

Synthesis of Boron-Nitrogen-Carbon (BNC) Hybrid Materials: From 2D Doped Polyphenylenes to 3D Porous Architectures

Francesco Fasano



Thesis submitted in accordance with the requirements for the
degree of Doctor of Philosophy

Prof. Davide Bonifazi

School of Chemistry
Cardiff University

December 2017

DECLARATION

This work has not been submitted in substance for any other degree or award at this or any other university or place of learning, nor is being submitted concurrently in candidature for any degree or other award.

Signed (Francesco Fasano) Date

STATEMENT 1

This thesis is being submitted in partial fulfilment of the requirements for the degree of PhD.

Signed (Francesco Fasano) Date

STATEMENT 2

This thesis is the result of my own independent work/investigation, except where otherwise stated, and the thesis has not been edited by a third party beyond what is permitted by Cardiff University's Policy on the Use of Third Party Editors by Research Degree Students. Other sources are acknowledged by explicit references. The views expressed are my own.

Signed (Francesco Fasano) Date

STATEMENT 3

I hereby give consent for my thesis, if accepted, to be available online in the University's Open Access repository and for inter-library loan, and for the title and summary to be made available to outside organisations.

Signed (Francesco Fasano) Date

STATEMENT 4: PREVIOUSLY APPROVED BAR ON ACCESS

I hereby give consent for my thesis, if accepted, to be available online in the University's Open Access repository and for inter-library loans **after expiry of a bar on access previously approved by the Academic Standards & Quality Committee.**

Signed (Francesco Fasano) Date

Acknowledgements

First and foremost, I would like to thank my supervisor *Prof. Davide Bonifazi*, for giving me the opportunity to pursue my doctoral studies in an international scientific environment. I will always be grateful for the enthusiasm that he transmitted me along these years in the challenging field of chemistry. Thank you for guiding me and for always being helpful and understanding through any ups and downs, both on personal and professional aspects.

Great thanks to *Dr. Timothy Easun* and *Prof. Steve Goldup* for accepting and being part of my doctoral commission. Thanks for the helpful comments and for spending your precious time in reading and correcting my thesis.

Of course, the work on the borazine 2D-MOCNs would not been realised without the collaboration of *Prof. Willi Auwärter*, *Martin Schwarz* and *Dr. Manuela Garnica*, from Technical University of Munich, Germany, who performed the Scanning Tunnelling Microscopy (STM) measurements and the data analysis.

Many thanks to *Dr. Nicola Demitri*, from the ELETTRA synchrotron in Trieste, Italy, for solving sometimes complicated crystal structures. Thank you for always being present to help me.

I am also thankful to *Dr. Robert Armstrong* for the time spent and the help provided.

Special thanks must also be given to *Maria, Lou* and *Rodolfo*, for the great support and help in the revision of this manuscript. Thank you guys for your patience!!!

I would like also to thank *Andrea F.* and *Tommaso* for the fruitful discussions regarding the photochemistry.

Numerous thanks to all the members of Bonifazi's group, past and present, who made this experience unbelievable. First of all, I want to express my gratitude to *Hamid, Jonathan, Francois K., Laurie-Elie, Silvia F., Irene, Andrey, Alex, Antoine, Nicolas, Oliwia, Olesia, Dmytro, Andre S., Deborah* and *Dong-Min Diem Lee*, it has been a great pleasure to work with all of you. Special thanks to the "Italian community": *Maria, Davide, Cataldo, Silvia R., Jacopo* and *Tanja*, along these years we have created a big family. Thank you for all the time that we spent together.

Un grazie davvero speciale va alla mia famiglia, sempre presente durante tutti questi anni nonostante anche le grandi difficoltà vissute. Grazie per aver supportato ogni mia scelta, non lo dimenticherò mai.

And last but not least, ringrazio *Francesca* per essermi sempre stata accanto, una presenza costante nella mia vita, un porto felice. Grazie per aver condiviso con me questa esperienza ogni singolo giorno, attraversando a volte momenti difficili ma spesso indimenticabili.

Thank you to everyone

Grazie a tutti

Francesco

Curriculum vitae

Francesco Fasano

61 Harriet Street, CF24 4BW Cardiff, UK
+44 7565487558 • fasanof@cardiff.ac.uk

Personal statement

I am highly motivated and professional organic synthetic chemist with extensive experience in organic synthesis and analysis of functional molecules, with an emphasis on the development of novel organic derivatives for material science applications. A highly organised and efficient person, whose accurate and precise approach to projects has yielded good results.

More in detail, working at the interface between organic and supramolecular chemistry, I had the opportunity to deal with the preparation of functional supramolecular materials, carbon-based nanostructure chemistry and synthesis and characterization of new highly emissive heteroatom-doped π -conjugated scaffolds.

Employment History

Ph.D. in Organic Chemistry – Cardiff University, United Kingdom (January 2014 – Present)

Main activities and responsibilities:

- Synthesis and characterization of polyphenylenes dendritic nanostructures doped with borazine scaffolds
- Synthesis and characterization of stable Metal Organic Frameworks and the evaluation of the gas storage properties
- Design, synthesis and characterization of borazine derivatives with emphasis in the self-assembly on metal surface
- Preparation of manuscripts for high impact journals
- Preparation of written reports to be presented in group meetings, project networks and conferences
- Co-supervision of undergraduate students
- Responsible of HPLC, GPC and elemental analysis

Research Collaborator in Organic Chemistry – University of Valencia, Spain

(July 2013 – December 2013)

Main activities and responsibilities:

- Conduct research independently based on the design and synthesis of Indole derivatives
- Prepare written reports to be presented in group meetings

Research Collaborator in Organic Chemistry – Synchimia s.r.l., Italy

(November 2010 – March 2011)

Main activities and responsibilities:

- Conduct research independently based on the design and synthesis of organic semiconductors for organic light emitted devices (OLEDs)
- Prepare written reports to be presented in group meetings

Scientific guide – Cittadella Mediterranea della Scienza

(September 2009 – June 2010)

Main activities and responsibilities:

- Guide of people with different backgrounds toward the chemistry and physics through the realization of small scientific laboratories.

Education

MSc in Chemical Science

Chemistry Department, University of Bari, Italy

Dissertation: “Synthesis of molecular semiconductors in organic optoelectronics”,
Supervisors: Prof. G.M. Farinola (University of Bari), Dr. O.H.Omar (University of Bari)

Mark: 110/110 with honor

(October 2009 – April 2013)

BSc in Chemical Science

Chemistry Department, University of Bari, Italy

Dissertation: “Synthesis of phosphorus heterocycles from aminobenzylnaphtol”,
Supervisors: Prof. F. Naso (University of Bari), Dr. C. Cardellicchio (University of Bari)

Mark: 110/110

(September 2005 – October 2009)

Key Skills

- Knowledge and competence in the field of organic chemistry: organic synthesis, microwaves synthesis.
- Experience in using different chromatography analytical techniques (GC, GPC, HPLC), thermal analysis (TGA, DSC), spectroscopy (NMR, UV-Vis, FT-IR, Fluorescence, Raman, XRD), spectrometry (GC-MS, MALDI, ESI-MS) and electron microscopy (SEM, TEM)
- Collaborative spirit and excellent ability to work both in a team and autonomously, good problem-solving skills, stress tolerance and ability to deal with conflicts and good ability to adapt to multicultural environments.
- Problem-solving attitude, good organizational capacity, excellent flexibility and fast learning, good presentation skills, high reliability and attention to details. Ability to motivation and dynamism. Good ability to manage projects and teams
- Excellent IT skills in a variety of programs including Microsoft Office (Word, Excel, PowerPoint), Scifinder Scholar, MestreNova, Mercury and Origin
- Native Italian
- Fluent in English and elementary Spanish
- Driving licence B category

List of Publications

Peer-reviewed Journal Articles (published and in preparation)

- 1) D. Bonifazi, **F. Fasano**, M. M. Lorenzo-Garcia, D. Marinelli, H. Oubaha, J. Tasseroul, 'Boron–Nitrogen Doped Carbon Scaffolding: Organic Chemistry, Self-Assembly and Materials Applications of Borazine and its Derivatives', *Chem. Comm.*, **2015**, 51, 15222.
- 2) J. Dosso, J. Tasseroul, **F. Fasano**, D. Marinelli, N. Biot, A. Fermi, D. Bonifazi, 'Synthesis and Optoelectronic Properties of Hexa- perihexabenzoborazinocoronene' *Angew. Chem. Int. Ed.* **2017**, 56, 4483.
- 3) D. Marinelli, **F. Fasano**, B. Najassari, N. Demitri, D. Bonifazi, 'Borazino-Doped Polyphenylenes' *J. Am. Chem. Soc.* **2017**, 139, 5503. (D. Marinelli and F. Fasano contributed equally).
- 4) M. Schwarz, M. Garnica, **F. Fasano**, J. V. Barth, N. Demitri, D. Bonifazi, W. Auwärter, 'BN-Patterning of Metallic Substrates through Metal Coordination of decoupled Borazines', *manuscript submitted*. (M. Schwarz, M. Garnica and F. Fasano contributed equally).

- 5) **F. Fasano**, F. Kerff, D. Reed, N. Dimitri, D. Book D. Bonifazi, `Synthesis of Borazine Organic Linker for Metal Organic Frameworks Applications, *manuscript in preparation*.
- 6) M. M. Lorenzo Garcia, N. Biot, **F. Fasano**, N. Dimitri, D. Bonifazi, `Substituent-Controlled Stereoselective Nucleophilic Aromatic Substitution Reaction of Borazines`, *manuscript in preparation*.

References

Prof. Davide Bonifazi - dbonifazi@cardiff.ac.uk

School of Chemistry, Cardiff University,
Main Building, Park place CF10 3AT Cardiff, United Kingdom

Prof. Alain Krief - alain.krief@unamur.be

Chemistry Department, University of Namur,
Rue de Bruxelles 61, 5000 Namur, Belgium

Prof. Gianluca Maria Farinola - gianlucamaria.farinola@uniba.it

Chemistry Department, University of Bari,
Via E. Orabona 4, 70125 Bari, Italy

Table of contents

Acknowledgements	I
Curriculum vitae	III
Abstract	VII
List of abbreviations	X

Chapter 1 - Introduction

1.1 Generalities	4
1.2 Synthesis of the borazine core	7
1.2.1 [1+1'+1+1'+1+1'] Hexamerisation <i>via</i> dehydrogenation reactions	8
1.2.2 [1+1'+1+1'+1+1'] Hexamerisation <i>via</i> condensation reactions	10
1.2.3 [2+2+2] Trimerisation reactions	11
1.3 Reactivity of the borazine core	15
1.3.1 Chemical stability and reactivity of B ₃ N ₃ core	15
1.3.2 Electrophilic addition reactions at the borazine core	16
1.3.3 Exchange reactions at the boron sites	17
1.4 Building an “outer shell”: peripheral functionalisation of the “inner shell”	20
1.5 Materials and applications	23
1.5.1 Materials for optoelectronic devices	24
1.5.2 Materials for gas storage	25
1.6 Outlines of the dissertation	27
1.7 References	28

Chapter 2 – BN-doped polyphenylenes

2.1 Research challenge: BN-doped graphene	35
2.2 Bottom-up synthetic approaches	38
2.3 Molecular design and divergent synthetic strategy	41

2.4 Aim of the project – borazine doped polyphenylenes	44
2.5 Results and discussion	47
2.5.1 Synthesis of borazine-derived ethynyl core modules	47
2.5.2 Synthesis of borazine-derived cyclopenta-2,4-dienone branching modules	50
2.5.3 Synthesis of carbon core modules	56
2.5.4 Synthesis of carbon branching module	58
2.5.5 Synthesis of three-branched borazine doped polyphenylenes	60
2.5.6 Synthesis of borazine monomeric references	71
2.5.7 Steady state UV-vis absorption and emission studies in solution	73
2.6 Conclusions and perspectives	81
2.7 References	83

Chapter 3 – Synthesis of borazine derivatives for metal organic frameworks applications

3.1 Boron-nitrogen (BN) materials for gas storage applications	87
3.2 Aim of the project	89
3.3 Results and discussion	90
3.3.1 Synthesis of three-carboxyl linkers	90
3.3.2 Synthesis and X-ray crystal structure of MOFs	99
3.3.3 Powder X-ray diffraction (PXRD)	108
3.3.4 Brunauer Emmett Teller (BET) surface area	111
3.3.5 Thermal stability	113
3.3.6 Synthesis of partially-protected borazine linker	115
3.4 Conclusions and perspectives	118
3.5 References	120

Chapter 4 – BN-patterning of metallic substrates through metal coordination of decoupled borazine

4.1 General overview on 2D molecular organic architectures on metal surfaces	124
---	------------

4.2 Aim of the project – borazine self-assembly on metal substrates	127
4.3 Results and discussion	131
4.3.1 Synthesis of three-pyridyl borazine modules	131
4.3.2 STM of three-pyridyl borazine modules	136
4.3.3 Self-assembly of three-pyridyl borazine 4-6 on Ag(100) surface	137
4.3.4 Self-assembly of three-pyridyl borazines on Cu(111) surface	139
4.4 Conclusions and perspectives	142
4.5 References	143

Chapter 5 – Experimental part

5.1 Instrumentations	146
5.2 Material and general methods	149
5.3 Experimental procedures	150
5.4 Life time measurements	191
5.5 X-ray data	192
5.6 References	203
Appendix A	204

Abstract

In the growing field of polycyclic aromatic hydrocarbons (PAHs), the replacement of carbon with isostructural atoms is becoming a versatile functionalisation strategy to tailor the optoelectronic properties of the materials. Among the different dopants, the substitution of C-C pairs by isoelectronic B-N covalent couples leads to isostructural molecular material bearing strong local dipole moments. This imparts a series of physical-chemical properties to the molecule, such as wider HOMO-LUMO gap, the introduction of anchoring points for gas storage and peculiar self-assembly behaviour on metal surfaces. The BN/CC isosterism concept goes back to the seminal discovery of the borazine ($\text{H}_3\text{B}_3\text{N}_3\text{H}_3$) by Stock and Pohland in 1926. Thus, in reference to its isoelectronic and isostructural relationship with benzene, borazine ring is commonly known as “inorganic benzene”. Hence, borazine and its derivatives are valuable molecular modules to be inserted as doping units in graphitic-based carbon materials to tailor their physical-chemical properties.

This dissertation focuses on the design, synthesis and characterisation of novel organic materials doped with borazine modules, with the aim of exploring the photophysics, electronics and self-assembly properties of hybrid boron-nitrogen-carbon (BNC) frameworks.

Before addressing the detailed investigations of this thesis work, in *Chapter I*, a brief introduction on the past and recent achievements in the organic synthesis of borazine and its derivatives are given to the reader. This chapter also includes the main synthetic methods used for their functionalisations, as well as their chemical properties and materials applications.

Chapter II addresses the design and synthesis of three-branched borazine doped polyphenylenes, in which one or more aryl units are replaced by borazine rings. Owing the possibility of functionalising the borazine ring with different groups on the aryl substituents at the *N* and *B* atoms, BNC polyphenylenes were prepared through the decarbonylative [4 + 2] Diels-Alder cycloaddition reaction. To achieve this, two types of molecular modules were synthesised: core and branching units. Therefore, having the possibility of introducing the borazine in different ratios, orientations and positions, three-branched hybrid

polyphenylenes featuring controlled orientation and dosages of the doping B_3N_3 -rings were prepared (Figure A.1).

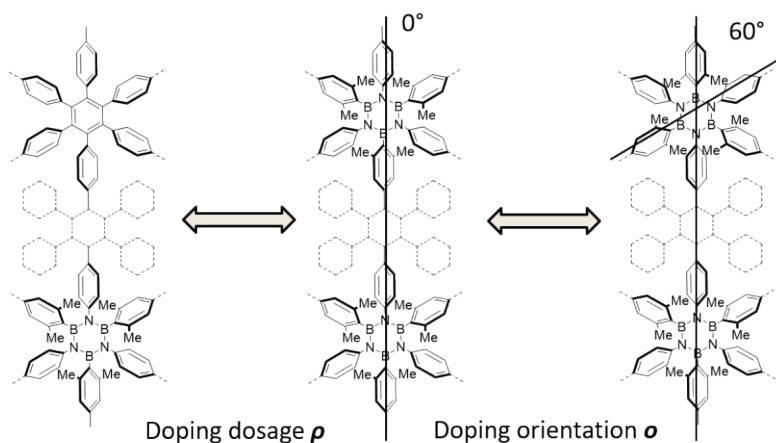


Figure A.1. Doping dosage and orientation of borazine in polyphenylenes frameworks.

At last, the photophysical properties of borazine-doped polyphenylenes have been investigated, describing the relation between the light emission properties and the orientation / dosage doping of these hybrid materials.

The second project tackled in this doctoral work is described in *Chapter III*. Inspiring by the local polar character of the borazine ring, B_3N_3 scaffold can theoretically interact with polar or polarisable gas molecules, thus making BN-materials promising candidates for tailoring the gas absorptions. In this chapter, the preparation of 3D BN metal organic framework (**BN-MOF**), composed by three-carboxyl borazine **3-1** as organic linker and $[Zn_4O(CO)_6]$ as metal cluster is described (Figure A.2). Additionally, to evaluate the effect of the BN doping units in gas storage, the isostructural 3D **C-MOF** reference, in which the borazine core is replaced by the benzene unit, has been prepared (Figure A.2). The last section of the chapter is dedicated to the description of the X-ray crystal structures of the MOFs as well as their morphology, surface area and thermal stability.

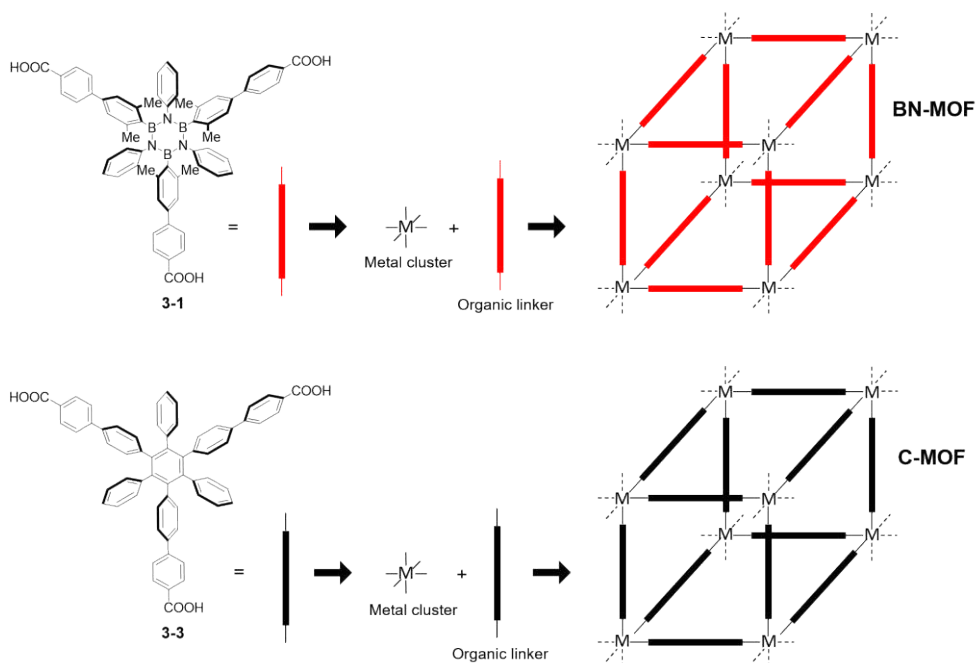


Figure A.2. Schematic illustration of the synthesis of 3D BN-MOF and C-MOF.

Finally, *Chapter IV* is dedicated to the investigation of three-pyridyl borazine derivatives, amenable to self-assemble and form 2D metal-organic porous network upon deposition on metal surfaces. The first part of the chapter deals with the synthesis of borazine **4-6** through a Suzuki cross-coupling reaction between borazine bearing three-OTf groups and an organoboron pyridyl moiety. The second part describes, by scanning tunnelling microscopy (STM), the tailoring of the 2D self-assembly of borazine **4-6** on Ag(100) and Cu(111) *via* coordination and thermal treatments. Specifically, densely packed honeycomb network on Ag(100) was observed, whereas interconnected chains were found on Cu(111). Upon deposition of additional Cu atoms at 420 K, a structural transformation can be induced on Cu(111), which leads to a fully three-fold coordinated triangular network (Figure A.3).

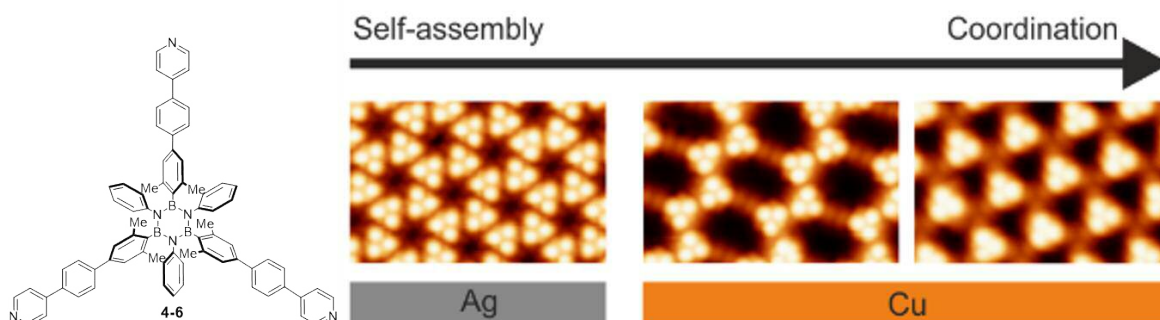


Figure A.3. 2D Self-assembly of three-pyridyl borazine **4-6** on Ag(100) and Cu(111).

List of Abbreviations

Å	Angstrom
Ar	Aryl
a.u.	Arbitrary unit
Abs.	Absorption
[A]	Concentration of molecule A
BET	Brunauer Emmett Teller
BIFs	Boron imidazolate frameworks
br	broad signal (NMR)
B.P.	Boiling point
Bu	Butyl
cal	Calories
CHX	Cyclohexane
COFs	Covalent organic frameworks
CPD	tetraphenylcyclopentadienone
CVD	Chemical vapour deposition
d	Doublet (NMR)
DMF	N,N-Dimethylformamide
DMSO	Dimethylsulfoxide
DTG	Derivative thermal gravimetric profile
Eg	Energy gap
Eq.	Equivalent
Em.	Emission
ESI	ESI Electrospray ionisation
EWG	Electron withdrawing group
FESEM	Field emission scanning electron microscopy
rec-GPC	Recycling gel permeation chromatography
h	Planck constant, hexagonal, hour
HOMO / LUMO	Highest occupied molecular orbital / Lowest occupied molecular orbital
rec-HPLC	Recycling high performance liquid chromatography
HR	High resolution

LR	Low resolution
IL	Ionic liquid
IR	Infra-red
k_f	Radiative rate constant
k_v	Vibrational rate constant
k_{ISC}	Intersystem-crossing rate constant
k_{CS}	Charge separated rate constant
LTSTM	Low temperature scanning tunnelling microscopy
m	Milli (10^{-3}), multiplet (NMR)
min	Minute
Mes	Mesityl (2,4,6-trimethylphenyl)
M.P.	Melting point
MALDI	Matrix-assisted laser desorption/ionisation
MD	Molecular dynamics
MS	Mass spectrometry
MOFs	Metal organic frameworks
NMP	N-methyl-pyrrolidone
NMR	Nuclear magnetic resonance
OTBDMS	O- <i>Tert</i> -butyldimethylsilyl
P	Pressure
P_0	Atmospheric pressure
PAHs	polycyclic aromatic hydrocarbons
Ph	Phenyl
Py	Pyridyl
P_{vol}	Pore volume
PXRD	Powder X-ray diffraction
r.t.	Room temperature
SA	Surface area
SEM	Scanning electron microscopy
STM	Scanning tunnelling microscopy
t	Time, <i>tert</i>
TBAF	tetrabutylammoniumfluoride
TGA	Thermal gravimetric analysis

THF	Tetrahydrofuran
TIPS	Triisopropylsilane
TLC	Thin layer chromatography
TMS	Trimethylsilane
TMSA	Trimethylsilylacetylene
ToF	Time of flight
UHV	Ultra high vacuum
vdW	van der Waals
ρ	Doping dosage, density
τ_f	Fluorescence life time
τ_{phos}	Phosphorescence life time

CHAPTER 1

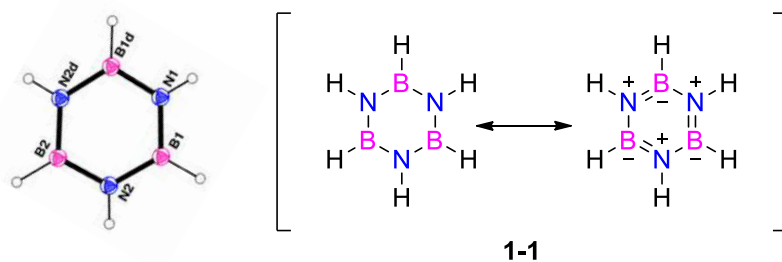
Introduction

The content described in this chapter has been published in the following article: Bonifazi D., **Fasano F.**, Lorenzo-Garcia M. M., Marinelli D., Oubaha H., Tasseroul J. *Chem. Comm.* **2015**, 51, 15222.

Borazines

1.1 Generalities

Borazine ($\text{H}_3\text{B}_3\text{N}_3\text{H}_3$, compound **1-1**, Scheme **1.1**), isolated by *Stock* and *Pohland* in 1926, is often named “inorganic benzene” due to its similarities with its carbon analogue, benzene. It is composed by three boron atoms and three nitrogen atoms in alternate positions in a six member ring. As benzene, borazine is liquid at room temperature, shows equalised bond lengths (1.40 Å for benzene, and 1.44 Å for borazine, with the latter being between B–N single bond at 1.51 Å and B–N double bond at 1.31 Å) and shares a planar hexagonal structure.¹⁻³



Scheme 1.1. Left: ORTEP representation of borazine **1-1**;⁴ right: resonance forms for borazine **1-1**.

Nevertheless, borazine shows only a weakly aromatic character,^{5,6} leading to a lower intrinsic stability that favour its hydrolysis to boric acid and ammonia in the presence of atmospheric moisture conditions. Another difference between borazine and benzene is the strong polar character of the B–N bonds with a dipole of 5.2 D and bond dissociation energy of $27.2 \text{ kcal mol}^{-1}$,⁷⁻⁹ resulting from the electron donation of the nitrogen atoms to the electrophilic boron centres. This strong polar character leads to a series of peculiar physical and structural properties to the $\text{H}_3\text{B}_3\text{N}_3\text{H}_3$. Specifically, a widening of the

HOMO-LUMO gap (6.2 eV compared to 6.0 eV for benzene) along with an increase of the HOMO energy level compared to benzene (ionization potentials measured by photoelectron spectroscopy as 10.1 eV for borazine, compared to 9.25 eV for benzene).^{10,11} This makes borazine a good UV emitter, showing a significantly blue shifted absorption spectrum in comparison with oligophenylenes.¹² Similarly, the change in the electron density of the nitrogen atoms dictates a peculiar reactivity of the borazine core that greatly differs from that of classical aromatic compounds.¹³

After a series of publications during the 1960's and 1970's, where borazine's fundamental structural, reactivity and electronic properties were firstly described,¹⁴⁻¹⁶ the interest toward borazine derivatives started only in the 1990's as precursors for boron nitride (BN) ceramics, in particular hexagonal boron nitride (h-BN), the insulating analogue of graphene.¹⁷⁻¹⁹ In 2005, the first investigations of borazine derivatives as active materials in optoelectronic devices started to appear.²⁰ Following the vigorous synthetic developments of polyaromatic hydrocarbons (PAHs),²¹ nanoribbons²²⁻²⁸ and graphene,²⁹⁻³¹ the substitution (*i.e.* doping) of sp^2 -carbon atoms with heteroatoms³²⁻³⁵ has been studied as one of the most versatile approaches to tune the optoelectronic properties of graphitic materials.

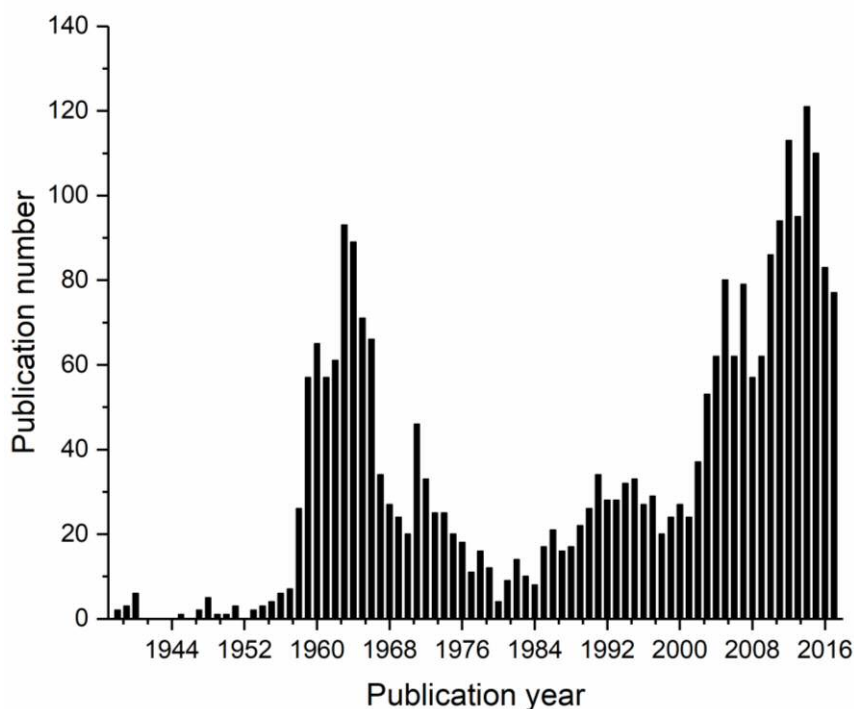


Figure 1.1. Histogram representation of publications about borazines and their derivatives, updated on the 9th of December 2017 (data taken from SciFinder).

This has prompted a deep research in the field, rediscovering the use of the isoelectronic and isostructural B-N couples as doping units to trigger the electronic properties^{36–41} of the all-*sp*²-carbon materials, leading to hybrids carbon-nitrogen-boron (CBN) monolayers.^{42–45} In particular, borazine derivatives and BN-doped PAHs (*e.g.*, azaborines,^{46,47} borazapyrene,^{48,49} borazaphenanthrene,^{50,51} borazanaphthalene^{52–56}) is now increasingly attracting the chemists attention in different applications such as: UV-emitting OLEDs, porous materials for gas storage, ceramics, coatings, and in supramolecular chemistry for engineering new functional frameworks both in solution and at interfaces. Figure 1.1 summarises the evolution of the yearly publication regarding borazine and its derivatives (sourced from SciFinder).

The aim of this chapter is to give a general overview about the synthesis, organic reactivity and material applications of borazine and its derivatives.⁵⁷ In particular, through a detailed description of the most significant examples coming from our group and others, it will be showed that, despite the intrinsic sensitivity of the borazine core towards hydrolysis, borazine derivatives can be rationally functionalised through a large variety of organic reactions (*e.g.*, metal-catalysed cross-coupling, nucleophilic addition and/or substitutions, photocyclisation, thermal dehydrogenation, electrophilic substitutions) and it can be compatible with commonly used organic transformations employed in the chemistry of protecting groups (*e.g.*, hydrogenation, fluoride, weak bases, metal-based reductions, hydrides, thermal cleavages to name a few). This lead to the preparation of different scaffolds that have expanded the spectrum of different applications where borazine derivatives can be exploited. To describe the different substitution patterns around the borazine core, the nomenclature depicted in Figure 1.2 will be used throughout this thesis. Being the central core of the molecule composed by substituted B₃N₃ motif, each nitrogen and boron atom can bear different functional groups that, depending on their chemical nature, can form an ‘inner’ and an ‘outer shell’, with the latter decorating the peripheral rim of the molecule.

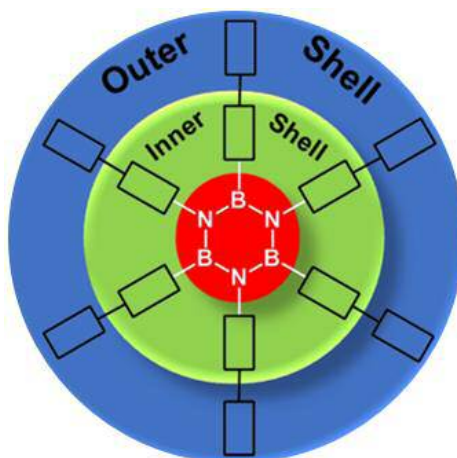


Figure 1.2. General representation of a borazine derivative, displaying the different substitution regions along with the labelling, as will be used in this manuscript.

1.2 Synthesis of the borazine core

As shown in Figure 1.3, the borazine core can be synthesised following two cyclisation approaches:

- $[1+1'+1+1'+1+1']$ hexamerisation route from a mixture of the selected borane (*i.e.*, hydro or halide) and amine precursors.
- $[2+2+2]$ trimerisation strategy using a pre-formed imino or aminoborane derivative.

Depending on the chemical nature of the borane, different reactions have been used: thermal or metal-catalysed dehydrogenation with boron hydrides and condensation reactions with BX_3 .

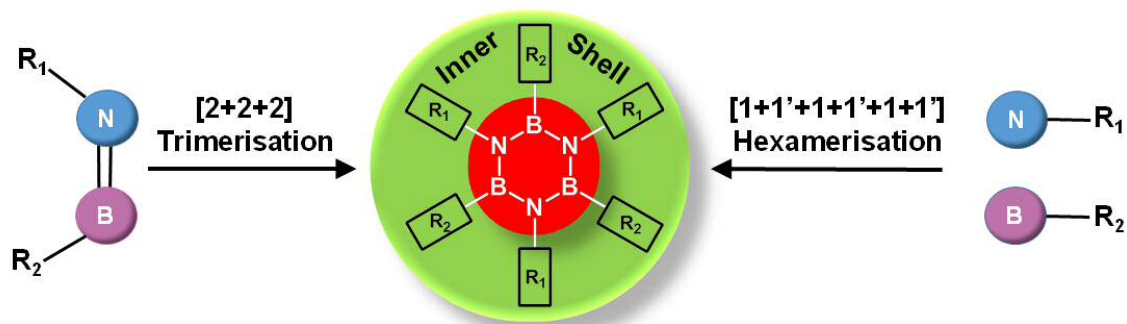
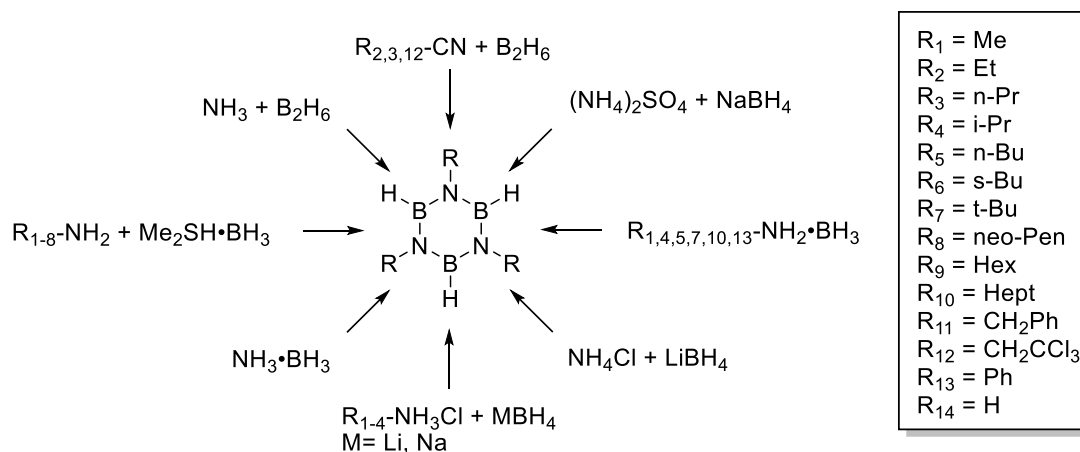


Figure 1.3. Synthetic strategies toward the synthesis of the borazine core, with $R_1 = R_2$ or $R_1 \neq R_2$ being an aryl, alkyl or hydrogen substituent.

1.2.1 [1+1'+1+1'+1+1'] Hexamerisation *via* dehydrogenation reactions

Thermal dehydrogenation of ammonia-borane complexes, firstly described by Stock and Pohland, was the first method used in order to prepare borazine **1-1** ($\text{H}_3\text{B}_3\text{N}_3\text{H}_3$).¹ The reaction consists of the formation of a $\text{NH}_3\cdot\text{BH}_3$ adduct that, upon thermal dehydrogenation at 200 °C, undergoes formation of $\text{H}_3\text{B}_3\text{N}_3\text{H}_3$. Following this method, other procedures were further developed (Scheme 1.2), which employed higher pressure (11 atm),⁵⁸ lower temperatures (140-160 °C),^{59,60} and different precursors as mixtures of NH_4Cl and LiBH_4 ⁶¹ or $(\text{NH}_4)_2\text{SO}_4$ and NaBH_4 .⁵⁵



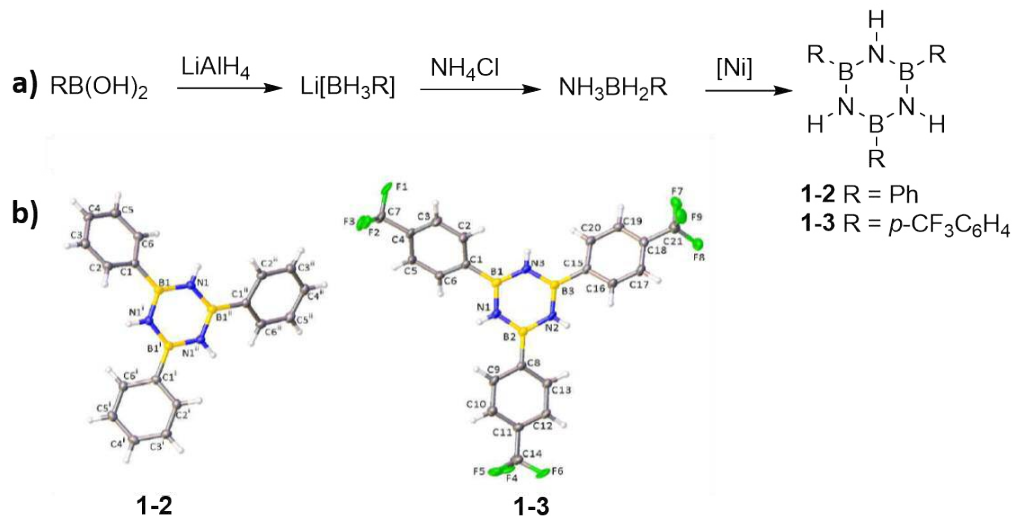
Scheme 1.2. Different protocols and precursors used for the thermal dehydrogenation of amino-borane complexes.

Analogously, both *N*-substituted alkyl- and aryl-borazines can be also synthesised (Scheme 1.2). For instance, *t*- $\text{BuNH}_2\cdot\text{BH}_3$ adduct in a sealed tube at 360 °C for 5 h gives tri-*N-tert*-butylborazine ($\text{H}_3\text{B}_3\text{N}_3t\text{-Bu}_3$) in nearly quantitative yield,⁶² as well as aromatic amino-borane adducts lead to tri-*N*-arylborazines.⁶⁰ Notably, tri-*N*-methylcyclotriborazine ($\text{H}_3\text{B}_3\text{N}_3\text{H}_3\text{Me}_3$) could be selectively obtained from $\text{MeNH}_2\cdot\text{BH}_3$ at 120 °C, and further converted into the corresponding tri-*N*-methylborazine ($\text{H}_3\text{B}_3\text{N}_3\text{Me}_3$) at 200 °C.⁶⁰ In a similar avenue, alkylammonium chlorides were used to prepare tri-*N*-ethyl-, tri-*N*-propyl-, and tri-*N*-isopropylborazine in high yields (94%, 92%, and 84%, respectively).^{63,64} Nitriles precursors were also found to be a valid alternative to amines.¹⁵ For instance, tri-*N*-methyl, tri-*N*-ethyl, and *N*-(2,2,2-trichloroethyl)borazine were synthesised in 50-60% yield, heating at 85 °C in dimethoxyethane of the corresponding alkylnitriles and B_2H_6 .^{15,65} Remarkably, the nitrile-borane adducts decomposed at room temperature in few days to give *N*-alkylborazines with comparable yields.

Miyaura and co-workers, proposed $\text{Me}_2\text{S}\cdot\text{BH}_3$ as boron source for the formation of borazines.⁶⁶ Several alkylamines were used to form borane adducts in solution that, after evaporation and heating at 120 °C, were transformed into a mixture of *N*-alkylcycloborazanes ($\text{H}_6\text{B}_3\text{N}_3\text{H}_3\text{Alk}_3$) and *N*-alkylborazines ($\text{H}_3\text{B}_3\text{N}_3\text{Alk}_3$). By further elimination of H_2 at 200 °C, *N*-alkylcycloborazanes were converted into the corresponding *N*-alkylborazines with yields between 73-85%, with the dehydrogenation rates depending on the steric demand of the *N*-substituents. *In situ* preparation protocols of the borane derivatives, e.g. $\text{MeNH}_2\cdot\text{BH}_3$ from NaBH_4 in the presence of $\text{BF}_3\cdot\text{Et}_2\text{O}$ and MeNH_2 in THF, also quantitatively yielded the corresponding methylborazine.⁶⁶

In the last years, metal-catalysed reaction pathways have also been designed for preparing borazine by dehydrogenation reaction. Manners and co-workers synthesised borazines from $\text{NH}_3\cdot\text{BH}_3$ or $\text{CH}_3\text{NH}_2\cdot\text{BH}_3$ at 45 °C, using $[\text{Rh}(1,5\text{-cod})(\mu\text{-Cl})_2]$ as catalyst.⁶⁷ Kinetic studies showed that the rate-determining step for both substrates is the loss of the last H_2 molecule, which has been demonstrated to be fast only at high temperature.⁶⁰ Tri-*N*-phenylborazine ($\text{H}_3\text{B}_3\text{N}_3\text{Ph}_3$) could be prepared from $\text{PhNH}_2\cdot\text{BH}_3$ in 56% yield after 16 h at 25 °C with the same rhodium complex. The higher tendency towards dehydrogenation of the tri-*N*-phenylcycloborazane compared to the tris-*N*-methyl and to the all-hydrogen analogues is rationalised by the steric hindrance of the *N*-substituents. In other words, the greater the steric hindrance is, the faster the dehydrogenation reaction occurs. Several Cr, Mo, and W complexes were studied as catalysts, with the Cr^{IV} complexes displaying the highest dehydrogenation activities with $\text{NH}_3\cdot\text{BH}_3$ or *t*- $\text{BuNH}_2\cdot\text{BH}_3$.⁶⁸ Cr^0 , Mo^0 , W^0 have been used as hexacarbonyl complexes for the synthesis of *N*-alkylborazines from alkylamine-borane adduct.⁶⁸ The catalyst and the boron-nitrogen precursors were initially dissolved in benzene and irradiated for 8 h with a Hg lamp, then left in the dark at room temperature for 24 h. The best results were obtained using Cr^0 complexes.⁶⁹ $\text{MeNH}_2\cdot\text{BH}_3$ and $\text{EtNH}_2\cdot\text{BH}_3$ gave comparable transformations in very high yields, whereas *t*- $\text{BuNH}_2\cdot\text{BH}_3$ yielded tri-*N*-*tert*-butylborazine in low yield. Moderate dehydrogenation yields (53%) were also achieved using nickel nanoparticles as catalysts in tetraglyme at 80 °C.^{70,71} Lewis acid can also catalysed dehydrogenation reaction leading to the formation of borazine.⁷² Reacting $(\text{NH}_4)_2\text{SO}_4$ with NaBH_4 in tetraglyme in the presence of a catalytic amount of AlCl_3 , borazine **1-1** was formed in 67% yield (purified by distillation), while in the absence of the catalyst only 30% yield was obtained. In contrast to the case of (*N*-

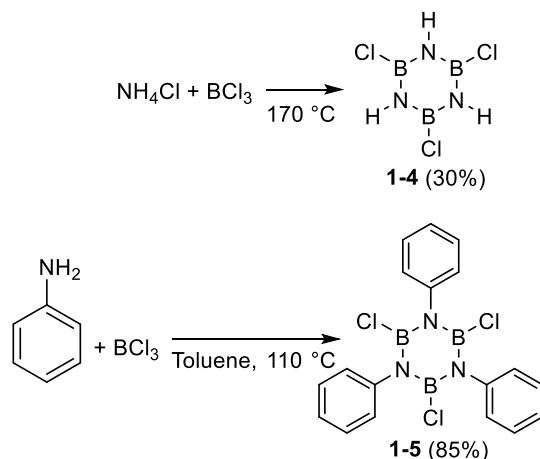
aryl)amino-boranes, the dehydrocoupling of the *B*-aryl analogues was relatively unexplored. In 2017, Manners and co-workers reported the catalytic dehydrogenation of *B*-aryl aminoborane.⁷³ Borazine **1-2** and **1-3** were obtained by heating the *B*-aryl amino-boranes in THF at 70 °C in the presence of skeletal nickel. The *B*-aryl amino-borane were synthesized by dehydrogenative salt metathesis of Li[BH₃R] and NH₄Cl (Scheme 1.3). The chemical structure identities of borazines **1-2** and **1-3** were unambiguously confirmed by X-ray diffraction analysis.



Scheme 1.3. a) Synthesis of borazine **1-2** and **1-3**; b) X-ray crystal structures of borazine **1-2** and **1-3**.⁷³

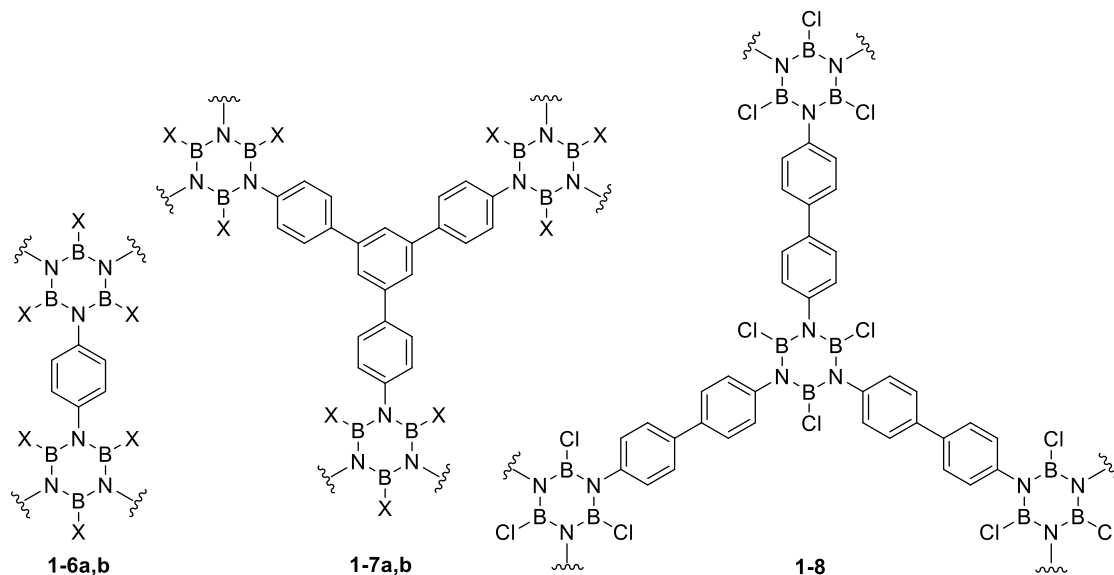
1.2.2 [1+1'+1+1'+1+1'] Hexamerisation *via* condensation reactions

In 1955, Brown and Laubencayer designed a new methodology for the synthesis of cyclic condensed boron-nitrogen systems, using boron halides (BX₃) as precursors. Reacting BCl₃ with NH₄Cl at 170 °C, tri-*B*-chloro-borazine **1-4** (Scheme 1.4) could be synthesised in 30% yield⁷⁴ and the chemical structure was confirmed by X-ray diffraction. Similarly, *B,B',B''*-trichloro-*N,N',N''*-tri(phenyl)borazine **1-5** can be prepared from BCl₃ and aniline in anhydrous toluene heating under reflux.⁷⁵ As shown in sections 1.3.3 and 1.4, trichloroborazines are versatile substrates for further functionalisation at the boron sites by nucleophilic substitution reactions.



Scheme 1.4. Synthesis of borazine derivatives **1-4** and **1-5**.

Besides aniline, different aryl derivatives functionalised with di and tri-amino groups have been used to prepare a large number of *N*-substituted borazines polymers (Scheme 1.5). El-Kaderi and co-workers show that by reacting *para*-phenylenediamine,^{76,77} 1-3-5-tris-(4-aminophenyl)benzene,⁷⁷ or 4,4'-diammino-biphenyl⁷⁸ with BCl_3 or BBr_3 , different covalent organic frameworks (**1-6**, **1-7**, and **1-8**) could be obtained for gas storage applications (see also *Section 1.5*).



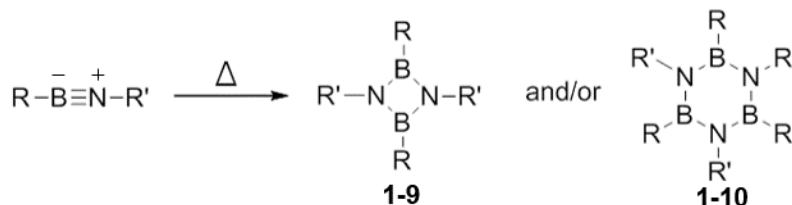
Scheme 1.5. Linear and branched borazine-linked polymers prepared with di, tri-amino aryl derivatives.⁷⁶⁻⁷⁸ **1-6a** X = Cl, **1-6b** X = Br, **1-7a** X = Cl, **1-7b** X = Br.

1.2.3 [2+2+2] Trimerisation reaction

As alternative to the hexamerisation approach, borazine can be prepared by trimerisation reaction of boron-nitrogen precursors. This pathway was firstly proposed by Paetzold and

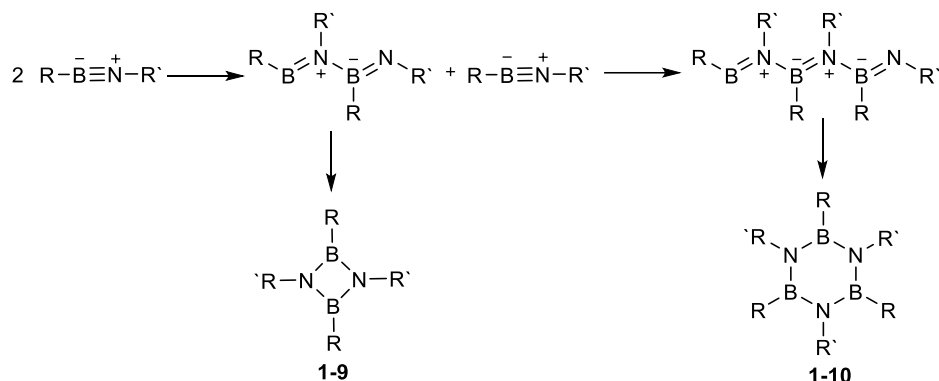
co-workers.⁷⁹ Starting from dialkyliminoboranes ($R-B=N-R'$), four and six-member rings can be formed through a cyclodimerisation or trimerisation reaction. In the presence of sterically hindered alkyl groups (*i.e.* $R = R' = \textit{tert}$ -butyl and $R = \textit{tert}$ -butyl, $R' = \text{Ph}$) the formation of four membered rings (**1-9**) were observed, otherwise six membered rings (borazines **1-10**) were obtained (*i.e.* $R = R' = \text{Me}$) (Table 1.1).⁷⁹

Table 1.1. Products obtained from the thermal cyclisation of $RB=NR'$.⁷⁹



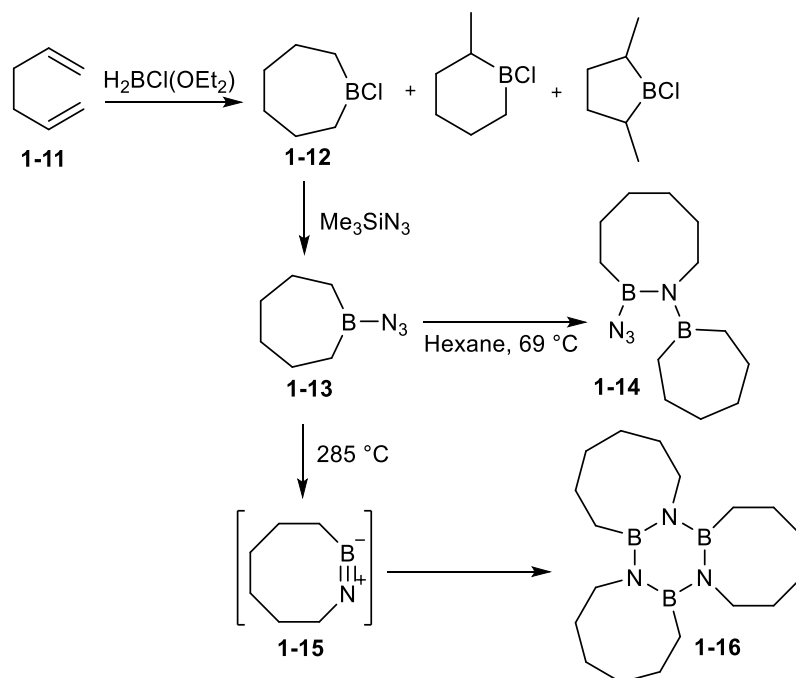
Entry	R/R'	Product	Entry	R/R'	Product
1	^t Bu/ ^t Bu	1-9	4	Me/Me	1-10
2	^t Bu/Ph	1-9	5	^t Bu/Et	1-10
3	sec-Bu/sec-Bu	1-9 and 1-10	6	ⁱ Pr/ ⁱ Pr	1-10

Depending on the alkyl groups, the synthesis of compound **1-9** and borazine **1-10** was described assuming the formation of a linear BN adduct structure as depicted in Scheme 1.6. Such adducts, can either be closed to four-member ring cycle **1-9** or can react with another molecule of iminoborane to give the formation of BN open chain trimers. At this stage, the ring closure can take place allowing the formation of borazine derivatives **1-10** as final product.



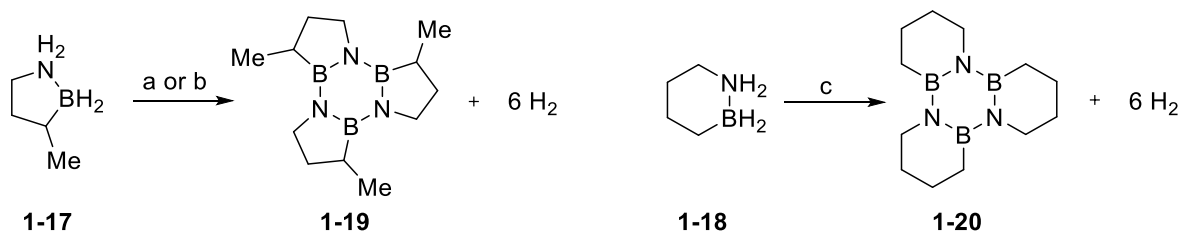
Scheme 1.6. Formation of BN four-member ring cycle **1-9** and borazine derivative **1-10** via thermic cyclomerisation reaction.

In 2004, the synthesis of four or six BN membered rings was obtained using cyclic iminoboranes as precursors.⁸⁰ Starting from hydroboration of 1,5-hexadiene **1-11**, chloroborane derivatives has been synthesised. Main product **1-12** can be separated from the other constitutional isomers thanks to ring-opening polymerisation at 20-80 °C. Afterwards, the polymeric form gives pure compound **1-12** upon depolymerisation at 160 °C. The azidation of **1-12** gives monomeric **1-13**, that yields **1-14** in refluxing hexane conditions. Conversely, in gas phase at 285 °C, the thermolysis reaction of azide derivative **1-13** allows the intramolecular rearrangement leading the formation of **1-15** which finally undergoes to cyclotrimerisation reaction, yielding borazine **1-16** as final product in 48% (Scheme 1.7).



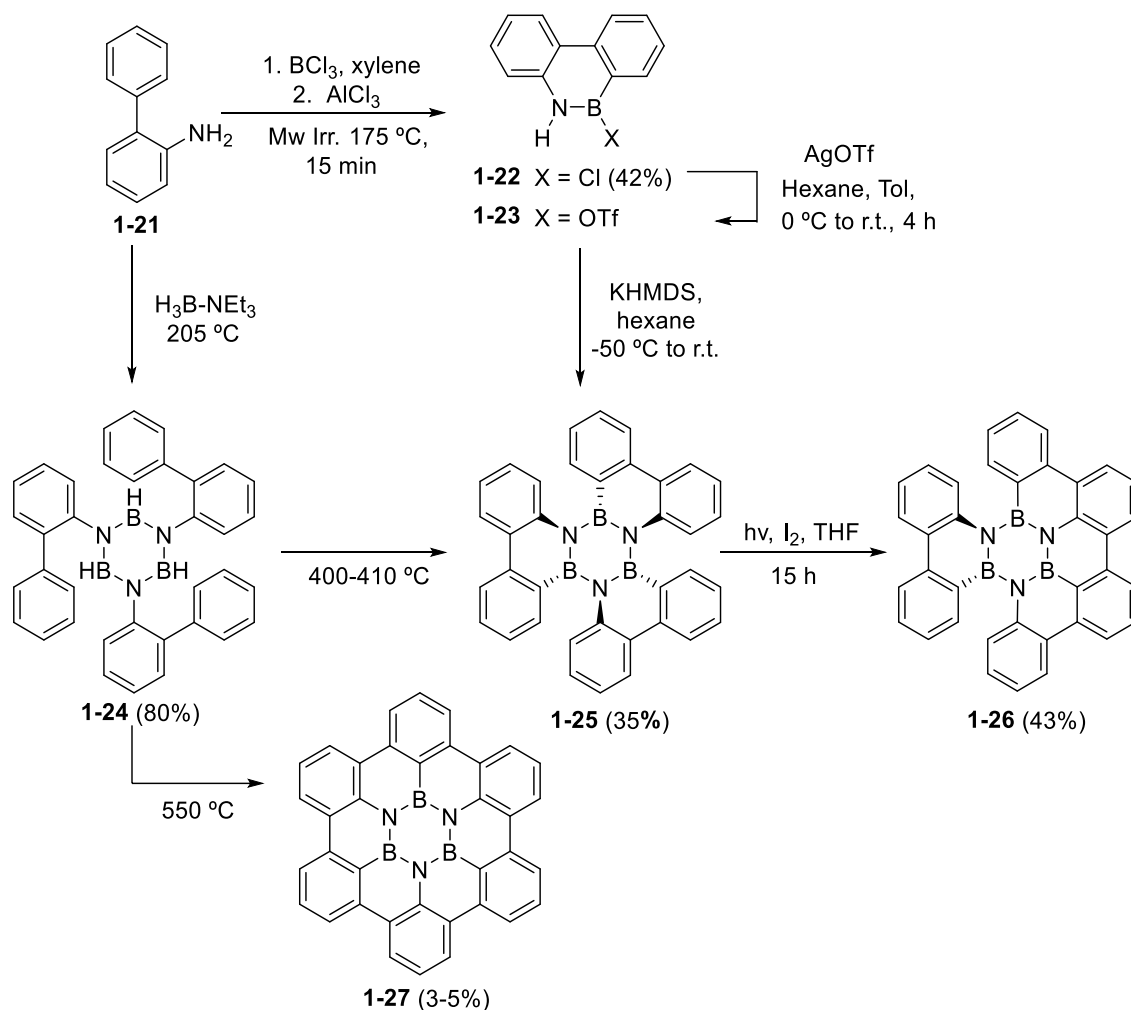
Scheme 1.7. Formation of borazine **1-16** via cyclic iminoboranes in the gas phase.⁸⁰

Alternatively, Liu and co-workers were able to prepare borazines **1-19** and **1-20** (Scheme 1.8) in quantitative yields via thermal or catalytic dehydrogenation reaction starting from aminoboranes 1,2-BN-cyclopentane⁷¹ **1-17** and 1,2-BN-cyclohexane⁸¹ **1-18**, respectively. This chemical reaction allowed a controlled release of H₂ at low temperatures or at the proton exchange membrane fuel cell waste-heat temperature of 80 °C. The reaction conditions are such that this chemical process can be considered as a suitable candidate for liquid-phase H₂ storage materials.



Scheme 1.8. Formation of borazine derivatives **1-19** and **1-20** by trimerisation from cyclic amino-boranes.^{71,81} a) FeCl₂ (5 mol%), 80 °C, 20 min, quant.; b) 150 °C, 1 h, 98%; c) toluene, 150 °C, 1 h, quant.

In 2012, Bettinger and co-workers developed a trimerisation procedure to prepare borazine **1-25**, in which three 9,10-BN-phenanthrene moieties are linked through a borazine core (Scheme 1.9).



Scheme 1.9. Formation of borazines **1-24** and **1-25**.^{82,83}

In a first venue, 2-aminobiphenyl **1-21** was reacting with BCl₃ in the presence of AlCl₃, yielding intermediate **1-22** in 42% yield.⁸² Either through direct transformation of **1-22** or

via triflate derivative **1-23**, base-induced elimination gave borazine **1-25** through cyclotrimerisation reactions.⁸² Further irradiation of **1-25** under Hg lamp in the presence of I₂ afforded borazine **1-26** in 43% yield (Scheme 1.9).⁸³ Alternatively, cyclotrimer **1-25** could be also obtained by the thermolysis of borazine **1-24**, which was obtained from 2-aminophenyl **1-21** in the presence of Et₃N·BH₃ at 205 °C. Recently, the same group, has reported the formation of an unprecedented borazinocoronene derivative **1-27** (yield 3-5%) through pyrolysis at 550 °C of **1-24**.⁸⁴

1.3 Reactivity of the borazine core

1.3.1 Chemical stability and reactivity of the B₃N₃ core

Borazine derivatives are known to be very reactive towards nucleophiles, which undergo addition to the electrophilic boron atoms favouring the opening of the cycle and inducing the degradation of the borazine cycle. This usually gives a mixture of the corresponding amine and boronic/boric acid precursors. For instance, borazine **1-1** (H₃B₃N₃H₃) rapidly decomposes to boric acid, ammonia and H₂ in the presence of ambient humidity. This has been one of the major limits toward the synthetic development of BN-doped aromatic hydrocarbons and their exploitation in material science. To avoid the hydrolytic decomposition of borazines, two main approaches have been developed: *i*) insertion of bulky substituents in proximity to the boron centres, and *ii*) introduction of electron-donating substituents on the nitrogen centres. The presence of sterically-hindered substituents at the nitrogen⁸⁵ or boron atoms⁸⁶ disfavour the hydrolysis, with 2,6-xylyl,¹⁶ 2-mesityl,⁸⁶ and 9-anthryl⁸⁷ groups displaying the greatest effect. X-ray crystal structure analyses of these compounds clearly show that the boron atoms are sterically protected by the *ortho*-substituents (Figure 1.4). On the other hand, the presence of electron-donating groups on the nitrogen centres increases the aromatic character of the BN core by allowing a better electron delocalisation from the nitrogen to the boron atoms, thus strengthening the B-N double bond character.⁸⁸ This in turn increases the chemical stability toward hydrolysis, and more in general decreases the reactivity toward any nucleophile addition.^{85,89} The opposite is true for electron-withdrawing substituents on the boron atoms, which also enhance the chemical stability of the borazine ring.⁹⁰

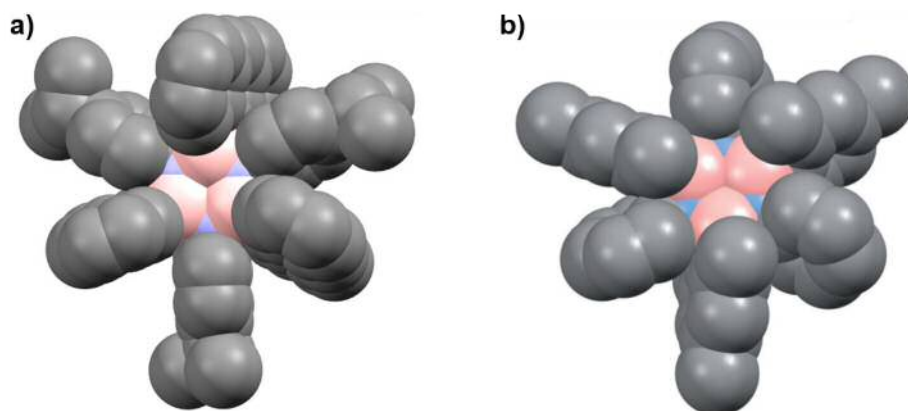
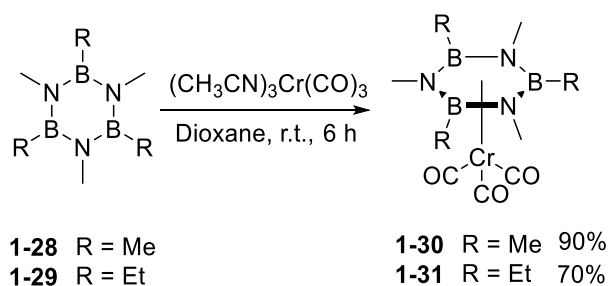


Figure 1.4. Space-filling representation of the crystal structure of a) tri-B-anthryl-tri-N-(4-isopropylphenyl)-borazine and b) tri-B-mesityl-tri-N-phenyl-borazine indicating the steric hindrance around the boron centres. Colour code: grey: C, pink: B, blue: N.

The weakly aromatic borazine ring is also able to complex metals, forming half-sandwiched “piano-stool” complexes with Cr^0 (Scheme 1.10).⁹¹ Hexa-alkylborazines form $\text{R}_3\text{B}_3\text{N}_3\text{R}_3 \cdot \text{Cr}(\text{CO})_3$ at room temperature, which can be crystallised and characterised as η^6 complexes.⁹² However, the weak interaction holding the borazine core to the metal can lead to the protodeborylation of the phenyl substituents at the *B* sites, decomposing the borazine core and yielding $\text{C}_6\text{H}_6 \cdot \text{Cr}(\text{CO})_3$ as the main product.⁹³ Complexation with Li is also possible, giving rise to multiple binding motifs (η^1 , η^2 or η^3 complexes) depending on the reagents and equivalents used.⁹⁴

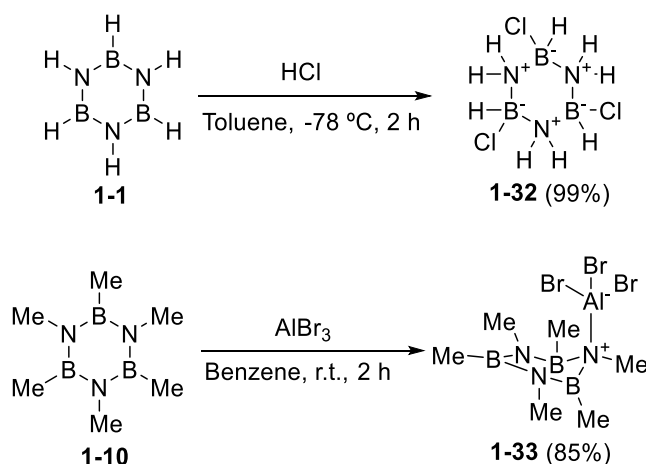


Scheme 1.10. Formation of borazine-chromium complexes **1-30** and **1-31**.⁹²

1.3.2 Electrophilic addition reactions at the borazine core

Borazine rings easily undergo addition of hydric acids, such as HCl and HBr at $-78\text{ }^\circ\text{C}$, obtaining molecular derivatives featuring a broken aromaticity and thus a non-planar conformation of the central ring.^{95–97} The reaction takes place on each B-N bond, breaking the partial double bond character, ultimately forcing the borazine core to adopt a chair-like conformation. For example, the addition of HCl to $\text{H}_3\text{B}_3\text{N}_3\text{H}_3$ **1-1** at low temperature in

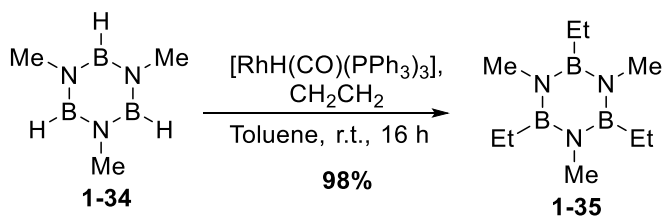
the absence of water, forms adduct $\text{H}_3\text{B}_3\text{N}_3\text{H}_3 \cdot 3\text{HX}$ **1-32** in quantitative yield (Scheme 1.11). Heating at 130 °C, *ate*-complex **1-32** dissociates in $\text{H}_3\text{B}_3\text{N}_3\text{H}_3$ **1-1** and HCl, thus favouring the formation of the weakly aromatic borazine core. The separation of the monoprotonated borazinium ion $\text{H}_3\text{B}_3\text{N}_3\text{H}_4^+$ proved to be very difficult with direct HX addition, but it could be achieved in the presence of Lewis acids. For instance, non-planar borazinium ion **1-33** could be prepared upon addition of AlBr_3 to borazine **1-10** (Scheme 1.11).^{98,99} Theoretical modelling investigations have been also evaluated to study the reactivity of the borazine core toward electrophilic substitution reactions and to explore the aromatic properties of the BN.⁵ Although the results did not show any magnetic anisotropy, the resonance stabilisation (9.6 kcal/mol for $\text{H}_3\text{B}_3\text{N}_3\text{H}_3$ **1-1**, compared to 21.9 kcal/mol for benzene)⁵ suggest that the borazine core is weakly aromatic, thus displaying a similar chemical behaviour to that of benzene.¹⁰⁰



Scheme 1.11. Electrophilic addition of HCl to borazine **1-1**⁹⁸ and AlBr_3 to borazine **1-10**.

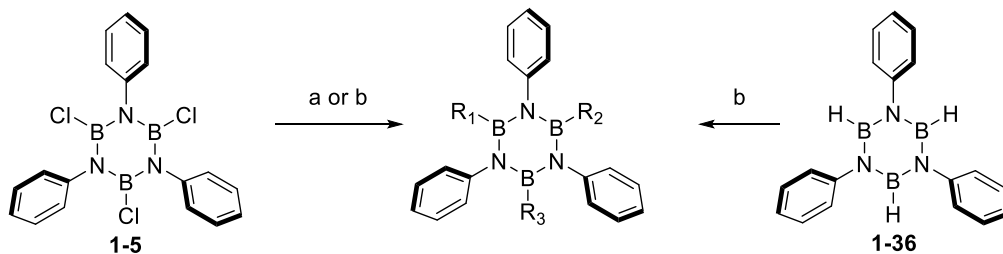
1.3.3 Exchange reactions at the boron sites

T. Schaeffer *et al.* reported the first halogenation exchange reactions at the boron sites of the borazine ring. This work revisited later by Niedenzu *et al.* who prepared at room temperature *B*-mono and *B*-dihalogeno borazines in moderate yields (25-35%) by reacting molecule **1-1** with BCl_3 and BBr_3 .^{59,101} Alternatively, halogenation with HCl, HBr,¹⁴ or with Br_2 ,¹⁰² also affords *B*-substituted mono-, di- and tri-haloborazines. In addition, $\text{H}_3\text{B}_3\text{N}_3\text{E}_3$ derivatives can be functionalised by hydroboration of alkenes using a rhodium catalyst,⁶⁶ allowing the isolation of mono-, bi- and tri-*B*-alkylborazine derivatives in 70-98% yield (Scheme 1.12).



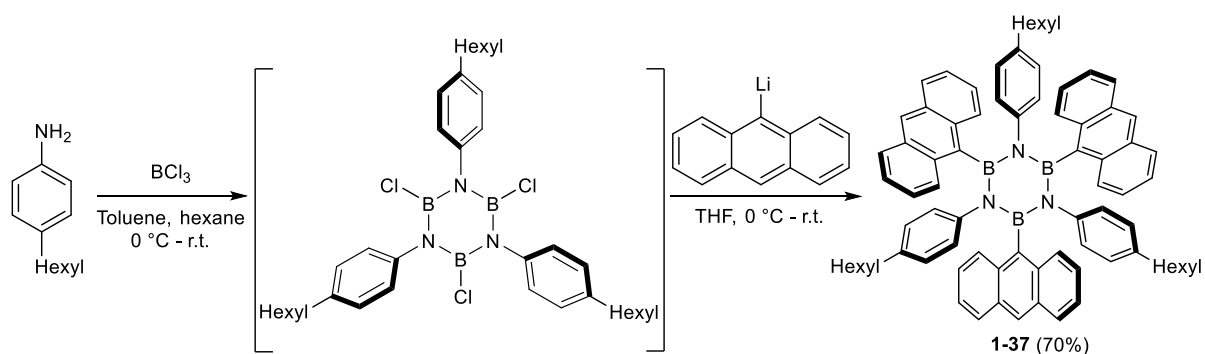
Scheme 1.12. Hydroboration of ethylene by $\text{H}_3\text{B}_3\text{N}_3\text{Me}_3$ **1-34**, catalysed by a Rh complex.⁶⁶

However, the most common synthetic approach to functionalise a borazine core is based on the substitution reaction at the boron site with *organolithium* or *organomagnesium* reagents. Since the reports of Groszos and Stafiej in 1958,¹⁰³ the alkylation or arylation of hydroborazines with RLi/ArLi or $\text{RMgBr}/\text{ArMgBr}$ has become one of the most versatile approaches to add substituents on the borazine core. In particular, following the BCl_3 -based synthetic methodology, for which a tri-*B*-chloroborazine intermediate is formed in the presence of an amine, substituents at the boron centres can be added through substitution reactions upon addition of the relevant organometallic species. For example, tri-*B*-chloroborazine **1-5** undergoes substitution reactions in the presence of an alkyl- or aryl Grignard or *organolithium* reagent into *B*-alkyl or *B*-aryl substituted derivatives (Scheme 1.13). Depending on the stoichiometry and the addition sequence, different *B*-substituted derivatives, *i.e.*, A_3 -, A_2C -, or ACD -, could be obtained. Alternatively, borazine **1-36** can be also used as effective substrates to give *B*-alkyl derivatives in the presence of a Grignard reagent.^{86,87,103–107}



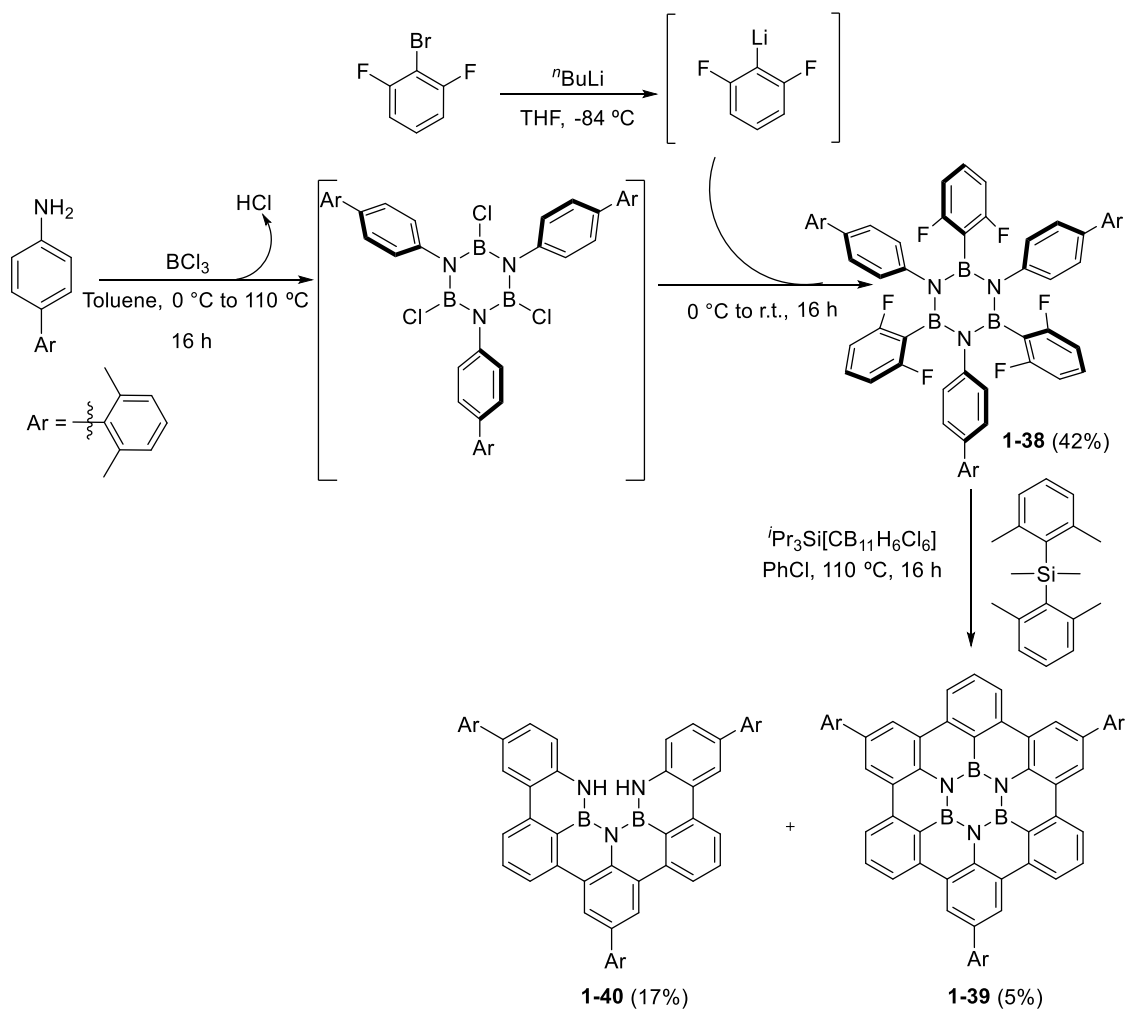
Scheme 1.13. Synthetic approaches toward the preparation of *B*-substituted borazines using organometallic reagents. a) Sequential additions of R_1Li , R_2Li , R_3Li in THF; b) Sequential additions of R_1MgBr , R_2MgBr , R_3MgBr in Et_2O . $\text{R}_1 = \text{R}_2 = \text{R}_3$, $\text{R}_1 = \text{R}_2 \neq \text{R}_3$, or $\text{R}_1 \neq \text{R}_2 \neq \text{R}_3$.

Following this synthetic strategy, Yamaguchi and co-workers reported in 2005 the synthesis of tri-*B*-anthryl-tri-*N*-(4-isopropylphenyl)-borazine derivatives **1-37** (Scheme 1.14).⁸⁷ BCl_3 was reacted with 4-hexyl-aniline producing the corresponding *B*,*B'*,*B''*-trichloro-*N*,*N'*,*N''*-triarylborazines, which was subsequently treated with 9-anthryllithium, affording trianthrylborazine **1-37** bearing the alkyl chain at the *N* atoms in 70% yield.



Scheme 1.14. Synthetic of tri-B-anthryl-tri-N-(4-isopropylphenyl)-borazine derivatives **1-37**.⁸⁷

More recently, our group has recently presented the first rational synthesis of BN-doped coronene derivative **1-39**. Hexafluoro borazine **1-38** was obtained after reaction of 4-xylyl aniline with BCl_3 upon subsequent addition of difluoro-ArLi (Scheme **1.15**).



Scheme 1.15. Synthetic path for preparing BN-doped coronene derivative **1-39**.¹⁰⁸

Capitalising on the Friedel–Crafts ring-closure reaction of fluoroarenes developed by Siegel and co-workers,¹⁰⁹ borazine **1-38** could be planarised into **1-39** (5% yield, 61% per C–C bond formation) in the presence of $[\text{iPr}_3\text{Si}\cdots\text{CB}_{11}\text{H}_6\text{Cl}_6]$ and $\text{Me}_2\text{SiMes}_2$ at 110 °C in PhCl. Together with BN-doped coronene **1-39**, partially fused BN-derivative **1-40** was obtained as major product (17% yield), suggesting that the ring closure proceeds stepwise with the last aryl fusion likely being the rate-determining step.

1.4 Building an ‘outer shell’: peripheral functionalisation of the ‘Inner Shell’

In this *section* different synthetic strategies undertaken to functionalise the ‘outer shell’ of substituted borazines by functionalisation of the ‘inner shell’ are described (Figure 1.5).

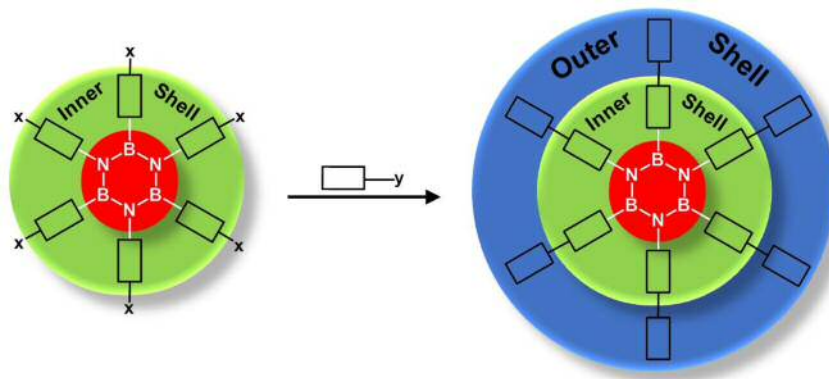
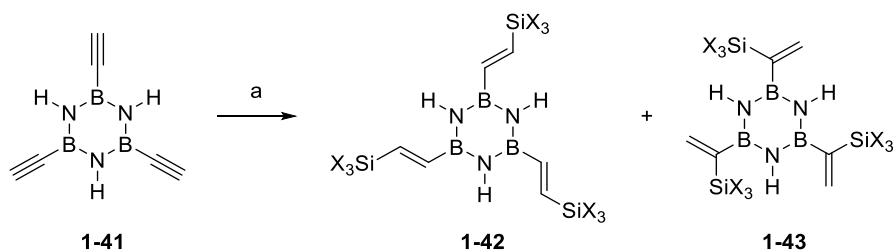


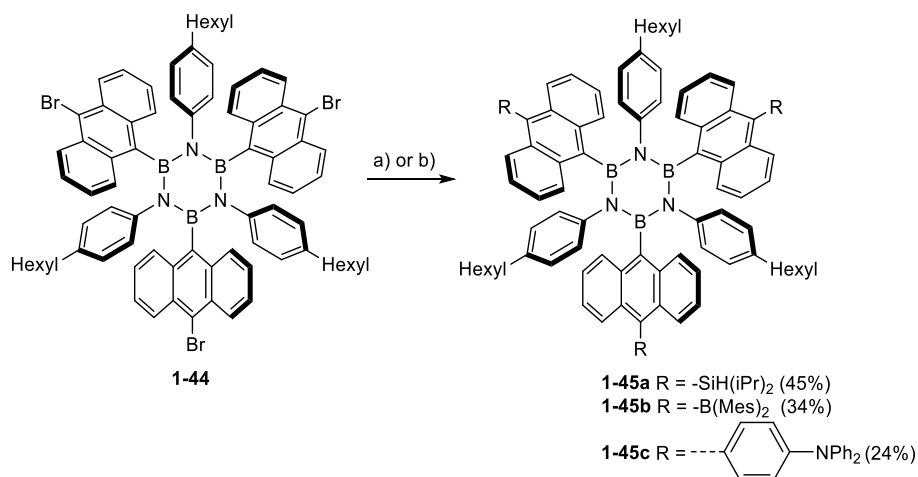
Figure 1.5. Formation of the borazine ‘outer shell’, with X and Y being the reactive functional groups.

In 2003, Grützmacher and co-workers reported the functionalisation of tri-*B*-ethynylborazine **1-41** through a platinum-catalysed hydrosilylation reaction.¹¹⁰ In the presence of a catalytic amount of Pt/C, HSiCl_3 or $\text{HSi}(\text{OR}')_3$ were reacting with **1-41** in toluene at 120 °C, yielding tri-vinylborazines **1-42** and **1-43** (Scheme 1.16). Notably, the addition of the silane on the triple bond proceeded with *cis*-stereoselectivity, thus affording the β -*trans* isomers as major products. The addition of trichlorosilane HSiCl_3 afforded isomer **1-42** in 80% yield; alkoxy silanes gave rise to a complex mixture of regioisomers.



Scheme 1.16. Pt-catalysed hydrosilylation of tri-ethynylborazine **1-41**.¹¹⁰ (a) HSiX_3 , Pt/C (1 wt%), toluene, 120 °C, 48 h, X = Cl (80%), X = OMe, OEt, O^tPr, **1-42** (60%) + **1-43** in mixture with other isomers (40%).

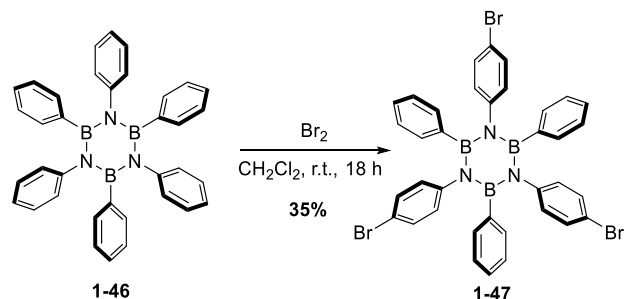
Yamaguchi and co-workers also reported the synthesis and functionalisation of 10-bromo-anthryl-bearing borazine **1-44**.⁸⁷ The anthryl hydrogen atom sitting on top the boron centers shields the electrophilic centres from nucleophile additions, thus allowing the use of a large variety of organometallic reagents (Scheme **1.17**). Consequently, the treatment of **1-44** with *t*-BuLi in THF at -78 °C followed by the addition of TIPSCl or Mes_2BF led to the formation of tri-(diisopropylsilyl) **1-45a** and tri-(dimesitylboryl) **1-45b** derivatives in 45% and 34% yield, respectively, leaving intact the central borazine core. Furthermore, Negishi cross-coupling reaction between tri-bromo derivative **1-44** with *p*-bromo(di-phenylamino) benzene yields the formation of tri-phenylamine-bound derivative **1-45c** in 24% yield,⁹¹ the latter revealing to be a very good blue emitter.



Scheme 1.17. Functionalisation strategies of trianthrylborazine **1-44**.⁸⁷ a) 1) *t*-BuLi, THF, -78 °C, 2) H(*i*-Pr)₂SiCl or Mes_2BF , r.t., 20 h, R = SiH(*i*-Pr)₂, **1-45a**, R = BMe₂, **1-45b**; b) 1) *t*-BuLi, THF, -78 °C. 2) $\text{ZnCl}_2(\text{tmen})$, 0 °C, 3) Ph₂NPhBr, [Pd(PPh₃)₄], THF, r.t., 24 h, **1-45c**.

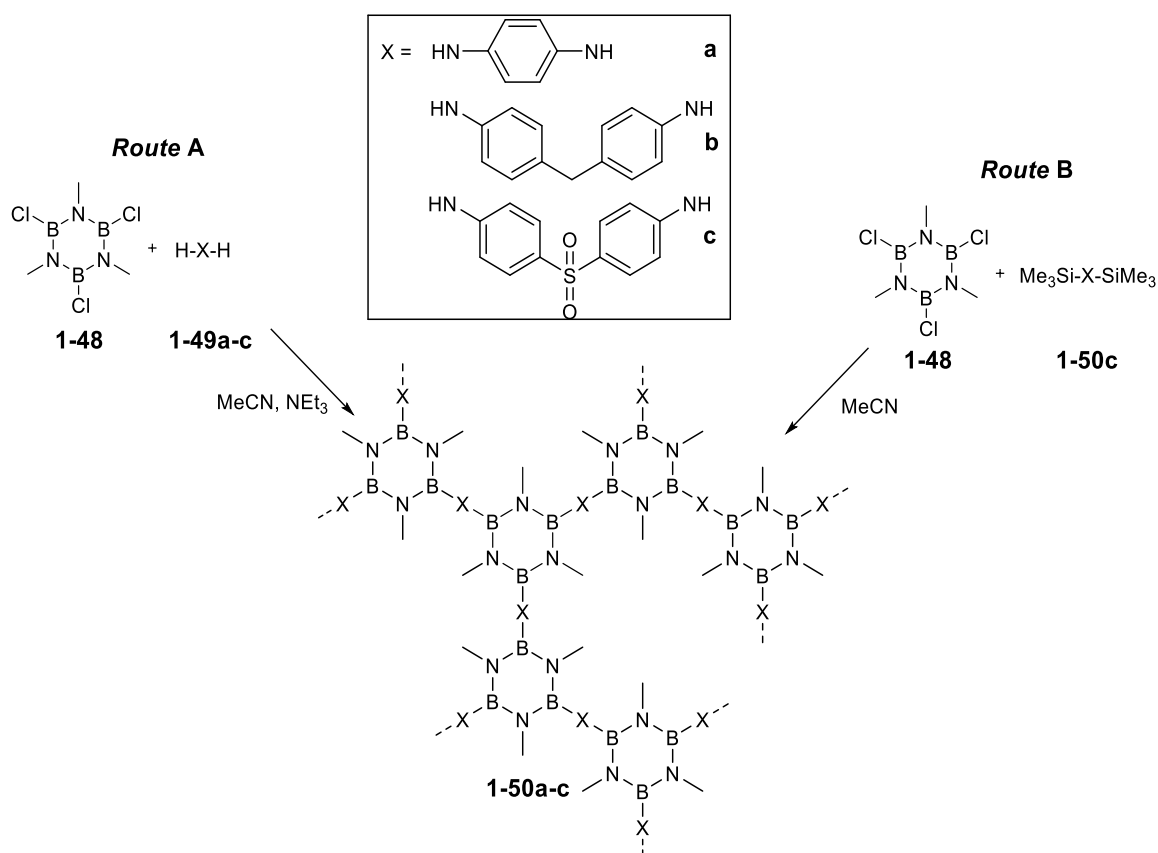
In 2013, Bettinger and co-workers reported the electrophilic aromatic bromination of hexaphenylborazine $\text{Ph}_3\text{B}_3\text{N}_3\text{Ph}_3$ **1-46**, to obtain selectively borazine **1-47** in 35% yield.¹¹¹ Only decomposition of the borazine core could be observed when tri-*N*-phenylborazine

$\text{H}_3\text{B}_3\text{NPh}_3$ **1-31** was reacted with Br_2 , further demonstrating the crucial role of the *B*-substituents on the chemical reactivity of the BN core (Scheme 1.18).



Scheme 1.18. Bromination of arylborazine **1-46**.¹¹¹

More recently, Helten and co-workers proposed *B,B',B''*-trichloro-*N,N,N''*-trimethylborazine **1-48** as monomeric unit for the preparation of cross-linker borazine polymers in the presence of different diamine derivative.¹¹² Two main strategies have been described. The first synthetic pathway was a polycondensation reaction in which borazine derivative **1-48** was dissolved in CH_3CN at room temperature, and then diamine derivative **1-49a**, **1-49b** or **1-49c** was added in ratio 2:3 (Scheme 1.19, *Route A*).



Scheme 1.19. Synthesis of polymer borazine **1-50a-c** via salt elimination (*Route A*), and synthesis of **1-50c** via silicon-boron exchange polycondensation (*Route B*).¹¹²

Investigations of the morphologies of polymers **1-50a-c** by field emission scanning electron microscopy (FESEM) revealed the formation of spherical particles with a diameter of $d = 184 \pm 21$ nm. In the second synthetic pathway (Scheme **1.19**, *Route B*), cross-linked borazine polymer **1-50c** was synthesised *via* silicon-boron exchange condensation reaction. Borazine derivative **1-48** was reacted with **1-50c** in CH_3CN , affording the cross-linked polymer **1-50c**. This showed a significantly bigger diameter size, $d = 331 \pm 21$ nm, than those obtained *via Route A*, ascribed to a better solubility of the trimethylsilyl monomers which favour the growth of the oligomer **1-50c** in the reaction medium compared to the non-silylated species.

1.5 Materials and applications

As depicted in the Figure **1.6**, borazine and its derivatives can find applications not only as precursors for optoelectronic organic materials but also as molecular materials for gas storage or supramolecular systems. The self-assembly of the borazine derivatives will be discussed in detail in *chapter 4*. In the following sections, an overview of the main achievements in the field of the optoelectronics and gas storage will be described.

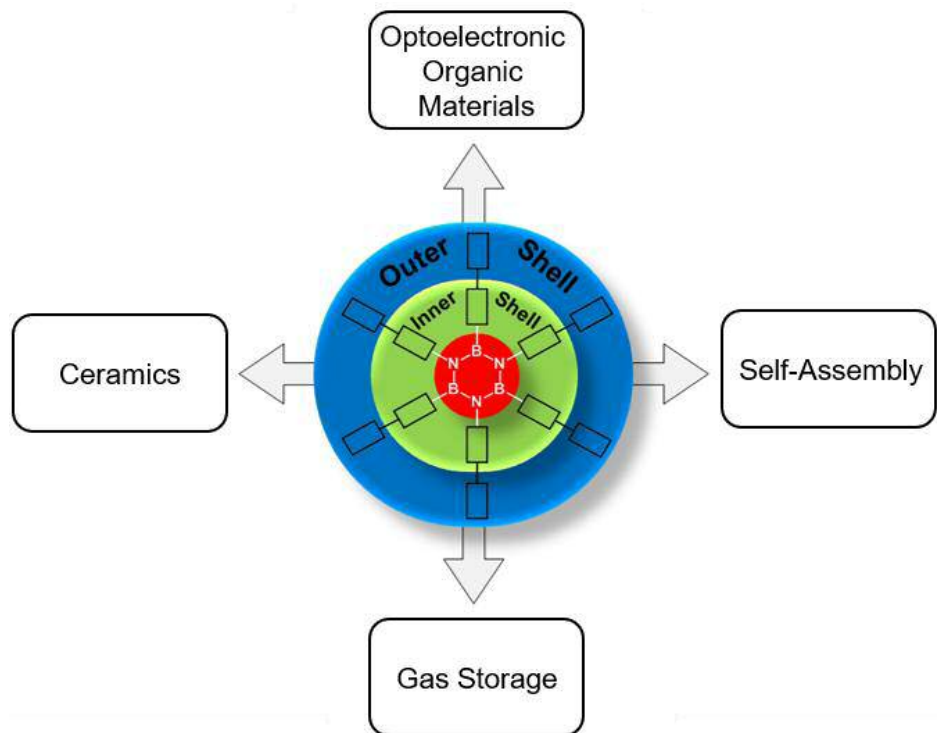


Figure 1.6. Schematic presentation of applications involving borazine and its derivatives. Along this *section*, the application related to ceramics will not be described as our interest is focused on the use of borazine derivatives for optoelectronic organic materials, self-assembly and gas storage.

1.5.1 Materials for optoelectronic devices

To achieve emission in the higher energy gap region, namely in the normal and deep UV regions, chemists have designed molecules that, relying on the idea of ‘broken conjugation’,⁴³ display short conjugation length thus featuring high-energy HOMO-LUMO gaps falling in the ultraviolet energy region. An efficient way to decrease the conjugation length of an organic aromatic hydrocarbons emitter would be to dope an all-carbon scaffold with boron-nitrogen units.^{43,86}

In this respect, with their high molecular bandgap (4 eV),^{20,113} borazine-based UV-emitters represent valuable scaffolds to be inserted in active layers of organic light emitting devices (OLEDs) for the emission in the UV or deep UV. In collaboration with group of Cacialli, our group has showed the use of a borazine-based UV-emitter as active layer in a light-emitting electrochemical cell (LEC).⁸⁶ In solution, the spectra profiles of $\text{Me}_3\text{B}_3\text{N}_3\text{Ph}_3$ **1-51** (Figure 1.7a) show photoluminescence quantum yields (Φ_{em}) between 6.6 and 7.7%, displaying little dependence on the solvent used. On the contrary, in the solid state, the emission profile changes depending on the obtained polymorph (Figure 1.7b). When borazine **1-51** was used to form the emissive layer of LEC, weak UV-emission was observed at high voltages. In particular, charge injection into the LEC is observed with a strong nonlinear dependence of the current density J on the applied voltage V .

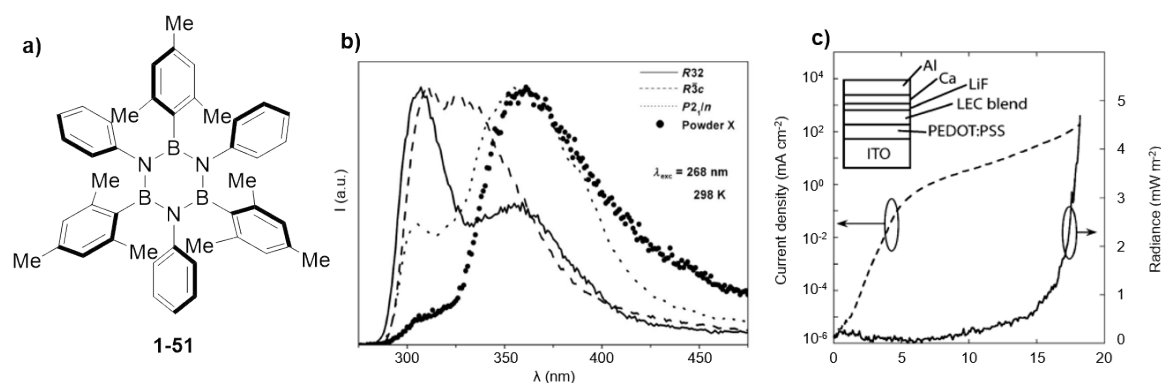
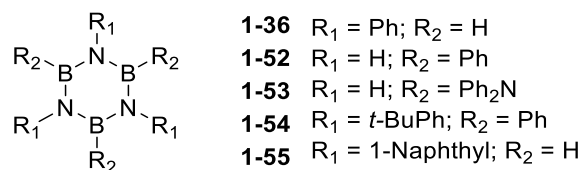


Figure 1.7. a) Chemical structure of borazine **1-51**; b) normalised emission spectra of different polymorphs formed by borazine **1-51**: space group $R3_2$ (solid line), $R3c$ (dashed line), $P2_1/n$ (dotted line), and ground powder (full circle); c) current and radiance versus light characteristics of an LEC incorporating an active layer of borazine emitter **1-51**, blended with PEO as ion transporter and LiOTf as mobile ions. The device was fabricated with vertical structure ITO/PEDOT:PSS(80 nm)/active layer/LiF (6 nm)/Ca (30 nm)/Al (150 nm).⁸⁶

Current densities of $> 100 \text{ mA/cm}^2$ were achieved at high voltage ($\sim 15 \text{ V}$), whereas a change of slope in the J/V characteristics suggests that a bipolar injection mechanism is

obtained at ~ 5 V. Similar results were obtained for the corresponding LEDs giving a promising EL quantum efficiency values of $\sim 10^{-4}$ % that, although rather weak, are the first of its kind and give hope to use borazine as suitable molecular scaffolds for UV-devices. Through the introduction of different substituents in the borazine ‘inner shell’, the ability to tune the physical properties of such organic materials, has been demonstrated.²⁰ Five borazine derivatives **1-36**, **1-52**, **1-53**, **1-54** and **1-55** have been prepared (Scheme **1.20**), and revealed to be suitable dopants due to their promising values of hole and electron mobilities ($\mu_h = 10^{-6}$ - 10^{-4} cm²/V·s and $\mu_e = 10^{-6}$ - 10^{-3} cm²/V·s respectively).



Scheme 1.20. Structure of borazine derivatives **1-36**, **1-52**, **1-53**, **1-54** and **1-55**.²⁰

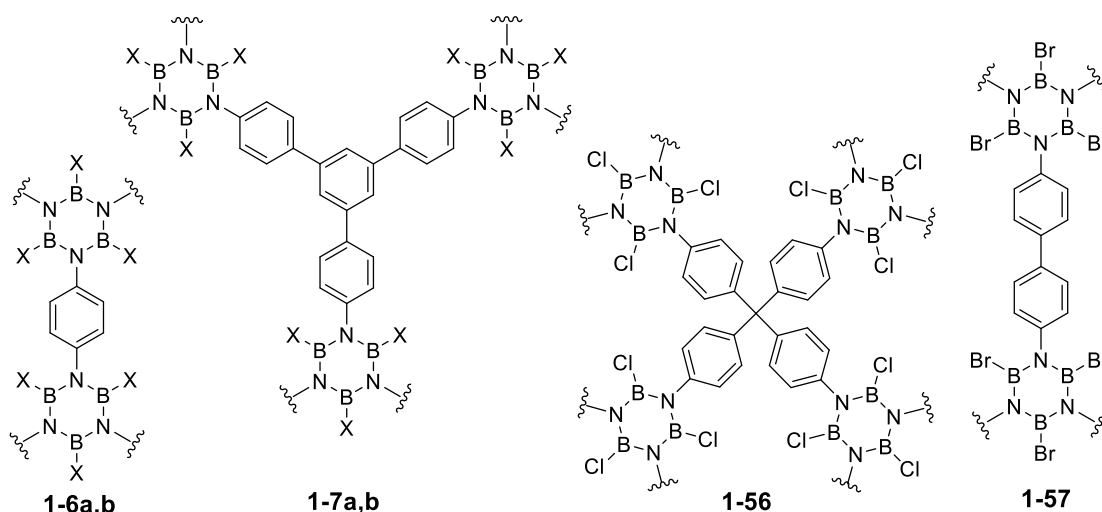
OLED devices fabricated with borazine derivative **1-54** as hole transporting materials gave yellow EL emission characteristic of Alq₃ (aluminium tri-(8-hydroxyquinoline)); and a luminance of 290 cd/m² at 11 V, with the maximum luminance of 6200 cd/m² at 21 V. The ability of the device to maintain high luminance at high voltages could be due in part to the high thermal stability of borazine compounds.

1.5.2 Materials for gas storage

The depletion of fossil oil deposits and the enhancement of global warming have pushed the scientific community towards the research of clean energy carriers such as hydrogen and methane as well as the reduction of carbon dioxide emissions. The problem of global warming has drawn the public attention to the issue of CO₂ emissions. Carbon dioxide, which is mainly generated through the combustion of fossil fuel, accumulates at an alarming rate due to the rapid development of the energy consumption worldwide.¹¹⁴ To alleviate CO₂ release to the environment, carbon dioxide capture and sequestration (CCS) strategies have been extensively studied.¹¹⁵ On the other hand, the choice of an alternative clean energy carrier such as H₂ and CH₄ may appeared as a long-term sustainable solution able to meet our future energy demands.^{116–118} However, the safe and economical storage of such gases remains one of the biggest limit for its implementation. A possible way to

solve these problems is the physical storage of gas molecules inside of porous materials. The synthesis of porous organic polymers with predefined porosity displaying high surface areas has attracted considerable attention due to their great potentials for gas storage and separation.¹¹⁹ To improve the gas uptake by porous materials, the strategy that can be developed is introduction of polarized building units. In this context, the polar BN bonds could serve as anchoring point for the non-covalent absorption of gas molecules. For instance, gases like CO₂ and CO can in principle interact with BN pairs through dipolar interactions, thus making BN-doped materials very good candidates for tailoring the gas absorptions (see *chapter 3*).^{120–124}

The synthesis and the gas uptake performance (Table 1.2) of six covalent organic frameworks (COFs) containing borazine units as polar molecular modules for gas absorption have been recently described for the first time (Scheme 1.21).^{76–78}



Scheme 1.21. Chemical formula of borazine covalent organic frameworks borazine. **1-6a** X = Cl, **1-6b** X = Br, **1-56**, **1-7a** X = Cl, **1-7b** X = Br, **1-57** and **1-8**.

Table 1.2. Porous properties of borazine covalent organic frameworks. ^aCalculated by BET methods. ^bCalculated from nitrogen adsorption at P/P₀ = 0.9.

Polymer	S _A BET (m ² /g) ^a	P _{vol} (cm ³ /g) ^b	H ₂ 77 K (mg/g)	CO ₂ 273 K (mg/g)	CH ₄ 298 K (mg/g)
1-6a (Cl)	1364	0.746	1.00	114	4.1
1-6b (Br)	503	0.303	0.68	72	1.9
1-7a (Cl)	1174	0.649	1.30	141	11.1
1-7b (Br)	849	0.571	0.98	68	2.6
1-56	1569	0.853	1.75	140	15.2
1-57	520	0.321	0.72	51	4.8

All the BN doped covalent organic frameworks reported in scheme **1.21** show a type I isotherm measured by N₂ uptake at 77 K which is indicative of microporous materials. The Brunauer-Emmett-Teller (BET) surface areas measure at 77 K reveal a higher surface area for BN-COF functionalised with chloride atoms: **1-56** (1569 m²/g) > **1-6a** (1364 m²/g) > **1-7a** (1174 m²/g) than Br-COFs **1-7b** (849 m²/g) > **1-6b** (503 m²/g). The enhancement of the BET surface area moving from **1-6a** to **1-56** and from **1-6b** to **1-7b** could be ascribed to the increasing of the length of borazine monomeric module which reduce the density of the networks, increasing the surface area of the polymers. On the other hand, COF **1-7a** should exhibit higher surface area than **1-6a**. However, COFs do not conform to such expectations due to their amorphous nature. The pore volumes calculated at P/P₀ = 0.9 show a remarkable dependence on the halide as the chlorinated polymers give rise to higher pore volumes compared to brominated analogues. This can be ascribed to a smaller atomic size of Cl atoms with respect to that of Br atoms. H₂, CO₂ and CH₄ isotherm were measured at 77 k, 273 k and 298 K, respectively. There is a clear relation between the surface area and the gas uptake performance of the porous materials. The higher the surface area is, the larger the volume pore and the gas uptake. Notably, the CO₂ isotherm adsorption for the borazine COFs shows good uptakes reaching the highest adsorption of 140 mg/g at 273 K for COF **1-56**. In contrast, the H₂ and CH₄ isotherms exhibit a very low uptake of 1.75 mg/g and 15.2 mg/g at 77 K and 298 K, respectively. The authors attribute the selective uptake of CO₂ over H₂ and CH₄ to the interactions between the borazine scaffold and CO₂, making them appealing material for gas storage and separation application.

1.6 Outlines of the dissertation

In this doctoral work, our research activities were directed toward the preparation of hybrid boron-nitrogen-carbon (BNC) organic frameworks with the aim of exploring the optoelectronic, gas adsorption and self-assembly properties. In this respect, the borazine scaffold has been used as molecular building block to be inserted as a doping unit in polyphenylene organic materials. Accordingly, the work here presented is divided into three main chapters. *Chapter II* describes the design and syntheses of three-branched borazine doped polyphenylenes, featuring a controlled orientation and dosage of B₃N₃ doping scaffold. The last section of the chapter provides a description of the photophysical

properties of BNC hybrid derivatives evaluating the relationship between the luminescence and the borazine doping. To assess the effect of borazine as an anchoring point for gas storage, in *Chapter III*, the design and synthesis of 3D BNC metal organic frameworks (MOFs) has been investigated. The last section of this chapter is dedicated to the description of the X-ray crystal structures of the porous materials as well as their BET surface area and thermal stability.

Chapter IV addresses the design and preparation of three-pyridyl borazine linkers, amenable to self-assembly to form 2D networks upon deposition on metal surfaces. The introduction of pyridine functionalities allows us to achieve distinct supramolecular architectures with control of the interdigitation of the molecules by surface templating on Ag(100) and Cu(111) substrates.

1.7 References

- (1) Stock A., Pholand E. *Berichte Dtsch. Chem. Ges. B Ser.* **1926**, *59*, 2215.
- (2) Jeffrey G. A., Ruble J. R., McMullan R. K., Pople J. A. *Proc. R. Soc. Math. Phys. Eng. Sci.* **1987**, *414*, 47.
- (3) Harshbarger W., Lee G. H., Porter R. F., Bauer S. H. *Inorg. Chem.* **1969**, *8*, 1683.
- (4) Bock H., Fuss W. *Angew. Chem. Int. Ed.* **1971**, *10*, 182.
- (5) Kiran B., Phukan A. K., Jemmis E. D. *Inorg. Chem.* **2001**, *40*, 3615.
- (6) Islas R., Chamorro E., Robles J., Heine T., Santos J. C., Merino G. *Struct. Chem.* **2007**, *18*, 833.
- (7) Grant D. J., Dixon D. A. *J. Phys. Chem.* **2006**, *110*, 12955.
- (8) Blanksby S. J., Ellison G. B. *Acc. Chem. Res.* **2003**, *36*, 255.
- (9) Thorne L. R., Suenram R. D., Lovas F. J. *J. Chem. Phys.* **1983**, *78*, 167.
- (10) Kaldor A. *J. Chem. Phys.* **1971**, *55*, 4641.
- (11) Frost D. C., Herring F. G., Mcdowell C. A., Stenhouse I. A. *Chem. Phys. Lett.* **1970**, *5*, 291.
- (12) Platt J. R., Klevens H. B., Schaeffer G. W. *J. Chem. Phys.* **1947**, *15*, 598.
- (13) Tossell J. A., Moore J. H., McMillan K., Subramaniam C. K., Coplan M. A. *J. Am. Chem. Soc.* **1992**, *114*, 1114.
- (14) Wagner R. I., Bradford J. L., Ross I. *Inorg. Chem.* **1962**, *1*, 93.
- (15) Leffler A. J. *Inorg. Chem.* **1964**, *3*, 145.

- (16) Nagasawa K. *Inorg. Chem.* **1966**, *5*, 442.
- (17) Narula C. K., Schaeffer R., Datye A., Paine R. T. *Inorg. Chem.* **1989**, *28*, 4053.
- (18) Maya L. *Appl. Organomet. Chem.* **1996**, *10*, 175.
- (19) Moon K., Min D., Kim D. *J. Ind. Eng. Chem.* **1997**, *3*, 288.
- (20) Sham I. H. T., Kwok C.-C., Che C.-M., Zhu N. *Chem. Commun.* **2005**, *2*, 3547.
- (21) Jishan Wu, Wojciech Pisula, Müllen K. *Chem. Rev.* **2007**, *107*, 718.
- (22) Fujita M., Wakabayashi K., Nakada K., Kusakabe K. *J. Phys. Soc. Japan* **1996**, *65*, 1920.
- (23) Liu J., Li B.-W., Tan Y.-Z., Giannakopoulos A., Sanchez-Sanchez C., Beljonne D., Ruffieux P., Fasel R., Feng X., Müllen K. *J. Am. Chem. Soc.* **2015**, *137*, 6097.
- (24) Narita A., Feng X., Müllen K. *Chem. Rec.* **2015**, *15*, 295.
- (25) Cai J., Ruffieux P., Jaafar R., Bieri M., Braun T., Blankenburg S., Muoth M., Seitsonen A. P., Saleh M., Feng X., Müllen K., Fasel R. *Nature* **2010**, *466*, 470.
- (26) Chen C., Wu J. Z., Lam K. T., Hong G., Gong M., Zhang B., Lu Y., Antaris A. L., Diao S., Guo J., Dai H. *Adv. Mater.* **2015**, *27*, 303.
- (27) Vo T. H., Shekhirev M., Kunkel D. A., Morton M. D., Berglund E., Kong L., Wilson P. M., Dowben P. A., Enders A., Sinitskii A. *Nat. Commun.* **2014**, *5*, 3189.
- (28) Kosynkin D. V., Higginbotham A. L., Sinitskii A., Lomeda J. R., Dimiev A., Price B. K., Tour J. M. *Nature* **2009**, *458*, 872.
- (29) Novoselov K. S., Geim A. K., Morozov S. V., Jiang D., Zhang Y., Dubonos S. V., Grigorieva I. V., Firsov A. *Science* **2004**, *306*, 666.
- (30) Schwierz F. *Nat. Nanotechnol.* **2010**, *5*, 487.
- (31) Park S., Ruoff R. S. *Nat. Nanotechnol.* **2009**, *4*, 217.
- (32) Bronner C., Stremlau S., Gille M., Brauße F., Haase A., Hecht S., Tegeder P. *Angew. Chem. Int. Ed.* **2013**, *52*, 4422.
- (33) Liang H.-W., Zhuang X., Brüller S., Feng X., Müllen K. *Nat. Commun.* **2014**, *5*, 4973.
- (34) Makarov N. S., Mukhopadhyay S., Yesudas K., Brédas J.-L., Perry J. W., Pron, A., Kivala M., Müllen K. *J. Phys. Chem. A* **2012**, *116*, 3781.
- (35) Cloke R., Marangoni T., Nguyen G. D., Joshi T., Rizzo D. J., Bronner C., Cao T., Louie S. G., Crommie M. F., Fischer F. R. *J. Am. Chem. Soc.* **2015**, *137*, 8872.
- (36) Liu Z., Marder T. B. *Angew. Chem. Int. Ed.* **2008**, *47*, 242.

- (37) Watanabe K., Taniguchi T., Niiyama T., Miya K., Taniguchi M. *Nat. Photonics* **2009**, *3*, 591.
- (38) Watanabe K., Taniguchi T., Kanda H. *Nat. Mater.* **2004**, *3*, 404.
- (39) Golberg D., Bando Y., Huang Y., Terao T., Mitome M., Tang C., Zhi C. *ACS Nano* **2010**, *4*, 2979.
- (40) Zhi C., Bando Y., Terao T., Tang C., Kuwahara H., Golberg D. *Adv. Funct. Mater.* **2009**, *19*, 1857.
- (41) Côté M., Haynes P. D., Molteni C. *Phys. Rev. B* **2001**, *63*, 125207.
- (42) Kawaguchi M., Kawashima T., Nakajima T. *Chem. Mater.* **1996**, *8*, 1197.
- (43) Ci L., Song L., Jin C., Jariwala D., Wu D., Li Y., Srivastava A., Wang Z. F., Storr K., Balicas L., Liu F., Ajayan P. M. *Nat. Mater.* **2010**, *9*, 430.
- (44) Kazemi A., He X., Alaie S., Ghasemi J., Dawson N. M., Cavallo F., Habteyes T. G., Brueck S. R. J., Krishna S. *Sci. Rep.* **2015**, *5*, 11463.
- (45) Huang, C., Chen C., Zhang M., Lin L., Ye X., Lin S., Antonietti M., Wang X. *Nat. Commun.* **2015**, *6*, 7698.
- (46) Dewar M. J. S., Marr P. A. *J. Am. Chem. Soc.* **1962**, *84*, 3782.
- (47) Campbell P. G., Marwitz A. J. V., Liu S.-Y. *Angew. Chem. Int. Ed.* **2012**, *51*, 6074.
- (48) Chissick S. S., Dewar M. J. S., Maitlis P. M. *Tetrahedron Lett.* **1960**, *23*, 8.
- (49) Bosdet M. J. D., Piers W. E., Sorensen T. S., Parvez M. *Angew. Chem. Int. Ed.* **2007**, *46*, 4940.
- (50) Dewar M. J. S., Kubba V. P., Pettit R. *J. Chem. Soc.* **1958**, 3073.
- (51) Bosdet, M. J. D., Jaska C. A., Piers W. E., Sorensen T. S., Parvez M. *Org. Lett.* **2007**, *9*, 1395.
- (52) Dewar M. J. S., Dietz R. *J. Chem. Soc.* **1959**, 2728.
- (53) Paetzold P., Stanescu C., Stubenrauch J. R., Bienmüller M., Englert U. *Z. Anorg. Allg. Chem.* **2004**, *630*, 2632.
- (54) Fang X., Yang H., Kampf J. W., Banaszak Holl M. M., Ashe A. J. *Organometallics* **2006**, *25*, 513.
- (55) Molander G. A., Wisniewski S. R. *J. Org. Chem.* **2014**, *79*, 6663.
- (56) Wisniewski S. R., Guenther C. L., Argintaru O. A., Molander G. A. *J. Org. Chem.* **2014**, *79*, 365.
- (57) Bonifazi D., Fasano F., Lorenzo-Garcia M. M., Marinelli D., Oubaha H., Tasseroul,

- J. Chem. Commun.* **2015**, *51*, 15222.
- (58) Schlesinger H. I., Ritter D. M., Burg A. B. *J. Am. Chem. Soc.* **1938**, *60*, 1296.
- (59) Schaeffer G. W., Schaeffer R., Schlesinger H. I. *J. Am. Chem. Soc.* **1951**, *73*, 1612.
- (60) Framery E., Vaultier M. *Heteroat. Chem.* **2000**, *11*, 218.
- (61) Wideman T., Sneddon L. *Inorg. Chem.* **1995**, *34*, 1002.
- (62) Meller A., Schaschel E. *Inorg. Nucl. Chem. Lett* **1966**, *2*, 41.
- (63) Schaeffer G. W., Anderson E. R. *J. Am. Chem. Soc.* **1949**, *71*, 2143.
- (64) Hough W. V., Schaeffer G. W., Dzurus M., Stewart A. C. *J. Am. Chem. Soc.* **1955**, *77*, 864.
- (65) Emeléus H. J. *J. Chem. Soc* **1960**, 2614.
- (66) Yamamoto Y., Miyamoto K., Umeda J., Nakatani Y., Yamamoto T., Miyaura N. *J. Organomet. Chem.* **2006**, *691*, 4909.
- (67) Jaska C. A., Temple K., Lough A. J., Manners I. *J. Am. Chem. Soc.* **2003**, *125*, 9424.
- (68) García-Vivó D., Huergo E., Ruiz M. A., Travieso-Puente R. *Eur. J. Inorg. Chem.* **2013**, *2013*, 4998.
- (69) Kawano Y., Uruichi M., Shimoi M., Taki S., Kawaguchi T., Kakizawa T., Ogino H. *J. Am. Chem. Soc.* **2009**, *131*, 14946.
- (70) Kim S.-K., Cho H., Kim M. J., Lee H.-J., Park J., Lee Y.-B., Kim H. C., Yoon C. W., Nam S. W., Kang S. O. *J. Mater. Chem. A* **2013**, *1*, 1976.
- (71) Luo W., Campbell P. G., Zakharov L. N., Liu S. Y. *J. Am. Chem. Soc.* **2011**, 19326.
- (72) Li J. S., Zhang C. R., Li B., Cao F., Wang S. Q. *Eur. J. Inorg. Chem.* **2010**, *5*, 1763.
- (73) Resendiz-Lara D. A., Stubbs N. E., Arz M. I., Pridmore N. E., Sparkes H. A., Manners I. *Chem. Commun.* **2017** DOI: 10.1039/C7CC07331C.
- (74) Laubencayer A. W., Brown C. A. *J. Am. Chem. Soc.* **1955**, *77*, 3699.
- (75) Smalley J. H., Stafiej S. F. *J. Am. Chem. Soc.* **1959**, *81*, 582.
- (76) Jackson K. T., Rabbani M. G., Reich T. E., El-Kaderi H. M. *Polym. Chem.* **2011**, *2*, 2775.
- (77) Reich T. E., Jackson K. T., Li S., Jena P., El-Kaderi H. M. *J. Mater. Chem.* **2011**, *21*, 10629.
- (78) Reich T. E., Behera S., Jackson K. T., Jena P., El-Kaderi H. M. *J. Mater. Chem.* **2012**, *22*, 13524.

- (79) Paetzold P. *Phosphorus. Sulfur. Silicon Relat. Elem.* **1994**, *93*, 39.
- (80) Münster J., Paetzold P., Schröder E., Schwan H., von Bennigsen-Mackiewicz T. *Zeitschrift für Anorg. und Allg. Chemie* **2004**, *630*, 2641.
- (81) Luo W., Zakharov L. N., Liu S.-Y. *J. Am. Chem. Soc.* **2011**, *133*, 13006.
- (82) Biswas S., Müller M., Tönshoff C., Eichele K., Maichle-Mössmer C., Ruff A., Speiser B., Bettinger H. F. *European J. Org. Chem.* **2012**, *2012*, 4634.
- (83) Müller M., Behnle S., Maichle-Mössmer C., Bettinger H. F. *Chem. Commun.* **2014**, *50*, 7821.
- (84) Krieg M., Reicherter F., Haiss P., Ströbele M., Eichele K., Treanor M. J., Schaub R., Bettinger H. F. *Angew. Chem. Int. Ed.* **2015**, *54*, 8284.
- (85) Atkinson I. B., Blundell D. C., Clapp D. B. *J. Inorg. Nucl. Chem.* **1972**, *34*, 3037.
- (86) Kervyn S., Fenwick O., Di Stasio F., Shin Y. S., Wouters J., Accorsi G., Osella S., Beljonne D., Cacialli F., Bonifazi D. *Chem. Eur. J.* **2013**, *19*, 7771.
- (87) Atsushi W., Toshihisa I., Yamaguchi S. *J. Am. Chem. Soc.* **2005**, *127*, 14859.
- (88) Newsom H., English W., McCloskey A. *J. Am. Chem. Soc.* **1961**, *83*, 4134.
- (89) Massey A. G., Park A. J. *J. Organomet. Chem.* **1964**, *2*, 461.
- (90) Watanabe H., Totani T., Yoshizaki T. *Inorg. Chem.* **1965**, *4*, 657.
- (91) Fischer E. O., Öfele K. *Chem. Ber.* **1957**, *90*, 2532.
- (92) Werner H., Prinz R., Deckelmann E. *Chem. Ber.* **1969**, *102*, 95.
- (93) Beckett M. A., Gilmore R. J., Idrees K. *J. Organomet. Chem.* **1993**, *455*, 47.
- (94) Nöth H., Troll A. *Eur. J. Inorg. Chem.* **2005**, *2005*, 3524.
- (95) Stock A., Wiberg E., Martini H. *Berichte der Dtsch. Chem. Gesellschaft A B Ser.* **1930**, *63*, 2927.
- (96) Wiberg E., Bolz A. *Berichte der Dtsch. Chem. Gesellschaft A B Ser.* **1940**, *73*, 209.
- (97) Laubengayer A. W., Beachley O. T., Porter R. F. *Inorg. Chem.* **1965**, *4*, 578.
- (98) Anton K., Fußstetter H., Nöth H. *Chem. Ber.* **1981**, *114*, 2723.
- (99) Gemünd B., Günther B., Nöth H. *ARKIVOC* **2008**, *136*, 152.
- (100) Carion R., Liégeois V., Champagne B., Bonifazi D., Pelloni S., Lazzeretti P. *J. Phys. Chem. Lett.* **2010**, *1*, 1563.
- (101) Bai J., Niedenzu K., Serwatowska J., Serwatowski J. *Inorg. Chem.* **1991**, *30*, 4631.
- (102) Riley R. F., Schack C. J. *Inorg. Chem.* **1964**, *3*, 1651.
- (103) Groszos S. J., Stafiej S. F. *J. Am. Chem. Soc.* **1958**, *80*, 1357.

- (104) Haworth D. T., Hohnstedt L. F. *J. Am. Chem. Soc.* **1960**, *82*, 3860.
- (105) Ryschkewitsch G. E., Harris J. J., Sisler H. H. *J. Am. Chem. Soc.* **1958**, *80*, 4515.
- (106) Melcher L. A., Adcock J. L., Lagowski J. J. *Inorg. Chem.* **1972**, *11*, 1247.
- (107) Jackson L. A., Allen C. W. *J. Chem. Soc. Dalt. Trans.* **1989**, *12*, 2423.
- (108) Dosso J., Tasseroul J., Fasano F., Marinelli D., Biot N., Fermi A., Bonifazi D. *Angew. Chem. Int. Ed.* **2017**, *56*, 4483.
- (109) Allemann O., Duttwyler S., Romanato P., Baldrige K. K., Siegel J. S. *Science* **2011**, *332*, 574.
- (110) Haberecht J., Krummland A., Breher F., Gebhardt B., Rügger H., Nesper R., Grützmacher H. *Dalt. Trans.* **2003**, *11*, 2126.
- (111) Müller M., Maichle-Mössmer C., Sirsch P., Bettinger H. F. *Chempluschem* **2013**, *78*, 988.
- (112) Riensch N. A., Deniz A., Kühl S., Müller L., Adams A., Pich A., Helten H. *Polym. Chem.* **2017**, *8*, 5264.
- (113) Kervyn S., Nakanishi T., Aimi J., Saeki A., Seki S., Champagne B., Bonifazi D. *Chem. Lett.* **2012**, *41*, 1210.
- (114) Doney S. C., Schimel D. S. *Annu. Rev. Environ. Resour.* **2007**, *32*, 31.
- (115) Markewitz P., Kuckshinrichs W., Leitner W., Linssen J., Zapp P., Bongartz R., Schreiber A., Müller T. E. *Energy Environ. Sci.* **2012**, *5*, 7281.
- (116) Winsche W. E., Hoffman K. C., Salzano F. J. *Science* **1973**, *180*, 1325.
- (117) Schlapbach L., Züttel A. *Nature* **2001**, *414*, 353.
- (118) Ma S., Zhou H.-C. *Chem. Commun.* **2010**, *46*, 44.
- (119) McKeown N. B., Budd P. M. *Macromolecules* **2010**, *43*, 5163.
- (120) Portehault D., Giordano C., Gervais C., Senkowska I., Kaskel S., Sanchez C., Antonietti M. *Adv. Funct. Mater.* **2010**, *20*, 1827.
- (121) Aijaz A., Akita T., Yang H., Xu Q. *Chem. Commun.* **2014**, *50*, 6498.
- (122) Si X., Zhang J., Li F., Jiao C., Wang S., Liu S., Li Z., Zhou H., Sun L., Xu F. *Dalt. Trans.* **2012**, *41*, 3119.
- (123) Sagynbaeva M., Hussain T., Panigrahi P., Johansson B., Ahuja, R. *Epl* **2015**, *109*.
- (124) Deng X., Zhang D., Si M., Deng M. *Phys. E Low Dimensional Syst. Nanostructures* **2011**, *44*, 495.

CHAPTER 2

BN-DOPED POLYPHENYLENES

This chapter describes the divergent synthesis of three-branched borazine doped polyphenylenes, in which one or more aryl units are replaced by borazine rings. Taking advantage of the decarbonylative [4+2] Diels-Alder cycloaddition reaction between ethynyl and tetraphenylcyclopentadienone derivatives, two molecular modules were prepared: a core and a branching unit. Indulging this approach, three-branched hybrid polyphenylenes featuring controlled orientation and dosages of the doping B₃N₃-rings have been synthesised. At last, the photophysical investigations of the borazine-doped polyphenylenes have been evaluated, describing the relation between the light emission properties and the doping orientation and dosage of the polyphenylenes.

The chapter is divided into 5 main sections: *i) section 2.1* includes a general introduction on BN-doped graphene; *ii) section 2.2* introduces the bottom-up synthetic approach towards the synthesis of borazine doped polyaromatic hydrocarbons (PAHs); *iii) section 2.3* will address to the divergent synthetic strategy of polyphenylenes; *iv) section 2.4* deals with the synthetic design of borazine doped-polyphenylenes; *v) section 2.5* reports the synthesis and the photophysical properties of three-branched borazine doped polyphenylenes.

The research work described in *sections 2.5.2, 2.5.4, 2.5.5 and 2.5.6* has been carried out jointly with Davide Marinelli (*Cardiff University, Wales*) who performed the syntheses of derivatives **2-39**, **2-41**, **2-42**, **2-47**, **2-48**, **2-52**, **2-54**, **2-63** and **2-64**. The X-Ray diffraction analyses were performed by Nicola Demitri (*Electra-Sincrotrone, Basovizza, Trieste, Italy*).

The results reported in this *chapter* have been published in the following article:

Marinelli D., **Fasano F.**, Btissam N., Demitri N., Bonifazi D. *J. Am. Chem. Soc.* **2017**, *139*, 5503. (Marinelli D. and Fasano F. contributed equally).

2.1 Research challenge: BN-doped graphene

After the first experimental demonstration of graphene in 2004 by Geim and Novoselov,¹ several research groups have been involved in the investigation of this material. Graphene presents remarkable properties, particularly high charge carrier mobility, making it an encouraging material for organic electronic applications.² However, the absence of a band gap precludes the possibility to use graphene as a semiconducting material in organic devices.³ Different ways have been used in order to overcome this problem, including covalent and non-covalent functionalisation strategies.^{4,5} Above all, the replacement of C-C pairs with isosteric groups, such as boron-nitrogen (BN) pairs, is becoming one of the most efficient ways to tune the energy band gap of graphitic nanostructure (Figure 2.1).⁶⁻⁸

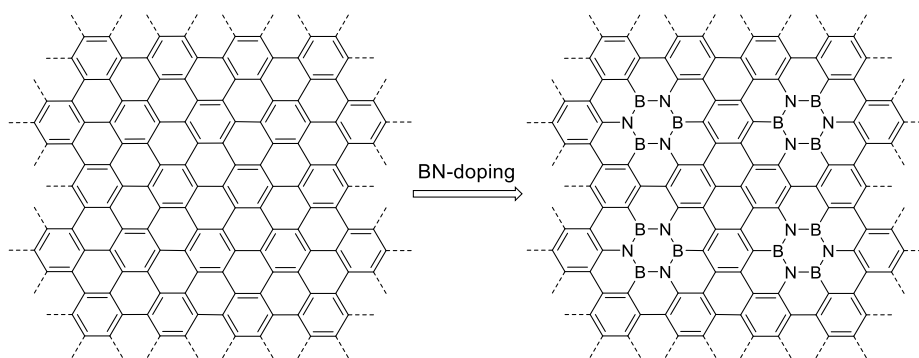


Figure 2.1. Schematic representation of the BN doping of graphitic nanostructures.

As it has been described in section 1.1 and 1.6.3, the strong polar character of the BN pair causes a series of particular properties, such as widening of the HOMO-LUMO gap with respect to the all carbon analogues. Considerable theoretical studies have demonstrated that small clusters of BN pairs embedded into a graphene carbon sheet allow for bandgap opening, increasing the charge transport mobility of the doped boron-nitrogen-carbon (BNC) material.^{9,10} The density functional theory (DFT) calculations reveal that *hexagonal*-BN (*h*-BN) possesses a bandgap of 4.56 eV (Figure 2.2a-b) which is 1 eV smaller than the experimental value¹¹ due to the limitation of the DFT method. Increasing the carbon component in the structure, moving from $B_{16}N_{16}$ to $B_{11}C_{12}N_9$ structure, a significantly reduced energy gap (E_g) from 4.56 to 2.00 eV was observed (Figure 2.2c-d). In contrast to the localised valence band of pure *h*-BN, the valence band in $B_{11}C_{12}N_9$ is more delocalised as depicted in the Figure 2.22d.

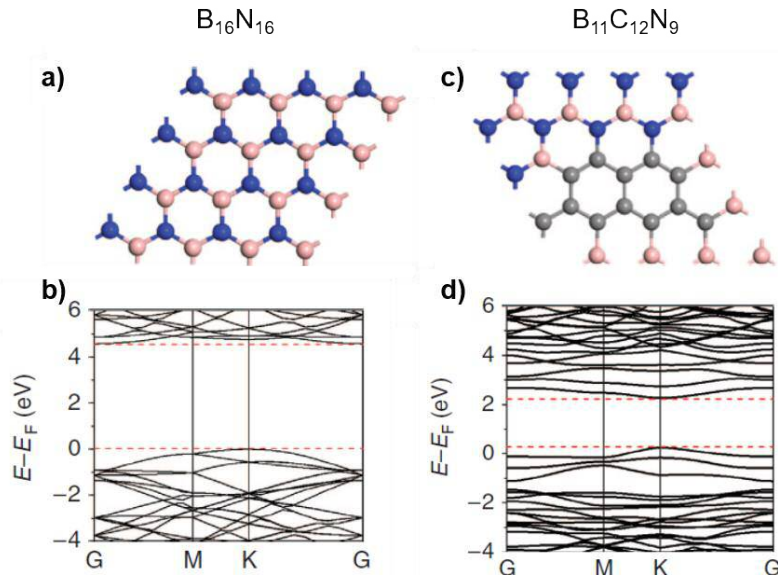


Figure 2.2. DFT calculations of *h*-BN and *h*-BNC.¹⁴ a) Optimised chemical structure of $B_{16}N_{16}$; b) Calculated energy band of $B_{16}N_{16}$; c) Optimized chemical structure of $B_{11}C_{12}N_9$; d) Calculated energy band of $B_{11}C_{12}N_9$.

The first experimental report of *h*-BN graphene was reported by Ajayan and co-workers in 2010.¹² They proposed a top-down synthetic approach of *h*-BNC monolayer starting from BH_3-NH_3 through chemical vapour deposition (CVD) process on copper substrates. By controlling the experimental conditions (temperature, time and ratio between BN and C sources), they were able to control the BN-doping from 10% to 100% (Figure 2.3).

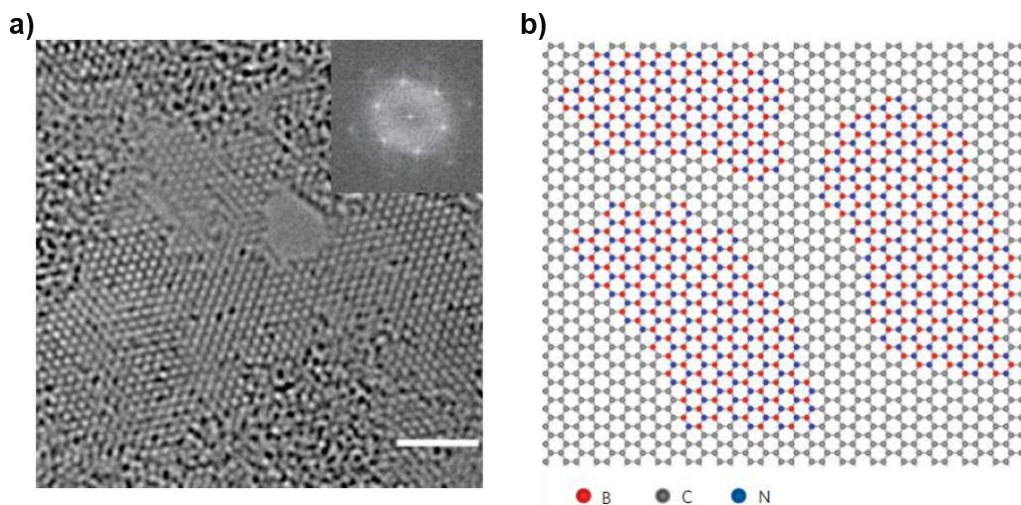


Figure 2.3. a) HRTEM image of a single-layer region of the *h*-BNC film. Scale bars: 2 nm. Inset: FFT pattern of the single-layer region.¹² b) Atomic model of *h*-BNC film showing hybridised *h*-BN and graphene domains.¹²

In 2013, Lu and co-workers reported the control growth of *h*-BNC using borazine as BN source.¹³ By treatment of Ru(0001)-grown graphene monolayer with vaporized borazine at 900 K, the replacement of C atoms with B and N atoms was observed, leading to the formation of *h*-BNC material. The morphology of the *h*-BNC monolayer follows the moiré pattern of graphene, yielding a triangular motif network (Figure 2.4a). The *h*-BNC mosaic patchwork on Ru(0001) is composed of domains where carbon atoms are close to Ru atoms (*e.g.*, valleys) and domains in which the carbon atoms are far from the metal (*e.g.*, hills). In valleys, the adjacency of C and Ru atoms catalyse the reduction of the graphene layer by borazine thermal decomposition products (B, N, and H reactive species), etching away CH_x fragments, and encapsulating B and N atoms into the graphene network (Figure 2.4b). By increasing the borazine ratio, formation of domains composed by *h*-BC₂N incorporated into the graphene network, has been observed (Figure 2.4c) with a measured energy gap of 2 eV.

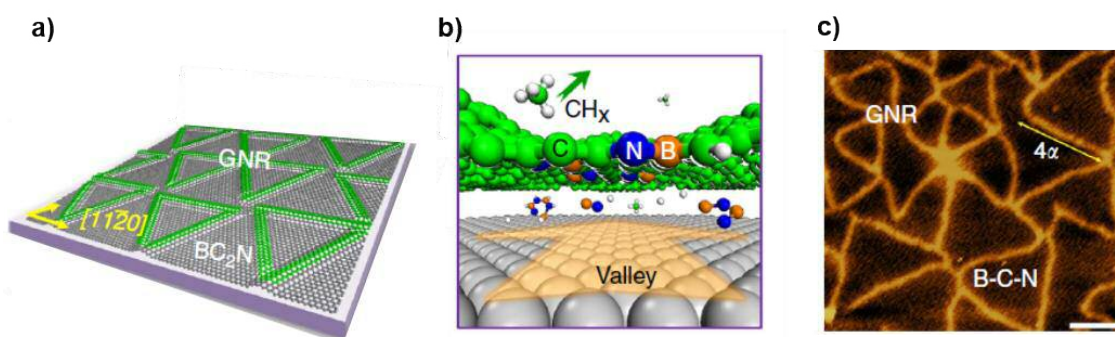


Figure 2.4. Formation of mixed BNC domains enclosed by graphene-nanoribbons (GNRs).¹³ a) Illustration of the substitutional doping of graphene/Ru(0001) by borazine leading to the formation of triangular motif network. b) Schematic shows the subsurface diffusion and catalytic decomposition of borazine to generate active B and N species which replace lattice carbon in graphene c) STM images show the evolution of mixed BCN domains (dotted dark regions) and GNR phases bright lines.

More recently, Wang and Antonietti reported the preparation of *h*-BNC using a pyrolysis method.¹⁴ Different ratio between glucose, boron oxide and urea, were mixed in ammonia atmosphere into a tube furnace at 1,525 K. Notably, the resulting *h*-BNC material has proven to be active as photocatalyst for the visible light photo-reduction of CO₂ to CO and the water splitting with a quantum efficiency of 0.54% at 405 nm. Furthermore, the *h*-BNC band gaps (2–3 eV) were estimated to straddle the H₂O redox potentials, producing molecules of H₂ and O₂, when coupled to NiCo layered co-catalyst. However, all the top-down approaches described cannot represent a feasible solution for the preparation of heteroatom BN doped graphene with atomic precision. BN segregations on the metal

substrates and edge termination impurities, B-O and N-H bonds, are always detected on the surface by XPS.¹⁴ Thus, precise structural control cannot be achieved and only monoatomic-thick sheets containing B, N and C atoms over wide compositional ranges featuring no structural order are known to date.

2.2 Bottom-up synthetic approaches

Alternatively to the top-down approach, the use of the bottom-up growth of structurally well-defined BN-doped graphene monolayers from BN incorporated building blocks, could allow the control of the doping with atomic precision. This synthetic approach aims to guide the assembly of atomic and molecular constituents into highly pure organised structures. The proof of concept was given by Zhang and co-workers in 2015. They proposed the synthesis of BN-heterosuperbenzene **2-2** through an electrophilic borylation reaction between triamino-triphenylene derivative **2-1** and dichloro-phenylborane (Figure 2.5a).¹⁵

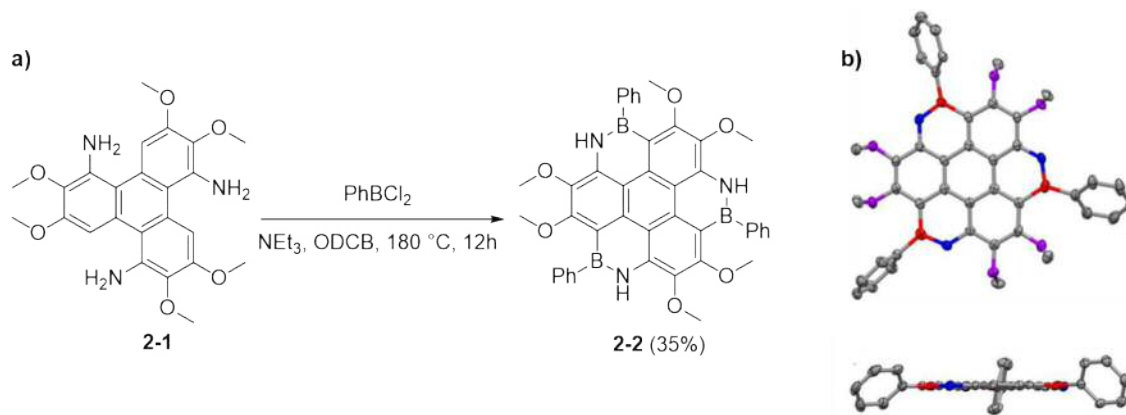


Figure 2.5. Synthesis a) and single crystal structure b) of BN-heterosuperbenzene **2-2**.¹⁵

The single crystal structure analysis of BN-heterosuperbenzene **2-2** clearly shows a fully planar geometry with the peripheral phenyl rings twisted off-plane by angles between 44° and 75° (Figure 2.5b). The optical E_g of **2-2** is 3.85 eV, which is larger than the corresponding full carbon coronene ($E_g = 3.07$ eV).¹⁶ However, the BN doping on the periphery of coronene does not allow the formation of a chemically stable compound. BN-heterosuperbenzene **2-2** undergoes hydrolysis in the presence of water leading to the cleavage of the B-Ph bonds. Very recently, Hatekeyama and co-workers reported the synthesis of BN doped hexaphenylcoronene **2-4**.¹⁷ Triarylamine **2-3** was treated with BI_3 and BPh_3 in trichlorobenzene at 200°C yielding compound **2-4** in 48% (Figure 2.6).

Interestingly, the single crystal structure of BN-hexaphenylcoronene **2-4** shows a distorted structure in which the dihedral angles between the planes of the peripheral benzene rings are very different to each other (A-A', 30.3°; A-B, 46.4°; B-C, 33.1°; C-C', 48.2°, Figure 2.6), while those of the carbon analogue are in the range of 43-45°.

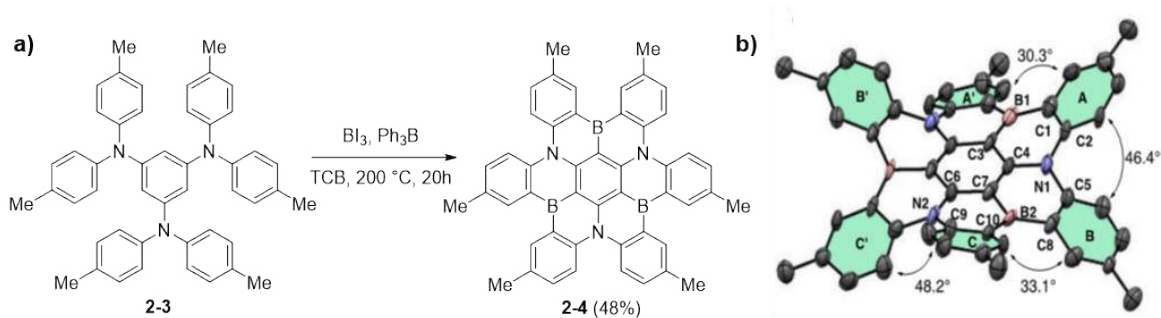


Figure 2.6. Synthesis a) and single crystal structure b) of BN-hexaphenylcoronene **2-4**.¹⁷

As described in *section 1.2.3*, the first example of stable borazine-doped coronene was achieved by Bettinger and co-workers through the pyrolysis at 550 °C of borazine **1-24**. Nonetheless, the poor solubility of **1-27** did not permit the evaluation of the optoelectronic properties of the molecule. In 2017, our group has reported the first rational synthesis of BN-doped coronene derivative **1-39** and the corresponding full carbon congener **2-5** (see *section 1.3.3*, Figure 2.7a and d). The identity of **1-39** was confirmed by X-ray diffraction analysis, a nearly flat shape of the structure can be observed, similar to all-carbon analogue **2-5** (Figure 2.7b and e). To evaluate the effect of the BN doping unit on the aromatic π -surface, the charge distribution of the crystal structure of **1-39** and **2-5** were calculated and mapped on Van der waals (Vdw) surface (Figure 2.7c and f). As expected, the introduction of borazine core in the carbon skeleton, lead to charge polarisation of the π -surface with the *N* and *B* atom negatively and positively charged, respectively. On the other hand, the full carbon congener **2-5** showed a homogeneous π electron density delocalised above and below the carbon framework. Finally, UV/Vis absorption, emission and electrochemical investigations reveals a widening of the HOMO-LUMO gap of 0.53 eV with respect to **2-5**.

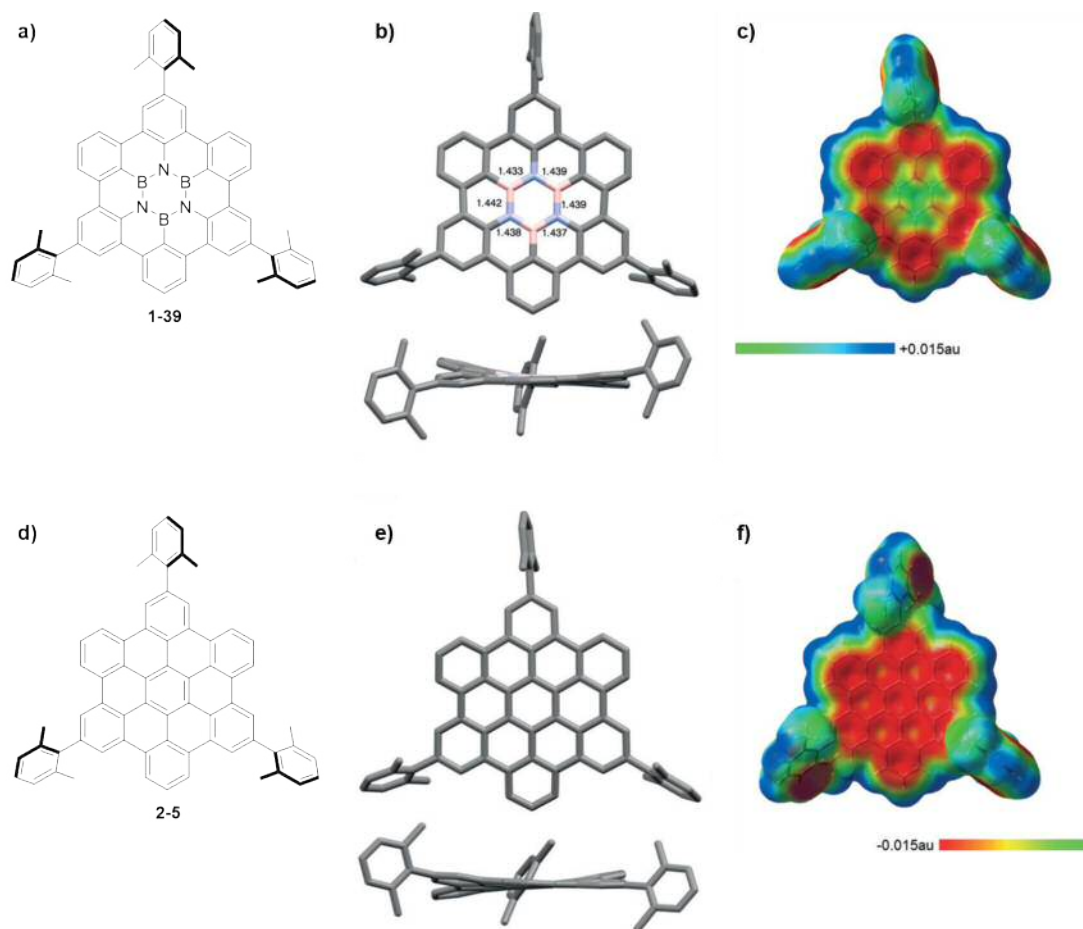


Figure 2.7. a) And d) Chemical structure of borazinocoronene derivative **1-39** and full-carbon congener **2-5**, respectively; b) And e) Horizontal (top) and side (bottom) view of the X-ray crystal structures of **1-39** (with the B-N distances in Å, space group: I2/a) and **2-5** (space group: P-1); Colour code: B pink, N blue, C gray; c) And f) ESP mapped on the vdW surface up to an electron density of 0.001 electronbohr⁻³ of **1-39** and **2-5**, respectively.

Even if great results have been achieved in the synthesis of BN doped coronene derivatives, no examples are reported in the literature about the synthesis in solution of extended well-defined BN-doped graphene monolayers. So far, the only example of a BN-doped covalent network featuring a regular doping pattern has been described through metal surface-assisted polymerisation of borazine **2-6** (Figure 2.8) reaction by Müllen and co-workers.¹⁸ Interlinked BN-HBC networks could be prepared on a Ag(111) surface under ultra-high vacuum (UHV) conditions through stepwise thermal methodology (Figure 1.7).¹⁸ In particular, thermal deposition of **2-6** on Ag(111) led to the formation of non-covalent flower-like assemblies at 425 K (Figure 2.9a). When temperature is raised to 475 K, phenyl-phenyl type cross-coupling reaction catalysed by Ag atoms occurred at the C-Br functionalities (Figure 2.9b), forming covalently assembled networks. Complete

cyclodehydrogenation of partially planarized molecule **2-6** could be achieved at 575 K (Figure 2.9c), ultimately leading to the formation of the covalently-linked borazinocoronene network.

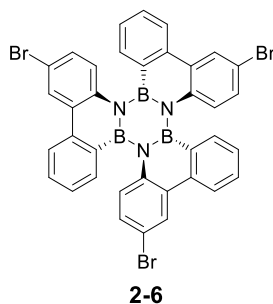


Figure 2.8. Chemical structure of borazine derivative **2-6**.¹⁸

Together with the first self-assembly studies on surfaces, this represents the first step toward the implementation of the BN-doped hybrid carbon materials and the assessment of their electronic properties and potentials applications in molecular devices. Given these premises, it is clear that the current state of research is still far from a bottom-up synthetic approach in solution of BN doped carbon structures exhibiting programmed optoelectronic properties.

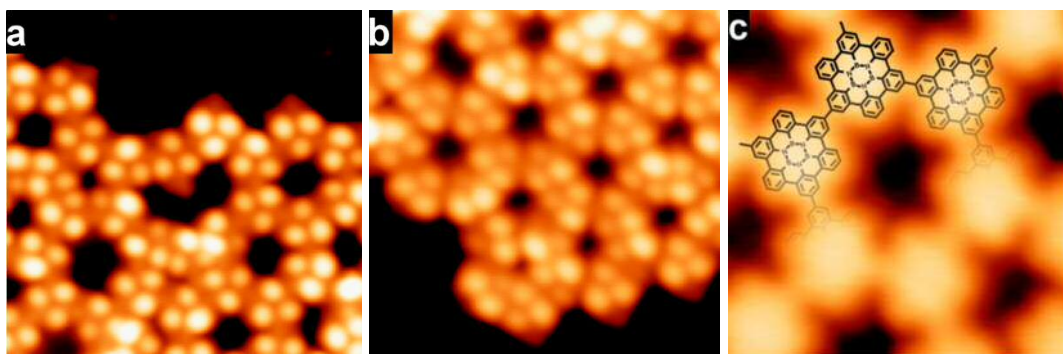
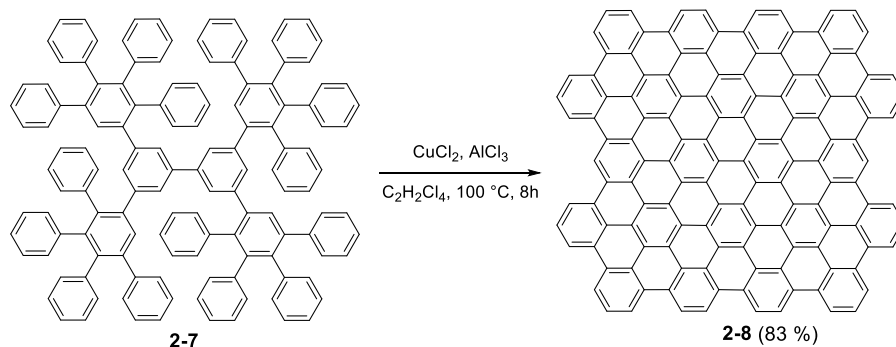


Figure 2.9. a) STM image of borazine **2-6** after deposition and annealing to 425 K; b) Covalent network after polymerization at 475 K and c) High resolution STM of the planar network after fully cyclodehydrogenation at 575 K. Adapted from reference.¹⁸

2.3 Molecular design and divergent synthetic strategy

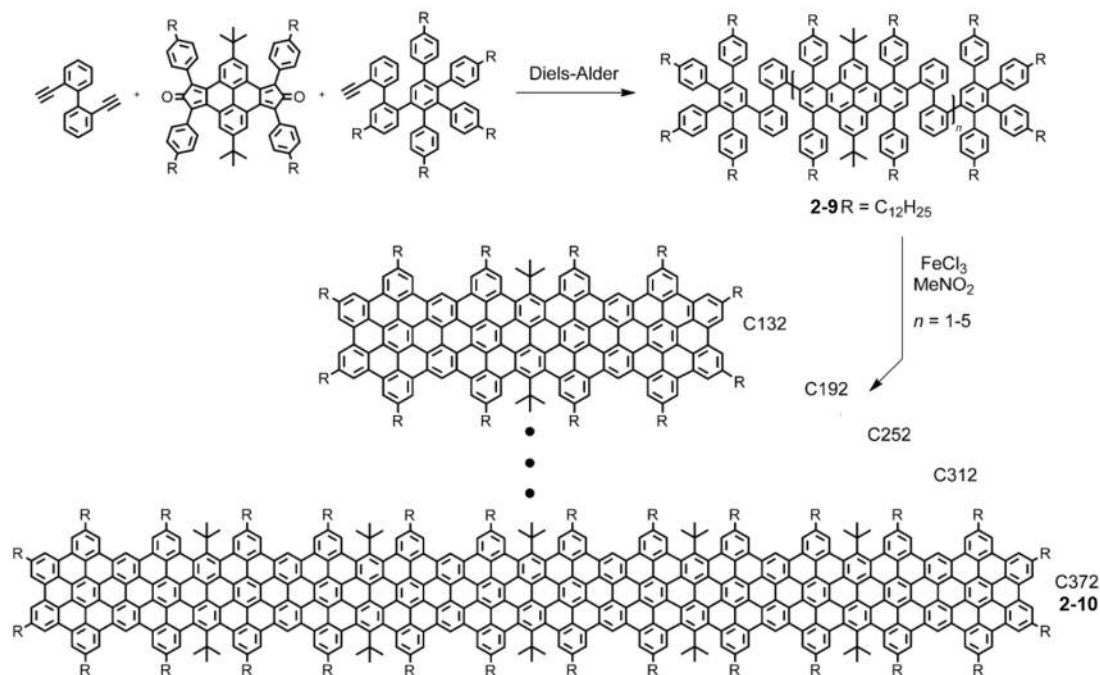
Polyphenylenes dendrimers (PPDs) have been extensively used as chemical precursors for the bottom-up design of graphitic nanostructures.^{19–21} In particular, the rational synthetic design of PPDs can lead to the formation of polycyclic aromatic hydrocarbons (PAHs) with atomic precision through a chemical graphitisation. The graphitisation was described by Müllen as the transformation of a 3D polyphenylene precursor into the corresponding 2D rigid and planar graphitic structure by intramolecular cyclodehydrogenation reaction.²² For

instance, he reported in 1997 the synthesis of extended PAHs **2-8** starting from polyphenylene **2-7** through intramolecular Scholl reaction in the presence of $\text{CuCl}_2/\text{AlCl}_3$ (Scheme 2.1).²³



Scheme 2.1. Synthesis of PAH **2-8** starting from polyphenylene dendrimer **2-7**.²³

In 2012, the same group described the synthesis of five linear polyphenylenes, owing a rigid dibenzo[*e,l*]pyrene core as repeating unit, which were prepared through a stoichiometrically controlled Diels-Alder cycloaddition reaction (Scheme 2.2).²² The obtained polyphenylene precursors **2-9** range from 132 ($n = 1$) to 372 ($n = 5$) carbon atom in the aromatic skeleton, underwent to chemical graphitisation in the presence of FeCl_3 , affording the corresponding graphene nanoribbons **2-10**.



Scheme 2.2. Synthesis of monodisperse polyphenylenes **2-9** and subsequent cyclodehydrogenated graphene nanoribbons **2-10**.²²

Inspired by this approach, the synthetic design of hybrid polyphenylenes bearing borazine units placed in selected positions appears as the natural direction for the preparation of BN-doped nano-graphenes with atomic precision (Figure 2.10). Taking this into consideration, Müllen's pioneering approach²³ for the preparation of polyphenylenes through cycloaddition reactions, could also lead to branched borazine-doped polyphenylene.

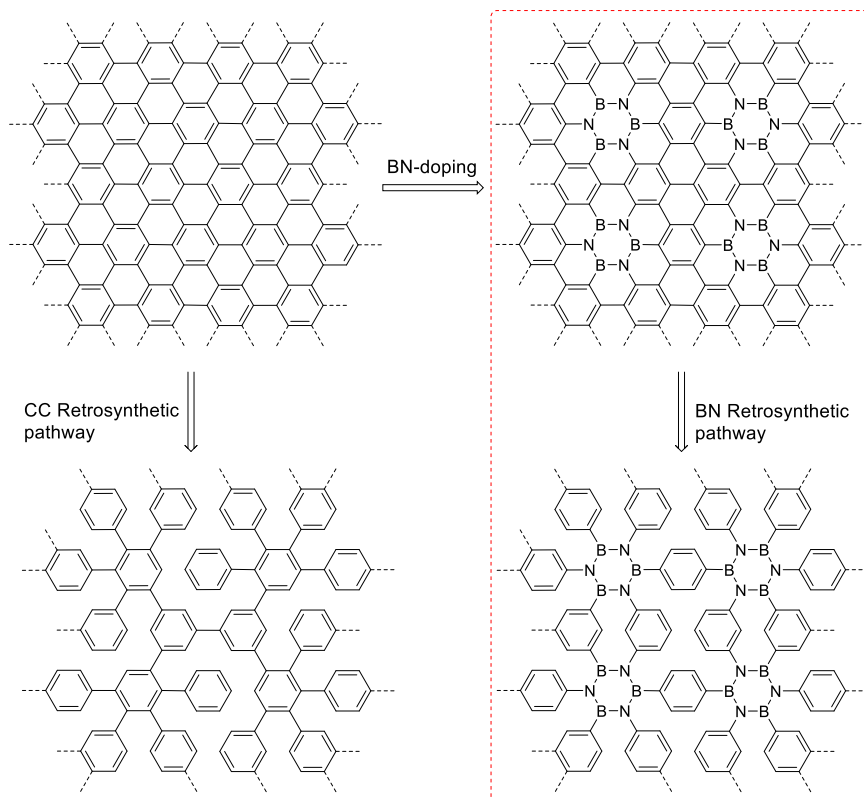
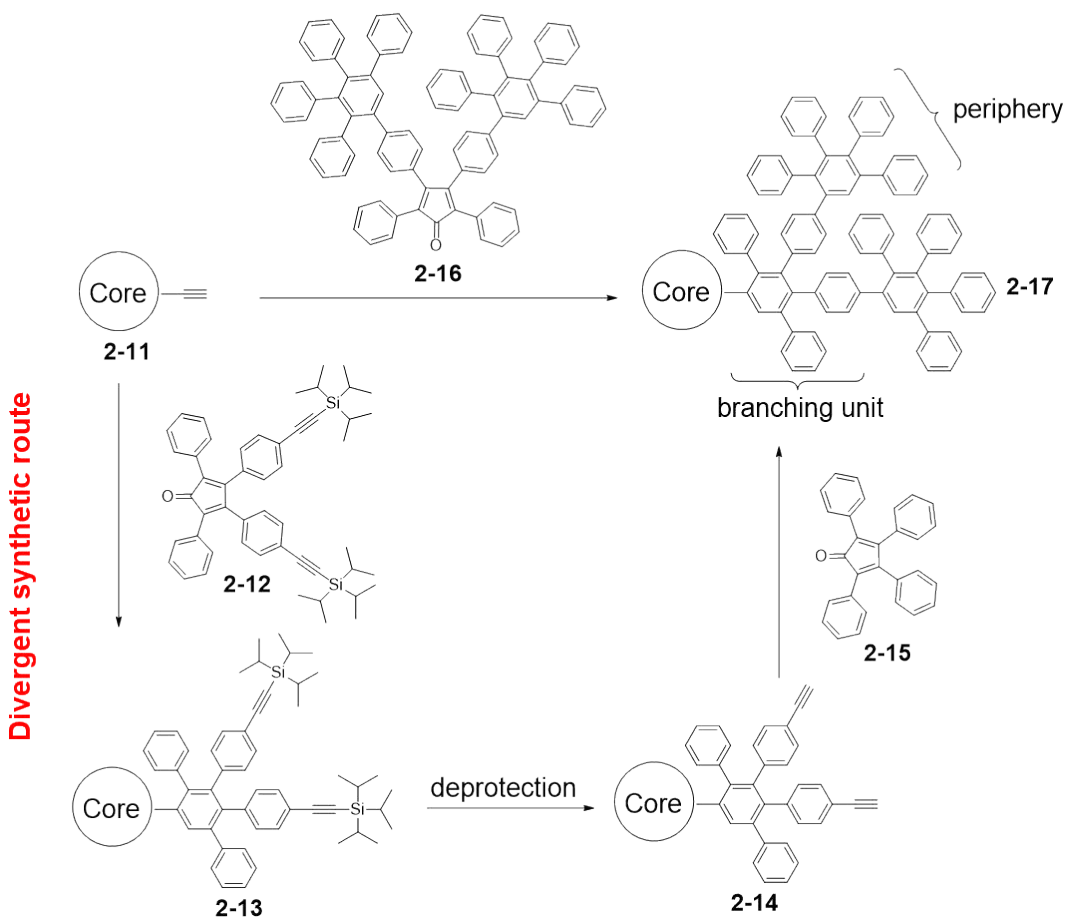


Figure 2.10. Schematic representation of the retrosynthetic pathways of PAHs and BN doped PAHs.

The two main approaches for the synthesis of polyphenylene dendrimers are shown in the Scheme 2.3. Both routes utilize decarbonylative Diels–Alder cycloadditions reaction of cyclopentadienones to alkynes. In the divergent approach the branching units are grown outwards from the core in an iterative manner. By addition of silyl-protected cyclopentadienone **2-12** to core derivative **2-11**, **2-13** can be obtained, then followed by deprotection and addition of second cyclopentadienone **2-15**, dendrimer **2-17** can be formed. On the other hand, in the convergent approach ethynyl-substituted core **2-11** can be reacted with a cyclopentadienone **2-16**, already branched, to make **2-17** directly.

Convergent synthetic route

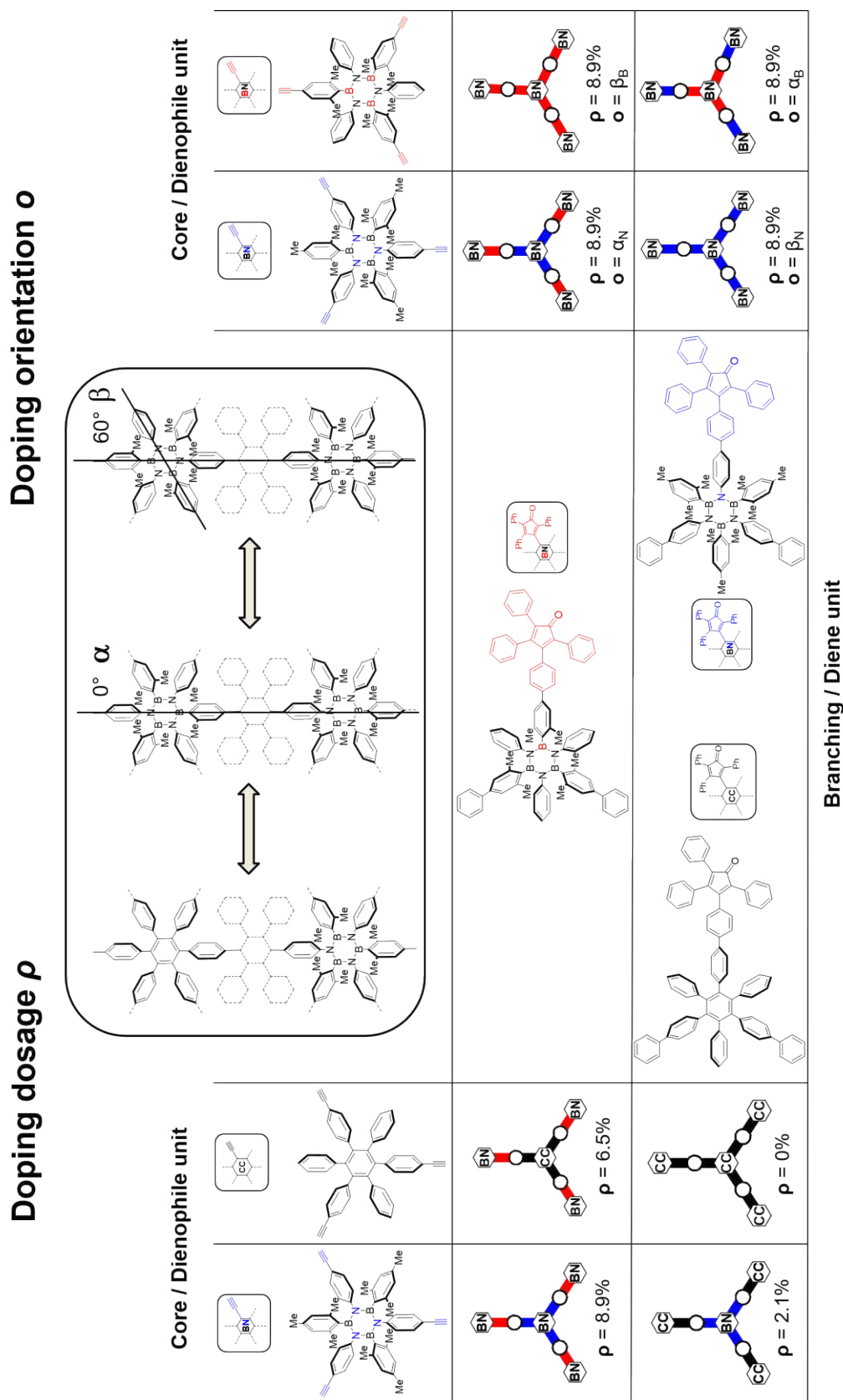


Scheme 2.3. Convergent (top) and divergent (left) approaches towards the synthesis of polyphenylene dendrimers.

2.4 Aim of the project – borazine doped polyphenylenes

Following the divergent synthetic route, and taking advantage of decarbonylative Diels-Alder cycloaddition reaction, boron-nitrogen-carbon (BNC) polyphenylenes from reactive borazine modules alternatively functionalised with peripheral ethynyl or tetraphenylcyclopentadienone groups, can be designed. In this respect, two main classes of compound will be synthesized: the core (dienophile) and the branching (diene) units (Figure 2.11). The cores bear ethynyl moieties, whereas the branching units expose tetraphenylcyclopentadienone. Having the possibility of introducing borazine units in different ratios, orientations, and positions, two different doping parameters should be considered when replacing benzene units with the borazine analogues (Figure 2.11): the doping dosage (ρ) and the doping orientation (θ). The doping dosage ρ is defined as the

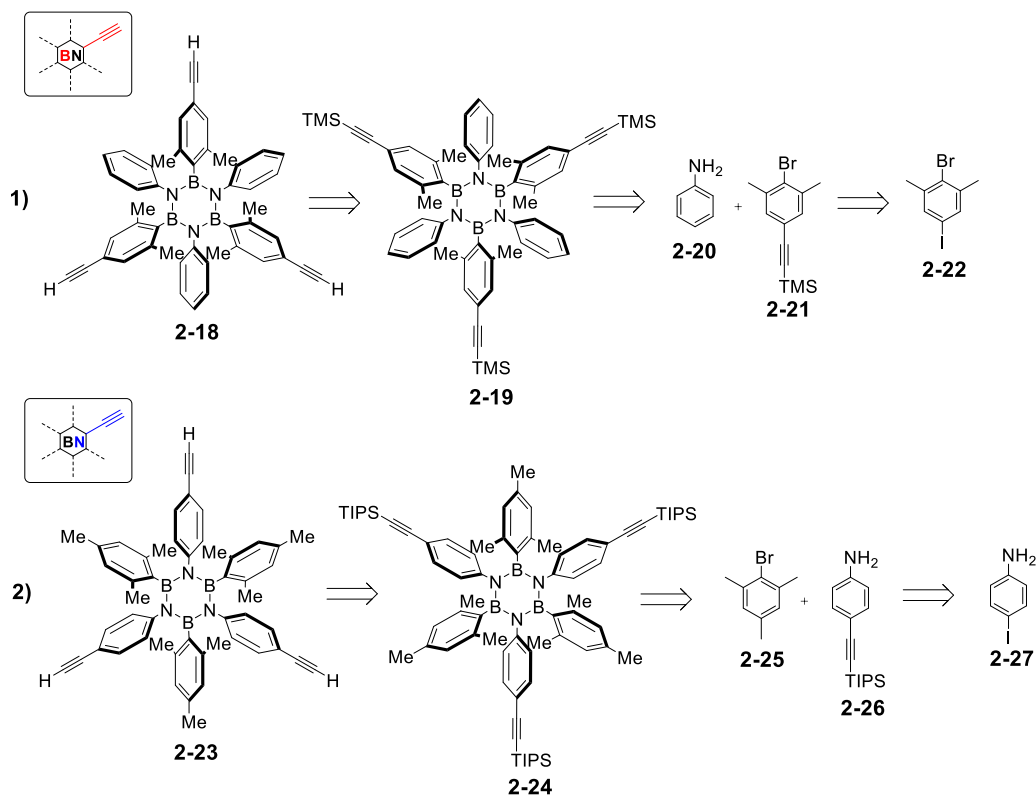
percentage of the aryl units that have been substituted with the borazine analogues. Hence, by a careful selection of the core and branching units, we have envisaged to prepare eight different three-branched polyphenylenes with a progressive replacement of aryl rings with B_3N_3 , moving from $\rho = 0\%$ (full-carbon polyphenylene) to $\rho = 8.9\%$ (three-branched polyphenylene in which four aryl units have been substituted with the borazine analogues). Moreover, owing to the possibility of functionalizing the core and the branching borazine units with different aryl groups at the N and B atoms (highlighted in blue and red, respectively, Figure 2.11), different doping orientation \boldsymbol{o} can be achieved. The doping orientation \boldsymbol{o} defines the relative orientations between the doping borazine rings. The \boldsymbol{o} descriptor is α when the BN ring placed on the periphery of the polyphenylene displays the same orientation as that of the borazine ring placed on the core, otherwise β when rotated of 60° (Figure 2.11). In this way, the three-branched polyphenylene bearing four borazine scaffolds will be depicted as \boldsymbol{o}_N (β_N or α_N) and \boldsymbol{o}_B (β_B or α_B) when describing the branching borazine units (with the 60° or 0° orientation, respectively) at the N and B positions in respect to the borazine core (Figure 2.11). Taken all together, the two descriptors ρ , and \boldsymbol{o} allow the precise description of the borazine-doping pattern of any polyphenylene. Depending on the chemical nature of the central aromatic module and of the reactive group, each covalent combination of the modules yields one exclusive doping pattern featuring controlled doping dosages and orientations.



2.5 Results and discussion

2.5.1 Synthesis of borazine-derived ethynyl core modules

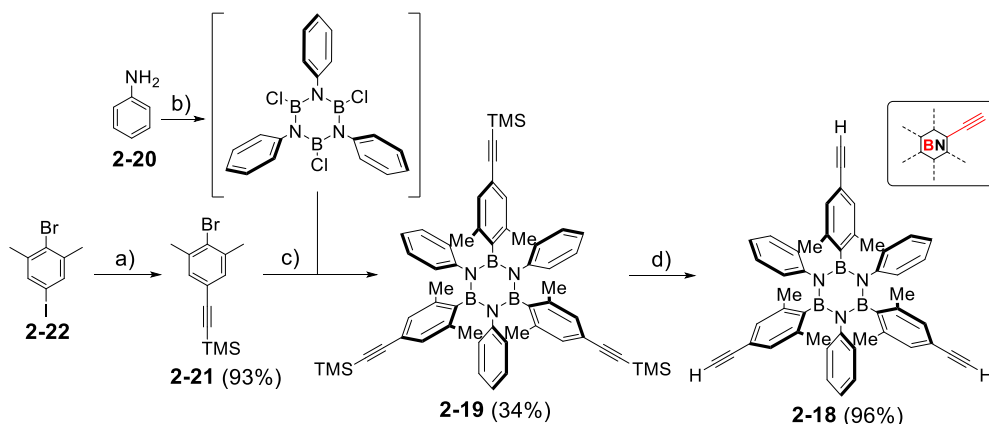
The retrosynthetic strategy for the preparation of borazine core units **2-18** and **2-23**, functionalised with peripheral ethynyl groups on the aryl substituents at the *B* and *N* atoms, respectively, is shown in Scheme 2.4. Since the synthesis of borazines requires BCl_3 and ArLi reagents, the ethynyl groups must be protected with trimethylsilyl (TMS) or triisopropylsilyl groups (TIPS) during the formation of borazine ring (**2-19** and **2-24**). Finally, borazine derivative **2-19** and **2-24** could be obtained starting from bromoarene derivative (**2-25** and **2-21**), and aniline derivatives (aniline **2-20** and **2-26**), following the synthetic protocol proposed in *section 1.3.3*.



Scheme 2.4. Retrosynthetic pathway of borazine-based core modules **2-18** and **2-23**.

As previously discussed in *section 1.3*, the borazine ring is sensitive to acids and oxidisers, without proper electronic or steric protection provided by its inner shell. Hence, we envisage to build the borazine ring from bromoarene derivatives bearing two methyl groups as protecting group of the boron atoms. For the core aryl-substituted borazine **2-18**, in the first

synthetic step, the synthesis started with Sonogashira cross coupling reaction between 2,6-dimethyl-4-iodo-bromobenzene **2-22** and trimethylsilylacetylene (TMSA), affording **2-21** TMS protected ethynyl group in 93% yield (Scheme 2.5). For the formation of the borazine ring, aniline was reacted with BCl_3 under refluxing conditions to give intermediate *B*-trichloro-*N*-triphenylborazine. Upon subsequent treatment with TMS-protected aryl-lithium derivative **2-21**, it was converted into borazine core **2-19** in 34% yield (Scheme 2.5). Deprotection of compound **2-19** with TBAF yields borazines **2-18**, exposing terminal phenylacetylene moieties at the *B*-sites.



Scheme 2.5. Synthesis of borazine-based core module **2-18**. Reagent conditions: a) trimethylsilylacetylene (TMSA), $[\text{PdCl}_2(\text{PPh}_3)_2]$, CuI, diisopropylamine, r.t., 16 h; b) BCl_3 , toluene, reflux, 24 h; c) *t*BuLi, THF, -84°C , 16 h; d) tetrabutylammonium fluoride (TBAF), THF, 0°C , 1 h.

To confirm the chemical identity of borazines **2-19** and **2-18**, single crystals suitable for X-ray diffraction analysis were obtained by slow diffusion of MeOH in CH_2Cl_2 .

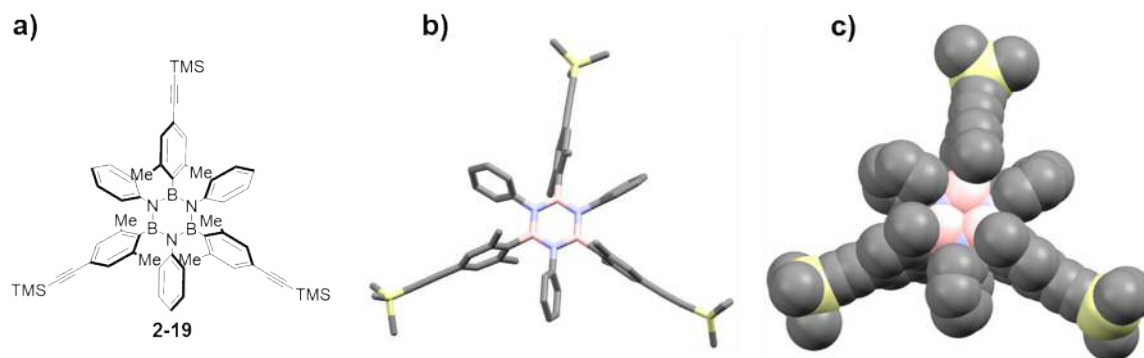


Figure 2.12. Crystal structure of borazine derivative **2-19**; a) molecular structure; b) crystal structure represented in capped sticks; c) crystal structure represented in spacefill. Space group: P-1. The crystal structure was grown by slow diffusion of MeOH in CH_2Cl_2 . Colour code: grey: C, pink: B, blue: N and yellow: Si. Hydrogen atoms were omitted for the sake of clarity.

The crystal structure clearly show that the boron atoms are sterically protected by the presence of the *ortho*-methyl substituents.

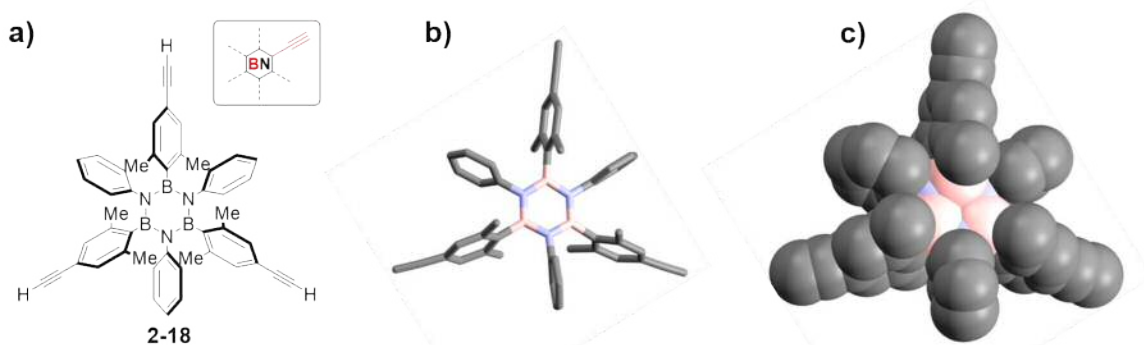
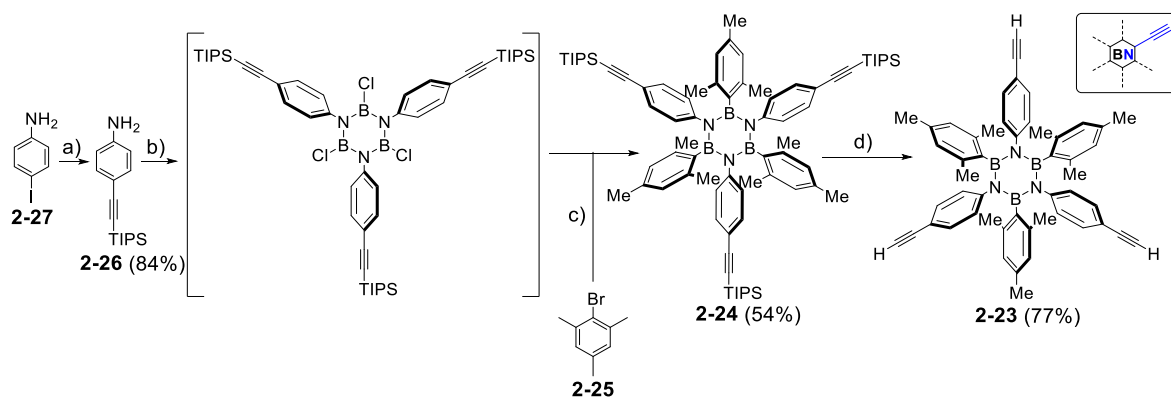


Figure 2.13. Crystal structure of borazine core module **2-18**; a) molecular structure; b) crystal structure represented in capped sticks; c) crystal structure represented in spacefill. Space group: P-1. The crystal structure was grown by slow diffusion of MeOH in CH₂Cl₂. Colour code: grey: C, pink: B and blue: N. Hydrogen atoms were omitted for the sake of clarity.;

Core aryl-substituted borazine **2-23**, exposing terminal phenylacetylene moieties at the *N*-sites has been synthesized following the synthetic procedure depicted in Scheme 2.6. TIPS protected aniline **2-26** was prepared starting from 4-iodo aniline **2-27** through Sonogashira cross coupling reaction in 84% yield. Reaction of compound **2-26** with BCl₃ under refluxing conditions, gave intermediate TIPS-protected B-trichloro-*N*-triphenylborazine, which was reacted with mesityl-lithium (MesLi), affording borazine core **2-24** in 54% yield (Scheme 2.6). Removal of the TIPS protecting group with TBAF yields borazines **2-23** bearing the ethynyl groups on the aryl substituents at the *N* atoms in 77% yield.



Scheme 2.6. Synthesis of borazine-based core modules **2-23**. Reagent conditions: a) triisopropylsilylacetylene, [PdCl₂(PPh₃)₂], CuI, diisopropylamine, r.t., 16 h; b) BCl₃, toluene, reflux, 18 h; c) *t*BuLi, THF, -84 °C, 16 h; d) TBAF, THF, 0 °C, 2 h.

The $^1\text{H-NMR}$ spectrum of borazine core module **2-23** in CDCl_3 is detailed in Figure 2.14. In the aromatic region, two doublets *a* and *b* at 6.91 and 6.72 ppm can be assigned to the 12 phenyl hydrogen atoms at the *N*-sites with the same *ortho* coupling constant of 8 Hz. One singlet *c* at 6.34 ppm is related to the 6 phenyl hydrogen atoms at the *B*-sites. In the aliphatic region, the singlet *d* at 2.89 ppm can be assigned to the ethynyl hydrogen atoms and the two singlets *e* and *f* at 2.16 and 2.01 ppm, respectively, corresponds to the methyl groups of the mesityl groups.

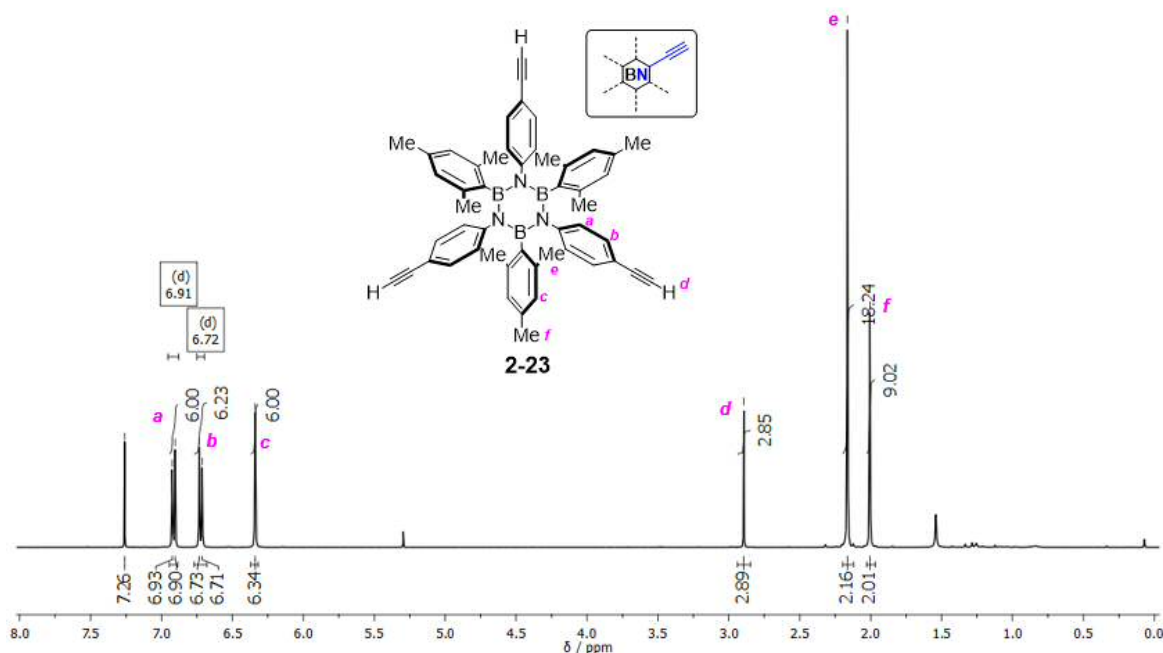
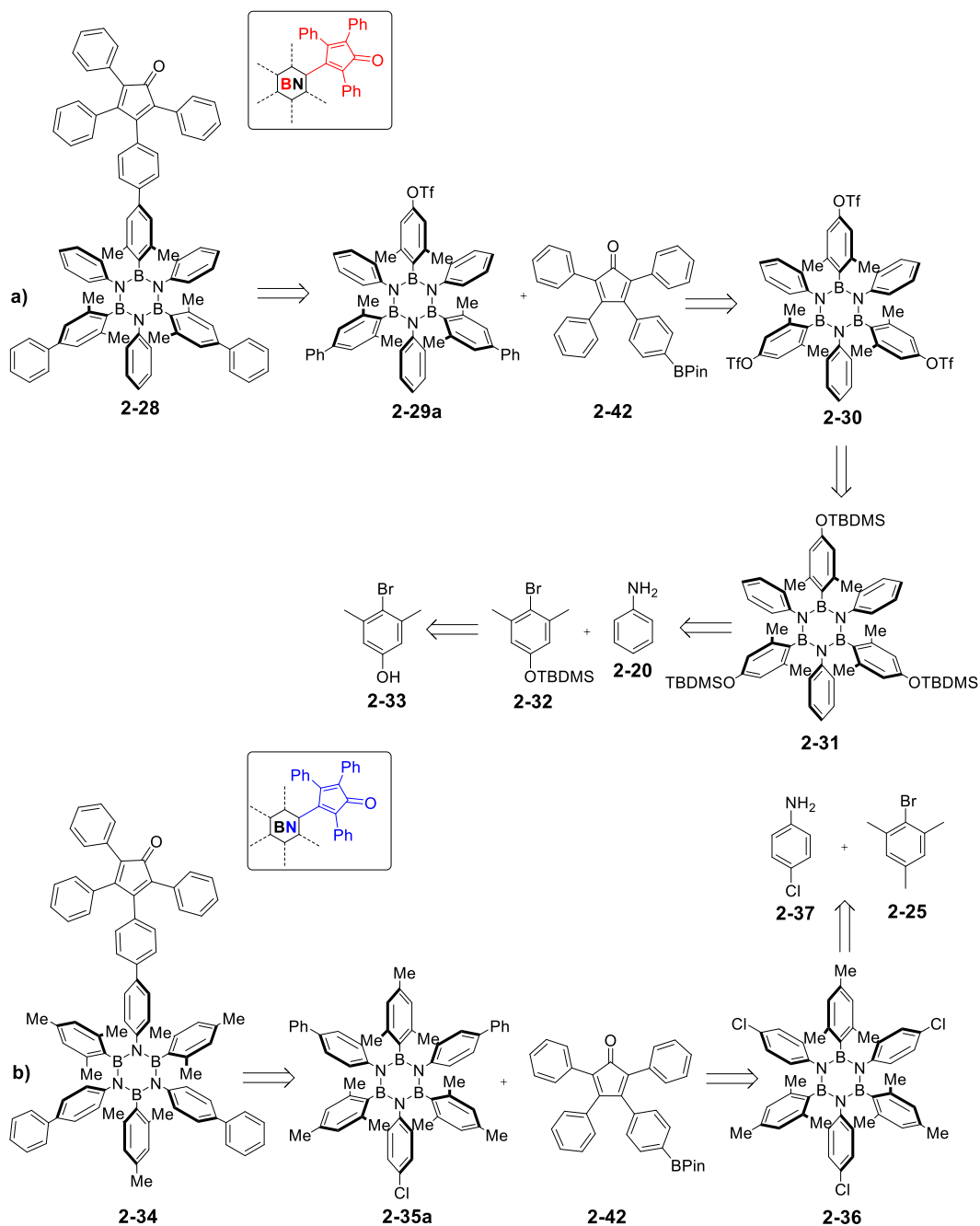


Figure 2.14. 400 MHz $^1\text{H-NMR}$ of borazine branching module **2-23** in CDCl_3 (Solvent residual peak: 7.26 ppm).

2.5.2 Synthesis of borazine-derived cyclopenta-2,4-dienone branching modules

The retrosynthetic strategy chosen to prepare the borazine branching units containing the cyclopenta-2,4-dienone on the aryl substituents at the *B* atoms (**2-28**, highlighted in red) and *N* atoms (**2-34**, highlighted in blue), is shown in Scheme 2.7. We conjectured that borazine branching scaffolds might be easily obtained from Suzuki cross-coupling reaction between organoboron derivative **2-42** and a borazine exposing a suitable aryl halide or related electrophile (*i.e.*, ArOTf) at either the *B* (**2-29a**) or *N* (**2-35a**) sites. The latter were both obtained through a controlled stepwise Suzuki cross-coupling reaction starting from borazine **2-30** and **2-36**, respectively. Finally, borazine derivatives **2-30** and **2-36** could be

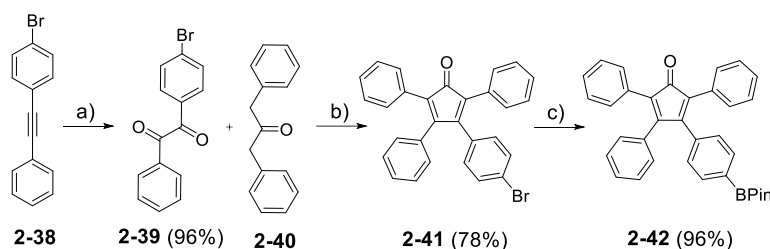
prepared starting from bromoaryl derivatives (**2-32** and **2-25**, respectively), and aniline derivatives (**2-20** and **2-37**, respectively).



Scheme 2.7. Retrosynthetic pathway of borazine derived cyclopenta-2,4-dienone branching units **2-28** and **2-34**.

Before starting with the synthesis of the branching units, we performed the preparation of tetraphenylcyclopentadienone pinacolate derivative **2-42** as described in Scheme **2.8**. The

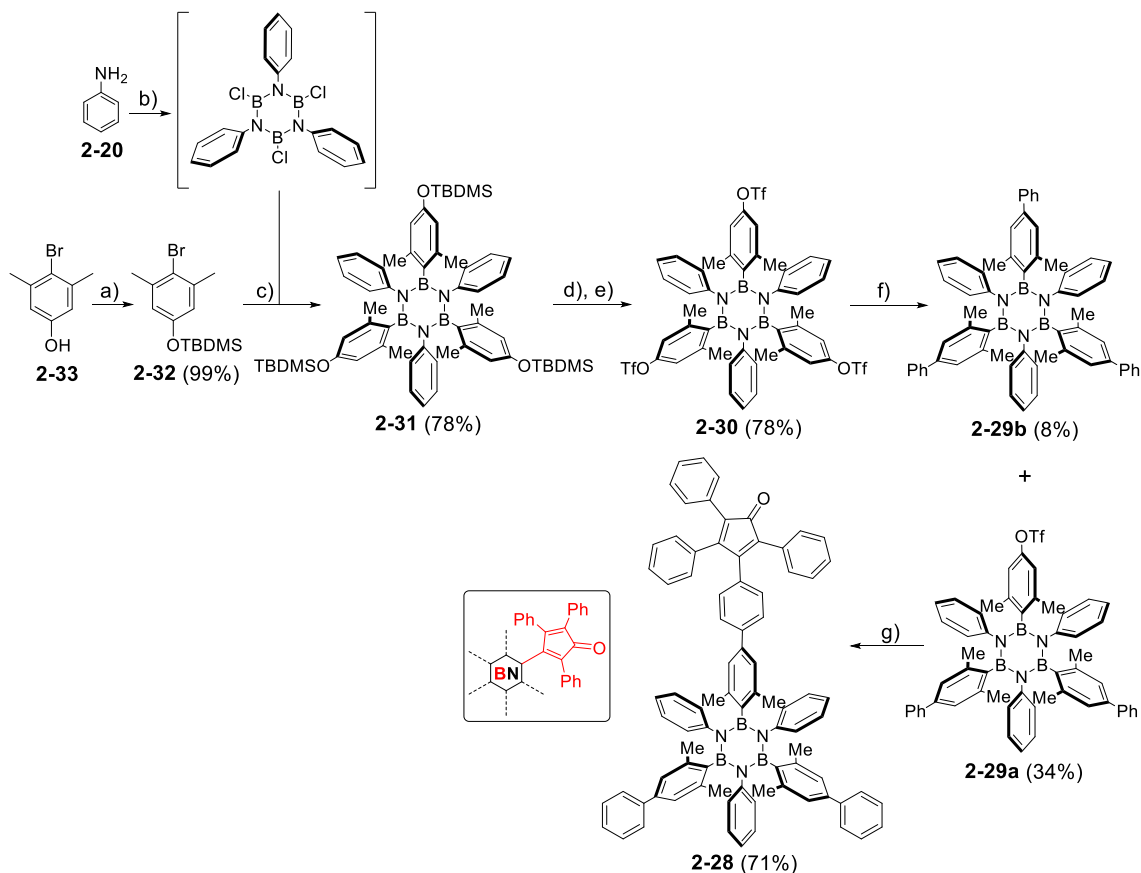
first synthetic step involved an oxidation reaction of **2-38** in the presence of KMnO_4 , affording **2-39** in 96%. Furthermore, the second step was a condensation reaction where diphenylketone **2-40** was reacted as nucleophile partner. As result, compound **2-41** was isolated in 78% yield. Finally, bromotetracyclone derivative **2-41** was successfully converted to the corresponding pinacolate moiety **2-42** through a Miyaura borylation in 96% yield.



Scheme 2.8. Synthesis of tetraphenylcyclopentadienone pinacolate derivative **2-42**. Reagent conditions: a) KMnO_4 , acetic acid, acetone, r.t., 24 h; b) KOH , EtOH , reflux, 20 min; c) bis(pinacolato)diborane, $[\text{Pd}(\text{dppf})\text{Cl}_2]$, KOAc , DMF , 80°C , 16 h.

Having in hand diene scaffold **2-42**, we moved on the synthesis of the electrophilic borazine partners to be reacted in the final Suzuki cross-coupling reaction (Scheme **2.9**). Hence, the first step involved a nucleophilic attack of **2-33** to *t*-butyl-dimethyl-silylchloride (TBDMS-Cl) in the presence of imidazole, yielding derivative **2-32** in 99%. The idea behind the choice of TBDMS as protecting group, was to prepare an aryl halide derivative bearing a functional group (-OH protected), able not only to be easily converted into suitable electrophile for the Suzuki cross coupling reaction, but also to be stable under the reaction conditions adopted for formation of the borazine ring. Furthermore, **2-20** was reacted with BCl_3 under refluxing conditions of toluene to give intermediate *B*-trichloro-*N*-triphenylborazine, which was reacted with TBDMS-protected aryllithium derivative **2-32**, affording TBDMS-protected borazine **2-31** in 78% yield. Through the removal of the TBDMS protecting group with tetrabutylammoniumfluoride (TBAF) and subsequent esterification reaction with Tf_2O in pyridine, borazine **2-31** was converted into tris(triflate)-substituted borazine **2-30** in 78% yield. Suzuki cross-coupling between molecule **2-30** and phenylboronic acid (1.8 eq.) led to diphenyl- and triphenyl-substituted borazine derivatives **2-29a** and **2-29b** (compound **2.29b** will be used as borazine reference to evaluate the photophysical properties of the BN doped polyphenylenes, see *section 2.5.7*) in 39% and 8% yields, respectively. Final Suzuki cross-coupling reaction between monotriflate-

substituted borazine **2-29a** and cyclopenta-2,4- dienone-derived boronic ester **2-42** gave targeted borazine derived **2-28** in 71% yield (Scheme 2.9).



Scheme 2.9. Syntheses of borazine branching derivative **2-28**. Reagent conditions: a) tert-butyl-dimethylsilylchloride, imidazole, DMF, 75 °C, 16 h; b) BCl_3 , toluene, reflux, 18 h; c) tBuLi , THF, -84 °C, 2 h; d) TBAF, THF, 0 °C, 2 h; e) trifluoromethanesulfonic anhydride (Tf_2O), pyridine, r.t., 16 h; f) PhB(OH)_2 , $[\text{Pd}(\text{PPh}_3)_4]$, K_2CO_3 , dioxane/ H_2O (5:1), 105 °C, 15 h; g) **2-42**, $[\text{Pd}(\text{PPh}_3)_4]$, K_2CO_3 , dioxane/ H_2O (5:1), 105 °C, 15 h.

Suitable single crystals of borazine derivatives **2-31**, **2-30** and branching module **2-28** were obtained by slow diffusion of MeOH in CHCl_3 and analysed through X-ray diffraction (Figures 2.15, 2.16 and 2.17).

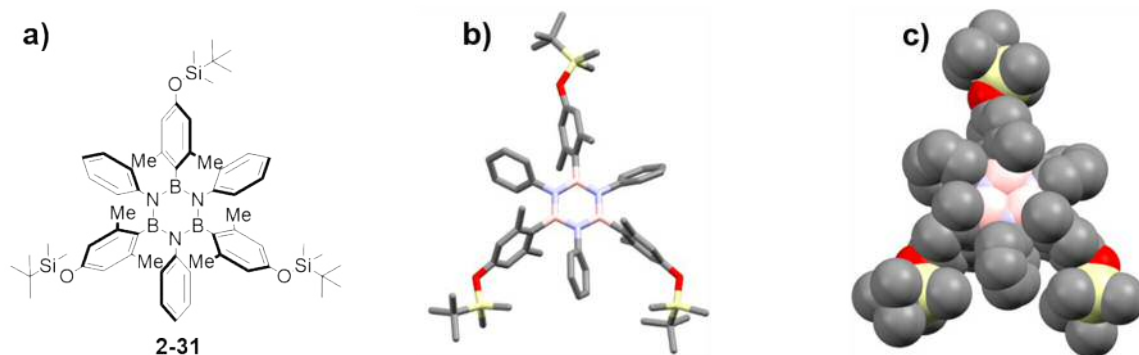


Figure 2.15. Crystal structure of borazine derivative **2-31**; a) molecular structure; b) crystal structure represented in capped sticks; c) crystal structure represented in spacefill. Space group: P-1. The crystal structure was grown by slow diffusion of MeOH in CHCl_3 . Colour code: grey: C, pink: B, blue: N, yellow: Si and red: O. Hydrogen atoms were omitted for the sake of clarity.

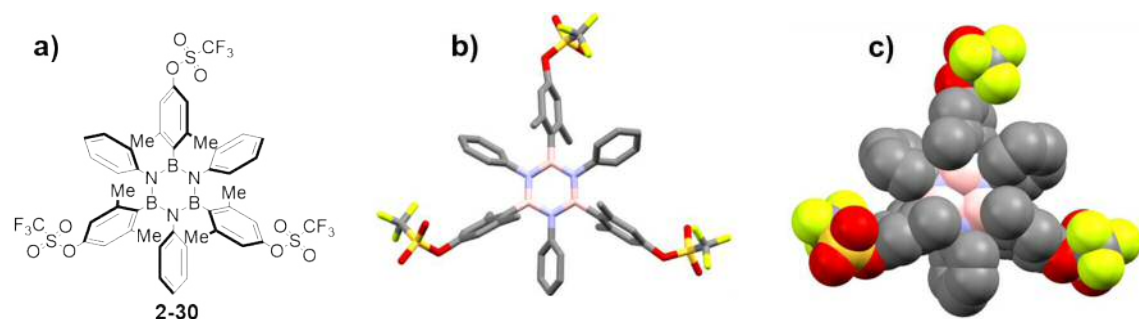


Figure 2.16. Crystal structure of borazine **2-30**; a) molecular structure; b) crystal structure represented in capped sticks; c) crystal structure represented in spacefill. Space group: $P2_1/n$. The crystal structure was grown by slow diffusion of MeOH in CHCl_3 . Colour code: grey: C, pink: B, blue: N, orange: S, green: F and red: O. Hydrogen atoms were omitted for the sake of clarity.

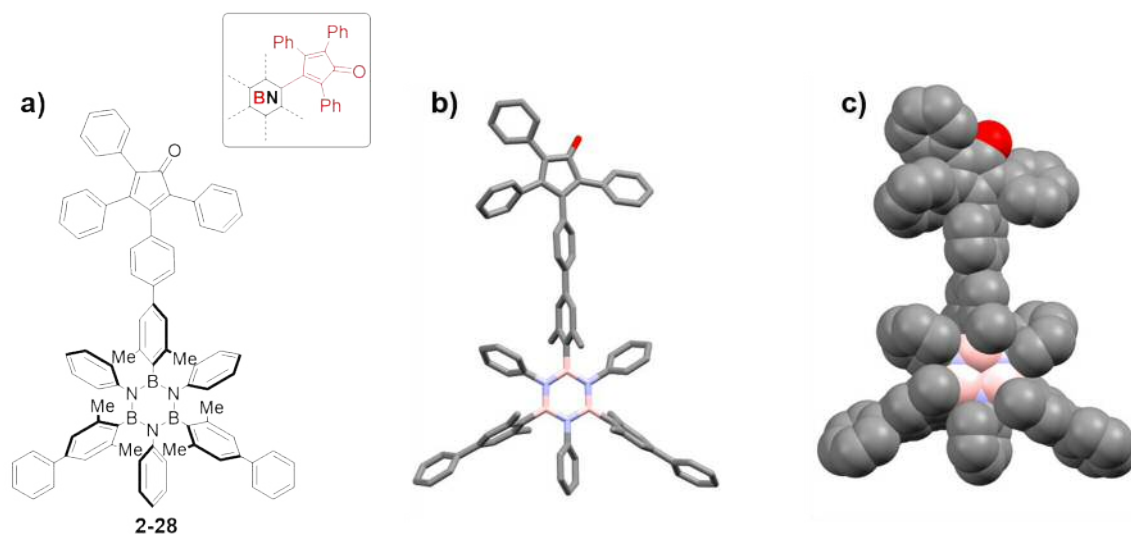
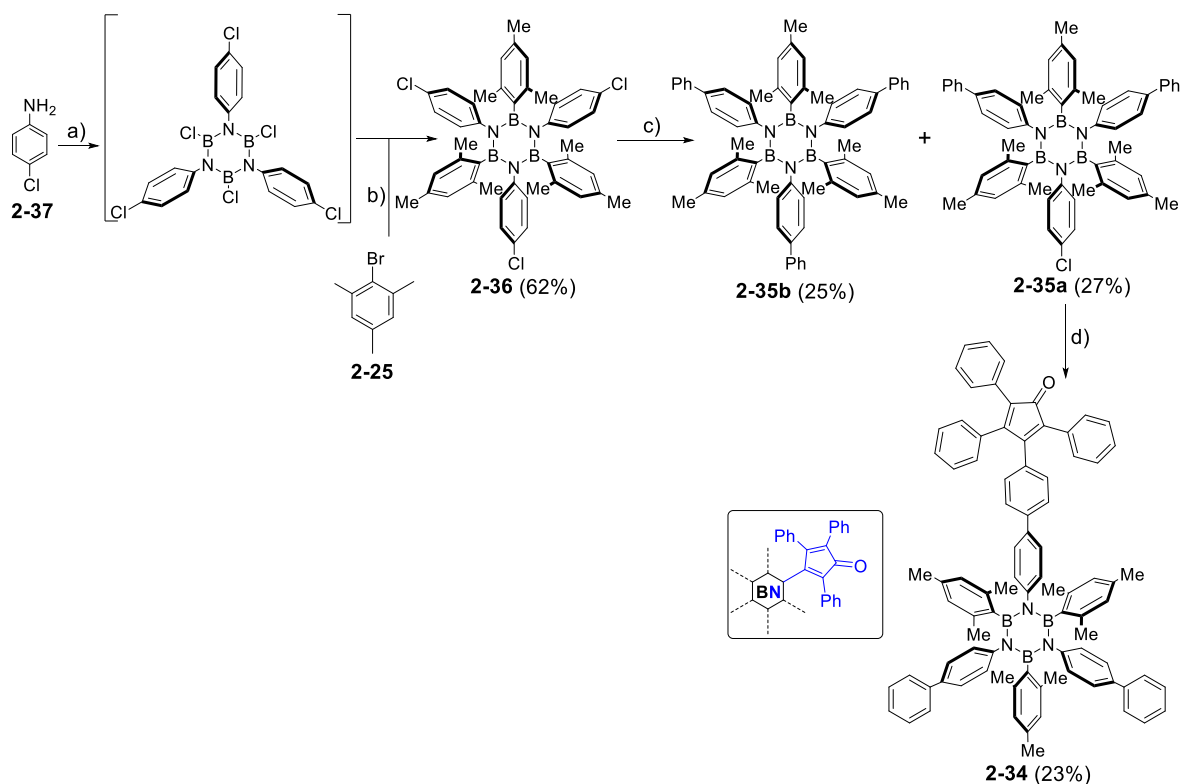


Figure 2.17. Crystal structure of borazine **2-28**; a) molecular structure; b) crystal structure represented in capped sticks; c) crystal structure represented in spacefill. Space group: P-1. The crystal structure was grown by slow diffusion of MeOH in CHCl_3 . Colour code: grey: C, pink: B, blue: N and red: O. Hydrogen atoms were omitted for the sake of clarity.

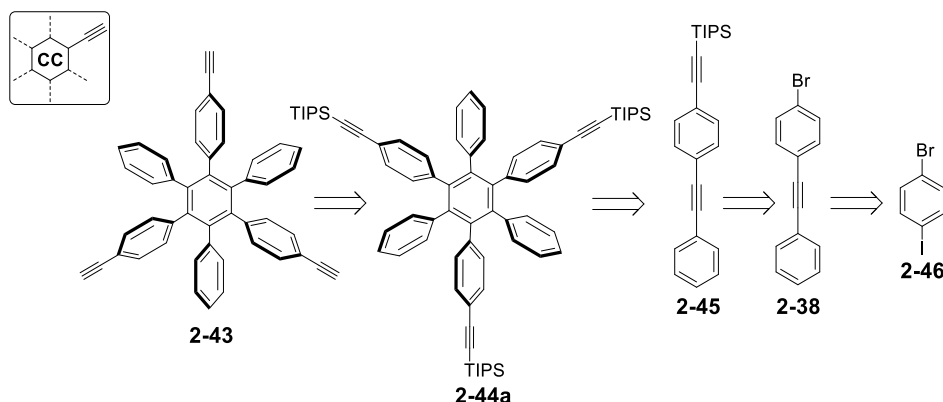
Moving on the synthesis of branching module **2-34**, due to the reactivity TBDMS protecting group under the acidic BCl_3 conditions, a different synthetic strategy was undertaken to introduce a suitable electrophile at the *N*-atoms of the borazine ring. Following these considerations, trichloro-substituted borazine **2-39** was first synthesised in 62% yield starting from 4-chloroaniline **2-37** following the BCl_3 route (Scheme **2.10**). Similarly to the synthetic strategy adopted for borazines **2-29a** and **2-29b**, Suzuki cross-coupling reactions between phenylboronic acid (2.2 eq.) and borazine **2-36** led to diphenyl and triphenyl derivatives **2-35a** and **2-35b** (the compound **2.35b** will be used as borazine reference in to evaluate the photophysical properties of the BN doped polyphenylenes, see *section 2.5.7*) in 27% and 25% yields, respectively. Final grafting of cyclopenta-2,4-dienone-derived functionality was performed through successive Suzuki cross-coupling reactions between boronic ester **2-42** and borazine monochloride **2-35a**, affording target molecule **2-34** bearing a cyclopenta-2,4-dienyl group on the *N*-aryl substituent.



Scheme 2.10. Synthesis of borazine branching derived **2-34**. Reagent conditions: a) BCl_3 , toluene, reflux, 18 h; b) tBuLi , THF, $-84\text{ }^\circ\text{C}$, 16 h; c) PhB(OH)_2 , $[\text{Pd}_2(\text{dba})_3]$, K_3PO_4 , dioxane/ H_2O (5:1), $150\text{ }^\circ\text{C}$, 16 h; d) **2-42**, $[\text{Pd}(\text{PPh}_3)_4]$, K_2CO_3 , dioxane/ H_2O (5:1), $150\text{ }^\circ\text{C}$, 20 h.

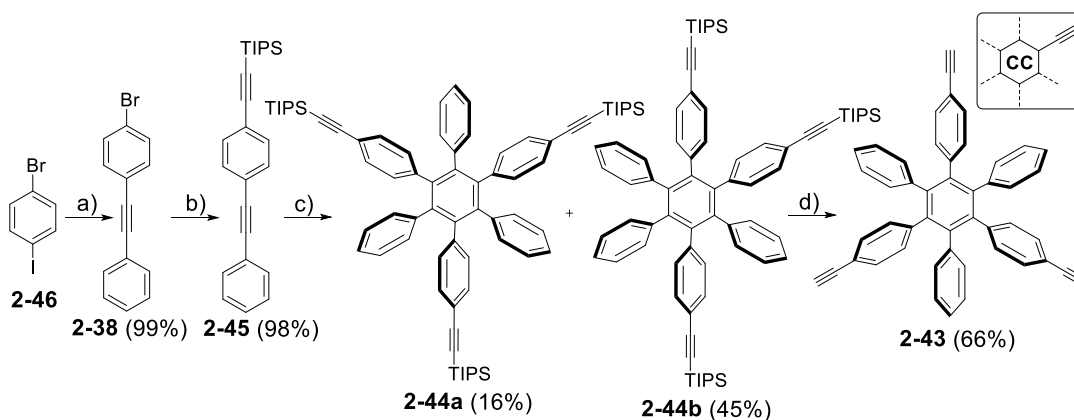
2.5.3 Synthesis of carbon core module

The retrosynthetic pathway for full-carbon core module **2-43** is outlined in Scheme 2.11. The target molecule could be obtained by deprotection of TIPS analogue derivative **2-44a**, being formed through a cyclotrimerisation reaction of **2-45** catalysed by $[\text{Co}_2(\text{CO})_8]$. The choice of the TIPS as protecting groups was driven by the steric hindrance of the silyl moiety, which does not allow the reaction between the external ethynyl groups TIPS protected and $[\text{Co}_2(\text{CO})_8]$ catalyst. Finally, *sp-sp*² cross-coupling reaction will allow the formation of derivative **2-45** from compound **2-46**.



Scheme 2.11. Retrosynthetic pathway of the carbon core module **2-43**.

For the synthesis of full-carbon modules **2-43**, in the first synthetic step, the synthesis commenced with Sonogashira cross-coupling reaction between 4-iodo-bromobenzene **2-46** and phenylacetylene in the presence of $[\text{PdCl}_2(\text{PPh}_3)_2]$, affording **2-38** derivative in 99% yield (Scheme 2.12).



Scheme 2.12. Syntheses of the carbon core modules **2-43**. Reagent conditions: a) Phenylacetylene, $[\text{PdCl}_2(\text{PPh}_3)_2]$, CuI, diisopropylamine, r.t., 16 h; b) triisopropylsilylacetylene, $[\text{PdCl}_2(\text{PPh}_3)_2]$, CuI, diisopropylamine, 70 °C., 16 h; c) $[\text{Co}_2(\text{CO})_8]$, dioxane, reflux, 18 h; d) TBAF, THF, 0 °C, 3 h.

Having in hand derivative **2-38**, a further Sonogashira cross-coupling reaction was performed in the presence of triisopropylsilylacetylene yielding **2-45** moieties as white solid in 98% yield. This was followed by Co-catalysed cyclotrimerisation²⁴ in which TIPS-protected diphenylacetylene **2-45** was reacted with $[\text{Co}_2(\text{CO})_8]$ in dioxane at 105 °C. The reaction gave a mixture of two regioisomers **2-44a** and **2-44b** which were separated by silica gel column chromatography. Interestingly, although the reaction gave the complete conversion of starting material **2-45**, the desired hexaphenylbenzene **2-44a** was isolated only in 16% yield whereas **2-44b** in 45% yield. This result could be explained following the mechanism proposed by C. Aubert and co-workers in 2007.²⁴ The cyclotrimerisation mechanism is [2+2+2] stepwise cycloaddition reaction, in which the statistical distribution of the products is observed. The ratio of the two regioisomers **2-44a** and **2-44b** is 1:3 in favour to the asymmetrical product **2-44b**. Finally, removal of the TIPS groups using TBAF gave tris(ethynylphenyl)triphenylbenzene **2-43** in 66% yield as white solid (Scheme 2.12). The ¹H-NMR spectrum of borazine branching unit **2-43** in CDCl_3 is detailed in Figure 2.16. It shows in the aromatic region the multiplet signals *a* and *b* between 7.01 and 6.76 ppm, which are related to the 24 phenyl hydrogen atoms. The singlet signal *c* at 2.93 ppm is attributed to the 3 ethynyl hydrogen atoms.

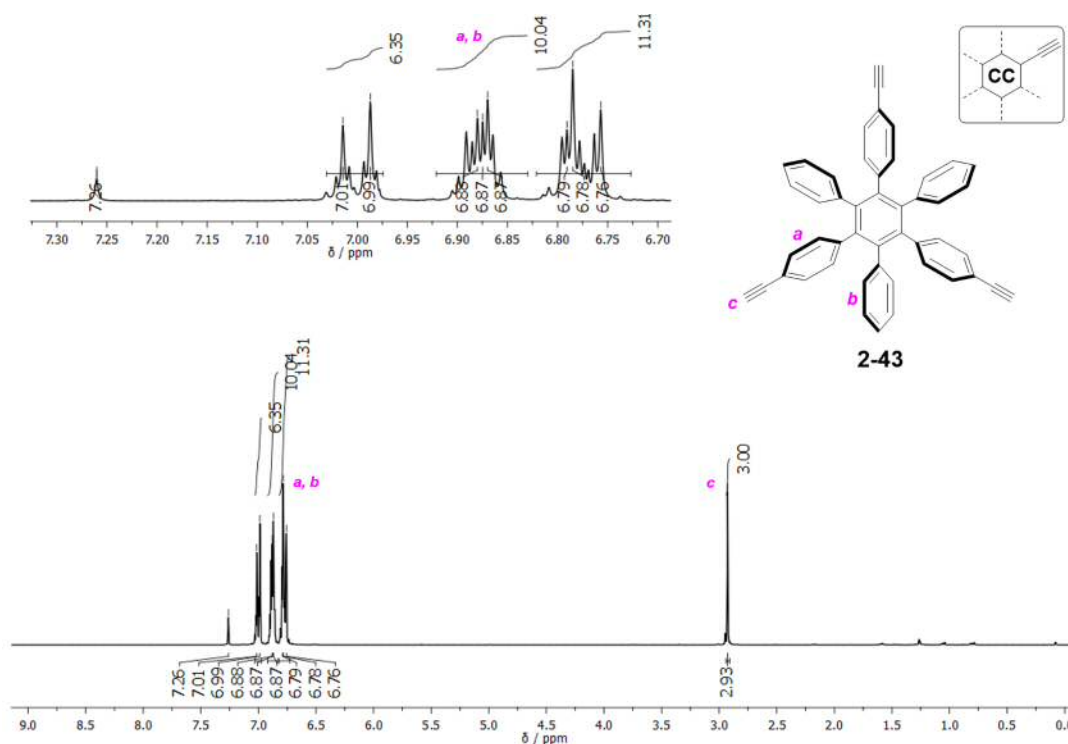
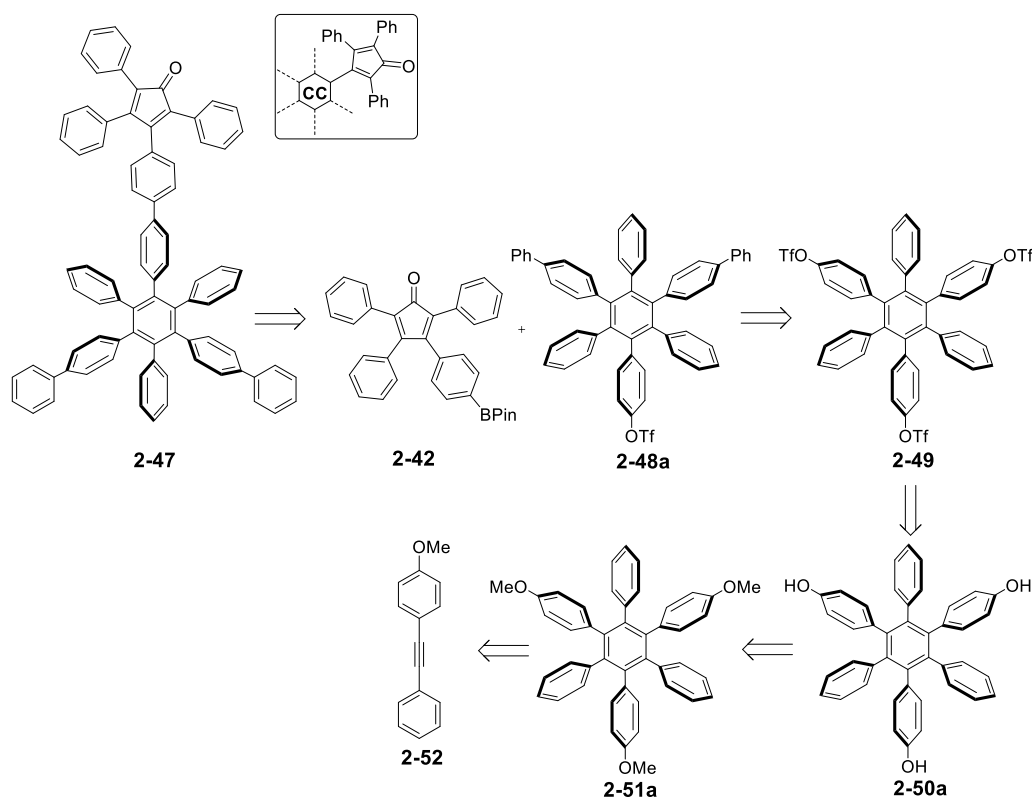


Figure 2.16. 400 MHz ¹H-NMR of borazine branching module **2-43** in CDCl_3 (Solvent residual peak: 7.26 ppm).

2.5.4 Synthesis of carbon branching module

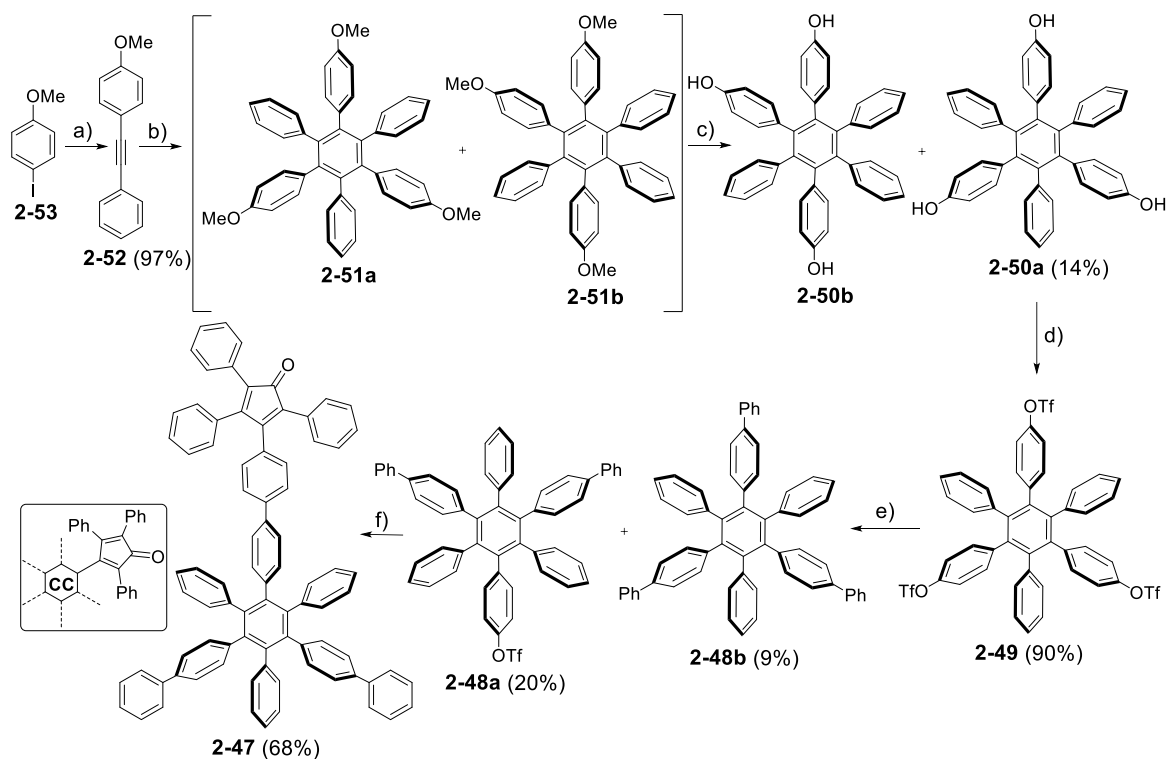
The full-carbon branching unit **2-47** bearing cyclopenta-2,4-dienone functional group can be obtained from Suzuki cross-coupling reaction between organoboron derivative **2-42** (previously synthesised, see *section 2.5.2*) and hexaphenylbenzene derivative exposing triflate groups (**2-48a**, Scheme **2.13**) as leaving groups. Compound **2-48a** can be prepared through a controlled stepwise Suzuki cross-coupling reaction starting from derivative **2-49**. Full-carbon triflate derivative **2-49** can be obtained by a functional group transformation of the corresponding hydroxy derivative **2-50a**, itself formed from a cyclotrimerisation of diphenylacetylene **2-52** [Co] catalysed and further deprotection of compound **2-51a**.



Scheme 2.13. Retrosynthetic pathway of the carbon branching module **2-47**.

For the preparation of full-carbon branching unit **2-47**, the synthesis commenced with Sonogashira cross-coupling reaction between phenylacetylene and **2-53**, yielding **2-52** in 97% (Scheme **2.14**). The following step was the cyclotrimerisation reaction of methoxydiphenylacetylene **2-52** in the presence of $[\text{Co}_2(\text{CO})_8]$ in dioxane, as described in the previous *section*, the mixture of two regioisomers **2-51a** and **2-51b** was observed. Taking into consideration that the purification of desired product **2-51a** was unfeasible due

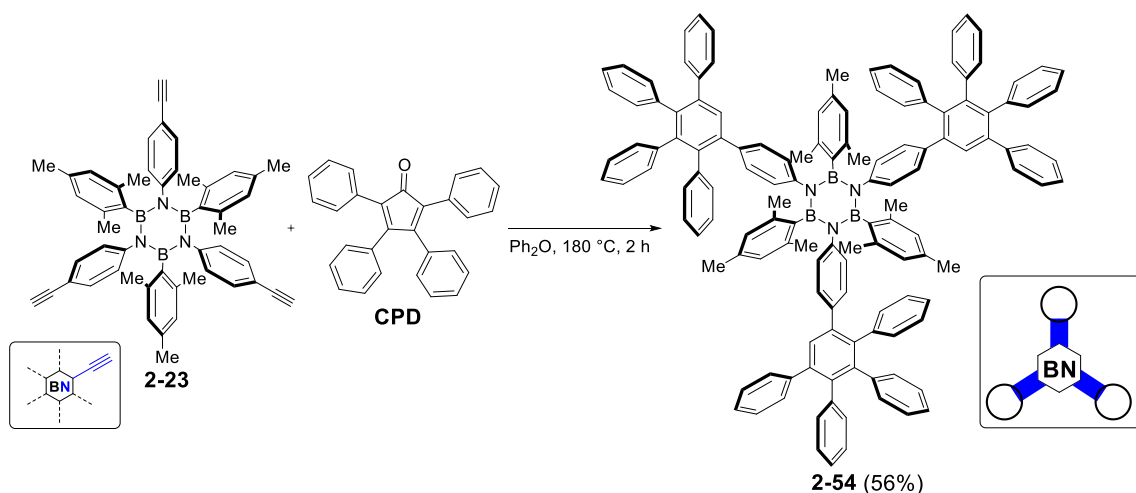
to the similar polarity of the two derivatives, the mixture **2-51a** and **2-51b** was directly treated with BBr_3 in CH_2Cl_2 at room temperature. The difference in polarity between the compounds bearing the hydroxy groups **2-50a** and **2-50b** allow us the purification of 1,3,5-tris(4-hydroxy)-2,4,6-triphenylbenzene **2-50a** by silica gel column chromatography in 14% yield. The reaction of **2-50a** with Tf_2O in pyridine gave tris(triflate) derivative **2-49**, which was subsequently reacted with phenyl boronic acid by Suzuki cross-coupling reaction, yielding di and tri-phenyl substituted derivatives **2-48a** and **2-48b**, isolated in 20% and 9% yield, respectively (compound **2-48b** will be used as full-carbon reference to evaluate and compare the optoelectronic properties of the BN doped polyphenylenes, see section 2.5.7). Monotriflate **2-48a** and boronic ester **2-42** were coupled together through a Suzuki cross-coupling reaction, yielding full-carbon branching module **2-47** in 68% yield (Scheme 2.14).



Scheme 2.14. Synthesis of the carbon branching modules **2-47**. Reagent conditions: a) $[\text{PdCl}_2(\text{PPh}_3)_2]$, CuI , diisopropylamine, THF, r.t., 4 h b) $[\text{Co}_2(\text{CO})_8]$, dioxane, reflux, 18 h; c) BBr_3 , CH_2Cl_2 , r.t., 3 h; d) Tf_2O , pyridine, r.t., 18 h; e) $\text{PhB}(\text{OH})_2$, $[\text{Pd}(\text{PPh}_3)_4]$, K_2CO_3 , dioxane/ H_2O (5:1), 105 °C, 15 h; f) **2-42**, $[\text{Pd}(\text{PPh}_3)_4]$, K_2CO_3 , dioxane/ H_2O (5:1), 105 °C, 15 h.

2.5.5 Synthesis of three-branched borazine doped polyphenylenes

Following the synthetic protocol described in *section 2.3*, to divergently construct BNC polyphenylenes from borazine and full-carbon modules, the decarbonylative Diels-Alder cycloaddition reaction was investigated. To ensure the thermal stability of the borazine core under the cycloaddition reaction conditions, the synthesis of **2-54** (Scheme 2.15), was first explored. Hence, when compound **2-23** was reacted with tetraphenylcyclopenta-2,4-dienone (**CPD**) in Ph₂O at 180 °C, borazine-oligophenylene molecule **2-54** decorated with three pentaphenylbenzene branches at the *N* sites was obtained in 56% yield (Scheme 2.15).



Scheme 2.15. Synthesis of borazine-doped polyphenylenes **2-54**.

The ¹H-NMR spectrum of borazine pentaphenylbenzene **2-54** in CDCl₃ is detailed in Figure 2.17. In the aromatic region, the multiplet signals *a* in the region between 7.31 and 6.50 ppm can be attributed to the 75 phenyl hydrogen atoms of the pentaphenylbenzene moiety at the *N*-sites of the borazine ring. The singlet *b* at 6.35 ppm is related to the 6 phenyl hydrogen atoms at the *B*-sites. In the aliphatic region, the singlets *c* and *d* at 2.09 and 2.03 ppm, respectively, corresponds to the methyl groups of the mesityl groups.

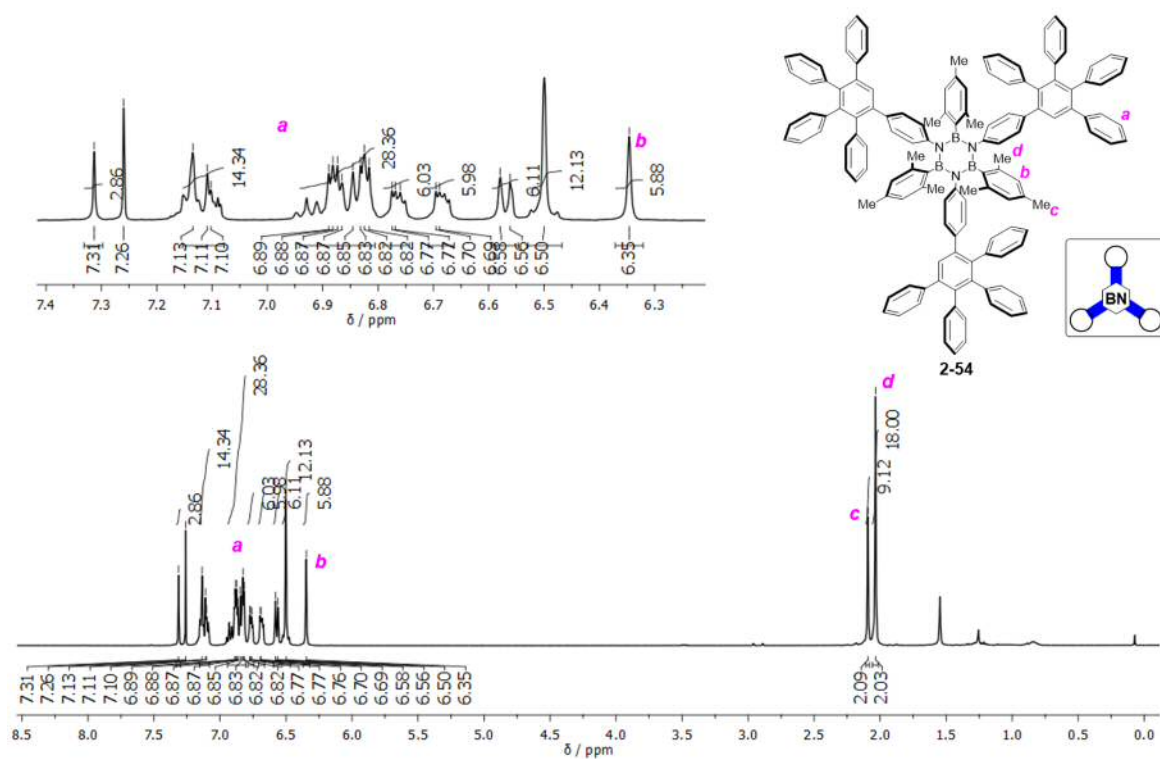


Figure 2.17. 400 MHz ¹H-NMR of borazine branching module **2-54** in CDCl₃ (Solvent residual peak: 7.26 ppm).

Furthermore, the chemical identification of borazine polyphenylene **2-54** was accomplished by MALDI-TOF HRMS analysis as displayed in Figure 2.18. The analysis revealed the presence of mass peak assigned to the molecule of **2-54** at m/z 1803.8802 (calc. for [C₁₃₅H₁₀₈B₃N₃]⁺: 1803.8822).

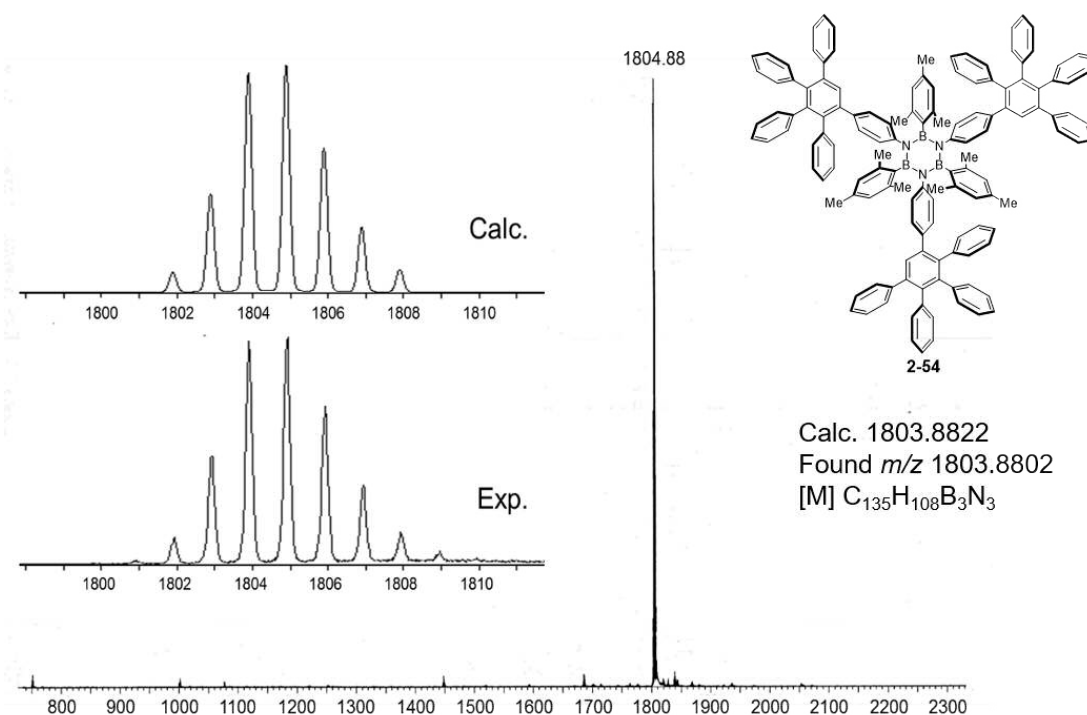


Figure 2.18. MALDI-TOF Mass spectrometry of borazine polyphenylene **2-54**, matrix: trans-2-[3-(4-tert-butyl-phenyl)-2-methyl-2-propenylidene]malonitrile (DCTB).

To prove the chemical identity of **2-54**, single crystal suitable for X-ray diffraction analysis was obtained by slow evaporation of CHCl_3 solution. As expected, the X-ray crystal structure shows the presence of the pentaphenylbenzene peripheries on the *N* atoms of the borazine core (Figure 2.19).

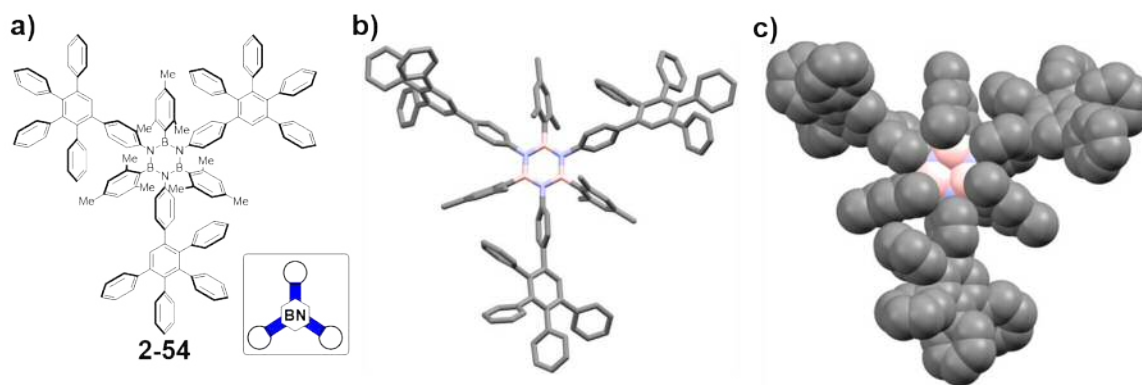
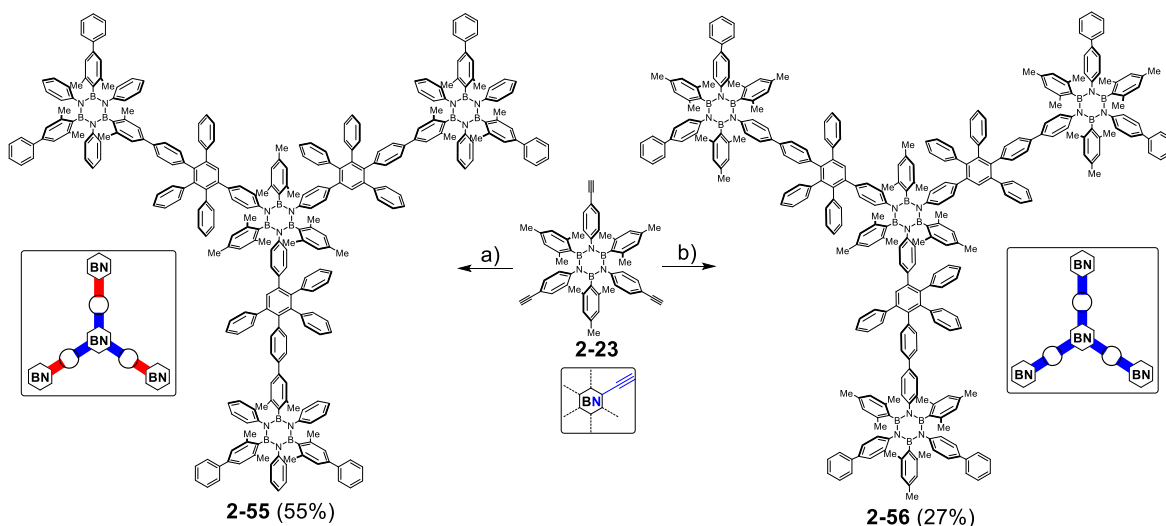


Figure 2.19. Crystal structure of borazine derivative **2-54**; a) molecular structure; b) crystal structure represented in capped sticks; c) crystal structure represented in spacefill. Space group: R-3c. The crystal structure was grown by solvent evaporation of CHCl_3 . Colour code: grey: C, pink: B, blue: N and red: O. Hydrogen atoms were omitted for the sake of clarity.

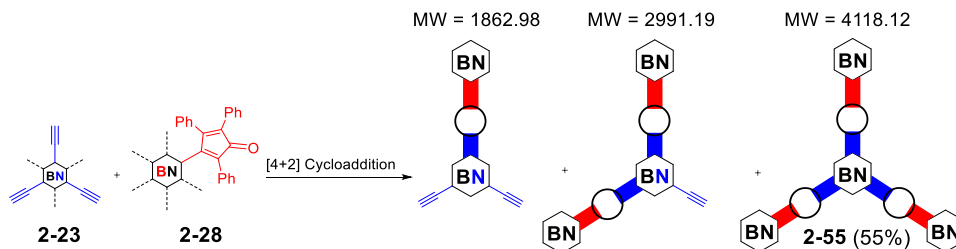
Inspired by this result, the synthesis of borazine-doped polyphenylenes was undertaken following the divergent covalent branching approach through decarbonylative [4 + 2] Diels-Alder cycloaddition reactions under heating conditions in Ph_2O containing the relevant core

and branching units. We started with the synthesis of four different borazine-doped polyphenylenes presenting a doping dosage $\rho = 8.9\%$. Using borazine module **2-23** as core of the polyphenylenes, the cycloaddition reaction with borazine branching unit **2-28** (Scheme 2.16) led to molecule **2-55** in 55% yield, in which three peripheral borazine units are attached to the *N* position of the central borazine core with α_N orientational doping pattern.



Scheme 2.16. Synthesis of borazine-doped polyphenylenes **2-55** and **2-56**. Reaction conditions: a) **2-28**, Ph₂O, 180 °C, 18 h; b) **2-34**, Ph₂O, 200 °C, 16 h.

On the other hand, when borazine core **2-23** was reacted with cyclopenta-2,4-dienone **2-34**, branched borazylene **2-56** was synthesised in 27% yield. Although the three peripheral borazine units are also attached to the *N* positions of the central BN core, they are organised in a β_N orientational doping pattern. It is worth pointing out that the [4+2] cycloaddition reaction between the borazine core modules and the branching units, even working in excess of the diene derivatives, led to the formation of side products resulting from mono and bis-cycloaddition reaction on the dienophile groups. Notably, as shown in Scheme 2.17, cycloadduct side products have been observed in addition to the product of interest **2-55**.



Scheme 2.17. Schematic representation of [4+2] cycloaddition reaction between borazine core module **2-23** and borazine branching module **2-28**.

In order to purify BN-doped polyphenylene **2-55**, recycling gel-permeation chromatography (Rec-GPC) was performed, using CHCl_3 as eluent (Figure 2.20). In this way, after 6 cycles, the desired product **2-55** has been isolated in 55% yield (collection 1).

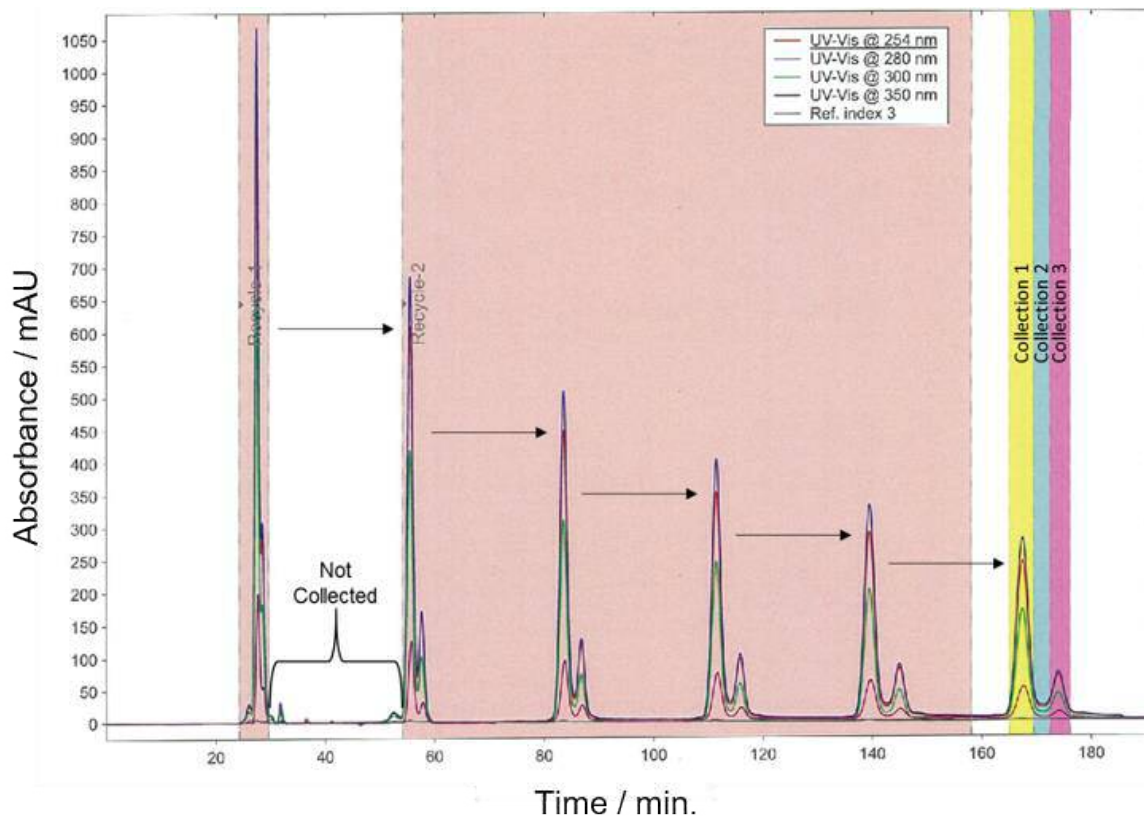


Figure 2.20. Rec-GP chromatogram of borazine-doped polyphenylene **2-55**. Product **2-55** in collection 1, mixture of **2-55**, bis and mono-cycloadduct in collection 2 and 3. GPC columns JAIGEL-2.5HH and 3HH in recycling CH_3Cl .

The chemical identity of borazine polyphenylene **2-55** was unambiguously proved by MALDI-TOF HRMS analysis as displayed in Figure 2.21. The analysis reveals the presence of mass peak assigned to molecule **2-55** at m/z 4118.1251 (calc. for $[\text{C}_{297}\text{H}_{252}\text{B}_{12}\text{N}_{12}]^+$: 4118.1344). The $^1\text{H-NMR}$ spectrum of BN-doped polyphenylene **2-55** in CD_2Cl_2 is detailed in Figure 2.22. In the aromatic region the multiplet signal between 7.43-6.74 ppm refers to the 165 phenyl hydrogen atoms and the singlet at 6.43 ppm can be assigned to the 6 hydrogen atoms of the mesityl moieties at the *B* sites of the borazine core. The aliphatic region is the fingerprint of polyphenylene **2-55**. The presence of two singlets *a* and *b* at 2.43 and 2.38 ppm, respectively, can be attributed to the methyl hydrogen atoms of the xyllyl groups at the *B* sites of the borazine peripheral units. The two singlet signals *c* and *d* at 2.13 and 2.08 ppm, respectively, correspond to the 26 methyl hydrogen atoms of the xyllyl groups

at the *B* sites of the borazine core.

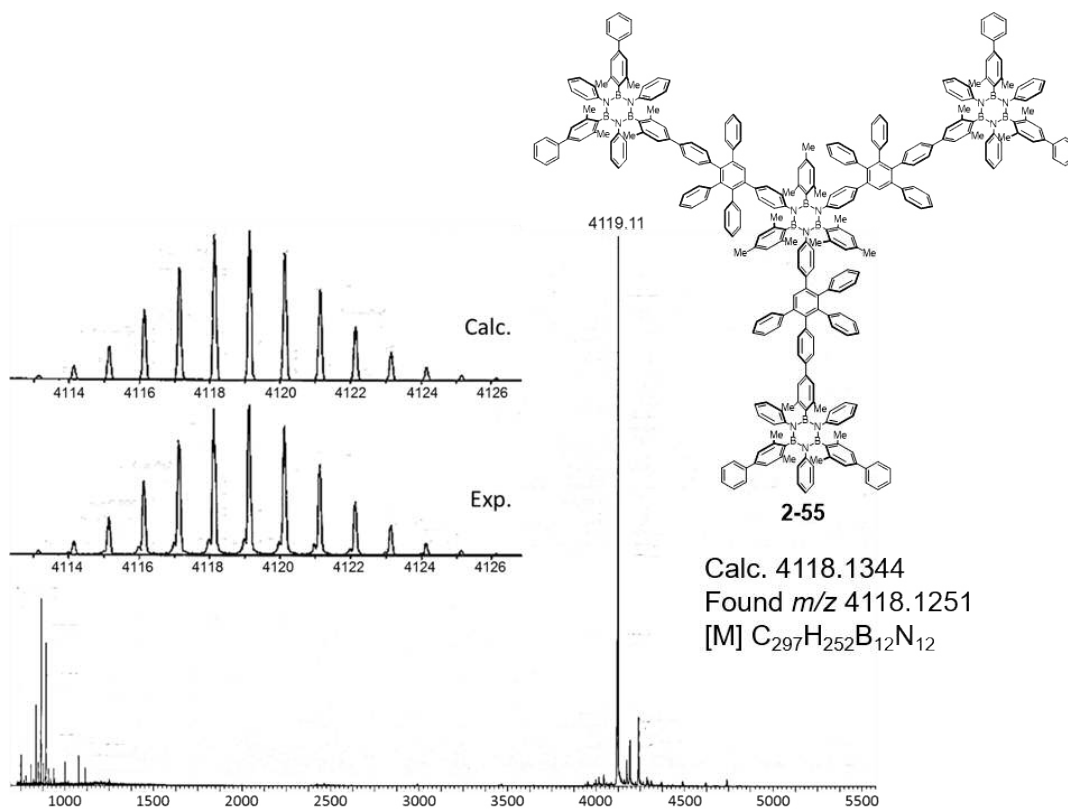


Figure 2.21. MALDI-TOF Mass spectrometry of borazine polyphenylene **2-55**, matrix: *trans*-2-[3-(4-*tert*-butyl-phenyl)-2-methyl-2-propenylidene]malonitrile (DCTB).

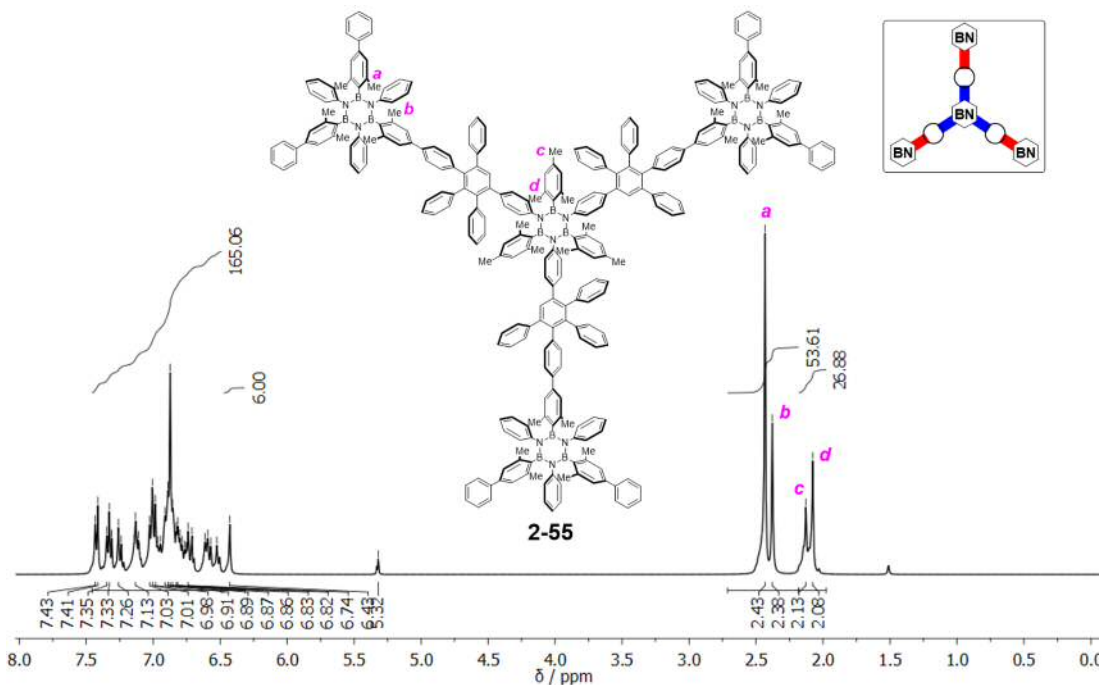
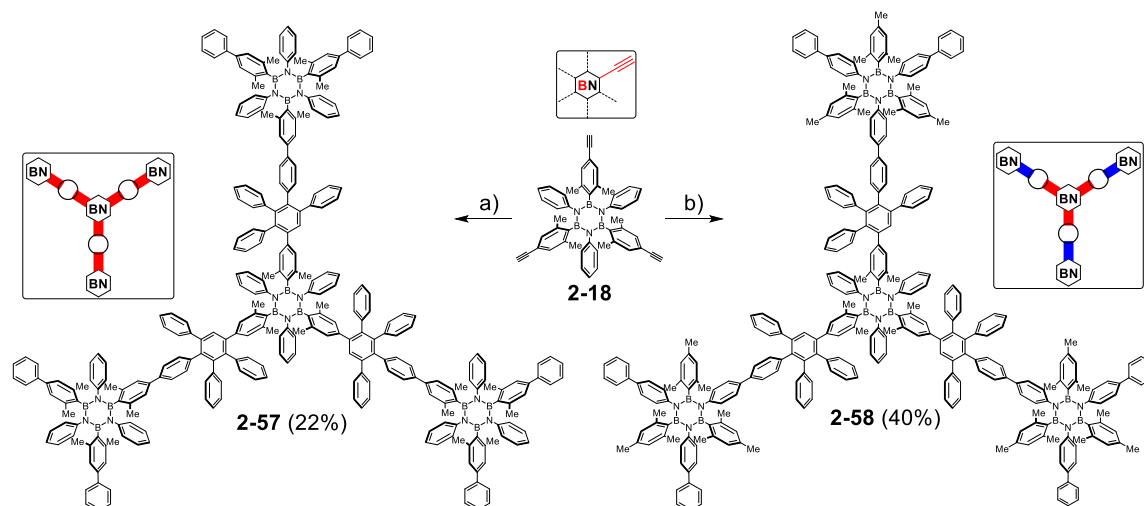


Figure 2.22. 400 MHz ¹H-NMR of borazine branching module **2-55** in CD₂Cl₂ (Solvent residual peak: 5.32 ppm).

Following the same line, by using borazine dienophile core **2-18**, branched hybrid polyphenylenes bearing substituents exclusively at the *B* sites has been prepared. Capitalizing on this building block, cycloaddition reactions of core **2-18** with borazine dienes **2-28** and **2-34** (Scheme 2.18) gave branched borazylenes **2-57** in 22 % yield and **2-58** in 40% yield featuring β_B and α_B orientational doping patterns, respectively.



Scheme 2.18. Synthesis of borazine-doped polyphenylenes **2-57** and **2-58**. Reaction conditions: a) **2-28**, Ph₂O, 190 °C, 18 h; b) **2-34**, Ph₂O, 210 °C, 16 h.

For compound **2-55**, the desired BN-doped polyphenylenes **2-58** was purified from incomplete cycloaddition side products through Rec-GPC (Figure 2.23). After 6 cycles, using CHCl₃ as eluent, we were able to isolate the desired product **2-58** in 40 % yield (collection 1).

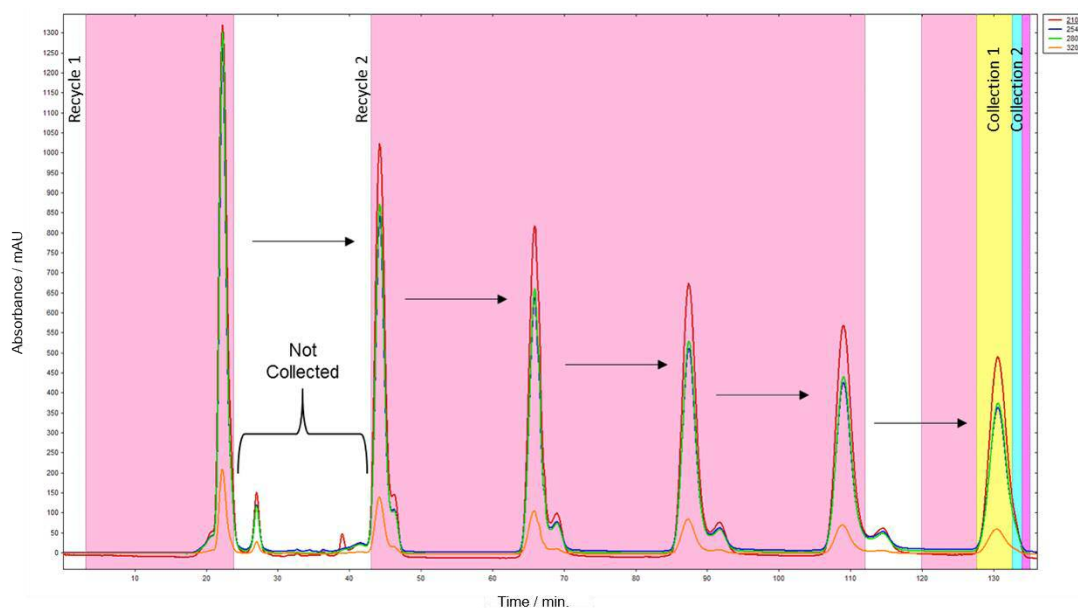


Figure 2.23. Chromatogram obtained from the purification of borazine-doped polyphenylene **2-58** by recycling gel permeation chromatography (rec-GPC). GPC columns JAIGEL-2.5HH and 3HH in recycling using CHCl_3 as eluent.

The chemical identity of borazine polyphenylene **2-58** (collection 1) was unambiguously confirmed by MALDI-TOF HRMS analysis as displayed in Figure 2.24. The analysis revealed the presence of mass peak assigned to molecule **2-58** at m/z 4202.2144 (calc. for $[\text{C}_{303}\text{H}_{264}\text{B}_{12}\text{N}_{12}]^+$: 4202.2241).

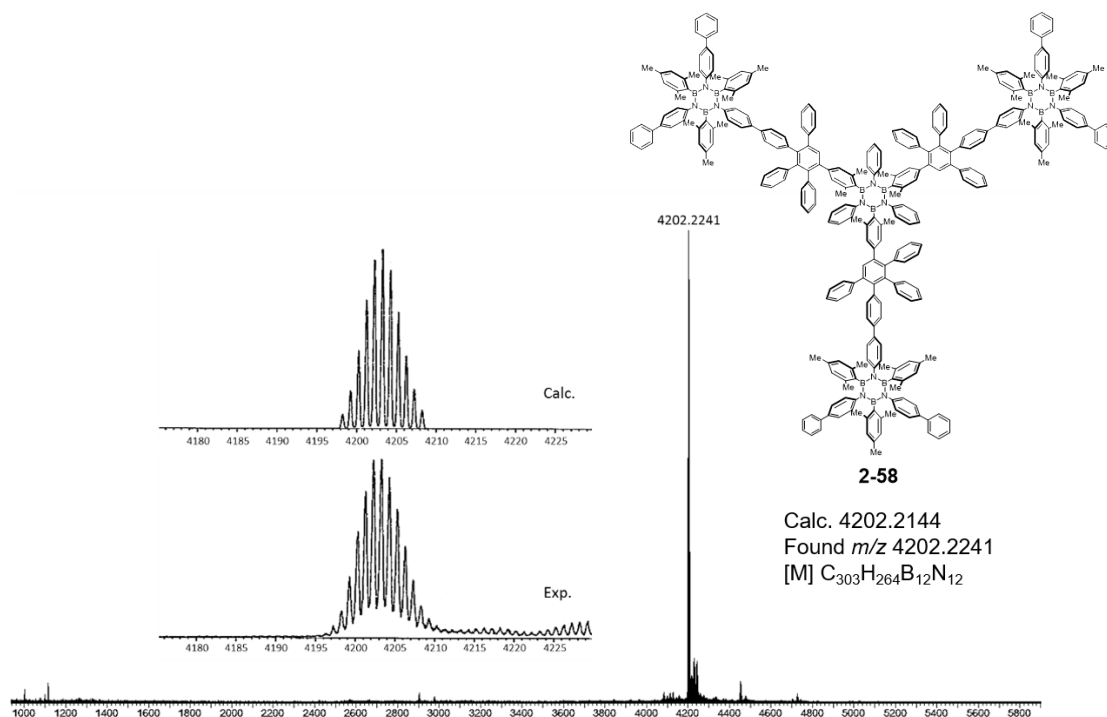


Figure 2.24. MALDI-TOF Mass spectrometry of borazine polyphenylene **2-58**, matrix: *trans*-2-[3-(4-*tert*-butyl-phenyl)-2-methyl-2-propenyldiene]malonitrile (DCTB).

The $^1\text{H-NMR}$ spectrum of BN-doped polyphenylene **2-58** in CDCl_3 is shown in Figure 2.25. In the aromatic region, the multiplet signal between 7.39-6.25 ppm can be assigned to the 162 phenyl hydrogen atoms. In the aliphatic region, two singlets *a* and *b* at 2.25 and 2.23 ppm, can be attributed to the methyl hydrogen atoms of the mesityl groups at the *B* sites of the borazine peripheral units. Furthermore, the three singlet signals *c*, *d*, and *e* at 2.01, 1.97 and 1.95 ppm, respectively, correspond to the 45 methyl hydrogen atoms at the *B* sites of the peripheral and core borazine units.

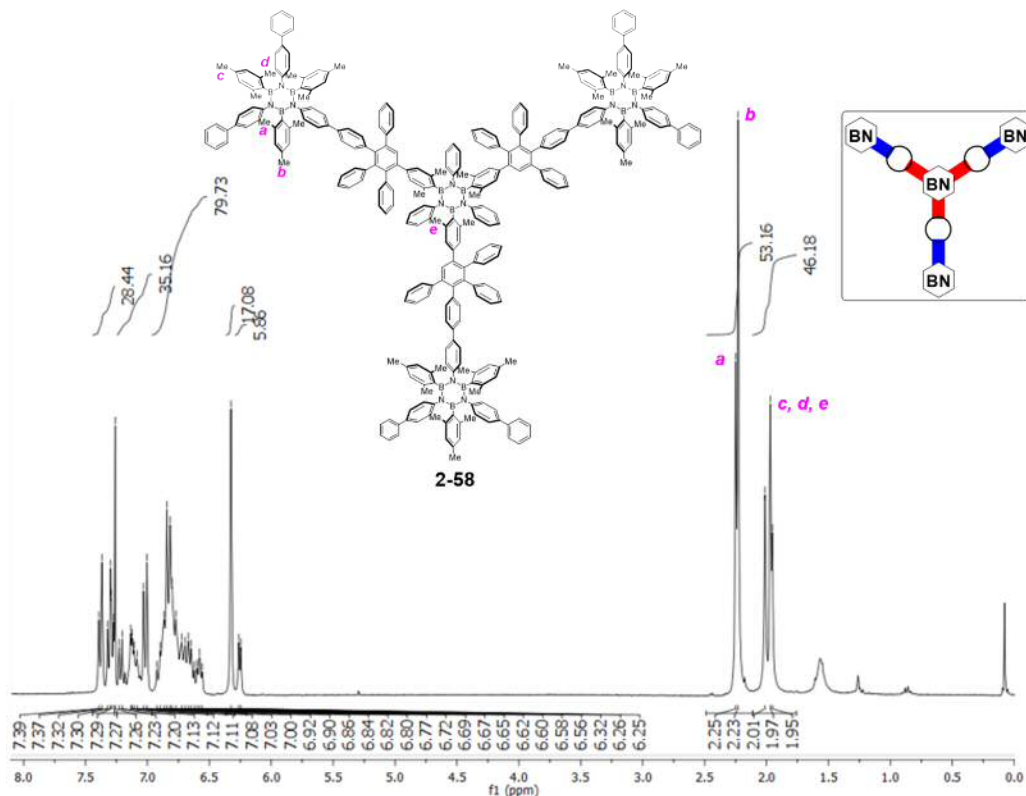
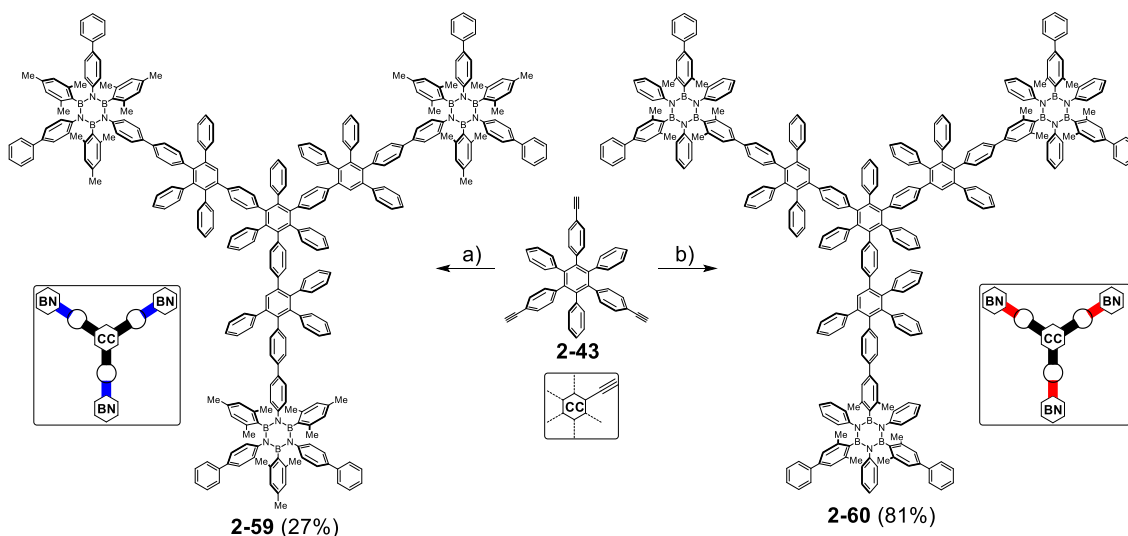


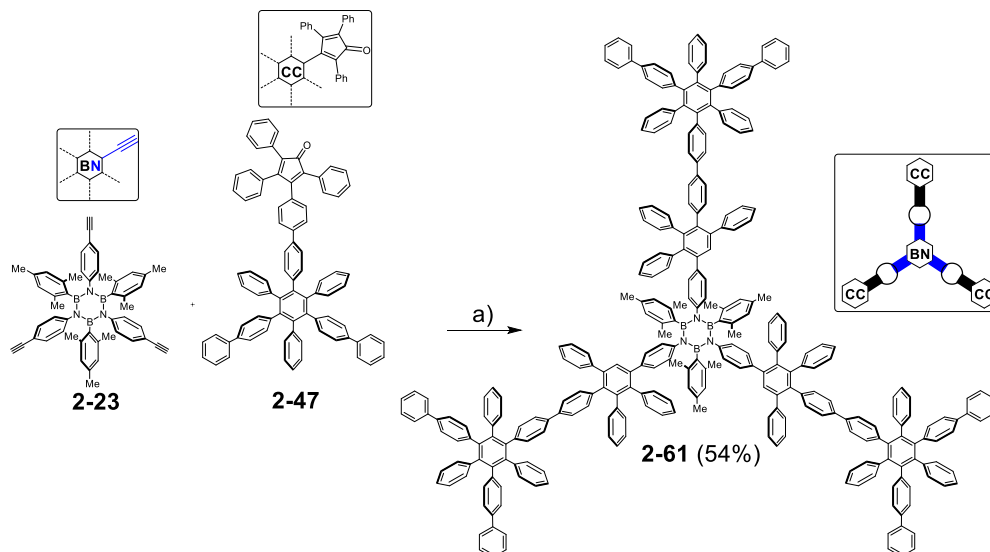
Figure 2.25. 400 MHz $^1\text{H-NMR}$ of borazine branching module **2-58** in CDCl_3 (Solvent residual peak: 7.26 ppm).

In a similar manner, upon replacement of the borazine core dienophile with full-carbon congener **2-43**, branched polyphenylenes **2-59** and **2-60** displaying an intermediate doping dosage ($\rho = 6.5\%$) were synthesised using dienes **2-34** and **2-28**, respectively (Scheme 2.19). Notably, branched polyphenylenes **2-59** and **2-60** present the peripheral borazine units at the *N* and *B* sites, respectively, all displaying the α orientational doping pattern (*i.e.*, α_{N} and α_{B}).

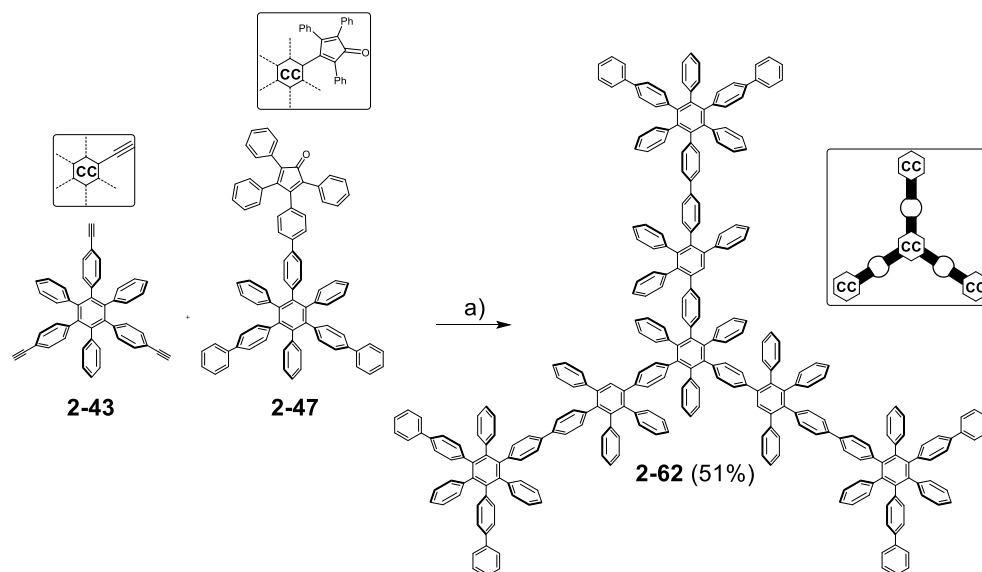


Scheme 2.19. Synthesis of the borazine-doped polyphenylenes **2-59** and **2-60**. Reaction conditions: a) **2-34**, Ph₂O, 230 °C, 2 h; b) **2-28**, Ph₂O, 190 °C, 18 h.

Moving down with the doping dosage, when borazine core **2-23** was reacted with cyclopenta-2,4-dienone **2-47**, branched molecule **2-61** has been obtained in 54% yield (Scheme 2.20). Notably, BN-doped polyphenylene **2-61** presents only a central doping borazine unit bearing all-carbon branches at the *N* sites with a doping dosage $\rho = 2.08\%$. In a similar manner, upon replacement of the borazine core dienophile with full-carbon congener **2-43**, full-carbon reference **2-62** was synthesised (Scheme 2.21).



Scheme 2.20. Synthesis of borazine-doped polyphenylenes **2-61**. Reaction conditions: a) Ph₂O, 190 °C, 18 h.



Scheme 2.21. Synthesis of full-carbon polyphenylene **2-62**. Reaction conditions: a) Ph₂O, 190 °C, 16 h.

The Rec-GPC of the full-carbon polyphenylene **2-62** is pointed out in Figure 2.26. After 11 cycles, using CHCl₃ as eluent, compound **2-62** was isolated in 51% yield (collection 2). The chemical identity of the full-carbon dendrimer was confirmed by MALDI-TOF HRMS analysis as displayed in Figure 2.27. The analysis revealed the presence of mass peak assigned to molecule **2-62** at m/z 3727.5566 (calc. for [C₂₉₄H₁₉₈]⁺: 3727.5494).

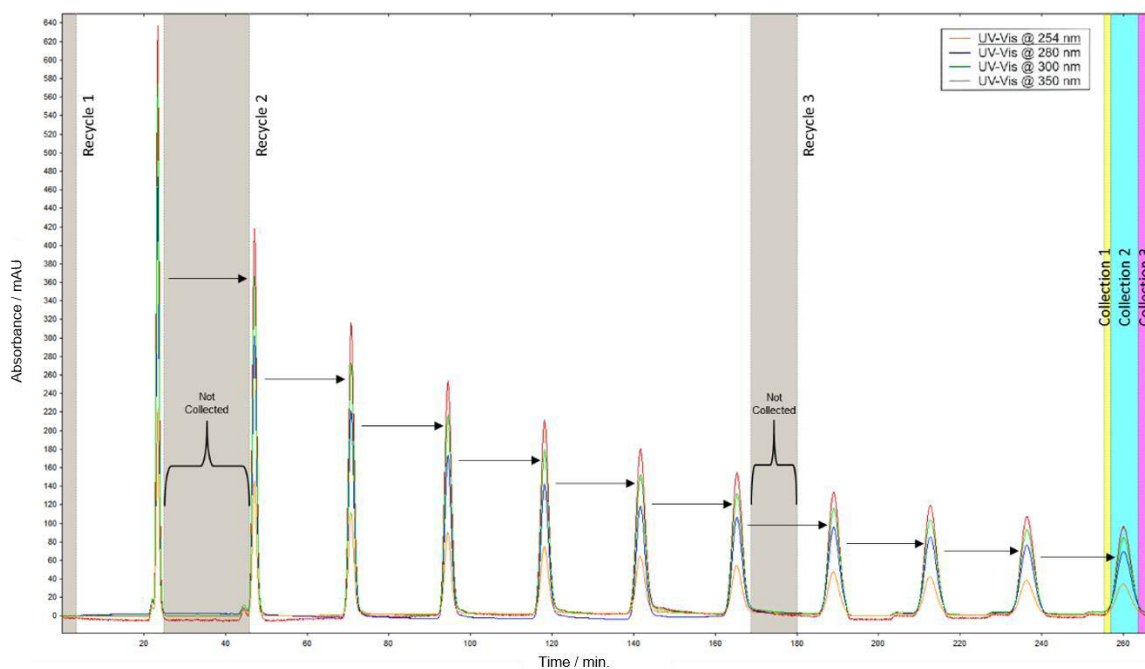


Figure 2.26. Chromatogram obtained from the purification of **2-62** by recycling gel permeation chromatography (rec-GPC). GPC columns JAIGEL-2.5HH and 3HH in recycling using CHCl₃ as eluent.

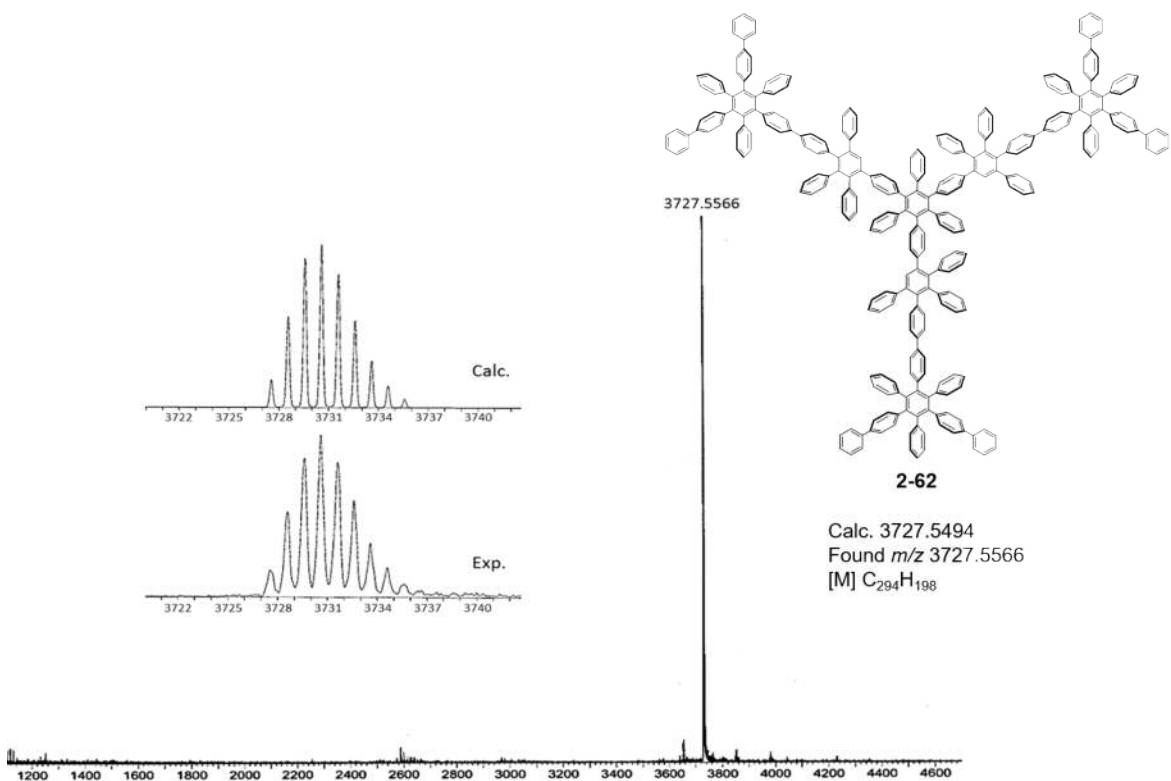
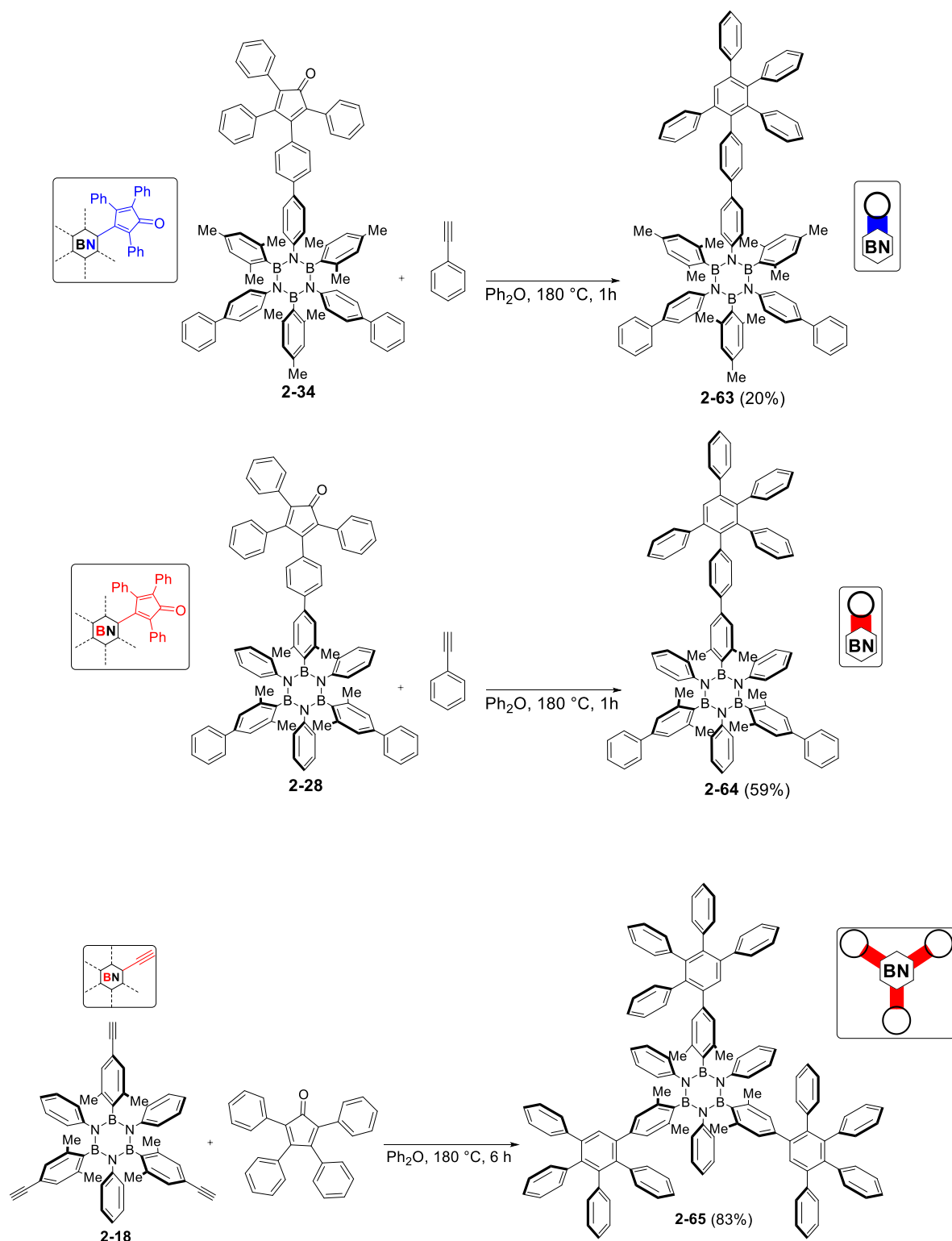


Figure 2.27. MALDI-TOF Mass spectrometry of borazine polyphenylene **2-62**, matrix: trans-2-[3-(4-tert-butyl-phenyl)-2-methyl-2-propenylidene]malonitrile (DCTB).

2.5.6 Synthesis of borazine monomeric references

For reference purposes, to describe the optoelectronic properties of the doped polyphenylenes properties, borazines derivative **2-63**, **2-64** and **2-65**, bearing pentaphenylbenzene moieties at the nitrogen and boron positions, respectively, have been synthesized. The synthesis of reference borazine **2-63** and **2-64** involved a [4+2] decarbonylative cycloaddition reaction between dienophiles **2-34** and **2-28** with phenylacetylene, leading to the desired products in 20% and 59% yield, respectively (Scheme 2.22). Finally, when compound **2-18** was reacted with tetraphenylcyclopenta-2,4-dienone in Ph₂O at 180 °C, borazine-oligophenylene **2-65** bearing three pentaphenylbenzene branches at the *B* sites was obtained in 83% yield (Scheme 2.22).

Scheme 2.22. Synthesis of borazine monomeric reference **2-54**, **2-55** and **2-56**.

2.5.7 Steady state UV-vis absorption and emission studies in solution

The UV-vis absorption spectra of the borazine monomeric references and the three-branched polyphenylenes series were measured in CH_2Cl_2 at room temperature (Fig. 2.28 and 2.29). All the references absorb in the UV region, with the maximum of the absorption between 259 and 275 nm. Increasing the branching, the ϵ_{max} of the borazine derivatives increase moving from 10^4 to $10^5 \text{ M}^{-1}\text{cm}^{-1}$. Notably, molecules bearing the functionalities exclusively at the *N* sites have a higher ϵ_{max} value than those functionalized at the *B* sites showing an hyperchromic effect (*i.e.*, ϵ_{max} (2-35b) > ϵ_{max} (2-29b); ϵ_{max} (2-63) > ϵ_{max} (2-64); ϵ_{max} (2-54) > ϵ_{max} (2-65), Table 2.1).

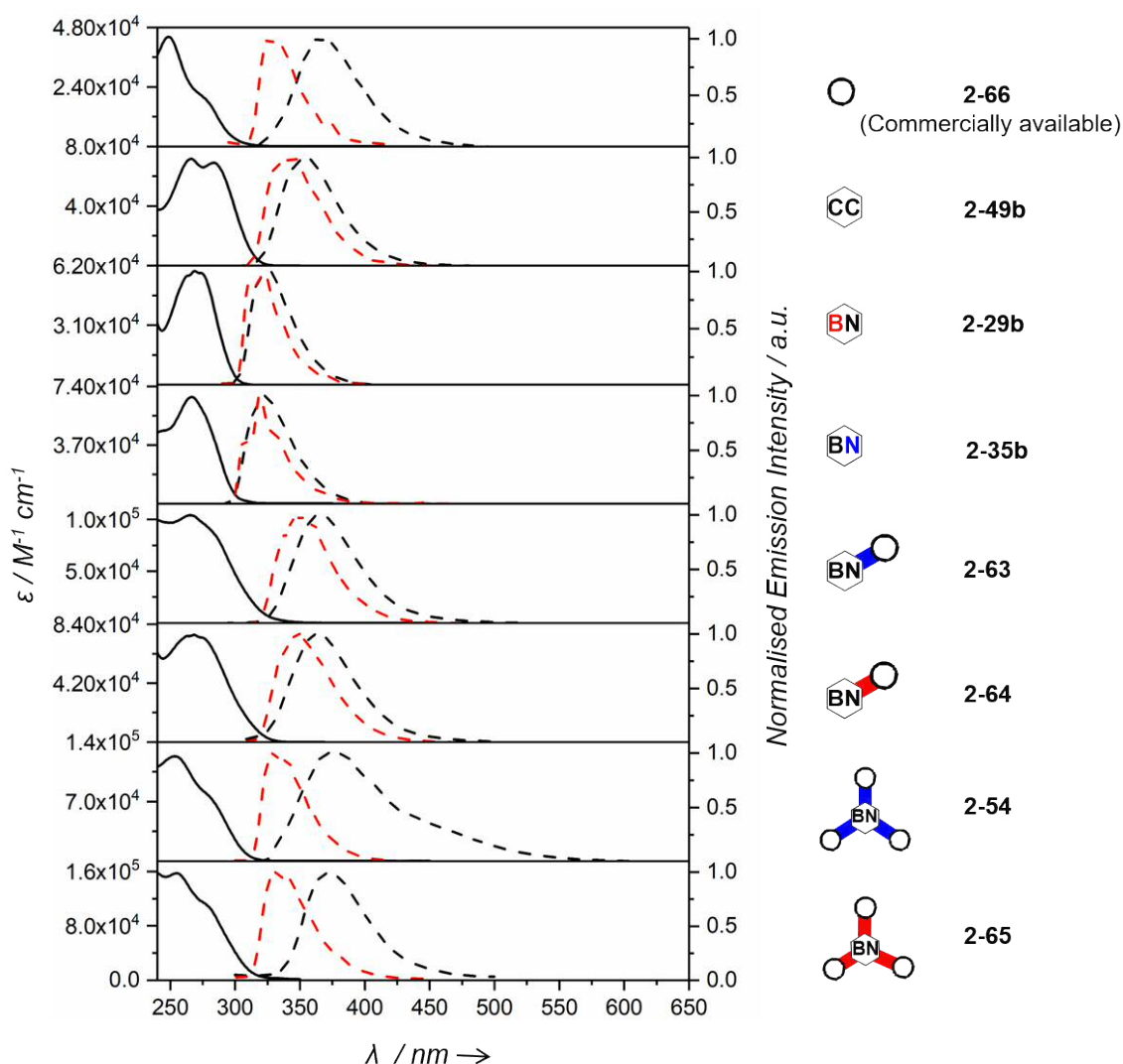


Figure 2.28. Absorption (black solid) at 298 K, emission (black dashed) at 298 K, and emission (red dashed) at 77 K spectra of monomeric borazine references in CH_2Cl_2 at 298 K.

Moving to the three-branched polyphenylene series, all the dendrimers absorb in the UV region, with the maximum of the absorption between 265 and 269 nm. Remarkably, the insertion of the borazine ring on the periphery of the dendrimers lead to an increase of the ϵ_{\max} value of the polyphenylenes from 10^4 to 10^5 $M^{-1}cm^{-1}$. Among the three-branched BN-doped polyphenylenes, the different orientation of the borazine ring led to an hyperchromic effect in the polyphenylene frameworks (*i.e.*, ϵ_{\max} (2-57) > ϵ_{\max} (2-56) > ϵ_{\max} (2-55) > ϵ_{\max} (2-58), Table 2.1), with the highest value for the BN dendrimers featuring the β_B and β_N orientations.

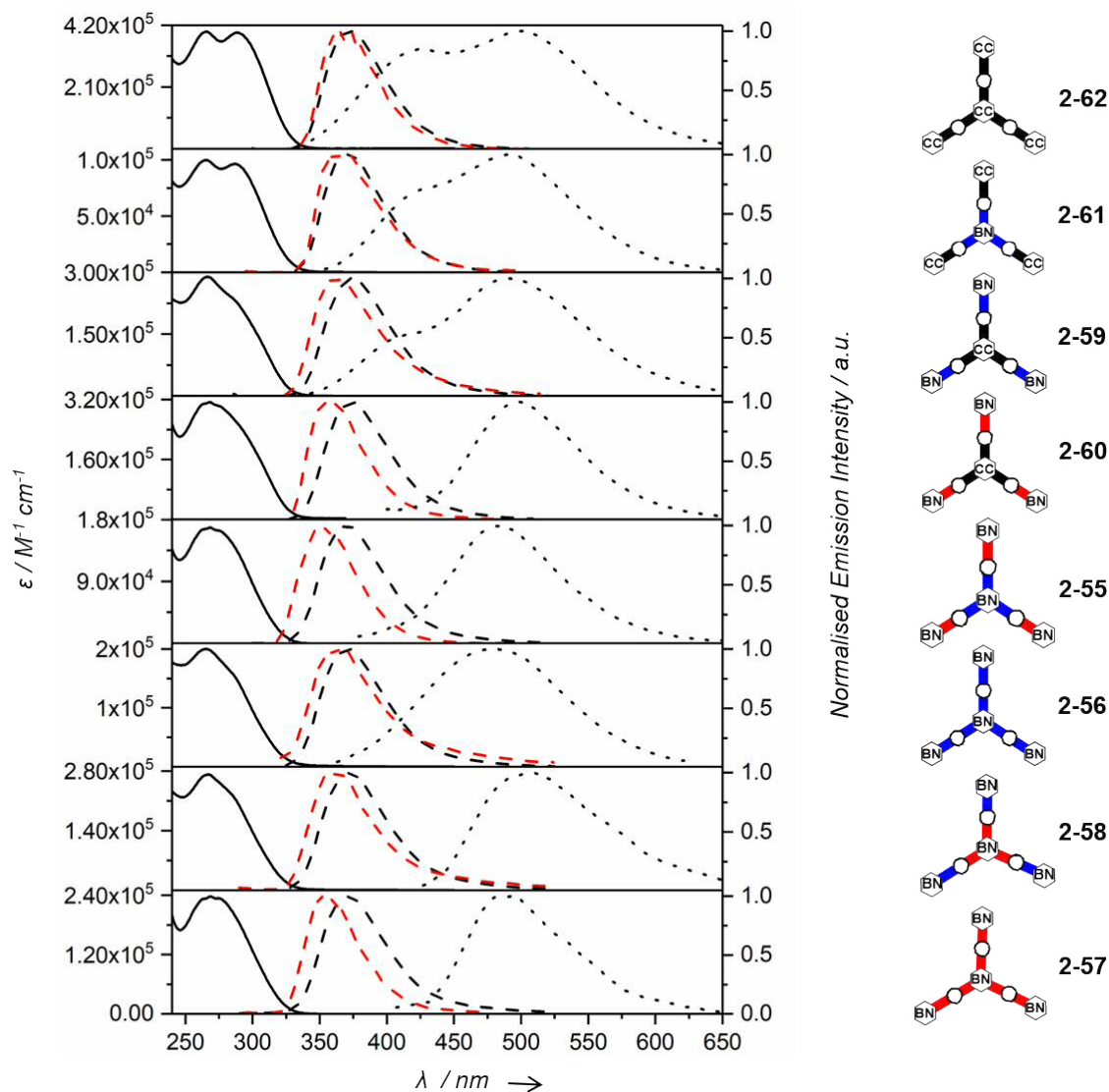


Figure 2.29. Absorption (black solid) at 298 K, emission (black dashed) at 298 K and emission (red dashed) at 77K spectra, and phosphorescence at 77 K (dotted) of three-branched polyphenylenes in CH_2Cl_2 .

The emission spectra have been also recorded at room temperature, the borazine references show the maximum of emission located in the near-UV region between 325 and 350 nm. When increasing the number of pentaphenylbenzene moving from **2-29b** to **2-65**, a red shift is observed (Figure 2.28) due to the enhancement of the conjugation in the compounds. The emission profile of the three-branched polyphenylene series present the maximum of emission in the near-UV region between 351 and 371 nm. For both the series of compounds, the comparison between the emission profile recorded at 77 K and the emission spectra at room temperature shows a hypsochromic shift ascribable to the reducing of the solvation of the excited state at low temperature known as rigidochromism effect.²⁵ Meanwhile the absorption spectra at r.t. of the BN dendrimers possess similar energetic profiles to the borazine core and periphery reference compounds, on the other hand their emission at 77 K seems to vary in accordance to the chemical functionalisation of the peripheral moieties. Consistently, the emission of compounds **2-56** and **2-58** ($\lambda_{\text{max}} = 363$ and 360 nm at 77 K, respectively) present a similar spectral shape and energy to the borazine reference **2-63** ($\lambda_{\text{max}} = 352$ nm at 77 K). Following the same trend, the emission of dendrimer **2-55** and **2-57** ($\lambda_{\text{max}} = 351$ and 352 nm at 77 K, respectively) are similar to periphery reference compound **2-64** ($\lambda_{\text{max}} = 352$ nm at 77 K). As a consequence, it can be reasonable postulated that the absorption of the BN three-branched polyphenylenes leads to an energy transfer process from the core to the periphery scaffolds with a subsequent emission localised in periphery of the dendrimers. The intersection of the emission spectra recorded at 77 K and the absorption spectra at r.t. (approximating the optical energy gap (E_g)) for the borazine derivatives has also been evaluated. Monomeric borazine references bearing the substituents exclusively at the *N* sites exhibit similar energy gaps to those functionalised at the *B* sites (*i.e.*, E_g (**2-35b**) \sim E_g (**2-29b**), E_g (**2-63b**) \sim E_g (**2-64b**) and E_g (**2-54**) \sim E_g (**2-65**), see table 2.1). Additionally, moving from one (**2-63b** and **2-64b**) to three (**2-54** and **2-65**) tetraphenylbenzene moieties at the *N* or *B* sites, the introduction of such functional groups does not affect the E_g of the borazine compounds which is ~ 4 eV (table 2.1). In accordance with this result, moving on to the three-branched polyphenylene series, the borazine doping orientation (α_N , α_B , β_N and β_B) has no effect on the E_g , whereas on increasing the doping dosage, an enhancement of the E_g is observed. The lowest value of E_g is measured for all-carbon polyphenylene **2-62** ($\rho = 0\%$, $E_g = 3.6$ eV).

Table 2.1. Photophysical properties of borazine monomeric references and three-branched polyphenylenes in CH₂Cl₂. a) Φ_{em} is the emission quantum yield; b) Life time measured with- λ_{exc} = 295 nm; c) Radiative rate constant, given by $k_f = \Phi_{em} / \tau_f$; d) Total nonradiative rate constant, given by $(1/\tau_f) - k_f$; e) Shoulder phosphorescence peaks, f) Optical energy gap, given by $E_g = 1240.5/\lambda_i$ in which λ_i is the intersection wavelength between the emission spectra recorded at 77 K and the absorption spectra at r.t.

	Absorption			Emission							
	Comp.	λ_{max} [nm]	ϵ [M ⁻¹ cm ⁻¹] (λ)	λ_{exc} [nm]	λ_{max} [nm] (Φ_{em}) ^a	τ_f^b [ns]	k_f^c [ns ⁻¹]	$k_v+k_{ISC}+k_{CS}^d$ [ns ⁻¹]	λ_{max}^{77k} [nm]	$\lambda_{Phosph.}^{77k}$ [nm]	E_g [eV] ^f
Monomeric references	2-66	248 278	4.4×10 ⁴ (248)	259	369 (0.8%)	< 0.1	-	-	325	-	4
	2-49b	266 283	7.1×10 ⁴ (266)	264	355 (9%)	0.3	0.3	3.03	344	-	4
	2-29b	263 269 274	5.9×10 ⁴ (269)	263	327 (20%)	0.7	0.28	1.15	322	-	4.2
	2-35b	267	6.7×10 ⁴ (267)	273	322 (34%)	2.7	0.12	0.25	319	-	4.1
	2-63	266 282	7.6×10 ⁵ (266)	273	362 (20%)	0.3	0.66	2.67	352	-	3.8
	2-64	263 268 275	1.0×10 ⁵ (268)	275	365 (16%)	0.3	0.53	2.8	352	-	3.9
	2-54	253 283	1.5×10 ⁵ (253)	264	373 (2%)	0.1	0.08	9.9	329	-	3.9
	2-65	253 282	1.2×10 ⁵ (253)	263	374 (0.8%)	0.7	0.02	1.4	330	-	4
Three-branched polyphenylenes	2-62	266 289	3.9x10 ⁴ (266)	274	372 (76%)	0.6	1.26	0.40	366	501 423 ^e	3.6
	2-61	266 288	9.9x10 ⁴ (266)	279	373 (64%)	0.8	0.8	0.45	373	489 432 ^e	3.6
	2-60	267 287	4x10 ⁵ (267)	266	373 (45%)	0.5	0.9	1.1	367	490 406 ^e	3.8
	2-59	264 268 275	3.1x10 ⁵ (268)	272	373 (44%)	0.6	0.73	0.93	355	499	3.9
	2-55	263 268 276	1.7x10 ⁵ (268)	272	370 (33%)	0.5	0.66	1.34	351	487	3.8
	2-56	265 286	1.9x10 ⁵ (265)	272	370 (29%)	0.5	0.58	1.42	363	477	3.9
	2-58	267 286	2.7x10 ⁴ (267)	274	373 (11%)	0.2	0.55	4.45	360	508	3.8
2-57	263 269 275	2.3x10 ⁵ (269)	275	372 (7%)	0.2	0.35	4.65	352	482	3.9	

The replacement of the aryl ring with B₃N₃ on the core (**2-61**) does not produce any relevant shift of the emission at 77 K compared with **2-62**, on the other hand, the borazine doping at the periphery (**2-59** and **2-60**, $\rho = 6.5\%$) or in the tetra-borazine polyphenylenes ($\rho = 8.9\%$)

gives as outcome a moderate enhancement of the E_g of 0.2 - 0.3 eV with respect to the full-carbon dendrimer (see table 2.1). The fluorescence quantum yields (Φ_{em}) of the borazines monomeric references and the three-branched polyphenylenes series have been calculated using equation (1):

$$\Phi_{em, X} = \Phi_{em, S} \times (A_S I_X / A_X I_S) \times (n_X / n_S)^2 \quad (\text{eq. 1})$$

Where Φ_{em} is the fluorescence quantum yield, A is the absorbance at the excitation wavelength, I is the integrated area of fluorescence emission, and n is the refractive index of the solvents used (cyclohexane: $n = 1.426$; CH_2Cl_2 : $n = 1.424$). Subscripts S and X refer to the standard and to the unknown, respectively. The $\Phi_{em, S}$ values were determined using naphthalene as reference ($\Phi_{em, S} = 0.036$ in cyclohexane).²⁶ Starting with reference borazine molecules **2-29b** and **2-35b**, the introduction of the phenyl substituents on the aryl rings linked to either the *B* or *N* sites significantly enhances the emission quantum yield ($\Phi_{em} = 20\%$ and 34% for borazines **2-29b** and **2-35b**, respectively see Table 2.1) but reduces the lifetime ($\tau = 0.7$ and 2.7 ns for borazines **2-29b** and **2-35b**, respectively) compared to *B, B', B''*-trimesityl-*N, N', N''*-triphenylborazine **1-51** ($\Phi_{em} = 7.7\%$ and $\tau = 7.1$ ns in CH_2Cl_2).²⁷ In any circumstances, these monomeric borazine derivatives are stronger emitters than their all-carbon congener, such as molecule **2-49b** ($\Phi_{em} = 9\%$). The observed emission enhancement could be ascribed to the presence of the *o*-methyl groups that, hampering rotational movements, rigidify the hexasubstituted borazine scaffold compared with that of hexaphenylbenzene derivatives, decreasing the vibrational relaxation pathway. When the borazine scaffold is branched, the emission intensity progressively diminishes as the number of pentaphenylbenzene spokes increases ($\Phi_{em} = 20\%$, 16% , 2% , and 0.8% for **2-63**, **2-64**, **2-54**, and **2-65**, respectively; see Table 2.1). In view of the negligible emissive nature of the pentaphenylbenzene moieties **2-66** ($\Phi_{em} < 1\%$), the observed weakening of the emission intensity for all reference molecules can be realistically attributed to non-radiative vibrational deactivations triggered by the pentaphenylbenzene moieties. Remarkably, molecules bearing the phenylenes exclusively at the *N* sites display higher emission than those functionalized at the *B* sites (*i.e.*, $\Phi_{em}(\mathbf{2-35b}) > \Phi_{em}(\mathbf{2-29b})$; $\Phi_{em}(\mathbf{2-63}) > \Phi_{em}(\mathbf{2-64})$; $\Phi_{em}(\mathbf{2-54}) > \Phi_{em}(\mathbf{2-65})$), suggesting that the functionalization pattern at the borazine core is not as innocent as one could think. The double-bond character for the BN bonds 22% ,²⁸ it can be considered that the *B* and *N* atoms are neutral. Thus, this suggests that each *N* atom

retains the major electron density while each *B* atom keeps its electronic deficiency generating a push-pull system. As previously reported for boron–nitrogen-containing donor–acceptor dendrimers,^{29–31} dynamic processes involving photoinduced short-lived charge separated (CS) states could take place between the electron-donating and electron-accepting moieties, deactivating the emissive excited states.

Moving to the three-branched polyphenylenes series, a significant decrease in the emission intensity with increasing doping dosage has been observed, as pointed out in Table 2.1 and Figure 2.30. The highest value of fluorescence quantum yield is measured for all-carbon polyphenylene **2-62** (76%), whereas the progressive replacement of aryl rings with B₃N₃ rings, surprisingly reduces the emission intensity, with the tetra-borazine derivatives being the weakest emitters. This trend is rather unexpected taking in consideration that borazine references **2-29b** and **2-35b** are more emissive than their hexaphenylbenzene analogue **2-49b**. The observed emission enhancement for molecule **2-62** could be reasonably attributed to an overcrowding effect that, generated by the simultaneous presence of multiple branching units,³² rigidifies the dendritic structure and enhances the emission intensity, as described by Mullen and co-workers with other full-carbon polyphenylenes.³³ Interestingly, while the insertion of the B₃N₃ ring in the core position of the polyphenylene seems to have a minor effect on the emissive properties ($\Phi_{\text{em}} = 64\%$ for **2-61**), a relevant decrease in the fluorescence intensity is observed when borazine units are present at the periphery of the dendrimers ($\Phi_{\text{em}} \approx 45\%$ for both **2-59** and **2-60**). Notably, no effects of the borazine *N* or *B* sites is observed for molecules **2-59** and **2-60**, as these two conjugates essentially display the same Φ_{em} value. As anticipated above, the major fluorescence quenching is observed for the four tetra-borazine derivatives ($\Phi_{\text{em}} < 33\%$), which bear both inner and peripheral borazine rings. In accordance with the emission trend observed for the borazine references functionalised at the *N*-sites, three-branched BN-doped polyphenylenes **2-57** and **2-58** featuring β_B and α_B orientational doping patterns display the weakest emissions ($\Phi_{\text{em}} = 7\%$ and 11% , respectively), whereas derivatives **2-56** and **2-55** display the highest values ($\Phi_{\text{em}} = 29\%$ and 33% , respectively). Additionally, although the fluorescence lifetime decays of the three-branched polyphenylenes do not show a significant difference among the dendrimers (representative fluorescence lifetime measurements are shown in Figure 2.31, the decays were deconvoluted on DAS6 analysis software), the calculation of the radiative (k_f , in which $k_f = \Phi_{\text{em}} / \tau_f$) and total non-radiative ($k_{\text{nr}} = k_v + k_{\text{ISC}} + k_{\text{CS}}$, in which $k_{\text{nr}} = (1/\tau_f) - k_f$)

rate constants (Table 2.1) allowed us to shed further light on the effect of the doping on the deactivation pathways. As it clearly appears from the derived rate constant values, increasing the BN dosage accelerates the non-radiative deactivation of the singlet excited state through a possible combination of intersystem crossing (ISC), increased CS character of the excited state or vibrational relaxation.

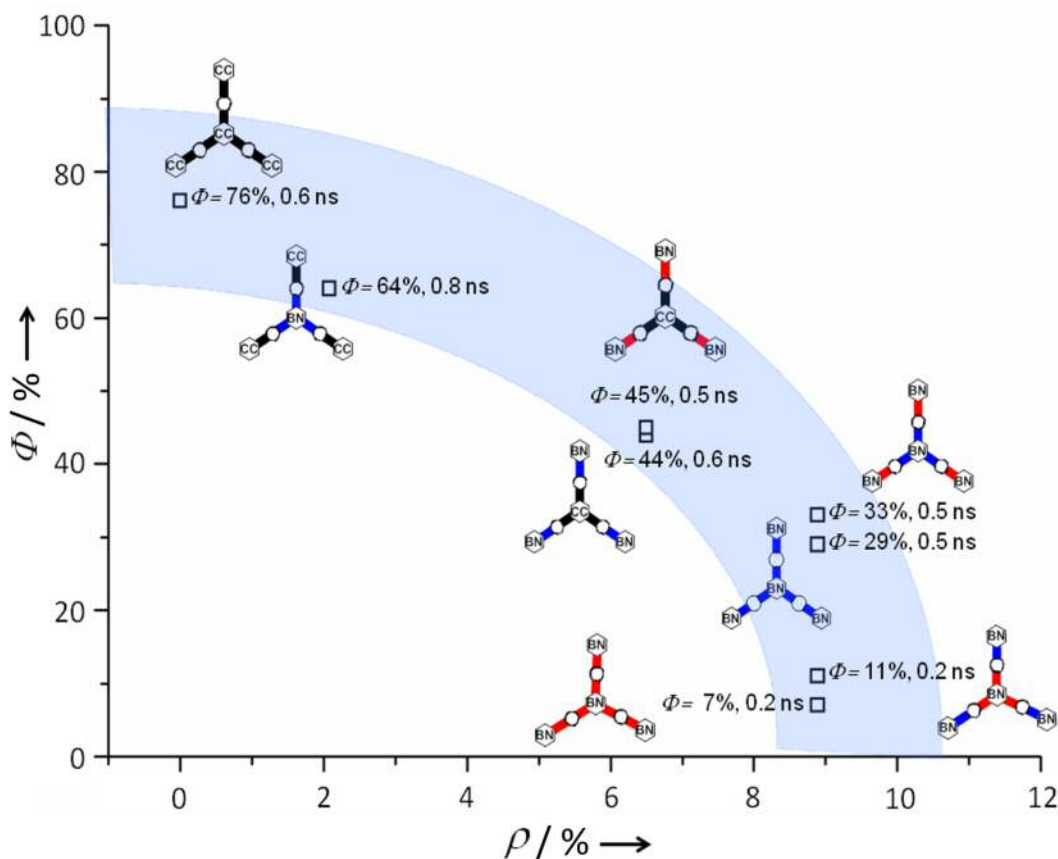


Figure 2.30. Emission quantum yield as a function of the dosage and orientational doping for the three-branched polyphenylene series. The fluorescence life time of each three-branched polyphenylenes is also reported together with the emission quantum yield.

Notably, the emission quenching is particularly high when the peripheral borazines branch out through the *B* sites (i.e., molecule 2-57) with a total non-radiative deactivation 12 times faster than that of full-carbon analogue 2-62. When the measurements were performed at 77 K, non-negligible phosphorescence emission was observed (Figure 2.29) with the borazine-doped molecules generally featuring the highest-energy triplet emission. Representative phosphorescence lifetime measurements (Figure 2.32) have been also performed, showing longer lasting emission profiles for the borazine-containing derivatives

($\tau_{\text{phos}} = 2.6, 2.1,$ and 2 s for **2-29b**, **2-65**, and **2-55**, respectively) compared to those of the full carbon analogues ($\tau_{\text{phos}} = 1.1$ s for **2-62**).

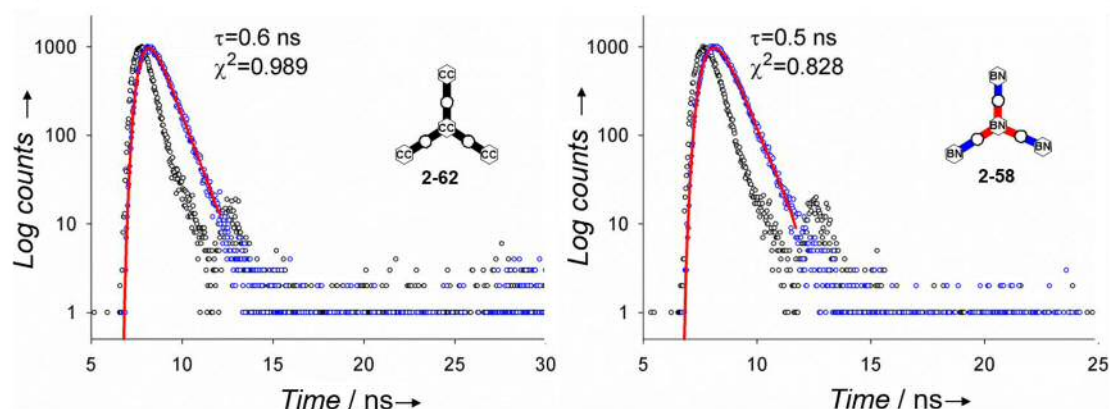


Figure 2.31. Emission lifetime decays (blue dots) and fittings (red lines) of three-branched polyphenylenes **2-62** and **2-58** excited at $\lambda_{\text{exc}} = 295$ nm in CH_2Cl_2 at r.t. All reported fittings are mono exponentials. Decay of the excitation source is reported as the black dots (Instrument response function).

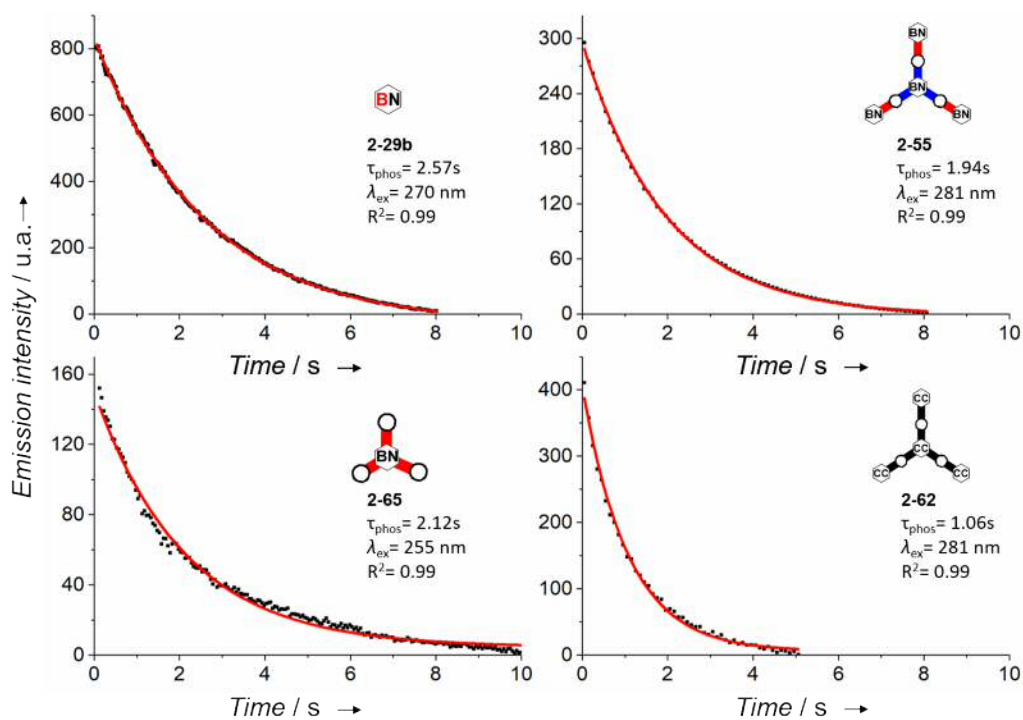


Figure 2.32. Phosphorescence lifetime decays (black dots) and fittings (red lines) of BN-doped polyphenylene **2-29b**, **2-65**, **2-55**, and **2-62** excited at $\lambda_{\text{ex}} = 270$ nm, 255 nm, 281 nm, and 281 nm, respectively, in CH_2Cl_2 at 77 K. All reported fittings are mono exponentials.

2.6 Conclusions and perspectives

In this chapter, we have reported the first example of the use of borazine as a versatile modular building block to prepare hybrid BNC polyphenylenes featuring doping borazine

cores at selected positions with specified doping ratios and orientation patterns (Figure 2.33).

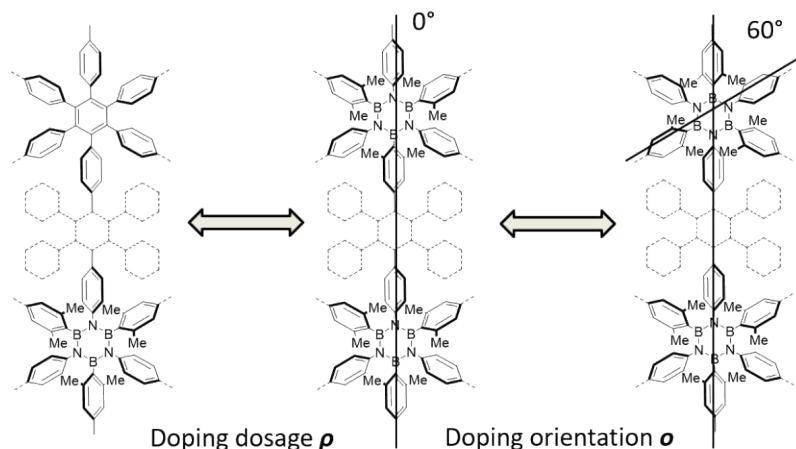


Figure 2.33. Doping dosage and orientation of borazine in polyphenylenes framework.

Recognizing the possibility of functionalising the borazine core with different groups on the aryl substituents at the *N* and *B* atoms, we have prepared BNC polyphenylenes by means of the decarbonylative [4 + 2] Diels–Alder cycloaddition reaction. To achieve this, two types of molecular modules were prepared: core and branching units. Depending on the chemical natures of the central aromatic module and the reactive group, each covalent combination of the modules could yield one exclusive doping pattern. As far as the borazine building blocks are concerned, di-*o*-methyl-substituted aryl moieties were used to protect the electrophilic boron atoms. Extending this approach, we have prepared the three-branched hybrid polyphenylenes featuring controlled orientations and dosages of the doping B_3N_3 rings. Detailed photophysical investigations showed that with increasing doping dosage the strong luminescence signal is progressively reduced ($\Phi_{em} = 76\%$ to 7%). This observation suggests that the presence of B_3N_3 rings possibly increases the ISC, photoinduced charge transfer or vibrational relaxation pathways in the dendrimers, favouring non-radiative deactivation of the singlet excited states. Notably, an effect of the borazine substitution pattern on the emission quantum yield was observed only for those hybrid BNC polyphenylenes featuring low doping dosages. The ability to acquire substitution and doping patterns “at will” make these BNC polyphenylene architectures versatile molecular precursors for synthesising planarised graphitic nanostructures featuring controlled doping patterns. Currently, we are investigating on the planarisation protocol allowing the formation of C–C bonds in the presence of BN type aromatics network. As described in the

sections 1.3.3 and 2.2, we recently proposed the synthesis of BN-doped coronene derivative **1-39**, starting from borazine derivative featuring six leaving group (*e.g.* the fluorine atoms) able to protect the B_3N_3 ring. Then in the presence of $[iPr_3Si^+][CB_{11}H_6Cl_6^-]$ and Me_2SiMes_2 , the six C-C ring-closure steps occur through an intramolecular Friedel-Crafts-type reaction yielding **1-39** derivative 5% yield (Figure 2.34).

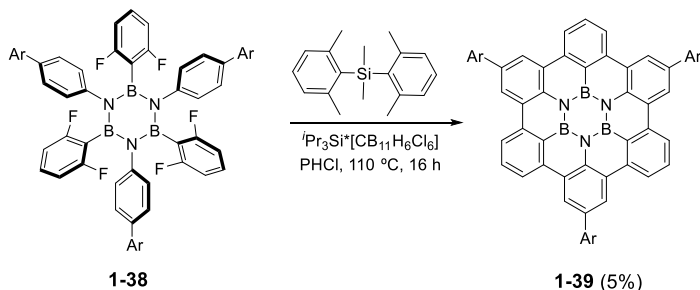


Figure 2.34. Doping dosage and orientation of borazine in polyphenylenes framework.

Nevertheless, the low yield for the full cyclisation calls for the development of more efficient synthetic strategies that, being compatible with the BN ring, will allow the planarization of extended BN-doped systems in higher yield. Together with the bottom-up synthetic approach developed in this work, the synthesis of BN-doped dendrimers featuring suitable leaving groups able to protect the B_3N_3 rings, will be the synthetic challenge of our future endeavours in the molecular BNC field (Figure 2.35).

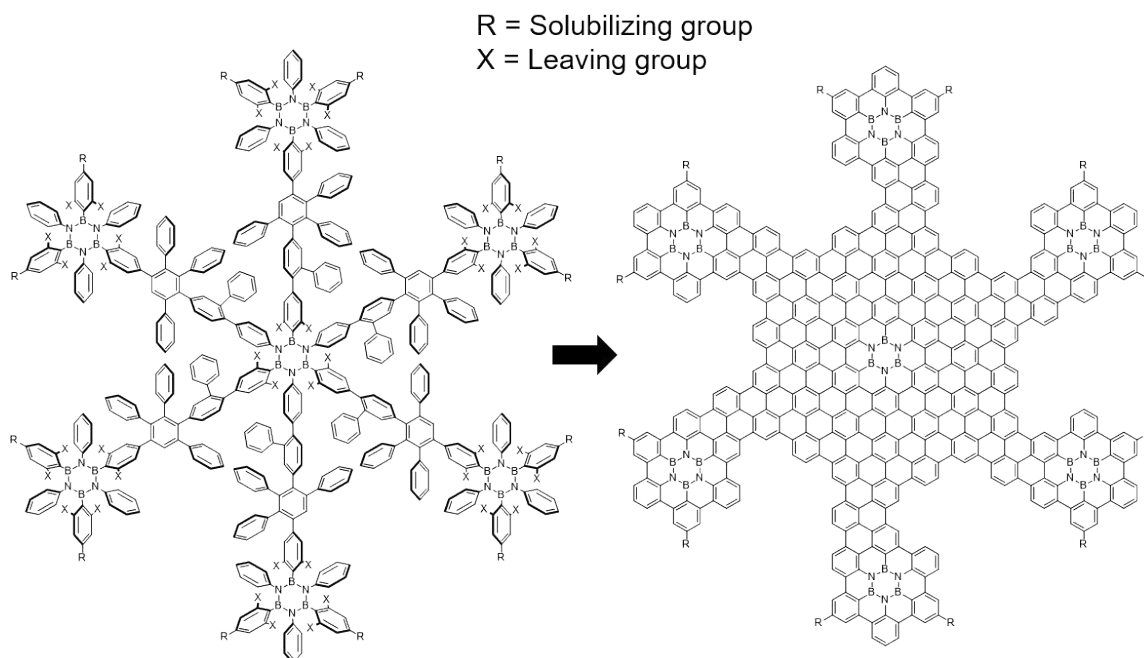


Figure 2.35. General strategy for the synthesis of borazine doped graphene.

2.7 References

- (1) Novoselov K. S., Geim A. K., Morozov S. V., Jiang D., Zhang Y., Dubonos S. V., Grigorieva I. V., Firsov A. A. *Science*. **2004**, *306*, 5696.
- (2) Geim A. K., Novoselov K. S. *Nat. Mater.* **2007**, *6*, 183.
- (3) Narita A., Wang X.-Y., Feng X., Müllen K., Iijima S., Arifin Sato K., Omachi H., Kitaura R., Irle S., Suenaga K., Shinohara H., Menges B., Reichert J., Feng X., Räder H. J., Klappenberger F., Rubio A., Müllen K., Barth J. V. *Chem. Soc. Rev.* **2015**, *44*, 6616.
- (4) Ohta T., Bostwick A., Seyller T., Horn K., Rotenberg E. *Science* **2006**, *313*, 5789.
- (5) Zhang Y., Tang T.-T., Girit C., Hao Z., Martin M. C., Zettl A., Crommie M. F., Shen Y. R., Wang F. *Nature* **2009**, *459*, 820.
- (6) Wang X.-Y., Wang J.-Y., Pei J. *Chem. Eur. J.* **2015**, *21*, 3528.
- (7) Liu Z., Marder T. B. *Angew. Chem. Int. Ed.* **2008**, *47*, 242.
- (8) Otero N., El-kelany K. E., Pouchan C., Rérat M., Karamanis P. J. *Phys. Chem. Chem. Phys.* **2016**, *18*, 25315.
- (9) Yu S., Zheng W., Wang C., Jiang Q. *ACS Nano* **2010**, *4*, 7619.
- (10) Fiori G., Betti A., Bruzzone S., Iannaccone G. *ACS Nano* **2012**, *6*, 2642.
- (11) Song L., Ci L., Lu H., Sorokin P. B., Jin C., Ni J. K., A. G. Kvashnin, Lou J., Yakobson B. I., Ajayan, P. M. *Nano Lett.* **2010**, *10* (8), 3209.
- (12) Ci L., Song L., Jin C., Jariwala D., Wu D., Li Y., Srivastava A., Wang Z. F., Storr K., Balicas L., Liu F., Ajayan P. M. *Nat. Mater.* **2010**, *9*, 430.
- (13) Lu J., Zhang K., Feng Liu X., Zhang H., Chien Sum T., Castro Neto A. H., Loh K. P. *Nat. Commun.* **2013**, *4*, 1.
- (14) Huang, C.; Chen, C.; Zhang, M.; Lin, L.; Ye, X.; Lin, S.; Antonietti, M.; Wang, X. *Nat. Commun.* **2015**, *6*, 1.
- (15) Li G., Xiong W.-W., Gu P.-Y., Cao J., Zhu J., Ganguly R., Li Y., Grimsdale A. C., Zhang Q. *Org. Lett.* **2015**, *17*, 560.
- (16) Wu D., Zhang H., Liang J., Ge H., Chi C., Wu J., Liu S. H., Yin J. *J. Org. Chem.* **2012**, *77*, 11319.
- (17) Matsui K., Oda S., Yoshiura K., Nakajima K., Yasuda N., Hatakeyama T. *J. Am. Chem. Soc.* jacs. 7b10578.

- (18) Sánchez-Sánchez C., Brüller S., Sachdev H., Müllen K., Krieg M., Bettinger H. F., Nicolaï A., Meunier V., Talirz L., Fasel R., Ruffieux P. *ACS Nano* **2015**, *9*, 9228.
- (19) Narita A., Wang X.-Y., Feng X., Müllen K. *Chem. Soc. Rev.* **2015**, *44*, 6616.
- (20) Chen L., Hernandez Y., Feng X., Müllen K. *Angew. Chem. Int. Ed.* **2012**, *51*, 7640.
- (21) Dössel L., Gherghel L., Feng X., Müllen K. *Angew. Chem. Int. Ed.* **2011**, *50*, 2540.
- (22) Chen L., Hernandez Y., Feng X., Müllen K. *Angew. Chem. Int. Ed.* **2012**, *51*, 7640.
- (23) Morgenroth F., Reuther E., Müllen K. *Angew. Chem. Int. Ed.* **1997**, *36*, 631.
- (24) Agenet N., Gandon V., Vollhardt K. P. C., Malacria M., Aubert C. *J. Am. Chem. Soc.* **2007**, *129*, 8860.
- (25) Damrauer N. H., McCusker J. K. *Inorg. Chem.* **1999**, *38*, 4268.
- (26) Montalti M., Credi A., Prodi L., Gandolfi M. T., Michl J., Balzani V. *Handbook of photochemistry* 3rd ed., CRC Press., Taylor & Francis, Boca Raton **2006**.
- (27) Kervyn S., Fenwick O., Di Stasio F., Shin Y. S., Wouters J., Accorsi G., Osella S., Beljonne D., Cacialli F., Bonifazi D. *Chem. Eur. J.* **2013**, *19*, 7771.
- (28) Pauling L. *Proc. Natl. Acad. Sci. USA* **1966**, *56*, 1646.
- (29) Kurata R., Kaneda K., Ito A. *Org. Lett.* **2017**, *19*, 392.
- (30) Proń A., Baumgarten M., Müllen K. *Org. Lett.* **2010**, *12*, 4236.
- (31) Ji L., Griesbeck S., Marder T. B. *Chem. Sci.* **2017**, *8*, 846.
- (32) Qin T., Zhou G., Scheiber H., Bauer R. E., Baumgarten M., Anson C. E., List E. J. W., Müllen K. *Angew. Chem. Int. Ed.* **2008**, *47*, 8292.
- (33) Liu D., De Feyter S., Cotlet M., Stefan A., Wiesler U.-M., Herrmann A., Grebel-Koehler D., Qu J., Müllen K., De Schryver F. C. *Macromolecules* **2003**, *36*, 5918.

CHAPTER 3

Synthesis of borazine derivatives for metal organic frameworks (MOFs) applications

In this chapter, the design and synthesis of metal organic frameworks decorated with borazine modules are described. To evaluate the influence of the B₃N₃ rings on the gas adsorption properties, the synthesis of the corresponding full-carbon MOF has been proposed. The first part addresses the synthesis of the organic linkers. The second part sets out the preparation of the MOFs arrays.

The chapter is divided into three main sections: *i) section 3.1* includes a general introduction on the gas storage in boron-nitrogen materials; *ii) section 3.2* focuses on the design of MOF functionalised with borazine moiety; *iii) section 3.3* gathers the results obtained with the synthesis of the organic linkers as well as the preparation of the corresponding MOFs.

The research works in *section 3.6.2* and *3.6.4* have been carried out jointly with François Kerff (*University of Mons, Belgium*) who performed the synthesis of compounds **3-3**, **3-4a** and **3-10** under my supervision. The X-Ray diffraction analyses were performed by Nicola Demitri (*Electra-Synchrotron, Basovizza, Trieste, Italy*). Brunauer-Emmett-Teller (BET) surface area measures and data analysis of MOFs were performed by Robert Armstrong, (*Cardiff University, Wales*). Furthermore, Greg Shaw (*Cardiff University, Wales*) is kindly acknowledged for the fruitful scientific discussions.

3.1 Boron-nitrogen (BN) materials for gas storage applications

The safe and economical storage of CO₂, H₂, CH₄ *etc.* is currently pushing the scientific community towards the research of porous materials which exhibit strong interaction with gas molecules (as described in *section 1.5.2*). In this context, the works of El-Kaderi, described in the same *section*, shows that boron-nitrogen (BN) modules in covalent organic frameworks (COFs), could act as anchoring points to enhance the non-covalent absorption of gas molecules. However, the modest surface areas and the amorphous nature of the BN-COFs are the major limitations of these porous materials. A way to overcome these problems was reported by F. Xu and co-workers.¹ They proposed, for the first time, metal-organic framework (MOF) as template to build a porous boron-nitrogen-carbon (BNC) material by post-synthetic modification. MOFs are infinitely extended metal-ligand network composed by metal centres and organic ligands. The self-assembly of these components, typically in solution, generates a crystalline material with rigid pores and incredibly high surface area (> 6000 m²/g).² In particular they described the preparation of BN-MOF achieved by the reaction between metal organic framework MIL-53 and ammonia-borane at 450 °C. CO₂ adsorption isotherm at 273 K of BN-MIL-53 was measured and compared with respect to MIL-53. Interestingly, the introduction of BN modules into the metal-organic framework produced as result an enhancement of 1 mmol/g of CO₂ uptake at 780 mmHg in BN-MIL-53 (4.6 mmol/g) compared to MIL-53 (3.6 mmol/g). This was ascribed to the specific interaction between the BN framework and the carbon dioxide.¹ Following the same synthetic principle, Q. Xu and co-workers proposed the synthesis of aluminium-based MOF, MIL-100(Al), grafted with BN.³ 1-ethyl-3-methylimidazolium (EMIM TCB, Figure 3.1a) was chosen as ionic liquid (IL) BN-precursor, which was reacted with MIL-100(Al) at 200 °C for 12 h, followed by calcination process at 800 °C (Figure 3.1b). As result, IL-MIL-100(Al) was obtained, showing appreciable CO₂ adsorption capacities (4.4 mmol/g) at 273 K.

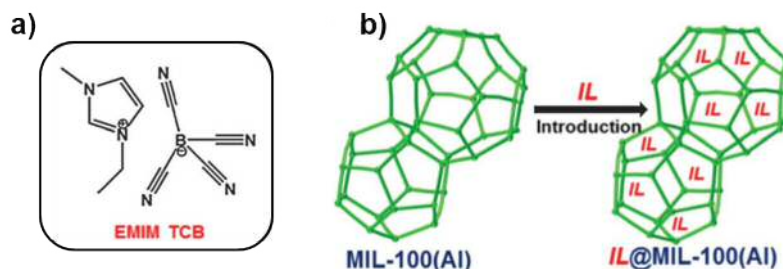


Figure 3.1 a) Chemical structure of 1-ethyl-3-methylimidazolium;³ b) schematic illustration of the synthetic procedure of IL-MIL-100(AI).³

Although the BN grafting of MOFs could represent a promising strategy to trigger the gas storage performance of the metal coordination polymers, experimental works about the preparation of BNC-frameworks are still in their infancy because of the difficulties to control with high purity the BN grafting by MOF post-synthetic modifications. Alternately, the BN functionalisation of MOFs can be achieved by modification of the organic linkers which then can be used to prepare the porous polymers. This synthetic bottom-up approach aims to guide the assembly between BN pre-formed organic linkers and the metal centres into highly pure organised porous structures. The proof of concept was given by Bakshi and Knop in 1995. Sodium boron imidazolate was reacted with LiCl at room temperature, leading the formation of B-N-Li 3D-crystalline polymer in which the imidazole rings coordinate Li atoms.⁴ In 2009, Feng and Bu reported the synthesis of stable 3D open porous boron imidazolate framework (BIF) that exhibited CO₂ adsorption properties.⁵ In this case the borate organic linker (Figure 3.2a) was reacted with CuI in CH₃CN at 120 °C. The resulting BIF-3 (Figure 3.2b) showed a surface area of 726 m²/g with CO₂ uptake of 1.52 mmol/g at 273 K.

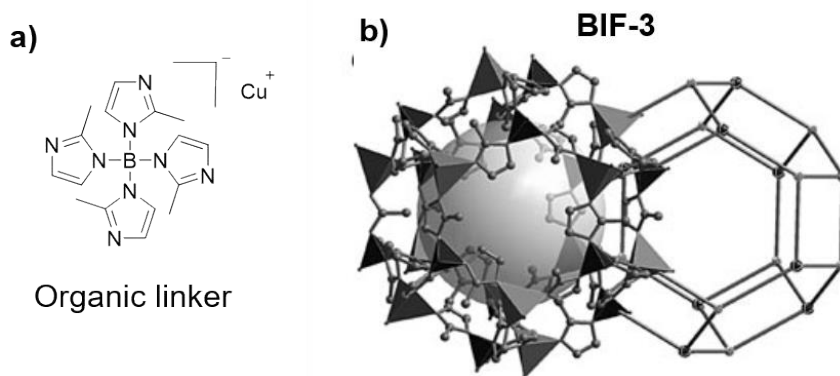


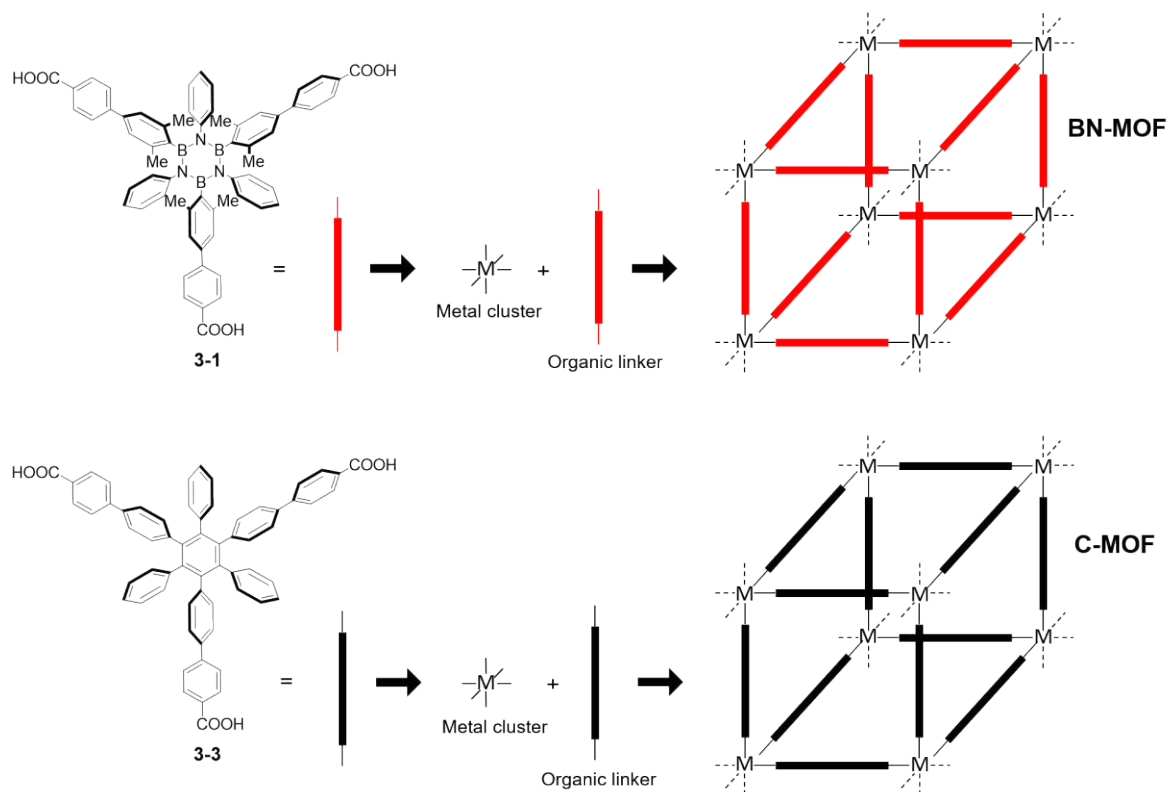
Figure 3.2 a) Boron imidazolate organic linker;⁵ b) BIF-3 crystal structure, the tetrahedra represents boron and copper sites.⁵

Recently, Zhang and co-workers described the preparation of BIFs in which the boron imidazolate was reacted with Co(II) metal centre in the presence of a second dicarboxylate linker in order to tune the porosity of the polymers.⁶ As result, a 3D microporous BIF with CO₂ uptake value of 3.44 mmol/g at 273 K was obtained.

3.2 Aim of the project

As described in the previous *section*, molecular systems based on boron-nitrogen have attracted much attention because of their local polar character. For instance, gases like CO₂ and CO can, in principle, interact with BN bonds through dipolar interactions, thus making BN-doped materials very good candidates for tailoring gas absorptions. In the context of porous materials, MOFs have attracted tremendous attention, due to the fact that they can be made porous, the porosity and incredibly high surface area of this frameworks initiated a new field of supramolecular chemistry for the gas storage.⁷⁻¹⁶

Inspired by these results, the design of metal organic frameworks with polar building blocks such as borazine, is expected to increase their affinity towards polar or polarisable gas molecules. Hence, we aimed to design a 3D BN-MOF composed by three-carboxyl borazine linker **3-1** (Scheme **3.1**). Borazine **3-1** is decorated with two π -conjugated frameworks, alternately at the boron and nitrogen sites. We also envisioned, to introduce the carboxylic groups at the *B*-sites as coordinating connector between the metal centres and the borazine scaffolds to ensure the metal-organic rigidity and stability.¹⁷ Additionally, to evaluate the real effect of the BN doping towards the gas storage, we have also designed the isostructural full-carbon analogue linker **3-3** (Scheme **3.1**), in which the borazine core is replaced by benzene. Notably, to achieve the best compromise between synthesis and similarity of the structures, *m*-xylene groups present in compound **3-1** are replaced by phenyl groups in compound **3-3** (the reason will be explained in detail in *section* 3.3.1). Finally, the synthesis of the corresponding full-carbon MOF will be carried out with the purpose of comparing the two reactivities and obtaining fundamental and information about their physical-chemical properties (BN-MOF vs C-MOF).

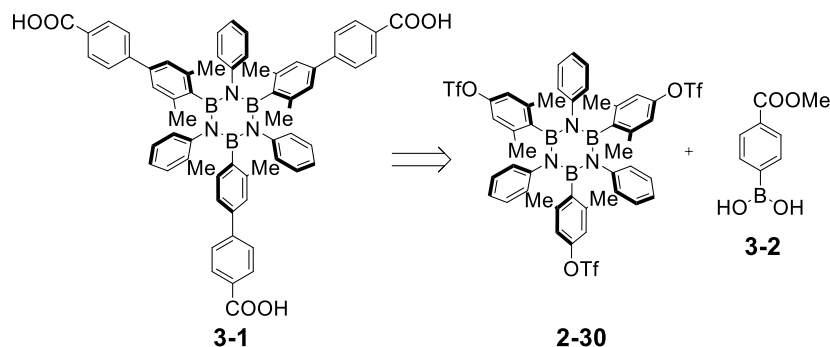


Scheme 3.1. Schematic illustration of the synthesis of BN-MOF and C-MOF.

3.3 Results and Discussion

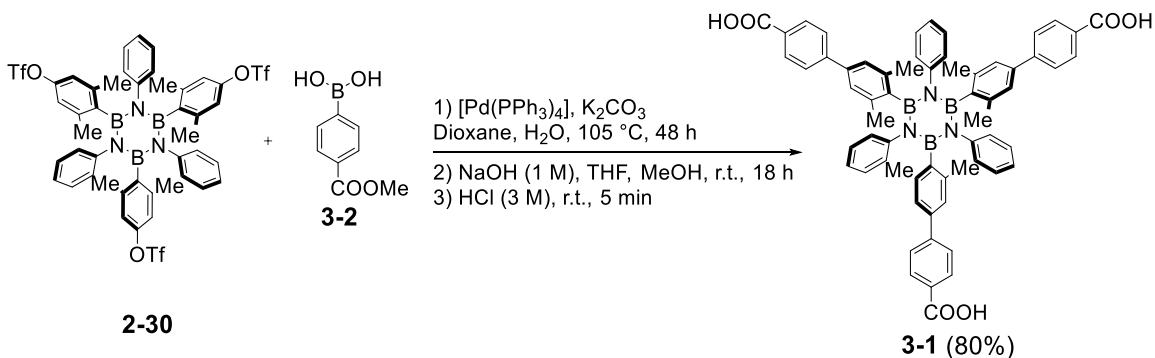
3.3.1 Synthesis of three-carboxyl linkers

The retrosynthetic strategy chosen to prepare three-carboxyl borazine **3-1** is showed in Scheme 3.2. Taking advantage of the synthesis of triflate borazine derivative **2-30**, mentioned in *section 2.5.2*, borazine **3-1** can be obtained from Suzuki cross-coupling reaction between 4-methoxycarbonyl-phenylboronic acid **3-2** and borazine bearing the triflate groups at the *B*-sites **2-23**, followed by saponification reaction of the methoxycarbonyl groups.



Scheme 3.2. Retrosynthetic pathway of borazine **3-1**.

The synthesis started with Suzuki cross-coupling reaction between compound **2-30** and **3-2** in the presence of $[\text{Pd}(\text{PPh}_3)_4]$, followed by saponification reaction. This afforded the expected borazine linker **3-1**, isolated in 80% yield over three steps (Scheme 3.3).



Scheme 3.3. Synthesis of three-carboxyl borazine **3-1**.

To prove the chemical identity of compound **3-1**, single crystals suitable for X-ray diffraction was obtained by slow diffusion of H_2O in DMSO solution. As expected, the X-ray molecular structure shows the presence of the carboxyl groups at the *B*-sites of the borazine outer shell (Figure 3.3).

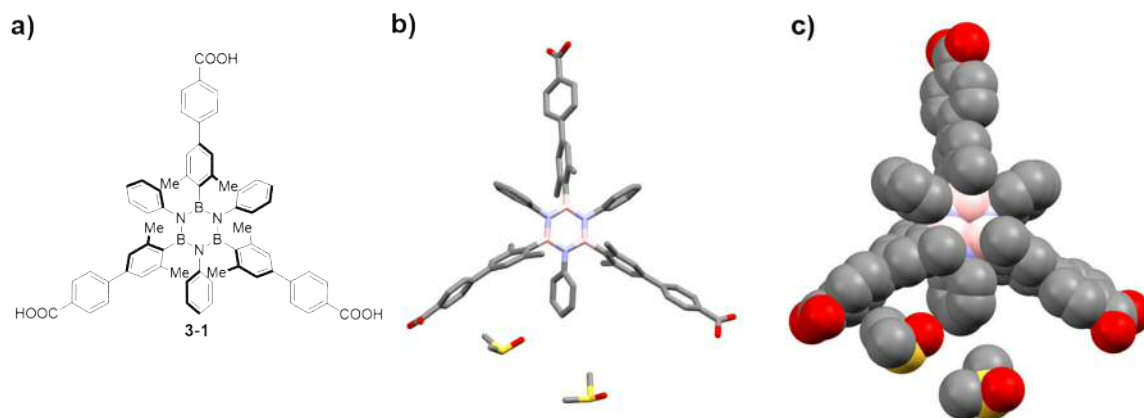


Figure 3.3. Crystal structure of borazine derivative **3-1**; a) molecular structure; b) crystal structure represented in capped sticks; c) crystal structure represented in spacefill. Space group: P21c. The crystal structure was grown by slow diffusion of H₂O in DMSO. Colour code: grey: C, pink: B, blue: N and red: O. Hydrogen atoms were omitted for the sake of clarity.

The crystal obtained belongs to the P21c space group. Borazine linker **3-1** possess supramolecular packing in a rectangular parallelepiped shape ($a = 17.57 \text{ \AA}$, $b = 19.98 \text{ \AA}$ and $c = 16.93 \text{ \AA}$) with the borazines core on side of the unit cell. Interestingly, the compound shows a highly dense supramolecular packing ($\rho = 1.28 \text{ g/cm}^3$, see X-ray data *chapter 5*) driving by H-bonding interactions between borazine **3-1**, H₂O and DMSO (Figure 3.4).

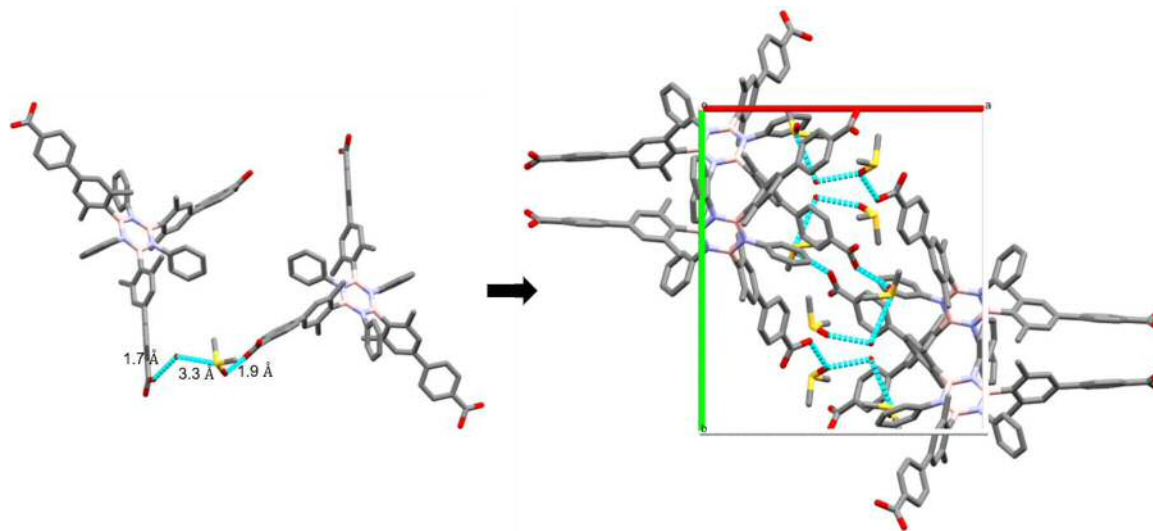


Figure 3.4. Crystal structure of borazine derivative **3-1** showing the different interactions present in the crystal lattice. Colour code: grey: C, pink: B, blue: N and red: O. Hydrogen atoms were omitted for the sake of clarity.

The ¹H-NMR spectrum of three-carboxyl borazine **3-1** in DMSO-*d*₆ is detailed in Figure 3.5. The broad singlet at 12.89 ppm corresponds to proton *a* and it is peculiar of the carboxylic groups. In the aromatic region, proton *b* and *c* appear distinctively as doublets at 7.87 and 7.58 ppm, respectively, with the same *ortho* coupling constant of 8.3 Hz, as

expected. The doublets *b* and *c* are related to the 6 phenyl hydrogen atoms in position 2 and 3, respectively, with respect to the carboxylic groups. The multiplet signal between 7-6.98 ppm refers to the 12 phenyl hydrogen atoms *d* and *e*. Multiplet signal *f* and triplet *g* ($J = 7.3$ Hz) are related to the 6 and 3 proton atoms of the phenyl rings at the *N* sites, respectively. In the aliphatic region, singlet *h* at 2.41 ppm is related to the 18 methyl hydrogen atoms.

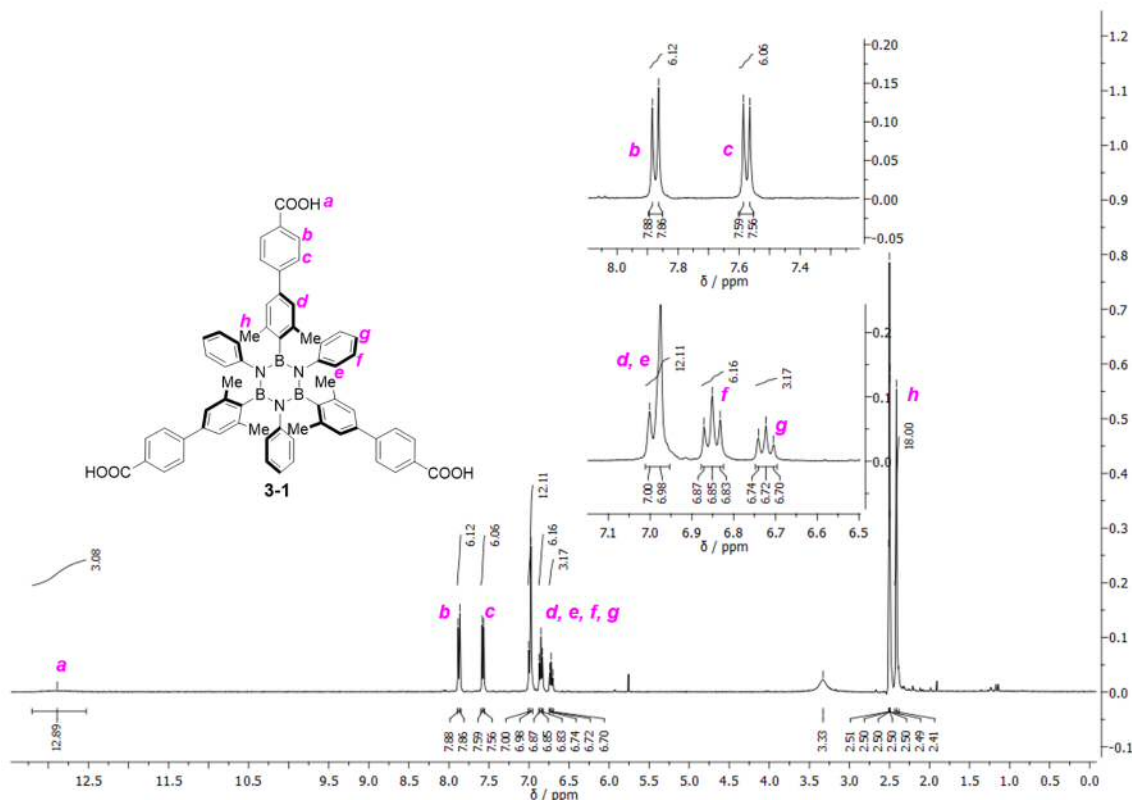
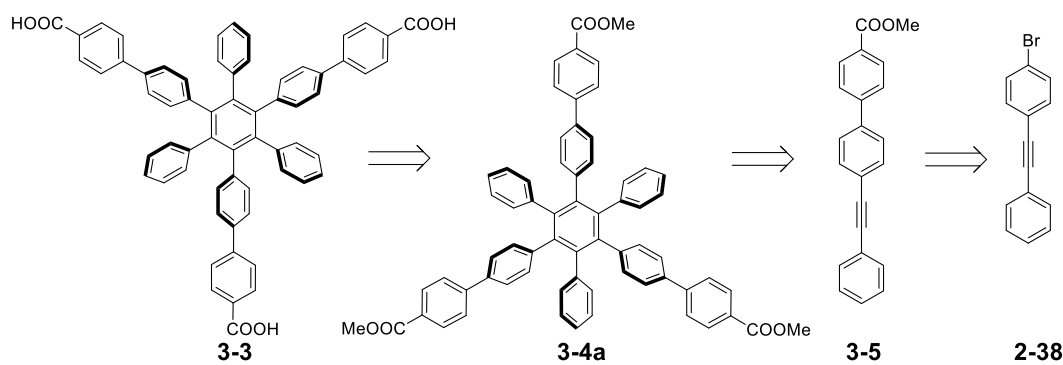


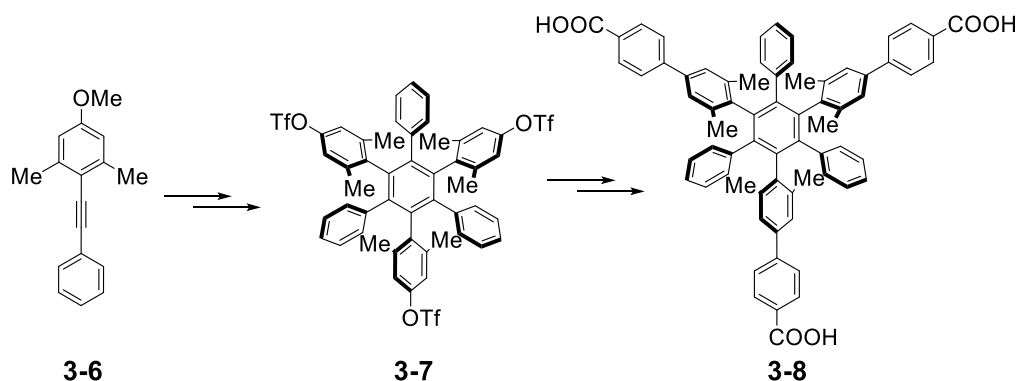
Figure 3.5. 400 MHz $^1\text{H-NMR}$ of borazine linker **3-1** in $\text{DMSO-}d_6$ (Solvent residual peak: 2.50 ppm).

Moving on the synthesis of full-carbon reference **3-3**, the proposed retrosynthetic pathways is pointed out in Scheme **3.4**. Three-carboxyl derivative **3-3** can be obtained through a saponification reaction of corresponding hexaphenyl ester derivative **3-4a**, itself prepared from a cyclotrimerisation reaction of **3-5**, catalysed by $[\text{Co}_2(\text{CO})_8]$.



Scheme 3.4. Retrosynthetic pathway of full-carbon linker **3-3**.

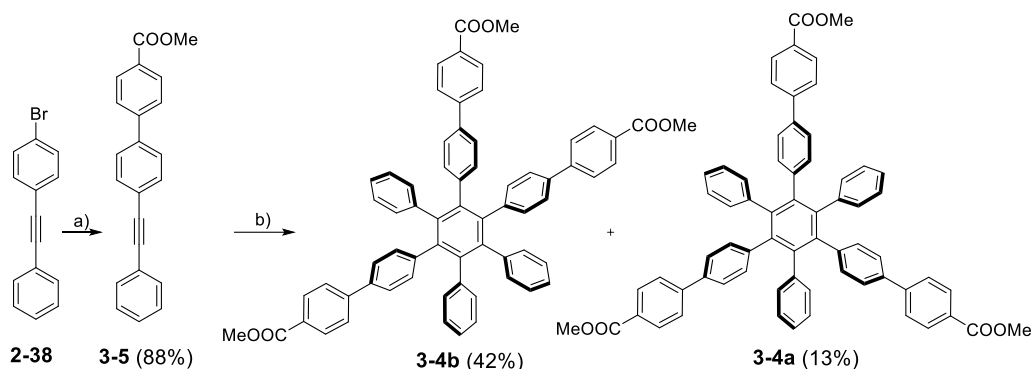
Starting from derivative **2-38** (previously synthesised in *section 2.5.3*), Suzuki cross-coupling reaction would allow the formation of **3-5** introducing the phenylmethoxycarbonyl moiety. The choice of compound **3-3** as molecular reference bearing phenyl rings instead of xylyl groups in position 2,4 and 6 of the benzene core was dictated by the best compromise between synthesis and chemical structure similarity with borazine derivative **3-1**. In particular, from a synthetic point of view, the only feasible way to prepare the real analogue full-carbon linker **3-8** is starting from the cyclotrimerisation reaction of 2-((4-methoxyphenyl)ethynyl)-1,3-dimethylbenzene **3-6** (Scheme **3.5**). Unfortunately, the cyclotrimerisation reaction of compound **3-6**, catalysed by $[\text{Co}_2\text{CO}_8]$, was previously attempted in our group without conclusive results, probably due to the presence of the two methyl groups which prevent the coordination of the triple bond on the $[\text{Co}]$ catalyst.



Scheme 3.5. Schematic synthetic scheme of full-carbon linker **3-8**.

In the first synthetic step, the synthesis commenced with Suzuki cross-coupling reaction between compound **2-38** and **3-2**, affording **3-5** derivative in 88% yield (Scheme **3.6**).

Having in hand **3-5**, the following step was the [Co] catalysed cyclotrimerisation reaction, obtaining the mixture of two regioisomers **3-4a** and **3-4b**.



Scheme 3.6. Synthesis of compound **3-4a**. Reaction conditions: a) Phenylmethoxycarbonyl boronic acid **3-2**, [Pd(PPh₃)₄], K₂CO₃, Dioxane, H₂O in ratio 1:3, 105 °C, 18 h, b) [Co₂CO₈], dioxane, 105 °C, 18 h.

The two regioisomers were firstly isolated from the reaction mixture through silica gel chromatography and then injected in recycling high performance liquid chromatography (rec-HPLC) normal phase. Notably, using CHCl₃/Hexane (in ratio 3:7), after 8 cycles, we were able to separate desired hexaphenylbenzene **3-4a** in 13% yield from **3-4b** (42% yield, Figure 3.6).

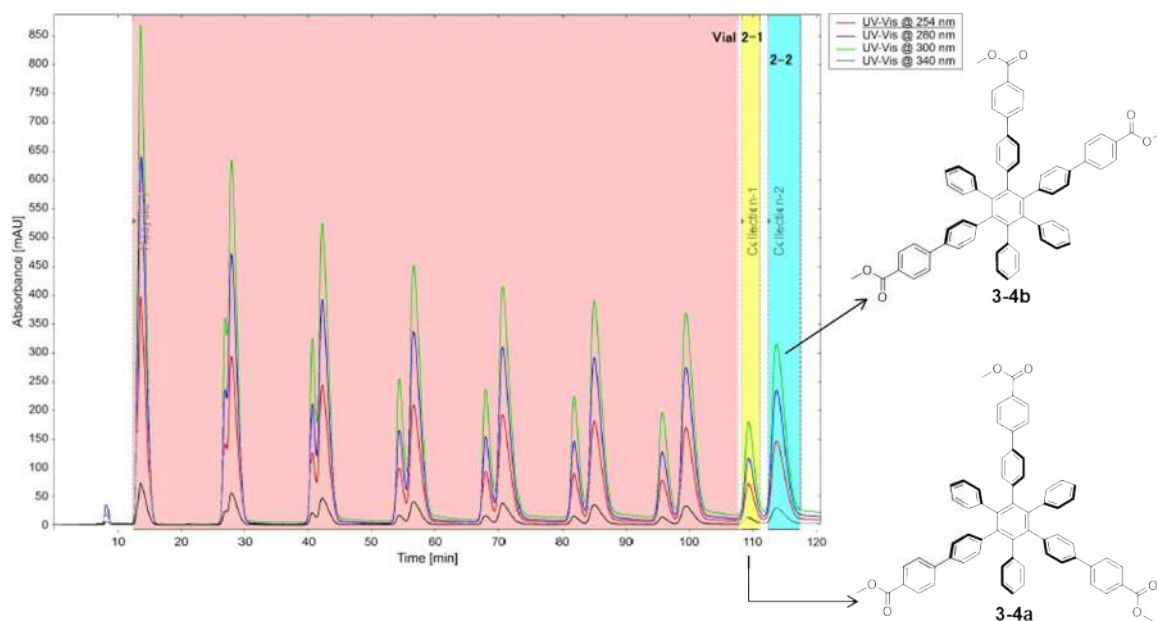
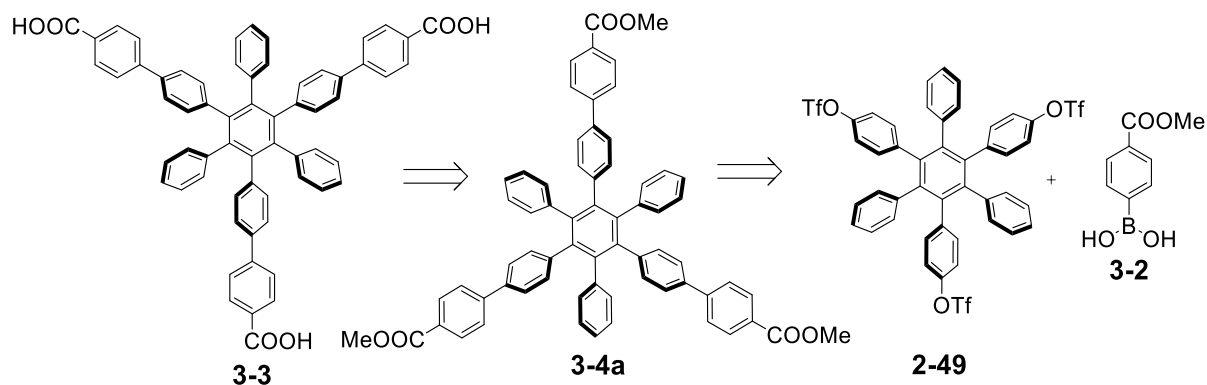


Figure 3.6. Chromatogram obtained from the purification of full-carbon derivative **3-4a** and **3-4b** by recycling-HPLC normal phase. Eluent: CHCl₃/Hexane 3:7.

Despite the desire to accomplish the final step of the synthesis through the saponification reaction of ester **3-4a**, we need to point out that, as mention in *section 2.5.3*, the cyclotrimerisation reaction always gives the formation of two regioisomers in ratio 1:3 in favour to the asymmetrical product (**3-4b**). Additionally, although the rec-HPLC is a powerful analytical method, the maximum amount that we can inject in the machine is only 15 mg. As result, an alternative retrosynthetic procedure was necessary to scale up the chemical reaction. At the same time, the synthesis of triflate-hexaphenyl derivative **2-49** was performed in large scale, as described in *chapter 2*. Hence, having in hand the derivative **2-49**, a second retrosynthetic pathway for three-carboxyl derivative **3-3** was designed (Scheme 3.7). Derivative **3-4a** can be synthesised by Suzuki cross-coupling reaction between 4-methoxycarbonyl-phenylboronic acid **3-2** and hexaphenyl derivative **2-49**.

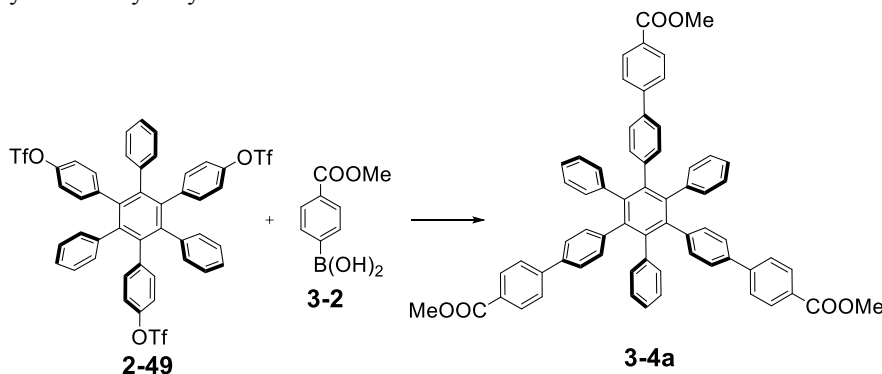


Scheme 3.7. Retrosynthetic pathway of three-carboxyl derivative **3-3**.

Different Suzuki cross-coupling reaction attempts were performed to yield hexaphenyl ester derivative **3-4a** (Table 3.1). At first, the reaction conditions proposed by M. D. Wendt and co-workers were reproduced (entry 1).¹⁸ In those conditions, the complete conversion of triflate derivative **2-49** was observed, only 4% yield of the desired product **3-4a** was recovered by silica gel chromatography. The remaining 96% of the material was a mixture of mono and bis-adducts. This result suggests us that the steps of oxidative addition and reductive elimination catalysed by [Pd] worked, but the reaction stop after the formation of the first adduct. As consequence, we envisage to move from conventional heating to microwave irradiation (entry 2). Many articles reported an higher conversion and reaction rate if compared with the classical heating.¹⁹ However, in our case, we did not observe any improvement. Then, we decided to change the reaction conditions following the work of E.

J Lavoie and co-workers²⁰ (entry 3). Notably, moving on Pd(OAc)₂/XPhos as catalytic system and K₂CO₃ as base, we did not isolate desired product **3-4a**, but the formation of the corresponding carboxylates (mono, bis and tris-adducts) were observed.

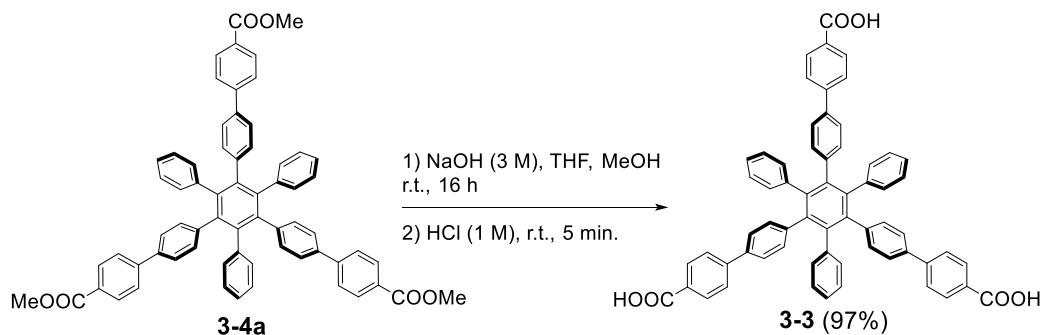
Table 3.1. Optimisation of Suzuki cross-coupling reaction to synthesise full-carbon derivative **3-4a**. XPhos = 2-Dicyclohexylphosphino-2',4',6'-triisopropylbiphenyl, Convent. = conventional, M.W. Irr. = microwave irradiation, Hyd = base hydrolysis.



Entry	Catalyst	Ligand	Base	Solvent	Temp.	Heating	Yield
1	[Pd(dppf)Cl ₂]	-	CsF	Dioxane	110 °C	Convent.	4%
2	[Pd(dppf)Cl ₂]	-	CsF	Dioxane	160 °C	M.W. Irr.	6%
3	Pd(OAc) ₂	XPhos	K ₂ CO ₃	Dioxane/H ₂ O	105 °C	Convent.	0%, hyd.
4	Pd(OAc) ₂	XPhos	K ₃ PO ₄	THF	75 °C	Convent.	83%

Unfortunately, we were not able to isolate them, but this result suggests that K₂CO₃ in the presence of water is able to hydrolyse ester **3-4a**. Inspired by this result, we decided to switch the base/solvent conditions from K₂CO₃/dioxane, H₂O to K₃PO₄/THF (dry) as showed in entry 4,²¹ affording desired three-ester derivative **3-4a** in 83%.

Finally, saponification reaction of compound **3-4a** in a mixture THF/MeOH 1:4, was performed by adding NaOH (1 M) at room temperature (Scheme 3.8). Then three-carboxyl derivative **3-3** was obtaining in 97% yield by acidification in the presence of HCl (3 M).



Scheme 3.8. Saponification reaction of full-carbon derivative **3-4a**.

The $^1\text{H-NMR}$ spectrum of three-carboxyl derivative **3-3** in DMSO-d_6 is shown in Figure 3.7. Broad singlet *a* at 12.93 ppm corresponds to the proton of the carboxylic group. In the aromatic region, protons *b*, *c*, and *d* appear distinctively as doublets at 7.90, 7.62 and 7.31 ppm, respectively, with the same *ortho* coupling constant of 8.3 Hz, which are attributed to the phenyl hydrogen atoms. The multiplet signal between 7-6.79 ppm refers to the 21 phenyl hydrogen atoms *e* and *f*.

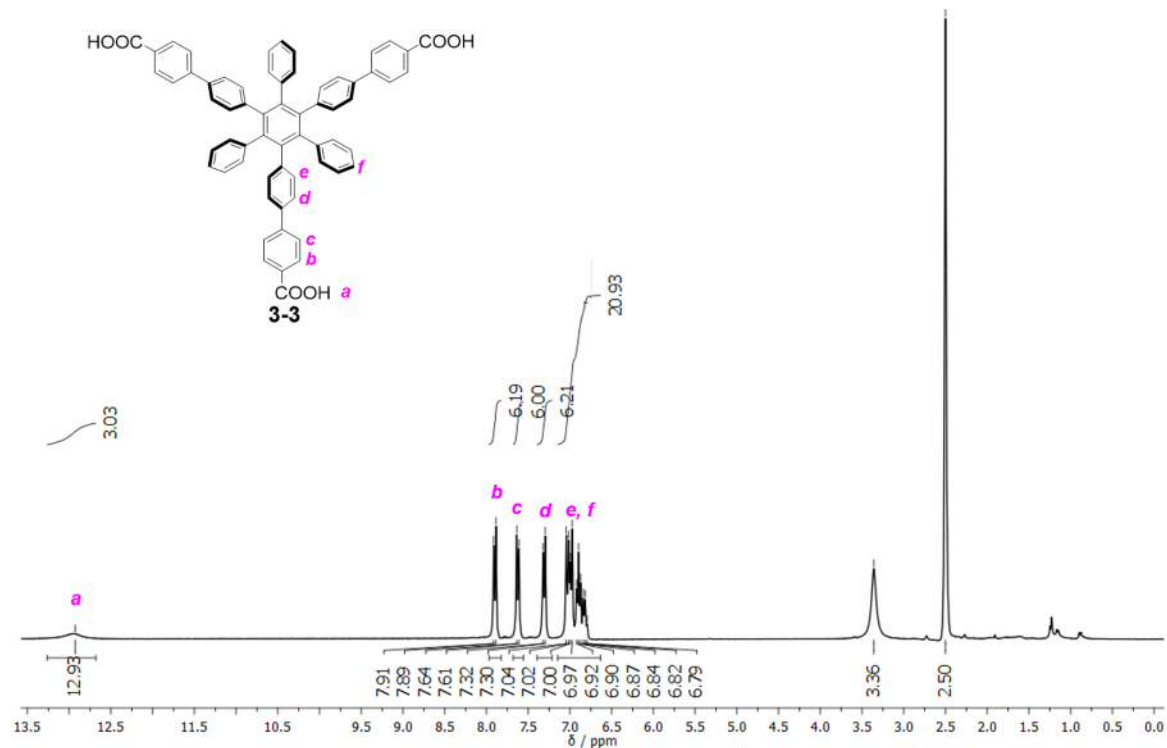
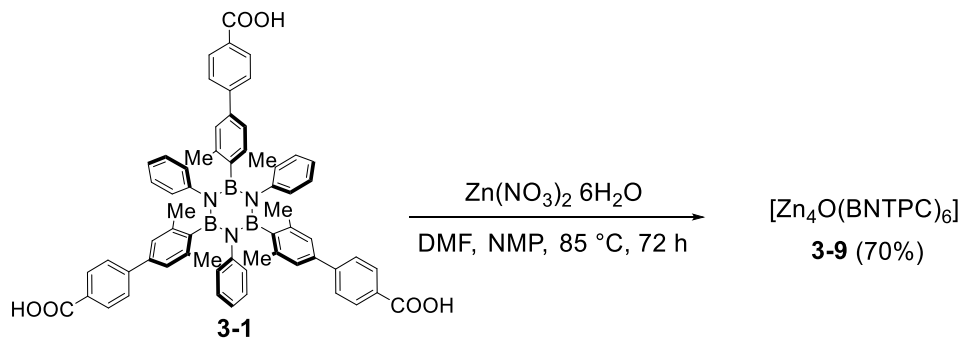


Figure 3.7. 400 MHz $^1\text{H-NMR}$ of borazine linker **3-3** in DMSO-d_6 (Solvent residual peak: 2.50 ppm).

3.3.2 Synthesis and X-ray crystal structure of MOFs

The synthesis of BN-MOF **3-9** was carried out following the solvothermal method proposed by O. Yaghi and co-workers,²² with the only exception that $\text{N,N}'$ -dimethylformamide (DMF) was replaced by DEF (Scheme 3.9). Three-carboxyl borazine (BNTCP) **3-1** was dissolved in a mixture 1:1 DMF/NMP. Then, $\text{Zn}(\text{NO}_3)_2 \cdot 6\text{H}_2\text{O}$ was added and the reaction mixture was heated at 85 °C. After 72 h, colourless crystals were observed, and BN-MOF **3-9** was isolated in 70% yield (the yield of the reaction has been measured taking in consideration the monomeric unit $[\text{Zn}_2\text{O}_{0.5}(\text{C}_{63}\text{H}_{51}\text{B}_3\text{N}_3\text{O}_6)]$ and the residual solvent calculated by TGA). The crystals obtained were firstly analysed by optical and electron

microscope (SEM), as shown in Figure 3.8. The SEM images of BN-MOF **3-9** (Figure 3.8c and d) shows the crystalline shape with maximum dimension between 0.5 and 0.6 mm. The SEM images of BN-MOF **3-9** (Figure 3.8c and d) shows the crystalline shape with maximum dimension between 0.5 and 0.6 mm.



Scheme 3.9. Synthesis of BN-MOF **3-9**.

In general, the interaction between the metal centre and the organic linker is dynamic in which the chemical bond can be formed or broken and reformed to obtain the polymer propagation. The dynamic bond formation plays a pivotal role in the formation of a crystalline porous material, so any erroneous bond that can cause disorder or early termination could affect dramatically the reaction performance.²³ In this context, it is worth to point out that the yield of the reaction depends on the heating system and on the size of the glassware in which the reactions have been performed. By changing the heating system and the glassware size, the heat transfers that take place during the chemical reaction can affect not only the crystal size but also the phase purity of the porous materials.²³ Given these premises, to ensure the reproducibility of the reactions, the syntheses have been performed in the same sealed vial (the specific size is reported in the *chapter 5*) heated by a bath of non-flammable silicon-based, keeping the same amount, ratio and concentration of the starting materials.

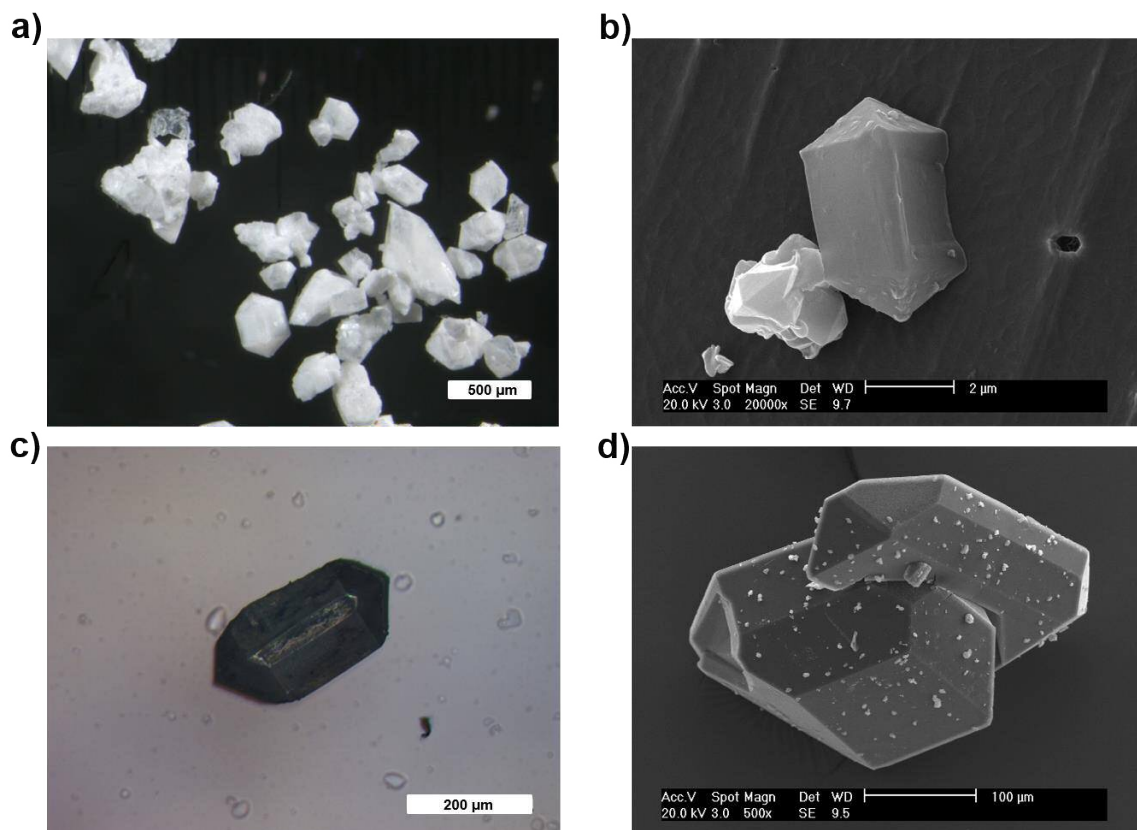


Figure 3.8. BN-MOF **3-9** crystals analysed by a), c) optical microscope and b), d) scanning electron microscope (SEM).

An X-ray crystal analysis of a single crystal from the reaction revealed that BN porous material **3-9** has an orthorhombic space group Pnmm and it crystallises with *rtl* topology. The refined crystal data is reported in *chapter 5*. A fragment of the structure is depicted in *Figure 3.9*, where six borazine linkers are coordinated to each of the Zn(II) centres. Each bi-dentate carboxyl moiety chelates the zinc ions in “bridging mode”, in which two metal centres are joined in close contact. The core of the structure proposed in *Figure 3.9* consists of a single O atom bonded to four Zn atoms, forming a regular Zn₄O tetrahedron. Each edge of each Zn tetrahedron is then capped by a -CO₂ group to form a Zn₄(O)(CO₂)₆ cluster.

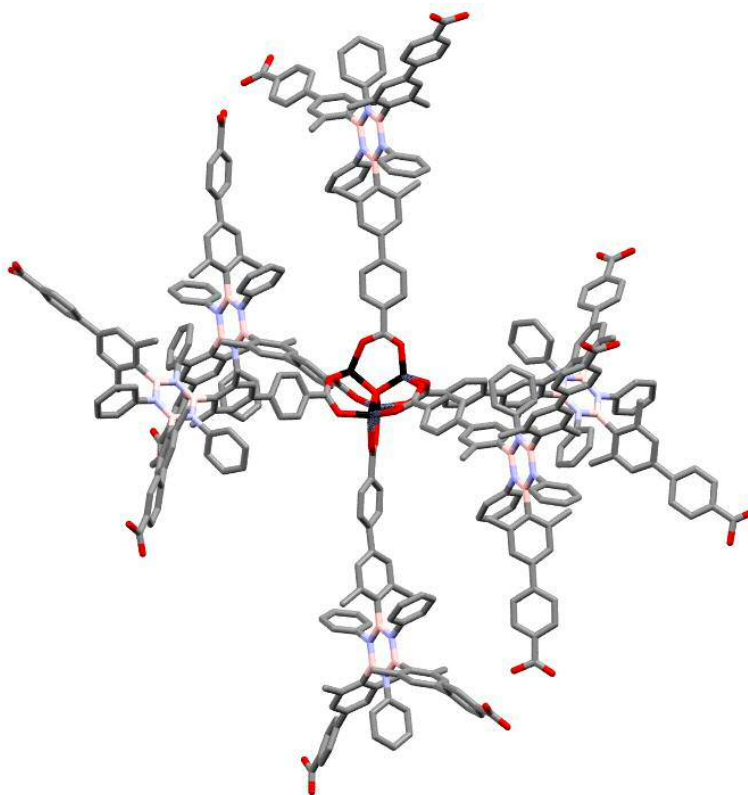


Figure 3.9. Crystal structure of BN-MOF **3-9** represented in capped sticks. Space group: Pnmn. Colour code: grey: C, pink: B, blue: N, red: O, black: Zn. Hydrogen atoms were omitted for the sake of clarity.

Interestingly, 3D BN-MOF **3-9** crystallised with the formation of a doubly interpenetrating network, composed by two infinite structurally regular motifs (highlighted in orange and green, see Figure **3.10**) that contain independent $[\text{Zn}_4\text{O}(\text{BNTCP})_6]$ units inextricably entangled. The distance between the two interpenetrated networks is 4.6 Å (Figure **3.10**). The origin of this phenomenon can be ascribed to the presence of free voids in the single network, which allows the interpretation by two BN polymers. Although this behaviour reduces the size of the pores, the interpenetration does not prevent the possibility of obtaining open porous materials.^{24,25}

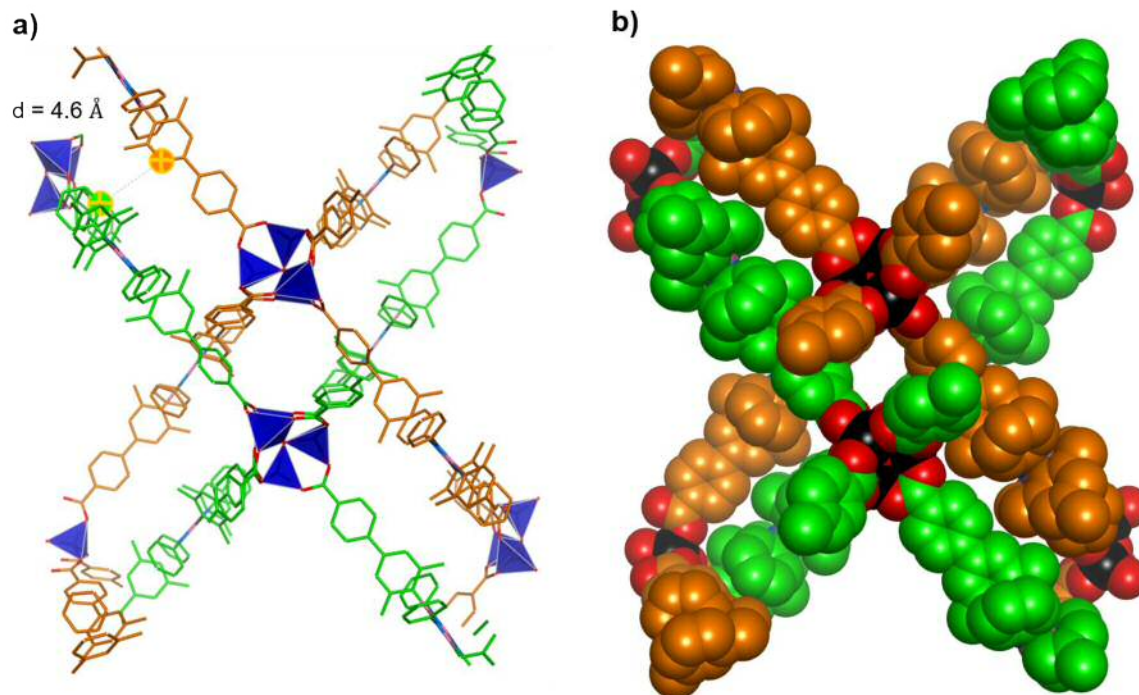


Figure 3.10. Crystal structure of BN-MOF **3-9** showing two interpenetrating networks a) the crystal structure is represented in capped sticks, the distance between the carbon atoms highlighted has been determined from the crystal structure taking in consideration the van der Waals radii; b) the crystal structure is represented in spacefill; colour code: the carbon atoms are coloured separately in orange and green, pink: B, blue: N, red: O, dark blue: cluster ZnO_4 . Hydrogen atoms were omitted for the sake of clarity.

The extension of $[Zn_4O(BNTCP)_6]$ units along the 3 dimensions revealed a remarkably open three-dimensional porous structure as pointed out in Figure 3.11. As result from Platon software, if overlapping spheres with van der Waals radii (2.25, 1.20, 1.70, 1.52, 1.55, 1.63 Å for Zn, H, C, O, N and B, respectively) are placed at the atomic positions, the non-occupied space is 70% (28300 \AA^3) of its cell volume. In conclusion, the framework atoms in BN-MOF **3-9** take up only a small fraction (30%) of the available space in the crystal, with a calculated density of 0.52 g/cm^3 (the theoretical measure has been performed with Platon software). The non-framework space is divided into two different types of pores namely C-cavities and BN-cavities. The C-cavities (highlighted in red, Figure 3.11) are formed by two metal clusters (one on each polymer) and also by the hydrocarbon moieties made of phenylenes. Resulting from the interpenetration of such two entangled networks, a pore diameter of approximately 6.3 \AA is generated (Figure 3.11). The BN-cavities are bigger than the C-counterpart, with a diameter of approximately 14.5 \AA , featuring borazine scaffolds which surround the cavity as clearly shown in Figure 3.11 (highlighted in black). The BN-cavities possess a peculiar pore constitution, made of borazine scaffolds. Such flat

rings surround the pore so that each one exposes its flat side towards the centre of the pores.

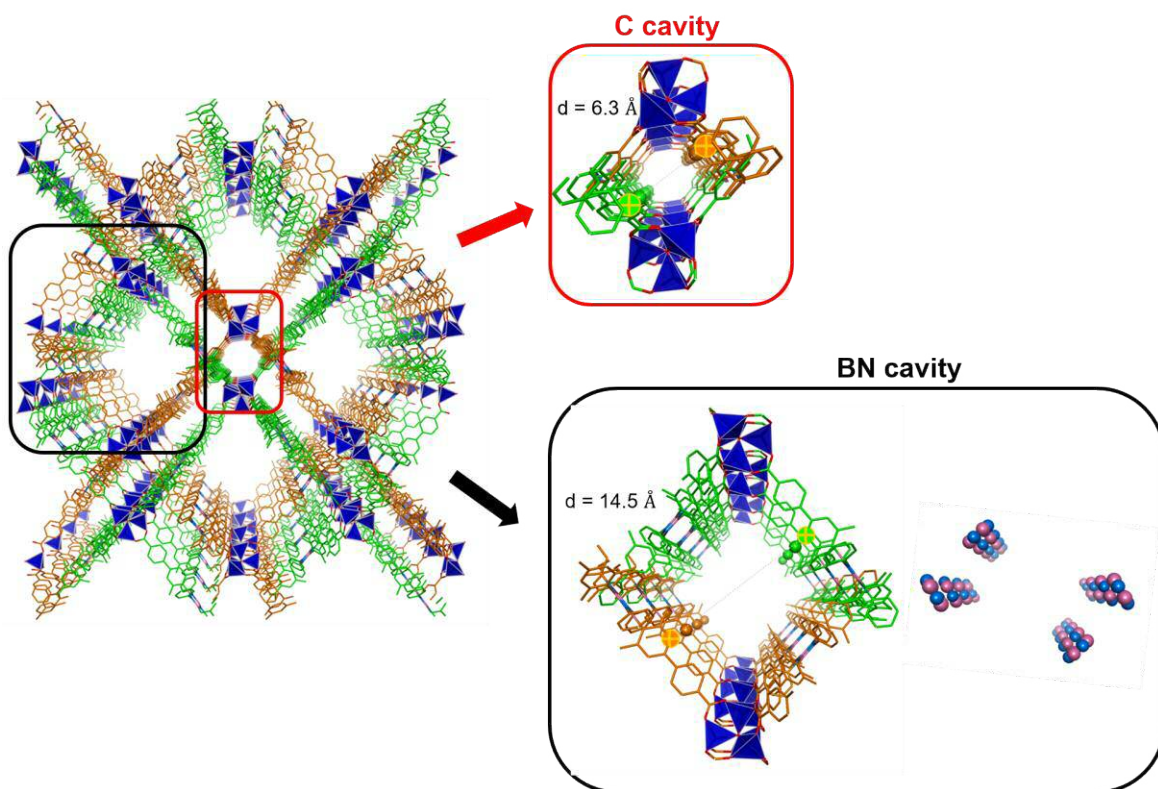
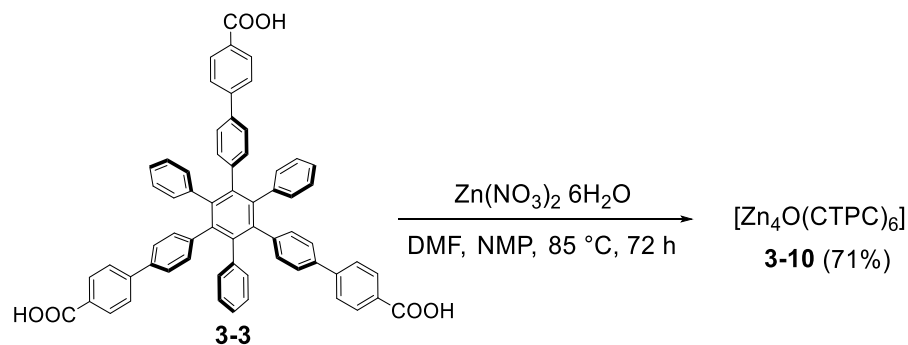


Figure 3.11. Crystal structure of BN-MOF **3-9** showing the C- and BN-cavities, the distances between the carbon atoms highlighted have been determined from the crystal structure taking in consideration the van der Waals radii. The crystal structure is represented in capped sticks. Colour code: the carbon atoms are coloured separately in orange and green, pink: B, blue: N, red: O, dark blue: cluster ZnO₄. Hydrogen atoms were omitted for the sake of clarity

As described for BN-MOF **3-9**, the formation of the porous crystal frameworks is strongly influenced by the reaction conditions, such as temperature, time, solvent and reagent concentrations. To obtain a comparable full-carbon analogue, C-MOF **3-10** was prepared following the same solvothermal procedure proposed for BN-MOF **3-9**. Three-carboxyl full-carbon linker (CTCP) **3-3** was dissolved in a mixture 1:1 DMF/NMP, then Zn(NO₃)₂·6H₂O was added and the reaction mixture was heated at 85 °C (Scheme **3.10**). After 72 h, colourless crystals were observed and filtered, yielding C-MOF **3-10** in 71% (the yield of the reaction has been measured taking in consideration the monomeric unit [Zn₂O_{0.5}(C₆₉H₃₉O₆)] and the residual solvent calculated by TGA). The crystals obtained were, once again, analysed by optical and electron microscope (SEM), as shown in Figure **3.12**. The SEM images of C-MOF **3-10** (Figure **3.12c** and **d**) shows the crystalline shape with maximum dimension between 0.5 and 0.6 mm.



Scheme 3.10. Synthesis of C-MOF 3-10.

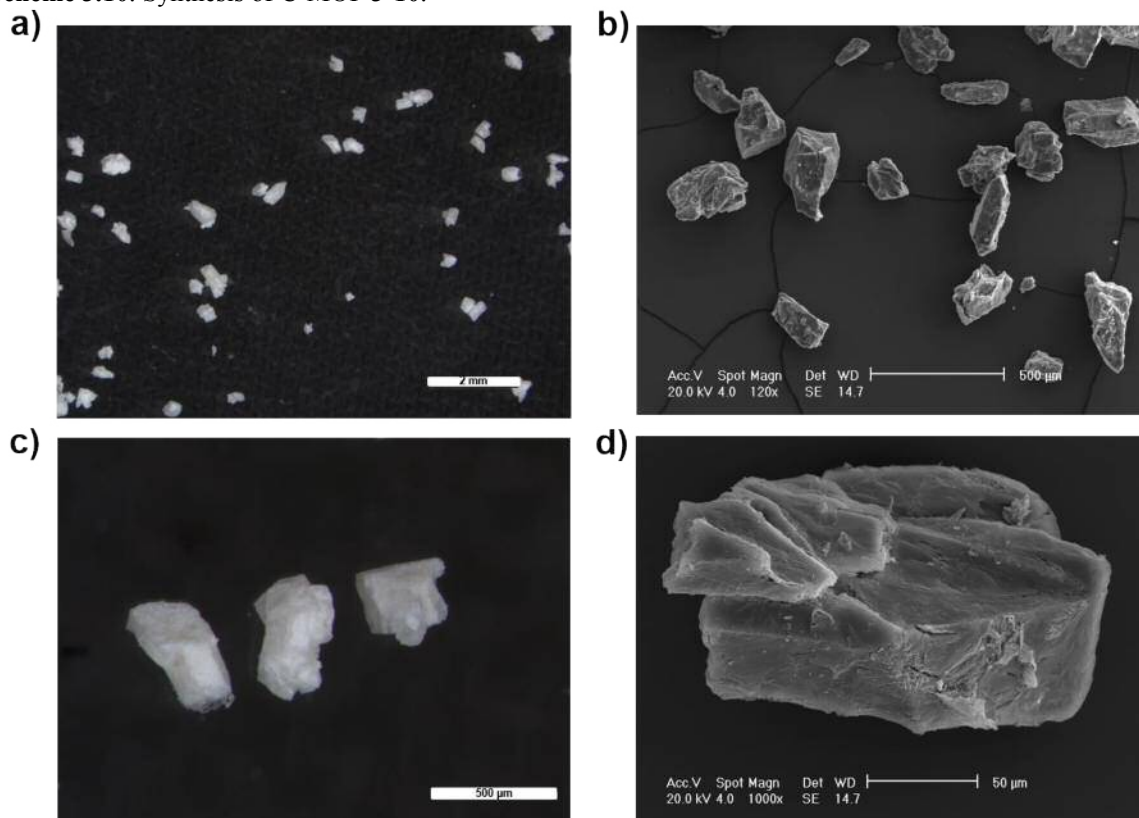


Figure 3.12. C-MOF 3-10 crystals analysed by a), c) optical microscope and b), d) scanning electron microscope (SEM).

A single crystal of C-MOF 3-10 was then analysed by X-ray diffraction. Once again, we observed a metal-organic framework (a fragment of the structure is shown in Figure 3.13) in which the core is composed by four Zn_4O tetrahedron subunits and the bi-dentate carboxylate linker chelates the zinc ions in bridging mode. The resulting metal cluster is surrounded by six full-carbon organic linker 3-3.

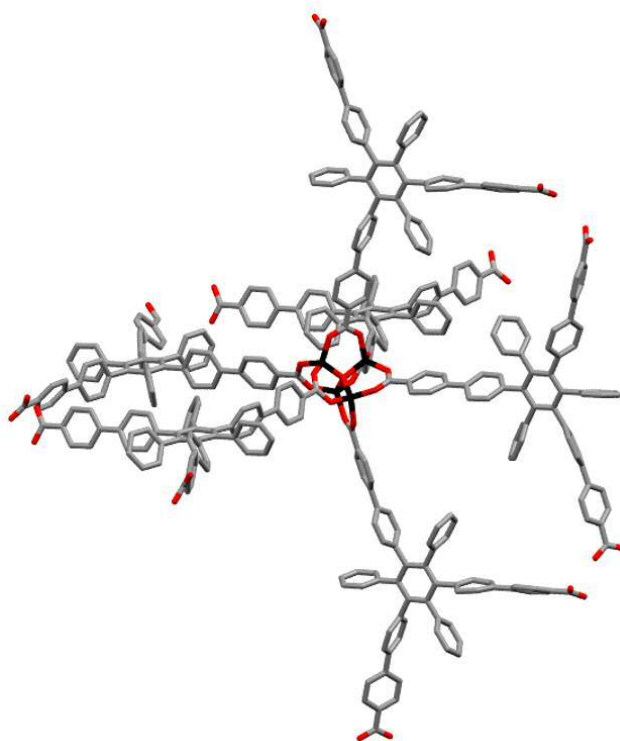


Figure 3.13. Crystal structure of C-MOF **3-10** represented in capped sticks. Space group: $Fdd2$. Colour code: grey: C, red: O, black: Zn. Hydrogen atoms were omitted for the sake of clarity.

Surprisingly, although C-MOF **3-10** belongs to the same crystal system of BN-MOF **3-9**, which is orthorhombic, the self-assembly in the solid state is described by the face centered Bravais lattice. Then, the presence of glide planes d and screw axis of order 2, defined the complete crystallographic space group $Fdd2$ ($R1 = 0.0595$, $wR2 = 0.1690$, the refined crystal data is shown in *chapter 5*). Comparing the two MOFs (**3-9** and **3-10**), $Zn_4(O)(CO_2)_6$ cluster are linked through the organic ligands in two different ways. The torsional angle between the plane of the organic ligands and the plane of the carboxylate cluster is 49° in C-MOF **3-10** and 56° in BN-MOF **3-9** (Figure **3.14**). The reason could be ascribed to the presence of the bulky *o*-methyl protecting groups on the aryl group at the *B*-sites in the inner shell of borazine **3-1** that, hampering rotational movements, rigidify the hexasubstituted borazine scaffold compared to that of hexaphenylbenzene derivative **3-3**. Moving from BN-MOF **3-9** to C-MOF **3-10**, interestingly the bond length between Zn atoms and O atoms is also different (Figure **3.14**). Notably, Zn-O bonds in the BN-MOF **3-9** cluster is 1.80 \AA compared to 1.93 \AA in analogue full-carbon MOF **3-10**, which is comparable to Zn-O bonds (1.91 \AA) reported by O. Yaghi and co-workers.¹⁷

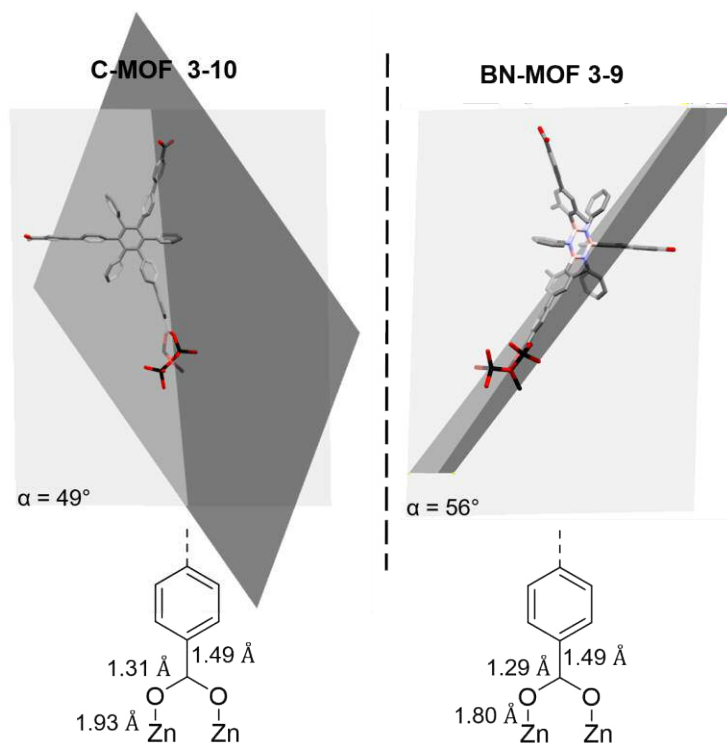


Figure 3.14. Crystal structures of C-MOF **3-10** and BN-MOF **3-9** showing the different atom disposition in the crystal lattice between the organic ligands and the carboxylate clusters.

As consequence of such different interactions, a change in the space group from Pnmm (BN-MOF **3-9**) to Fdd2 (C-MOF **3-10**) was observed leading to a different interpenetrated structure (Figure 3.15).

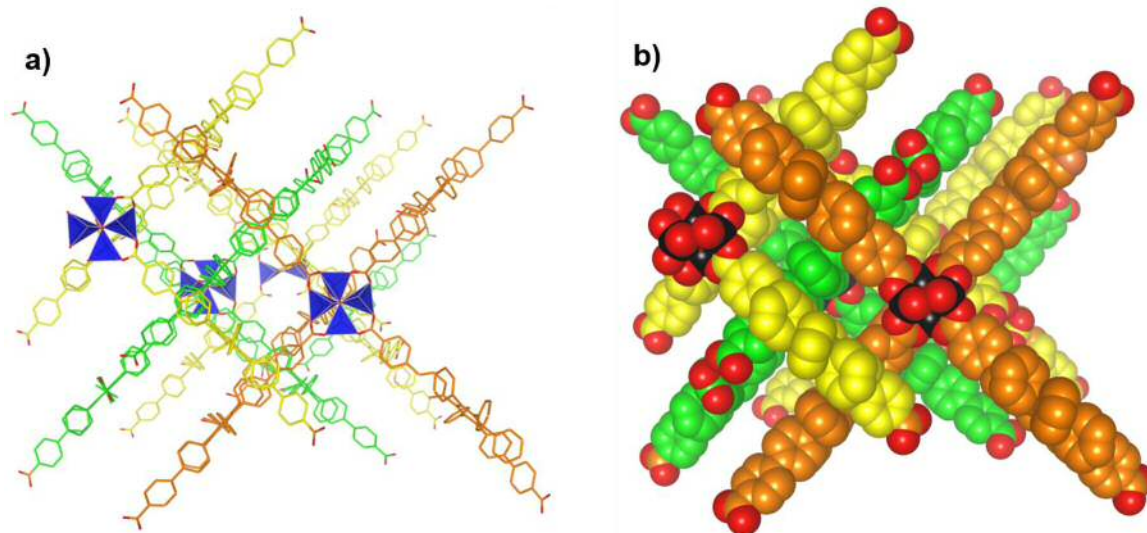


Figure 3.15. Crystal structure of C-MOF **3-10** showing three interpenetrating networks a) the crystal structure is represented in capped sticks; b) the crystal structure is represented in spacefill; colour code: the carbon atoms are coloured separately in orange, green and yellow, red: O, black: Zn, dark blue: cluster ZnO_4 . Hydrogen atoms were omitted for the sake of clarity.

3D C-MOF **3-10** crystallised with a *ant* topology, in which three interpenetrating networks composed by three infinite structurally regular motifs (highlighted in orange, yellow and green, Figure 3.16) are inextricably entangled.

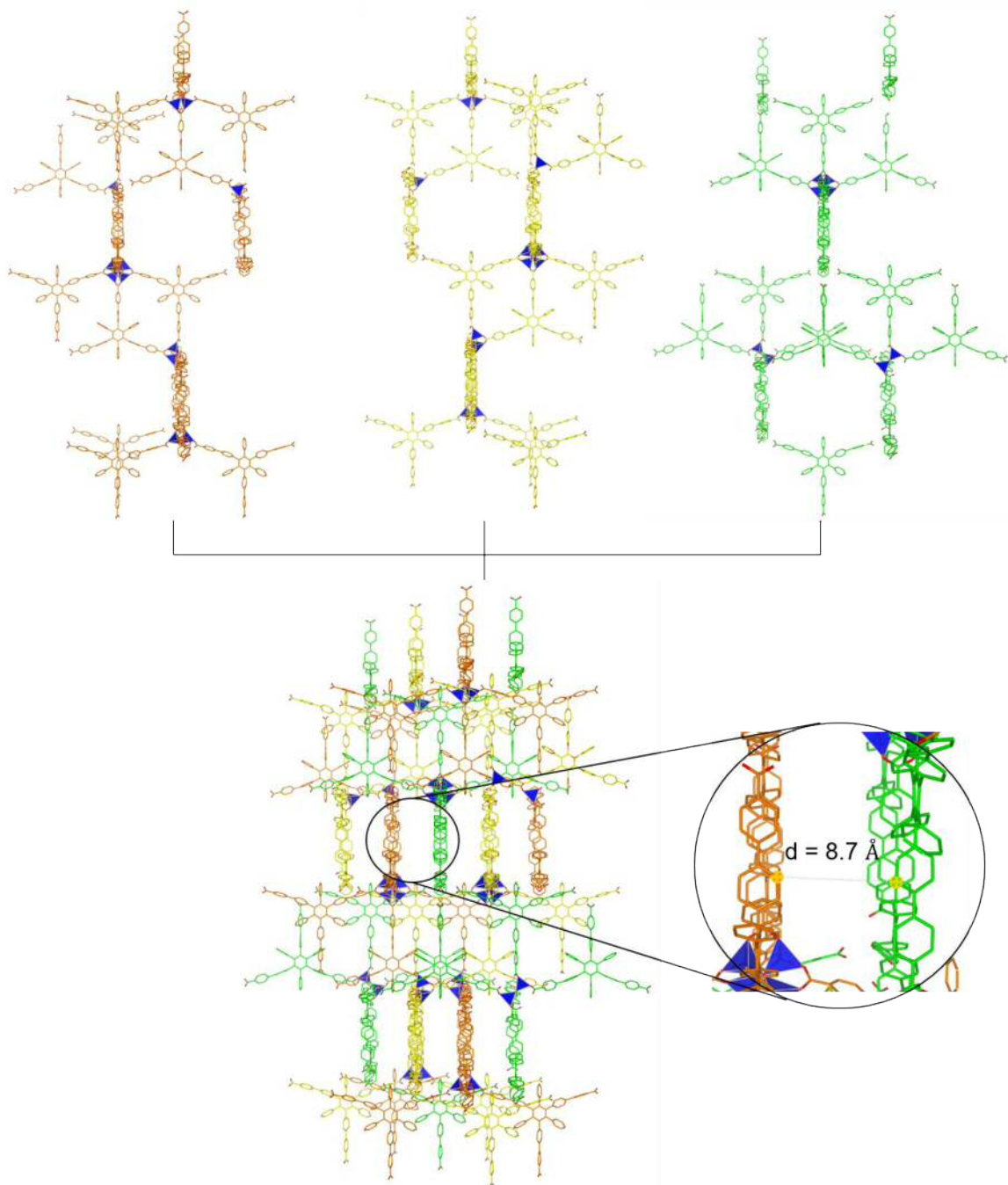


Figure 3.16. Crystal structure of C-MOF **3-10** showing three interpenetrating networks. The crystal structure is represented in capped sticks, the distance between the carbon atoms highlighted has been determined from the crystal structure taking in consideration the van der Waals radii. Colour code: the carbon atoms are coloured separately in orange, yellow and green, red: O, dark blue: cluster ZnO_4 . Hydrogen atoms were omitted for the sake of clarity.

The distance between each interpenetrated network respect to the others is approximately 8.7 Å (Figure 3.16). Moving on the description of the $[\text{Zn}_4\text{O}(\text{CTCP})_6]$ extended along the 3 dimensions, it also revealed an interesting open three-dimensional porous structure as shown in Figure 3.17. As result from theoretical calculation perform with Platon software, if overlapping spheres with van der Waals radii (2.25, 1.20, 1.70, 1.52, Å for Zn, H, C, and O, respectively) are placed at the atomic positions, the space not occupied is 63% (41771 Å³) of its cell volume. As result, the framework atoms in C-MOF 3-10 take up only the 37% of the available space in the lattice crystal, with a calculated density of 0.65 g/cm³ (against the 30% in BN-MOF 3-9). Additionally, by turning 90° the crystal along the z-axes, the interpenetration of such three entangled networks generates the formation of square channels. These cavities have a dimension of approximately 11.5 x 15.8 Å (Figure 3.17).

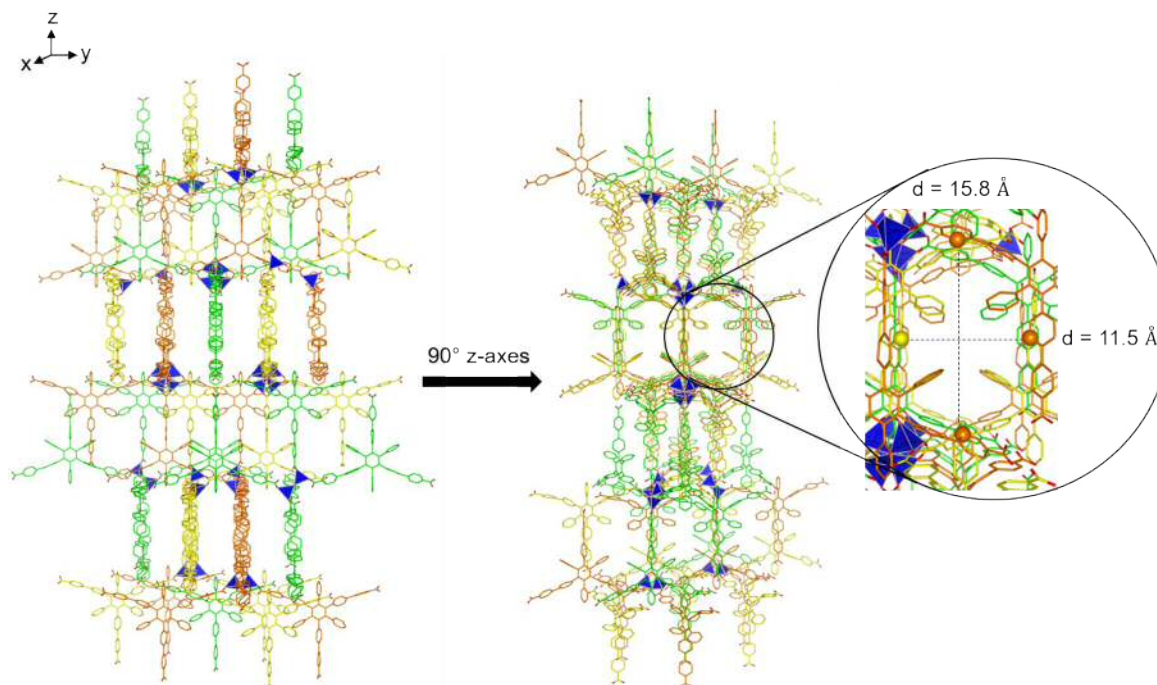


Figure 3.17. Crystal structure of C-MOF 3-10 showing the porous nature of the material, the distances between the carbon atoms highlighted have been determined from the crystal structure taking in consideration the van der Waals radii. The crystal structure is represented in capped sticks. colour code: the carbon atoms are coloured separately in orange, yellow and green, red: O, dark blu: cluster ZnO_4 . Hydrogen atoms were omitted for the sake of clarity.

3.3.3 Powder X-ray diffraction (PXRD)

The Powder X-ray diffraction (PXRD) has been measured to confirm the bulk crystallinity of BN-MOF 3-9 and C-MOF 3-10 (Figure 3.18). MOFs phase purity can be evaluated by comparing the experimental with the simulated powder patterns, the latter generated from

single crystal X-ray data. Before starting the analysis, the porous materials were freshly prepared and dried under air for 12 hours. Then the samples were loaded on aluminium flat plates and PXRD was performed. The results are shown in Figure 3.18 and the 2-theta values are reported in Table 3.2.

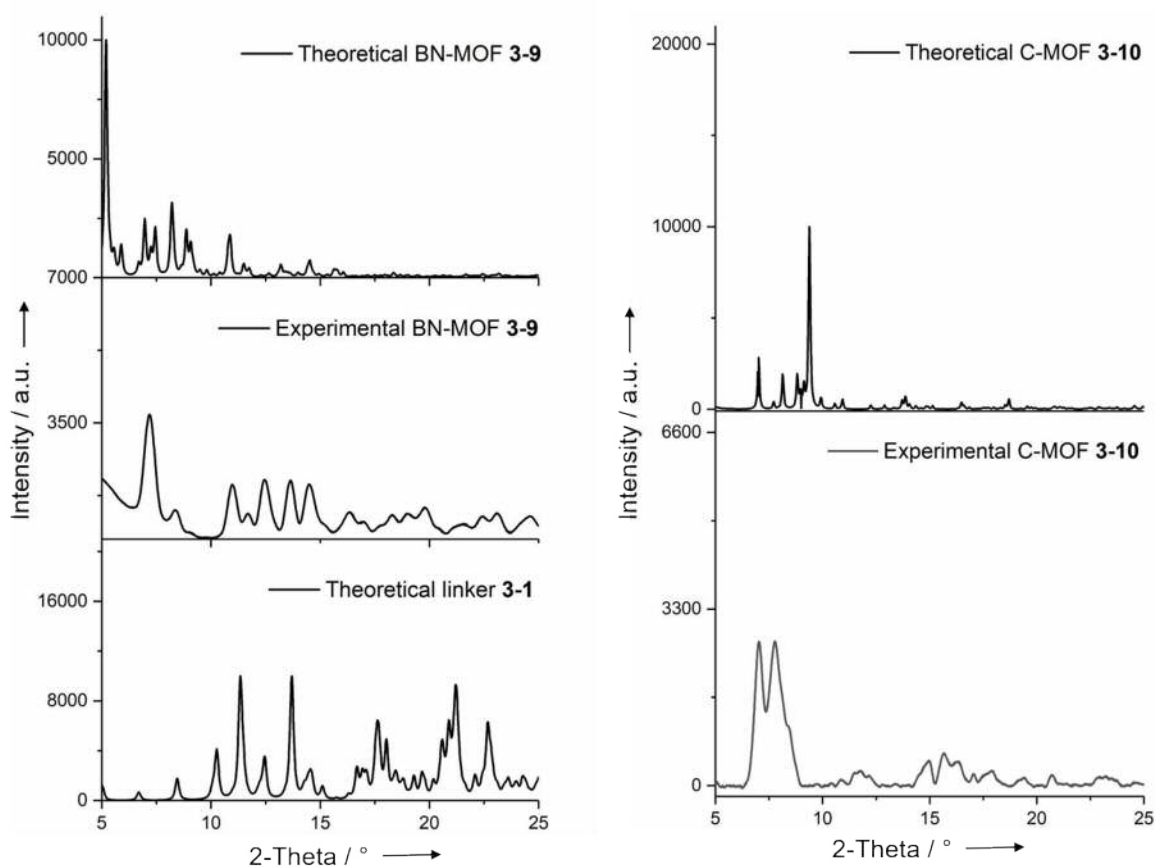


Figure 3.18. Theoretical and experimental PXRD spectra of BN-MOF 3-9, boraizne linker 3-1 (left) and C-MOF 3-10 (right).

When comparing the PXRD profile of BN-MOF 3-9 air dried with the simulated one, similarities in the peak positions can be found at 2-theta of 7.2°, 8.4°, 10.9°, 11.7°, 13.7° and 14.5°. Although this agreement on the peak positions between the model and the BN-MOF 3-9 air dried PXRD profile is observed, the relative intensities do not match up. Such differences in peak intensity are common when comparing theoretical and experimental PXRD profiles in MOFs because the structure is simulated in the absence of guests in the pores, while the experimental pattern is obtained in the presence of solvent molecules (the TGA clearly shows the presence of solvent in the cavities of the MOFs, *section 3.2.6*).

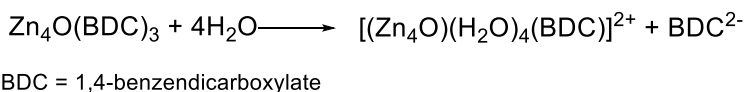
Because guest molecules are not considered while predicting PXRD, the calculated patterns do not reproduce all the expected peak intensities, but only the peak positions.

Table 3.2. Theoretical and experimental 2-theta data of BN-MOF **3-9**, borazine linker **3-1** and C-MOF **3-10**. Intensity lower than 400 counts have not been reported.

BN-MOF 3-9		Linker 3-1	C-MOF 3-10	
Theoret. 2-theta	Experim. 2-theta	Theoret. 2-theta	Theoret. 2-theta	Experim. 2-theta
5.2	7.2	6.7	6.9	7.1
5.5	8.4	8.4	7.9	7.8
5.8	10.9	10.2	8.8	
6.6	11.7	11.3	9.4	
6.9	12.4	12.4		
7.2	12.9	13.7		
7.4	13.7	14.5		
8.3	14.5	15.1		
8.9	14.8	16.6		
9.0	16.5	17.1		
10.9	17.1	17.6		
11.4	18.1	18.1		
11.7	18.4	18.4		
13.5	18.9	18.7		
14.5	19.8	19.3		
	21.4	19.7		
	21.9	20.2		
	22.4	20.5		
	23.1	20.9		
	23.5	21.1		
	23.8	22.1		
	24.4	22.6		
	24.8	23.6		
		23.9		
		24.2		

However, remarkable differences have been observed in the experimental PXRD patterns, that lack all the bulk crystallinity informations in the region between 5° and 7°. Another important difference seems to be the presence of new peaks that appear between 14° and 25° and are not found in the simulated pattern, which may indicate that BN-MOF **3-9** partially collapsed. Some peaks pattern from 14° to 25° of the experimental BN-MOF **3-9** are consistent with the theoretical PXRD of borazine linker **3-1** alone (Figure 3.18, table 3.2). This outcome seems likely to be due to a decomposition of the MOF, in line with a similar reports by M. D. Allendorf and co-workers in 2006.²⁶ Allendorf reports that Zn-

MOFs can undergo hydrolysis in the presence of ambient humidity, losing their crystallinity over time as described in the reaction below:



In conclusion, the mismatch between experimental and theoretical PXRD can be ascribed to the decomposition of BN-MOF **3-9** under air storage conditions, undergoing release of borazine linker **3-1** with a consequent loss of crystallinity of the porous material.

Moving on to C-MOF **3-10**, a good agreement of the PXRD peak positions between the theoretical and the experimental patterns is observed at 2-theta of 7.1° and 7.8° (Table **3.2**). However, the simulated peaks at 6.9° and 7.9° appear in a higher intensity, which is possibly due to the lack of the solvent molecules in the cavities of the framework or different orientation of the crystals, as already discussed above for BN-MOF **3-9**. Remarkably, two peaks are missing at 8.8° and 9.4° in the experimental data when compared to the simulated pattern, which could be ascribed to a preferential orientation effect of the crystals.

Brunauer Emmett Teller (BET) surface area

The BET surface areas of BN-MOF **3-9** was measured with Micromeritics 3Flex machine. Before N₂ adsorption at 77 K, the sample was degassed with N₂ at 403 K for 16 h under vacuum to remove any residual DMF/NMP from the cavities of the material. Figure **3.19a** shows that the nitrogen adsorption is a typical type I isotherm for microporous material as defined by the IUPAC classification scheme,²⁷ but it has an upward curvature due to pore filling at high relative pressure. The isotherm is very steep at p/p₀ ~ 0.01 due to rapid filling of the pores. The maximum N₂ uptake at 945 mbar (P/P₀ = 0.945) is 3.49 mmol/g. These uptake values and densities of N₂ (0.808 g/cm³) was used to estimate the total pore volume, which is 0.099 cm³g⁻¹. BET plot (Figure **3.19b**) reveals a surface area of 162.3 m²/g. At this point we were concerned about the strong degassing conditions that has been used to remove high boiling point solvents such as DMF and NMP. It is well described in literature that the heating under high vacuum condition of MOF could lead to lower surface areas than expected due to framework collapse.^{28,29} Framework can often collapse due to the high

surface tension forces imposed by the liquid-gas phase transformation of trapped solvent molecules especially when they have a high boiling points.

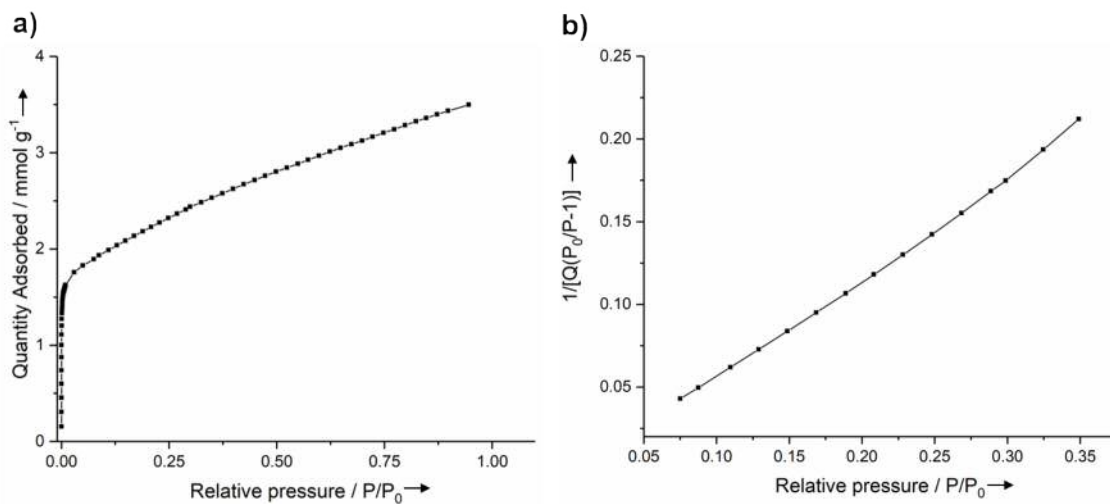


Figure 3.19. a) Nitrogen adsorption isotherm of BN-MOF 3-9 at 77 K; b) BET plot analysis of BN-MOF 3-9.

The easiest way to overcome this problem is to exchange the solvent with a lower-boiling point solvent prior to heating the sample under vacuum. In particular, the preparation of BN-MOF 3-9 in DMF/NMP was followed by acetone solvent-exchange (the procedure is described in chapter 5). Then BN-MOF 3-9 was degassed with N₂ at 303 K for 16 h under high vacuum and finally the N₂ adsorption at 77 K was recorded (Figure 3.20a).

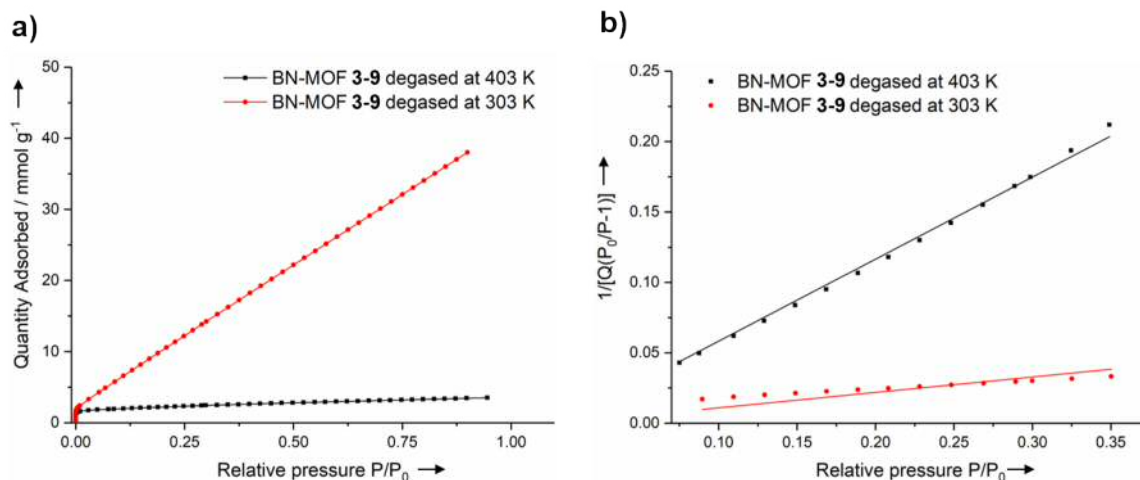


Figure 3.20. a) Nitrogen adsorption isotherm at 77 K of BN-MOF 3-9 previously degassed at 403 K (black) and 303 K (red); b) BET plot analysis of BN-MOF 3-9 previously degassed at 403 K (black) and 303 K (red).

Remarkably, the maximum N₂ uptake at 899 mbar (P/P₀ = 0.899) is 38 mmol/g, with the total pore volume of 0.98 cm³/g. As expected by such high pore volume, the BET graphs

(Figure 3.19b), clearly show an enhancement of the surface area to 1351.5 m²/g. Moving on C-MOF 3-10, the synthesis of the porous material was followed by acetone solvent-exchange. Then, following the same conditions proposed for BN-MOF 3-9, C-MOF 3-10 was degassed with N₂ at 303 K for 16 h under high vacuum and finally the N₂ adsorption at 77 K was recorded (Figure 3.21a). Once again, the nitrogen adsorption isotherm shows a typical microporous type I profile with the maximum N₂ uptake at 942 mbar (P/P₀ = 0.942) of 1.6 mmol/g and the total pore volume calculated is 0.063 cm³/g. Surprisingly, the BET plot (Figure 3.21b) reveals a surface area of 90.8 m²/g. This surface area of C-MOF 3-10 is lower than many commonly reported MOFs in literature.² This result can be explained by the possible collapse of the framework, supported by the PXRD analyses showing limited crystallinity (see Figure 3.17). The hypothesis of structural collapse points to the intrinsic low stability of the material towards moisture in air at room temperature.

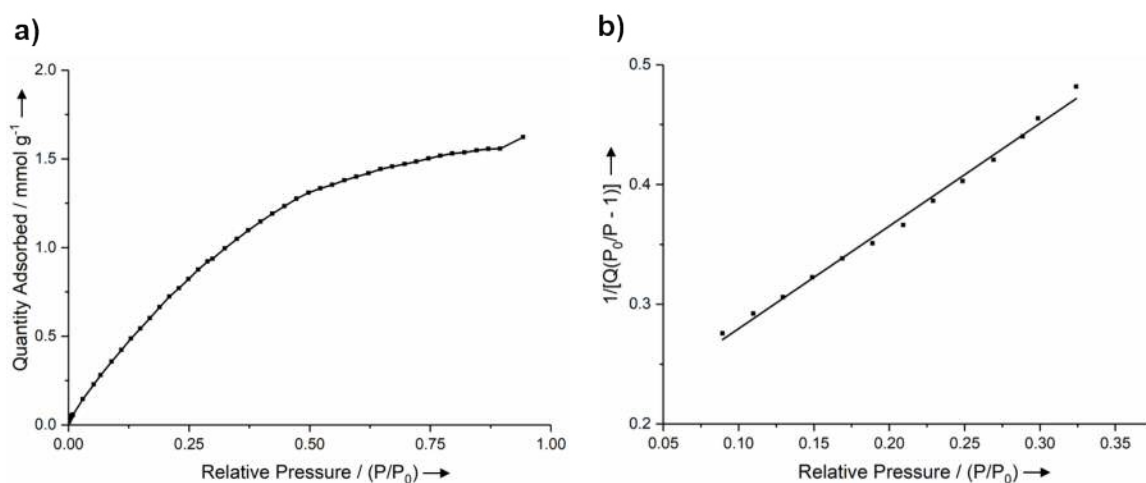


Figure 3.21. a) Nitrogen adsorption isotherm of C-MOF 3-10 at 77 K; b) BET plot analysis of C-MOF 3-10.

3.3.5 Thermal stability

The thermal stability of the MOFs has been evaluated through the thermal gravimetric analysis (TGA). The samples were placed in Pt pans using the following procedure: isotherm at 30 °C for 30 min, then a ramp from 30 to 900 °C at 5° C/min, under N₂ (flow rate on the sample of 90 mL/min). The temperatures were taken from the onset of the transition. The TGA and the derivative thermal gravimetric profiles (DTG) of BN-MOF 3-9, C-MOF 3-10, 3-1 and 3-3 are pointed out in Figure 3.22. The TGA of 12 hours air-dried BN-MOF 3-9 (Figure 3.22a) clearly shows two distinct steps of loss weight, the first step of 16% loss weight at 100 °C could be attributed to the gradual loss of DMF and NMP from

the outer surface and the pores of the sample. Remarkably, BN polymer **3-9** shows a high thermal stability up to 430 °C, then the frameworks started to decompose losing the 58% weight. Such loss of weight can be ascribed to the decomposition of three-carboxyl borazine **3-1** (Figure 3.22d).

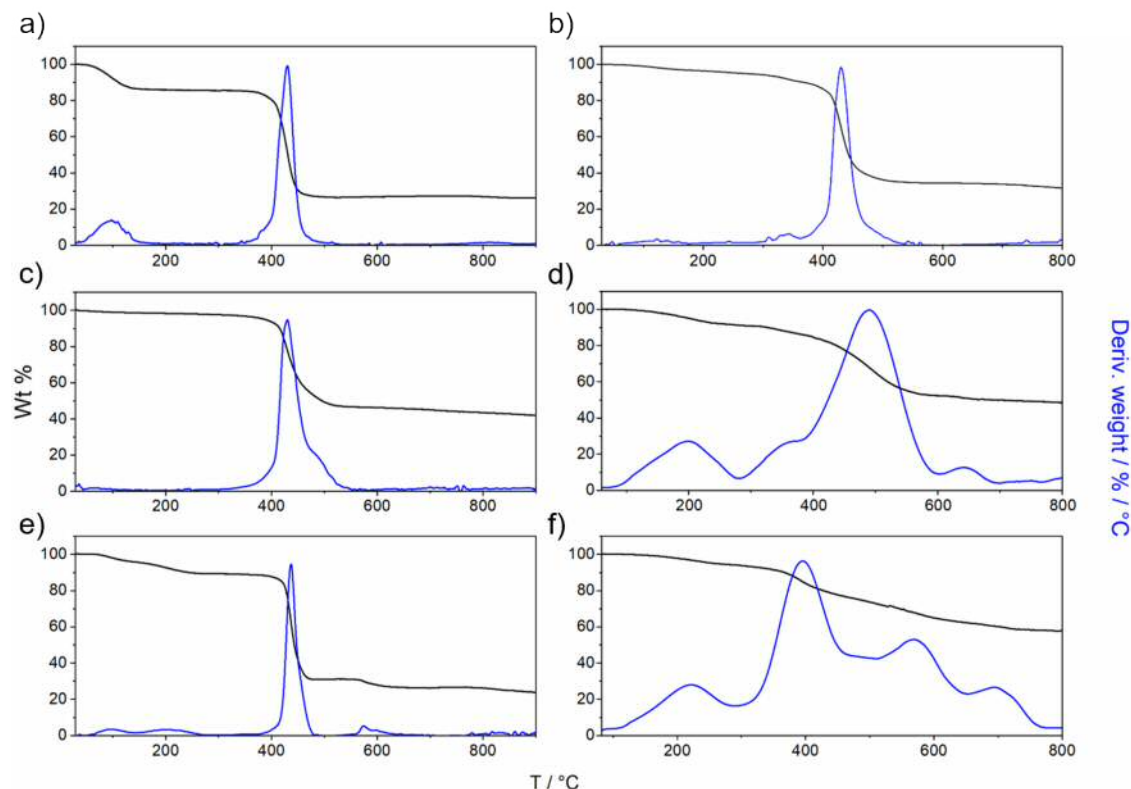


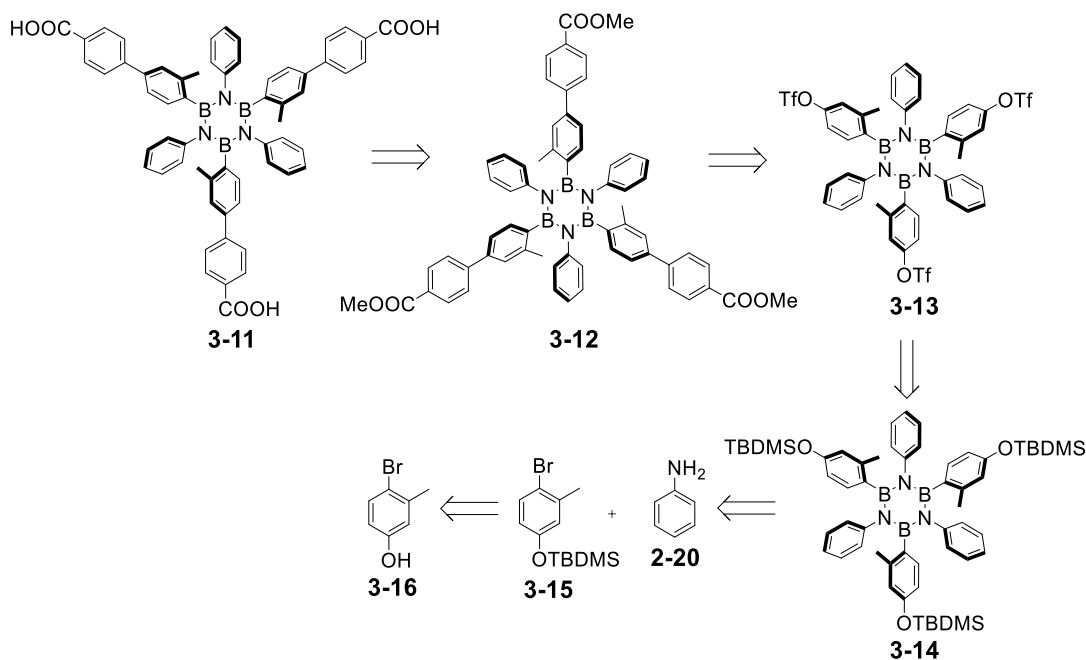
Figure 3.22. TGA curves (black) and corresponding DTG curves (blue) of a) BN-MOF **3-9**; b) BN-MOF **3-9** acetone solvent-exchange; c) BN-MOF **3-9** degassed at 403 K for 16h under vacuum; d) Three-carboxyl borazine derivative **3-1**; e) C-MOF **3-10**; f) Three-carboxyl derivative **3-3**.

The TGA of BN-MOF **3-9** after the acetone solvent exchange is shown in the Figure 3.22b. The sample was dried for 6 hours under air, the TGA profile shows a progressive loss of 8% weight from 30 °C to 340 °C. Once again, this could be ascribed to the gradual loss of acetone from the cavities of porous material **3-9**, then the decomposition of the MOF is observed at 430 °C. The TGA of degassed BN-MOF **3-9** is shown in Figure 3.33c. As expected, the porous material is stable until 430 °C, then 54% loss of weight has been observed. Moving on C-MOF **3-10**, the thermal stability of the material does not show any relevant difference compare to BN-MOF **3-9**. The TGA (Figure 3.22e) reveal three main steps of loss of weight, the first two steps at 93 °C and 202 °C clearly show the loss of 5% and 6%, respectively, attributed to the gradual loss of DMF and NMP. As described for BN-MOF **3-9**, C-MOF **3-10** displays a high thermal stability up to 430 °C then the frameworks

start to decompose losing the 58% of weight. Such weight lost can be ascribed to the decomposition of three-carboxyl derivative **3-3** (Figure 3.22f).

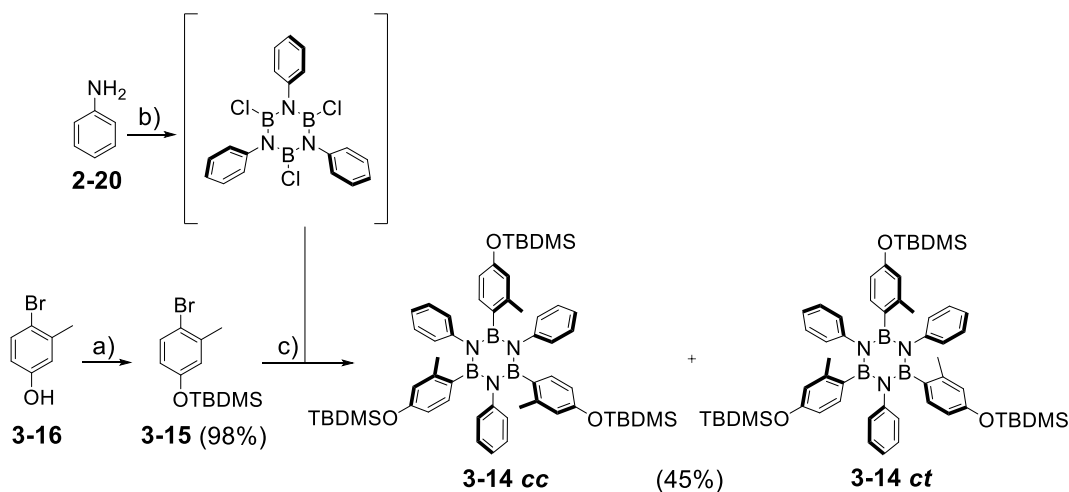
3.3.6 Synthesis of partially-protected borazine linker

As described in *section* 3.3.2, BN-MOF **3-9** presents an open three-dimensional porous structure in which the borazine units are facing the BN-cavities exposing its flat side towards the centre of the pores. The insertion of methyl groups, on the aryl substituent at the *B*-sites, is crucial to avoid the decomposition of the borazine core, however it could reduce the gas adsorption performance of the material because of the steric hindrance. In particular, the presence of -CH₃ groups, namely above and below the borazine ring, could reduce the interaction between the gas molecule and the B₃N₃ ring. For such reason we envisaged a BN-MOF in which each boron atom of the borazine scaffold is protected by only one methyl group instead of two. The retrosynthetic pathway of three-carboxyl borazine **3-11** is reported in Scheme 3.11. Following the same synthetic strategy proposed for borazine **3-1**, desired organic linker **3-11** could be prepared through saponification reaction of borazine ester derivative **3-12**. Once again, borazine ester **3-12** could be obtained from Suzuki cross-coupling reaction between 4-metoxycarbonyl-phenylboronic acid **3-2** and borazine exposing the aryl triflate group at *B*-sites **3-13**. A functional group transformation would allow the synthesis of triflate derivative **3-13** starting from the corresponding partially-protected borazine **3-14**, itself synthesised through the synthetic procedure proposed in *section* 2.5.1.



Scheme 3.11. Retrosynthetic pathway of borazine derivative **3-11**.

The first synthetic step involved a nucleophilic attack of **3-16** to *t*-butyl-dimethylsilylchloride (TBDMS-Cl) in the presence of imidazole, obtaining derivative **3-15** as colourless oil in 98% yield (Scheme **3.12**). The idea behind this reaction was to prepare an aryl halide with one methyl group and bearing a functional group (-OH protected) not only to be easily converted into suitable electrophile for the Suzuki cross coupling reaction, but also to be stable under the reaction conditions adopted for formation of the borazine ring. In the presence of **2-20** and compound **3-15**, TBDMS partially protected borazine **3-9** was prepared in 45% yield. Notably, the substituents that provide the steric protection were introduced in only one of the two *ortho*-positions of the *B*-aryl moieties. Therefore, two different isomers can be produced (Scheme **3.12**, isomer **3-14 cc** and isomer **3-14 ct**), depending on the position of the substituents, in respect to the borazine plane. Note that isomer **cc** is obtained when the three *ortho*-substituents of the *B*-aryl moieties are all pointing in the same direction (*cis-cis*), while isomer **ct** corresponds to two *ortho*-groups pointing in one direction, while the third one is pointing in the opposite one (*cis-trans*).



Scheme 3.12 Syntheses of borazine derivative **3-14**. Reagent conditions: a) tert-butyl-dimethylsilylchloride, imidazole, DMF, 75 °C, 16 h; b) BCl₃, toluene, reflux, 18 h; c) tBuLi, THF, -84 °C, 2 h.

The chemical identity of molecule **3-14** was unambiguously confirmed by X-Ray diffraction analysis. Borazine **3-14** was crystallised by slow diffusion of MeOH in CHCl₃. Isomer *ct* was found, where two of the methyl groups are on the same side, and the third one is on the opposite with respect to the borazine ring (Figure 3.23).

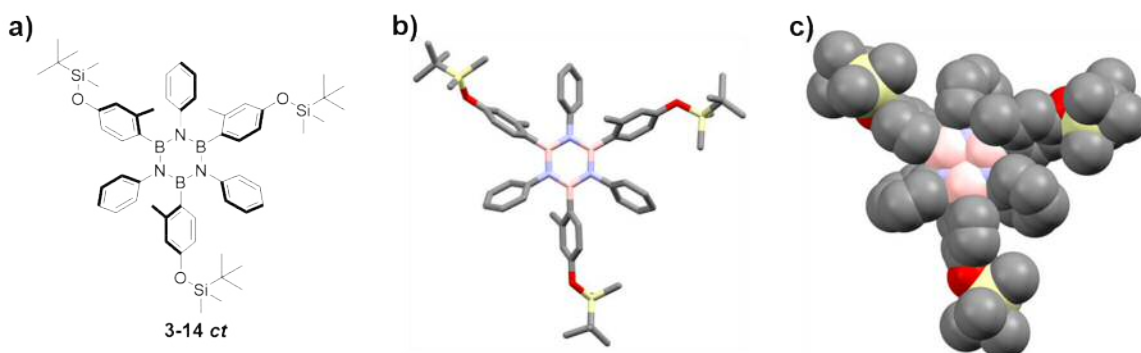
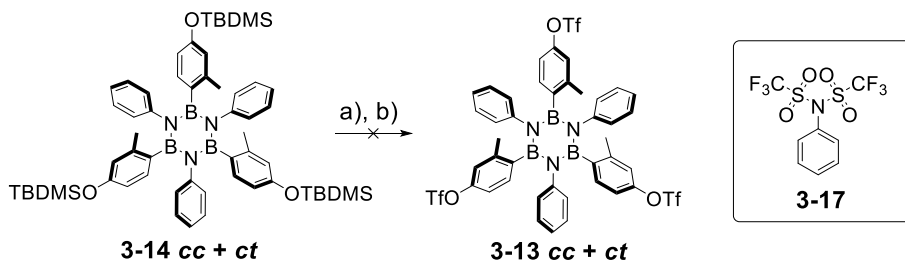


Figure 3.23. Crystal structure of borazine derivative **3-14 ct**; a) molecular structure; b) crystal structure represented in capped sticks; c) crystal structure represented in spacefill. Space group: P-1. The crystal structure was grown by slow diffusion of MeOH in CHCl₃. Colour code: grey: C, pink: B, blue: N, red: O and yellow: Si. Hydrogen atoms were omitted for the sake of clarity.

The next synthetic attempt was the functional group transformation of -TBDMS groups of the partially-protected borazine **3-14** to the corresponding triflate groups (Scheme 3.13). However, when we applied the same reaction conditions proposed in section 2.5.2 to partially-protected borazine **2-31**, total degradation of the borazine core was observed. The reaction entails a deprotection reaction with TBAF, to form the corresponding hydroxy-derivative. Subsequent esterification with Tf₂O in pyridine would end up with the formation of three-triflate derivative **3-13** (Scheme 3.12). Presumably, during the first step, F⁻ can

attack the boron atoms of partially-protected borazine **3-14**. This addition involves the ring-opening of the borazine core. The degradation of the core produces aniline **2-20**, which reacts with Tf_2O forming amino-derivative **3-17** in 60% yield. Suitable crystals for X-ray diffraction analysis of derivative **3-17** were obtained by slow diffusion of MeOH in CH_2Cl_2 (Figure 3.24). In conclusion, the synthesis of borazine **3-11** could not be completed using these conditions.



Scheme 3.13 Synthetic attempt for the formation of borazine derivative **3-13**. Reagent conditions: 45%. a) TBAF, THF, 0 °C, 2 h; b) trifluoromethanesulfonic anhydride (Tf_2O), pyridine, r.t., 16 h.

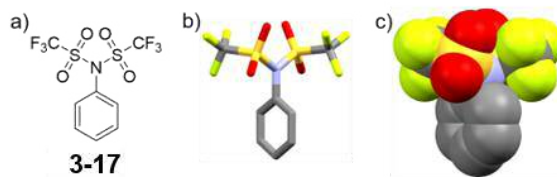


Figure 3.24. Crystal structure of the side product **3-17**; a) molecular structure; b) crystal structure represented in capped sticks; c) crystal structure represented in spacefill. Space group: $Fdd2$. The crystal structure was grown by slow diffusion of MeOH in CH_2Cl_2 . Colour code: grey: C, blue: N, red: O, orange: S and green: F. Hydrogen atoms were omitted for the sake of clarity.

3.4 Conclusions and Perspectives

The work presented in this part of the thesis focused on the preparation of BN metal organic framework **3-9**, composed by three-carboxyl borazine **3-1** as organic linker and $[\text{Zn}_4\text{O}(\text{CO})_6]$ as metal cluster. Additionally, to evaluate the effect of the BN doping units in the gas storage, we have also prepared the isostructural MOF reference **3-10**, in which the borazine core has been replaced by benzene unit. To achieve this, the synthesis of borazine-linker **3-1** and full-carbon linker **3-3** have been carried out following the same synthetic strategy in which triflate derivative **2-30** and **2-49** were coupled with **3-2**, followed by saponification reaction. The crystalline nature of BN-MOF **3-9** and C-MOF **3-10** allows the characterisation by X-ray diffraction. Although, the two porous polymers have the same

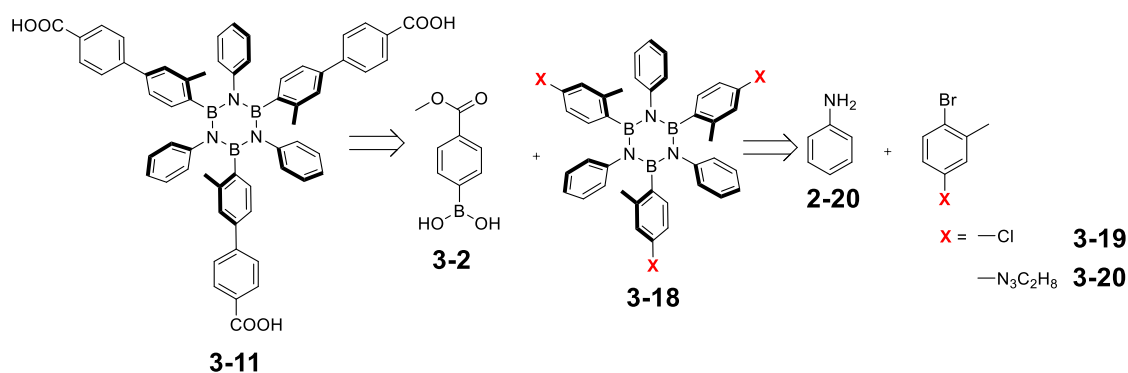
orthorhombic crystal system, BN-MOF **3-9** and C-MOF **3-10** belong to Pnmm and Fdd2 space groups, respectively. As consequence of such space configuration, the two polymers reveal unique chemical-physical features remarkably different in the solid state (see Table **3.3**). BN-MOF **3-9** crystallised with the formation of a doubly interpenetrating network, composed by two infinite structurally regular motifs that contain independent $[\text{Zn}_4\text{O}(\text{BNTCP})_6]$ octahedral units inextricably entangled. The distance between the two interpenetrated networks is 4.6 Å and the framework atoms in BN-MOF **3-9** take up only a small fraction (30%) of the available space in the crystal, with a calculated density of 0.52 g/cm³. Whereas, in C-MOF **3-10** the formation of three interpenetrating networks composed by three infinite structurally regular motifs have been observed. As consequence of such entangled interpenetration, a higher density of 0.65 g/cm³ has been determined with respect to BN-MOF **3-9**, in which the framework atoms take up the 37% of the available space in the crystal lattice. The BET measures have been successful carried out showing a notable high surface area of 1351.5 m²/g in BN-MOF **3-9** with a maximum N₂ uptake at 77 K of 38 mmol/g. On the other hand, the BET surface area of C-MOF **3-10** (90.8 m²/g) is lower than BN-MOF **3-9**, which explain also the low N₂ uptake at 77 K of 1.6 mmol/g. Additionally, the TGA analysis of the porous polymers, reveal a high thermal stability, upon solvent removing, of 430 °C. However as confirmed by PXRD, the MOFs tends to decompose in the presence of moisture and generally to ambient conditions unveiling a low stability of the framework.

Table 3.3.: Chemical-physical properties of BN-MOF **3-9** and C-MOF **3-10**.

	BN-MOF 3-9	C-MOF 3-10
Yield	90%	92%
Space group	Pnmm	Fdd2
Distance between the interpenetrate networks	4.6 Å	8.7 Å
Free-space in the cell volume	70 %	63 %
Density calculated	0.52 g/cm ³	0.65 g/cm ³
N ₂ uptake at 77 K	38 mmol/g	1.6 mmol/g
Pore volume calculated	0.98 cm ³ /g	0.063 cm ³ /g
BET surface area	1351.5 m ² /g	90.8 m ² /g
Thermal stability	430 °C	430 °C
Crystal dimension	0.5-0.6 mm	0.5-0.6 mm

The results of this research lead to the conclusion that full-protected borazine linkers can be exploited for the preparation of new 3D BN doped porous materials with remarkable high surface area and N₂ uptake. However, to fully-evaluate the gas storage performance of such porous material, a systematic screening of the gas adsorption (H₂, CO and CO₂) will be accomplished in the next months.

In the second part of this project we envisage the synthesis of partially-protected borazine linker **3-11** to enhance the gas uptake performance of the BN-MOF. To achieve this, borazine derivate **3-14** (Figure 3.23a), bearing only three methyl groups on the aryl substituent at the *B* sites, was successfully prepared. However, it decomposed in the presence of TBAF, obtaining the ring-opening of the borazine ring and the formation of aniline triflate moiety **3-17** (Figure 3.24) as main product. An alternative synthetic methodology is necessary, hence we designed another possible retrosynthetic pathway avoiding the reaction with TBAF, that will be addressed to prepare the desired three-carboxyl borazine linker **3-11** (Scheme 3.13). BN organic linker **3-11** might be easily obtained from Suzuki cross-coupling reaction between **3-2** and borazine exposing an aryl chloride or related electrophile (*i.e.*, triazene moiety) at *B*-sites **3-18**. Thus, starting from **3-19** or **3-20**, in the presence of aniline **2-20**, we could synthesise borazine derivatives **3-18** bearing an electrophilic partner to be reacted in Suzuki cross-coupling reaction. Unfortunately, due to time constraints, the synthesis will be performed in the next months.



Scheme 3.13. Retrosynthetic pathway of borazine linker **3-11**.

3.5 References

- (1) Si X., Zhang J., Li F., Jiao C., Wang S., Liu S., Li Z., Zhou H., Sun L., Xu F. *Dalt. Trans.* **2012**, *41*, 3119.

- (2) M. P. Suh, H. J. Park, T. K. Prasad, D.-W. Lim *Chem. rev.* **2012**, *112*, 782.
- (3) Aijaz A., Akita T., Yang H., Xu Q. *Chem. Commun.* **2014**, *50*, 6498.
- (4) Knop O., Bakshi P. K. *Can. J. Chem.* **1995**, *73*, 151.
- (5) Zhang J., Wu T., Zhou C., Chen S., Feng P., Bu X. *Angew. Chem. Int. Ed.* **2009**, *48*, 2542.
- (6) Zhang H.-X., Liu M., Xu G., Liu L., Zhang J. *Chem. Commun.* **2016**, *52*, 3552.
- (7) Suh M. P., Cheon Y. E., Lee E. Y. *Coord. Chem. Rev.* **2008**, *252*, 1007.
- (8) Kepert C. J. *Chem. Commun.* **2006**, *7*, 695.
- (9) Düren T., Bae Y.-S., Snurr R. Q. *Chem. Soc. Rev.* **2009**, *38*, 1237.
- (10) Rowsell J. L. C., Yaghi O. M. *Angew. Chem. Int. Ed.* **2005**, *44*, 4670.
- (11) Li J.-R., Kuppler R. J., Zhou H.-C. *Chem. Soc. Rev.* **2009**, *38*, 1477.
- (12) Panella B., Hirscher M., Pütter H., Müller U. *Adv. Funct. Mater.* **2006**, *16*, 520.
- (13) Li C.-J., Lin Z., Peng M.-X., Leng J.-D., Yang M.-M., Tong M.-L. *Chem. Commun.* **2008**, *47*, 6348.
- (14) Iremonger S. S., Southon P. D., Kepert C. J. *Dalt. Trans.* **2008**, *44*, 6103.
- (15) Rosi N. L., Eckert J., Eddaoudi M., Vodak D. T., Kim J., O’Keeffe M., Yaghi, O. M. *Science* **2003**, *300*, 1127.
- (16) Kitagawa S., Kitaura R., Noro S. *Angew. Chem. Int. Ed.* **2004**, *43*, 2334.
- (17) Li H., Eddaoudi M., O’Keeffe M., Yaghi O. M. *Nature* **1999**, *402*, 276.
- (18) Wendt M. D., Shen W., Kunzer A., McClellan W. J., Bruncko M., Oost T. K., Ding H., Joseph M. K., Zhang H., Nimmer P. M., Ng S. C., Shoemaker A. R., Petros A. M., Oleksijew A., Marsh K., Bauch J., Oltersdorf T., Belli B. A., Martineau D., Fesik S. W., Rosenberg S. H., Elmore S. W. *J. Med. Chem.* **2006**, *49*, 1165.
- (19) De la Hoz A., Díaz-Ortiz Á., Moreno A. *Chem. Soc. Rev.* **2005**, *34*, 164.
- (20) Zhang Y., Giurleo D., Parhi A., Kaul M., Pilch D. S., Lavoie E. J. *Bioorganic Med. Chem. Lett.* **2013**, *23*, 2001.
- (21) Duthion B., Pardo D. G., Cossy J. *Org. Lett.* **2010**, *12*, 4620.
- (22) Bruinsma R. F., Gennes P. G., Freund J. B., Levine D. *Nature* **2004**, *427*, 523.
- (23) Howarth A. J., Peters A. W., Vermeulen N. A., Wang T. C., Hupp J. T., Farha O. K. *Chem. Mater.* **2017**, *29*, 26.
- (24) Reineke T. M., Eddaoudi M., Moler D., O’Keeffe M., Yaghi O. M. *J. Am. Chem. Soc.* **2000**, *122*, 4843.

- (25) Kondo M., Shimamura M., Noro S.-I., Minakoshi S., Asami A., Seki K., Kitagawa S. *Chem. Mater.* **2000**, *12*, 1288.
- (26) Greathouse J. A., Allendorf M. D. *J. Am. Chem. Soc.* **2006**, *128*, 10678.
- (27) Sing K. S. W. *Pure Appl. Chem.* **1985**, *57*, 603.
- (28) Mondloch J. E., Katz M. J., Planas N., Semrouni D., Gagliardi L., Hupp J. T., Farha O. K. *Chem. Commun* **2014**, *50*, 8944.
- (29) Wilmer C. E., Leaf M., Lee C. Y., Farha O. K., Hauser B. G., Hupp J. T., Snurr R. Q. *Nat. Chem.* **2011**, *4*, 83.

CHAPTER 4

BN-patterning of metallic substrates through metal coordination of decoupled borazines

In this chapter the syntheses of two three-pyridyl borazine modules together with their scanning tunnelling microscopy (STM) measurements are reported and described. These borazine scaffolds were designed and synthesised in order to prepare 2D metal organic frameworks (2D MOFs) on various substrates, exploiting the metal-ligand coordinative interactions, driven by the presence of pyridine groups and metal atoms.

The chapter is divided into three main sections: *i) section 4.1* includes a general introduction on 2D MOFs on surfaces; *ii) section 4.2* presents an overview of the self-assembly properties of borazine modules on metal substrates, followed by the design of new borazine linkers; *iii) section 4.3* reports the syntheses and STM measurements of three-pyridyl borazine modules as well as the preparation of 2D coordination metal-organic polymers on copper metal surface.

The work presented in this chapter has been accomplished thanks to the collaboration with Martin Schwarz, Manuela Garnica, Johannes V. Barth and Willi Auwärter (*Technical University of Munich, Germany*) who performed the STM measurements and data analysis. The X-Ray diffraction analyses were performed by Nicola Demitri (*Elettra-Sincrotrone, Basovizza, Trieste, Italy*).

4.1 General overview on 2D molecular organic architectures on metal surfaces

The interactions between molecular electronic materials and metal surfaces constitutes a valuable source of knowledge for technological applications. The technological potential of chemically controlled surface patterning has driven growing interest in the rational design of highly-ordered and regular networks at solid surfaces.¹ A balance between molecule-substrate (Figure 4.1a and b) and molecule-molecule (Figure 4.1c-f) interactions is crucial as it determines the arrangement of the molecular species involved, as well as the final electronic properties of the system. In the first case, the ordering of molecules (highlighted in green) on the metal substrate is mainly governed by van der Waals interactions^{2,3} (Figure 4.1a and b). On the other hand, molecules can interact with each other on the substrate driving the formation of regular networks due to the presence of polar groups (Figure 4.1c)⁴, hydrogen bonding (Figure 4.1d)⁵⁻⁷ or through the formation of covalent bonds (Figure 4.1e)⁸. Finally, introducing metal atoms (highlighted in pink) is possible to control the growth of the framework by metal-organic coordination (Figure 4.1f).⁹⁻¹¹

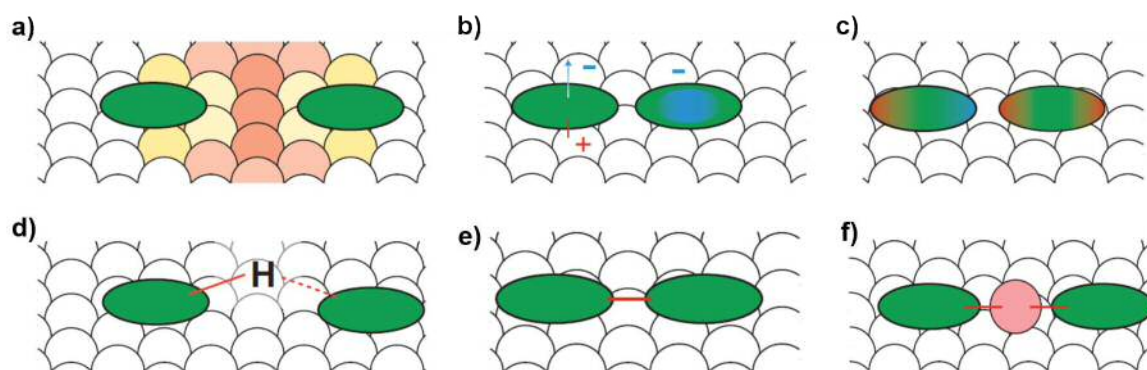


Figure 4.1. Schematic representation of the intermolecular interaction on the surface between molecule-substrate molecule-molecule.³

In this context, by a careful selection of the metal centre (Cu, Ag, Co, Au, etc.) and the design of the linkers (most frequently organic backbones with pyridyl, carbonitrile, or carboxylate functional groups), diverse highly-ordered polymer coordination networks (extending in one dimension 1D^{12,13} or two 2D¹⁴⁻¹⁷) can be obtained. In 2007, Tait and co-workers reported the preparation of 1D molecular nanostructure stabilised by 2-fold metal-ligand coordination.¹⁸ The organic linker **4-1** (Figure 4.2) was loaded on Cu(100) at 300 K

under ultra-high vacuum (UHV) condition and analysed by scanning tunnelling microscopy (STM). Upon deposition, molecule **4-1** self-assembled in one-dimensional chains at room temperature, where Cu atoms can be added on Cu(100) leading to pyridyl-Cu-pyridyl 1D nanostructure as shown in Figure 4.2.

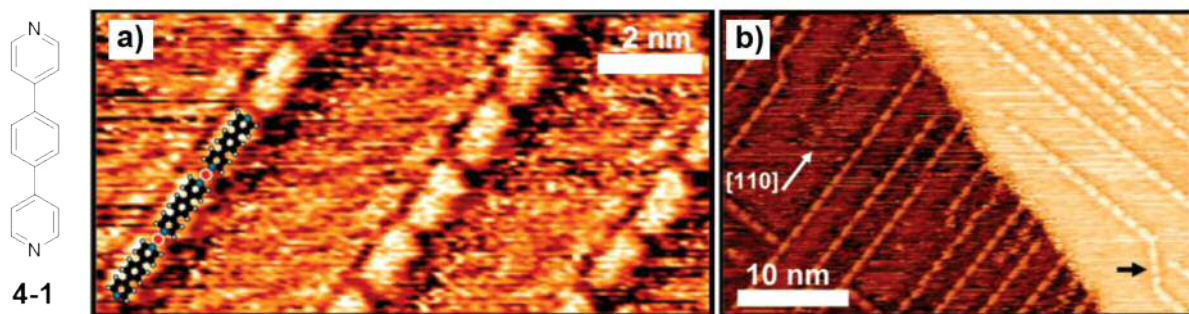


Figure 4.2. STM images of **4-1** adsorbed on Cu(100) at 300 K: a) detail of 1-D Cu chains with a structural model illustrating N-Cu-N coordination bonding (Cu centres red with white highlight) and b) overview of 1D-Cu chains. Adapted from reference.¹⁸

In 2008, Kern and co-workers demonstrated that the self-assembly of metal organic coordination systems on surface can overcome differences of the substrate structure and symmetry.¹⁹ In particular, using 5,5'-bis(4-pyridyl)(2,2'-bipyrimidine) **4-2** as ligand and copper atoms as coordination centres, they observed the formation of three-fold geometry, which lead to the construction of identical supramolecular square networks on Ag(100), Ag(111) and Cu(100), as showed in Figure 4.3.

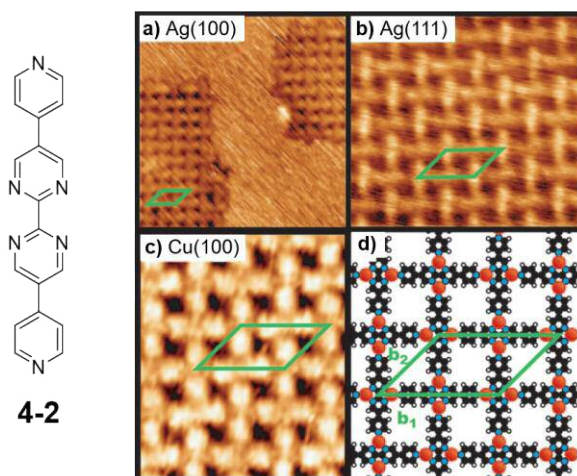


Figure 4.3. STM images of **4-2**-Cu two-dimensional coordination networks formed at the a) Ag(100), b) Ag(111), and c) Cu(100) surfaces; d) molecular model of the supramolecular network.¹⁹

Moreover, the formed coordination networks can be also modified by external stimuli such as pressure, temperature and light irradiation. One example of such stimuli driven

modifications is the use of 1,3,5-tripyridylbenzene (TPyB) as molecular ligand, in which the structural transformation of TPyB-Cu coordination networks can be promoted by the increase of the linker dosage on Copper surface under UHV conditions at 300 K.²⁰ Firstly, an highly ordered honeycomb network was observed by Lin and co-workers (Figure 4.4a) with a molecular density of 0.31 TPyB/nm². Enhancing the organic linker dosage at 0.34 TPyB/nm², a pentagonal (Figure 4.4b) or rhombic (Figure 4.4c) metal-organic network have been obtained. Moving from a molecular density of 0.40 TPyB/nm² to 0.47 TPyB/nm² the 2D-supramolecular organisation changes from a triangular structure (Figure 4.4d) to a zig-zag network (Figure 4.4e), respectively. The authors ascribe this structural in-plane transformations to the coordination binding mode, which shifts from 2-fold Cu-pyridyl binding in the honeycomb, pentagonal, rhombic and zig-zag structures to 3-fold Cu-pyridyl coordination in the triangular network as shown below.

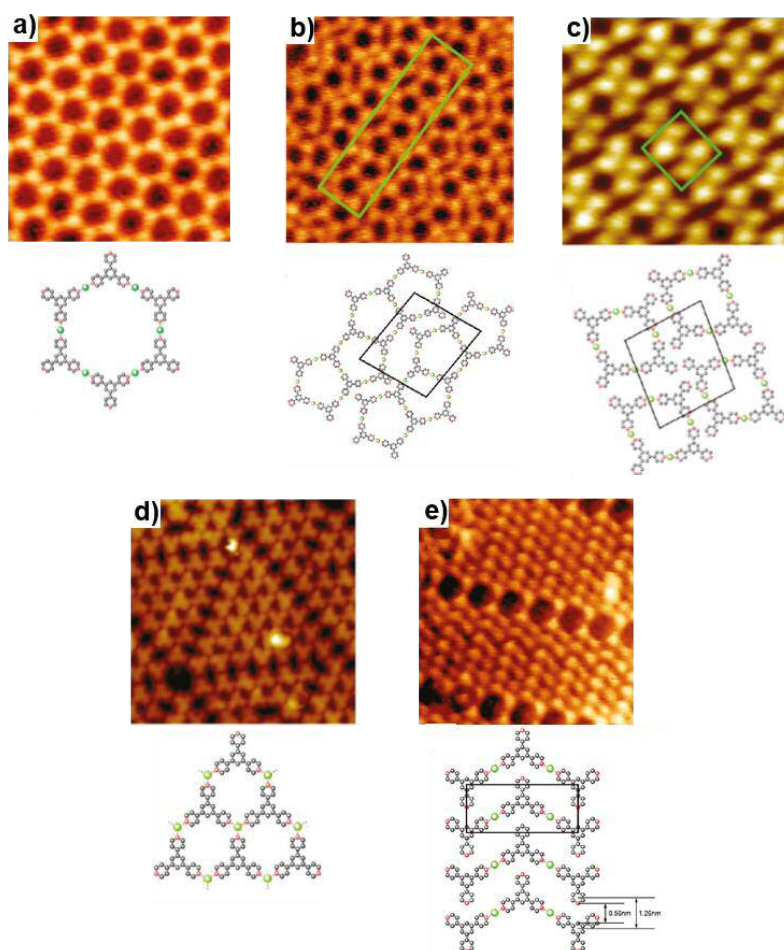


Figure 4.4. STM image of: a) TPyB-Cu honeycomb networks; b) Pentagon network; c) Rhombic cyclic network; d) triangular network; e) zig-zag network. Adapted from reference.²⁰

The pores of metal-organic networks can also be tuned by increasing the chain length of the ligands. Barth and co-workers showed that 2D honeycomb networks on Ag(111) composed by 4,4'-biscyanoterphenyl as linker and cobalt ions, can be increased by replacing the terphenyl backbone with quaterphenyl and quinquiphenyl derivatives without affecting the geometry of the network (Figure 4.5).²¹ The scaling up directly follows the increasing of the ligand backbone length, in particular, moving from biscyano-*tert*phenyl to biscyano-pentaphenyl, a shift of the inner diameter cavities from 34 to 47 Å have been observed.

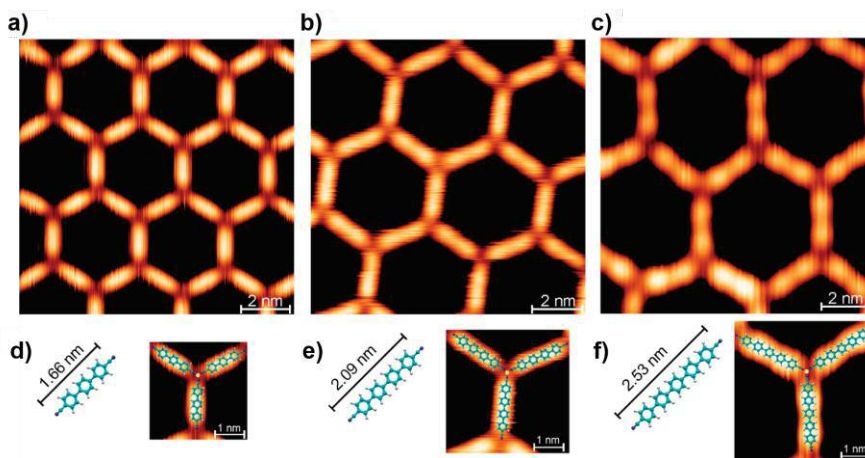


Figure 4.5. Tuning the cavities size of metal-organic honeycomb networks with designed linkers. The STM images show the results of Co-directed assembly of a) NC-Ph₃-CN; b) NC-Ph₄-CN; and c) NC-Ph₅-CN; respectively. d-f) Structure of the organic linkers including their lengths and models of the three-fold Co-carbonitrile coordination motifs. Adapted from reference.²¹

4.2 Aim of the project - borazine self-assembly on metal substrates

The rapid development of molecule-based technologies has created a new impetus for studying supramolecular assemblies and their interactions between functional molecular units on surfaces.^{22–25} Understanding and controlling the assembly of borazine molecular layers will provide the conceptual basis to engineer functional borazine-based supramolecular materials.^{26–29} In 2013, Kervyn *et al.* reported the first bottom-up preparation of borazine-based supramolecular architectures on metal surfaces.³⁰ Borazines **1-51** (Mes₃B₃N₃Ph₃) and **4-3** (Figure 4.6) assemble in very different architectures on Cu(111) surfaces, as revealed by low temperature (LT)-STM measurements. While molecule **1-51** self-organizes into large islands forming full monolayers most likely held

by van der Waals (vdW) interactions, borazine **4-3** bearing a hydroxyl group ((Ph)₂(OH)B₃N₃Ph₃) undergoes exclusive “magic” clustering forming architectures composed of 7, 10, 11, 12 and 13 molecules (Figure 4.6). While the formation of 7-mers and 13-mers take place with high frequency, molecular architectures larger than 13-mers are less likely to be obtained. These findings are rationalised as a delicate interplay of short-range vdW attractions between neighbouring molecules and long-range Coulomb repulsions between deprotonated charged molecules.

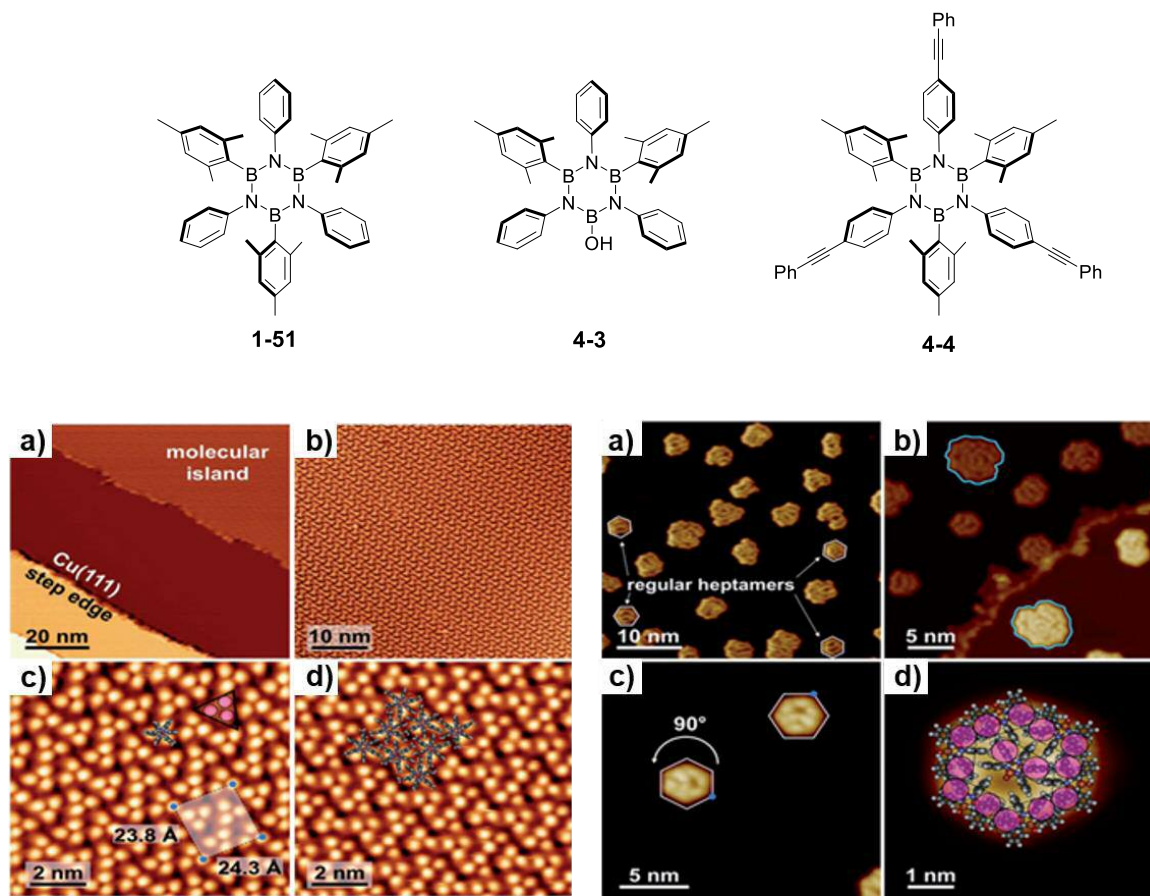


Figure 4.6. Top: Chemical formula of borazine derivatives **1-51**, **4-3** and **4-4**. Bottom-left: STM images for borazine **1-51** on Cu(111), deposited at 300 K, imaged at 77 K. a) Large area of the Cu(111) surface; b) and c) Expanded views of the molecular island; d) Calculated structure superimposed on the imaged.³⁰ Bottom-right: STM images of borazine **4-3** on Cu(111). a) Isolated molecular cluster, highlighting the regular 7-mers; b) expanded view of Cu(111) step edge, revealing two enantiomers of an irregular cluster; c) expanded view of two 90° rotated regular 7-mers; d) Calculated molecular model superimposed onto 7-mers.³⁰

In a successive work, Kalashnyk *et al.* investigated how the self-assembly of borazine derivatives **1-51** and **4-4** is dramatically affected by the peripheral substituents.³¹ Notably, while driving the assembly, the outer shell substituents interact with the metal substrate eventually dictating the formation of porous networks on Au(111) or Cu(111) surfaces.

Specifically, molecule **1-51** formed identical close-packed networks on Au(111) and Cu(111) surfaces, with a structure that is only governed by short-range attractive vdW interactions (Figure 4.7).

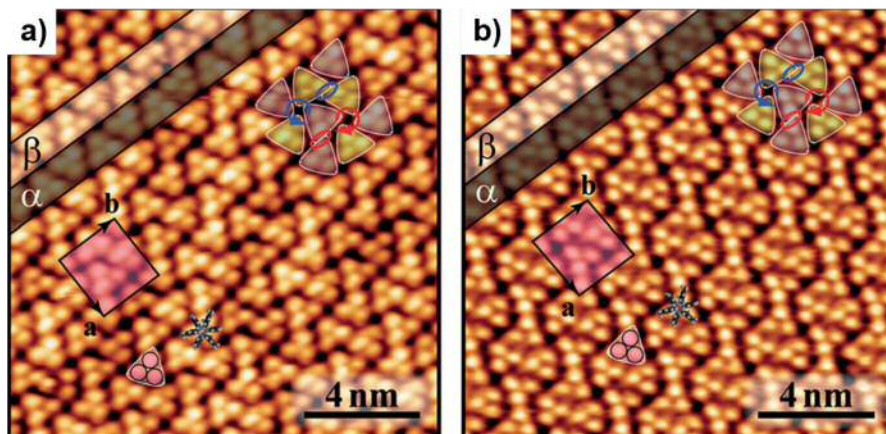


Figure 4.7. STM high resolution images of parallel supramolecular stripes constituting the general assembly of borazine **1-51** deposited on a) Au(111) and b) Cu(111) surfaces held at 300 K. The images were acquired at 77 K.³¹

Conversely, derivative **4-4** arranged into porous motifs. The porosity of the network was revealed to be strongly dependent on the nature of the metal substrate and the affinity of the outer rim with the surface (Figure 4.8). Notably, the protruding phenyl-1,4-phenylethynyl substituents of molecule **4-4** act as intermolecular spacers, thus driving the formation of a porous network. Their flexibility allows a stronger interaction with the substrate which, in the case of the more reactive Cu(111) surface, causes a higher porosity.

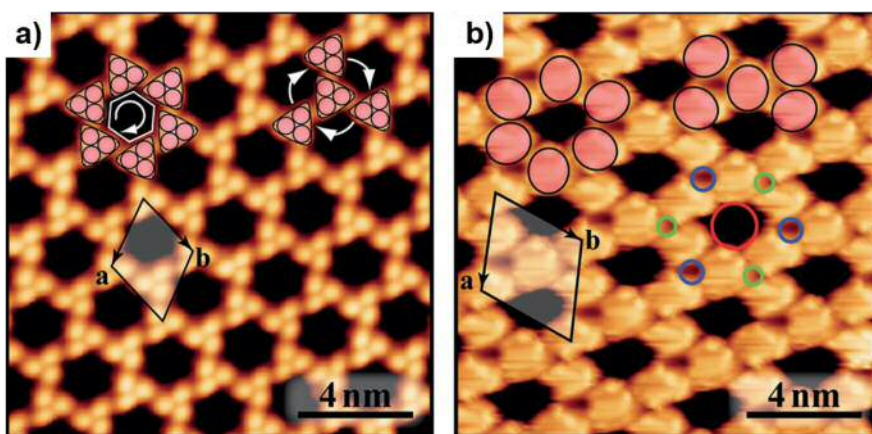


Figure 4.8. STM high resolution images of the porous network of borazine **4-4** deposited at r.t. on a) Au(111) and b) Cu(111). The images were acquired at 77 K.³¹

Molecular Dynamics (MD) simulations rationalised the behaviour of the two main borazine scaffolds in terms of the structural differences of the peripheral substituents. Additionally, the mutual steric hindrance between aryl and mesityl functional groups in molecules **1-51** and **4-4** force the substituents to adopt an almost perpendicular orientation with respect to the borazine core. As consequence, compounds **1-51** and **4-4** physisorb on the metal substrates not experiencing any in-plane modulation, presenting the borazine core on a higher plane compared to the substituents that stay lower on metal surfaces (Figure 4.9).

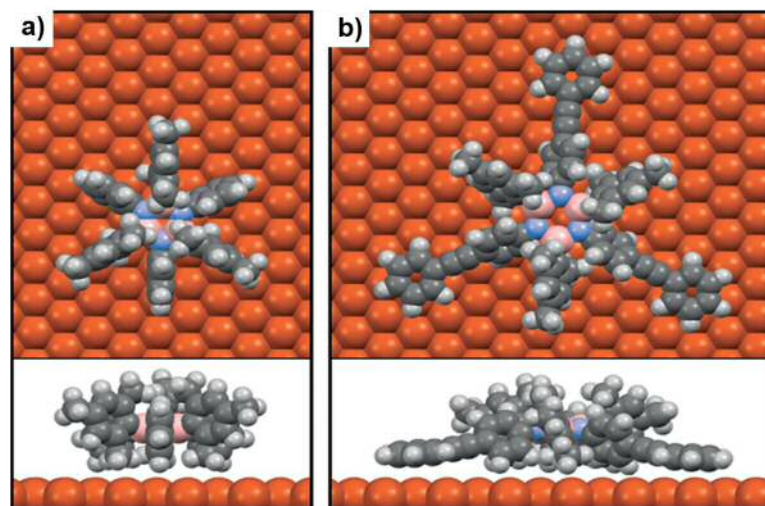
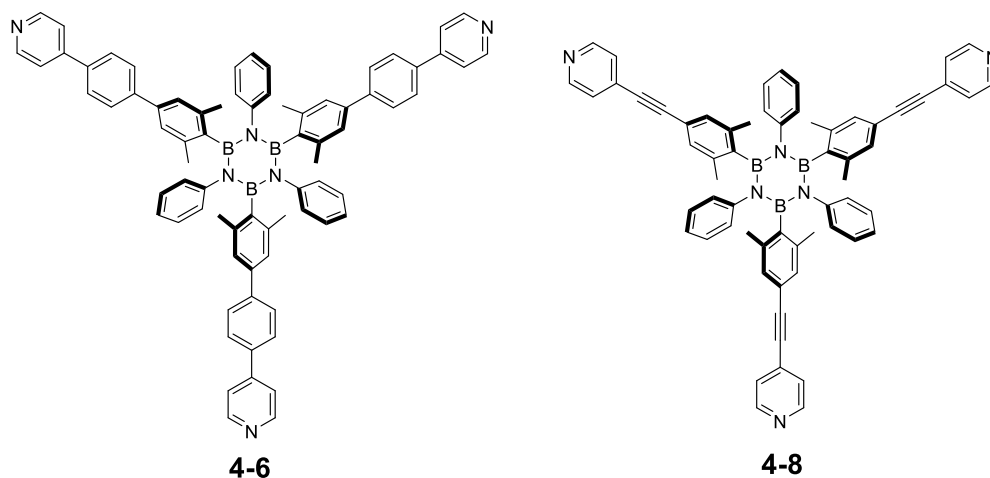


Figure 4.9. Calculated minimum energy adsorption configuration of a) borazines **1-51** and b) **4-4** on a Cu(111) surface. The steric hindrance between the Ph- and Mes- substituents results in the effective decoupling of the central borazine core from the surface for both molecules.³¹

It can be reasonably concluded that the B-N core does not influence the molecular ability to adsorb, self-assemble, or interact on different surfaces when there are six bulky perpendicular substituents in the inner shell. Moreover, the decoupling of the borazine unit from the metal substrates, which can be achieved with the rational synthetic design of the appropriate peripheral functional groups, preserves the properties of the B_3N_3 ring. Given these premises, we conjectured that 2D metal-organic coordination networks (2D-MOCNs) formed through the interaction between a borazine linker and a metal centre on the surface could act as unique model architectures to study the self-assembly and the coordination network of decoupled BN-materials through STM. Inspired by the results described above, we have designed three-pyridyl borazine linkers **4-6** and **4-8** (Scheme 4.1) in which the mutual steric hindrance between the aryl groups in the borazine inner

shell would allow the decoupling of the B_3N_3 rings from the metal substrate. The outer shell of linkers **4-6** and **4-8** are decorated with phenyl and alkynyl spacer groups at the *B* sites, respectively, themselves in turn functionalised with pyridyl moieties. The election of the pyridyl moiety as peripheral groups was driven by the possibility of steering the supramolecular interactions, leading to the formation of 2D-MOCNs in the presence of copper. The formation of such 2D-MOCN combining borazine and copper on Cu(111) and Ag(100) surfaces has not been reported to date, although those porous architectures are highly appealing as they can act as templates featuring cavities and molecular units on regular and well-defined sites linked by metallic nodes.³²

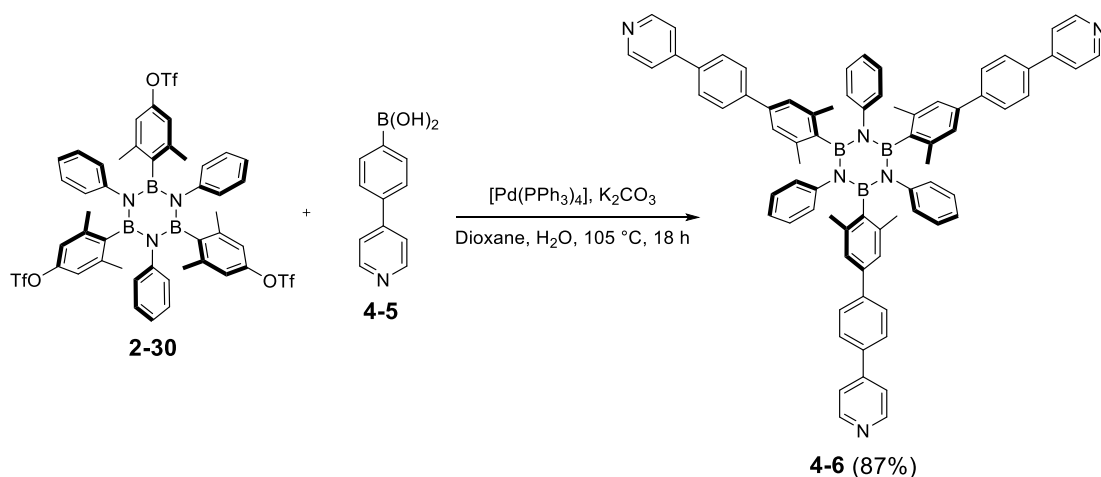


Scheme 4.1. Chemical formula of three-pyridyl borazine **4-6** and **4-8**.

4.3 Results and discussion

4.3.1 Synthesis of three-pyridyl borazine modules

Taking advantage of the synthesis of triflate borazine **2-30** described in *section 2.5.2*, three-pyridyl borazine **4-6** could be obtained from Suzuki cross-coupling reaction between **4-5** and borazine exposing the aryl triflate group at the *B* atoms **2-30** (Scheme 4.2). Hence, borazine derivative **2-30** was reacted with 4-pyridyl-phenylboronic acid **4-5** in the presence of $[Pd(PPh_3)_4]$ in dioxane- H_2O at 105 °C, affording desired product **4-6** in 87% yield.



Scheme 4.2. Synthesis of three-pyridyl borazine module **4-6**.

The $^1\text{H-NMR}$ spectrum of three-pyridyl borazine **4-6** in CDCl_3 is detailed in Figure 4.10. In the aromatic region, the broad singlet *a* at 8.68 ppm corresponds to the 6 pyridyl hydrogen atoms in position 2 with respect to the nitrogen atoms. The doublets at 7.60 ppm can be assigned to the 6 phenyl hydrogen atoms *b* with the *ortho* coupling constant of 8.5 Hz.

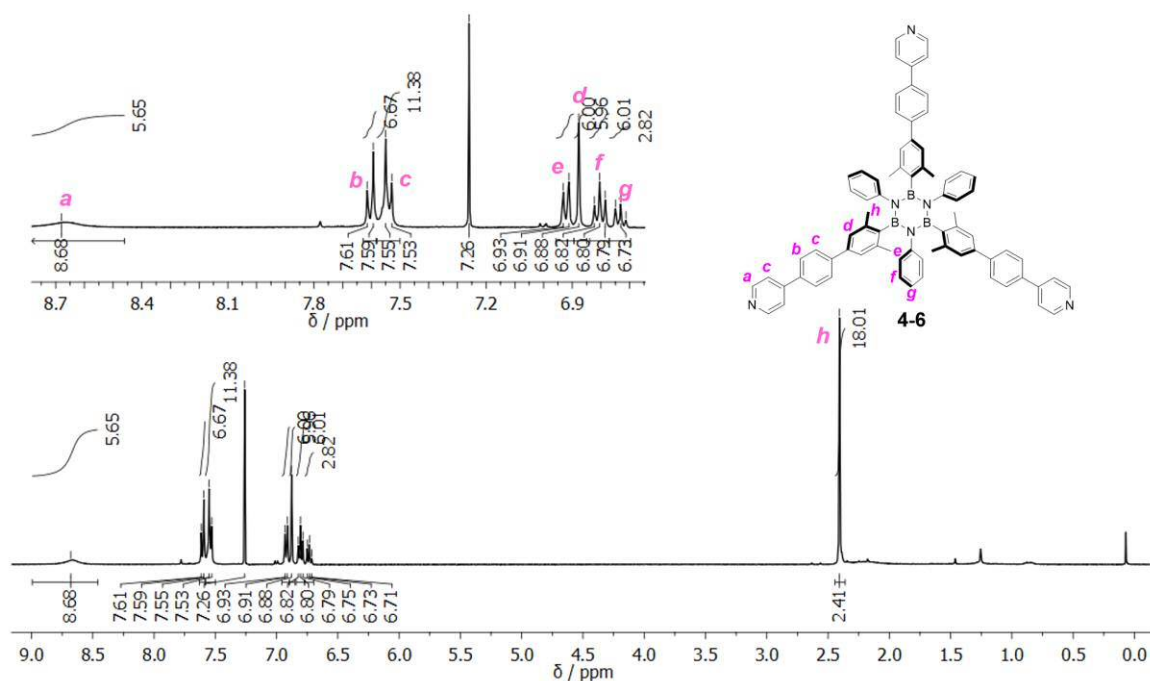


Figure 4.10. 400 MHz $^1\text{H-NMR}$ of borazine branching module **4-6** in CDCl_3 (Solvent residual peak: 7.26 ppm).

The multiplet signal between 7.55 and 7.53 ppm refers to the 18 hydrogen atoms *c*. The singlet at 6.82 ppm is related to proton *d* of the phenyl rings at the *B* sites. The 15 phenyl

hydrogen atoms *e*, *f* and *g* at the *N* sites appears as apparent (*app.*) doublet at 6.92 ppm ($J = 7.8$ Hz), *app.* triplet at 6.80 ppm ($J = 7.5$ Hz) and *app.* triplet at 6.73 ppm ($J = 7.3$ Hz), respectively. In the aliphatic region, the singlet at 2.41 ppm is consistent with the 18 methyl hydrogen atoms *h*.

To confirm the chemical identity of borazine **4-6**, single crystals suitable for X-ray diffraction analysis was obtained by slow diffusion of *n*-hexane in CH_2Cl_2 . As expected, the X-ray molecular structure showed the presence of the pyridyl moieties at the boron sites in the outer shell of B_3N_3 ring (Figure 4.11).

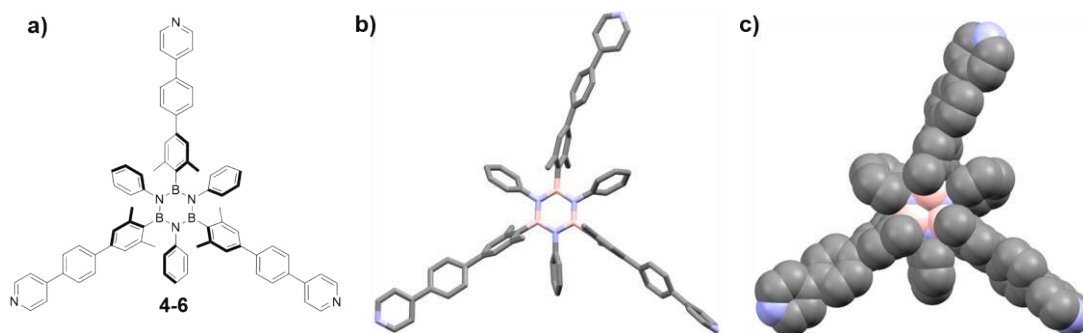


Figure 4.11. Crystal structure of borazine **4-6**; a) molecular structure; b) crystal structure represented in capped sticks; c) crystal structure represented in spacefill. Space group: $C2/c$. The crystal structure was grown by slow diffusion of *n*-hexane in CH_2Cl_2 . Colour code: grey: C, pink: B and blue: N. Hydrogen atoms were omitted for the sake of clarity.

The crystal obtained belongs to $C2/c$ space group in which three-pyridyl borazine **4-6** possess supramolecular packing in a rectangular parallelepiped shape ($a = 47.95 \text{ \AA}$, $b = 21.63 \text{ \AA}$ and $c = 13.87 \text{ \AA}$). The crystal shows a 3D organisation driven by van der Waals (labelled as *i*, *ii* and *iii*) and H-bonding (*iv*) interactions (highlighted in pale blue, Figure 4.12A and B) between the aryl moieties of the B_3N_3 rings. The effective packing of three-pyridyl borazine **4-6** in the solid phase gives rise to distorted planar arrangement of the molecules, piled up along the crystallographic *c* axis leading to partial overlaps of outer pyridine moieties of neighbour molecules (Figure 4.12C).

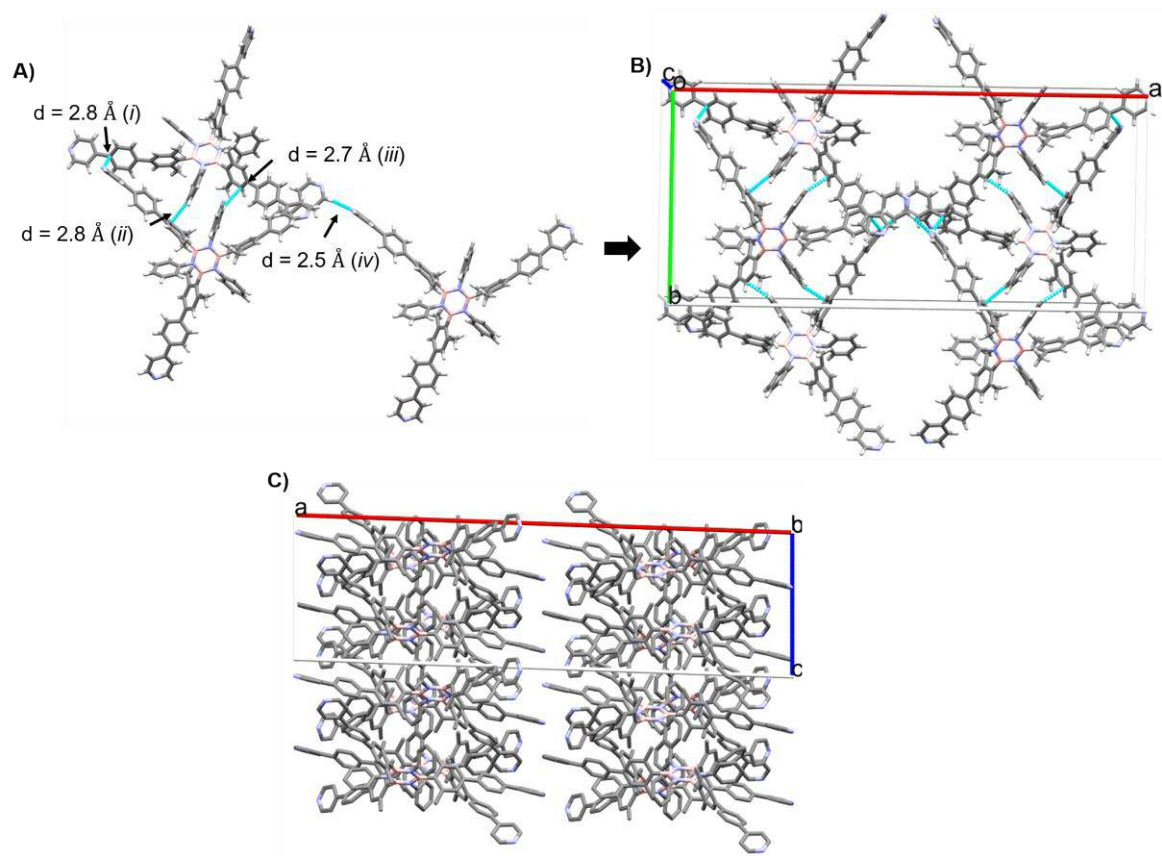
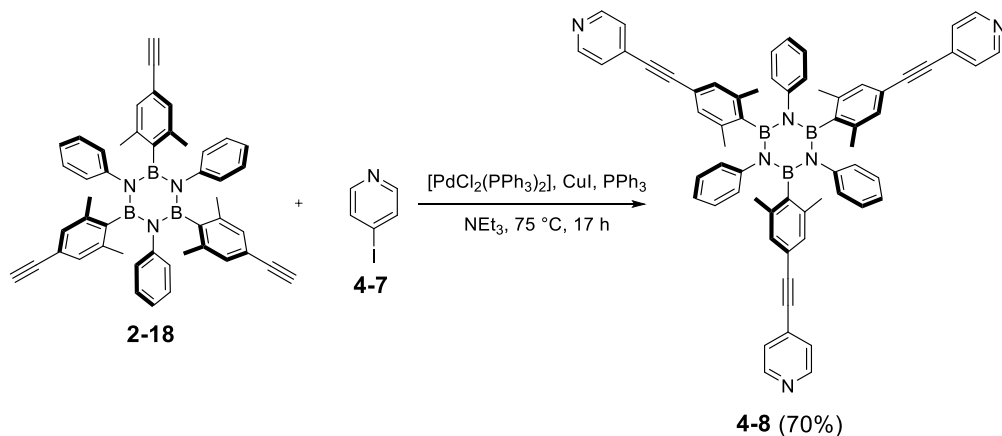


Figure 4.12. Crystal structure of three-pyridyl borazine 4-6 (colour code: grey: C, pink: B, blue: N, and white: H). A) Interactions present in the crystal lattice; B) Crystal packing showing the rectangular parallelepiped shape of the lattice; C) View of the crystal packing along the crystallographic c axis.

Following a similar synthetic approach described for compound 4-6, borazine derivative 4-8 could be synthesised by Sonogashira cross-coupling reaction between derivative 2-18 (previously synthesised in *section 2.5.1*) and 4-7 (Scheme 4.3) in 70% yield.



Scheme 4.3. Synthesis of three-pyridyl borazine 4-8.

The $^1\text{H-NMR}$ spectrum of 4-6 in CDCl_3 is shown in Figure 4.13. In the aromatic region of

the spectrum, the doublets at 8.51 and 7.25 ppm, with the same *ortho* coupling constant of 8.5 Hz, correspond to protons *a* and *b* in *ortho* and *meta* positions with respect to the *N*-atoms of the pyridine moieties. The multiplet between 6.93-6.84 ppm can be assigned to the phenyl hydrogen atoms *d* at the nitrogen sites of the borazine ring. The singlet at 6.80 ppm is related to the proton atoms *c*. In the aliphatic region, the singlet at 2.36 ppm can be reasonably attributed to the 18 methyl hydrogen atoms *e*.

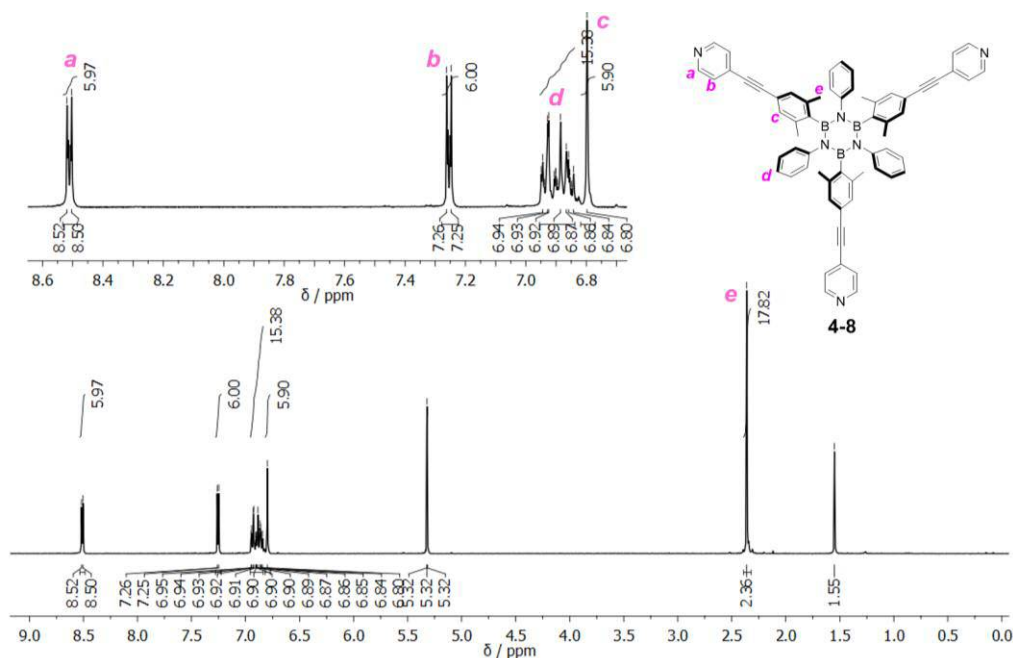


Figure 4.13. 400 MHz $^1\text{H-NMR}$ of borazine branching module **4-8** in CD_2Cl_2 (Solvent residual peak: 5.32 ppm).

Single crystals of borazine **4-8** suitable for X-ray diffraction were obtained by slow diffusion of MeOH in CHCl_3 solution (Figure 4.14) and relative characterisation confirmed the expected structure (see experimental section in *chapter 5*).

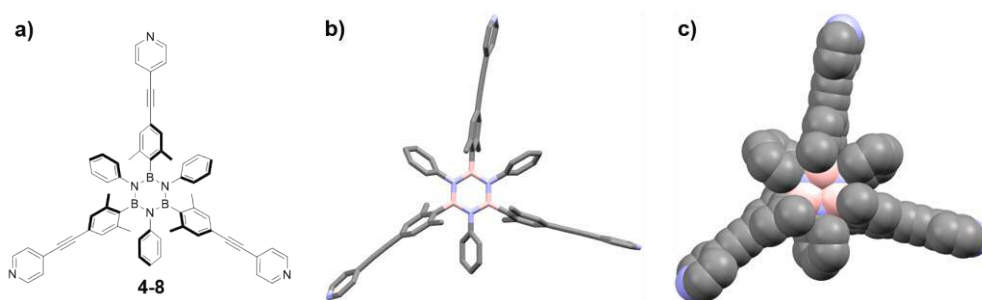


Figure 4.14. Crystal structure of borazine **4-8**; a) molecular structure; b) crystal structure represented in capped sticks; c) crystal structure represented in spacefill. Space group: P-1. The crystal structure was grown by slow diffusion of MeOH in CHCl_3 . Colour code: grey: C, pink: B and blue: N. Hydrogen atoms were omitted for the sake of clarity.

4.3.2 STM of three-pyridyl borazine modules

High-resolution STM images of single borazine **4-6** deposited by thermal sublimation under ultra-high vacuum (UHV) conditions on Cu(111) and Ag(100) are reported in Figure **4.15b** and **c**, respectively. Three bright lobes are visible at the center of the molecule along the axes defined by the peripheral pyridyl moieties, which are dimmer in the images below. The molecular contrast does not change for moderate bias voltages of both polarities, suggesting that it reflects the molecular conformation. The three lobes observed in STM imaging can be associated to the methyl groups on the phenyl ring at the *B*-sites of the borazine inner shell. This assignment is in line with STM observations and complementary MD modeling for xyl-yl-functionalised borazine derivatives **1-51** and **4-4** on copper substrate, described in *section 4.2*.

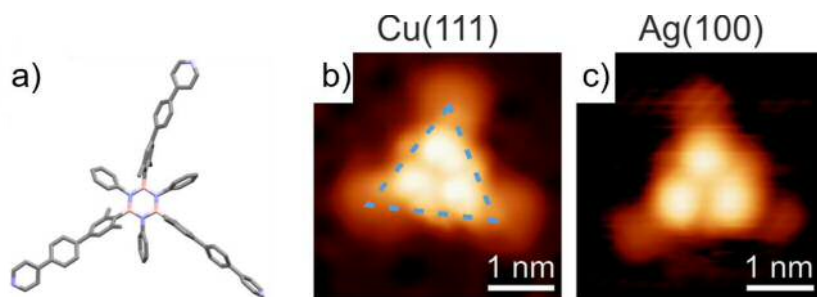


Figure 4.15. a) Crystal structure of borazine **4-6** determined by X-ray diffraction (atom colours: N in blue, B in pink, C in grey). Hydrogen atoms were omitted for the sake of clarity. STM images of borazine **4-6** on b) Cu(111) and c) Ag(100). The superimposed dashed triangle in b) indicates the orientation of the molecule. Scan parameters: b) $U_b = 1.9$ V, $I_t = 170$ pA, c) $U_b = 0.5$ V, $I_t = 81$ pA.

Simulated STM images (Figure **4.16**) of different adsorption geometries, suggest that three-pyridyl borazine **4-6** deforms upon surface adsorption. The best agreement on the geometry between experimental (Figure **4.16b**) and simulated STM (Figure **4.16d** and **f**) is found where the borazine core and the peripheral pyridyl groups are aligned (nearly) parallel to the surface plane while the phenyl rings are rotated out of this plane. Additionally, the distortion of borazine **4-6** on Cu(111) (Figure **4.16b**) with respect to the expected three-fold symmetry (Figure **4.16d**) can be ascribed to the flexibility of the substituents of the borazine which are slightly bent in-plane.

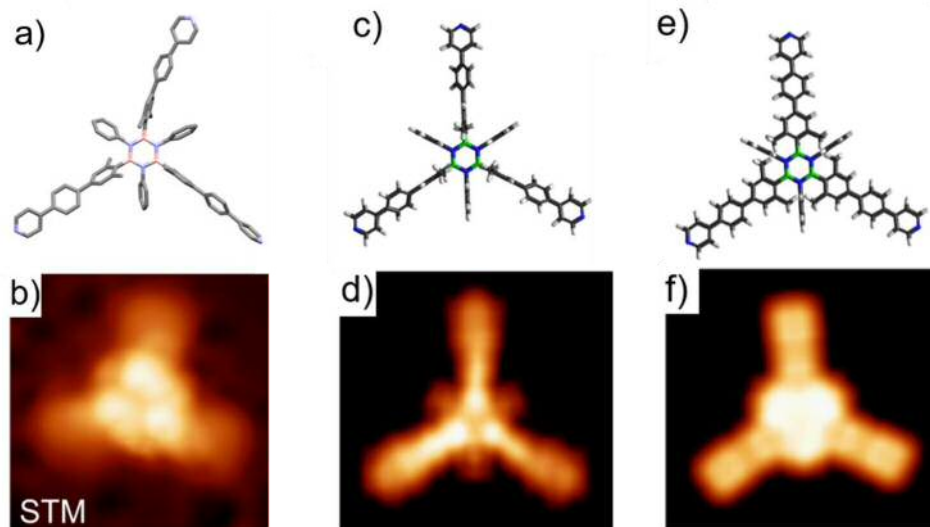


Figure 4.16. a) Crystal structure of borazine **4-6**; b) STM images of an individual borazine **4-6** on Cu(111); c) and e) model structure of **4-6** with different geometries of the substituents; d) and f) Simulated STM images of the corresponding borazine model structure c) and e), respectively.

4.3.3 Self-Assembly of three-pyridyl borazine **4-6** on Ag(100) surface

We started the investigation with three-pyridyl borazine **4-6**, which was deposited by thermal sublimation under UHV conditions on Ag(100) surfaces kept at room temperature, and their self-assembly behaviour was evaluated by low temperature (LT)-STM. Interestingly, three-pyridyl linker **4-6** shows 3D crystal packing with supramolecular organization driven by van der Waals and H-bonding interactions between the aryl moieties of the borazine scaffold as previously described (Figure 4.17a, see also Figure 4.12). On the other hand, compound **4-6** on Ag(100) arranges and forms 2D porous honeycomb networks controlled in the same fashion by van der Waals and H-bonding interactions (Figure 4.17b). Extended and highly ordered molecular islands of **4-6** were observed on Ag(100), as displayed in the STM image in Figure 4.18a. A high-resolution close-up view (inset in Figure 4.18a) reveals that each molecule in the honeycomb structure is surrounded by three neighbouring borazines and three pores. The rhombic unit cell (white lines in the inset in Figure 4.18a) has the parameters $a = b = (26.0 \pm 0.5) \text{ \AA}$ and $\theta = (60 \pm 3)^\circ$, which results in a packing density of $0.34 \text{ molecules} \cdot \text{nm}^{-2}$. The 2D network is stabilised by inter-molecular van der Waals and H-bonding interactions between the

aryl moieties decorating the BN core. Such high packing density suggests that the flexible protruding substituents are presumably bent towards the center of the pores.

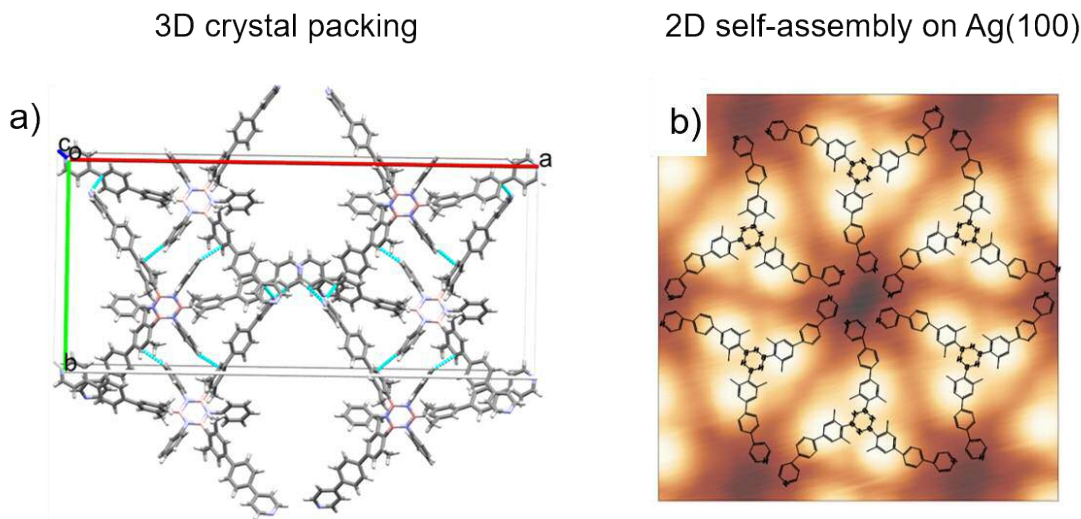


Figure 4.17. a) Crystal structure of three-pyridyl borazine **4-6** showing the different interaction present in the crystal lattice. Colour code: grey: C, pink: B, blue: N, and white: H. b) STM image overlaid with a tentative structural model of **4-6**.

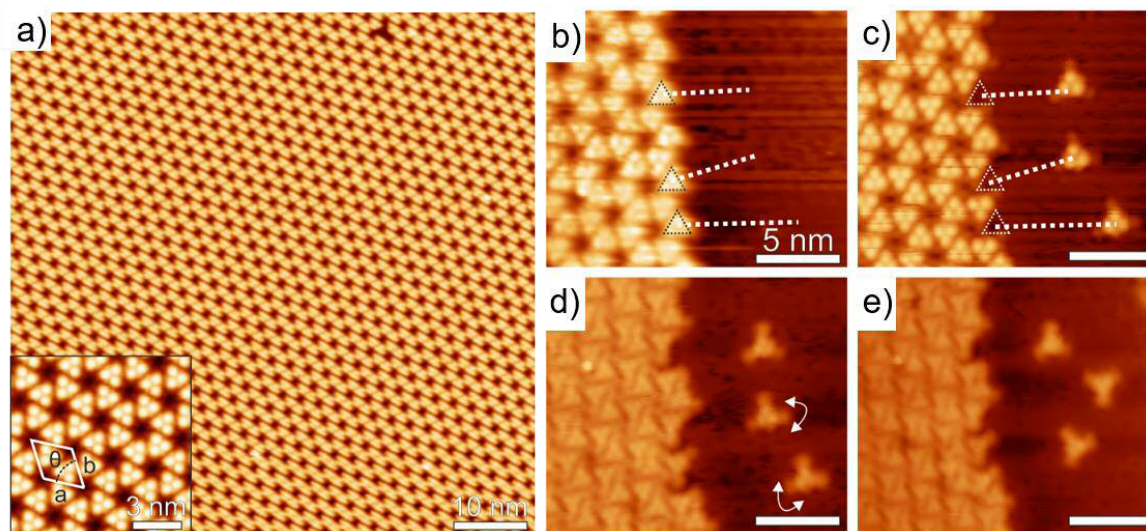


Figure 4.18. STM images of borazine derivative **4-6** on Ag(100). a) Large scale image of the close-packed hexagonal network of three-pyridyl borazine **4-6**. Scan parameters: $U_b = 1.0$ V, $I_t = 64$ pA. The inset shows a high-resolution STM image where the unit cell is highlighted. Scan parameters: $U_b = 0.2$ V, $I_t = 40$ pA; b) individual molecules can be manipulated via STM in a controlled way along the indicated dotted white lines; c) Three individual borazine **4-6** were detached from the dense-packed island; (Scan parameters of b) and c): $U_b = 0.5$ V, $I_t = 81$ pA d), e) additionally, the orientation of the protruding substituents can be changed as indicated by the white arrows in d); Scan parameters of d) and e): $U_b = 1.7$ V, $I_t = 81$ pA.

A clear indication of the weak intermolecular interactions between the borazine derivatives and the substrate is that individual borazine modules can be removed from the

edges of the islands in a controlled way by STM manipulation (Figure 4.18b and c). For this purpose, the STM tip is positioned above a rim molecule, which is dragged out (indicated by the white dashed lines) while a bias voltage $U_b = 50$ mV and a tunneling current $I_t = 20$ nA are applied. Moreover, the molecules can be rotated and the orientation of the peripheral substituents with respect to the molecular axes can be changed by STM manipulation (Figure 4.18d and e). The flexibility of the substituents is clearly revealed in Figure 4.18d where angles between 120° and almost 180° of adjacent substituents are observed. The most abundant arrangement in six-membered rings is not the only one, and a second phase embedded in the honeycomb network is occasionally observed (Figure 4.19a and c). In the latter, borazine 4-6 is assembled in rows consisting of pairs of molecules, which are rotated by 60° relatively to each other (Figure 4.19c). After annealing of the sample at 570 K, although some disordered regions can be found, the honeycomb networks are still observed, demonstrating a high thermal stability of the hexagonal borazine framework (Figure 4.19d).

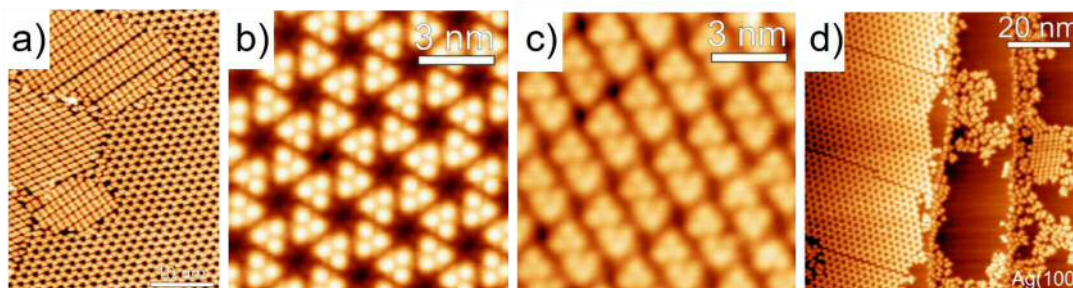


Figure 4.19. Self-assembly of borazine 4-6 on Ag(100) surface. a) Large-scale STM image reveals that within the well-ordered phase of 6-membered rings, several domains with a different phase occur; b) the most abundant phase, the molecules arrange in six-membered rings with hexagonal symmetry; c) In the second phase, the tripod molecules assemble in lines consisting of two molecules rotated by 60° relative to each other; d) STM image after annealing at 570 K. The close-packed assembly with 6-membered rings is mostly intact and only some disordered molecules are observed on the substrate.

4.3.4 Self-Assembly of three-pyridyl borazine on Cu(111) surface

The self-assembly of borazine 4-6 on Cu(111) is displayed in Figure 4.20b. As described for Ag(100) surface, compound 4-6 was deposited by thermal sublimation under UHV conditions and its self-assembly behaviour was investigated by LT-STM. A highly ordered network with molecules and pores arranged into interconnected chains is formed. Interestingly, this network does not reflect the intrinsic three-fold symmetry of 4-6 module, but base on interconnected rows where only one out of three pyridyl-substituents

seems to engage in Cu coordination although an excess of copper atoms is provided at room temperature. The trapezoidal unit cell of the borazine network has the parameters $a = (38.4 \pm 2.9) \text{ \AA}$, $b = (26.5 \pm 2.3) \text{ \AA}$ and $\theta = (75 \pm 5)^\circ$. The packing density is $0.20 \text{ molecules}\cdot\text{nm}^{-2}$ and the short axis of the unit cell is found to be parallel to one of the $\langle 110 \rangle$ directions of the Cu(111) surface. The measured centre-to-centre distance along the pyridyl substituents is $(20.5 \pm 0.5) \text{ \AA}$. A similar self-assembled chain-like structure was observed for borazine **4-8** on the same surface (Figure 4.20c). Due to the reduced length of the substituents at the *B-sites*, they presents a smaller trapezoidal unit cell with the parameters $a = (32.6 \pm 2.6) \text{ \AA}$, $b = (19.2 \pm 2.4) \text{ \AA}$ and $\theta = (75 \pm 4)^\circ$. Along the rows, the molecules are alternately rotated by $(60 \pm 6)^\circ$, showing a distance centre-to-centre of $(17.9 \pm 0.4) \text{ \AA}$. Interestingly, due to the flexibility of the lateral substituents, the borazine modules are not necessarily connected in a straight line, obtaining an uneven pore size distribution in the network. Adjacent rows are connected via opposing substituents in **4-6** and **4-8** networks with a centre-to-centre distance of $(32.2 \pm 0.6) \text{ \AA}$ and $(27.2 \pm 0.5) \text{ \AA}$, respectively. This long distance suggests a pyridine-Cu-pyridine (py-Cu-py) coordination where the *N* atoms of the peripheral pyridine groups are coordinated to copper ions. Interestingly, taking in consideration the distance between the peripheral aryl units at the *B-sites* and the centre of the borazine ring (14.4 \AA), the py-Cu-py bond length is 3.4 \AA , which is slightly shorter than 3.6 \AA reported by Li *et al.*³³ It can be ascribed to the flexibility of the protruding substituents giving an in-plane bending of the substituents as outcome.

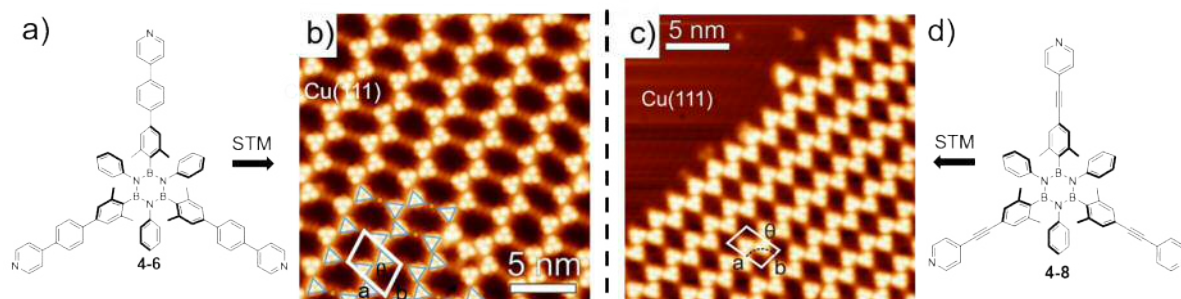


Figure 4.20. Self-assembly of borazine linkers **4-6** and **4-8** on the Cu(111) surface. a) Structural model of borazine linker **4-6**; b) STM image of borazine derivative **4-6** on Cu(111), scan parameters: $U_b = 1.2 \text{ V}$, $I_t = 100 \text{ pA}$; c) STM image of borazine derivative **4-8** on Cu(111), scan parameters: $U_b = 1.0 \text{ V}$, $I_t = 100 \text{ pA}$.; d) Structural model of borazine linker **4-8**.

The anisotropic island growth proceeds parallel to the step edges indicating that the intermolecular interactions along this direction are stronger compared to the interactions along the coordinated substituents. Deposition of additional copper atoms followed by subsequent annealing of three-pyridyl borazine **4-6** at 420 K gives rise to a structural transformation of the chain-like network. Patches of a fully Cu-coordinated triangular network are observed embedded in the chain-like assembly of the borazine on Cu(111) (Figure 4.21b). In this new network structure, three **4-6** modules are linked through the *N* atoms of their terminal py groups which presumably coordinates a single Cu atom. Remarkably, increasing the dosage of additional Cu atoms, a transformation of the molecular assembly into a three-fold coordinated metal-organic network has been observed on a larger scale (Figure 4.21c).

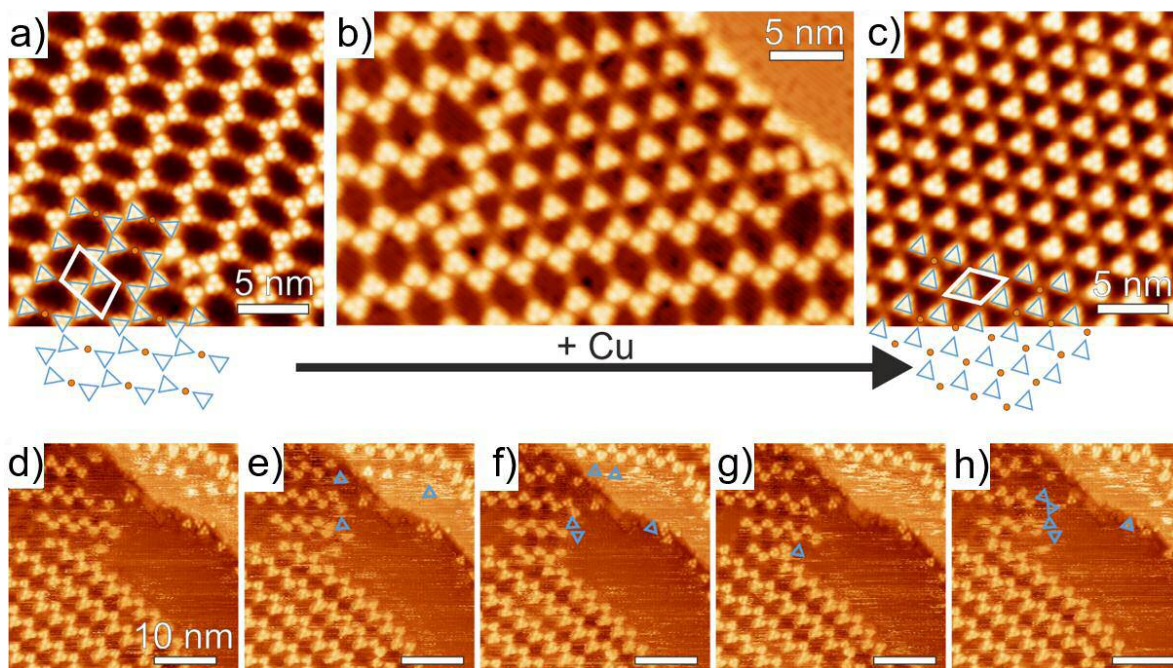


Figure 4.21. STM images displaying the self-assembly of **4-6** on Cu(111): a) In the self-assembled nanostructure, borazine **4-6** form rows that are interconnected by the protruding substituents coordinated to a Cu atom. Scan parameters: $U_b = 1.2$ V, $I_t = 100$ pA; b) Deposition of additional Cu adatoms while the sample is held at 370 K, leads to a structural transformation and patches of molecules with all three substituents coordinated to Cu atoms are formed. Scan parameters: $U_b = 1.0$ V, $I_t = 64$ pA; c) With a sufficient number of available Cu atoms, extended islands with fully three-fold coordinated borazine linker **4-6** are observed. The models of the molecular network is superimposed on the STM images in a) and c). Scan parameters: $U_b = 0.96$ V, $I_t = 40$ pA. d)-h) Series of STM images acquired at 300 K reveal that the metal-organic network is stable at room temperature. Individual molecules (highlighted in blue triangles) at the edge of the molecular islands are moving as can be seen in consecutive scans of the same region. Scan parameters: $U_b = 1.0$ V, $I_t = 110$ pA.

This behaviour could be due to the low steric hindrance of the extended lateral substituents in the outer shell of borazine **4-6** that allow the three-fold coordination with Cu ions. The trapezoidal unit cell presents the parameters $a = (25.5 \pm 1.7) \text{ \AA}$, $b = (24.2 \pm 1.6) \text{ \AA}$ with an internal angle $\theta = (60 \pm 2)^\circ$ and a packing density of $0.18 \text{ molecules} \cdot \text{nm}^{-2}$. STM measurements conducted at 300 K (Figure 4.21d-h) reveal that compound **4-6** forms the same network as that observed on Cu(111) at low-temperature (Figure 4.21a). However, subsequent scans of the edge region of a molecular island suggest that the borazine modules are mobile, while the bulk of the self-assembled architecture remains mostly unperturbed. Likely, this is a consequence of the weak molecule-substrate interaction combined with the high mobility of the Cu adatoms at room temperature that, enabling the diffusion of the molecules, allow the dynamic formation of new coordination bonds at the periphery of the self-assembled islands. Further annealing of the metal-organic network to temperatures higher than 470 K lead to the formation of a polymeric phase where covalent structures, formed through thermal activation of C-H bonds, are presumably present (Figure 4.22).

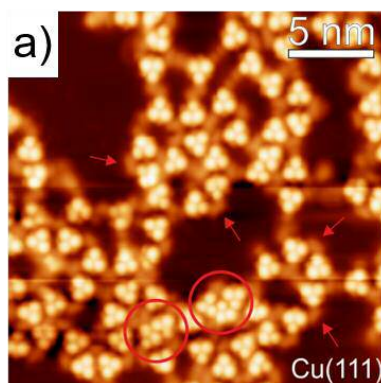


Figure 4.22. STM image of borazine linker **4-6** on Cu(111) after annealing to 470 K showing highly unordered islands. Presumably, covalent bonds are formed between some molecules (indicated by red arrows) while other molecules might have lost at least parts of their legs (indicated by red circles) leading to very densely packed structures.

Conclusions and Perspectives

The work presented in this last chapter of the thesis was focused on the influence of the metal substrate on the borazine self-assembly driven by metal-organic coordination. To achieve this, borazine linkers **4-6** and **4-8** bearing pyridyl moieties as coordinating connectors have been designed and successfully synthesised. The synthesis of borazine-linkers **4-6** and **4-8** have been carried out through cross-coupling reactions. In the first

case, Suzuki cross-coupling reaction allow us to couple triflate borazine derivative **2-30** with 4-pyridyl-phenylboronic acid **4-5**, achieving borazine-linker **4-6**. Whereas, Sonogashira cross-coupling between borazine derivative **2-18** and **4-7**, permit us to obtain three-pyridyl borazine **4-8**. Individual borazine **4-6** and **4-8** presents a remarkable flexibility, which is expressed by the possibility of their protruding substituents to bend in-plane on metal substrates. On Ag(100) surfaces, borazine **4-6**-substrate interactions are weak and no influence on the surface termination was observed. The self-assembly is driven by intermolecular van der Waals (vdW) interactions leading to a very dense-packed network. Different supramolecular networks have been observed with STM imaging for borazine **4-6** on Cu(111). While such molecules form a densely packed honeycomb network on Ag(100), interconnected chains were found on Cu(111). Upon deposition of additional Cu atoms at 420 K, a structural transformation can be induced on Cu(111), which lead to a fully three-fold coordinated triangular network. As result, thanks to an appropriate selection of the metal substrate together with the alteration of the molecular self-assembly *via* coordination and thermal treatment, the 2D borazine framework can be tailored.

In order to assess the effect of the protruding substituents of the borazine outer shell on the 2D metal organic network, the self-assembly on Ag(100) and Cu(111) of borazine **4-8** decorated with ethynyl groups as organic spacer has to be further investigate. Additionally, the scanning tunnelling spectroscopy (STS) has to be performed to evaluate the decoupling of the borazine linker from the metal substrate driving by the inner shell functionalisations.

4.4 References

- (1) Dong L., Gao Z. A., Lin N. *Prog. Surf. Sci.* **2016**, *91*, 101.
- (2) Lukas S., Witte G., Wöll C. *Phys. Rev. Lett.* **2002**, *88*, 283011.
- (3) Bartels L. *Nat. Chem.* **2010**, *2*, 87.
- (4) Wong K., Kwon K.-Y., Rao B. V, Liu A., Bartels L. *J. Am. Chem. Soc.* **2004**, *126*, 7762.
- (5) Yamamoto T., Yokoyama S., Kamikado T., Okuno Y., Mashiko S. *Nature* **2001**,

413, 619.

- (6) Stepanow S., Strunskus T., Lingenfelder M., Dmitriev A., Spillmann H., Lin N., Barth J. V., Wöll C., Kern K. *J. Phys. Chem. B* **2004**, *108*, 19392.
- (7) Mamdouh W., Dong M., Xu S., Rauls E., Besenbacher F. *J. Am. Chem. Soc.* **2006**, *128*, 13305.
- (8) Gourdon A. *Angew. Chem. Int. Ed.* **2008**, *47*, 6950.
- (9) Matena M., Riehm T., Stöhr M., Jung T. A., Gade L. H. *Angew. Chem. Int. Ed.* **2008**, *47*, 2414.
- (10) Lingenfelder M. A., Spillmann H., Dmitriev A., Stepanow S., Lin N., Barth J. V., Kern K. *Chem. Eur. J.* **2004**, *10*, 1913.
- (11) Langner A., Tait S. L., Lin N., Rajadurai C., Ruben M., Kern K. *Proc. Natl. Acad. Sci.* **2007**, *104*, 17927.
- (12) Surin M., Samorì P., Jouaiti A., Kyritsakas N., Hosseini M. W. *Angew. Chem. Int. Ed.* **2007**, *46*, 245.
- (13) Semenov A., Spatz J. P., Möller M., Lehn J. M., Sell B., Schubert D., Weidl C. H., Schubert U. S. *Angew. Chem. Int. Ed.* **1999**, *38*, 2547.
- (14) Marschall M., Reichert J., Weber-Bargioni A., Seufert K., Auwärter W., Klyatskaya S., Zoppellaro G., Ruben M., Barth J. V. *Nat. Chem.* **2010**, *2*, 131.
- (15) Stepanow S., Lin N., Payer D., Schlickum U., Klappenberger F., Zoppellaro G., Ruben M., Brune H., Barth J. V., Kern K. *Angew. Chem. Int. Ed.* **2007**, *46*, 710.
- (16) Stepanow S., Lingenfelder M., Dmitriev A., Spillmann H., Delvigne E., Lin N., Deng X., Cai C., Barth J. V., Kern K. *Nat. Mater.* **2004**, *3*, 229.
- (17) Spillmann H., Dmitriev A., Lin N., Messina P., Barth J. V., Kern K. *J. Am. Chem. Soc.* **2003**, *125*, 10725.
- (18) Tait S. L., Langner A., Lin N., Stepanow S., Rajadurai C., Ruben M., Kern K. *J. Phys. Chem. C* **2007**, *111*, 10982.
- (19) Tait S. L., Langner A., Lin N., Chandrasekar R., Fuhr O., Ruben M., Kern K. *ChemPhysChem* **2008**, *9*, 2495.

- (20) Liu J., Lin T., Shi Z., Xia F., Dong L., Liu P. N., Lin N. *J. Am. Chem. Soc.* **2011**, *133*, 18760.
- (21) Schlickum U., Decker R., Klappenberger F., Zoppellaro G., Klyatskaya S., Ruben M., Silanes I., Arnau A., Kern K., Brune H., Barth J. V. *Nano Lett.* **2007**, *7*, 3813.
- (22) Forrest S. R. *Nature* **2004**, *428*, 911.
- (23) Fréchet J. M. J. *Chem. Rev.* **2007**, *104*, 1066.
- (24) Facchetti A. *Chem. Mater.* **2011**, *23*, 733.
- (25) Della Pia A., Riello M., Floris A., Stassen D., Jones T. S., Bonifazi D., De Vita A., Costantini G. *ACS Nano* **2014**, *8*, 12356.
- (26) Bonifazi D., Mohnani S., Llanes-Pallas A. *Chem. Eur. J.* **2009**, *15*, 7004.
- (27) Barth J. V., Costantini G., Kern K. *Nature* **2005**, *437*, 671.
- (28) Elemans J. A. A. W., Lei S., De Feyter S. *Angew. Chem. Int. Ed.* **2009**, *48*, 7298.
- (29) Otero R., Gallego J. M., De Parga A. L. V., Martín N., Miranda R. *Adv. Mater.* **2011**, *23*, 5148.
- (30) Kervyn S., Kalashnyk N., Riello M., Moreton B., Tasseroul J., Wouters J., Jones T. S., De Vita A., Costantini G., Bonifazi D. *Angew. Chem. Int. Ed.* **2013**, *52*, 7410.
- (31) Kalashnyk N., Ganesh Nagaswaran P., Kervyn S., Riello M., Moreton B., Jones T. S., De Vita A., Bonifazi D., Costantini G. *Chem. Eur. J.* **2014**, *20*, 11856.
- (32) K. Ariga, V. Malgras, Q. Ji, M. B. Zakaria, Y. Yamauchi, *Coord. Chem. Rev.* **2016**, *320-321*, 139.
- (33) Li Y., Xiao J., Shubina T. E., Chen M., Shi Z., Schmid M., Steinrück H.-P., Gottfried J. M., Lin N. *J. Am. Chem. Soc.* **2012**, *134*, 6401.

CHAPTER 5

Experimental Part

5.1 Instrumentations

Thin layer chromatography (TLC) was conducted on pre-coated aluminium sheets with 0.20 mm Merk Millipore Silica gel 60 with fluorescent indicator F254.

Column chromatography was carried out using *Merck Gerduran silica gel 60* (particle size 40-63 μm).

Gel permeation chromatography (GPC). GPC analysis and purifications on a preparative scale (50 mg max.) were performed by the Japan Analytical Industry on a JAI LC-9160NEXT using GPC columns JAIGEL-2.5HH and 3HH in recycling mode and CHCl_3 (HPLC grade) as eluent.

Melting points (M.P.) were measured on a *Büchi Melting Point B-545* or were measured on a *Gallenkamp* apparatus. All of the melting points have been measured in open capillary tubes.

Nuclear magnetic resonance (NMR) ^1H , ^{11}B , ^{13}C , and ^{19}F spectra were obtained on a 300 MHz NMR (*Bruker Fourier*), 400 MHz NMR (*Jeol JNM EX-400* or *Bruker AVANCE III HD*), and 500 MHz NMR (*Jeol JNM EX-500R*). Chemical shifts were reported in ppm according to tetramethylsilane using the solvent residual signal as an internal reference (CDCl_3 : $\delta_{\text{H}} = 7.26$ ppm, $\delta_{\text{C}} = 77.16$ ppm, CD_2Cl_2 : $\delta_{\text{H}} = 5.32$ ppm, $\delta_{\text{C}} = 53.84$ ppm, Coupling constants (J) were given in Hz and were averaged. Resonance multiplicity was described as *s* (singlet), *d* (doublet), *t* (triplet), *m* (multiplet), *br* (broad signal). Carbon, fluorine and boron spectra were acquired with a complete decoupling for the proton. All spectra were recorded at 25 °C unless specified otherwise. Signals observed in ^1H spectra at 1.27 ppm and 0.8 ppm are traces of grease.

Infrared spectra (IR) were recorded on a *Perkin-Elmer Spectrum II FT-IR System UATR*,

mounted with a diamond crystal, on a *BIO-RAD FTS-165 apparatus*, or on a *Shimadzu IR Affinity 1S FTIR spectrometer* in ATR mode with a diamond mono-crystal. Selected absorption bands are reported in wavenumber (cm^{-1}).

ESI-High resolution mass spectrometry (ESI-HRMS). ESI-HRMS was performed by the *Fédération de Recherche; ICOA/CBM (FR2708)* platform of Orléans in France, on a Bruker maXis Q-TOF in the positive ion mode. The analytes were dissolved in a suitable solvent at a concentration of 1 mg/mL and diluted 200 times in methanol (≈ 5 ng/mL). The diluted solutions (1 μL) were delivered to the ESI source by a Dionex Ultimate 3000 RSLC chain used in FIA (Flow Injection Analysis) mode at a flow rate of 200 $\mu\text{L}/\text{min}$ with a mixture of $\text{CH}_3\text{CN}/\text{H}_2\text{O} + 0.1\%$ of HCO_2H (65/35). ESI conditions were as follows: capillary voltage was set at 4.5 kV; dry nitrogen was used as nebulizing gas at 0.6 bars and as drying gas set at 200 $^\circ\text{C}$ and 7.0 L/min. ESI-MS spectra were recorded at 1 Hz in the range of 50-3000 m/z . Calibration was performed with ESI-TOF Tuning mix from Agilent and corrected using lock masses at m/z 299.294457 (methyl stearate) and 1221.990638 (HP-1221). Data were processed using Bruker Data Analysis 4.1 software. Besides, ESI-HRMS analysis were performed on LCT HR TOF mass spectrometer in the positive or negative ion mode, at *Cardiff University*.

Matrix-Assisted Laser Desorption-Ionisation Time-of-Flight Mass Spectrometry analysis (MALDI-TOF). MALDI-HRMS was performed by the *Centre de spectrométrie de masse* at the *Université de Mons* in Belgium, using the following instrumentation: QToF Premier mass spectrometer equipped with a nitrogen laser, operating at 337 nm with a maximum output of 500 mW delivered to the sample in 4 ns pulses at 20 Hz repeating rate. Time-of-flight analyses were performed in the reflectron mode at a resolution of about 10.000. The matrix, trans-2-[3-(4-tertbutyl-phenyl)-2-methyl-2-propenylidene]malonitrile (DCTB), was prepared as a 40 mg/mL solution in chloroform. The matrix solution (1 μL) was applied to a stainless-steel target and air dried. Analyte samples were dissolved in a suitable solvent to obtain 1 mg/mL solutions. 1 μL aliquots of these solutions were applied onto the target area already bearing the matrix crystals, and air dried. For the recording of the single-stage MS spectra, the quadrupole (rf-only mode) was set to S3 pass ions from 100 to 1000 THz and all ions were transmitted into the pusher region of the time-offlight analyser where they were analysed with 1s integration time. Besides, High-resolution

MALDI mass spectra (HRMS) were performed on a Synapt G2-Si QTOF mass spectrometer, all this analysis was carried out at *Cardiff University*.

Powder X-ray diffraction (PXRD). Powder X-ray diffraction patterns were obtained on a PAN analytical X'Pert Pro diffractometer using Cu K α ray source operating at 40 kV and 40 mA. The signal was recorded for 2θ between 10° and 25° with a step of 0.02° . The XRD patterns were analysed following the JCPDS database, all this analysis was carried out at *Cardiff University*.

Scanning electron microscopy (SEM). Scanning electron microscopy images were obtained using a Carl Zeiss EVO 40 operated at 25 kV. All samples were mounted on carbon Leit adhesive discs. Images were collected using backscattered and secondary electron detectors. For EDX (X-ray energy dispersive spectroscopy) analysis, high probe currents (up to 25 nA) were required to allow sufficient generation of X-rays. The data was collected using an Oxford EDX analyser coupled to the EVO 40 SEM, all this analysis was carried out at *Cardiff University*.

UV-Vis spectroscopy. UV-Vis absorption spectra were recorded on a Varian Cary 5000 Bio UV-Vis spectrophotometer using a quartz cell (path length of 1 cm). **Fluorescence** was measured on a Cary Eclipse Fluorescence Spectrophotometer using a quartz cell (path length of 1 cm). The emission spectra have been recorded exciting the samples at their absorption maxima. **Luminescence lifetime.** Photophysical data were obtained on a JobinYvon-Horiba Fluorolog spectrometer fitted with a JY TBX picoseconds photodetection module as chloroform solutions. Emission spectra were uncorrected and excitation spectra were instrument corrected. The pulsed source was a NanoLED configured for 295 nm output operating at 1 MHz. Luminescence lifetime profiles were obtained using the JobinYvon-Horiba FluoroHub single photon counting module and the data fits yielded the lifetime values using the provided DAS6 deconvolution software.

Scanning tunnelling microscopy (STM). All STM experiments were performed at low temperature (if not explicitly stated differently) in a custom-designed ultra-high vacuum (UHV) chamber housing a CreaTec STM operated at 5K. Additional STM experiments were conducted at room temperature in a second UHV chamber equipped with a SPECS X-

ray source with an Al anode, a SPECS PHOIBOS 100 electron analyzer and a CreaTec room temperature STM. The base pressure during all experiments was 5×10^{-10} mbar. The Cu(111) and the Ag(100) single crystals were prepared by repeated cycles of Ar⁺ ion sputtering and annealing to 775K and 725K, respectively. The samples were dosed from a thoroughly degassed quartz crucible held at 600 K onto the sample held at room temperature. All STM images were recorded in constant-current mode using an electrochemically etched tungsten tip. The WsXM software was used to process the STM raw data.

5.2 Material and general Methods

Chemicals were purchased from *Sigma Aldrich*, *Acros Organics*, *Fluorochem*, *TCI*, *Carbosynth*, and *ABCR*, and were used as received unless specified otherwise. Solvents were purchased from *Sigma Aldrich* and *Acros Organics*. Deuterated solvents were purchased from *Eurisotop*.

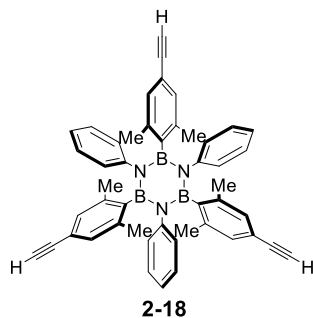
General solvents were distilled *in vacuo*. Anhydrous THF was distilled from Na/benzophenone. Anhydrous toluene was distilled from CaH₂.

Low temperature baths were prepared using different solvent mixtures depending on the desired temperature: -196 °C with liquid N₂, -84 °C with EtOAc/liquid N₂, -78 °C Et₂O/N₂ liquid, and 0 °C with ice/H₂O.

Anhydrous conditions were achieved by drying *Schlenk* lines, 2-neck flasks or 3-neck flasks by heating with a heat gun under vacuum and then purging with argon. The inert atmosphere was maintained using argon-filled balloons equipped with a syringe and needle that was used to penetrate the silicon stoppers used to close the flasks' necks. The addition of liquid reagents was done by means of dried plastic syringes or by cannulation.

5.3 Experimental procedures

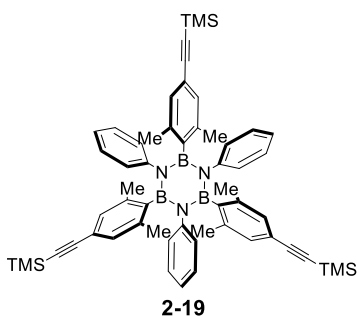
Synthesis of N,N',N''-triphenyl-B,B',B''- tri(2,6-dimethyl-4-acetyl phenyl)borazine 2-18



To a solution of **2-19** (0.57 g, 0.626 mmol) in THF (15 mL), TBAF (1M solution in THF, 2.10 mL, 2.10 mmol) was added dropwise at 0 °C. The reaction mixture was stirred at room temperature for 1 h, then diluted with EtOAc (30 mL), washed with H₂O (3 x 30 mL), and brine (30 mL). The organic phase was dried over MgSO₄ and the solvents removed under reduced pressure. The residue was purified by silica gel column chromatography (pentane/EtOAc, 95:5) affording **2-18** as white solid (0.417 g, 96%).

¹H-NMR (400 MHz, CDCl₃) δ: 6.80-6.75 (m, 15 H), 6.70 (s, 6 H), 2.87 (s, 3 H), 2.26 (s, 18 H). ¹³C-NMR (100 MHz, CDCl₃) δ: 145.38, 137.71, 129.23, 127.30, 126.58, 125.13, 120.41, 84.42, 76.19, 23.00 (the ¹³C resonance corresponding to the carbon atom bonded to the boron atom is not observed probably due to the quadrupolar relaxation). ¹¹B-NMR (128 MHz, CDCl₃) δ: 35.47. MALDI-HRMS calc. for [C₄₈H₄₂B₃N₃]⁺: 693.3658, found 693.3664. IR (film in CH₂Cl₂) ν_{max} (cm⁻¹): 3285, 2970, 2131 (weak), 1738, 1538, 1354, 1216, 700.

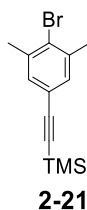
Synthesis of N,N',N''-triphenyl-B,B',B''-tri(2,6-dimethyl-4-(trimethylsilyl)acetynyl)phenyl borazine 2-19



To a solution of aniline (0.55 g, 5.90 mmol) in dry toluene (10 mL) under Ar, a solution of BCl_3 (1 M in heptane, 13.00 mL, 13.00 mmol) was added dropwise at 0 °C. The resulting white suspension was refluxed for 24 h. The solution was cooled down to room temperature and subjected to five freeze-pump-thaw cycles to remove the excess of HCl. In parallel, to a solution of **2-21** (2.00 g, 7.10 mmol) in anhydrous THF (31 mL), $t\text{BuLi}$ (1.7 M in hexane, 9.00 mL, 14.86 mmol) was added dropwise at -84 °C. The solution was allowed to warm up at 0 °C and stirred for 10 min. The degassed toluene mixture containing the chloro-borazine intermediate was cannulated dropwise to the organometallic-containing solution at 0 °C and allowed to react at room temperature for 16 h. The reaction mixture was diluted with EtOAc (100 mL), washed with H_2O (3 x 100 mL) and brine (1 x 100 mL). The organic layer was dried over MgSO_4 and evaporated under reduced pressure. The residue was purified by silica gel column chromatography (cyclohexane/ CH_2Cl_2 , 9:1) affording **2-19** as white solid (0.60 g, 34%).

M.P.: 256-259 °C. $^1\text{H-NMR}$ (400 MHz, CDCl_3) δ : 6.78-6.74 (m, 15 H), 6.69 (s, 6 H), 2.25 (s, 18 H), 0.15 (s, 27 H). $^{13}\text{C-NMR}$ (100 MHz, CDCl_3) δ : 145.46, 137.61, 129.13, 127.32, 126.58, 125.14, 121.26, 106.10, 92.88, 23.02, 0.09 (the ^{13}C resonance corresponding to the carbon atom bonded to the boron atom is not observed probably due to the quadrupolar relaxation). $^{11}\text{B-NMR}$ (128 MHz, CDCl_3) δ : 36.53. MALDI-HRMS calc. for $[\text{C}_{57}\text{H}_{66}\text{B}_3\text{N}_3\text{Si}_3]^+$: 909.4844, found: 909.4872. IR (film in CH_2Cl_2) ν_{max} (cm^{-1}): 2969, 2151, 1491, 1358, 1216, 1157, 840, 759.

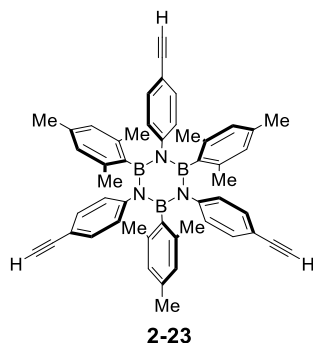
Synthesis of ((4-bromo-3,5-dimethylphenyl)ethynyl)trimethylsilane **2-21**



To a solution of 2-bromo-5-iodo-*m*-xylene **2-22** (0.50 g, 1.6 mmol) in diisopropylamine (10 mL), [PdCl₂(PPh₃)₂] (0.034 g, 0.048 mmol) and CuI (0.018 g, 0.096 mmol) were added. The mixture was subjected to three freeze-pump-thaw cycles and then trimethylsilyl acetylene (TMSA) (0.272 mL, 1.92 mmol) was added. The mixture was stirred for 16 h at room temperature, then diluted with EtOAc (30 mL) washed with H₂O (3 x 100 mL) and brine (30 mL). The organic phase was dried over MgSO₄ and the solvents removed under reduced pressure. The residue was purified by silica gel column chromatography (cyclohexane), affording **2-21** as yellow oil (0.42 g, 93%).

¹H-NMR (400 MHz, CDCl₃) δ: 7.18 (s, 2 H), 2.37 (s, 6 H), 0.25 (s, 9 H). ¹³C-NMR (100 MHz, CDCl₃) δ: 138.39, 131.44, 128.27, 121.59, 104.55, 94.54, 23.78, 0.09. ESI-HRMS: calc. for [C₁₃H₁₇BrSi]⁺: 280.0283, found 280.0287. IR (film in CH₂Cl₂) ν_{max} (cm⁻¹): 2956, 2154, 1561, 1248, 1173, 835, 757, 689.

Synthesis of N,N',N''-tri(4-ethynyl)phenyl-B,B',B''-trimesitylborazine **2-23**

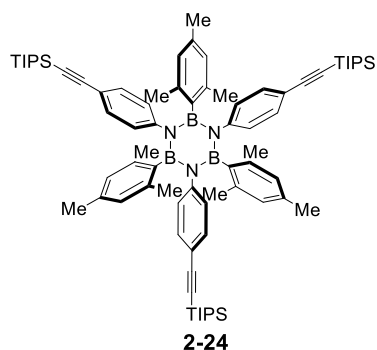


To a solution of **2-24** (0.162 g, 0.134 mmol) in THF (5 mL), TBAF (1M solution in THF, 0.536 mL, 0.536 mmol) was dropwise added at 0 °C. The reaction mixture was stirred at room temperature for 2 h, then diluted with EtOAc (30 mL), washed with H₂O (3 x 30 mL)

and brine (30 mL). The organic phase was dried over MgSO_4 and the solvents removed under reduced pressure. The residue was purified by silica gel column chromatography (pentane/EtOAc, 95:5) affording **2-23** as white solid (0.104 g, 77%).

$^1\text{H-NMR}$ (400 MHz, CD_2Cl_2) δ : 6.94 (d, $J = 8.6$ Hz, 6 H), 6.82 (d, $J = 8.6$ Hz, 6 H), 6.42 (s, 6 H), 2.97 (s, 3 H), 2.22 (s, 18 H), 2.03 (s, 9 H). $^{13}\text{C-NMR}$ (100 MHz, CD_2Cl_2) δ : 147.70, 137.83, 137.52, 131.47, 127.66, 126.99, 118.47, 83.69, 77.42, 23.37, 21.35 (the ^{13}C resonance corresponding to the carbon atom bonded to the boron atom is not observed probably due to the quadrupolar relaxation). $^{11}\text{B-NMR}$ (128 MHz, CD_2Cl_2) δ : 35.68. MALDI-HRMS calc. for $[\text{C}_{51}\text{H}_{48}\text{B}_3\text{N}_3]^+$: 735.4127, found 735.4114. IR (film in CH_2Cl_2) ν_{max} (cm^{-1}): 3295, 2919, 1537, 1355, 1264, 733, 703.

Synthesis of N,N',N'' -tri(4-triisopropylsilylethynyl)phenyl- B,B',B'' -trimesitylborazine **2-24**

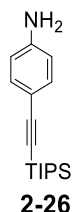


To a solution of **2-26** (2.07 g, 7.56 mmol) in dry toluene (20 mL) under Ar a solution of BCl_3 (1 M in heptane, 8.40 mL, 8.40 mmol) was added dropwise at 0 °C. The resulting scarlet-red solution was refluxed for 16 h. The solution was cooled down to room temperature and subjected to five freeze-pump-thaw cycles to remove the excess of HCl. In parallel, to a solution of MesBr (1.84 g, 9.28 mmol) in anhydrous THF (20 mL) $t\text{BuLi}$ (1.7 M in hexane, 11.5 mL, 19.5 mmol) was added dropwise at -84 °C. The solution was allowed to warm up at 0 °C and stirred for 10 min. The degassed toluene mixture containing the chloro-borazine intermediate was cannulated dropwise to the organometallic-containing solution at 0 °C and allowed to react at room temperature for 16 h. The reaction mixture was diluted with EtOAc (100 mL) and washed with H_2O (3 x 100 mL) and brine (1 x 100 mL). The organic layer was dried over MgSO_4 and evaporated under reduced pressure. The

residue was purified by silica gel column chromatography (cyclohexane/CH₂Cl₂, 9:1) affording **2-24** as white solid (1.60 g, 54%).

¹H-NMR (400 MHz, CDCl₃) δ: 6.89 (d, J= 8.5 Hz, 6 H), 6.71 (d, J= 8.5 Hz, 6 H), 6.37 (s, 6 H), 2.19 (s, 18 H), 2.02 (s, 9 H), 1.05 (s, 63 H). ¹³C-NMR (100 MHz, CDCl₃) δ: 146.96, 137.49, 137.01, 131.38, 127.17, 127.05, 119.65, 107.85, 89.70, 23.42, 21.47, 19.10, 11.81 (the ¹³C resonance corresponding to the carbon atom bonded to the boron atom is not observed probably due to the quadrupolar relaxation). ¹¹B-NMR (128 MHz, CDCl₃) δ: 35.96. MALDI-HRMS calc. for [C₇₈H₁₀₈B₃N₃Si₃]⁺: 1204.4280, found: 1204.8236. IR (film in CH₂Cl₂) ν_{max} (cm⁻¹): 3355, 2944, 2152, 1499, 1356, 1264, 839, 733.

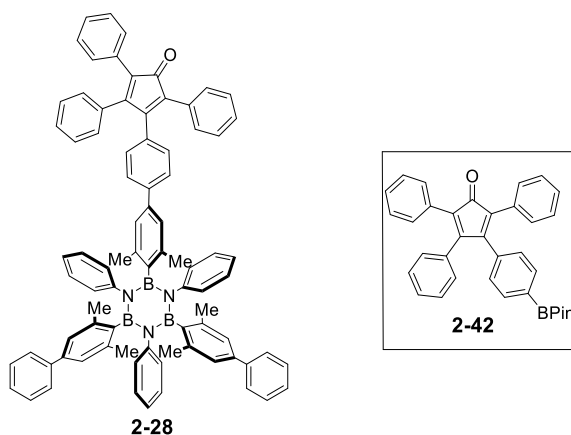
Synthesis of 4-(trisisopropylsilylethynyl)aniline **2-26**



To a solution of **2-27** (5.00 g, 22.8 mmol) in diisopropylamine (70 mL), trisisopropylsilylacetylene (5.60 mL, 25.0 mmol), [Pd(PPh₃)₂Cl₂] (0.323 g, 0.46 mmol) and CuI (0.089 g, 0.46 mmol) were added. The reaction mixture was subjected to three freeze-pump-thaw cycles. The mixture was stirred at room temperature for 24 h, then diluted with EtOAc (200 mL), washed with H₂O (3 x 200 mL) and brine (1 x 100 mL). The organic layer was dried over MgSO₄ and evaporated under reduced pressure. The residue was purified by silica gel column chromatography (cyclohexane/EtOAc, 8:2), affording **2-26** as yellow oil (5.25 g, 84%).

¹H-NMR (400 MHz, CDCl₃) δ: 7.28 (d, J= 8.7 Hz, 2 H), 6.58 (d, J= 8.7 Hz, 2 H), 1.11 (s, 21 H). ¹³C-NMR (100 MHz, CDCl₃) δ: 147.12, 133.82, 130.35, 123.56, 104.87, 97.57, 18.68, 11.29. ESI-HRMS calc. for [C₁₇H₂₈NSi]⁺: 274.4950, found 274.2390. IR (neat film) ν_{max} (cm⁻¹): 3425, 3382, 2941, 2147, 1605, 1510, 1289, 657.

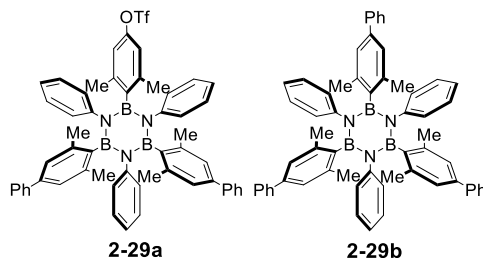
Synthesis of N,N',N''-triphenyl-B,B'-di(2,6-dimethyl-4-phenyl)-B''-2,6-dimethyl-4-(2,3,5-triphenyl-4-(phenyl-4'-yl))cyclopenta-2,4-dienone borazine 2-28



To a suspension of **2-29a** (0.07 g, 0.075 mmol) in dioxane/ H₂O 3:1 (8 mL), K₂CO₃ (0.042 g, 0.304 mmol) was added. The mixture was subjected to three freeze-pump-thaw cycles and then [Pd(PPh₃)₄] (0.005 g, 0.005 mmol) and **2-42** (0.077 g, 0.152 mmol) were added. The mixture was stirred at 105 °C for 16 h, diluted with EtOAc (20 mL), washed with H₂O (3 x 20 mL) and brine (30 mL). The organic phase was dried over MgSO₄ and the solvents removed under reduced pressure. The residue was purified by silica gel column chromatography (cyclohexane/EtOAc 9:1) affording **2-28** as red solid (0.061 g, 71%).

M.P.: 284-286 °C. ¹H-NMR (400 MHz, CD₂Cl₂) δ: 7.41-7.740 (m, 4 H), 7.33-7.16 (m, 23 H), 7.01-6.93 (m, 7 H), 6.89-6.77 (m, 16 H), 2.42 (s, 12 H), 2.41 (s, 6 H). ¹³C-NMR (100 MHz, CDCl₃) δ: 200.39, 154.50, 154.28, 138.04, 130.28, 128.53, 128.21, 128.17, 128.12, 127.10, 127.08, 126.99, 126.75, 124.20, 115.14, 23.41, 23.40 (some peaks are missing probably due to overlap). ¹¹B-NMR (128 MHz, CDCl₃) δ: 35.79. MALDI-HRMS calc. for [C₈₃H₆₈B₃N₃O]⁺: 1155.5642, found: 1155.5642. IR (film in CH₂Cl₂) ν_{max} (cm⁻¹): 3059, 2915, 1711, 1554, 1359, 1026, 815, 748, 698.

Synthesis of N,N',N''-triphenyl-B,B'-di(2,6-dimethyl-4-phenyl)-B''-2,6-dimethyl-4-(trifluoromethane sulphonate) phenylborazine 2-29a and N,N',N''-triphenyl-B,B',B''-tri((2,6-dimethyl-4-phenyl)phenyl)borazine 2-29b



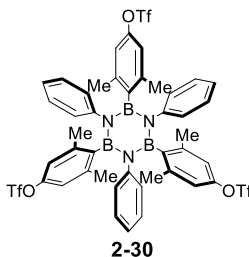
To a suspension of **2-30** (0.65 g, 0.61 mmol) in dioxane/H₂O 3:1 (3 mL), K₂CO₃ was added (0.73 g, 5.25 mmol). The reaction mixture was degassed by Ar bubbling (40 minutes) and then [Pd(PPh₃)₄] (0.028 g, 0.025 mmol) and phenylboronic acid (0.13 g, 1.10 mmol) were added. The mixture was stirred at 105 °C for 16 h, then diluted with EtOAc (100 mL), washed with H₂O (3 × 100 mL) and brine (100 mL). The organic phase was dried over MgSO₄ and evaporated under reduced pressure. The residue was purified by silica gel column chromatography (cyclohexane/EtOAc 9:1) affording products **2-29a** and **2-29b**.

2-29a (0.219 g, 39%). M.P.: 188-190 °C. ¹H-NMR (400 MHz, CDCl₃) δ: 7.41-7.38 (m, 4 H), 7.31-7.27 (m, 4 H), 7.22-7.20 (m, 2 H), 6.88-6.75 (m, 21 H), 2.36 (s, 6 H), 2.35 (s, 12 H). ¹³C-NMR (100 MHz, CDCl₃) δ: 149.15, 149.09, 146.01, 145.77, 145.54, 141.35, 141.24, 140.45, 139.56, 139.37, 138.05, 137.98, 128.50, 127.20, 126.73, 126.72, 117.94, 117.84, 23.34, 23.22 (some peaks are missing probably due to overlap). ¹¹B-NMR (128 MHz, CDCl₃) δ: 36.66. ¹⁹F-NMR (376 MHz, CDCl₃) δ: -72.72. MALDI-HRMS calc. for [C₅₅H₄₉B₃F₃N₃O₃S]⁺: 921.3726, found: 921.3757. IR (film in CH₂Cl₂) ν_{max} (cm⁻¹): 3061, 2947, 1554, 1355, 1309, 1239, 1206, 813, 732, 697.

2-29b (0.042 g, 8%). M.P.: 259-261 °C. ¹H-NMR (400 MHz, CDCl₃) δ: 7.44-7.41 (m, 5 H), 7.33-7.20 (m, 10 H), 6.93-6.70 (m, 21 H), 2.40 (s, 18 H). ¹³C-NMR (100 MHz, CDCl₃) δ: 146.01, 141.34, 139.36, 138.06, 128.50, 127.03, 127.00, 126.76, 126.74, 124.62, 124.19, 23.39 (13C resonance corresponding to the carbon atom bonded to the boron atom is not observed probably due to the quadrupolar relaxation). ¹¹B-NMR (128 MHz, CDCl₃) δ:

35.96. MALDI-HRMS calc. for $[\text{C}_{60}\text{H}_{54}\text{B}_3\text{N}_3]^+$: 849.4597, found: 849.4607. IR (film in CH_2Cl_2) ν_{max} (cm^{-1}): 3060, 2915, 1554, 1361, 1103, 815, 726, 698.

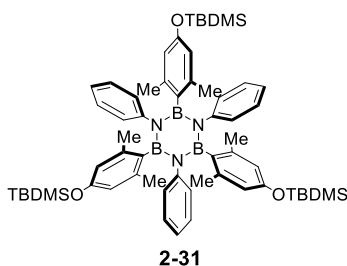
Synthesis of N,N',N'' -triphenyl- B,B',B'' -tri(2,6-dimethyl-4-(trifluoromethanesulphonate) phenyl)borazine 2-30



To a solution of **2-31** (1.60 g, 1.58 mmol) in THF (30 mL) at 0 °C, TBAF (tetrabutylammonium fluoride, 1 M in THF, 5.22 mL, 5.22 mmol) was dropwise added. The white suspension formed was stirred for 2 h. The white solid was recovered by filtration and dried under high vacuum for 3 h. Dry pyridine (24 mL) was directly added to the solid and the resulting suspension cooled down at 0 °C, then Tf_2O (2.28 mL, 17.0 mmol) was added dropwise. The orange solution was stirred for 16 h at room temperature. The mixture was diluted with EtOAc (100 mL), washed with H_2O (100 mL) and brine (100 mL). The organic layer was dried over MgSO_4 and evaporated under reduced pressure. The residue was purified by silica gel column chromatography (cyclohexane/EtOAc 8:2) affording **2-30** as white powder (1.30 g, 78%).

M.P.: 236-238 °C. $^1\text{H-NMR}$ (400 MHz, CDCl_3) δ : 6.82-6.74 (m, 15 H), 6.49 (s, 6 H), 2.31 (s, 18 H). $^{13}\text{C-NMR}$ (100 MHz, CDCl_3) δ : 149.18, 144.80, 140.32, 127.47, 126.37, 125.44, 120.22, 118.03, 23.19. $^{11}\text{B-NMR}$ (128 MHz, CDCl_3) δ : 35.68. $^{19}\text{F-NMR}$ (376 MHz, CDCl_3) δ : -72.77. MALDI-HRMS calc. for $[\text{C}_{45}\text{H}_{40}\text{B}_3\text{F}_9\text{N}_3\text{O}_9\text{S}_3]^+$: 1066.4195, found: 1066.2067. IR (film in CH_2Cl_2) ν_{max} (cm^{-1}): 3080, 2924, 1492, 1364, 1239, 1207, 1141, 813, 748.

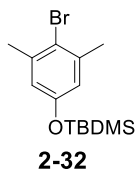
Synthesis of **N,N',N''-triphenyl-B,B',B''-tri(2,6-dimethyl-4-(tertbutyl dimethylsilyloxy) phenyl) borazine 2-31**



To a solution of aniline **2-20** (1.0 mL, 10.95 mmol) in dry toluene (20 mL) under Ar a solution of BCl_3 (1 M in heptane, 12.0 mL, 12.0 mmol) was added dropwise at 0 °C. The resulting mixture was refluxed for 18 h. The reaction mixture was cooled down to room temperature and subjected to five freeze-pump-thaw cycles to remove the excess of HCl. In parallel, to a solution of **2-32** (3.78 g, 12.0 mmol) in dry THF (20 mL), $t\text{BuLi}$ (1.7 M in hexane, 14.7 mL, 25.0 mmol) was added dropwise at -84 °C. The solution was allowed to warm up at 0 °C and stirred for 10 min. The degassed toluene mixture containing the chloro-borazine intermediate was slowly transferred to the organometallic-containing solution at 0°C and allowed to react at room temperature for 16 h. The mixture was diluted with EtOAc (100 mL), washed with H_2O (3 x 100 mL) and brine (100 mL). The organic phase was dried over MgSO_4 and the solvents removed under reduced pressure. The yellow deliquescent solid was re-dissolved in CH_2Cl_2 (2 mL) and CH_3OH was added. The precipitate was filtered off affording **2-31** as white solid (2.89 g, 78%).

M.P.: 205-207 °C. $^1\text{H-NMR}$ (400 MHz, CDCl_3) δ : 6.78-6.67 (m, 15 H), 6.05 (s, 6 H), 2.19 (s, 18 H), 0.84 (s, 27 H), -0.04 (18 H). $^{13}\text{C-NMR}$ (100 MHz, CDCl_3) δ : 154.60, 146.24, 138.98, 127.15, 126.72, 124.15, 117.64, 25.84, 23.11, 18.30, -4.47 (the ^{13}C resonance corresponding to the carbon atom bonded to the boron atom is not observed probably due to the quadrupolar relaxation). $^{11}\text{B-NMR}$ (128 MHz, CDCl_3) δ : 36.05. MALDI-HRMS calc. for $[\text{C}_{60}\text{H}_{85}\text{B}_3\text{N}_3\text{O}_3\text{Si}_3]^+$: 1011.6100 found 1011.6081. IR (film in CH_2Cl_2) ν_{max} (cm^{-1}): 3039, 2955, 1562, 1356, 1251, 839, 778, 698.

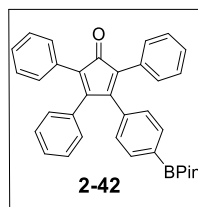
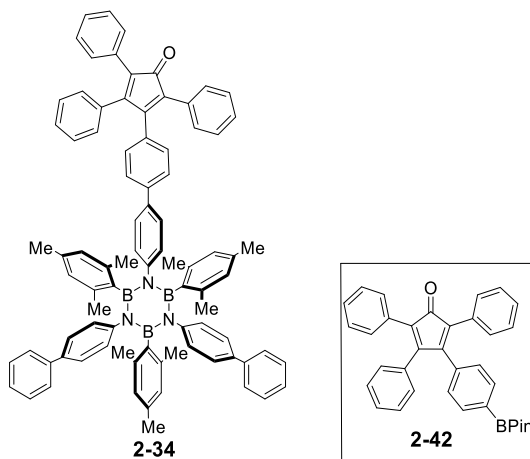
Synthesis of 2,6-dimethyl-4-(tertbutyldimethylsilyloxy)bromo benzene **2-32**



To a solution of 3,5-dimethyl-4-bromophenol **2-33** (10 g, 49.8 mmol) in DMF (60 mL), TBDMSCl (10.5 g, 69.7 mmol) and imidazole (10.2 g, 150 mmol) were added. The reaction mixture was stirred at 50 °C for 15 h, then diluted with EtOAc (200 mL), washed with H₂O (3 x 200 mL) and brine (100 mL). The organic layer was dried over MgSO₄, filtered and concentrated under reduced pressure. The residue was purified by silica gel column chromatography (pentane) affording **2-32** as pale-yellow oil (15.6 g, 99%).

¹H-NMR (400 MHz, CDCl₃) δ: 6.57 (s, 2 H), 2.34 (s, 6 H), 0.97 (s, 9 H), 0.18 (s, 6 H). ¹³C-NMR (100 MHz, CDCl₃) δ: 154.39, 139.27, 120.20, 119.27, 25.94, 24.19, 18.45, -4.15. ESI-HRMS calc. for [C₁₄H₂₃BrOSi]⁺: 315.3293, found 315.0774. IR (neat film) ν_{max} (cm⁻¹): 3039, 2954, 1581, 1464, 1321, 1251, 1166, 778.

N,N'-tri(4-phenyl)phenyl-N''-4-(2,3,5-triphenyl-4-(phenyl-4'-yl)cyclopenta-2,4-dienone borazine)- B,B',B''-trimesityl borazine **2-34**

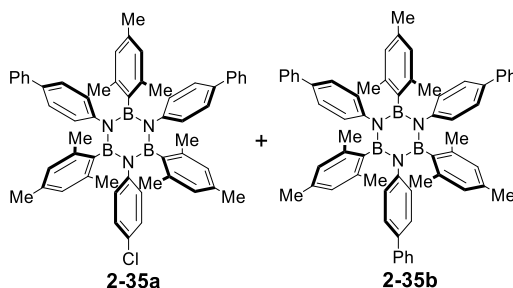


To a solution of **2-35a** (0.52 g, 0.61 mmol) in dioxane/H₂O (5:1) mixture (20 mL), boronic ester **2-42** (0.63 g, 1.23 mmol), K₃PO₄ (0.39 g, 1.85 mmol), [Pd₂(dba)₃] (0.036 g, 0.039 mmol) and XPhos (0.039 g, 0.081 mmol) were added and placed under inert N₂ atmosphere.

The reaction mixture was degassed by N₂ bubbling under sonication at 50 °C for 1.5 h. The red mixture heated at 150 °C and stirred for 20 h, then diluted with EtOAc (100 mL), washed with H₂O (3 x 100 mL) and brine (100 mL). The organic layer was evaporated under reduced pressure, and the residue was purified by silica gel column chromatography (petroleum ether/CH₂Cl₂ 7:3) affording **2-34** as red solid (0.17 g, 23%).

M.P.: 265-267 °C. ¹H-NMR (400 MHz, CDCl₃) δ: 7.40-6.85 (m, 41 H), 6.38-6.36 (m, 6 H), 2.30 (s, 18 H), 2.00-1.98 (m, 9 H). ¹³C-NMR (100 MHz, CDCl₃) δ: 200.23, 154.35, 154.04, 146.29, 145.66, 140.56, 137.27, 137.21, 136.27, 135.35, 133.27, 131.10, 130.98, 130.77, 130.18, 129.82, 129.36, 128.52, 128.13, 128.03, 127.46, 127.33, 126.72, 126.57, 126.44, 125.90, 125.64, 125.30, 125.15, 23.07, 21.09 (some peaks are missing probably due to overlap). ¹¹B-NMR (128 MHz, CDCl₃) δ: 33.96. MALDI-HRMS calc. for [C₈₆H₇₄B₃N₃O]⁺: 1197.6111, found 1197.6112. IR (film in CH₂Cl₂) ν_{max} (cm⁻¹): 3194, 2981, 1616, 1585, 1087, 810, 700, 686.

Synthesis of N,N'-tri(4-phenyl)phenyl-N''-4-chlorophenyl-B,B',B''-tri mesitylborazine **2-35a** and N,N',N''-tri(4-phenyl)phenyl-B,B',B''-trimesityl borazine **2-35b**

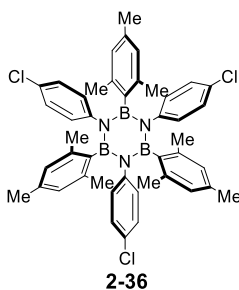


To a solution of **2-36** (1.32 g, 1.72 mmol) in dioxane/H₂O (5:1) mixture (20 mL), phenylboronic acid (0.46 g, 3.79 mmol), K₃PO₄ (1.47 g, 6.91 mmol), [Pd₂(dba)₃] (0.079 g, 0.086 mmol) and XPhos (0.083 g, 0.174 mmol) were added and placed under inert N₂ atmosphere. The reaction mixture was degassed by N₂ bubbling under sonication at 50 °C for 1.5 h. The red mixture was heated at 150 °C and stirred for 16 h, then diluted with EtOAc (100 mL), washed with H₂O (3 x 100 mL) and brine (100 mL). The organic layer was evaporated, and the product purified by silica gel column chromatography (petroleum ether/CH₂Cl₂ 8:2) affording products **2-35a** and **2-35b** as white solids.

2-35a (0.39 g, 27%). M.P.: 215-217 °C. $^1\text{H-NMR}$ (400 MHz, CDCl_3) δ : 7.41-7.21 (m, 10 H), 7.09-6.74 (m, 12 H), 6.36-6.33 (m, 6 H), 2.28-2.18 (s, 18 H), 2.00-1.96 (s, 9 H). $^{13}\text{C-NMR}$ (100 MHz, CDCl_3) δ : 145.61, 140.47, 137.39, 137.24, 137.17, 136.55, 136.40, 136.01, 129.72, 128.50, 128.33, 127.75, 127.47, 127.37, 127.31, 126.96, 126.74, 126.59, 126.52, 126.31, 125.31, 125.26, 23.21, 23.13, 23.08, 21.11, 21.08, 20.96, 20.01 (some peaks are missing probably due to overlap). $^{11}\text{B-NMR}$ (128 MHz, CDCl_3) δ : 36.21. MALDI-HRMS calc. for $[\text{C}_{57}\text{H}_{55}\text{B}_3\text{N}_3]^+$ (de-chlorination during analysis): 814.4670, found: 814.4672. IR (film in CH_2Cl_2) ν_{max} (cm^{-1}): 3035, 2970, 1527, 1348, 1014, 796, 783, 700, 690.

2-35b (0.33 g, 25%). M.P.: 249-252 °C. $^1\text{H-NMR}$ (400 MHz, CDCl_3) δ : 7.41-7.38 (m, 6 H), 7.32-7.27 (m, 6 H), 7.23-7.18 (m, 3 H), 7.05-7.03 (d, 6 H), 6.88-6.85 (d, 6 H), 6.34 (s, 6 H), 2.27 (s, 18 H), 1.97 (s, 9 H). $^{13}\text{C-NMR}$ (100 MHz, CDCl_3) δ : 145.76, 140.50, 137.29, 136.29, 136.24, 128.50, 127.38, 126.69, 126.57, 126.48, 125.20, 23.15, 21.10 (13C resonance corresponding to the carbon atom bonded to the boron atom is not observed probably due to the quadrupolar relaxation). $^{11}\text{B-NMR}$ (128 MHz, CDCl_3) δ : 36.02. MALDI-HRMS calc. for $[\text{C}_{63}\text{H}_{60}\text{B}_3\text{N}_3]^+$: 891.5093, found: 891.5066. IR (film in CH_2Cl_2) ν_{max} (cm^{-1}): 3035, 2970, 1527, 1386, 1014, 792, 717.

Synthesis of N,N',N''-tri(4-chlorophenyl)-B,B',B''-trimesityl borazine **2-36**



To a solution of 4-chloroaniline **2-37** (1.50 g, 11.80 mmol) in dry toluene (20 mL) under Ar, BCl_3 (1 M in heptane, 14.20 mL, 14.20 mmol) was added dropwise at 0 °C. The resulting white suspension was refluxed for 16 h. The solution was cooled down to room temperature and subjected to five freeze-pump-thaw cycles to remove the excess of HCl. In parallel, to a solution of **2-25** (2.59 g, 13.00 mmol) in anhydrous THF (40 mL), $t\text{BuLi}$ (1.7 M in hexane, 15.60 mL, 26.65 mmol) was added dropwise at -84 °C. The solution was

warmed up at 0 °C and stirred for 10 min. The degassed toluene mixture containing the chloro-borazine derivative was cannulated dropwise to the organometallic-containing solution at 0 °C and allowed to react at room temperature for 16 h. The reaction mixture was diluted with EtOAc (100 mL), washed with H₂O (3 x 100 mL) and brine (1 x 100 mL). The organic layer was dried over MgSO₄ and evaporated under reduced pressure. The residue was purified by silica gel column chromatography (petroleum ether/CH₂Cl₂, 9:1) affording **2-36** as white solid (1.86 g, 62%).

M.P.: 236-237 °C. ¹H-NMR (400 MHz, CDCl₃) δ: 6.75-6.67 (m, 12 H), 6.37 (s, 6 H), 2.16 (s, 18 H), 2.03 (s, 9 H). ¹³C-NMR (100 MHz, CDCl₃) δ: 144.72, 136.94, 136.79, 129.83, 128.11, 127.01, 126.65, 22.95, 21.11 (13C resonance corresponding to the carbon atom bonded to the boron atom is not observed probably due to the quadrupolar relaxation). ¹¹B-NMR (128 MHz, CDCl₃) δ: 34.01. MALDI-HRMS calc. for [C₄₅H₄₅B₃N₃Cl₃]⁺: 765.2983, found 765.2958.

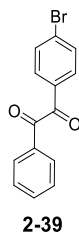
Synthesis of 1-bromo-4-(phenylacetynyl)benzene **2-38**



To a solution of 4-bromo-iodobenzene **2-46** (5.00 g, 17.67 mmol) in diisopropylamine (40 mL), [Pd(PPh₃)₂Cl₂] (0.12 g, 0.17 mmol) and CuI (0.033 g, 0.17 mmol) were added. The reaction mixture was degassed by three freeze-pump-thaw cycles, then phenylacetylene (1.95 mL, 17.76 mmol) was added and further three freeze-pump-thaw cycles have been done. The mixture was placed under inert atmosphere (N₂) and stirred at room temperature for 16 h. The mixture was diluted with EtOAc (100 mL), washed with H₂O (3 x 100 mL) and brine (100 mL). The organic layer was dried over MgSO₄ and concentrated under reduced pressure. The residue was purified by silica gel column chromatography (petroleum ether) affording **2-38** as white solid (4.50 g, 99%).

M.P.: 77-78 °C. $^1\text{H-NMR}$ (400 MHz, CD_2Cl_2) δ : 7.54-7.36 (m, 9 H). $^{13}\text{C-NMR}$ (100 MHz, CDCl_3) δ : 133.57, 132.20, 132.10, 129.13, 129.02, 123.42, 123.00, 122.80, 90.98, 88.75. ESI-HRMS calc. for $[\text{C}_{14}\text{H}_9\text{Br}]^+$: 256.9960, found: 256.9960. IR (film in CH_2Cl_2) ν_{max} (cm^{-1}): 3049, 1580, 1490, 1178, 828, 821, 755.

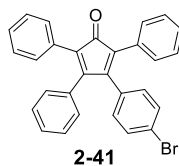
Synthesis of 1-(4-bromophenyl)-2-phenylethane-1,2-dione **2-39**



To a solution of 1-bromo-4-(phenylacetynyl)benzene **2-38** (1.77 g, 6.88 mmol) in acetone (260 mL), acetic acid (2.60 mL) and KMnO_4 (2.78 g, 17.20 mmol) were added. The purple mixture was stirred at room temperature for 24 h and then filtered through celite. The solution was concentrated under reduced pressure and the residue was dissolved in EtOAc (100 mL), washed with H_2O (3 x 100 mL) and brine (50 mL). The yellow organic layer was dried over MgSO_4 and evaporated under reduced pressure affording **2-39** as yellow solid. (1.91 g, 96%).

M.P.: 74-75 °C. $^1\text{H-NMR}$ (400 MHz, DMSO) δ : 7.95-7.88 (m, 2 H), 7.86-7.79 (m, 5 H), 7.63-7.61 (m, 2 H). $^{13}\text{C-NMR}$ (100 MHz, DMSO) δ : 194.59, 194.12, 136.11, 133.13, 132.61, 131.97, 131.75, 130.51, 130.26, 129.97. ESI-HRMS calc. for $[\text{C}_{14}\text{H}_{10}\text{O}_2\text{Br}]^+$: 288.9858, found: 288.9862. IR (film in CH_2Cl_2) ν_{max} (cm^{-1}): 3064, 2923, 2853, 1665, 1579, 1205, 1172, 708, 681.

Synthesis of 3-(4-bromophenyl)-2,4,5-triphenylcyclopenta-2,4-dien-1-one **2-41**

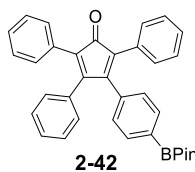


To a solution of **2-39** (2.00 g, 6.92 mmol) in ethanol (10 mL), 1,3-diphenylacetone **2-40** (1.45 g, 6.92 mmol) was added. The reaction mixture was stirred under reflux for 10 min.

Then a solution of KOH (0.20 g, 3.46 mmol) in ethanol (0.5 mL) was added through the condenser in two portions. The yellow solution immediately turned dark red and after 20 minutes it was cooled down to 0 °C. The solid residue was filtrated and washed with cold ethanol affording **2-41** (2.50 g, 78%).

M.P.: 206-207 °C. ¹H-NMR (400 MHz, CDCl₃) δ: 7.31-7.19 (m, 17 H), 6.96-6.91 (d, 2 H), 6.80-6.78 (d, 2 H). ¹³C-NMR (100 MHz, CDCl₃) δ: 200.06, 154.12, 153.14, 132.93, 132.02, 131.41, 131.15, 130.64, 130.52, 130.23, 129.37, 128.82, 128.32, 128.18, 127.85, 127.69, 125.83, 125.56, 123.05 (some peaks are missing probably due to overlap). MALDI-HRMS calc. for [C₂₉H₁₉OBr]⁺: 462.0619, found: 462.0615. IR (film in CH₂Cl₂) ν_{max} (cm⁻¹): 3055, 1708, 1558, 1442, 1025, 737, 716, 687.

Synthesis of 2,3,5-triphenyl-4-(4-(4,4,5,5-tetramethyl-1,3,2-dioxaborolan-2-yl)phenyl) cyclopenta-2,4-dienone **2-42**

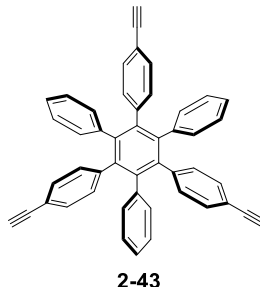


To a suspension of 2,3,5-triphenyl-4-(4-bromophenyl) cyclopenta-2,4-dienone **2-41** (0.104 g, 0.224 mmol) in dry DMF (5 mL) under Ar, KOAc (0.068 g, 0.672 mmol) was added. The mixture was subjected to three freeze-pump-thaw cycles and then [Pd(dppf)Cl₂] (0.010 g, 0.011 mmol) and bis(pinacolate) diboron (0.061 g, 0.235 mmol) were added. The mixture was stirred at 80 °C for 16 h, diluted with EtOAc (30 mL) and washed with H₂O (3 x 50 mL). The organic layer was dried over MgSO₄, filtered and concentrated under reduced pressure. The brownish solid was filtered through a short silica gel column chromatography (cyclohexane/EtOAc 7:3) to give **2-42** as deep purple solid. (0.110 g, 96 %).

M.P.: 250-252 °C. ¹H-NMR (400 MHz, CDCl₃) δ: 7.60-7.58 (m, 2 H), 7.25-7.15 (m, 13 H), 6.93-6.90 (m, 4 H), 1.33 (s, 12 H). ¹³C-NMR (100 MHz, CDCl₃) δ: 200.38, 154.868, 154.35, 135.97, 134.32, 133.07, 130.84, 130.73, 130.25, 129.37, 128.72, 128.64, 128.19, 128.13, 127.61, 127.56, 125.76, 125.41, 84.08, 25.03 (some peaks are missing probably due to

overlap). MALDI-HRMS calc. for $[\text{C}_{35}\text{H}_{32}\text{BO}_3]^+$: 511.4400, found: 511.2439. IR (film in CH_2Cl_2) ν_{max} (cm^{-1}): 3053, 2978, 1709, 1513, 1353, 1142, 710, 694.

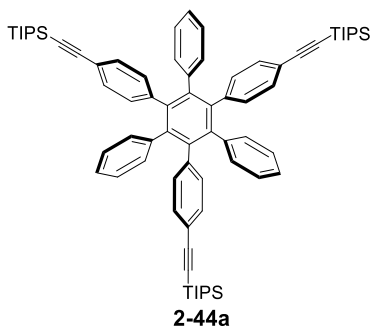
Synthesis of 2,4,6-triphenyl-1',3',5'-tri(4-triacetynyl)phenylbenzene 2-43



To a solution of **2-44a** (0.065 g, 0.006 mmol) in THF (4 mL), TBAF 1 M solution (0.250 mL, 0.21 mmol) was slowly added at room temperature. The reaction mixture was stirred for 3 h and the diluted with CH_2Cl_2 (50 mL), washed with H_2O (3 x 100 mL) and brine (50 mL). The organic layer was dried over MgSO_4 and evaporated under reduced pressure. The residue was purified by silica gel column chromatography (petroleum ether/ CH_2Cl_2 1:1) affording **2-43** as a white solid (24 mg, 66%).

$^1\text{H-NMR}$ (300 MHz, CDCl_3) δ : 7.01-6.99 (m, 6 H), 6.88-6.87 (m, 10 H), 6.79-6.76 (m, 11 H), 2.93 (s, 3 H). $^{13}\text{C-NMR}$ (100 MHz, CDCl_3) δ : 141.34, 140.90, 139.88, 139.87, 131.38, 131.29, 130.73, 127.13, 125.87, 118.91, 84.02, 76.84. ESI-HRMS calc. for $[\text{C}_{48}\text{H}_{30}]^+$: 606.2348, found: 606.2347. IR (film in CH_2Cl_2) ν_{max} (cm^{-1}): 3290, 2992, 2852, 2360, 1581, 1267, 842, 702, 651.

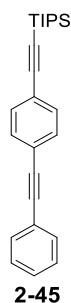
Synthesis of 2,4,6-triphenyl-1',3',5'-tri(4-triisopropylsilylacetynyl) phenyl benzene 2-44a



To a solution of **2-45** (0.400 g, 1.11 mmol) in dioxane (10 mL), $[\text{Co}_2(\text{CO})_8]$ (0.038 g, 0.11 mmol) was added under inert atmosphere of N_2 . The solution was degassed by 3 freeze-pump-thaw cycles. The reaction mixture was stirred and refluxed under N_2 atmosphere for 18 h. The precipitate was filtered off and the solution was concentrated under reduced pressure. The residue was purified by silica gel column chromatography (petroleum ether/ CH_2Cl_2 8:2) affording **2-44a** as white solid (65 mg, 16%).

$^1\text{H-NMR}$ (300 MHz, CDCl_3) δ : 6.99-6.73 (m, 27 H), 1.07 (s, 63 H). $^{13}\text{C-NMR}$ (100 MHz, CDCl_3) δ : 140.82, 140.51, 140.12, 140.01, 131.37, 131.28, 130.62, 127.16, 125.80, 107.54, 107.54, 89.84, 18.79, 11.47. ESI-HRMS calc. for $[\text{C}_{75}\text{H}_{90}\text{Si}_3]^+$: 1075.6429, found: 1075.6381. IR (film in CH_2Cl_2) ν_{max} (cm^{-1}): 2941, 2889, 2360, 2154, 1508, 1462, 829, 719, 677.

Synthesis of 1-(triisopropylsilylacetynyl)-4-(phenylacetynyl)benzene **2-45**

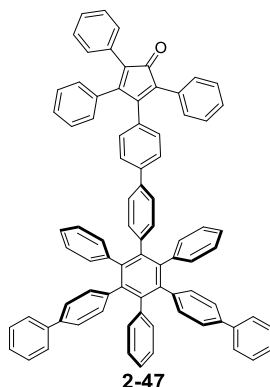


To a solution of **2-38** (1.26 g, 4.92 mmol) in diisopropylamine (20 mL), $[\text{Pd}(\text{PPh}_3)_2\text{Cl}_2]$ (0.070 g, 0.10 mmol) and CuI (0.019 g, 0.10 mmol) were added. The reaction mixture was degassed by three freeze-pump-thaw cycles, then triisopropylsilylacetylene (1.11 mL, 4.95 mmol) was added and further 3 freeze-pump-thaw cycles have been done. The suspension was stirred at 70 °C for 20 h, then diluted with EtOAc (200 mL), washed with H_2O (3 x 100 mL) and brine (100 mL). The organic layer was dried over MgSO_4 and evaporated under reduced pressure. The residue was purified by silica gel column chromatography (petroleum ether) affording **2-45** as white solid (1.73 g, 98%).

M.P.: 93-95 °C. $^1\text{H-NMR}$ (300 MHz, CD_2Cl_2) δ : 7.55-7.44 (m, 6 H), 7.39-7.36 (m, 3 H), 1.14 (s, 21 H). $^{13}\text{C-NMR}$ (100 MHz, CD_2Cl_2) δ : 132.48, 132.12, 131.94, 129.12, 129.02, 123.90, 123.73, 123.51, 107.12, 93.42, 91.69, 84.45, 19.02, 11.89. ESI-HRMS calc. for

$[\text{C}_{25}\text{H}_{30}\text{BrSi}]^+$: 358.5912, found: 358.6233. IR (film in CH_2Cl_2) ν_{max} (cm^{-1}): 2943, 2864, 2154, 1232, 906, 731, 673.

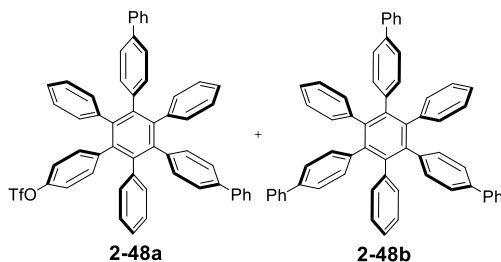
Synthesis of 1,3-bis-(biphenyl)-5-(4'-(2,3,5-triphenyl-4-(phenyl-4'-yl)) cyclopenta-2,4-dienone)-2,4,6-phenylbenzene 2-47



To a solution of **2-48a** (0.208 g, 0.25 mmol) in dioxane/ H_2O (5:1) mixture (6 mL), **2-42** (0.32 g, 0.63 mmol), $[\text{Pd}(\text{PPh}_3)_4]$ (0.018 g, 0.016 mmol) and K_2CO_3 (0.138 g, 0.99 mmol) were added and placed under inert atmosphere of N_2 . The reaction mixture was degassed by N_2 bubbling under sonication for 3 h, then was stirred and heated at 105°C for 15 h. The solution was diluted with EtOAc (50 mL), washed with H_2O (3 x 100 mL) and brine (100 mL). The dark organic solution was dried over MgSO_4 and evaporated under reduced pressure. The product was purified by silica gel column chromatography (cyclohexane/ CH_2Cl_2 7:3) affording **2-47** as a red solid (0.18 g, 68%).

M.P.: $294\text{--}296^\circ\text{C}$. $^1\text{H-NMR}$ (300 MHz, CD_2Cl_2) δ : 7.47-7.15 (m, 31 H), 6.99-6.90 (m, 25 H). $^{13}\text{C-NMR}$ (100 MHz, CDCl_3) δ : 200.24, 154.36, 154.04, 140.73, 140.66, 140.59, 140.50, 140.29, 140.25, 139.80, 139.74, 137.42, 136.50, 133.19, 132.02, 131.86, 131.49, 131.38, 130.93, 130.77, 130.20, 129.86, 129.39, 128.60, 128.14, 128.10, 128.05, 127.48, 126.95, 126.85, 126.73, 126.08, 125.59, 125.37, 125.28, 125.19, 125.04 (some peaks are missing probably due to overlap). ESI-MS calc. for $[\text{C}_{83}\text{H}_{56}\text{O}]^+$: 1069.4409, found: 1069.4395. IR (film in CH_2Cl_2) ν_{max} (cm^{-1}): 3028, 2980, 1710, 1598, 1487, 1026, 804, 731, 694.

Synthesis of 1,3-bis-(4-(phenyl)phenyl)-5-(4'-trifluoromethane sulphonylphenyl)-2,4,6-phenylbenzene 2-48a and 1,3,5-tris-(4-(phenyl) phenyl)-2,4,6-phenylbenzene 2-48b

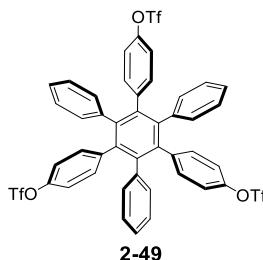


To a solution of **2-49** (0.547 g, 0.56 mmol) in dioxane/H₂O (5:1) mixture (24 mL), phenylboronic acid (0.109 g, 0.896 mmol), Pd(PPh₃)₄ (0.045 g, 0.038 mmol) and K₂CO₃ (0.621 g, 4.49 mmol) were added and placed under inert atmosphere of N₂. The reaction mixture was degassed by N₂ bubbling under sonication for 3 h and then stirred and heated at 105 °C for 15 h. The solution was diluted with EtOAc (50 mL), washed with H₂O (3 x 100 mL) and brine (100 mL). The dark organic solution was dried over MgSO₄ and evaporated under reduced pressure. The product was purified by silica gel column chromatography (cyclohexane/CH₂Cl₂ 8:2) affording products **2-48a** and **2-48b** as white solids.

2-48a (0.093 g, 20%). M.P.: 282-285 °C. ¹H-NMR (300 MHz, CD₂Cl₂) δ: 7.46-7.42 (m, 4 H), 7.37-7.31 (m, 4 H), 7.28-7.22 (m, 2 H), 7.18-7.15 (m, 4 H), 6.96-6.79 (m, 22 H). ¹³C-NMR (100 MHz, CD₂Cl₂) δ: 147.34, 141.60, 141.10, 140.37, 140.25, 140.13, 139.64, 138.72, 137.54, 133.06, 131.82, 131.32, 131.29, 128.63, 127.09, 126.87, 126.73, 126.48, 125.58, 125.48, 124.99, 119.35 (some peaks are missing probably probably due to overlap). ESI-MS calc. for [C₅₅H₃₇F₃O₃S]⁺: 834.2416, found: 834.2425. IR (film in CH₂Cl₂) ν_{max} (cm⁻¹): 3055, 1598, 1500, 1249, 1209, 1176, 839, 734, 696.

2-48b (0.038 g, 9%). ¹H-NMR (300 MHz, CD₂Cl₂) δ: 7.46-7.43 (m, 6 H), 7.36-7.32 (m, 6 H), 7.28-7.23 (m, 3 H), 7.18-7.15 (m, 6 H), 6.97-6.86 (m, 21 H). ¹³C-NMR (100 MHz, CD₂Cl₂) δ: 140.65, 140.54, 140.31, 140.07, 139.96, 137.38, 131.90, 131.41, 128.62, 127.05, 126.69, 126.48, 125.37, 124.92. ESI-MS calc. for [C₆₀H₄₂]⁺: 762.3287, found: 762.3287. IR (film in CH₂Cl₂) ν_{max} (cm⁻¹): 3028, 1598, 1485, 823, 738, 696.

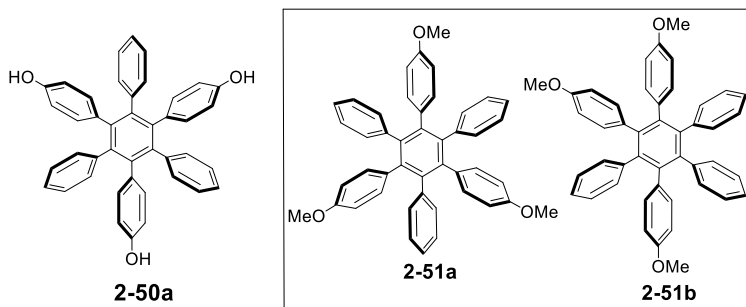
Synthesis of 1,3,5-(4'-trifluoromethansulphonylphenyl)-2,4,6-phenyl benzene 2-49



To a solution of **2-50a** (0.143 g, 0.245 mmol) in dry pyridine (5 mL), Tf₂O (0.494 mL, 2.94 mmol) was slowly added at 0 °C. The mixture was stirred for 18 h, then the reaction mixture was concentrated under reduced pressure. The residue was purified by silica gel column chromatography (petroleum ether/EtOAc 8:2) affording **2-49** as white solid (0.216 g, 90%).

M.P.: 235-237 °C. ¹H-NMR (300 MHz, CD₂Cl₂) δ: 6.95-6.90 (m, 15 H), 6.83-6.79 (m, 12 H). ¹³C-NMR (100 MHz, CD₂Cl₂) δ: 147.49, 140.96, 140.80, 139.34, 138.82, 132.95, 131.07, 127.09, 125.90, 120.71, 119.52. ESI-MS calc. for [C₄₅H₂₈F₉O₉S₃]⁺: 979.08, found: 978.06. IR (film in CH₂Cl₂) ν_{max} (cm⁻¹): 1502, 1247, 1205, 1178, 840, 700, 665.

Synthesis of 1,3,5-(4'-hydroxyphenyl)-2,4,6-phenylbenzene 2-50a



To a solution of **2-52** (3.99 g, 19.2 mmol) in dioxane (10 mL), [Co₂(CO)₈] (0.329 g, 1.92 mmol) was added under inert atmosphere of N₂. The solution was degassed by five freeze-pump-thaw cycles. A condenser was applied to the flask and the mixture was stirred and refluxed under N₂ atmosphere for 18 h. The solvent was removed under reduced pressure. The solid residue was purified by silica gel column chromatography (petroleum ether/CH₂Cl₂ 7:3) affording products **2-51a** and **2-51b** (3.24 g, 81%). To a solution of **2-51a** and **2-51b** in dry CH₂Cl₂ (50 mL), BBr₃ (1 M solution in CH₂Cl₂) (31 mL, 31.0 mmol)

at -84 °C. The reaction mixture stirred at room temperature for 3 h, then H₂O was slowly added. The mixture was diluted with EtOAc (200 mL) washed with H₂O (3 x 200 mL) and brine (100 mL). The yellow organic layer was dried over MgSO₄ and evaporated under vacuum. The crude was purified by silica gel column chromatography (petroleum ether/CH₂Cl₂ 9:1) affording **2-50a** as white solid (0.513 g, 14%).

¹H-NMR (300 MHz, CD₃OD) δ: 6.86-6.80 (m, 15 H), 6.61-6.58 (d, 6 H), 6.25-6.22 (d, 6 H). ¹³C-NMR (100 MHz, CD₃OD) δ: 154.21, 141.30, 140.69, 140.07, 132.21, 131.31, 126.19, 124.57, 113.07 (one peak corresponding to quaternary carbon is missing). ESI-HRMS calc. for [C₄₂H₃₀O₃]⁺: 582.2195, found: 582.2194. IR (film in CH₂Cl₂) ν_{max} (cm⁻¹): 3554, 1516, 1261, 817, 702.

Synthesis of 1-methoxy-4-(phenylethynyl)benzene **2-52**

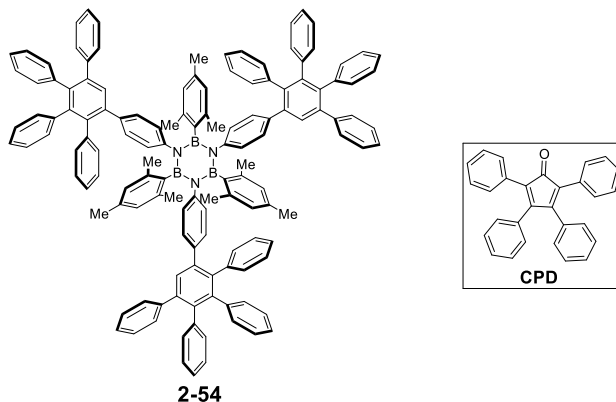


To a solution of **2-53** (5.00 g, 21.4 mmol) in a mixture diisopropylamine (25 mL) and THF (25 mL), [Pd(PPh₃)₂Cl₂] (0.155 g, 0.214 mmol) and CuI (0.042 g, 0.214 mmol) were added. The mixture was degassed by three freeze-pump-thaw cycles, then phenylacetylene (2.35 mL, 21.41 mmol) was added and further 2 freeze-pump-thaw cycles have been done. The suspension was stirred at room temperature for 4 h and then diluted with EtOAc (300 mL), washed with H₂O (3 x 200 mL) and brine (100 mL). The organic layer was dried over MgSO₄ and evaporated under reduced pressure. The crude was purified by silica gel column chromatography (petroleum ether/CH₂Cl₂ 8:2) affording **2-52** as colourless oil (4.30 g, 97%).

¹H-NMR (300 MHz, CDCl₃) δ: 7.53-7.46 (m, 4 H), 7.35-7.32 (m, 3 H), 6.91-6.86 (m, 2 H), 3.83(s, 3 H). ¹³C-NMR (100 MHz, CDCl₃) δ: 159.64, 133.08, 131.48, 128.35, 127.97, 123.61, 115.38, 114.02, 89.41, 88.10, 55.32 (one peak corresponding to quaternary carbon

is missing). ESI-HRMS calc. for $[C_{15}H_{12}O]^+$: 208.0888, found: 208.0880. IR (film in CH_2Cl_2) ν_{max} (cm^{-1}): 3051, 2895, 1508, 1246, 1024, 819.

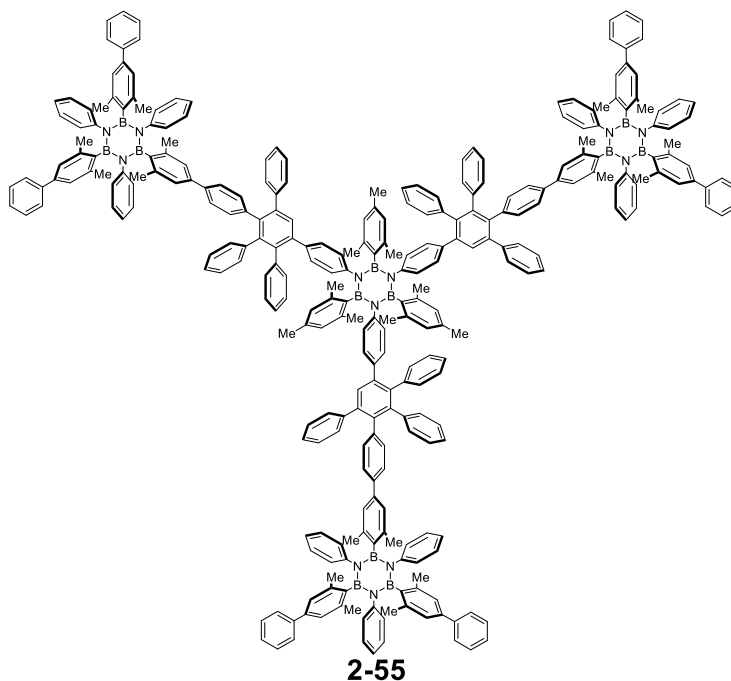
Synthesis of N,N',N''-tri(4-(1',2',3',4'-tetraphenyl)phenyl)phenyl-B,B',B''-trimesityl borazine **2-54**



To a solution of **2-23** (0.035 g, 0.048 mmol) in Ph_2O (1 mL), **CPD** (0.066 mg, 0.172 mmol) was added. The dark red solution was degassed by Ar bubbling for 45 minutes at 40 °C, then stirred at 180 °C for 2 h. The reaction mixture was directly introduced in a silica gel column chromatography and the product was purified (pentane/EtOAc 95:5) affording **2-54** as white solid (0.048 g, 56%).

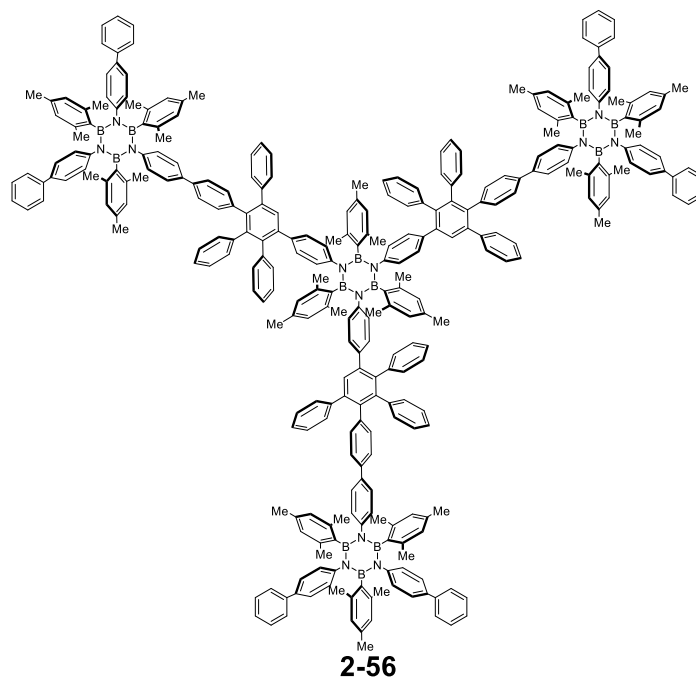
M.P.: 267-270 °C (decomp.). 1H -NMR (400 MHz, $CDCl_3$) δ : 7.31 (s, 3 H), 7.13-7.10 (m, 14 H), 6.89-6.70 (m, 40 H), 6.58-6.50 (m, 18 H), 6.35 (s, 6 H), 2.09 (s, 9 H), 2.03 (s, 18 H). ^{13}C -NMR (100 MHz, $CDCl_3$) δ : 144.68, 141.93, 141.68, 140.68, 140.53, 140.42, 140.12, 139.91, 139.06, 139.01, 137.45, 136.84, 137.78, 131.59, 131.47, 131.34, 130.02, 128.53, 127.64, 126.95, 126.65, 126.43, 126.31, 126.25, 125.62, 125.34, 125.26, 22.99, 21.29 (some peaks are missing probably due to overlap). ^{11}B -NMR (128 MHz, $CDCl_3$) δ : 35.84. MALDI-HRMS calc. for $[C_{135}H_{108}B_3N_3]^+$: 1803.8822, found 1803.8802. IR (film in CH_2Cl_2) ν_{max} (cm^{-1}): 3024, 2920, 1511, 1354, 796, 727, 695.

Synthesis of borazine-polyphenylene 2-55



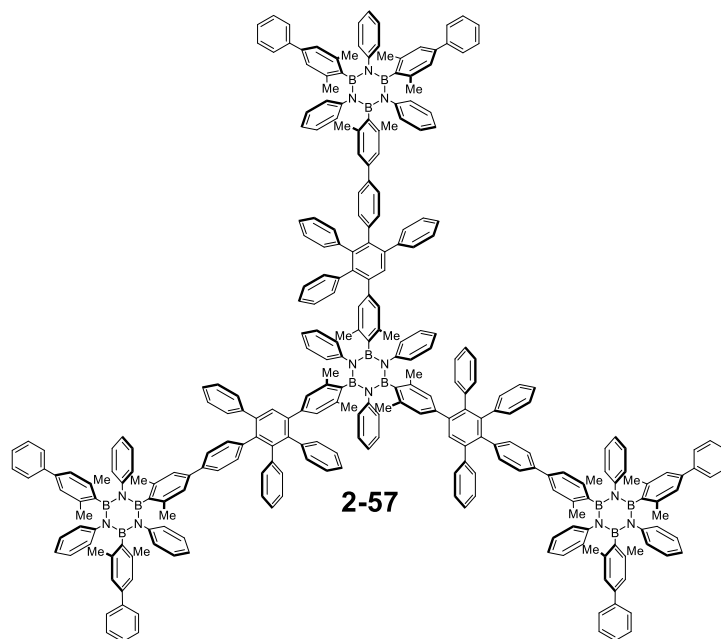
To a solution of **2-23** (0.014 g, 0.019 mmol) in Ph₂O (1 mL), **2-28** (0.080 mg, 0.069 mmol) was added. The dark red solution was degassed by Ar bubbling for 45 minutes at 40 °C, then stirred at 180 °C for 18 h. The reaction mixture was directly introduced in a silica gel column chromatography (cyclohexane/CH₂Cl₂ 7:3), then the solid residue was further purified by Rec-GPC (CHCl₃) affording **2-55** as white solid (0.043 g, 55%).

M.P. > 300 °C. ¹H-NMR (400 MHz, CD₂Cl₂) δ: 7.43-6.74 (m, 165 H), 6.43 (s, 6 H), 2.43-2.38 (s, 54 H), 2.13-2.08 (s, 27 H). ¹³C-NMR (100 MHz, CD₂Cl₂) δ: 146.87, 146.81, 145.34, 142.44, 142.37, 142.17, 141.77, 141.32, 141.29, 141.24, 141.08, 140.65, 140.61, 140.38, 140.10, 139.69, 139.61, 139.54, 139.50, 139.18, 138.83, 138.73, 138.60, 138.05, 137.72, 137.55, 136.51, 132.35, 131.97, 131.82, 131.76, 131.51, 130.44, 130.38, 129.68, 128.89, 128.07, 127.99, 127.65, 127.54, 127.42, 127.36, 127.32, 127.03, 126.92, 126.79, 126.74, 125.30, 125.28, 125.20, 124.96, 124.65, 124.39, 123.83, 123.79, 23.76, 23.70, 23.28, 21.44 (some peaks are missing probably due to overlap). ¹¹B-NMR (128 MHz, CD₂Cl₂) δ: 33.39. MALDI-HRMS calc. for [C₂₉₇H₂₅₂B₁₂N₁₂]⁺: 4118.1344, found 4118.1251. IR (film in CH₂Cl₂) ν_{max} (cm⁻¹): 3057, 2916, 1553, 1355, 1022, 839, 717, 696.

Synthesis of borazine-polyphenylene **2-56**

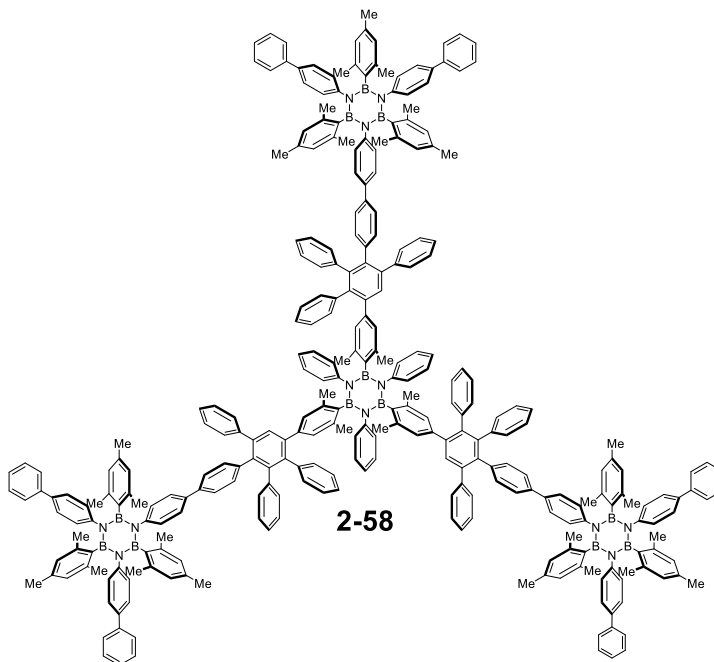
To a solution of **2-23** (0.005 g, 0.0067 mmol) in Ph₂O (1 mL), **2-34** (0.032 mg, 0.026 mmol) was added. The dark red solution was degassed by Ar bubbling for 30 minutes at 40 °C, then stirred at 200 °C for 16 h. The reaction mixture was directly introduced in a silica gel column chromatography (petroleum ether/CH₂Cl₂ 1:1), then the solid residue was furtherly purified by Rec-GPC (CHCl₃) affording **2-56** as white solid (0.005 g, 27%).

M.P.: > 300 °C. ¹H-NMR (400 MHz, CD₂Cl₂) δ: 7.40-7.22 (m, 34 H), 7.10-7.07 (m, 27 H), 6.99-6.67 (m, 79 H), 6.40 (s, 23 H), 2.31-2.29 (s, 56 H), 2.10-1.98 (s, 52 H). ¹¹B-NMR (128 MHz, CD₂Cl₂) δ: 37.50. MALDI-LRMS calc. for [C₃₀₆H₂₇₀B₁₂N₁₂]⁺: 4246.3, found 4244.1. IR (film in CH₂Cl₂) ν_{max} (cm⁻¹): 3015, 2899, 1598, 1356, 1014, 822, 725, 685.

Synthesis of borazine-polyphenylene **2-57**

To a solution of **2-18** (0.008 g, 0.012 mmol) in Ph₂O (2 mL), **2-28** (0.072 mg, 0.062 mmol) was added. The dark red solution was degassed by Ar bubbling for 45 minutes at 40 °C, then stirred at 190 °C for 18 h. The reaction mixture was directly introduced in a silica gel column chromatography (petroleum ether/CH₂Cl₂ 7:3), then the solid residue was further purified by Rec-GPC (CHCl₃) affording **2-57** as white solid (0.011 g, 22%).

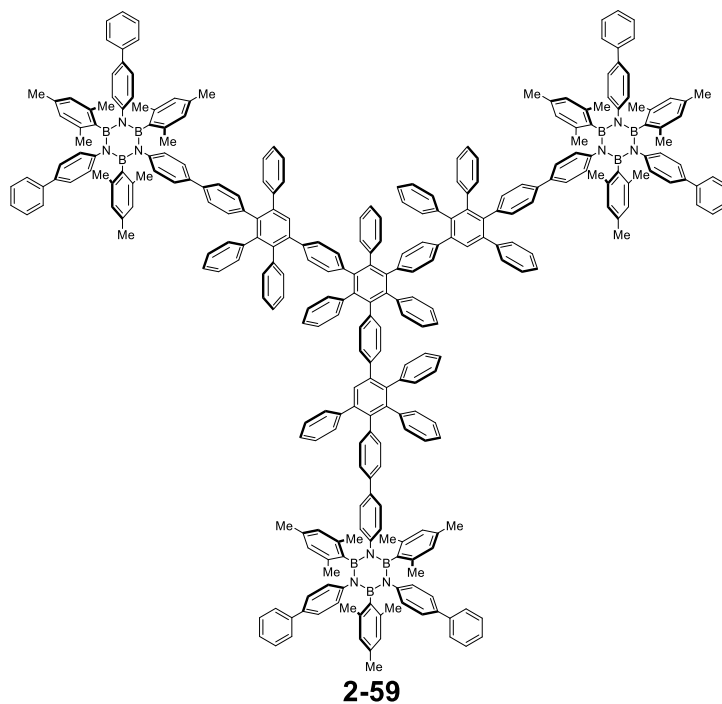
M.P. > 300 °C. ¹H-NMR (300 MHz, CDCl₃) δ: 7.38-7.29 (m, 26 H), 7.22-7.09 (m, 23 H), 6.96-6.58 (m, 119 H), 6.26-6.25 (m, 6 H), 2.34-2.29 (s, 54 H), 2.01 (s, 18 H). ¹¹B-NMR (128 MHz, CDCl₃) δ: 35.40. MALDI-HRMS calc. for [C₂₉₄H₂₄₆B₁₂N₁₂]⁺: 4077.0813, found 4077.0969. IR (film in CH₂Cl₂) ν_{max} (cm⁻¹): 3056, 2932, 1598, 1370, 1011, 822, 725, 684.

Synthesis of borazine-polyphenylene **2-58**

To a solution of **2-18** (0.007 g, 0.010 mmol) in Ph₂O (1 mL), **2-34** (0.039 mg, 0.033 mmol) was added. The dark red solution was degassed by Ar bubbling for 45 minutes at 40 °C, then stirred at 210 °C for 16 h. The reaction mixture was directly introduced in a silica gel column chromatography (petroleum ether/CH₂Cl₂ 7:3), then the solid residue furtherly purified by Rec-GPC (CHCl₃) affording **2-58** as white solid (0.016 g, 40%).

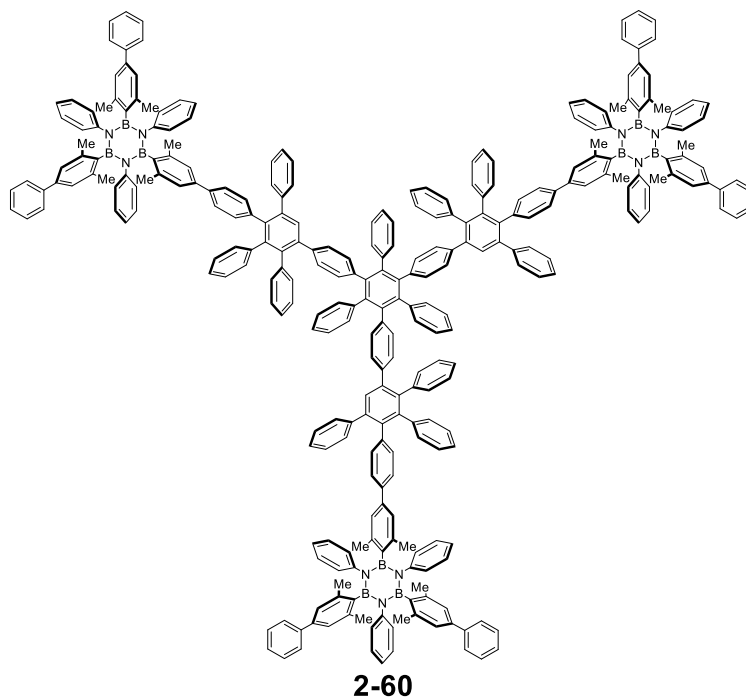
M.P. > 300 °C. ¹H-NMR (300 MHz, CDCl₃) δ: 7.39-7.27 (m, 28 H), 7.26-7.00 (m, 35 H), 6.92-6.56 (m, 79 H), 6.32 (s, 17 H), 6.26-6.25 (m, 6 H), 2.25-2.23 (s, 53 H), 2.01-1.95 (s, 46 H). ¹¹B-NMR (128 MHz, CDCl₃) δ: 35.31. MALDI-HRMS calc. for [C₃₀₃H₂₆₄B₁₂N₁₂]⁺: 4202.2144, found 4202.2241. IR (film in CH₂Cl₂) ν_{max} (cm⁻¹): 3024, 2954, 1567, 1312, 1011, 805, 725, 692.

Synthesis of borazine-polyphenylene 2-59



To a solution of **2-43** (0.0076 g, 0.013 mmol) in Ph₂O (1 mL), **2-34** (0.050 g, 0.042 mmol) was added. The dark red solution was degassed by Ar bubbling for 30 minutes at 40 °C, then stirred at 230 °C for 18 h. The reaction mixture was directly introduced in a silica gel column chromatography (petroleum ether/CH₂Cl₂ 7:3), then the solid residue was further purified by Rec-GPC using (CHCl₃) affording **2-59** as white solid (0.014 g, 27%).

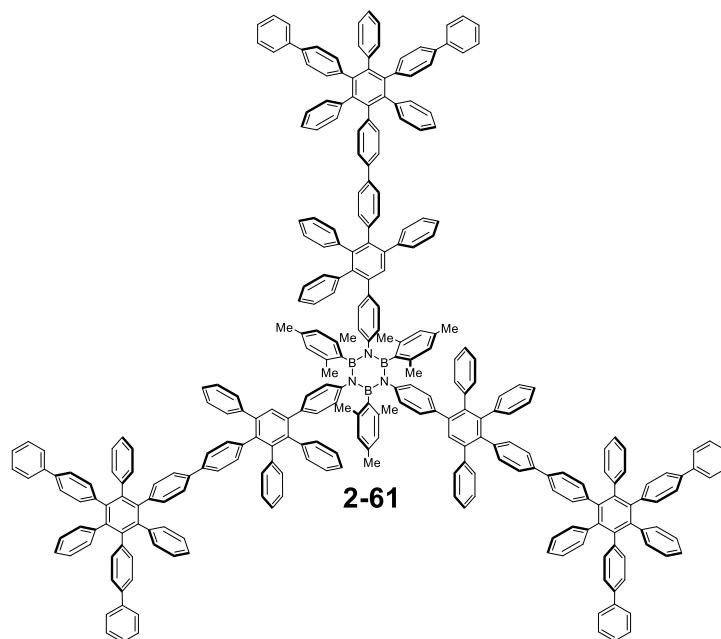
M.P.: > 300 °C. ¹H-NMR (300 MHz, CDCl₃) δ: 7.39-7.30 (m, 27 H), 7.23-7.00 (m, 35 H), 6.90-6.79 (m, 60 H), 6.66-6.51 (m, 33 H), 6.33 (s, 18 H), 2.25-2.23 (m, 54 H), 1.97-1.95 (m, 27 H). ¹³C-NMR (100 MHz, CDCl₃) δ: 145.71, 145.34, 141.94, 141.65, 141.02, 140.80, 140.74, 140.59, 140.50, 140.44, 140.19, 140.04, 139.99, 139.89, 139.18, 139.11, 139.06, 138.66, 138.46, 137.55, 137.33, 137.22, 137.19, 136.29, 136.18, 136.14, 131.61, 131.48, 130.84, 129.87, 128.32, 128.48, 127.63, 127.48, 127.31, 127.05, 127.00, 126.93, 126.80, 126.66, 126.54, 126.39, 126.35, 125.08, 124.78, 29.72, 23.03, 23.00, 21.02 (some peaks are missing probably due to overlap). ¹¹B-NMR (128 MHz, CDCl₃) δ: 34.43. MALDI-HRMS calc. for [C₃₀₃H₂₅₂B₉N₉]⁺: 4117.0990, found 4117.1094. IR (film in CH₂Cl₂) ν_{max} (cm⁻¹): 3005, 2965, 1546, 1345, 1054, 813, 721, 692.

Synthesis of borazine-polyphenylene **2-60**

To a solution of **2-43** (0.012 g, 0.019 mmol) in Ph₂O (1 mL), **2-28** (0.090 g, 0.077 mmol) was added. The dark red solution was degassed by Ar bubbling for 30 minutes at 40 °C and was heated at 190 °C 18 h. The reaction mixture was directly introduced in a silica gel column chromatography (petroleum ether/CH₂Cl₂ 7:3), then the solid residue was further purified by Rec- GPC (CHCl₃) affording **2-60** as white solid (0.063 g, 81%).

M.P.: > 300 °C. ¹H-NMR (300 MHz, CDCl₃) δ: 7.46-7.43 (m, 11 H), 7.37-7.7.32 (m, 14 H), 7.28-7.23 (m, 6 H), 7.16-7.15(m, 14 H), 7.05-6.71 (m, 124 H), 6.65-6.57 (m, 11 H), 2.45 (s, 36 H), 2.40 (s, 18 H). ¹³C-NMR (100 MHz, CDCl₃) δ: 146.87, 146.82, 142.43, 142.37, 142.27, 141.66, 141.34, 141.28, 141.23, 141.07, 140.85, 140.66, 140.53, 140.47, 140.36, 140.08, 139.72, 139.64, 139.32, 138.84, 138.62, 137.77, 137.44, 132.36, 131.98, 131.69, 131.36, 130.44, 130.38, 129.08, 128.72, 128.12, 128.04, 127.66, 127.42, 127.37, 127.33, 127.06, 126.94, 126.81, 126.72, 126.23, 126.01, 125.95, 125.31, 125.21, 124.99, 124.68, 124.41, 123.85, 123.81, 23.77, 23.71 (some peaks are missing probably due to overlap). ¹¹B-NMR (128 MHz, CDCl₃) δ: 33.38. MALDI-LRMS calc. for [C₂₉₄H₂₃₄B₉N₉]⁺: 3988.4 found: 3988.0. IR (film in CH₂Cl₂) ν_{max} (cm⁻¹): 2980, 1598, 1355, 1022, 837, 736, 696.

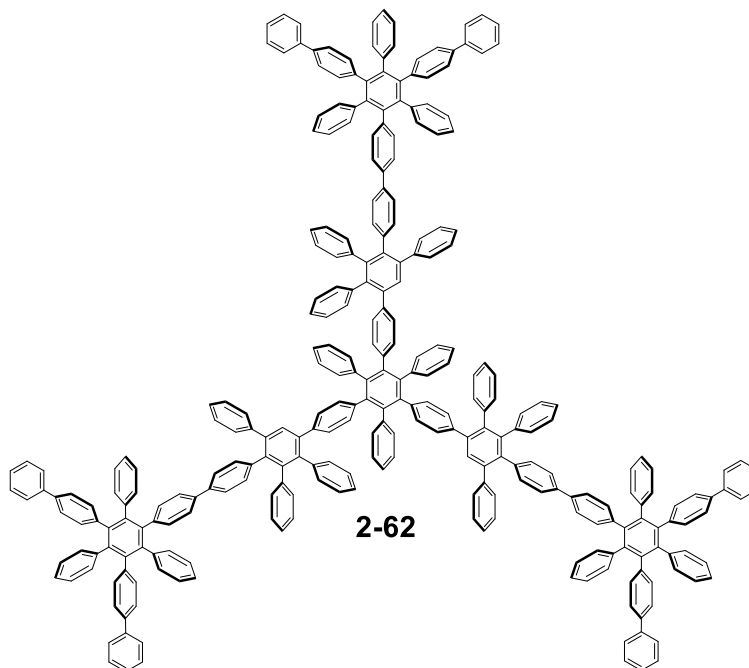
Synthesis of borazine-polyphenylene 2-61



To a solution of **2-23** (0.004 g, 0.0053 mmol) in Ph₂O (1 mL), **2-47** (0.020 g, 0.018 mmol) was added. The dark red solution was degassed by Ar bubbling for 30 minutes at 40 °C and then heated at 190 °C for 18 h. The reaction mixture was directly introduced in a silica gel column chromatography (petroleum ether/CH₂Cl₂ 1:1), then the solid residue was further purified by Rec-GPC (CHCl₃) affording **2-61** as white solid (0.011 g, 54%).

M.P.: > 300 °C. ¹H-NMR (300 MHz, CD₂Cl₂) δ: 7.45-7.42 (m, 12 H), 7.36-7.731 (m, 12 H), 7.27-7.22 (m, 9 H), 7.16-7.07(m, 27 H), 7.03-6.70 (m, 106 H), 6.60-6.48 (m, 17 H), 6.41 (s, 6 H), 2.11 (s, 9 H), 2.05 (s, 18 H). ¹³C-NMR (100 MHz, CD₂Cl₂) δ: 144.75, 141.84, 141.80, 141.69, 141.05, 140.72, 140.61, 140.56, 140.47, 140.29, 140.01, 139.92, 139.87, 139.72, 139.25, 138.92, 138.43, 138.39, 137.46, 137.32, 136.91, 136.70, 136.39, 136.35, 135.91, 131.84, 131.78, 131.62, 131.37 131.30, 131.22, 130.98, 130.90, 129.84, 129.80, 128.60, 128.28, 127.53, 127.40, 127.03, 126.86, 126.78, 126.64, 126.45, 126.34, 126.26, 126.15, 125.43, 125.34, 124.86, 124.53, 124.49, 124.34. 124.32, 124.22, 22.69, 20.86 (some peaks are missing probably due to overlap). ¹¹B-NMR (128 MHz, CD₂Cl₂) δ: 33.94. MALDI-HRMS calc. for [C₂₉₇H₂₁₆B₃N₃]⁺: 3856.7393 found: 3856.7273. IR (film in CH₂Cl₂) ν_{max} (cm⁻¹): 3026, 2980, 1599, 1359, 1028, 829, 734, 696.

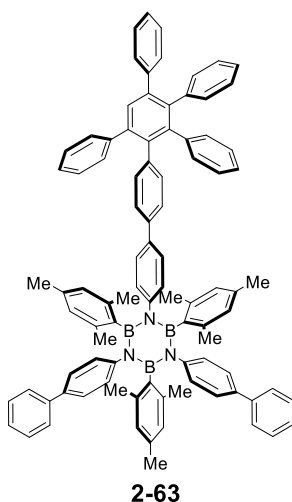
Synthesis of polyphenylene 2-62



To a solution of **2-43** (0.0044 g, 0.0073 mmol) in Ph₂O (1 mL), **2-47** (0.039 g, 0.036 mmol) was added. The dark red solution was degassed by Ar bubbling for 30 minutes at 40 °C and then heated at 190 °C for 18 h. The reaction mixture was directly introduced in a silica gel column chromatography (petroleum ether/CH₂Cl₂ 1:1), then the solid residue was furtherly purified by Rec-GPC (CHCl₃) affording **2-62** (0.014 g, 51%).

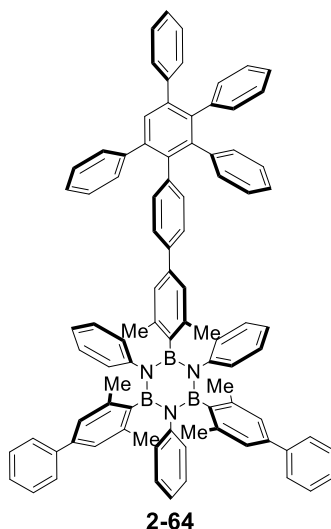
M.P. > 300 °C. ¹H-NMR (300 MHz, CD₂Cl₂) δ: 7.45-6.56 (m, 198 H). ¹³C-NMR (100 MHz, CD₂Cl₂) δ: 142.42, 142.38, 142.27, 141.67, 141.28, 141.21, 141.15, 141.07, 140.90, 140.81, 140.64, 140.51, 140.46, 140.33, 140.27, 139.83, 139.74, 139.69, 139.32, 139.15, 138.80, 137.93, 137.36, 137.02, 132.43, 132.37, 131.96, 131.90, 131.64, 131.34, 130.42, 130.38, 129.18, 128.69, 128.14, 128.02, 127.61, 127.50, 127.38, 127.23, 127.11, 127.04, 126.86, 126.72, 126.23, 126.02, 125.91, 125.86, 125.45, 125.14, 124.95, 124.92, 124.84 (some peaks are missing probably due to overlap). MALDI-HRMS calc. for [C₂₉₄H₁₉₈]⁺: 3727.5494 found: 3727.5566. IR (film in CH₂Cl₂) ν_{max} (cm⁻¹): 3026, 1598, 1495, 833, 734, 698.

Synthesis of N,N'-tri(4-phenyl)phenyl-N''-4-(2,3,4,6-tetraphenyl-(phenyl-4'-yl))-B,B',B''-trimesityl borazine 2-63



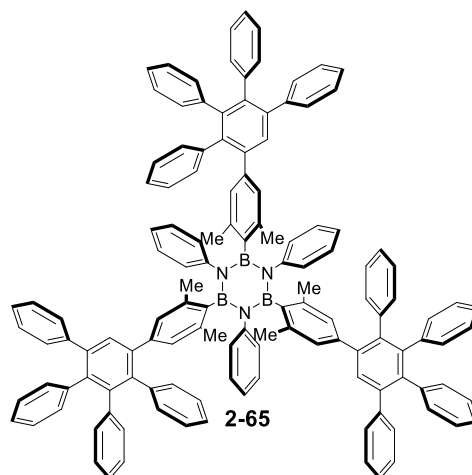
To a solution of **2-34** (0.022 g, 0.018 mmol) in Ph₂O, phenylacetylene (0.009 g, 0.091 mmol) was added. The dark red solution was degassed by N₂ bubbling for 30 minutes, then heated at 180 °C for 1 h in a microwave reactor. The reaction mixture was directly introduced in a silica gel column chromatography (petroleum ether/CH₂Cl₂ 6:4), then the solid residue was further purified by Rec-HPLC (hexane/CHCl₃ 3:7) affording **2-63** as a white solid (0.0045 g, 20 %).

M.P.: 249-253 °C. ¹H-NMR (400 MHz, CDCl₃) δ: 7.54 (s, 1 H), 7.40-7.27 (m, 8 H), 7.23-7.18 (m, 2 H), 7.15-7.13 (m, 8 H), 7.03-6.71 (m, 28 H), 6.33 (s, 6 H), 2.25-2.23 (s, 18 H), 1.98-1.96 (s, 9 H). ¹³C-NMR (100 MHz, CDCl₃) δ: 145.27, 145.31, 141.78, 140.60, 140.06, 137.25, 136.16, 131.56, 129.96, 128.52, 127.59, 127.34, 127.05, 126.41, 126.70, 126.57, 16.41, 125.10, 23.05, 21.08 (some peaks are missing probably due to overlap). MALDI-LRMS calc. for [C₉₃H₈₀B₃N₃]⁺: 1272.1, found: 1271.8. IR (film in CH₂Cl₂) ν_{max} (cm⁻¹): 3021, 2984, 1554, 1344, 1002, 824, 752, 691.

Synthesis of N,N',N''-triphenyl- B,B'-di(2,6-dimethyl-4-phenyl)-B''-2,6-dimethyl-4-(2,3,4,6-tetraphenyl-(phenyl-4'-yl)) borazine 2-64

To a solution of **2-28** (0.016 g, 0.014 mmol) in Ph₂O (0.4 mL), phenylacetylene (0.004 g, 0.04 mmol) was added. The dark red solution was degassed by N₂ bubbling for 30 minutes, then heated at 180 °C for 1 h in a microwave reactor. The reaction mixture was directly introduced in a silica gel column chromatography (petroleum ether/CH₂Cl₂ 6:4), then the solid residue was furtherly purified by Rec-HPLC (hexane/CHCl₃ 2:8) affording **2-64** as a white solid (0.010 g, 59 %).

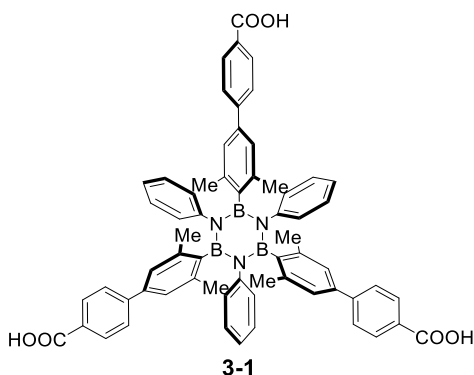
M.P.: 258-260 °C. ¹H-NMR (400 MHz, CDCl₃) δ: 7.54 (s, 1 H), 7.41-7.39 (m, 4 H), 7.32-7.27 (m, 4 H), 7.23-7.14 (m, 11 H), 7.01-6.64 (m, 34 H), 2.35-2.30 (m, 18 H). ¹³C-NMR (100 MHz, CDCl₃) δ: 146.33, 142.19, 141.63, 141.26, 139.59, 138.32, 132.01, 131.93, 131.86, 130.34, 128.81, 128.12, 127.97, 127.43, 127.35, 127.27, 127.14, 127.03, 126.60, 125.47, 124.90, 124.44, 124.20, 23.69 (some peaks are missing probably due to overlap). MALDI-HRMS calc. for [C₉₀H₇₄B₃N₃]⁺: 1228.6198, found: 1228.6228. IR (film in CH₂Cl₂) ν_{max} (cm⁻¹): 3218, 2958, 1548, 1345, 1053, 852, 741, 620.

**Synthesis of N,N',N''triphenyl- B,B',B''-tri-(4-(1',2',3',4'-tetra phenyl)phenyl)borazine
2-65**

To a solution of **2-18** (0.022 g, 0.03 mmol) in Ph₂O (0.5 mL), **CPD** (0.046 mg, 0.12 mmol) was added. The dark red solution was degassed by Ar bubbling for 1 h at 40 °C, then stirred at 180 °C for 6 h. The reaction mixture was directly introduced in a silica gel column chromatography (pentane/CH₂Cl₂ 7:3), then the solid residue affording furtherly purified was by Rec-HPLC (hexane/CHCl₃ 3:7) affording **2-65** as white solid (0.044 g, 83 %).

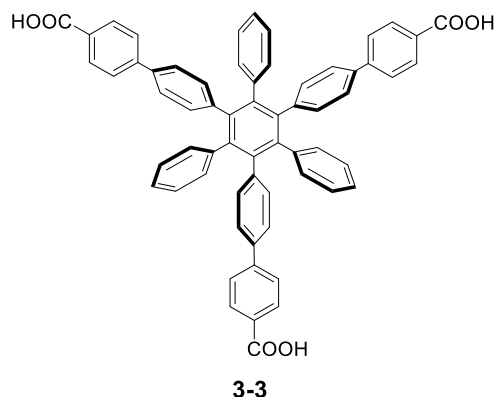
¹H-NMR (400 MHz, CDCl₃) δ: 7.34 (s, 3 H), 7.14-7.10 (m, 15 H), 6.90-6.60 (m, 60 H), 6.30 (s, 6 H), 2.04 (s, 18 H). ¹³C-NMR (100 MHz, CDCl₃) δ: 145.85, 142.00, 141.50, 140.72, 140.56, 140.51, 140.13, 139.97, 139.01, 138.79, 136.72, 131.55, 131.40, 129.96, 127.54, 127.26, 126.96, 126.83, 126.76, 126.73, 126.52, 126.16, 125.19, 125.14, 22.91 (some peaks are missing probably due to overlap). MALDI-HRMS calc. for [C₁₃₂H₁₀₂B₃N₃]⁺: 1761.8353, found 1761.8291. IR (film in CH₂Cl₂) ν_{max} (cm⁻¹): 3028, 2948, 1586, 1356, 1086, 820, 712, 644.

Synthesis of N,N',N''-triphenyl-B,B',B''-tri(2,6-dimethyl-4-(4-(carboxy)phenyl)phenyl)borazine 3-1



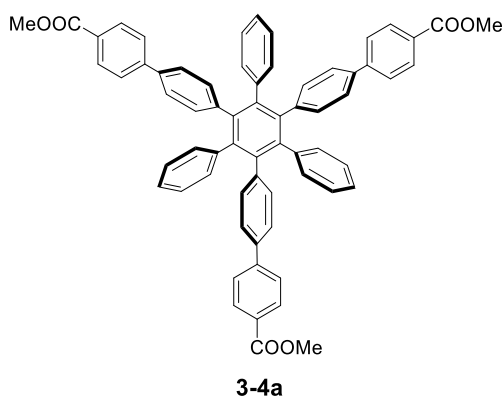
To a solution of **2-30** (0.350 g, 0.33 mmol) in a mixture 5:1 dioxane/H₂O (15 mL), 4-metoxycarbonyl-phenylboronic acid **3-2** (0.245 g, 1.48 mmol), [Pd(PPh₃)₄] (0.038 g, 0.032 mmol) and K₂CO₃ (0.542 g, 3.93 mmol) were added and placed under inert atmosphere of N₂. The reaction mixture was degassed by N₂ bubbling under sonication for 3 h, then heated at 105 °C for 48 h. The solution was diluted with EtOAc (50 mL) and washed with H₂O (3 x 100 mL). The H₂O solution was concentrated under reduced pressure. The solid residue was dissolved in a mixture 4:1 THF/CH₃OH (35 mL), then a solution of NaOH (1 M) was added dropwise until pH: 13-14 was obtained. The reaction mixture was stirred at room temperature for 18 h. Then CH₃OH and THF were removed under reduced pressure and HCl (1 M) was added dropwise at 0 °C until pH: 1 was obtained. The white solid was filtered off affording **3-1** (0.26 g, 80%).

¹H-NMR (300 MHz, DMSO) δ : 12.89 (s, 3 H), 7.87 (d, J = 8.3 Hz, 6 H), 7.58 (d, J = 8.3 Hz, 6 H), 7.00-6.98 (m, 12 H), 6.87-6.83 (m, 6 H), 6.74-6.70 (m, 3 H) 2.41 (s, 18 H). ¹³C-NMR (100 MHz, DMSO) δ : 167.11, 145.67, 143.73, 139.52, 138.13, 136.87, 129.73, 129.16, 127.22, 126.26, 125.98, 124.90, 123.47, 23.01. ¹¹B-NMR (128 MHz, CDCl₃) δ : 30.10. ESI-LRMS calc. for [C₆₃H₅₄B₃N₃O₆]⁺: 981.43, found: 981.57. FT-IR (solid) ν_{\max} (cm⁻¹): 3044, 2911, 1695, 1606, 1357, 1015, 702, 651.

Synthesis of 1,3,5-tris-(4-(4-carboxyphenyl)phenyl)-2,4,6-phenylbenzene 3-3

To a solution of **3-4a** (0.22 g, 0.23 mmol) in a mixture 4:1 THF/ CH₃OH (35 mL), a solution of NaOH (1 M) was added dropwise until pH: 13-14 was obtained. The reaction mixture was stirred at room temperature for 16 h. Then CH₃OH and THF were removed under reduced pressure and HCl (1 M) was added at 0 °C until pH: 1 was obtained. The white solid was filtered affording **3-3** (0.19 g, 90%).

¹H-NMR (300 MHz, DMSO) δ : 12.93 (s, 3 H), 7.90 (d, J = 8.3 Hz, 6), 7.62 (d, J = 8.3 Hz, 6 H), 7.31 (d, J = 8.3 Hz, 6 H), 7.62 (d, J = 8.3 Hz, 6 H), 7.00-6.79 (m, 15 H). ¹³C-NMR (100 MHz, DMSO) δ : 167.11, 143.26, 140.37, 140.20, 139.91, 139.63, 135.20, 131.74, 130.96, 129.91, 129.39, 126.79, 126.17, 125.69, 124.87. IR ν_{\max} (cm⁻¹): 3026, 1604, 1392, 1004, 750, 698.

Synthesis of 1,3,5-tris-(4-(4-methoxycarbonyl-phenyl)phenyl)-2,4,6-phenylbenzene 3-4a

Procedure 1

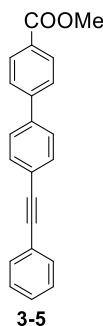
To a solution of **3-5** (0.4 g, 1.28 mmol) in dioxane (10 mL), [Co₂(CO)₈] (0.044 g, 0.12 mmol) was added under inert atmosphere of N₂. The solution was degassed by five freeze-pump-thaw cycles. The reaction mixture was stirred and refluxed for 18 h. The solvent was removed under reduced pressure. The precipitate was filtered off and the solution was concentrated under reduced pressure. The residue was purified by silica gel column chromatography (petroleum ether/CH₂Cl₂ 7:3) affording two regioisomers **3-4a** and **3-4b**. The mixture of **3-4a** and **3-4b** was furtherly purified by rec-HPLC normal phase (CHCl₃/Hexane in ratio 3:7) affording **3-4a** (52 mg, 13%).

Procedure 2

To a solution of **2-49** (0.27 g, 0.27 mmol) in dry THF (22 mL), **3-2** (0.451 g, 2.50 mmol), Pd(OAc)₂ (0.003 g, 0.008 mmol), XPhos (0.011 g, 0.02) and K₃PO₄ (0.565 g, 2.50 mmol) were added and placed under inert atmosphere of N₂. The reaction mixture was degassed by N₂ bubbling under sonication for 3 h, then heated at 75 °C for 15 h. The solution was diluted with EtOAc (50 mL), washed with H₂O (3 x 100 mL) and brine (100 mL). The dark organic solution was dried over MgSO₄ and concentrated under reduced pressure. The residue was purified by silica gel column chromatography (cyclohexane/EtOAc 7:3) affording **3-4a** as white solids (0.22 g, 83%).

¹H-NMR (300 MHz, CD₃Cl) δ: 8.00 (d, J = 8.7 Hz, 6 H), 7.50 (d, J = 8.7 Hz, 6 H), 7.17 (d, J = 8.5 Hz, 6 H), 6.93 (d, J = 8.4 Hz, 6 H), 6.90-6.86 (m, 15 H), 3.91 (s, 9 H). ¹³C-NMR (100 MHz, CD₃Cl) δ: 167.15, 145.30, 140.79, 140.67, 140.42, 140.06, 136.42, 132.11, 131.50, 130.02, 128.55, 127.01, 126.72, 125.63, 125.52, 52.24. ESI-HRMS calc. for [C₆₆H₄₈O₆]⁺ 936.3451, found 937.3515. IR ν_{max} (cm⁻¹) 3034, 2947, 1714, 1606, 1274, 1004, 738, 700.

Synthesis of 1-(4-metoxycarbonyl)phenyl-4-phenylethynyl-benzene **3-5**



To a solution of **2-38** (1.34 g, 5.23 mmol) in a mixture dioxane/H₂O 3:1 (20 mL), **3-2** (0.954 g, 5.75 mmol), [Pd(PPh₃)₄] (0.605 g, 0.523 mmol) and K₂CO₃ (2.38 g, 17.26 mmol) were added and placed under inert atmosphere of N₂. The reaction mixture was degassed by N₂ bubbling under sonication for 3 h, then heated at 105 °C for 15 h. The solution was diluted with EtOAc (50 mL), washed with H₂O (3 x 100 mL) and brine (100 mL). The dark organic layer was dried over MgSO₄ filtered and concentrated under reduced pressure. The residue was purified by silica gel column chromatography (cyclohexane/CH₂Cl₂ 8:2) affording **3-5** as white solids (1.43 g, 83%).

¹H-NMR (300 MHz, CDCl₃) δ: 8.12 (d, J = 8.6 Hz, 2 H), 7.68 (d, J = 8.6 Hz, 2 H), 7.63 (s, 4 H), 7.58-7.54 (m, 2 H), 7.38-7.35 (m, 3 H), 3.95 (s, 3 H).

Synthesis of [Zn₄O(BNTCP)₆] **3-9**

To a microwave vial (Biotage vial, size L x W x H: 1.5 x 1.5 x 8 cm) **3-1** (0.015 g, 0.015 mmol) and Zn(NO₃)₂·6H₂O (0.075 g, 0.25 mmol) were added and dissolved in a mixture 1:1 DMF/NMP (4 mL). The reaction mixture was heated at 85 °C for 72 h. The crystals obtained were filtered and dried under air affording [Zn₄O(CTCP)₆] **3-9** (0.013 g, 70%). See section 5.5 for X-ray crystal data.

Solvent exchange procedure: BN-MOF **3-9** was washed thoroughly with a mixture of 1:1 DMF/NMP (30 mL) to remove any non-coordinated three-carboxyl borazine **3-1**. In a centrifuge tube, BN-MOF **3-9** and acetone were added and the suspension was left to soak in the new solvent for 20 min. Subsequently, the suspension was washed with centrifugation

(5000 rpm, 30 min) and then the supernatant was carefully removed. This procedure was applied for 5 cycles.

FT-IR (solid) ν_{\max} (cm^{-1}): 3455 (broad peak, probably -OH stretching due to some uncoordinated borazine linker), 2983, 1652, 1560, 1350, 1082, 705, 662, 562, 539.

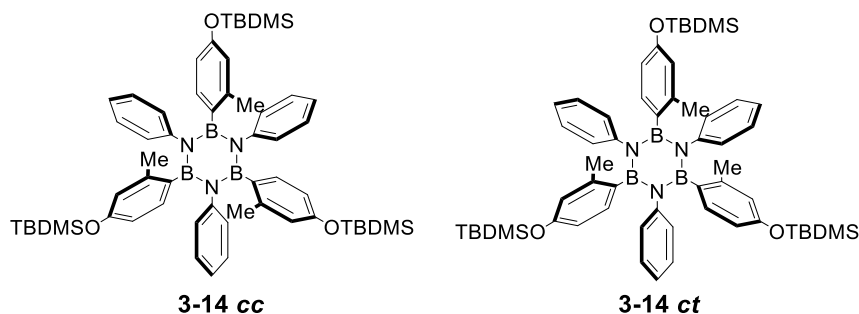
Synthesis of $[\text{Zn}_4\text{O}(\text{CTCP})_6]$ **3-10**

To a microwave vial (Biotage vial, size L x W x H: 1.5 x 1.5 x 8 cm) **3-3** (0.014 g, 0.016 mmol) and $\text{Zn}(\text{NO}_3)_2 \cdot 6\text{H}_2\text{O}$ (0.077 g, 0.26 mmol) were added and dissolved in a mixture 1:1 DMF/NMP (4 mL). The reaction mixture was heated at 85 °C for 72 h. The crystals obtained were filtered and dried under air affording $[\text{Zn}_4\text{O}(\text{CTCP})_6]$ **3-10** (0.013 g, 71%). See section 5.5 for X-ray crystal data.

Solvent exchange procedure: C-MOF **3-10** was washed thoroughly with a mixture of 1:1 DMF/NMP (30 mL) to remove any non-coordinated three-carboxyl linker **3-3**. In a centrifuge tube, C-MOF **3-10** and acetone were added and the suspension was left to soak in the new solvent for 20 min. Subsequently, the suspension was washed with centrifugation (5000 rpm, 30 min) and then the supernatant was carefully removed. This procedure was applied for 5 cycles.

FT-IR (solid) ν_{\max} (cm^{-1}): 3354 (broad peak, probably -OH stretching due to some uncoordinated linker), 3064, 1597, 1394, 767, 659, 566, 533.

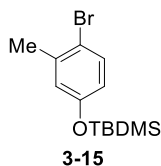
Synthesis of N,N,N'' -triphenyl- B,B',B'' -tri(2,6-dimethyl-4-(tertbutyl dimethylsilyloxy) phenyl) borazine **3-14 cc** and **3-14 ct**



To a solution of **2-20** (0.5 mL, 5.3 mmol) in dry toluene (6 mL) under Ar, a solution of BCl_3 (1 M in heptane, 6.0 mL, 5.8 mmol) was added dropwise at 0 °C. A white precipitate formed during the addition. The resulting mixture was refluxed for 18 h. The final mixture was cooled down to room temperature and subjected to five freeze-pump-thaw cycles to remove the excess of HCl. In parallel, to a solution of **3-15** (1.9 g, 6.36 mmol) in dry THF (15 mL), $t\text{BuLi}$ (1.7 M in hexane, 7.8 mL, 13.36 mmol) was added dropwise at -84 °C. The solution was allowed to warm up at 0 °C and stirred for 10 min. The degassed toluene mixture containing the chloro-borazine intermediate was slowly transferred to the organometallic-containing solution at 0°C and allowed to react at room temperature for 16 h. The mixture was diluted with EtOAc (100 mL), washed with H_2O (3 x 100 mL) and brine (100 mL). The organic phase was dried over MgSO_4 and the solvents removed under reduced pressure. The yellow deliquescent solid was re-dissolved in EtOAc (10 mL) and CH_3OH was added. The white formed precipitate was filtered off affording **3-14 cc** and **3-14 ct** in a mixture 1:3 (1.04 g, 45%).

M.P.: 200-202 °C. $^1\text{H-NMR}$ (400 MHz, CDCl_3) δ : 6.88-6.86 (m, 3 H), 6.79-6.65 (m, 69 H), 6.27-6.24 (m, 12 H), 6.19-6.12 (m, 12 H), 2.13 (s, 9 H), 2.07 (s, 18 H), 2.00 (s, 9 H), 0.84 (s, 107 H), -0.03 (s, 72 H). $^{13}\text{C-NMR}$ (100 MHz, CDCl_3) δ : 154.30, 154.28, 146.65, 146.59, 146.44, 139.71, 139.64, 139.58, 133.46, 133.18, 132.92, 132.52, 129.69, 129.65, 128.84, 127.55, 127.12, 127.04, 126.96, 123.83, 120.15, 116.21, 116.09, 115.96, 25.87, 23.01, 22.92, 22.82, 18.34, -4.44 (some peaks are missing probably due to overlap). $^{11}\text{B-NMR}$ (128 MHz, CDCl_3) δ : 36.05. MALDI-HRMS calc. for $[\text{C}_{57}\text{H}_{79}\text{B}_3\text{N}_3\text{O}_3\text{Si}_3]^+$: 970.5444 found 970.5736. IR (film in CH_2Cl_2) ν_{max} (cm^{-1}): 3050, 2980, 1562, 1363, 1026, 763, 729, 696.

Synthesis of 2,6-dimethyl-4-(tertbutyldimethylsilyloxy)bromo benzene **3-15**

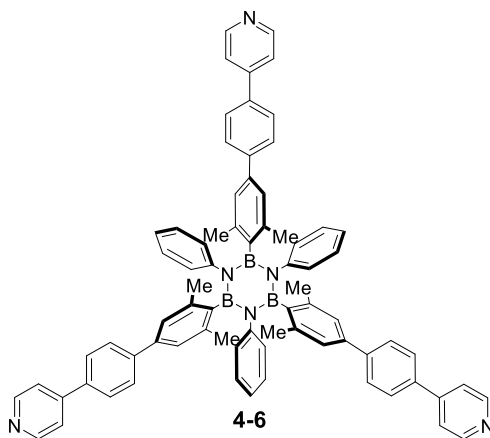


To a solution of 3-methyl-4-bromophenol **3-16** (5.5 g, 29.1 mmol) in DMF (35 mL), TBDMSCl (6.2 g, 41.7 mmol) and imidazole (6 g, 87 mmol) were added. The reaction mixture was stirred at 50 °C for 15 h, then diluted with EtOAc (200 mL), washed with H_2O

(3 x 200 mL) and brine (100 mL). The organic layer was dried over MgSO₄, filtered and concentrated under reduced pressure. The residue was purified by silica gel column chromatography (pentane) affording **3-15** as pale-yellow oil (8.5 g, 99%).

¹H-NMR (400 MHz, CDCl₃) δ: 7.35 (d, J = 8.5 Hz, 1 H), 6.75 (s, 1 H), 6.56 (d, J = 8.5 Hz, 1 H), 2.34 (s, 3 H), 1.00 (s, 9 H), 0.20 (s, 6 H). ¹³C-NMR (100 MHz, CDCl₃) δ: 154.97, 138.91, 132.89, 122.74, 119.25, 116.32, 25.77, 23.17, 18.31, -4.33. ESI-HRMS calc. for [C₁₃H₂₁BrOSi]⁺: 300.0545, found 300.0544. IR (neat film) ν_{max} (cm⁻¹): 2950, 1571, 1230, 1038, 824, 750, 685.

Synthesis of N,N',N''-triphenyl-B,B',B''-tri(2,6-dimethyl-4-(4-(pyridinyl)phenyl)phenyl)borazine 4-6

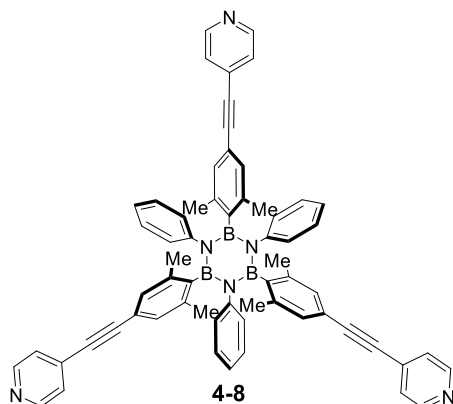


To a solution of **2-30** (0.05 g, 0.047 mmol) in dioxane/H₂O 3:1 (4 mL), [Pd(PPh₃)₄] (0.003 g, 0.0028 mmol), 4-pyridinphenylboronic acid **4-5** (38 mg, 0.188 mmol) and K₂CO₃ were added (0.078 g, 0.564 mmol). The reaction mixture was degassed by Ar bubbling 40 minutes and then stirred at 105 °C for 16 h. The solution was diluted with EtOAc (100 mL), washed with H₂O (3 × 100 mL) and brine (100 mL). The organic phase was dried over MgSO₄ and evaporated under reduced pressure. The residue was purified by silica gel column chromatography (CH₂Cl₂/CH₃OH, 95:5) affording **4-6** as yellow solid (0.044 g, 87%).

¹H-NMR (400 MHz, CDCl₃) δ: 8.68 (s, bs, 6H), 7.61-7.53 (m, 18 H), 6.93-6.71 (m, 21 H), 2.41 (s, 18 H). ¹³C-NMR (100 MHz, CDCl₃) δ: 150.17, 148.08, 145.92, 142.11, 139.37, 138.36, 138.26, 136.23, 127.37, 127.13, 127.09, 126.95, 124.74, 124.13, 121.54, 23.44. ¹¹B-NMR (128 MHz, CDCl₃) δ: 37.04. MALDI-HRMS *m/z*: Calcd for [C₇₅H₆₃B₃N₆]⁺ : calc:

1081.5593 found 1081.5472. IR (film in CH₂Cl₂, cm⁻¹) ν_{\max} (cm⁻¹): 3088, 2954, 1594, 1355, 1230, 1026, 750, 698.

Synthesis of N,N',N''-triphenyl-B,B',B''-tri(2,6-dimethyl-4-(pyridylacetynyl)phenyl)borazine 4-8



To a solution of **2-18** (0.41 g, 0.59 mmol) in NEt₃ (30 mL), [PdCl₂(PPh₃)₂] (0.043 g, 0.06 mmol), and CuI (0.034 g, 0.018 mmol) were added. The mixture was subjected to three freeze-pump-thaw cycles, then 4-iodopyridine **4-7** (0.424 g, 2.07 mmol) was added. The reaction mixture was stirred for 16 h at 75 °C, then diluted with EtOAc (30 mL), washed with H₂O (3 x 100 mL) and brine (30 mL). The organic phase was dried over MgSO₄ and the solvents removed under reduced pressure. The residue was purified by silica gel column chromatography (CH₂Cl₂/ CH₃OH, 95:5) affording **4-8** as yellow solid (0.39 g, 70%).

¹H-NMR (400 MHz, CD₂Cl₂) δ : 8.51 (d, J = 6.1 Hz, 6 H), 7.25 (d, J = 6.1 Hz, 6 H), 6.95-6.84 (m, 15 H), 6.80 (s, 6 H), 2.36 (s, 18 H). ¹³C-NMR (100 MHz, CDCl₃) δ : 149.64, 145.27, 141.32, 137.90, 131.67, 128.94, 127.32, 126.53, 125.45, 125.19, 120.45, 94.91, 85.99, 23.01. ¹¹B-NMR (128 MHz, CDCl₃) δ : 36.89. MALDI-HRMS m/z : [C₅₇H₆₇B₃N₃Si₃]⁺: calc. 925.4533 found 925.4554. IR (film in CH₂Cl₂, cm⁻¹) ν_{\max} : 3050, 2970, 2211, 1738, 1537, 1361, 1216, 1025, 698, 675.

5.4 Life time measurements

Fluorescence life times were measured of Time Correlated Single Photon Counting (TCSPC) on a JobinYvon-Horiba Fluorolog spectrometer using a pulsed laser source having an output of 295 nm. The decays $F(t)$ were deconvoluted on DAS6 decay analysis software. The statistical method used is the iterative least squares reconvolution, the basis of which is the calculation of the convolution integral using assumed fit parameters to obtain $F'(t)$. $F'(t)$ and the decay data $F(t)$ are then compared to assess the “goodness of fit”, which is quantified by the parameter χ^2 . $F'(t)$ is then recalculated using a range of fit parameters until the best possible agreement of $F'(t)$ and $F(t)$ is obtained and χ^2 has been minimised. The χ^2 is defined as:

$$\chi^2 = \sum_{\text{data}} \left[\frac{\text{actual deviation}}{\text{expected deviation}} \right]^2 = \sum_{\text{data}} \left[\frac{F(i) - F'(i)}{\sigma(i)} \right]^2$$

Where $\sigma(i)$ is the standard deviation of the i th data point.

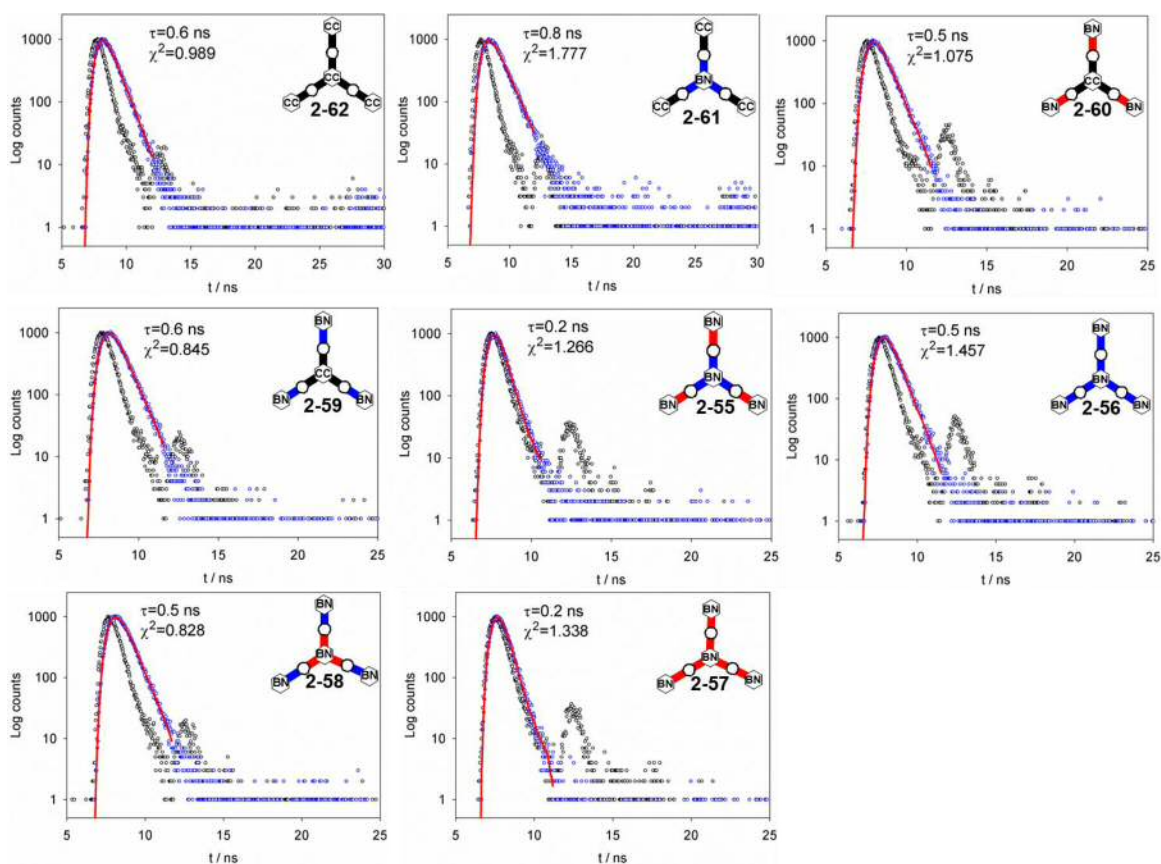


Figure 5.1. Emission lifetime decays (blue dots) and relative fittings (red lines) of three branched BN polyphenylenes excited at $\lambda_{\text{exc}} = 295$ nm in CH_2Cl_2 at r.t.. All reported fittings are mono exponentials. Decay of the excitation source is reported as the black dots (Instrument response function).

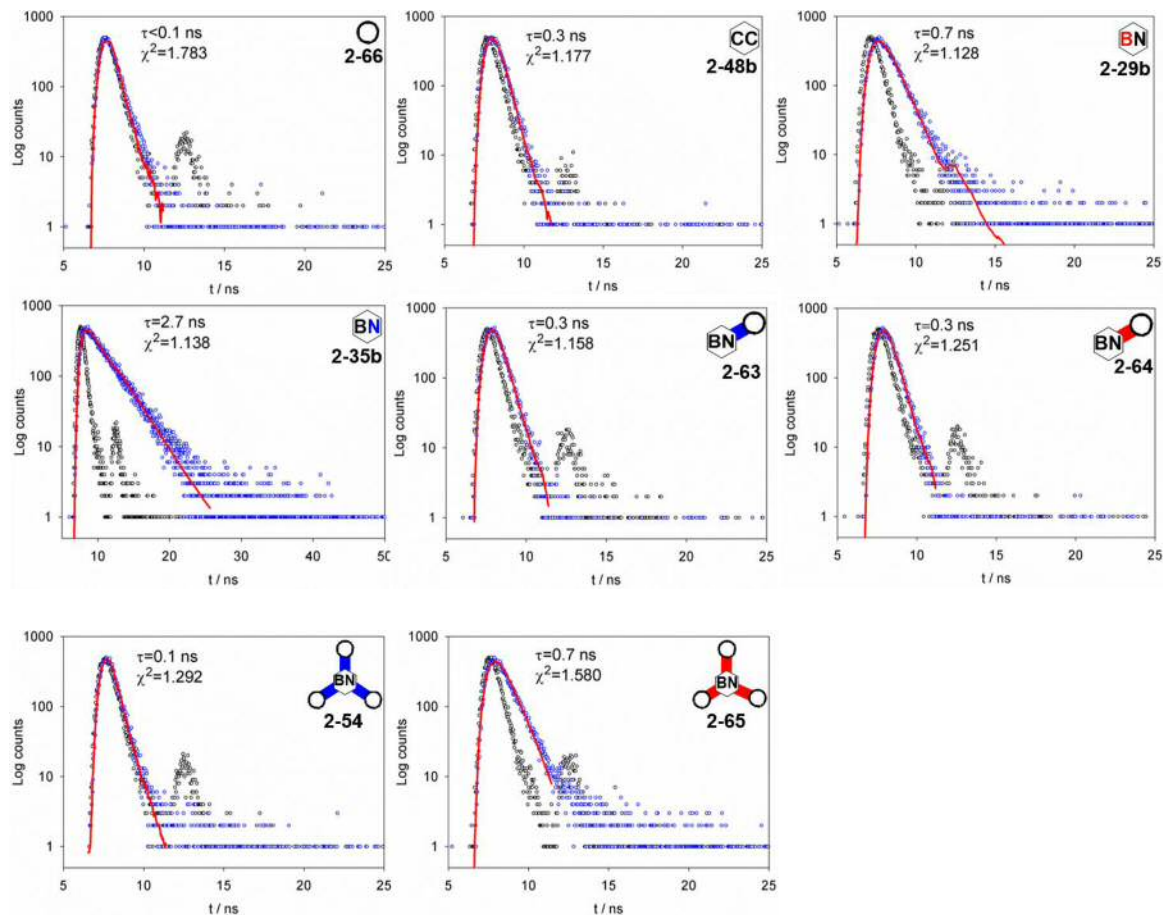


Figure 5.2. Emission lifetime decays (blue dots) and relative fittings (red lines) of borazine monomeric references excited at $\lambda_{\text{exc}} = 295 \text{ nm}$ in CH_2Cl_2 at r.t.. All reported fittings are mono exponentials. Decay of the excitation source is reported as the black dots (Instrument response function).

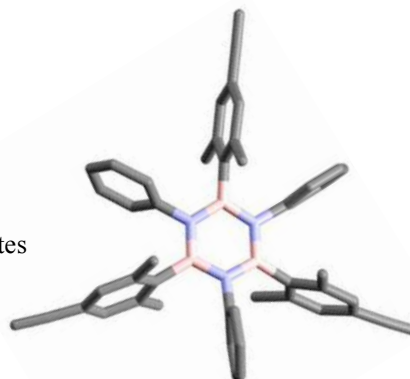
5.5 X-ray data

Data collections were performed by Nicola Demitri, at the X-ray diffraction beamLine (XRD1) of the Elettra Synchrotron, Trieste (Italy).² The crystals were dipped in NHV oil (Jena Bioscience, Jena, Germany) and mounted on the goniometer head with kapton loops (MiTeGen, Ithaca, USA). Complete datasets were collected at 100 K for compounds **2-18**, **2-28**, **2-30**, **2-31**, **2-54**, **3-1** and **4-6** (nitrogen stream supplied through an Oxford Cryostream 700 - Oxford Cryosystems Ltd., Oxford, United Kingdom) through the rotating crystal method. For compounds **3-9** and **3-10**, no ordered solvent molecules have been identified in the asymmetric units (ASUs) of MOFs and the complete datasets were collected at 298 K through the rotating crystal method. Data collection at cryogenic temperatures (100 K) shown a significant degradation of diffraction. Data were acquired using a monochromatic wavelength of 0.700 \AA , on a Pilatus 2M hybrid-pixel area detector (DECTRIS Ltd., Baden-

Daettwil, Switzerland). The diffraction data were indexed and integrated using XDS.³ Crystals **3-9** and **3-10** were sensitive to radiation damage, therefore complete datasets have been obtained merging sets from two different crystals for both, using CCP4-AimLess code.^{4,5} The structures were solved by the dual space algorithm implemented in the SHELXT code.⁶ Fourier analysis and refinement were performed by the full-matrix least-squares methods based on F^2 implemented in SHELXL (Version 2017/1).⁷ The Coot program was used for modeling.⁸ Anisotropic thermal motion refinement have been used for all atoms. Hydrogen atoms were included at calculated positions with isotropic $U_{\text{factors}} = 1.2 \cdot U_{\text{eq}}$ or $U_{\text{factors}} = 1.5 \cdot U_{\text{eq}}$ for methyl groups (U_{eq} being the equivalent isotropic thermal factor of the bonded non-hydrogen atom).

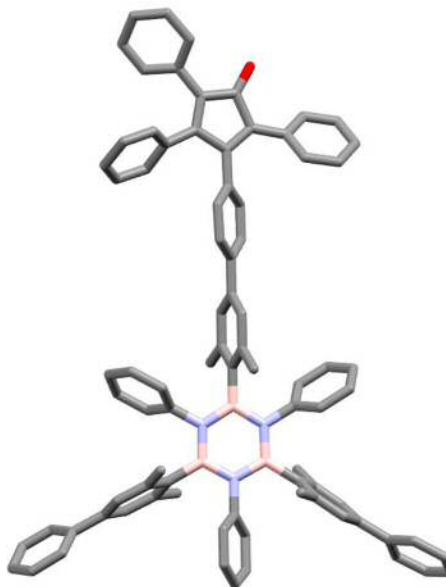
Crystal data and structure refinement of **2-18**.

CCDC Number	1567026
Chemical Formula	C ₅₀ H ₄₆ B ₃ N ₃ O
Formula weight (g/mol)	737.33
Temperature (K)	100(2)
Wavelength (Å)	0.700
Crystal system	Triclinic
Space Group	<i>P</i> -1
Unit cell dimensions	<i>a</i> = 8.818(2) Å <i>b</i> = 12.108(2) Å <i>c</i> = 21.120(4) Å α = 96.28(3)° β = 91.23(3)° γ = 110.54(3)°
Volume (Å ³)	2094.4(8)
Z	2
Density (calculated) (g·cm ⁻³)	1.169
Absorption coefficient (mm ⁻¹)	0.065
F(000)	5141
Crystal size (mm ³)	0.05 x 0.03 x 0.01
Crystal habit	Colorless thin plates
Theta range for data collection	0.96° to 29.99°
Index ranges	-12 ≤ <i>h</i> ≤ 12 -17 ≤ <i>k</i> ≤ 17 -30 ≤ <i>l</i> ≤ 30
Reflections collected	74477
Independent reflections (data with <i>I</i> > 2σ(<i>I</i>))	12480 (11995)
Resolution (Å)	0.70
Data multiplicity (max resltn)	5.82 (4.96)
<i>I</i> /σ(<i>I</i>) (max resltn)	40.60 (32.80)
R _{merge} (max resltn)	0.0339 (0.0347)
Data completeness (max resltn)	97.6% (94.6%)
Refinement method	Full-matrix least-squares on F ²
Data / restraints / parameters	12480 / 11 / 549
Goodness-of-fit on F ²	1.024
Final R indices [<i>I</i> > 2σ(<i>I</i>)]	R ₁ = 0.0501, wR ₂ = 0.1406
R indices (all data)	R ₁ = 0.0511, wR ₂ = 0.1419
Largest diff. peak and hole (eÅ ⁻³)	0.424 and -0.389
R.M.S. deviation from mean (eÅ ⁻³)	0.058



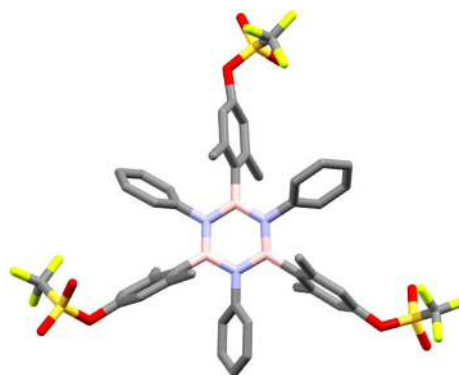
Crystal data and structure refinement of **2-28**.

Chemical Formula	C ₈₄ H _{70.8} B ₃ N ₃ Cl _{1.2} O _{1.4}
Formula weight (g/mol)	1219.61
Temperature (K)	100(2)
Wavelength (Å)	0.700
Crystal system	Triclinic
Space Group	<i>P</i> -1
Unit cell dimensions	<i>a</i> = 14.339(3) Å <i>b</i> = 14.788(3) Å <i>c</i> = 17.315(4) Å α = 77.56(3)° β = 72.01(3)° γ = 70.78(3)°
Volume (Å ³)	3271.0(14)
Z	2
Density (calculated) (g·cm ⁻³)	1.238
Absorption coefficient (mm ⁻¹)	0.115
F(000)	1285
Crystal size (mm ³)	0.10 x 0.05 x 0.05
Crystal habit	Colorless rods
Theta range for data collection	1.23° to 24.32°
Resolution (Å)	0.85
Index ranges	-16 ≤ <i>h</i> ≤ 16 -17 ≤ <i>k</i> ≤ 17 -20 ≤ <i>l</i> ≤ 20
Reflections collected	50940
Independent reflections (data with <i>I</i> > 2σ(<i>I</i>))	10976 (8854)
Data multiplicity (max resltn)	4.58 (4.48)
<i>I</i> /σ(<i>I</i>) (max resltn)	20.63 (8.30)
R _{merge} (max resltn)	0.0480 (0.1614)
Data completeness (max resltn)	98.7% (98.1%)
Refinement method	Full-matrix least-squares on F ²
Data / restraints / parameters	10976 / 12 / 839
Goodness-of-fit on F ²	1.030
Final R indices [<i>I</i> > 2σ(<i>I</i>)] ^a	R ₁ = 0.0935, wR ₂ = 0.2576
R indices (all data) ^a	R ₁ = 0.1090, wR ₂ = 0.2743
Largest diff. peak and hole (e·Å ⁻³)	1.032 and -1.180
R.M.S. deviation from mean (e·Å ⁻³)	0.088



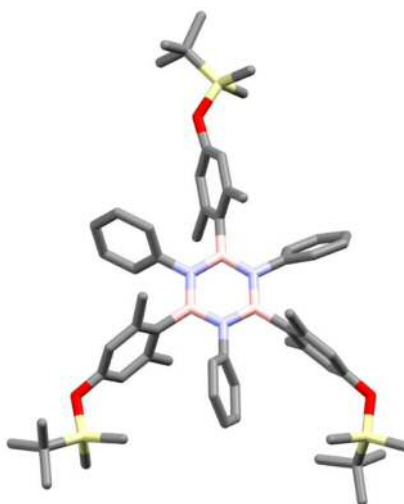
Crystal data and structure refinement of **2-30**.

Chemical Formula	C ₄₅ H ₃₉ B ₃ N ₃ F ₉ O ₉ S ₃
Formula weight (g/mol)	1065.42
Temperature (K)	100(2)
Wavelength (Å)	0.700
Crystal system	Monoclinic
Space Group	<i>P21/n</i>
Unit cell dimensions	<i>a</i> = 13.370(3) Å <i>b</i> = 19.684(4) Å <i>c</i> = 18.969(4) Å α = 90° β = 97.14(3)° γ = 90°
Volume (Å ³)	4953.4(17) Å ³
<i>Z</i>	4
Density (calculated) (g·cm ⁻³)	1.429
Absorption coefficient (mm ⁻¹)	0.227
<i>F</i> (000)	2184
Crystal size (mm ³)	0.50 x 0.31 x 0.20
Crystal habit	Colorless prisms
Theta range for data collection	1.5° to 29.1°
Reflections collected	170784
Independent reflections	13671
(data with <i>I</i> > 2σ(<i>I</i>))	
Data completeness (max resltn)	97.2% (95.4%)
Refinement method	Full-matrix least-squares on <i>F</i> ²
Data / restraints / parameters	13671 / 1059 / 696
Goodness-of-fit on <i>F</i> ²	0.882
Final R indices	<i>R</i> ₁ = 0.0503, <i>wR</i> ₂ = 0.1340
[<i>I</i> > 2σ(<i>I</i>)] ^a	
R indices (all data) ^a	<i>R</i> ₁ = 0.0548, <i>wR</i> ₂ = 0.1389



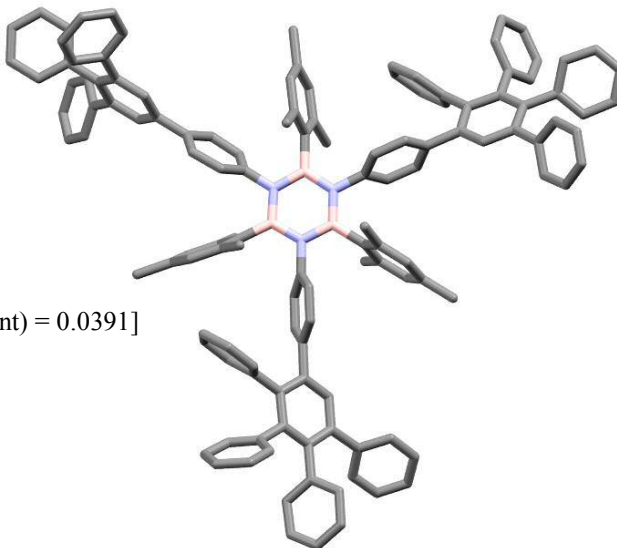
Crystal data and structure refinement of **2-31**.

Chemical Formula	C ₆₀ H ₈₄ B ₃ N ₃ O ₃ Si ₃
Formula weight (g/mol)	1012.02
Temperature (K)	100(2)
Wavelength (Å)	0.700
Crystal system	Triclinic
Space Group	<i>P</i> -1
Unit cell dimensions	<i>a</i> = 10.839(1) Å <i>b</i> = 17.2580(9) Å <i>c</i> = 18.414(5) Å α = 114.815(6)° β = 95.046(6)° γ = 90.999(6)°
Volume (Å ³)	3108.7(5) Å ³
<i>Z</i>	2
Density (calculated) (g·cm ⁻³)	1.112
Absorption coefficient (mm ⁻¹)	0.115
F(000)	1124
Crystal size (mm ³)	0.50 x 0.31 x 0.20
Crystal habit	Colorless prisms
Theta range for data collection	1.2° to 24.6°
Reflections collected	68917
Independent reflections (data with <i>I</i> > 2σ(<i>I</i>))	10731
<i>I</i> /σ(<i>I</i>) (max resltn)	6.61 (1.80)
R _{merge} (max resltn)	0.0864 (0.2970)
Data completeness (max resltn)	97.2% (95.4%)
Refinement method	Full-matrix least-squares on F ²
Data / restraints / parameters	10820/ 46 / 753
Goodness-of-fit on F ²	1.023
Final R indices	R ₁ = 0.0468, wR ₂ = 0.1197
[<i>I</i> > 2σ(<i>I</i>)] ^a	R ₁ = 0.0474, wR ₂ = 0.1197
R indices (all data) ^a	



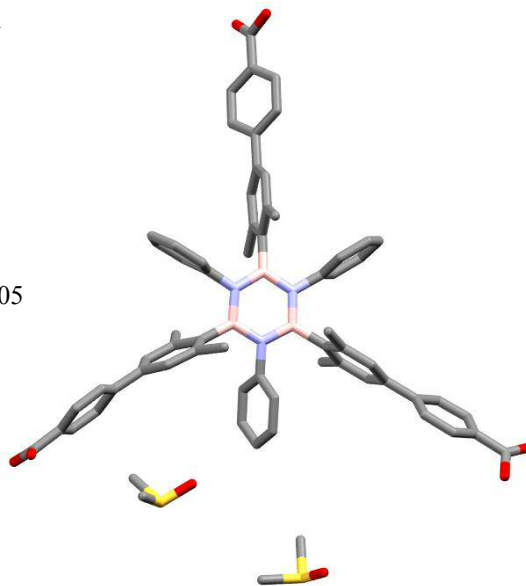
Crystal data and structure refinement of **2-54**.

CCDC Number	1418730
Moiety Formula	$C_{135}H_{108}B_3N_3 \cdot 1.67CHCl_3$
Sum Formula	$C_{136.67}H_{109.67}B_3Cl_5N_3$
Formula weight (Da)	2003.77
Temperature (K)	100(2)
Wavelength (Å)	0.700
Crystal system	Trigonal
Space Group	$R\bar{3}c$
a (Å)	38.284(5)
b (Å)	38.284(5)
c (Å)	47.377(9)
α (°)	90
β (°)	90
γ (°)	120
V (Å ³)	60136(21)
Z	18
ρ (g·cm ⁻³)	0.996
F(000)	18912
μ (mm ⁻¹)	0.145
θ min,max (°)	1.6, 24.3
Resolution (Å)	0.85
Total refl. collectd	67502
Independent refl.	11251 [R(int) = 0.0391]
Obs. Refl. [Fo>4 σ (Fo)]	9344
I/ σ (I) (all data)	15.83
I/ σ (I) (max resltn)	4.20
Completeness (all data)	1.00
Completeness (max resltn)	1.00
Rmerge (all data)	0.054
Rmerge (max resltn)	0.375
Multiplicity (all data)	5.9
Multiplicity (max resltn)	5.7
Data/restraint/parameters	11251/58/726
Goof	1.081
R ₁ ^a [I>2.0 σ (I)], wR ₂ ^a [I>2.0 σ (I)]	0.1438, 0.3349
R ₁ ^a (all data), wR ₂ ^a (all data)	0.1551, 0.3418



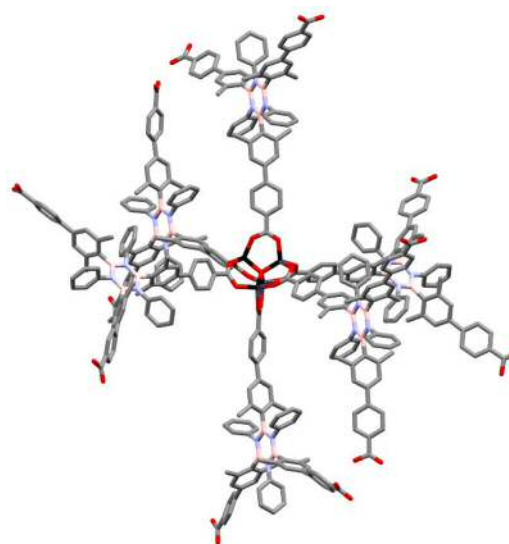
Crystal data and structure refinement of **3-1**.

Chemical Formula	C ₆₇ H _{66.5} B ₃ N ₃ O _{8.25} S ₂
Formula weight (g/mol)	1142.28
Temperature (K)	100(2)
Wavelength (Å)	0.700
Crystal system	Monoclinic
Space Group	<i>P</i> 2 ₁ / <i>c</i>
Unit cell dimensions	<i>a</i> = 17.572(4) Å <i>b</i> = 19.982(4) Å <i>c</i> = 16.937(3) Å α = 90° β = 90.71(3)° γ = 90°
Volume (Å ³)	5947(2)
<i>Z</i>	4
Density (calculated) (g·cm ⁻³)	1.276
Absorption coefficient (mm ⁻¹)	0.142
<i>F</i> (000)	2410
Crystal size (mm ³)	0.10 x 0.05 x 0.05
Crystal habit	Colorless rods
Theta range for data collection	1.14° to 28.17°
Resolution (Å)	0.74
Index ranges	0 ≤ <i>h</i> ≤ 23 -26 ≤ <i>k</i> ≤ 0 -22 ≤ <i>l</i> ≤ 22
Reflections collected	82428
Independent reflections (data with <i>I</i> > 2σ(<i>I</i>))	14881 (9461)
Data multiplicity (max resltn)	5.24 (4.54)
<i>I</i> /σ(<i>I</i>) (max resltn)	13.08 (3.81)
<i>R</i> _{merge} (max resltn)	0.0627 (0.3120)
Data completeness (max resltn)	94.1% (92.7%)
Refinement method	Full-matrix least-squares on <i>F</i> ²
Data / restraints / parameters	14881 / 3 / 771
Goodness-of-fit on <i>F</i> ²	1.069
Final <i>R</i> indices [<i>I</i> > 2σ(<i>I</i>)] ^a	<i>R</i> ₁ = 0.0846, <i>wR</i> ₂ = 0.1982
<i>R</i> indices (all data) ^a	<i>R</i> ₁ = 0.1393, <i>wR</i> ₂ = 0.2435
Largest diff. peak and hole (e·Å ⁻³)	0.867 and -0.799
R.M.S. deviation from mean (e·Å ⁻³)	0.083



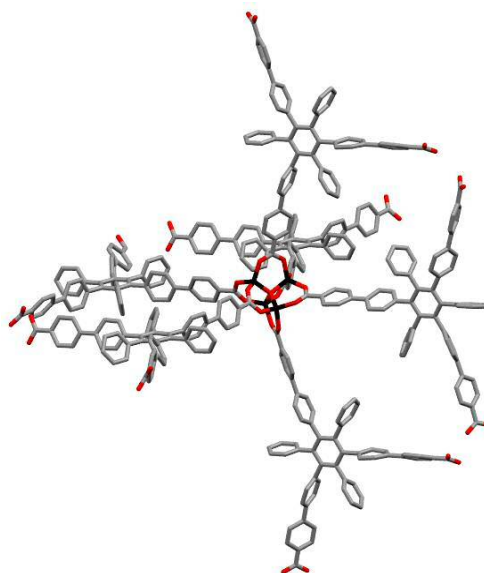
Crystal data and structure refinement of **3-9**.

Chemical Formula	C ₆₃ H ₅₁ B ₃ N ₃ O _{6.5} Zn ₂
Formula weight (g/mol)	1117.23
Temperature (K)	298(2)
Wavelength (Å)	0.700
Crystal system	Orthorhombic
Space Group	<i>Pnmm</i>
Unit cell dimensions	$a = 32.955(7)$ Å $b = 36.243(7)$ Å $c = 23.702(5)$ Å $\alpha = 90^\circ$ $\beta = 90^\circ$ $\gamma = 90^\circ$
Volume (Å ³)	28309(10)
Z	8
Density (calculated) (g·cm ⁻³)	0.524
Absorption coefficient (mm ⁻¹)	0.329
F(000)	4616
Crystal size (mm ³)	0.15 x 0.10 x 0.10
Crystal habit	Colorless prisms
Theta range for data collection	1.01° to 24.62°
Resolution (Å)	0.84
Index ranges	$-36 \leq h \leq 39$ $-43 \leq k \leq 43$ $-27 \leq l \leq 24$
Reflections collected	124140
Independent reflections (data with $I > 2\sigma(I)$)	25014 (16477)
Data multiplicity (max resltn)	4.75 (4.27)
$I/\sigma(I)$ (max resltn)	6.61 (1.80)
R_{merge} (max resltn)	0.0864 (0.2970)
Data completeness (max resltn)	97.2% (95.4%)
Refinement method	Full-matrix least-squares on F^2
Data / restraints / parameters	25014 / 0 / 744
Goodness-of-fit on F^2	1.052
Final R indices [$I > 2\sigma(I)$] ^a	$R_1 = 0.1430$, $wR_2 = 0.3196$
R indices (all data) ^a	$R_1 = 0.1676$, $wR_2 = 0.3329$
Largest diff. peak and hole (e·Å ⁻³)	0.782 and -0.809
R.M.S. deviation from mean (e·Å ⁻³)	0.087



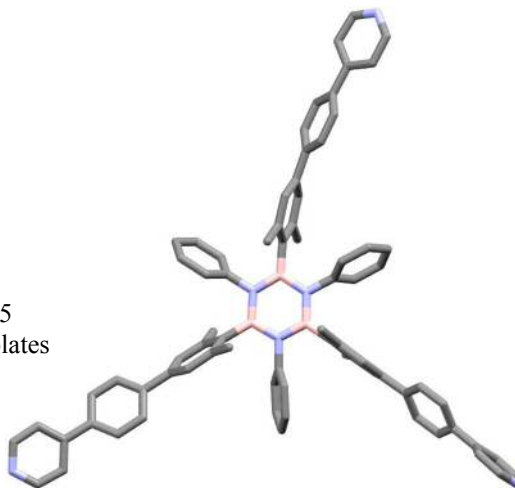
Crystal data and structure refinement of **3-10**.

Chemical Formula	C ₆₉ H ₃₉ O _{6.5} Zn ₂
Formula weight (g/mol)	1030.68
Temperature (K)	298(2)
Wavelength (Å)	0.700
Crystal system	Orthorhombic
Space Group	<i>Fdd2</i>
Unit cell dimensions	$a = 13.467(3) \text{ \AA}$ $b = 40.065(8) \text{ \AA}$ $c = 77.417(15) \text{ \AA}$ $\alpha = 90^\circ$ $\beta = 90^\circ$ $\gamma = 90^\circ$
Volume (Å ³)	41771(14)
Z	16
Density (calculated) (g·cm ⁻³)	0.656
Absorption coefficient (mm ⁻¹)	0.444
F(000)	8464
Crystal size (mm ³)	0.15 x 0.10 x 0.10
Crystal habit	Colorless prisms
Theta range for data collection	1.13° to 28.23°
Resolution (Å)	0.70
Index ranges	$-18 \leq h \leq 17$ $-54 \leq k \leq 53$ $-100 \leq l \leq 103$
Reflections collected	47620
Independent reflections (data with $I > 2\sigma(I)$)	22231 (17259)
Data multiplicity (max resltn)	3.10 (2.26)
$I/\sigma(I)$ (max resltn)	14.07 (1.74)
R_{merge} (max resltn)	0.0415 (0.3613)
Data completeness (max resltn)	92.9% (85.0%)
Refinement method	Full-matrix least-squares on F^2
Data / restraints / parameters	22231 / 1 / 584
Goodness-of-fit on F^2	0.997
Final R indices [$I > 2\sigma(I)$] ^a	$R_1 = 0.0595,$ $wR_2 = 0.1690$
R indices (all data) ^a	$R_1 = 0.0679,$ $wR_2 = 0.1800$
Largest diff. peak and hole (e·Å ⁻³)	0.401 and -0.433
R.M.S. deviation from mean (e·Å ⁻³)	0.059



Crystal data and structure refinement of **4-6**.

CCDC Number	1567027
Chemical Formula	C _{82.80} H _{81.71} B ₃ N ₆
Formula weight (g/mol)	1193.25
Temperature (K)	100(2)
Wavelength (Å)	0.700
Crystal system	Monoclinic
Space Group	<i>C</i> 2/ <i>c</i>
Unit cell dimensions	<i>a</i> = 47.956(1) Å <i>b</i> = 21.634(2) Å <i>c</i> = 13.878(1) Å α = 90° β = 92.020(12)° γ = 90°
Volume (Å ³)	14389(4)
Z	8
Density (calculated) (g·cm ⁻³)	1.102
Absorption coefficient (mm ⁻¹)	0.061
F(000)	5084
Crystal size (mm ³)	0.10 x 0.05 x 0.05
Crystal habit	Colourless thin plates
Theta range for data collection	0.84° to 27.42°
Index ranges	-61 ≤ <i>h</i> ≤ 62 -26 ≤ <i>k</i> ≤ 27 -18 ≤ <i>l</i> ≤ 18
Reflections collected	54317
Independent reflections (data with <i>I</i> > 2σ(<i>I</i>))	16976 (11154)
Resolution (Å)	0.76
Data multiplicity (max resltn)	3.13 (2.89)
<i>I</i> /σ(<i>I</i>) (max resltn)	7.73 (3.53)
<i>R</i> _{merge} (max resltn)	0.0816 (0.2434)
Data completeness (max resltn)	98.9% (97.6%)
Refinement method	Full-matrix least-squares on <i>F</i> ²
Data / restraints / parameters	16976 / 16 / 811
Goodness-of-fit on <i>F</i> ²	1.024
Final <i>R</i> indices [<i>I</i> > 2σ(<i>I</i>)]	<i>R</i> ₁ = 0.0603, <i>wR</i> ₂ = 0.1544
<i>R</i> indices (all data)	<i>R</i> ₁ = 0.0978, <i>wR</i> ₂ = 0.1760
Largest diff. peak and hole (eÅ ⁻³)	0.439 and -0.410
R.M.S. deviation from mean (eÅ ⁻³)	0.064



$$^a R_1 = \frac{\sum \|F_o\| - \|F_c\|}{\sum \|F_o\|}, wR_2 = \left\{ \frac{\sum [w(F_o^2 - F_c^2)^2]}{\sum [w(F_o^2)^2]} \right\}^{1/2}.$$

5.6 References

- (1) Horcas I., Fernández R., Gómez-Rodríguez J. M., Colchero J., Gómez-Herrero J., Baro A. M. *Rev. sci. instrum.* **2007**, 78, 13705.
- (2) Lausi A., Polentarutti M., Onesti S., Plaisier J. R., Busetto E., Bais G., Barba L., Cassetta A., Campi G., Lamba D., Pifferi A., Mande S. C., Sarma D. D., Sharma S. M., Paolucci G. *Eur. Phys. J. Plus*, **2015**, 130, 1.
- (3) Kabsch W. XDS. *Acta Crystallograph. D*, **2010**, 66, 125.
- (4) Winn M. D., Ballard C. C., Cowtan K. D., Dodson E. J., Emsley P., Evans P. R., Keegan R. M., Krissinel E. B., Leslie A. G. W., McCoy A., McNicholas S. J., Murshudov G. N., Pannu N. S., Potterton E. A., Powell H. R., Read R. J., Vagin A., Wilson K. S., *Acta Crystallograph. D*, **2011**, 67, 235.
- (5) Evans P. R., Murshudov G. N. *Acta Crystallograph. D*. **2013**, 69, 1204.
- (6) Sheldrick G. M. *Acta Crystallograph. A*, **2015**, 71, 3.
- (7) Sheldrick G. M. *Acta Crystallograph. C*, **2015**, 71, 3.
- (8) Emsley P., Lohkamp, B., Scott, W. G., Cowtan K. *Acta Crystallograph. D*, **2010**, 66, 486.

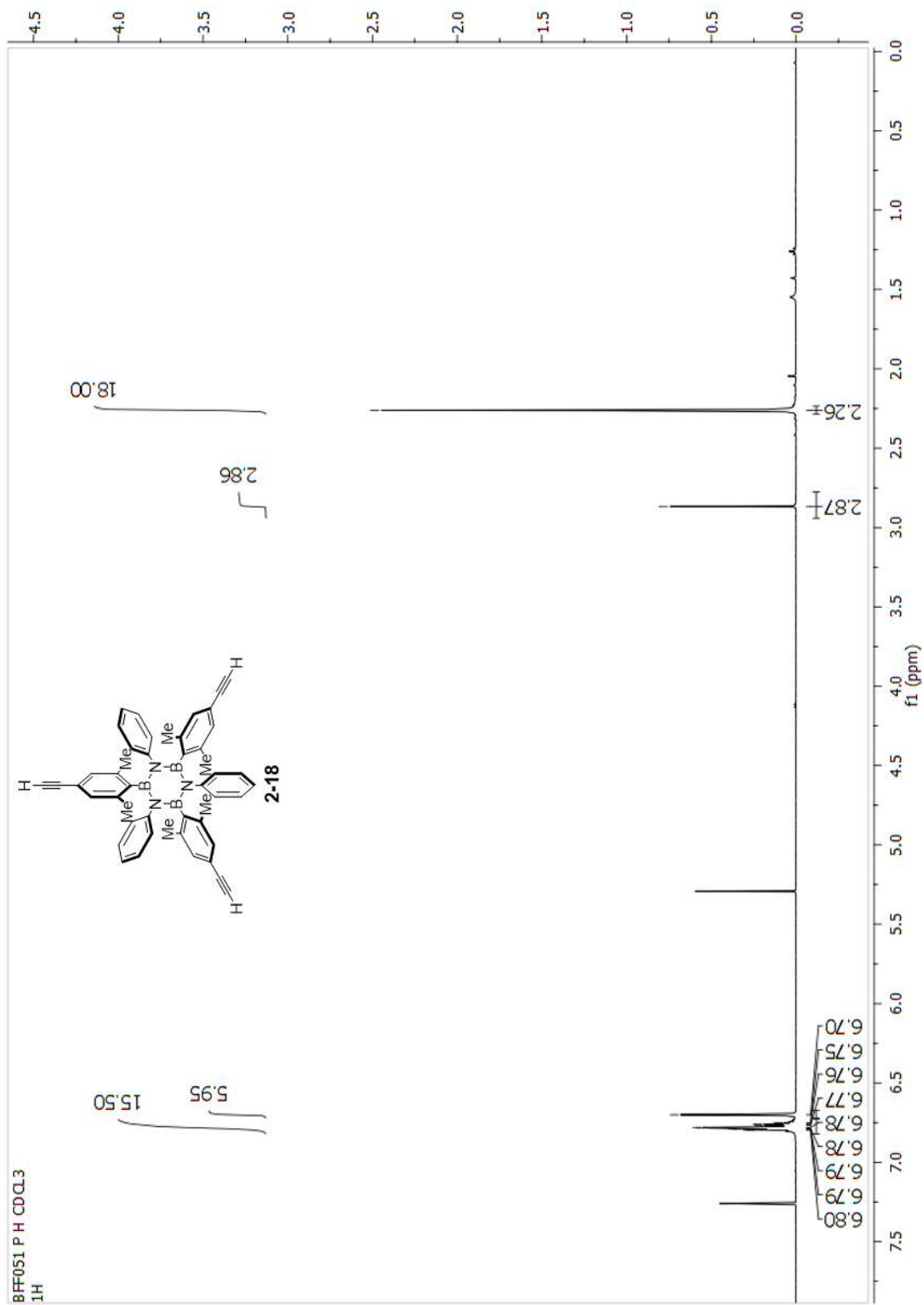
APPENDIX A

NMR, MS and GPC characterisations

Characterisation of 2-18	206
Characterisation of 2-19	209
Characterisation of 2-21	212
Characterisation of 2-23	214
Characterisation of 2-24	216
Characterisation of 2-26	219
Characterisation of 2-28	221
Characterisation of 2-29a	224
Characterisation of 2-29b	228
Characterisation of 2-30	231
Characterisation of 2-31	235
Characterisation of 2-32	238
Characterisation of 2-34	240
Characterisation of 2-35a	243
Characterisation of 2-35b	246
Characterisation of 2-36	249
Characterisation of 2-38	252
Characterisation of 2-39	254
Characterisation of 2-41	256
Characterisation of 2-42	258
Characterisation of 2-43	260
Characterisation of 2-44a	261
Characterisation of 2-45	263
Characterisation of 2-47	265
Characterisation of 2-48a	267
Characterisation of 2-48b	269
Characterisation of 2-49	271

Characterisation of 2-50a	273
Characterisation of 2-52	275
Characterisation of 2-54	277
Characterisation of 2-55	279
Characterisation of 2-56	281
Characterisation of 2-57	285
Characterisation of 2-58	289
Characterisation of 2-59	290
Characterisation of 2-60	295
Characterisation of 2-61	300
Characterisation of 2-62	305
Characterisation of 2-63	307
Characterisation of 2-64	309
Characterisation of 2-65	311
Characterisation of 3-1	313
Characterisation of 3-3	316
Characterisation of 3-4a	318
Characterisation of 3-5	320
Characterisation of 3-14 <i>cc + ct</i>	321
Characterisation of 3-15	323
Characterisation of 4-6	325
Characterisation of 4-8	328

Characterisation of 2-18

Figure A.1: $^1\text{H-NMR}$, 400 MHz, CDCl_3 .

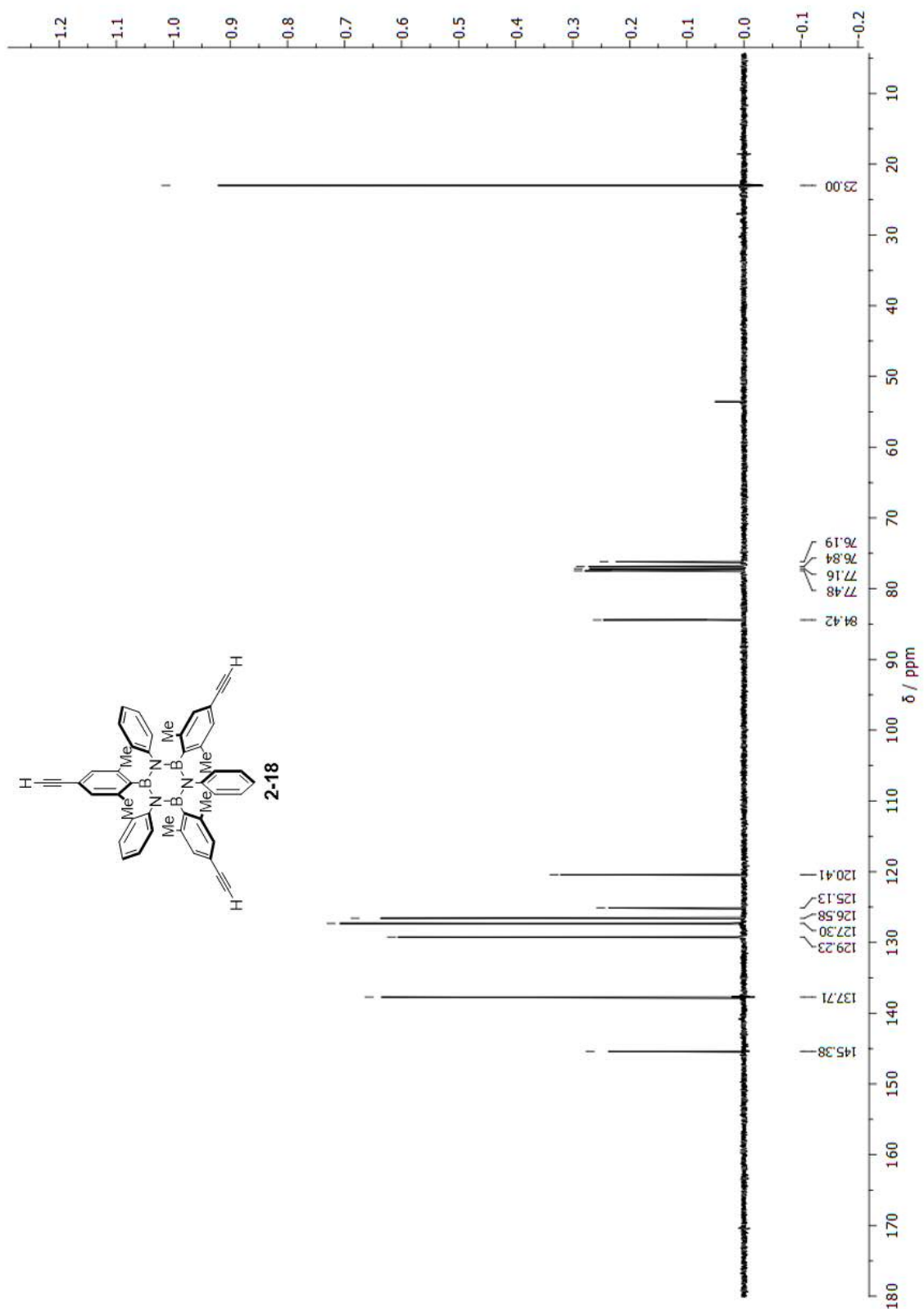


Figure A.2: ^{13}C -NMR, 100 MHz, CDCl_3 .

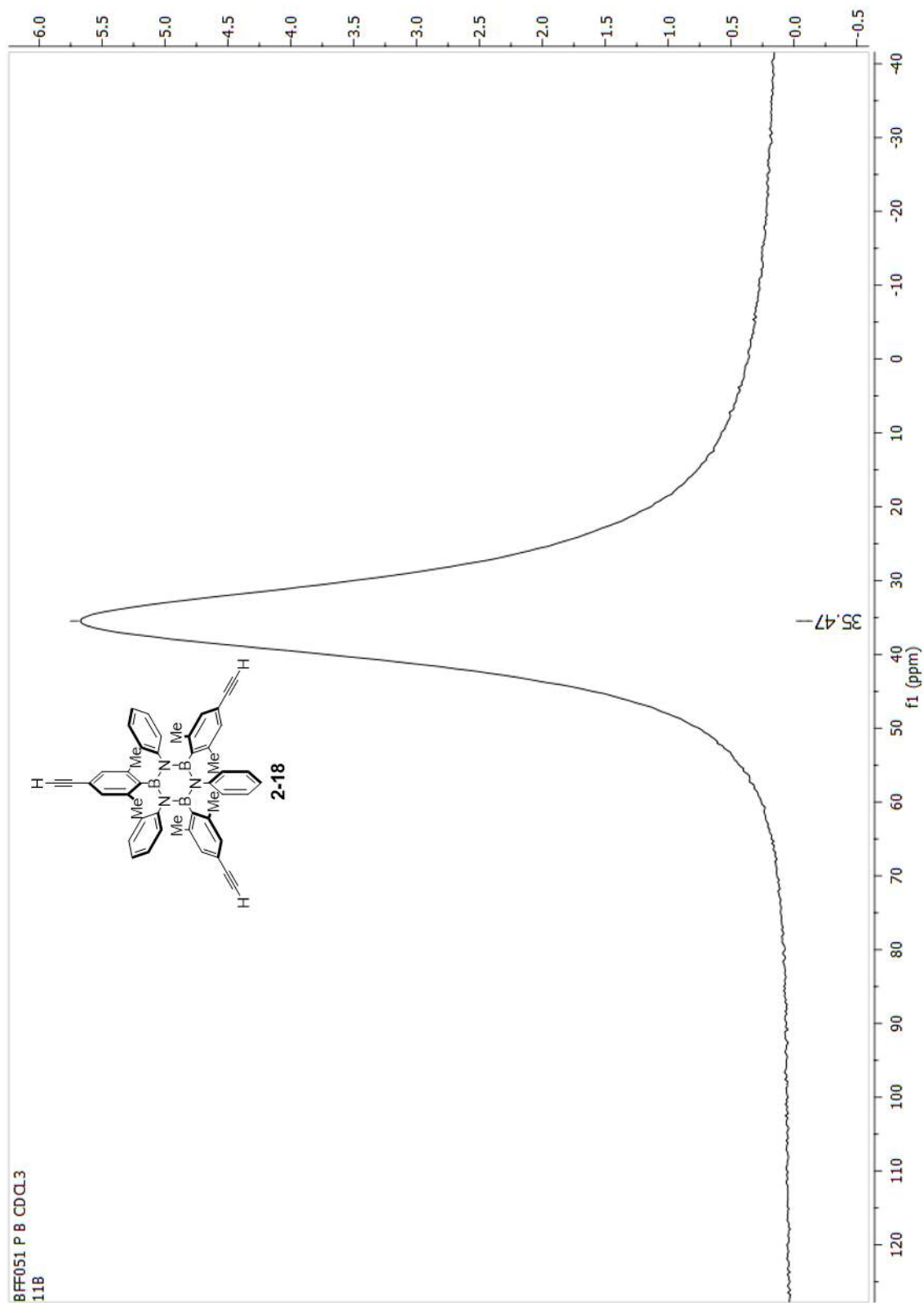


Figure A.3: ^{11}B -NMR, 128 MHz, CDCl_3 .

Characterisation of 2-19

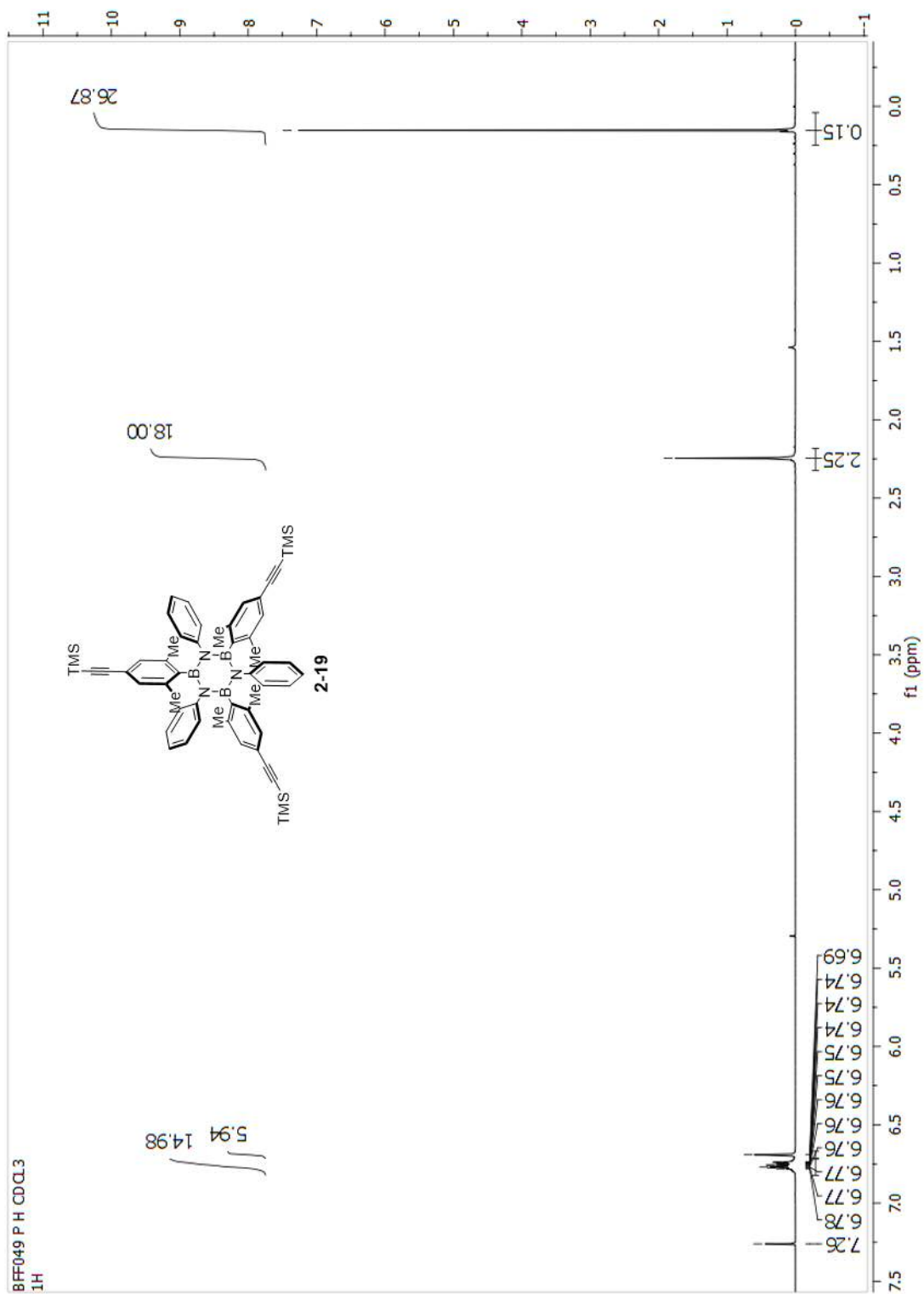


Figure A.4: $^1\text{H-NMR}$, 400 MHz, CDCl_3 .

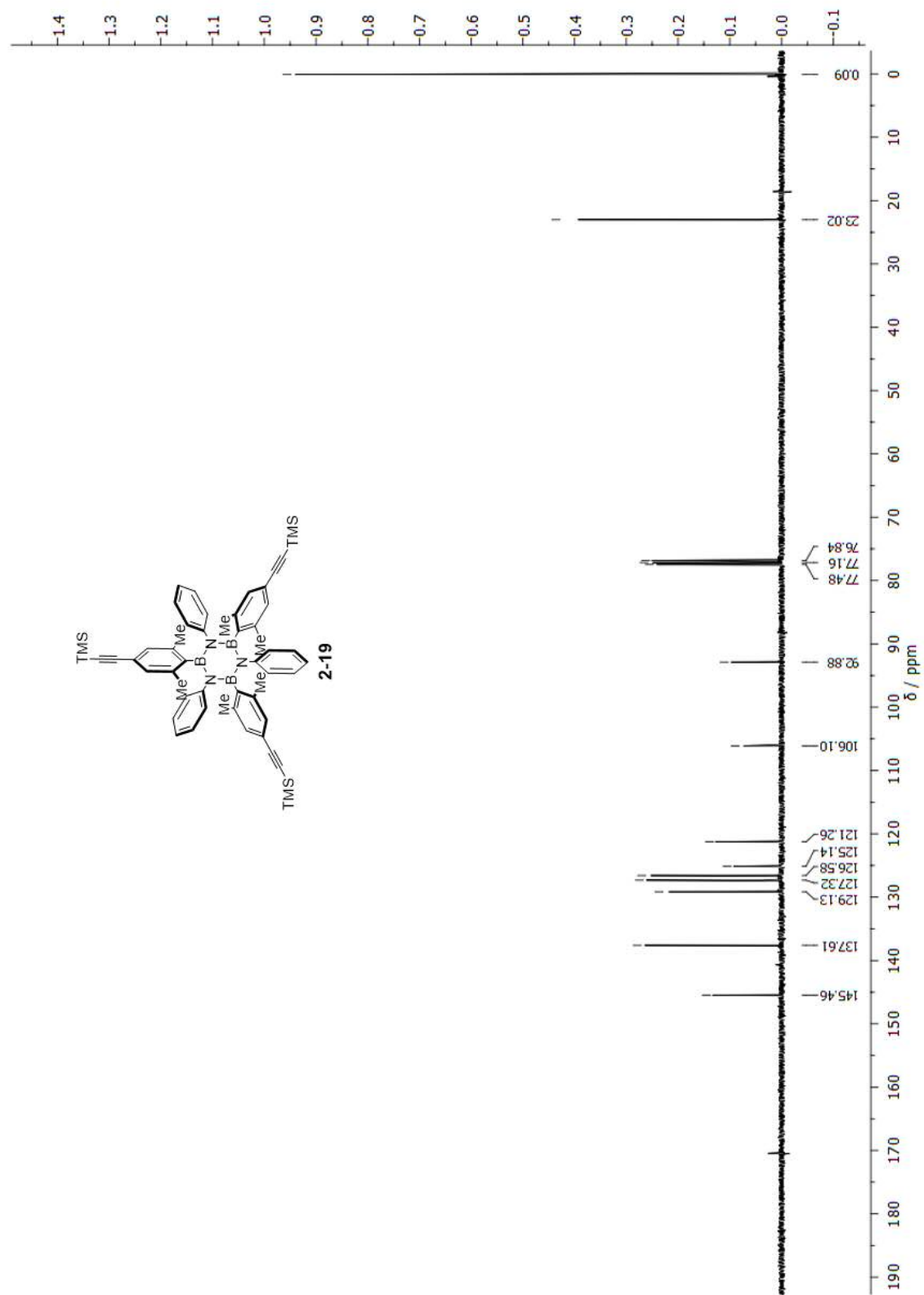


Figure A.5: ^{13}C -NMR, 100 MHz, CDCl_3 .

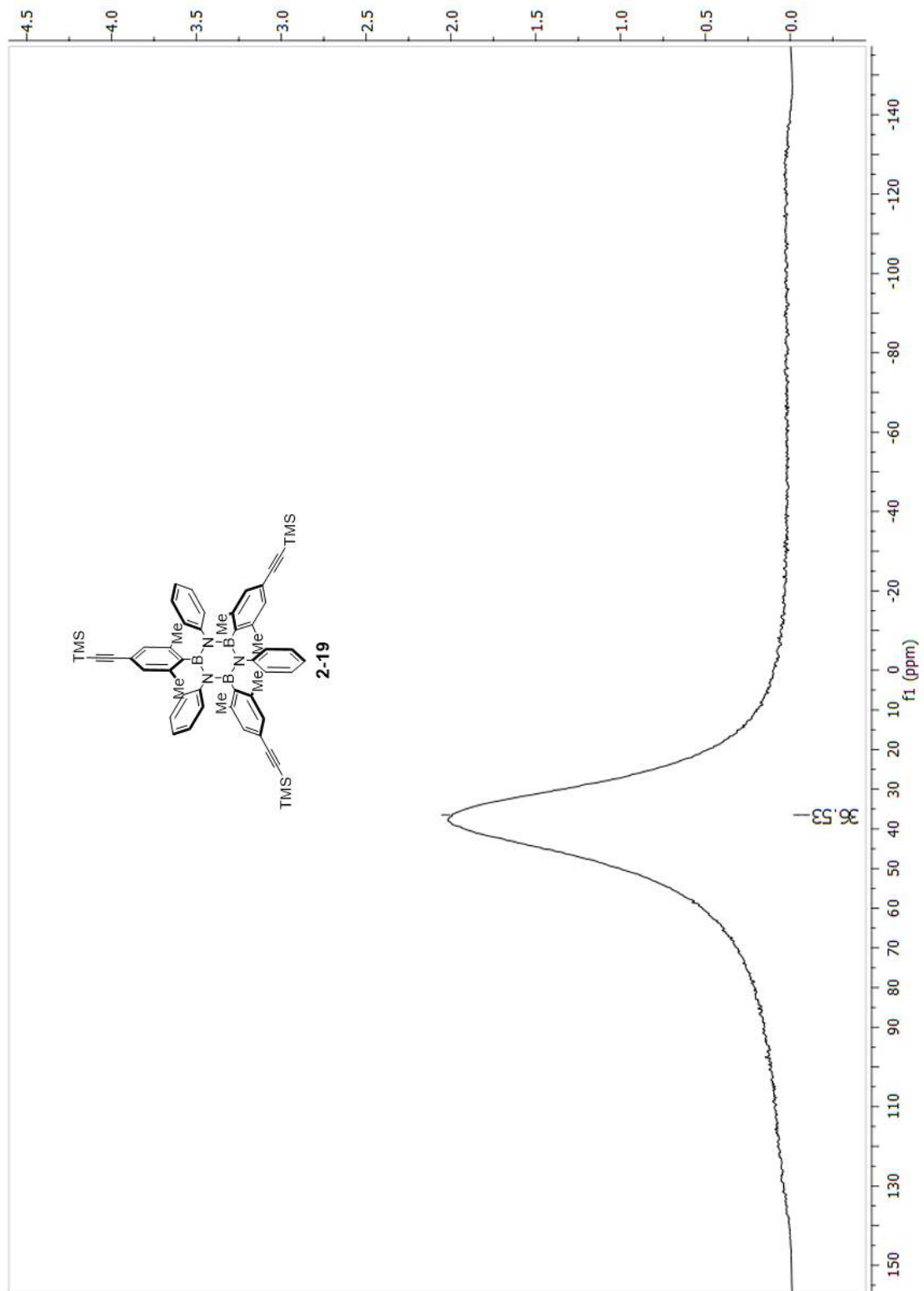
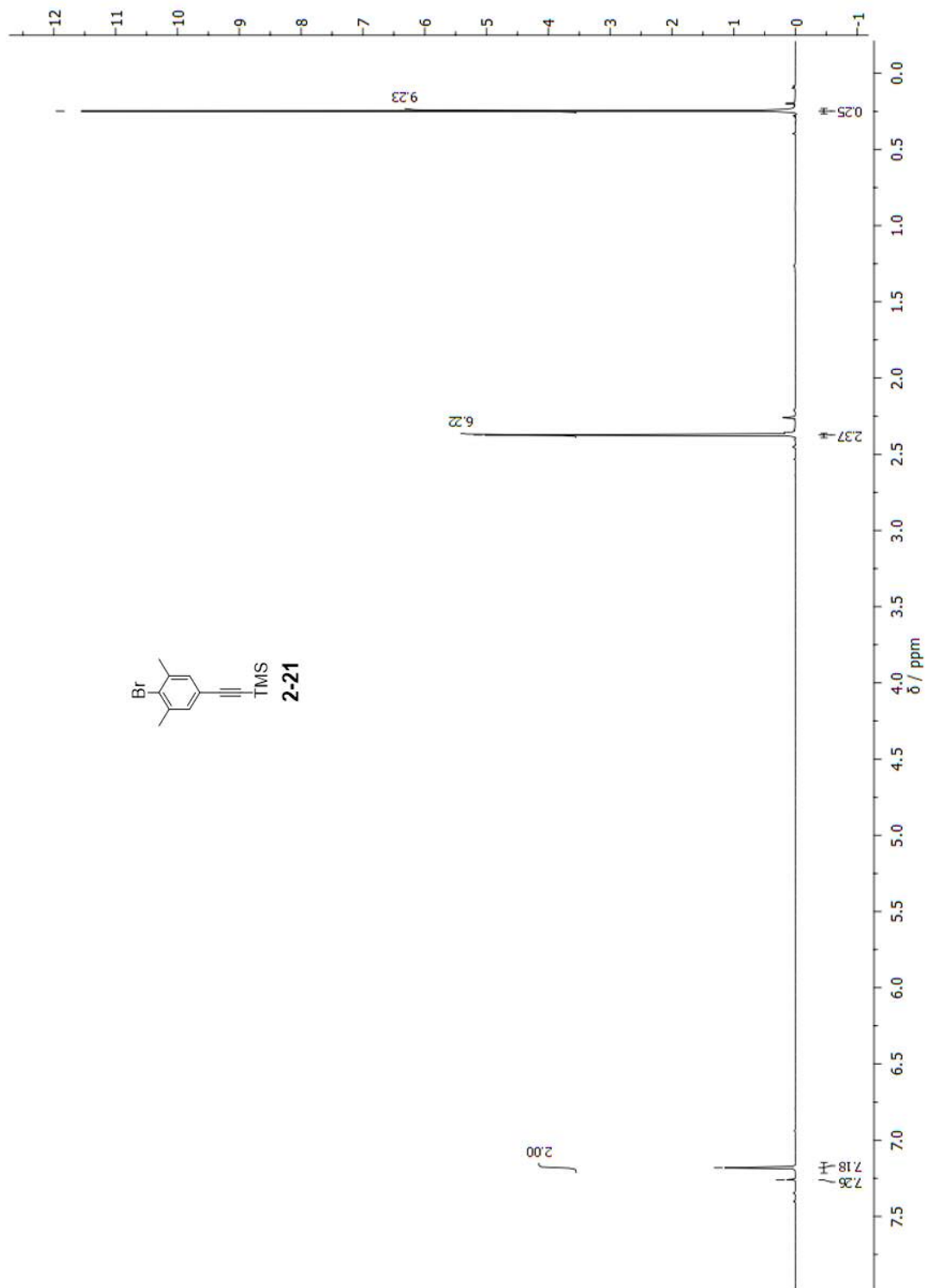


Figure A.6: ^{11}B -NMR, 128 MHz, CDCl_3 .

Characterisation of 2-21

Figure A.7: $^1\text{H-NMR}$, 400 MHz, CDCl_3 .

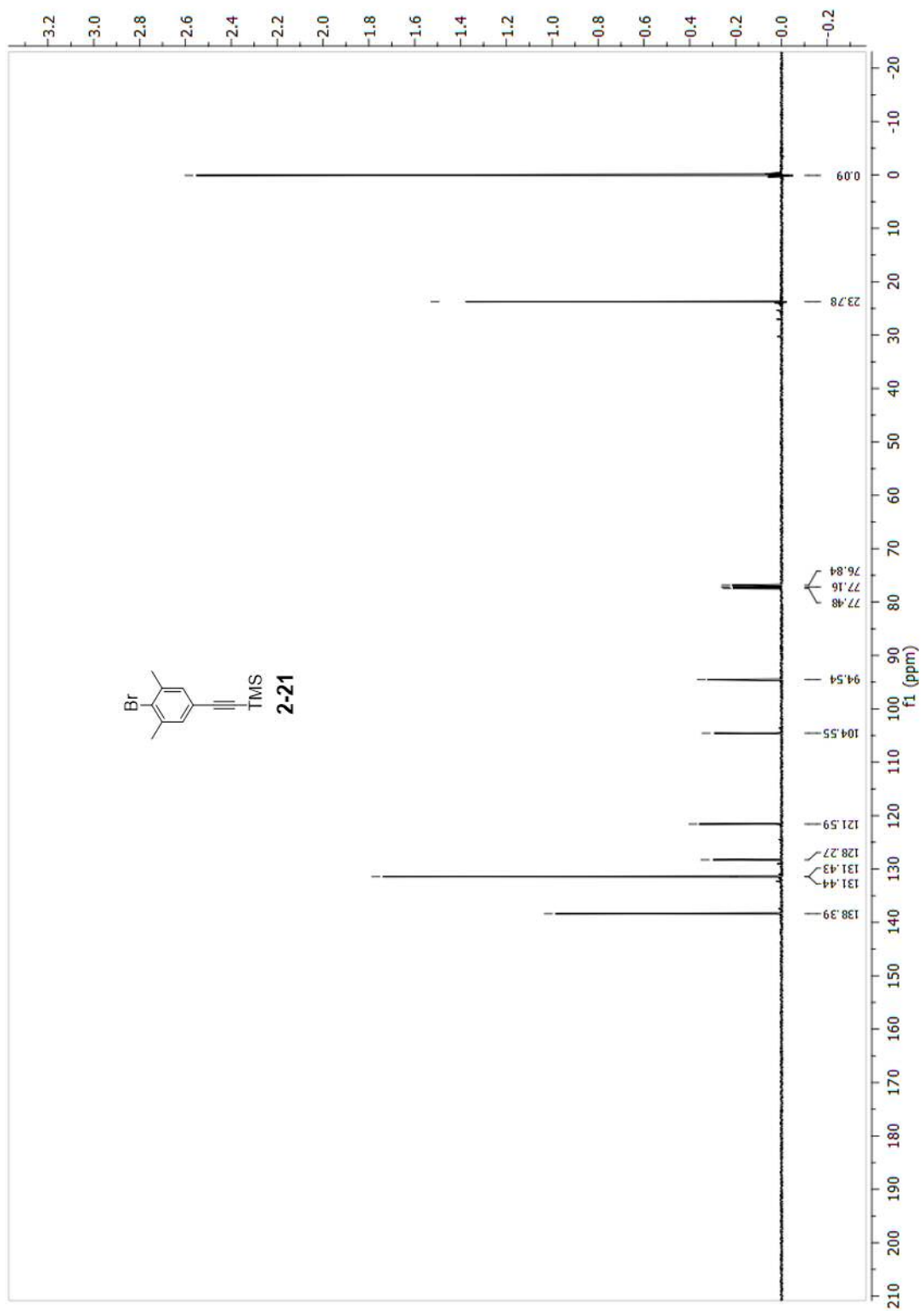
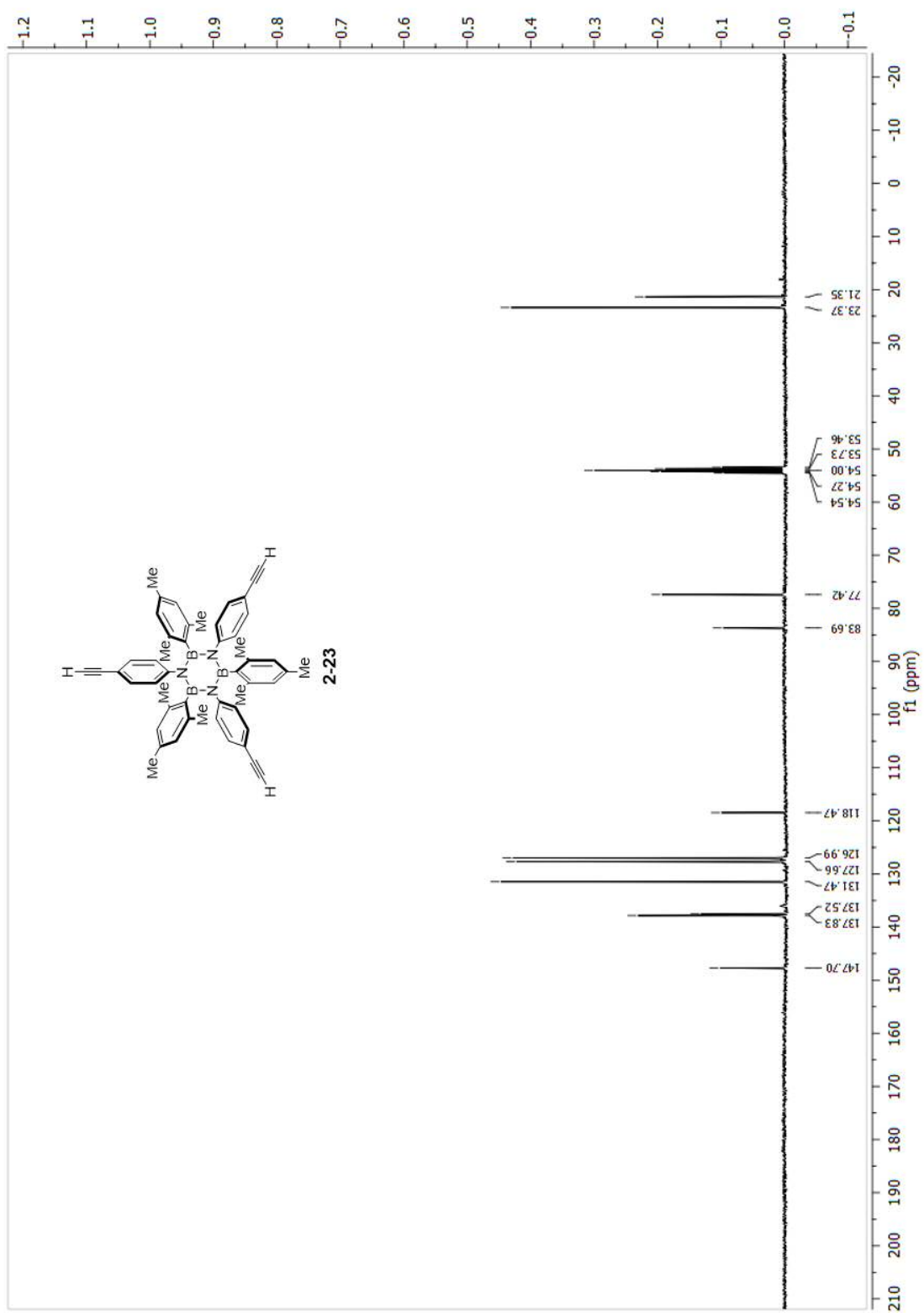


Figure A.8: ^{13}C -NMR, 100 MHz, CDCl_3 .

Characterisation of 2-23

Figure A.9: ^{13}C -NMR, 100 MHz, CDCl_3 .

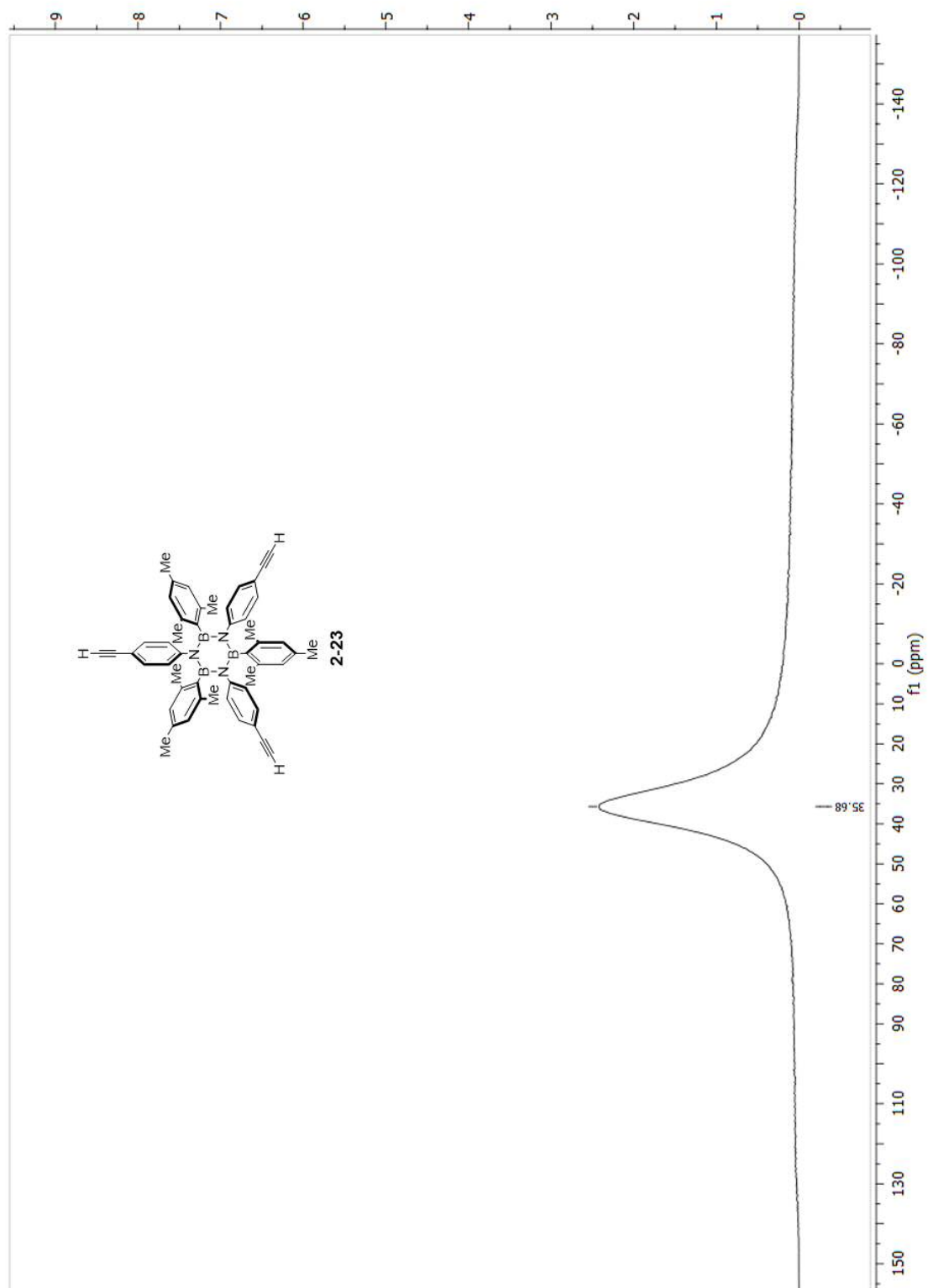
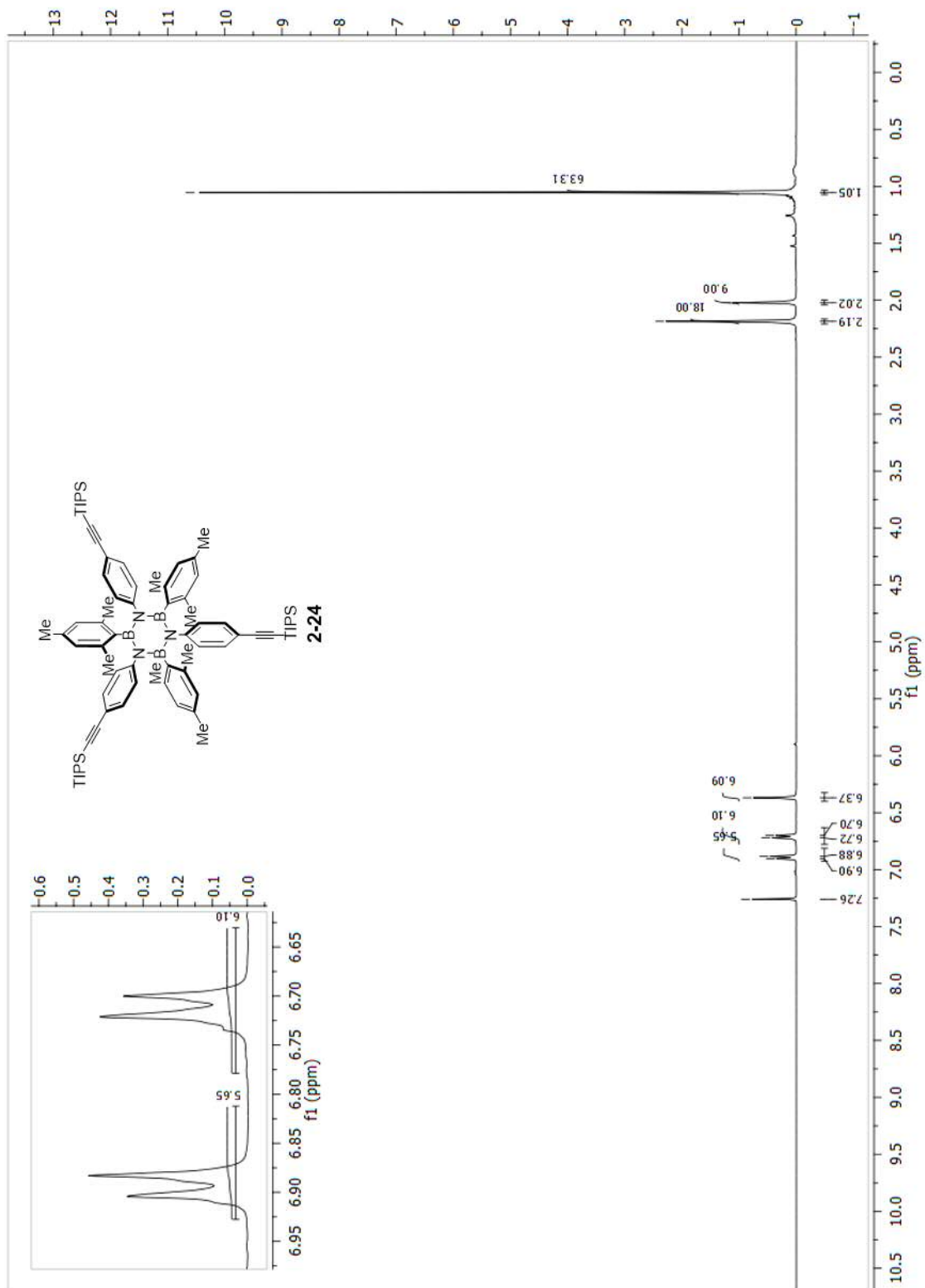


Figure A.10: ^{11}B -NMR, 128 MHz, CDCl_3

Characterisation of 2-24

Figure A.11: $^1\text{H-NMR}$, 400 MHz, CDCl_3 .

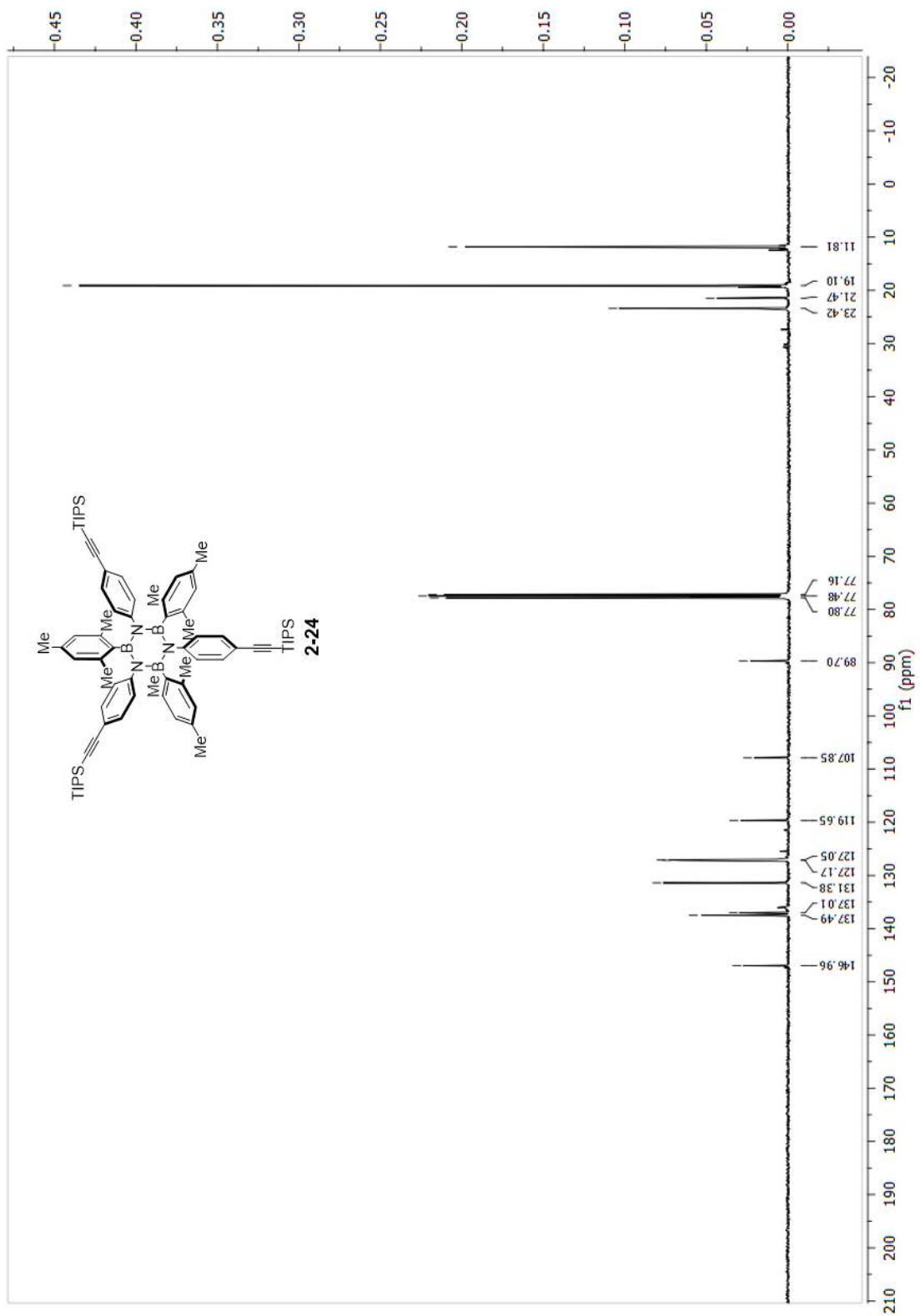


Figure A.12: ^{13}C -NMR, 100 MHz, CDCl_3 .

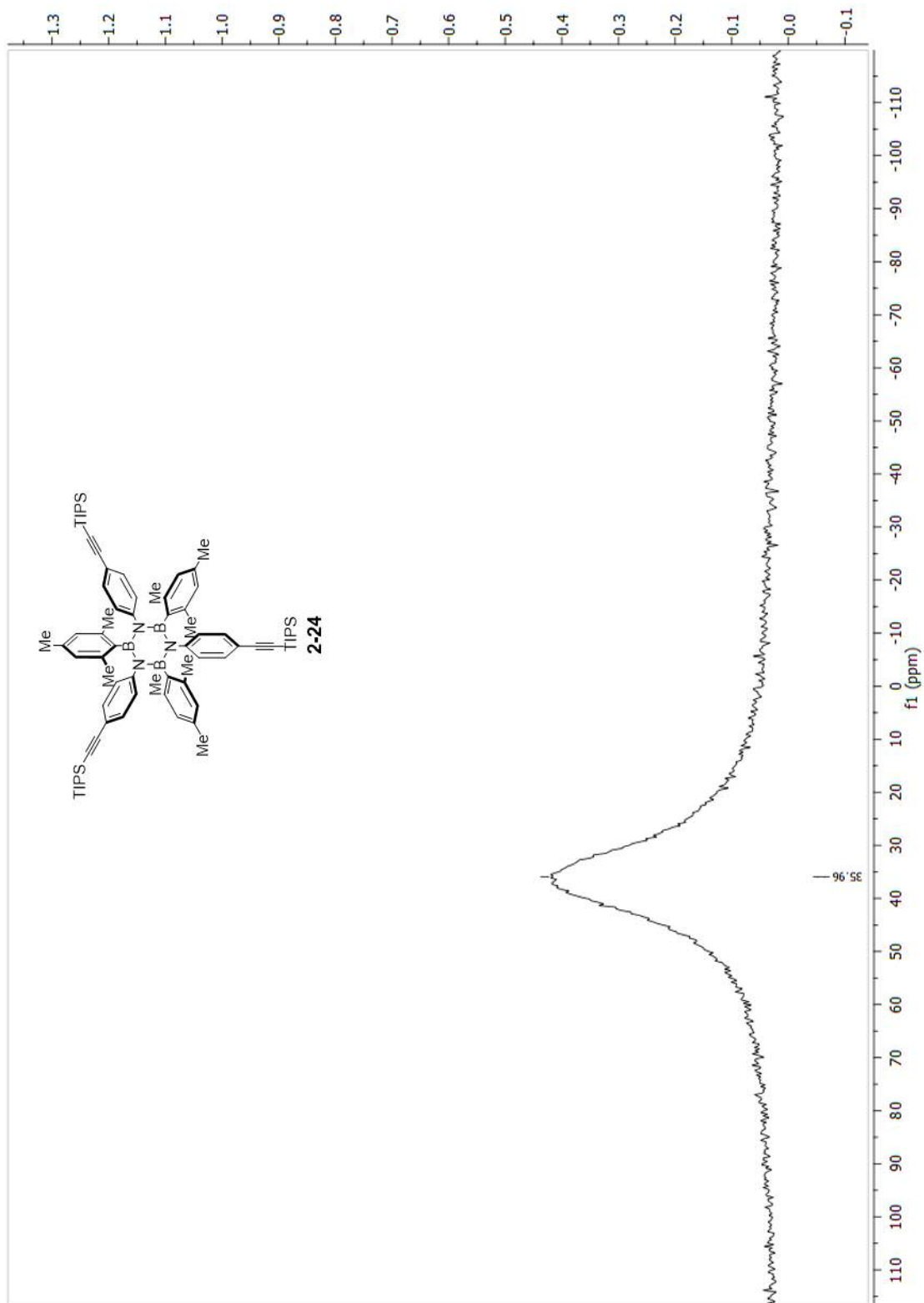


Figure A.13: ^{11}B -NMR, 128 MHz, CDCl_3 .

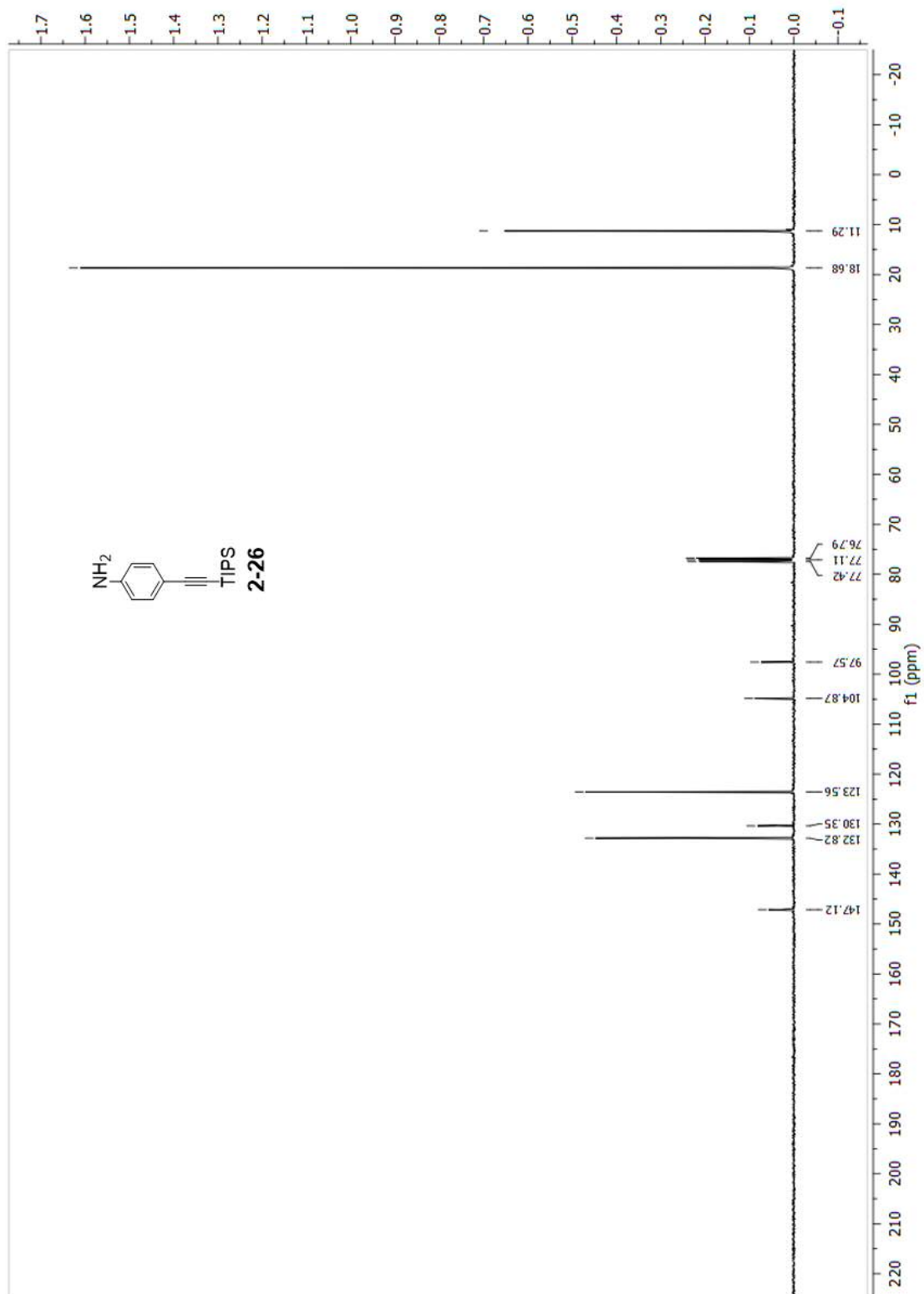
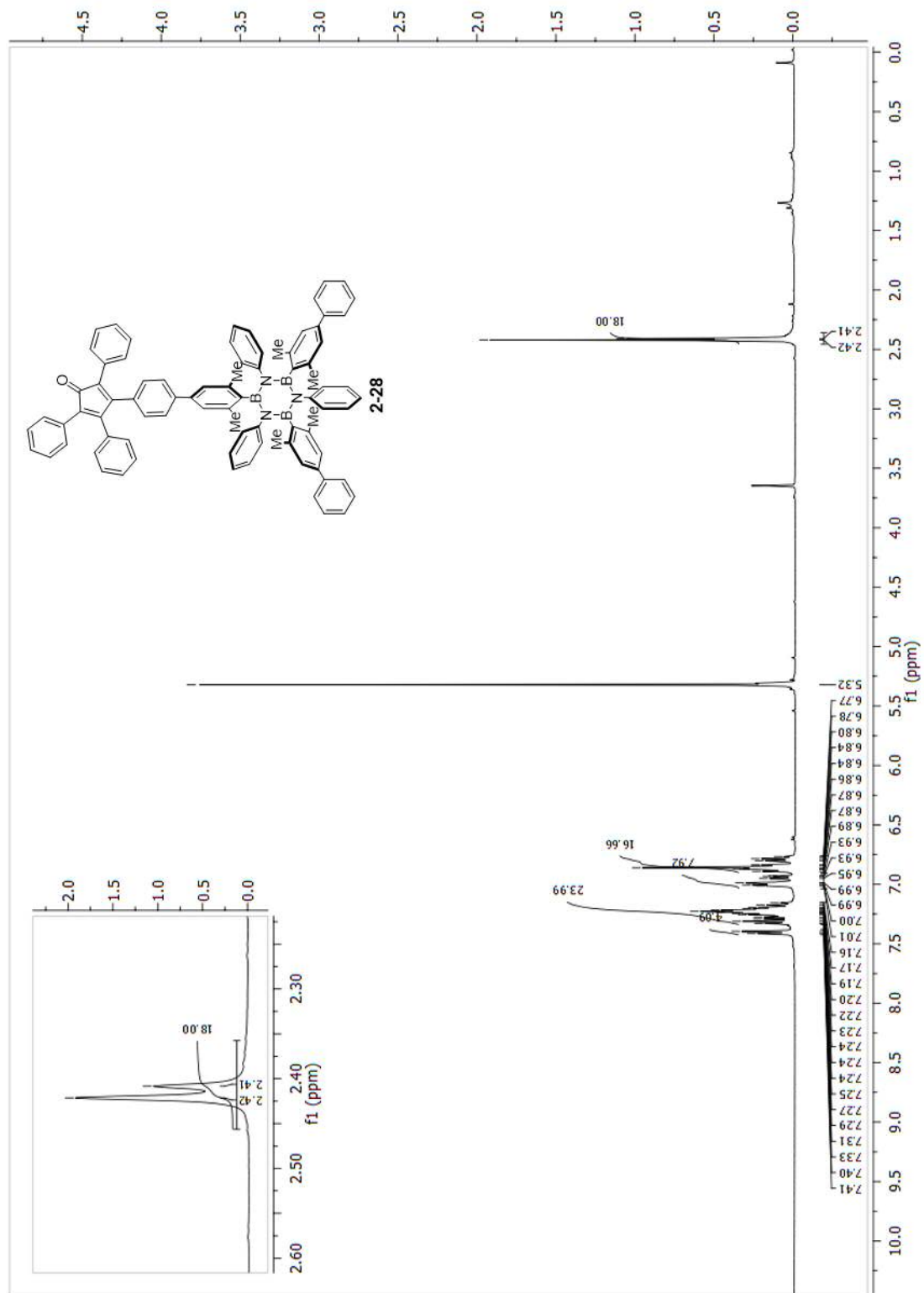


Figure A.15: ^{13}C -NMR, 100 MHz, CDCl_3 .

Characterisation of 2-28

Figure A.16: $^1\text{H-NMR}$, 400 MHz, CDCl_3 .

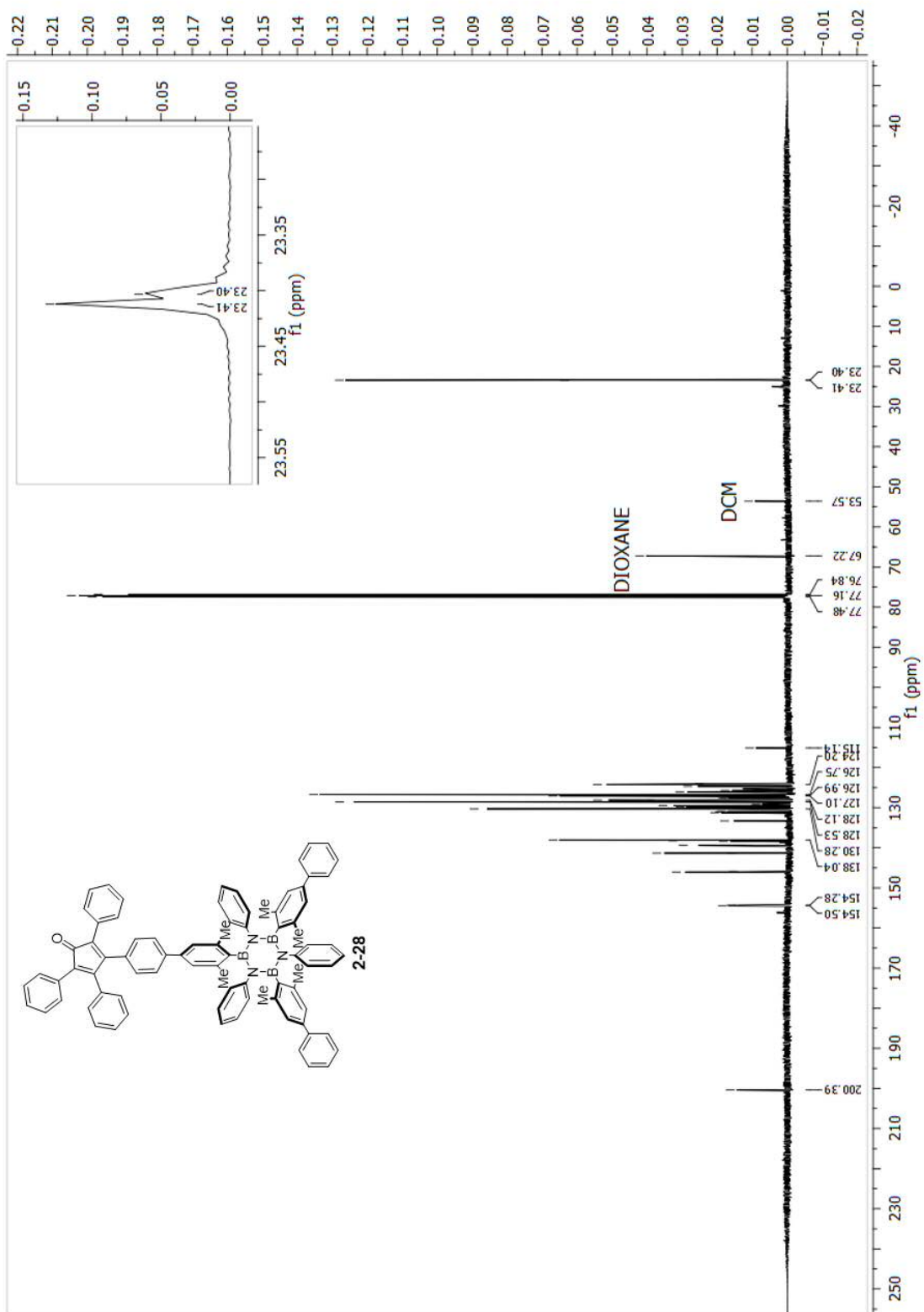


Figure A.17: ^{13}C -NMR, 100 MHz, CDCl_3 .

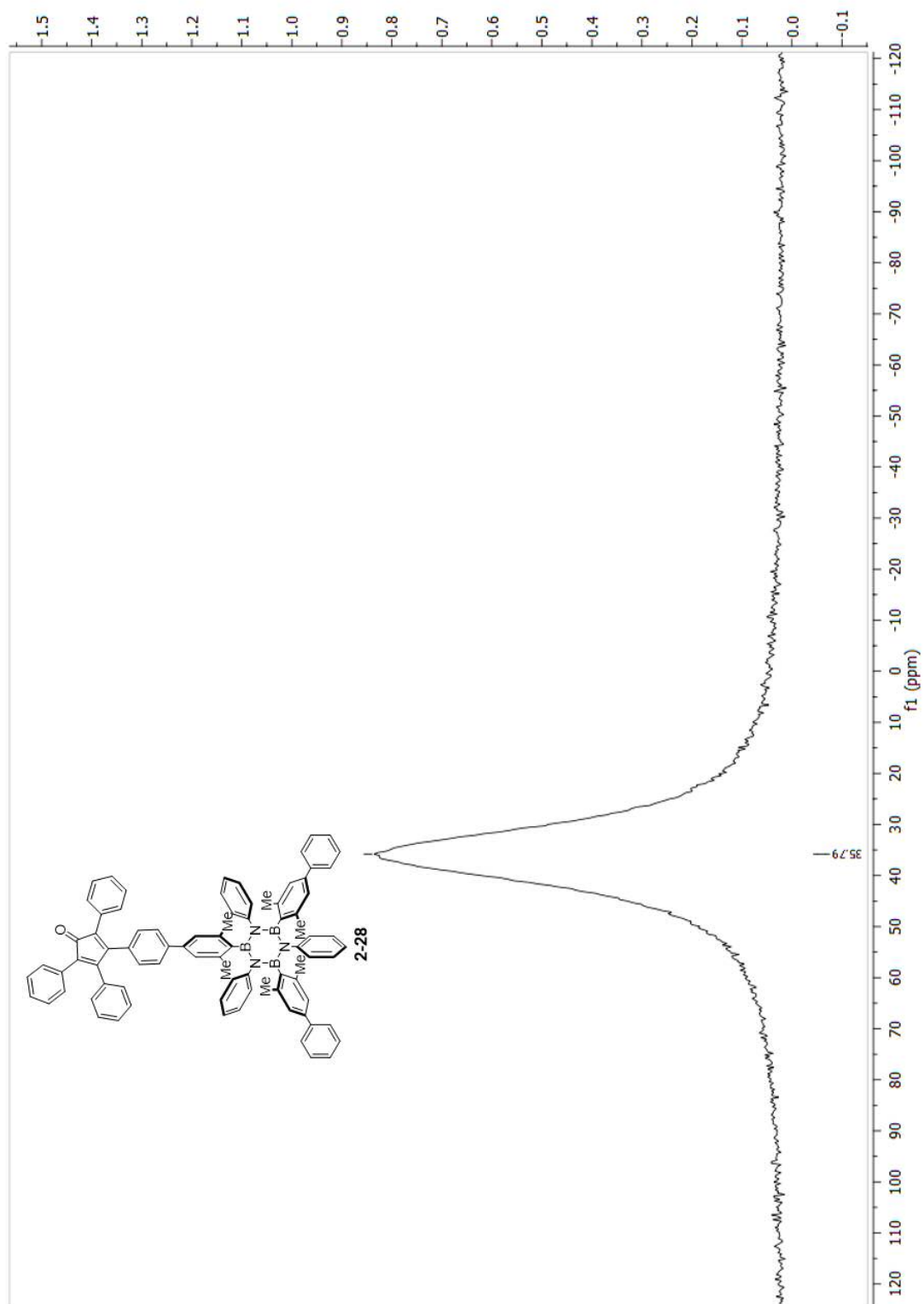
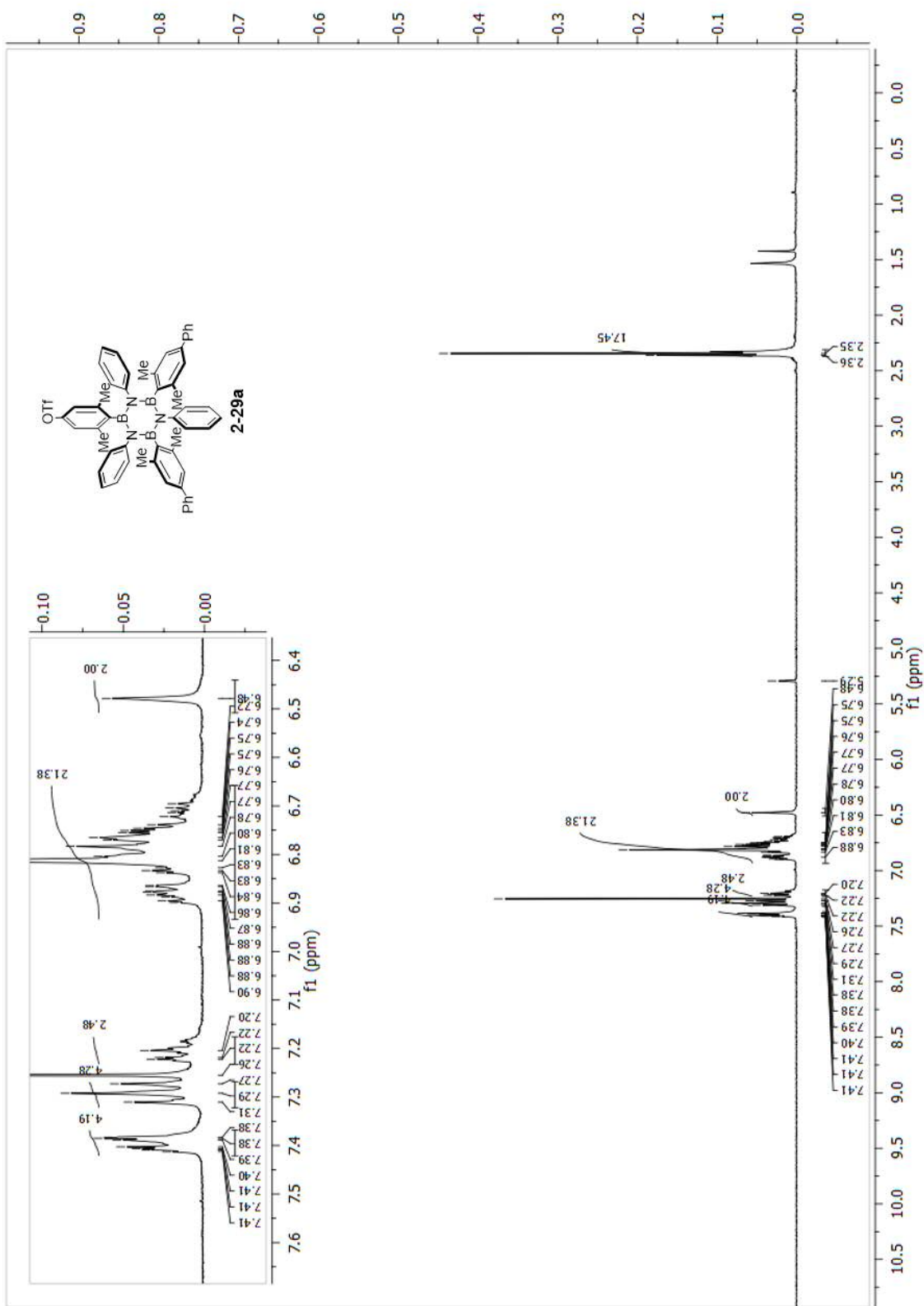


Figure A.18: ^{11}B -NMR, 128 MHz, CDCl_3 .

Characterisation of 2-29a

Figure A.19: $^1\text{H-NMR}$, 400 MHz, CDCl_3 .

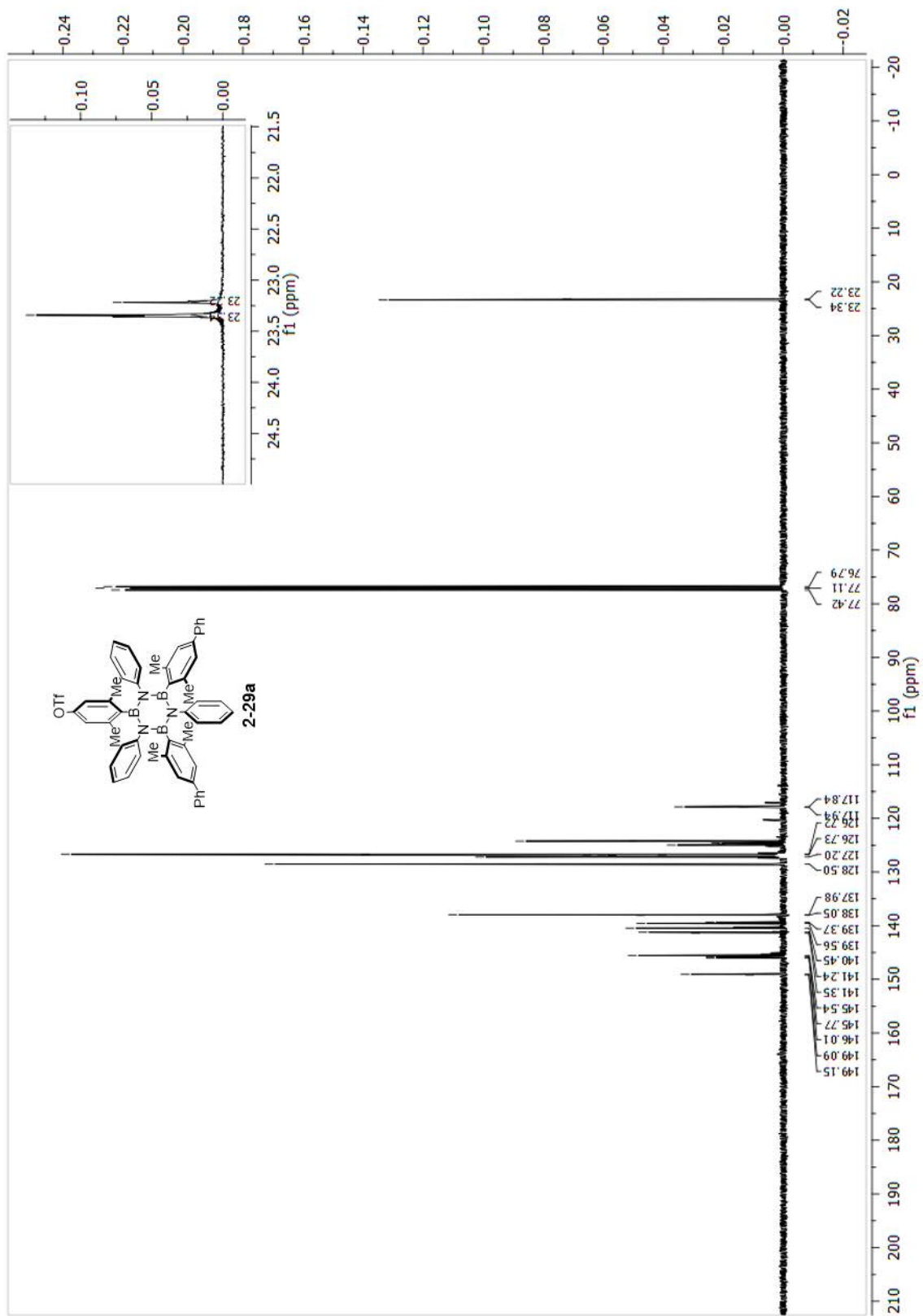


Figure A.20: $^{13}\text{C-NMR}$, 100 MHz, CDCl_3 .

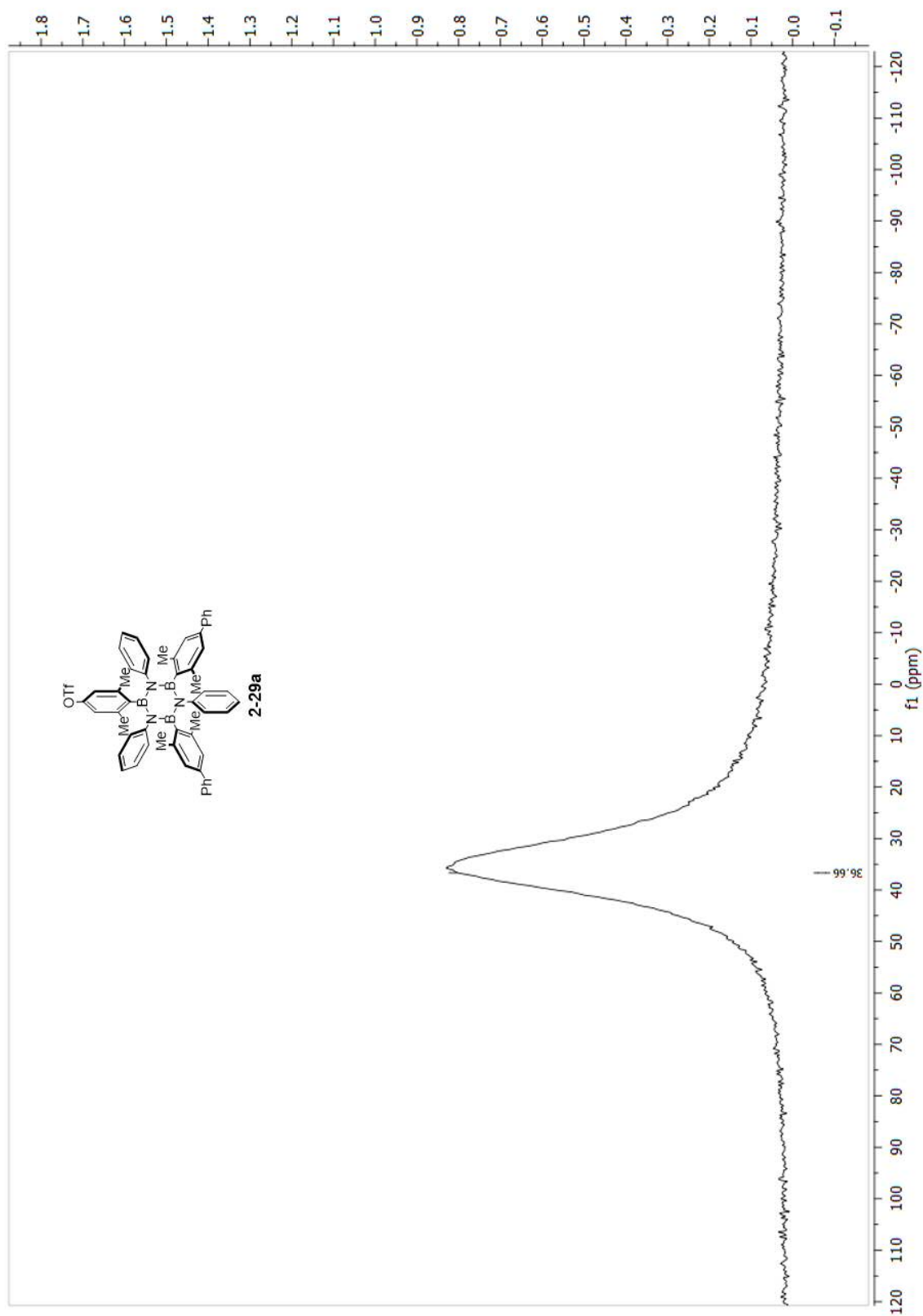


Figure A.21: ^{11}B -NMR, 128 MHz, CDCl_3 .

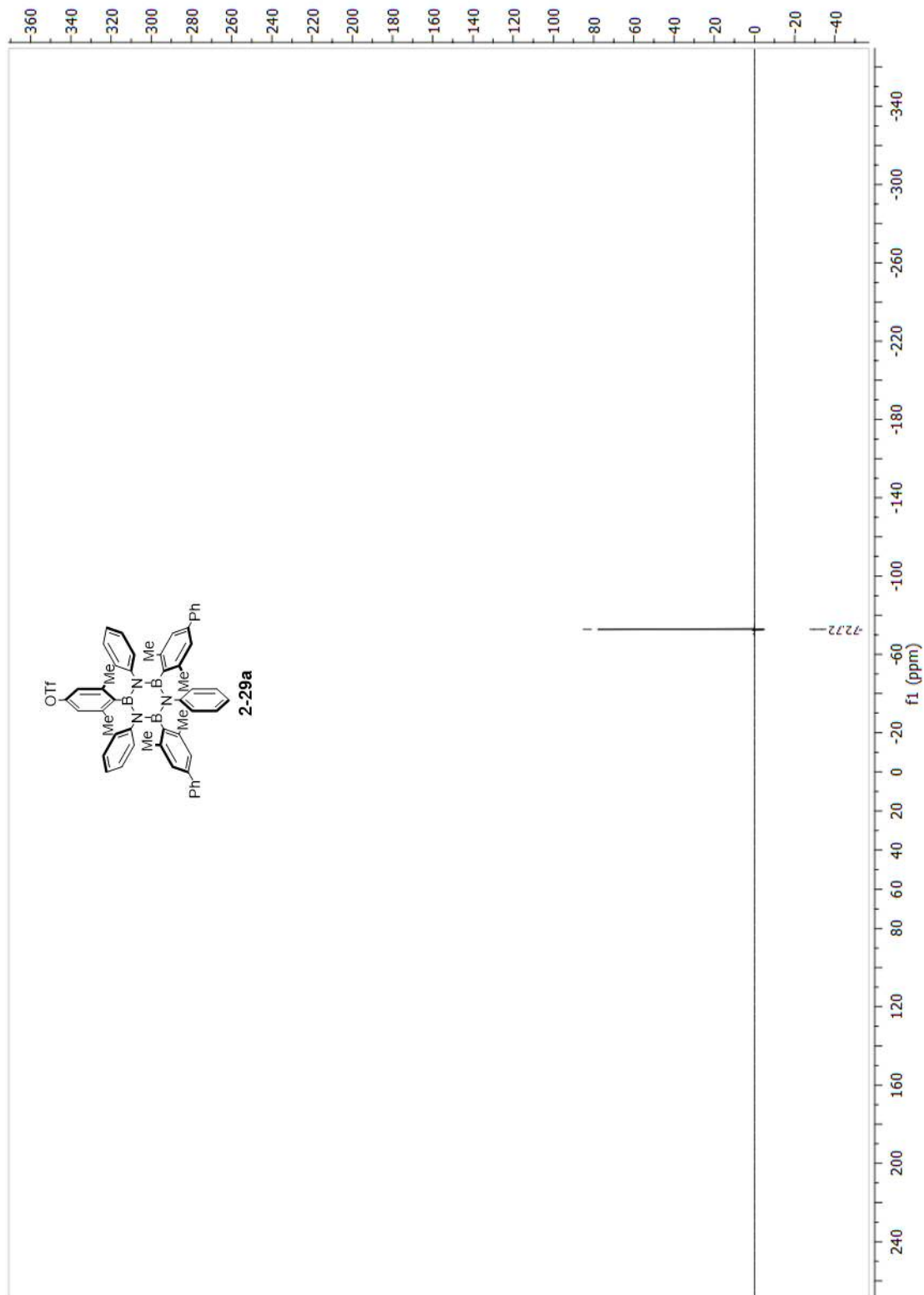
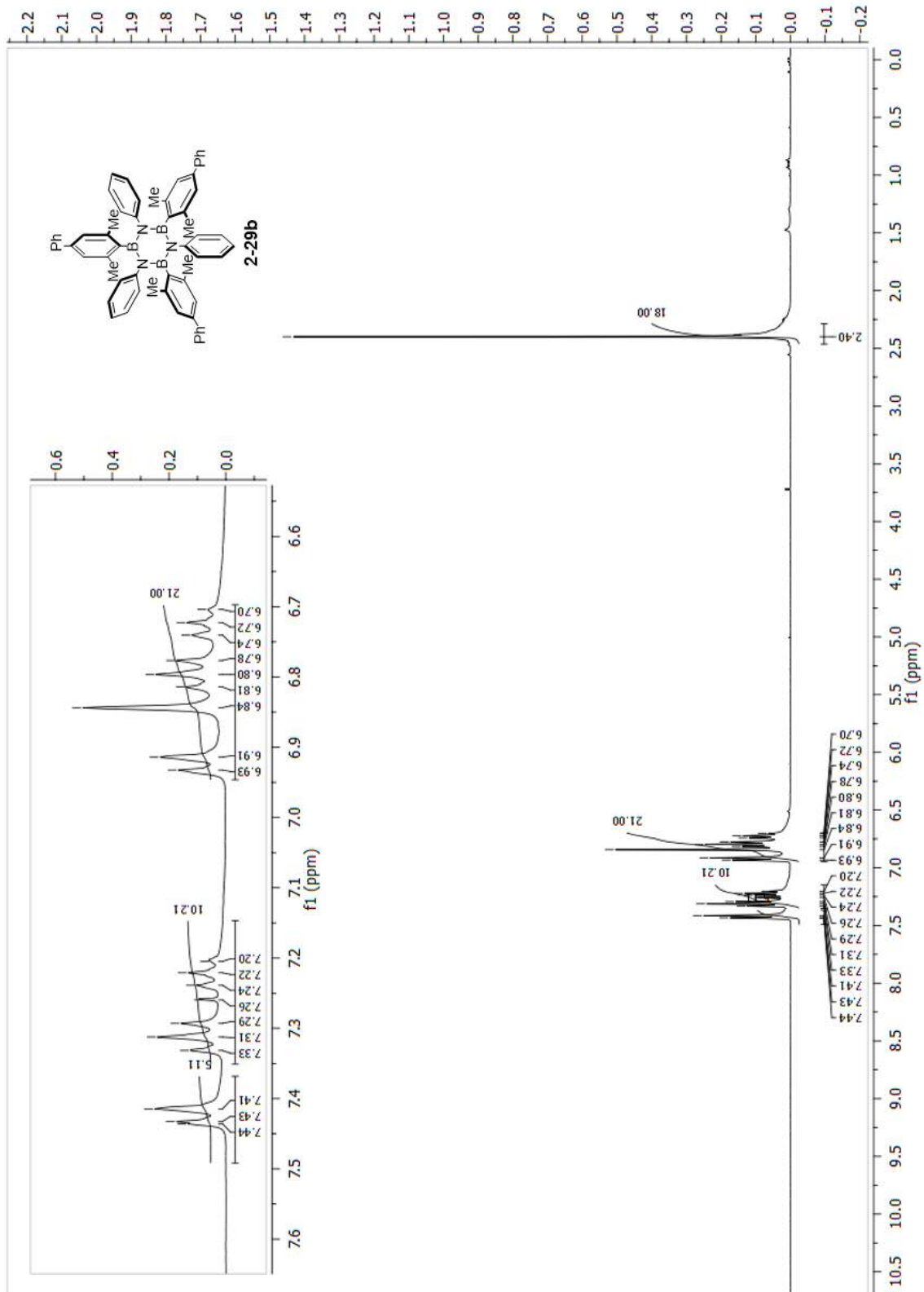


Figure A.22 ^{19}F -NMR, 376 MHz, CDCl_3 .

Characterisation of 2-29b

Figure A.23: $^1\text{H-NMR}$, 400 MHz, CDCl_3 .

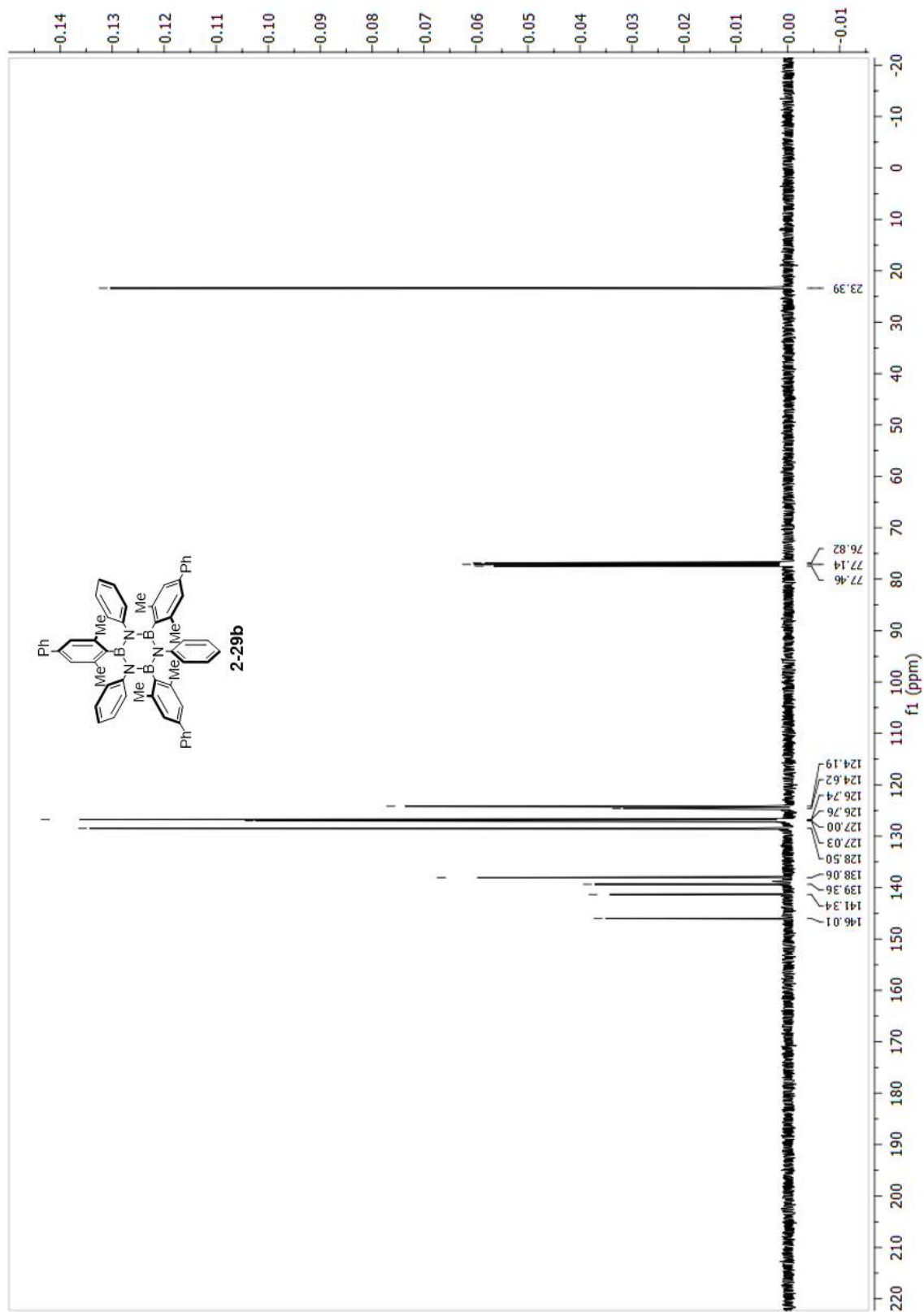


Figure A.24: ^{13}C -NMR, 100 MHz, CDCl_3 .

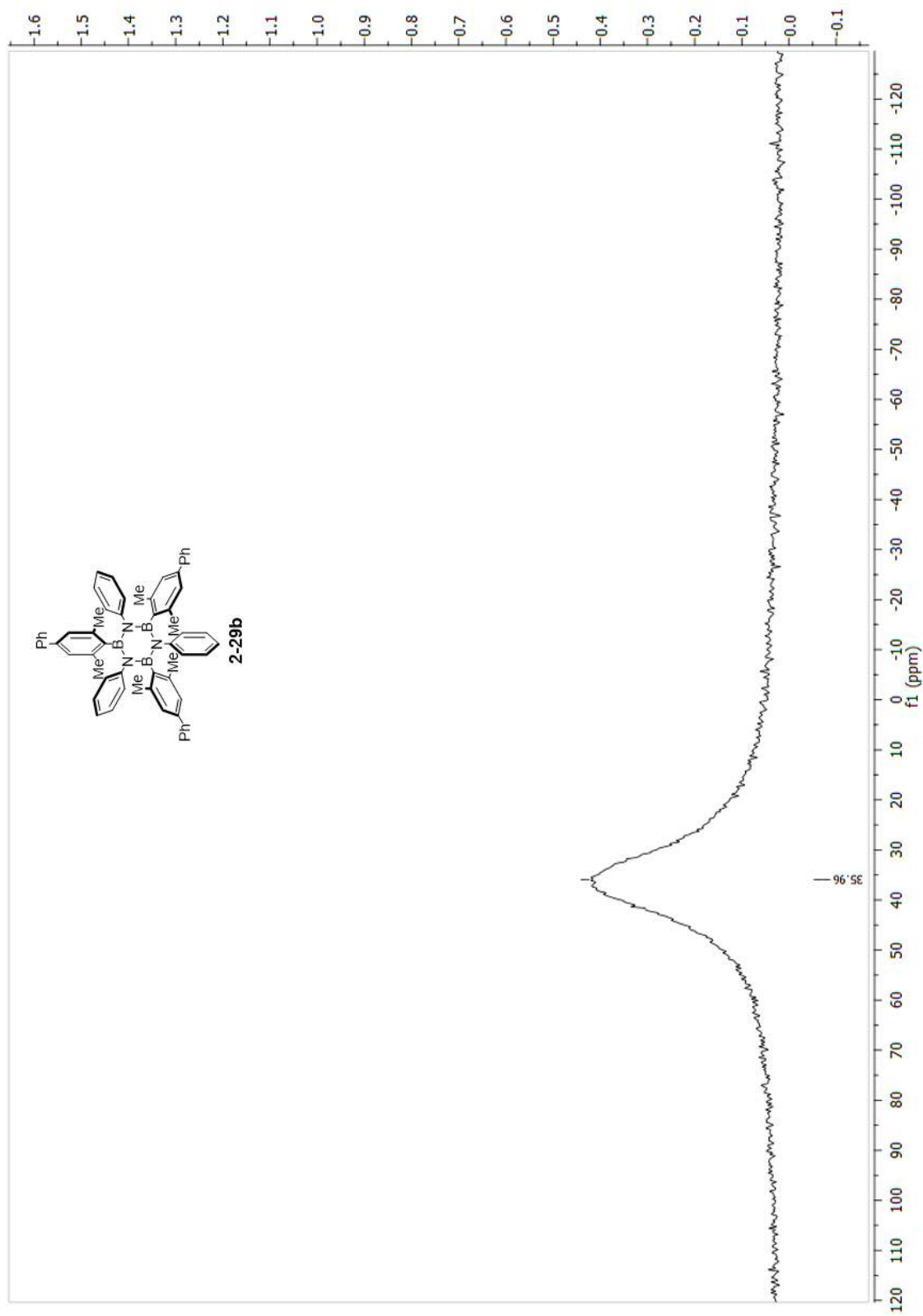
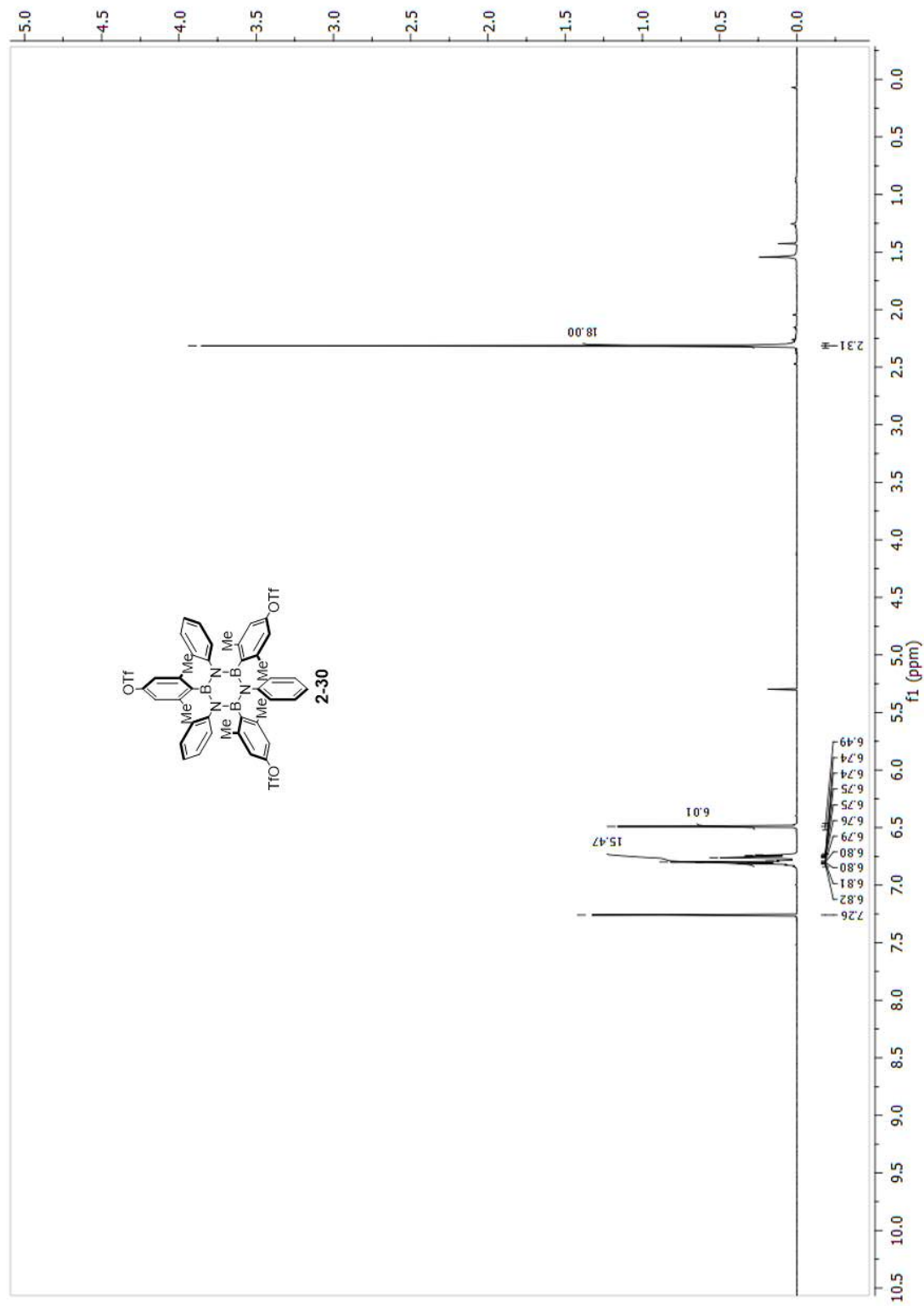


Figure A.25: ^{11}B -NMR, 128 MHz, CDCl_3 .

Characterisation of 2-30

Figure A.26: $^1\text{H-NMR}$, 400 MHz, CDCl_3 .

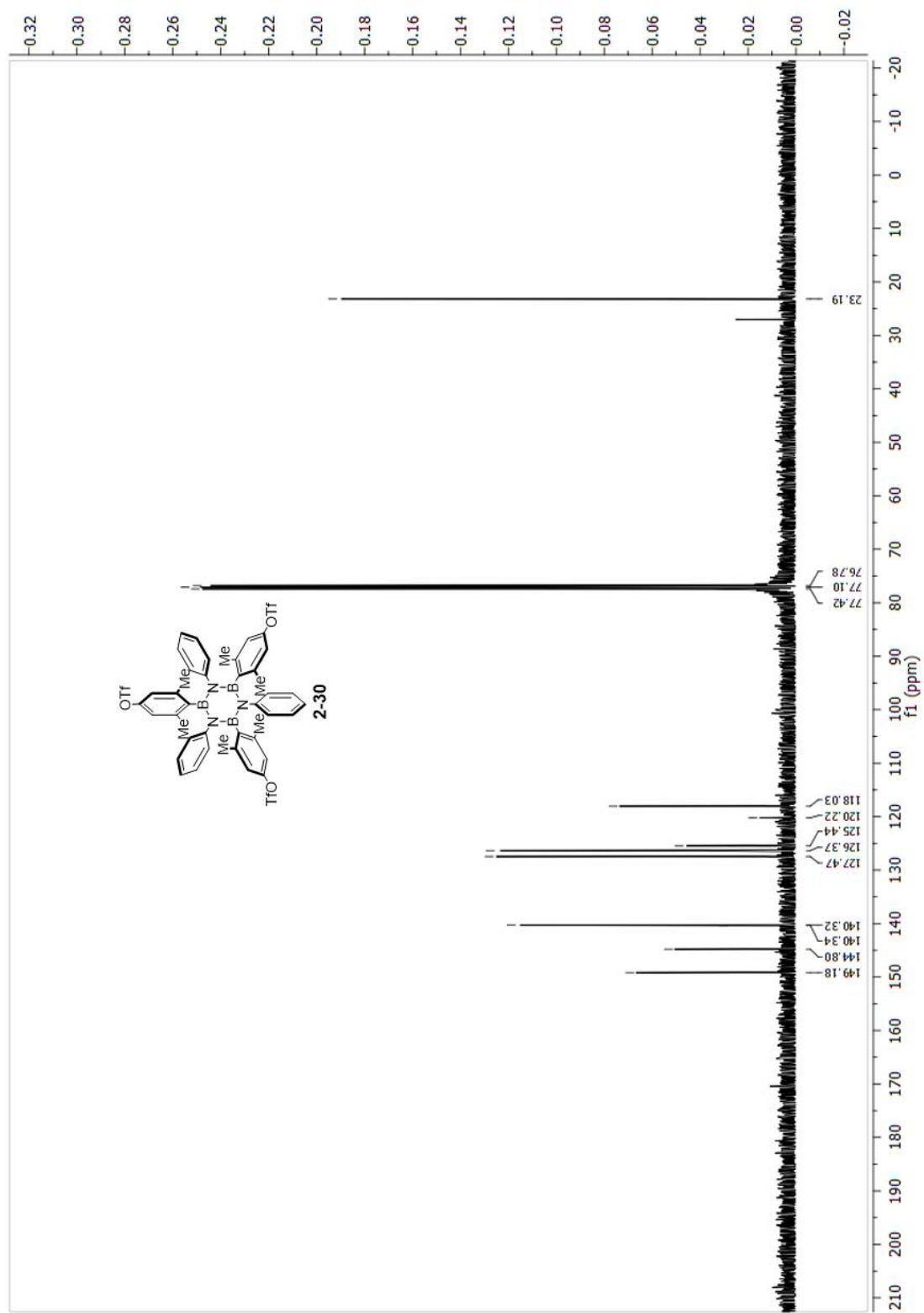


Figure A.27: ^{13}C -NMR, 100 MHz, CDCl_3 .

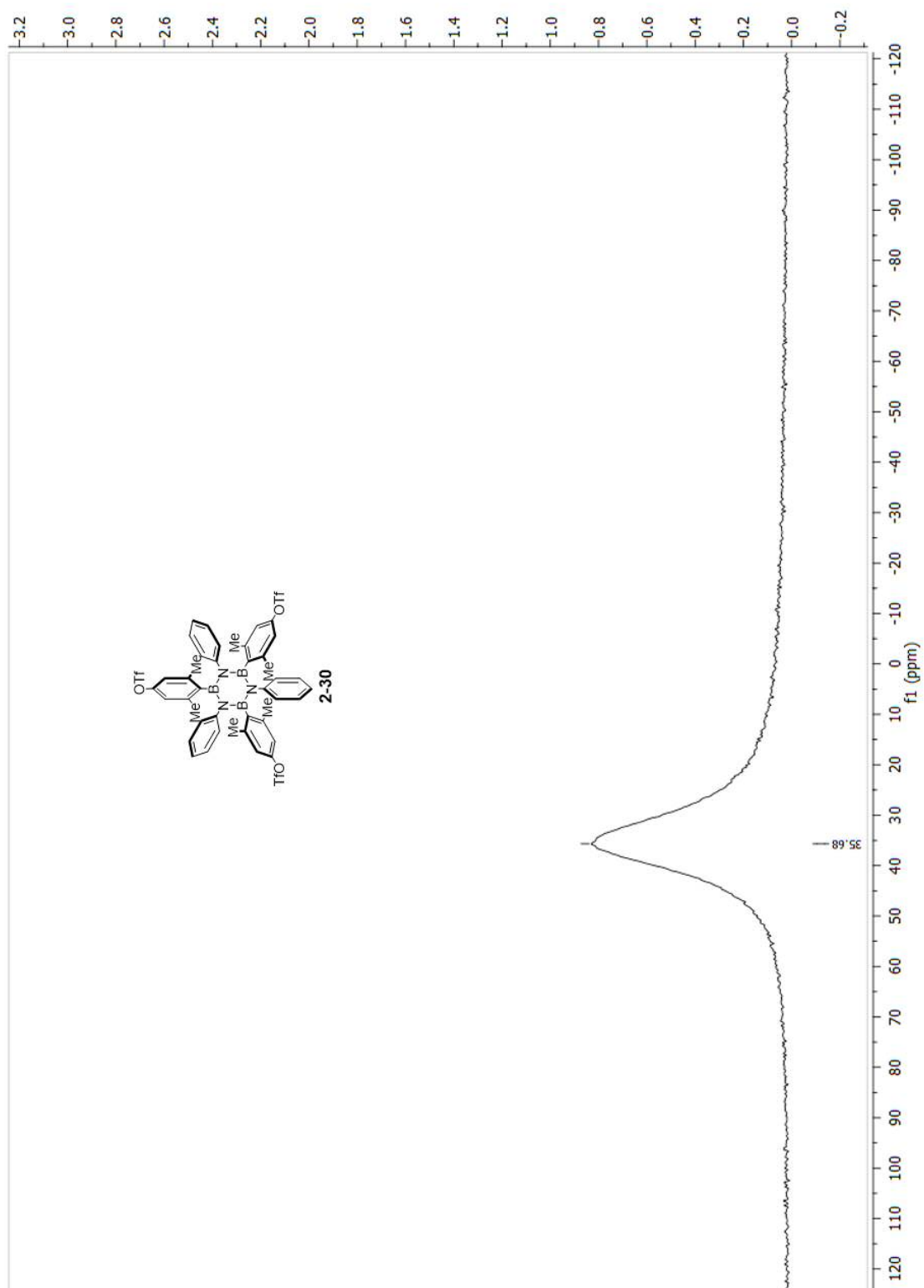


Figure A.28: ^{11}B -NMR, 128 MHz, CDCl_3 .

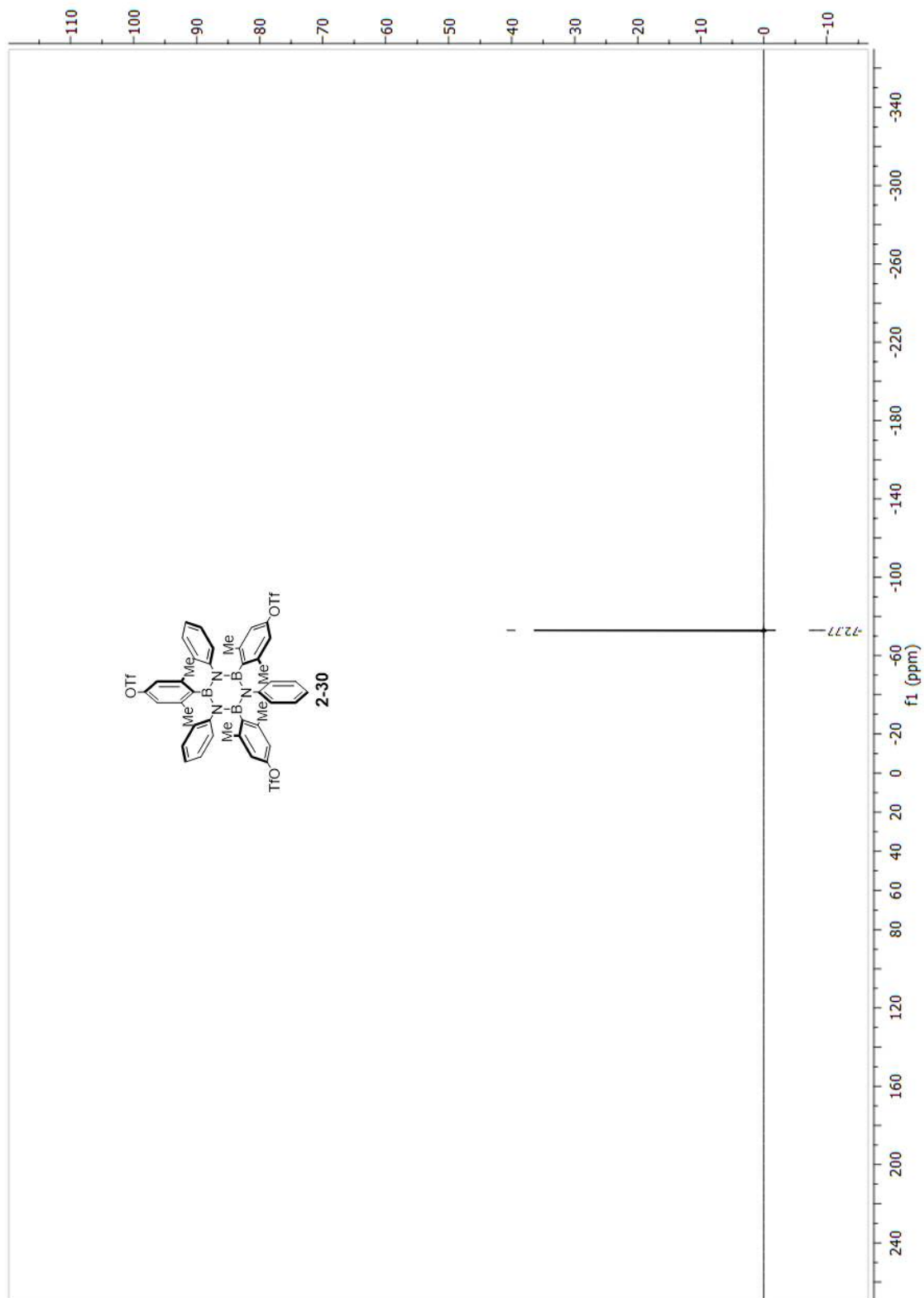
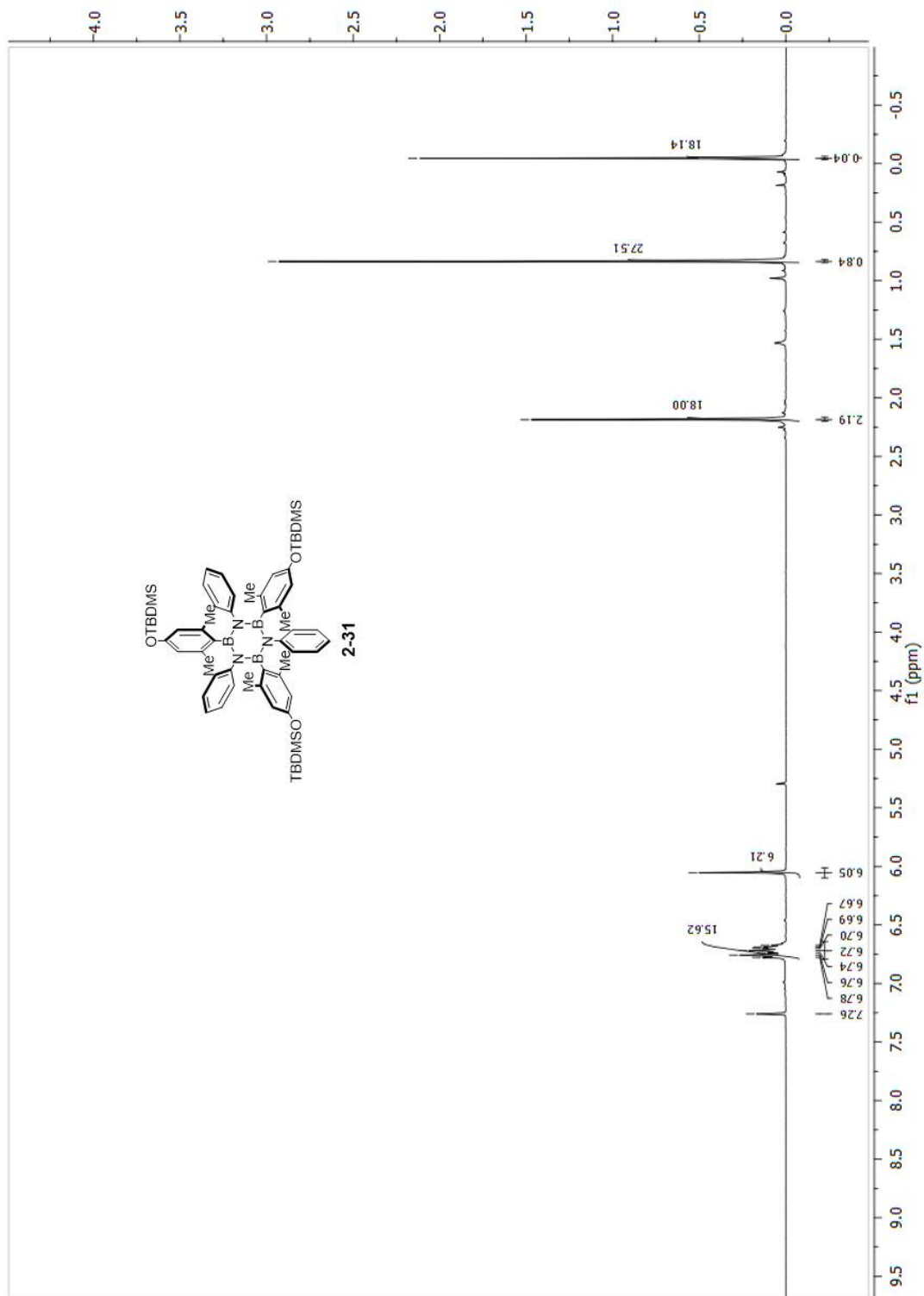


Figure A.29: ^{19}F -NMR, 376 MHz, CDCl_3 .

Characterisation of 2-31

Figure A.30: $^1\text{H-NMR}$, 400 MHz, CDCl_3 .

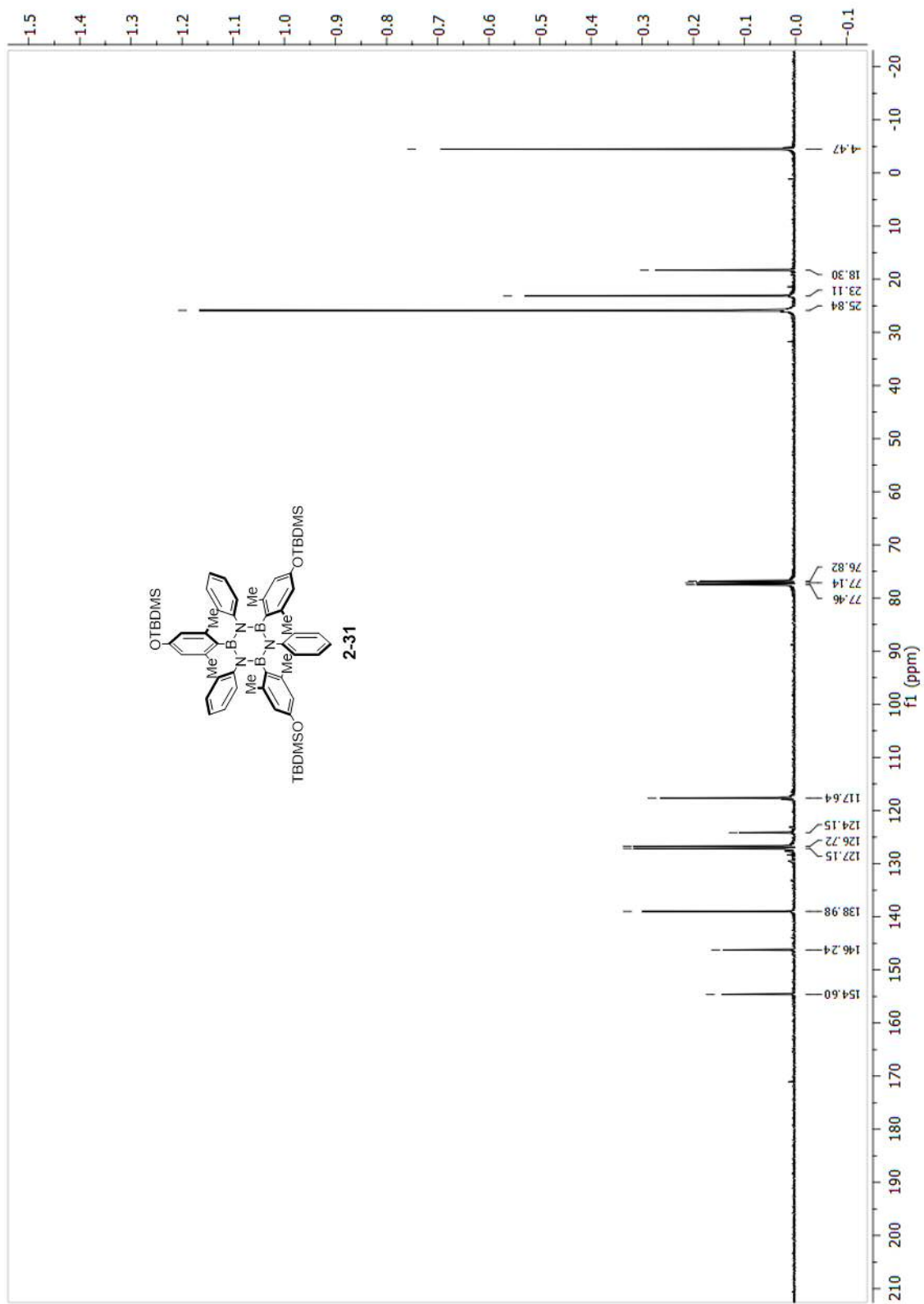


Figure A.31: ¹³C-NMR, 100 MHz, CDCl₃.

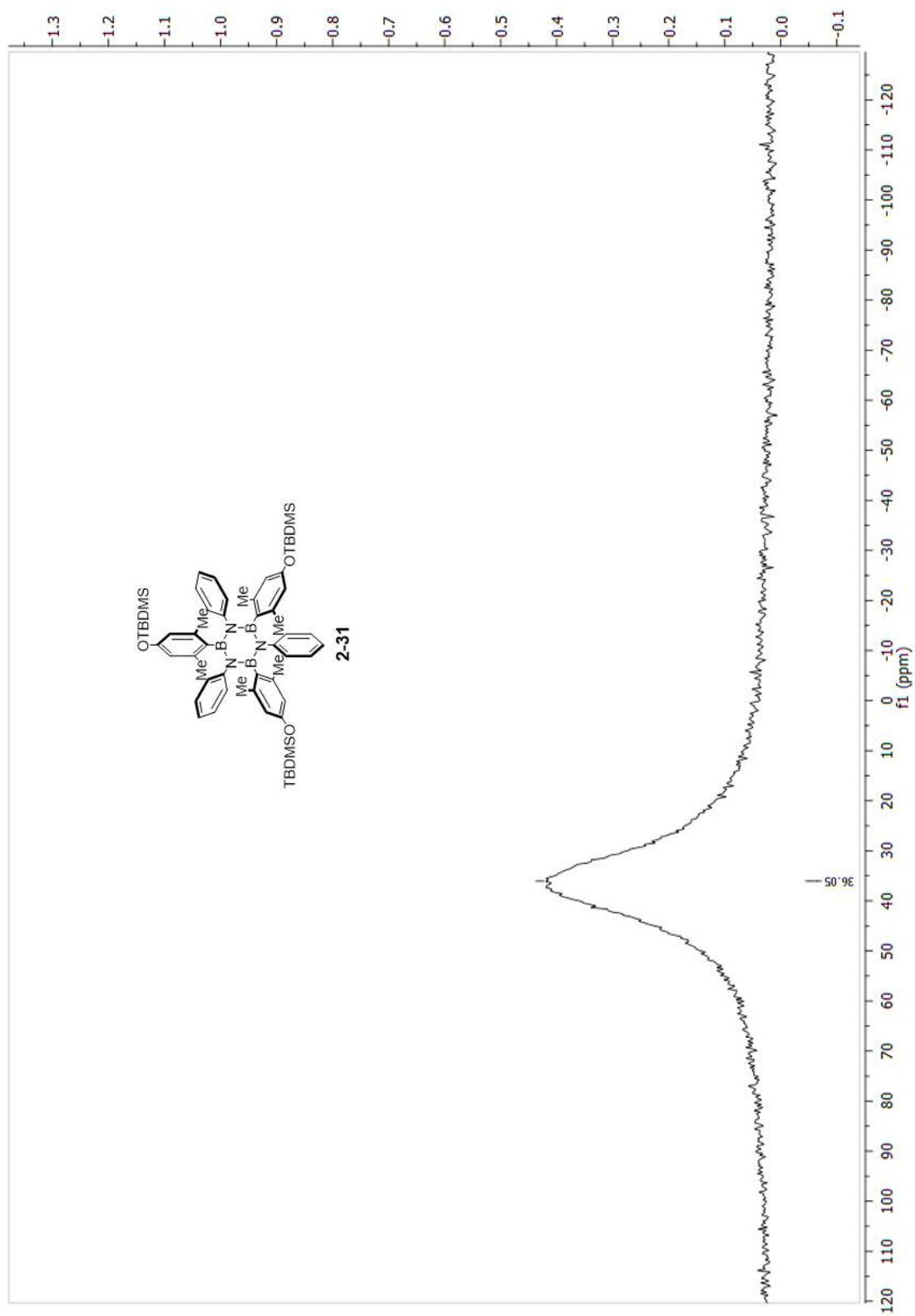
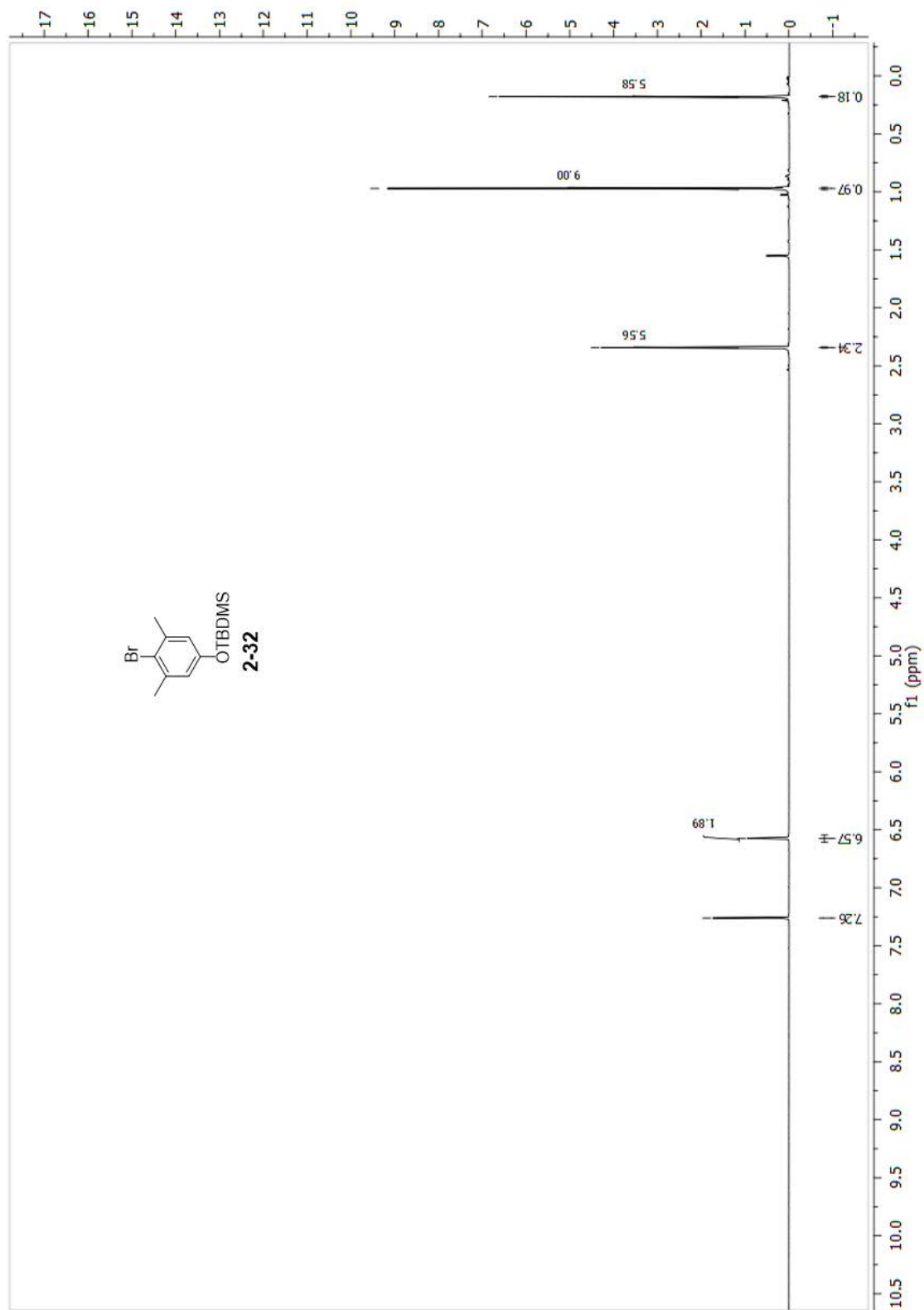


Figure A.32: ^{11}B -NMR, 128 MHz, CDCl_3 .

Characterisation of 2-32

Figure A.33: $^1\text{H-NMR}$, 400 MHz, CDCl_3 .

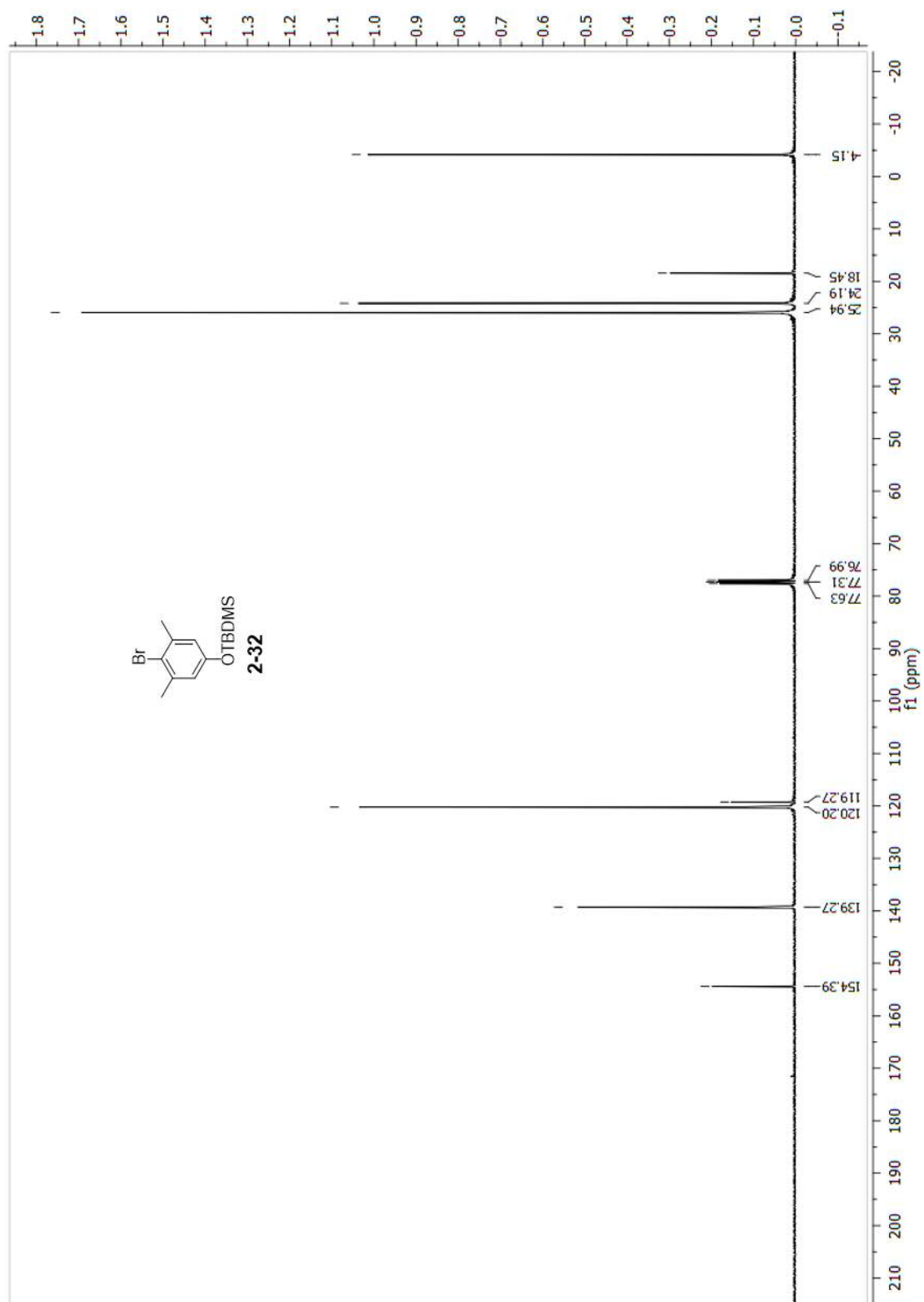
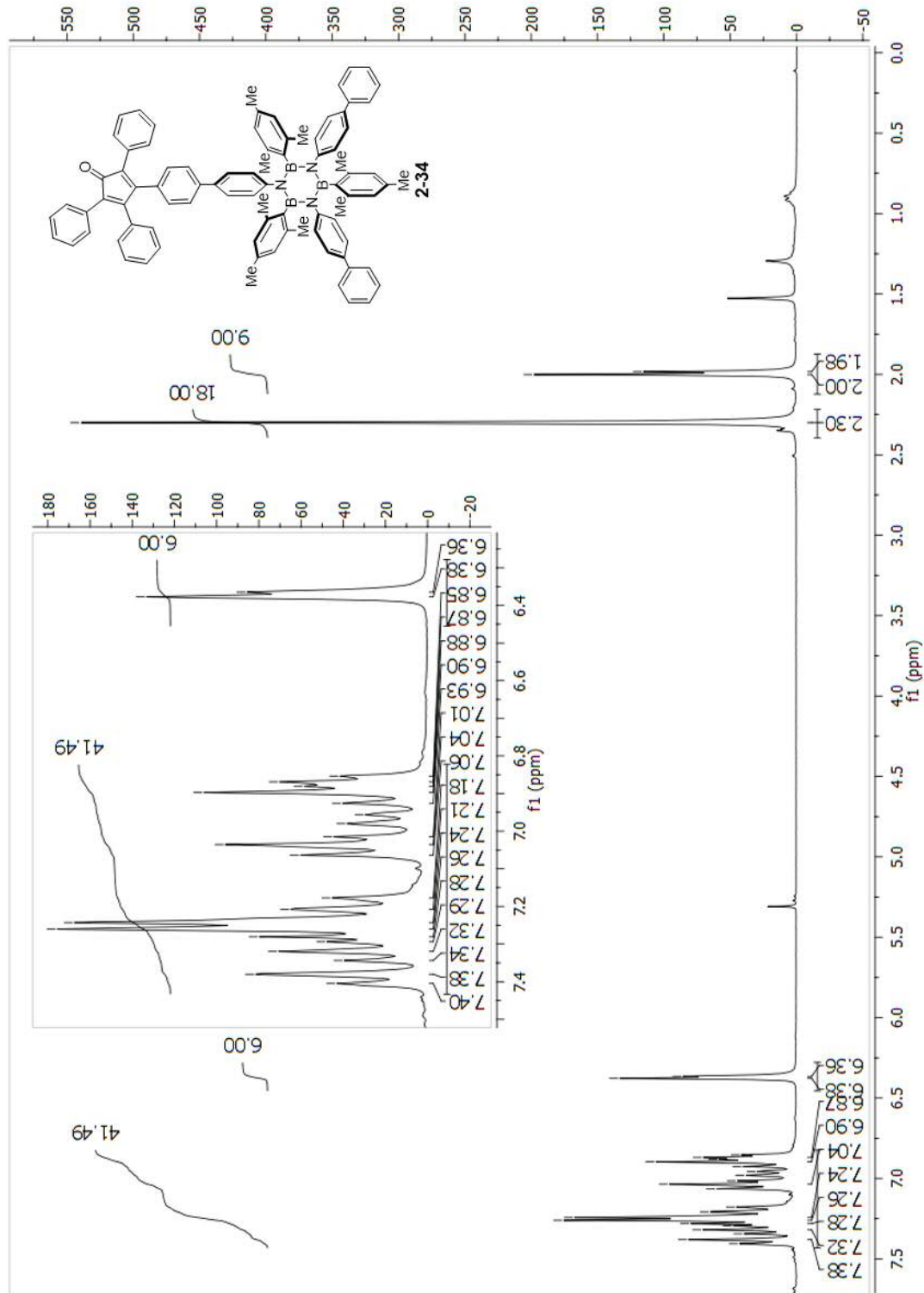


Figure A.34: ^{13}C -NMR, 100 MHz, CDCl_3 .

Characterisation of 2-34

Figure A.35: $^1\text{H-NMR}$, 400 MHz, CDCl_3 .

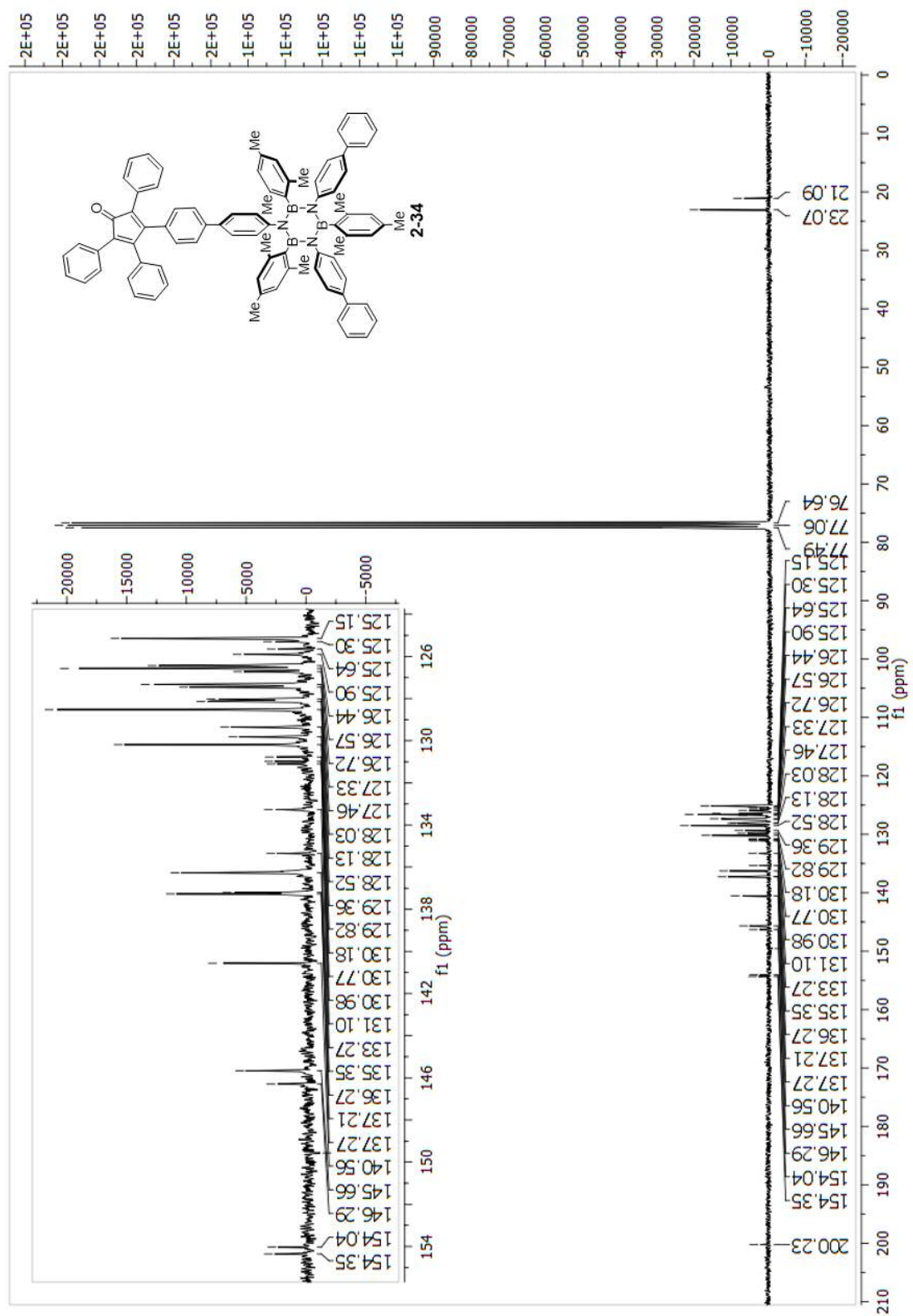


Figure A.36: ^{13}C -NMR, 100 MHz, CDCl_3 .

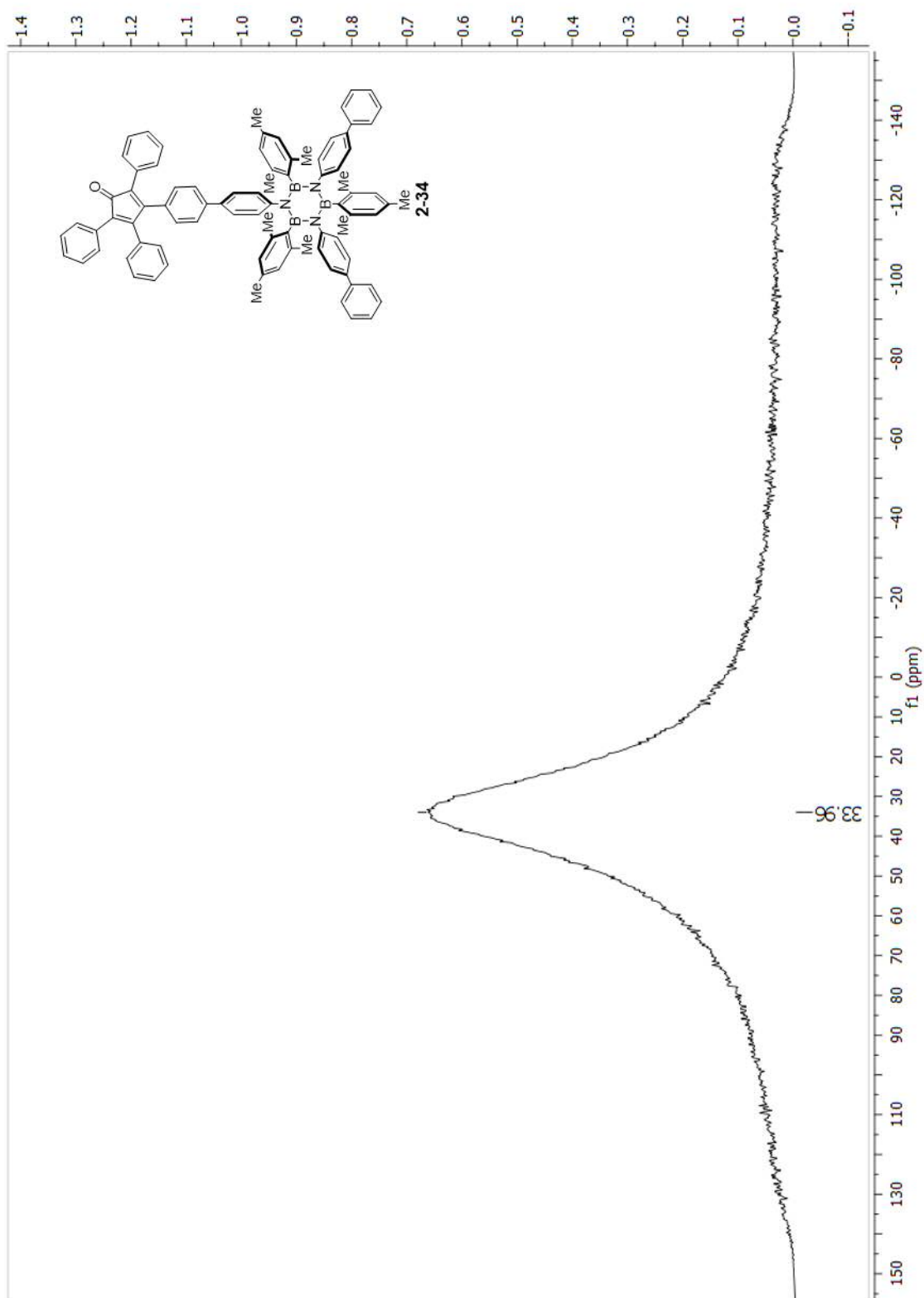
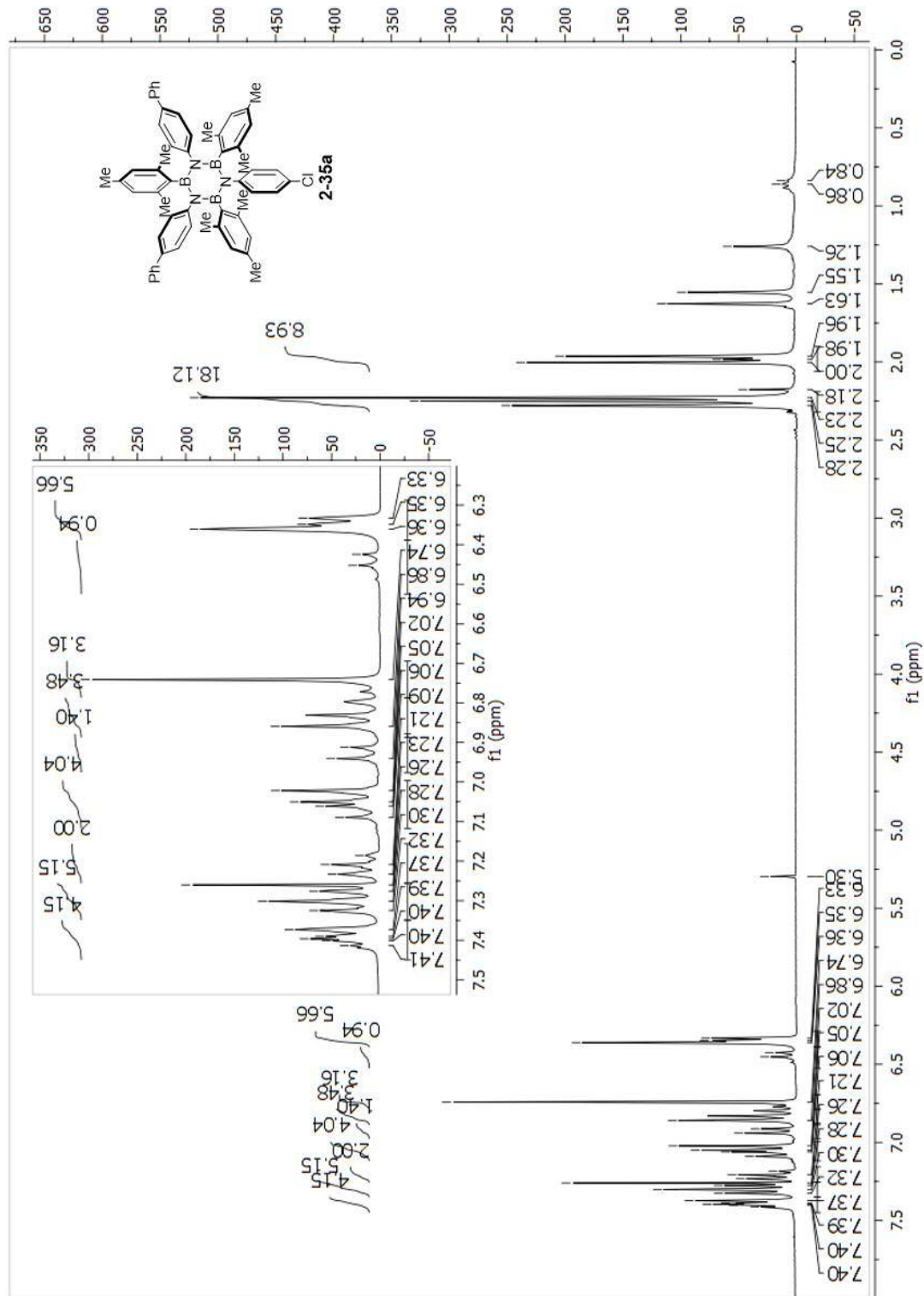


Figure A.37: ^{11}B -NMR, 128 MHz, CDCl_3 .

Characterisation of 2-35a

Figure A.38: $^1\text{H-NMR}$, 400 MHz, CDCl_3 .

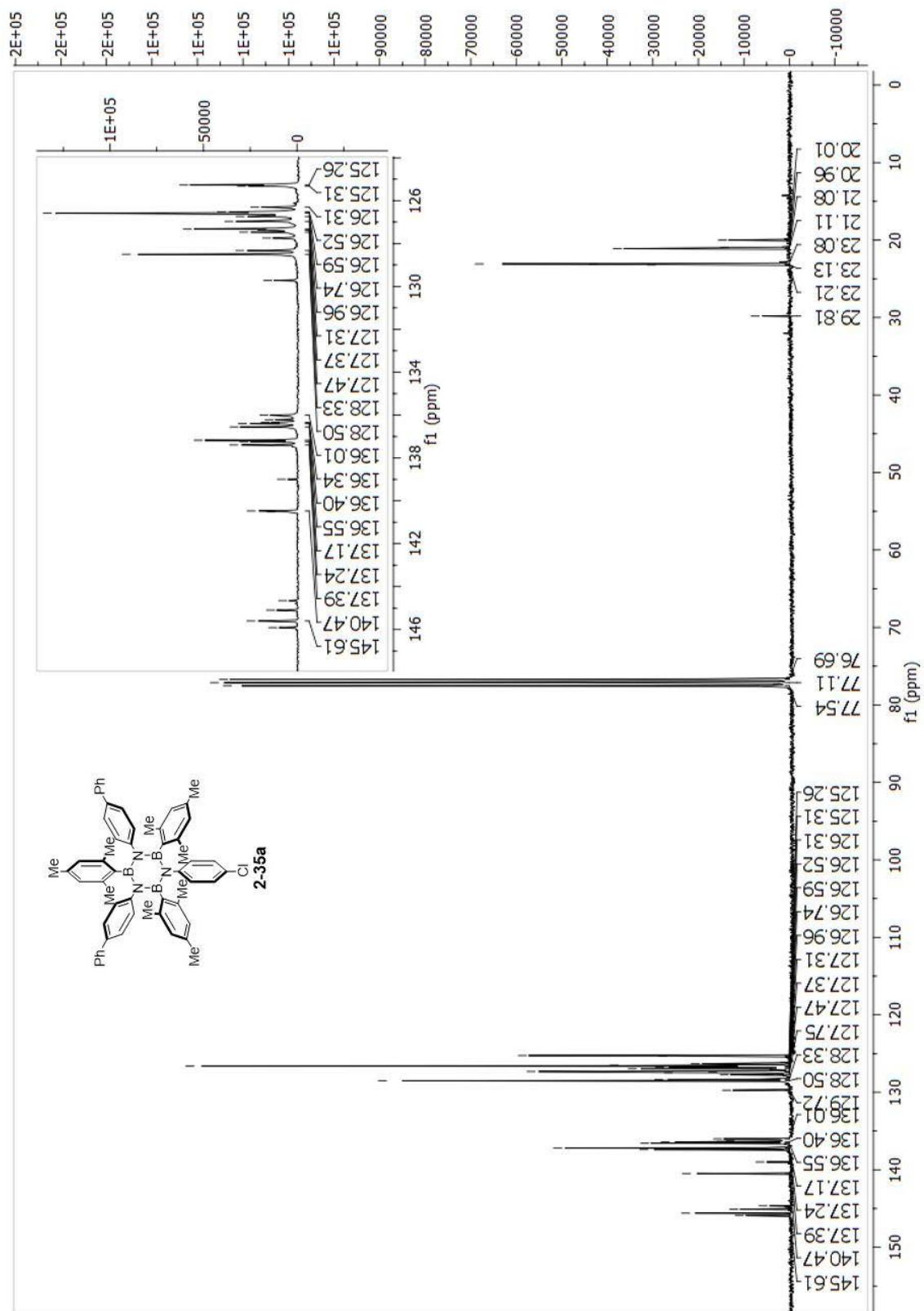


Figure A.39: $^{13}\text{C-NMR}$, 100 MHz, CDCl_3 .

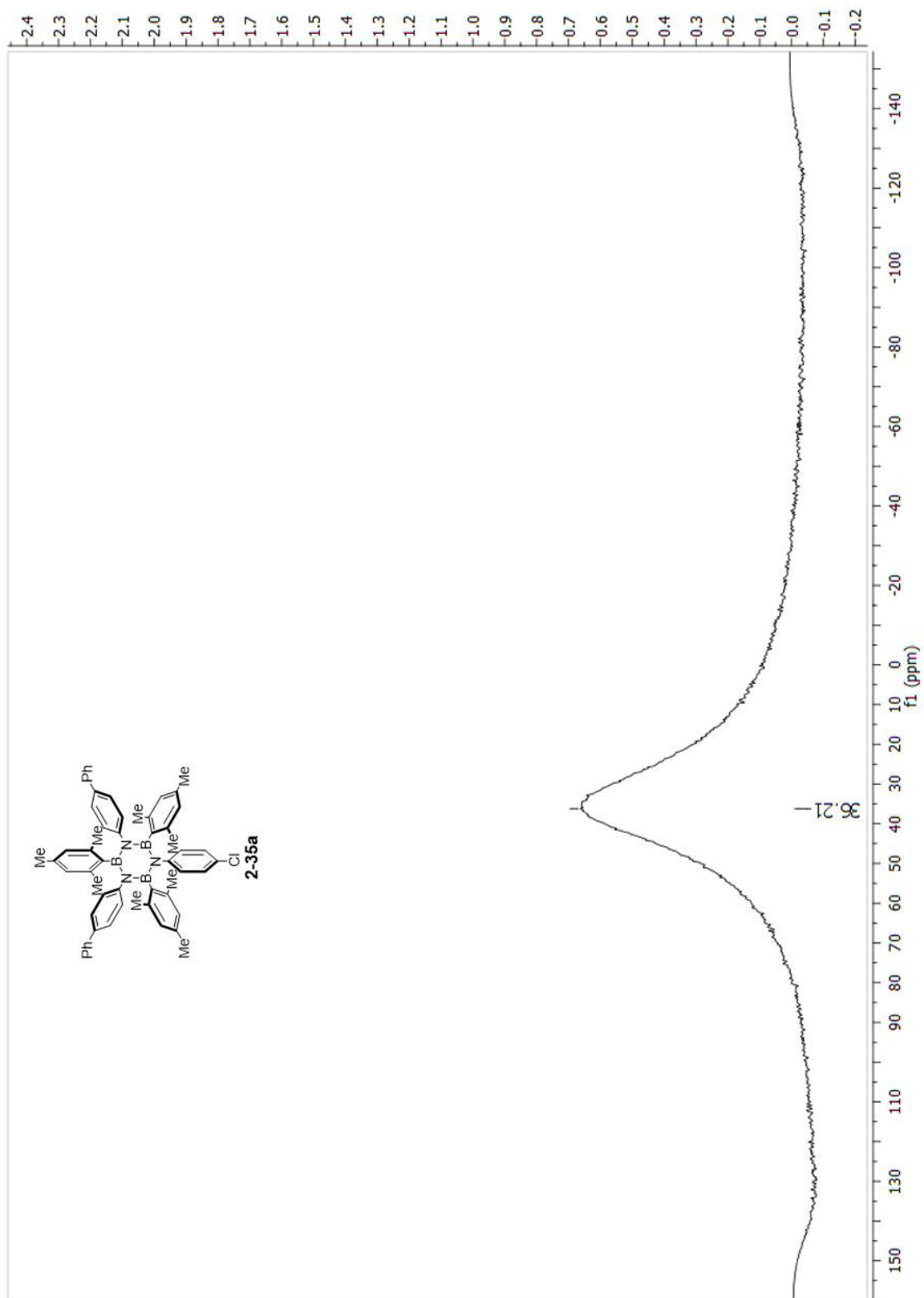
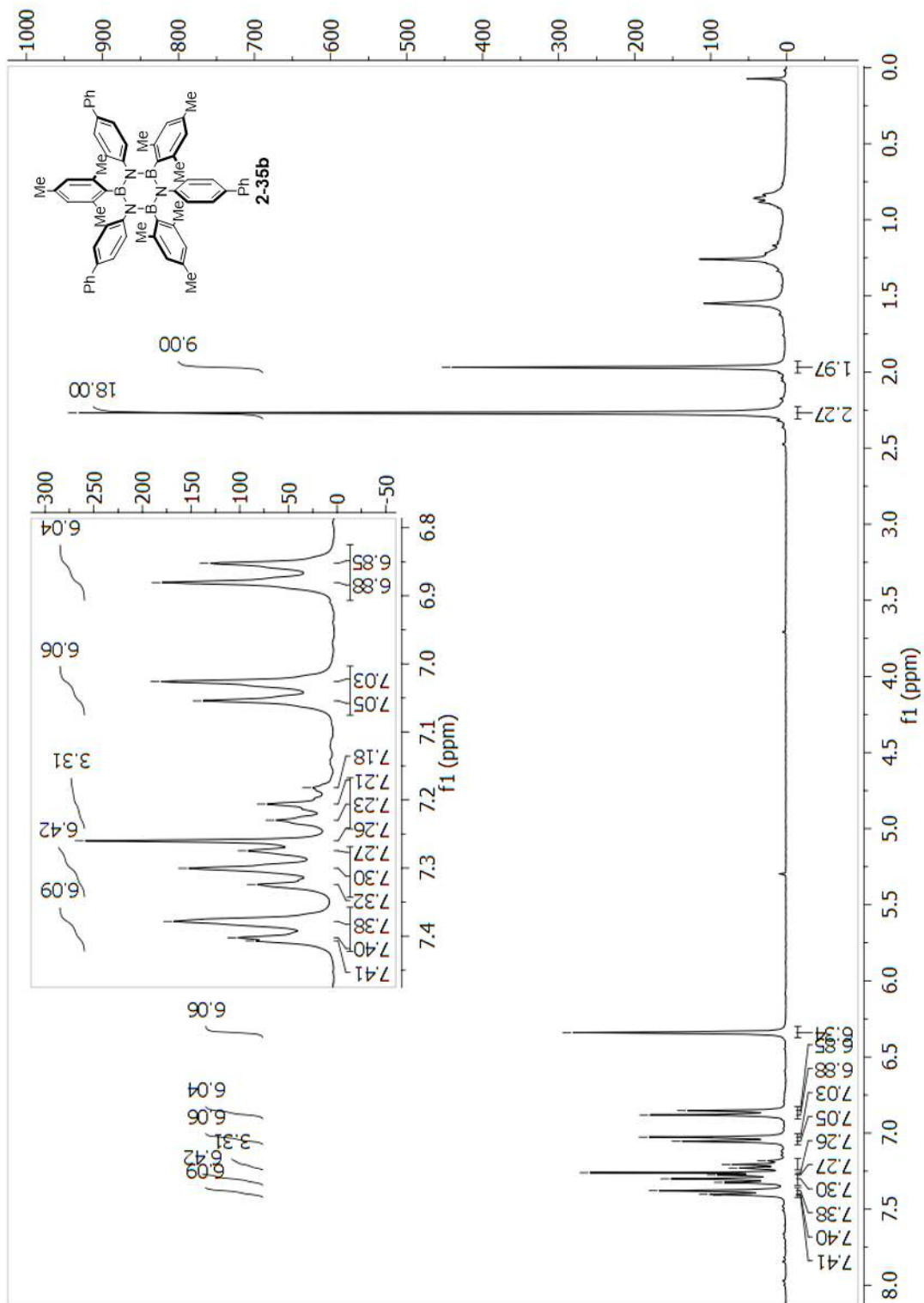


Figure A.40: ^{11}B -NMR, 128 MHz, CDCl_3 .

Characterisation of 2-35b

Figure A.41: $^1\text{H-NMR}$, 400 MHz, CDCl_3 .

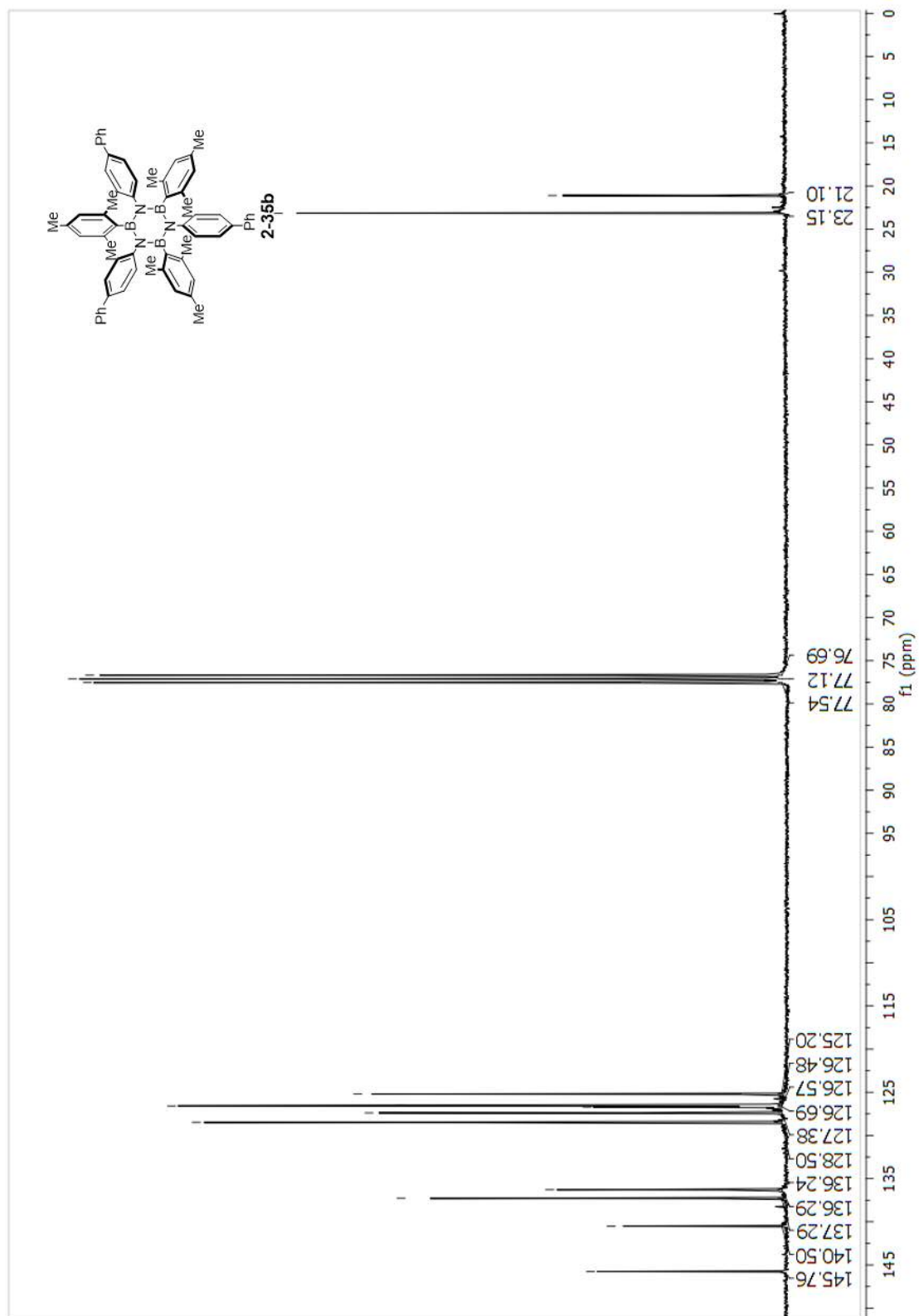


Figure A.42: ^{13}C -NMR, 100 MHz, CDCl_3 .

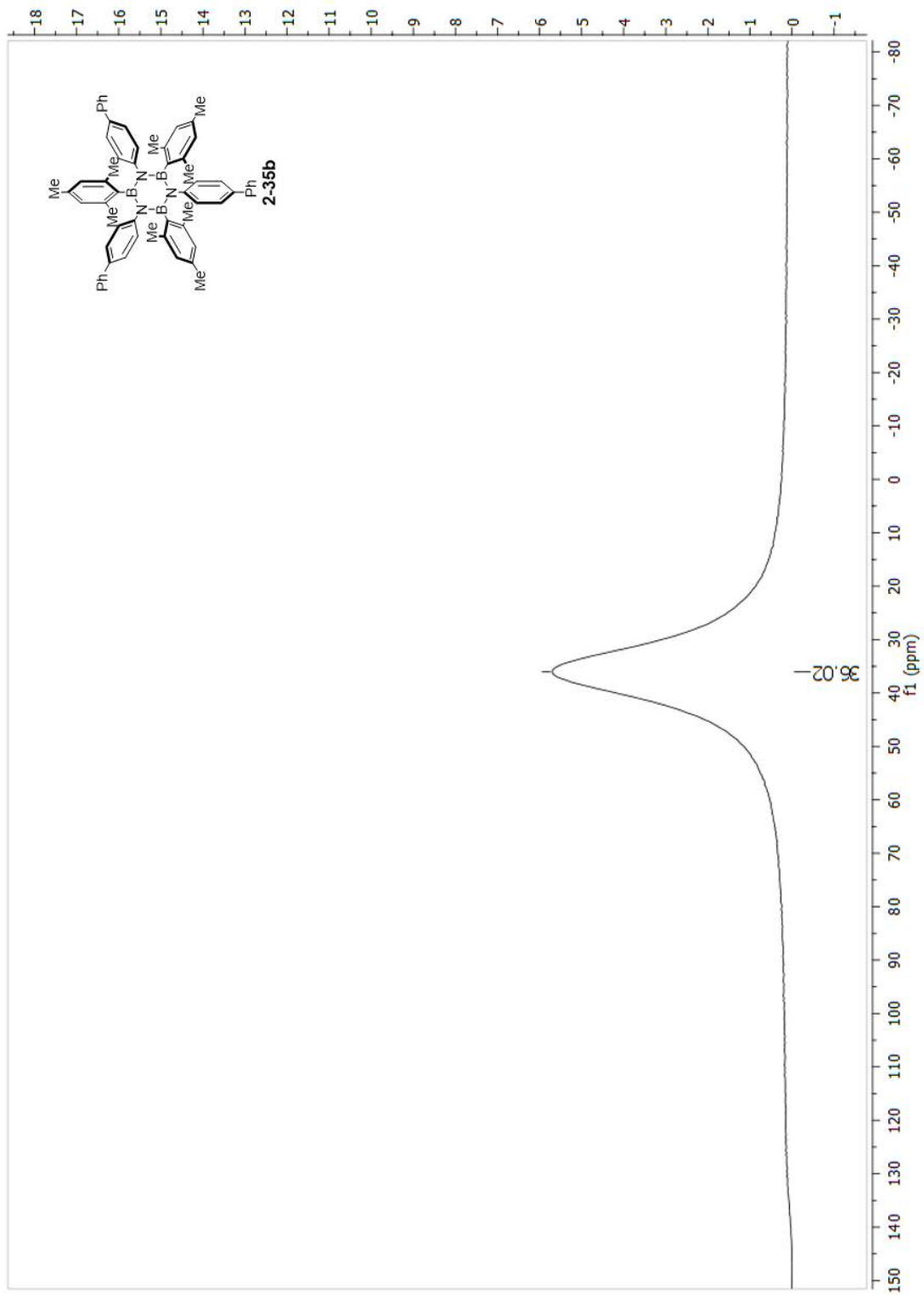
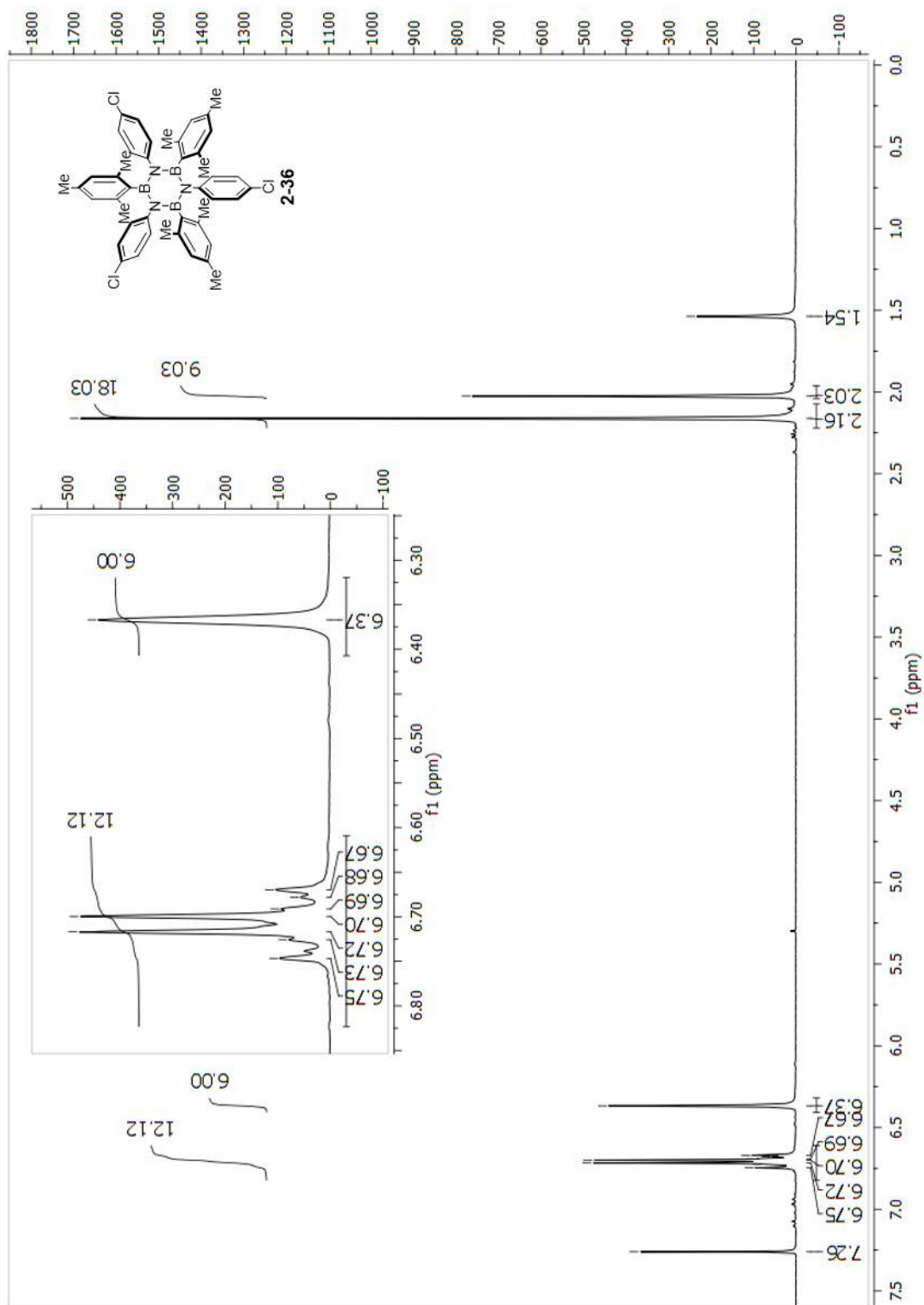


Figure A.43: ^{11}B -NMR, 128 MHz, CDCl_3 .

Characterisation of 2-36

Figure A.44: $^1\text{H-NMR}$, 400 MHz, CDCl_3 .

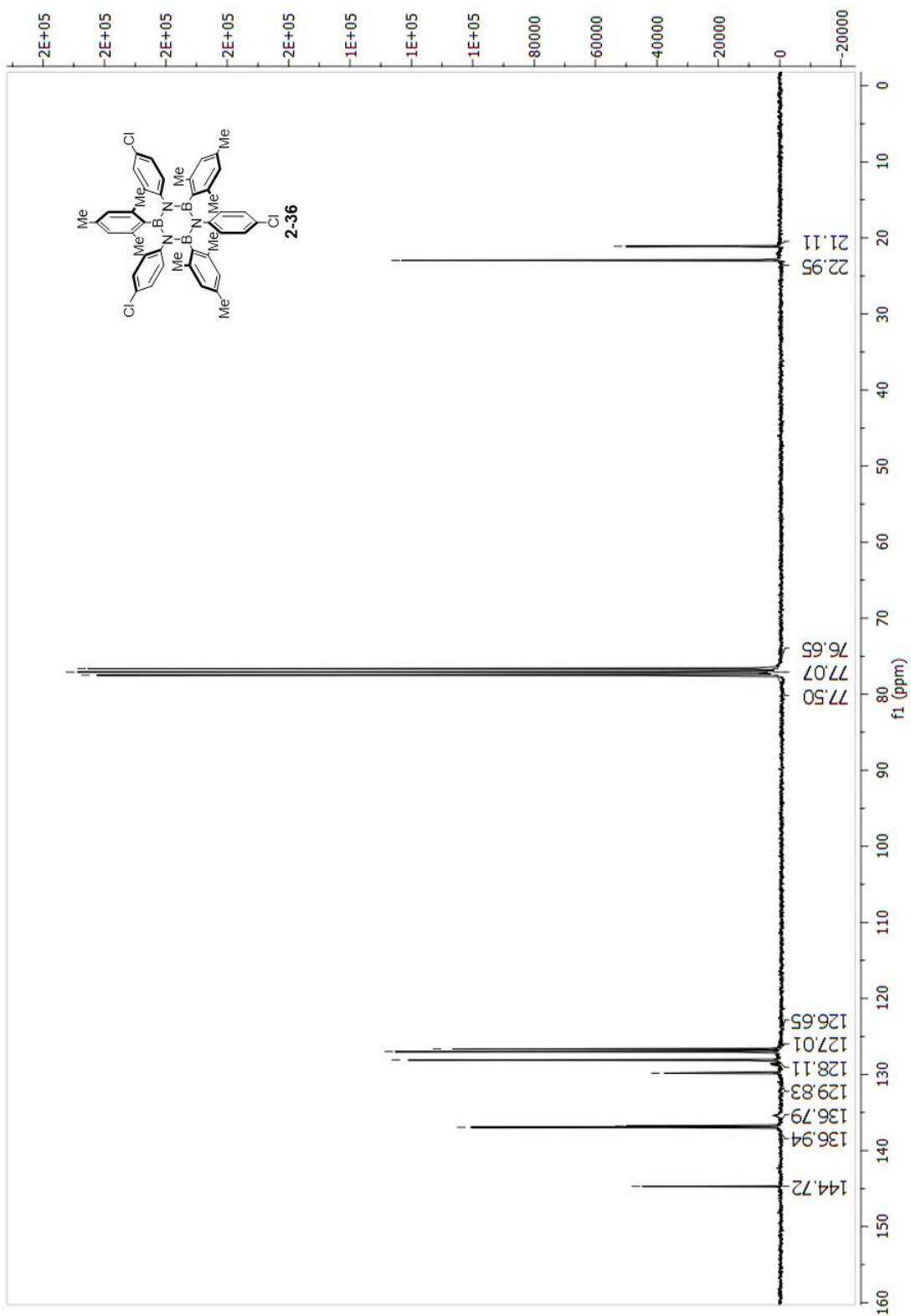


Figure A.45: ^{13}C -NMR, 100 MHz, CDCl_3 .

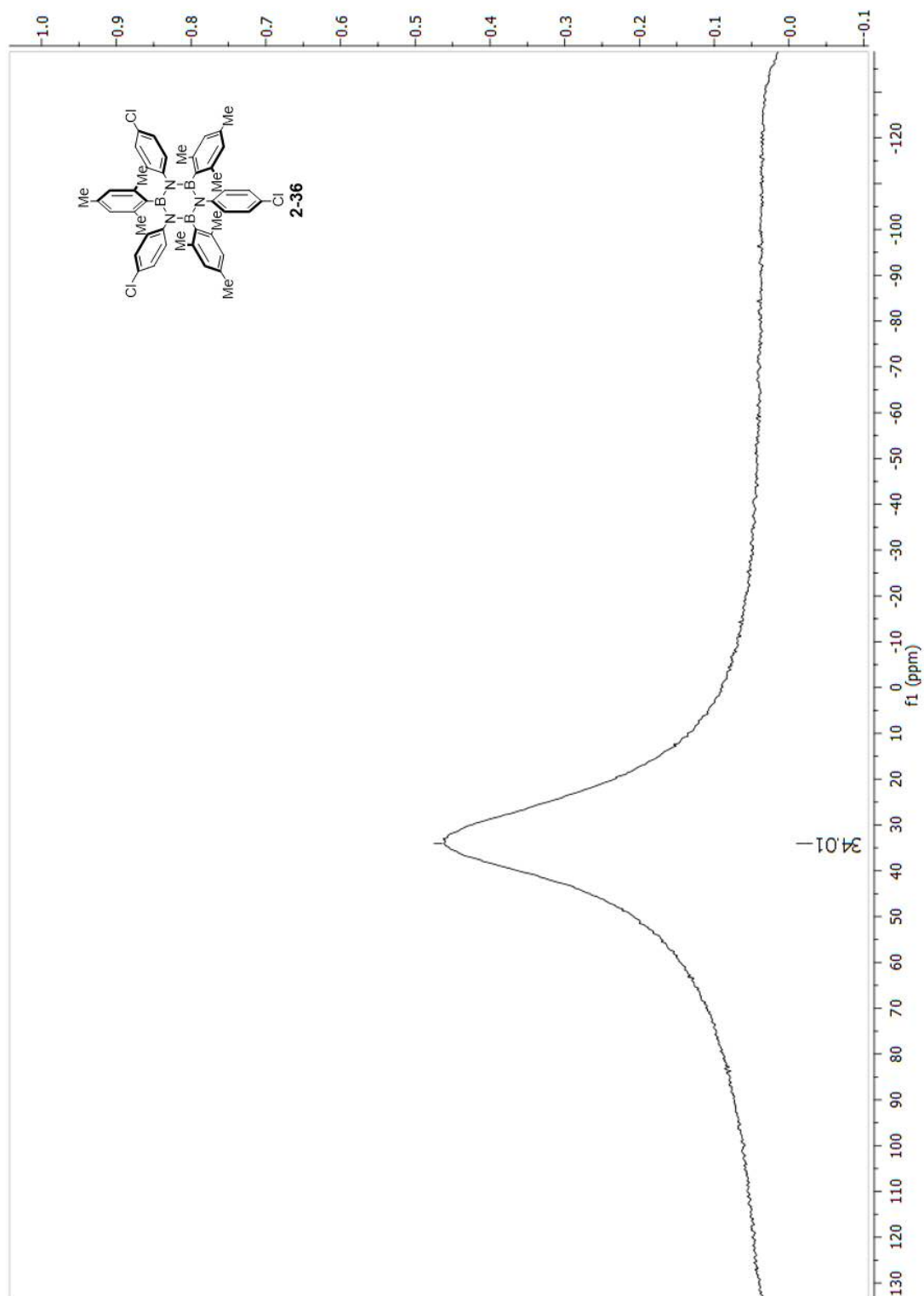
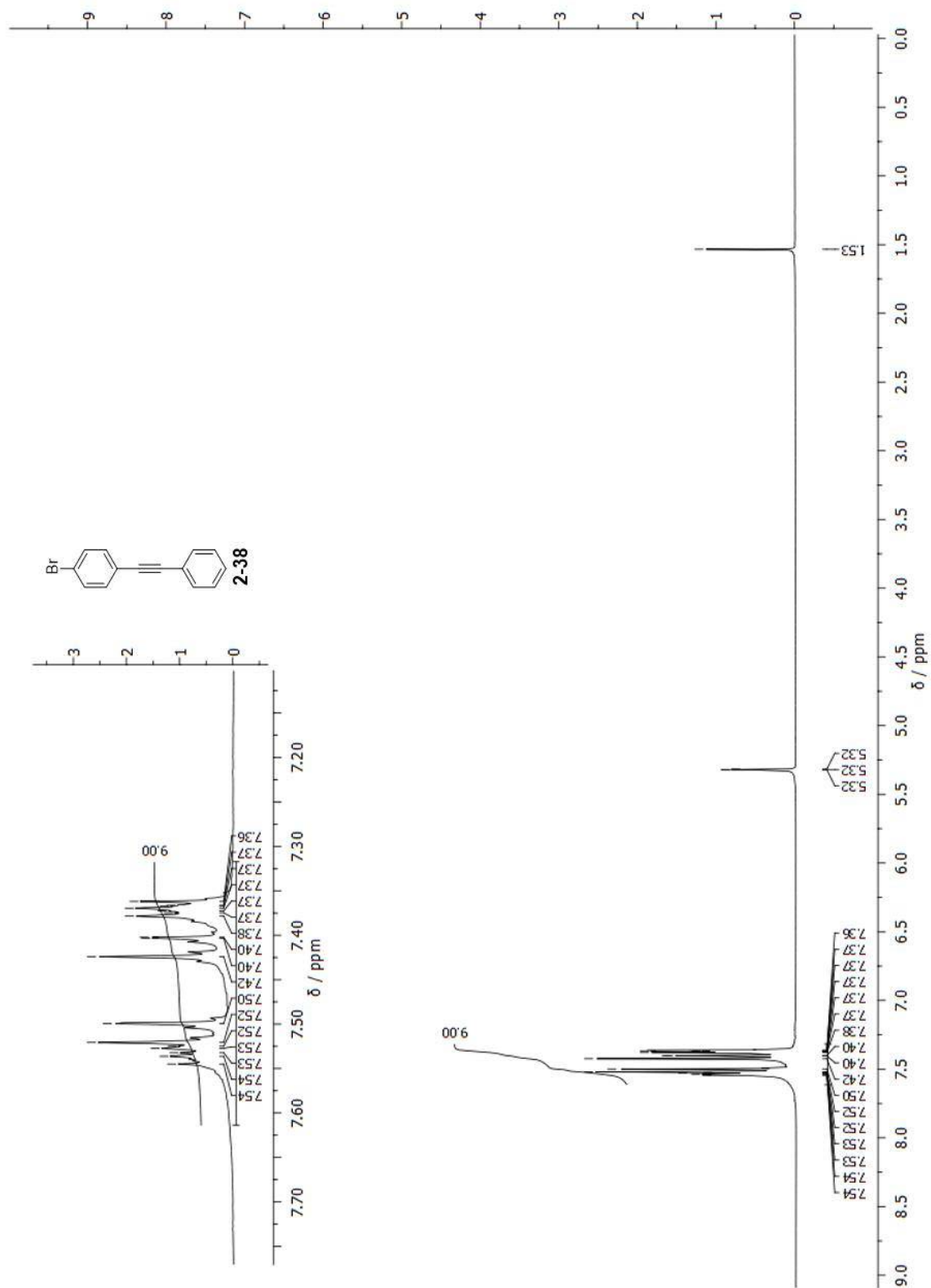


Figure A.46: ^{11}B -NMR, 128 MHz, CDCl_3 .

Characterisation of 2-38

Figure A.47: $^1\text{H-NMR}$, 400 MHz, CD_2Cl_2 .

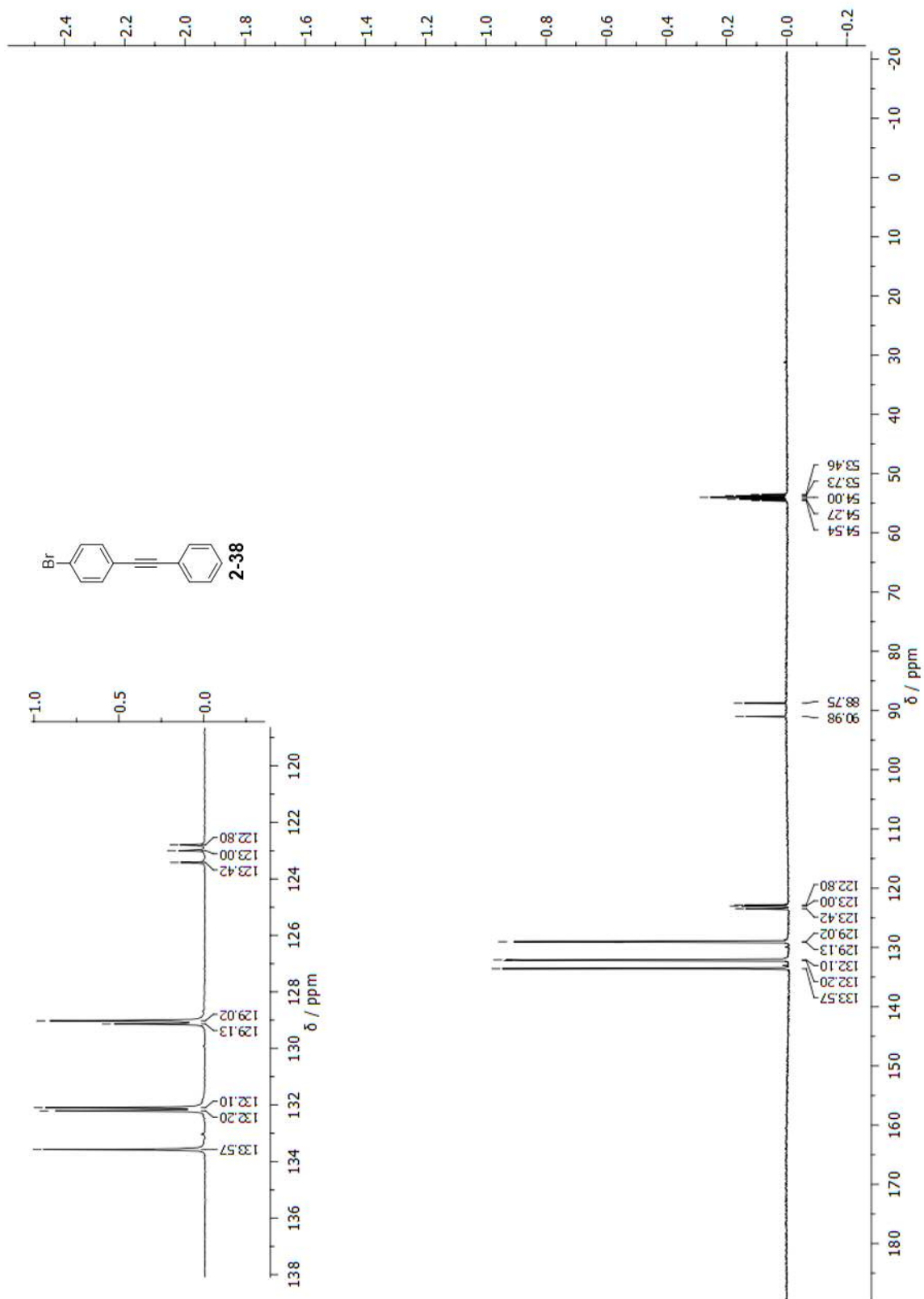
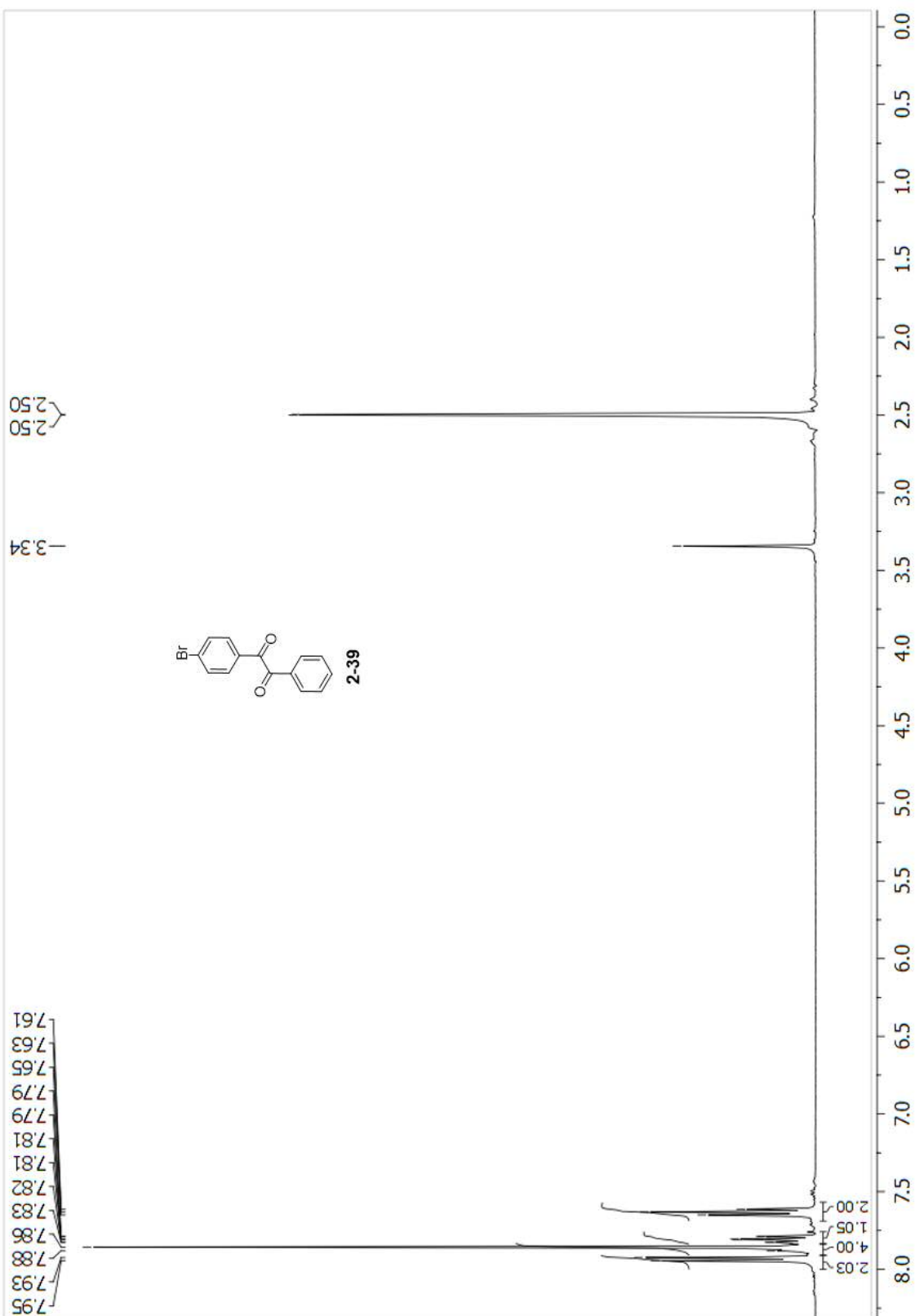


Figure A.48: ^{13}C -NMR, 100 MHz, CD_2Cl_2 .

Characterisation of 2-39

Figure A.49. $^1\text{H-NMR}$ 400 MHz, DMSO-d_6 .

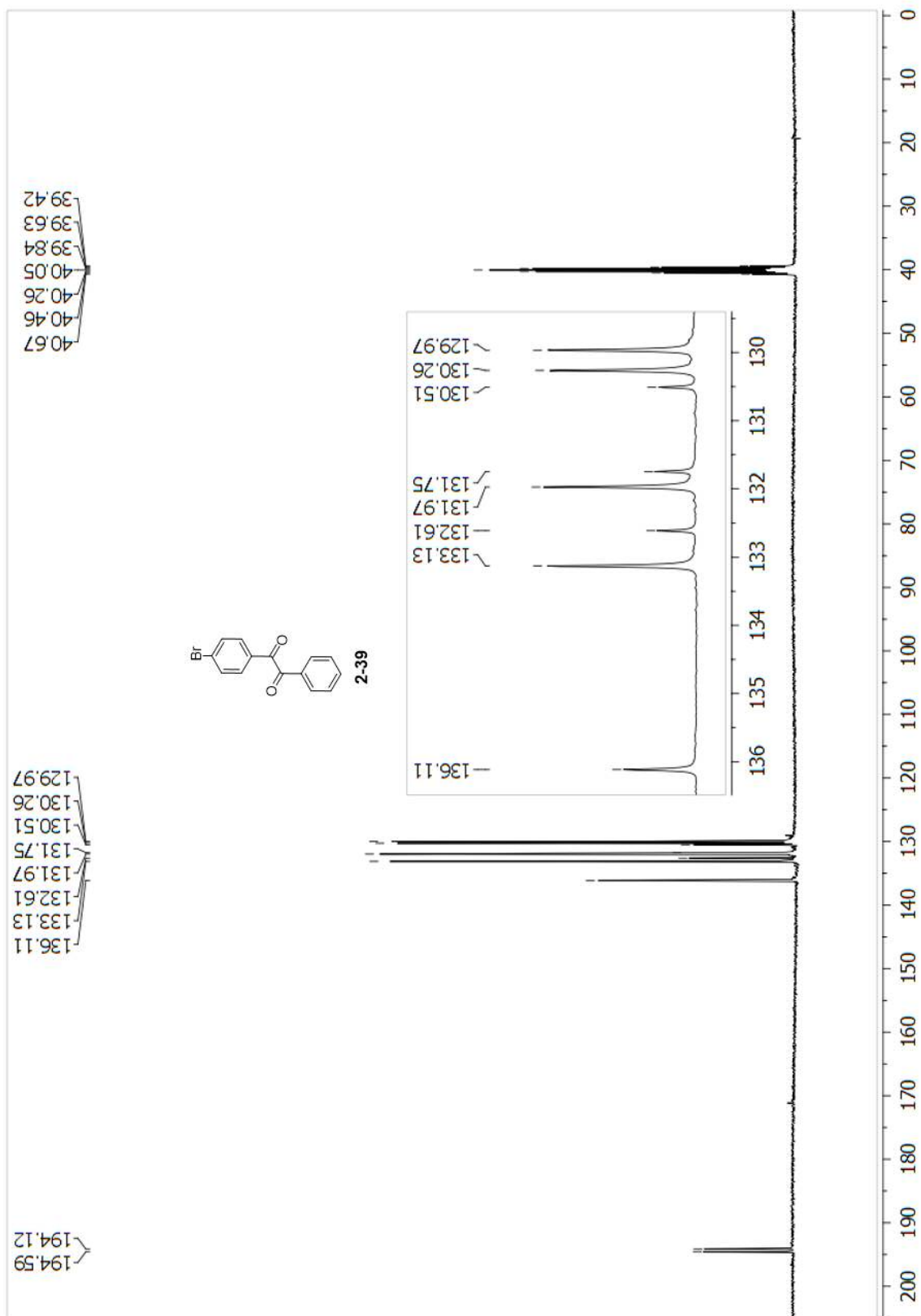
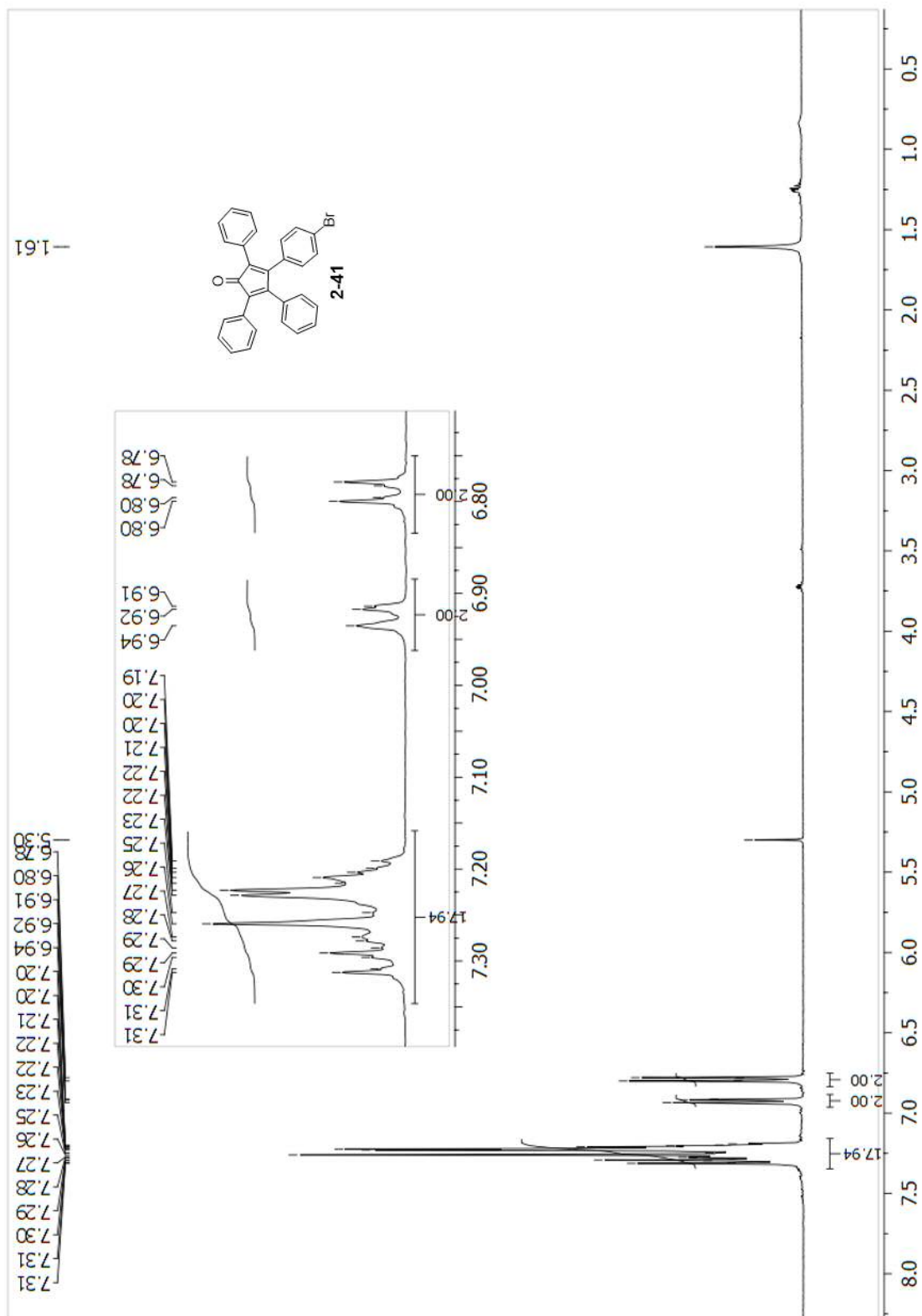


Figure A.50. ^{13}C -NMR 100 MHz, DMSO-d_6 .

Characterisation of 2-41

Figure A.51. $^1\text{H-NMR}$ 400 MHz, CDCl_3 .

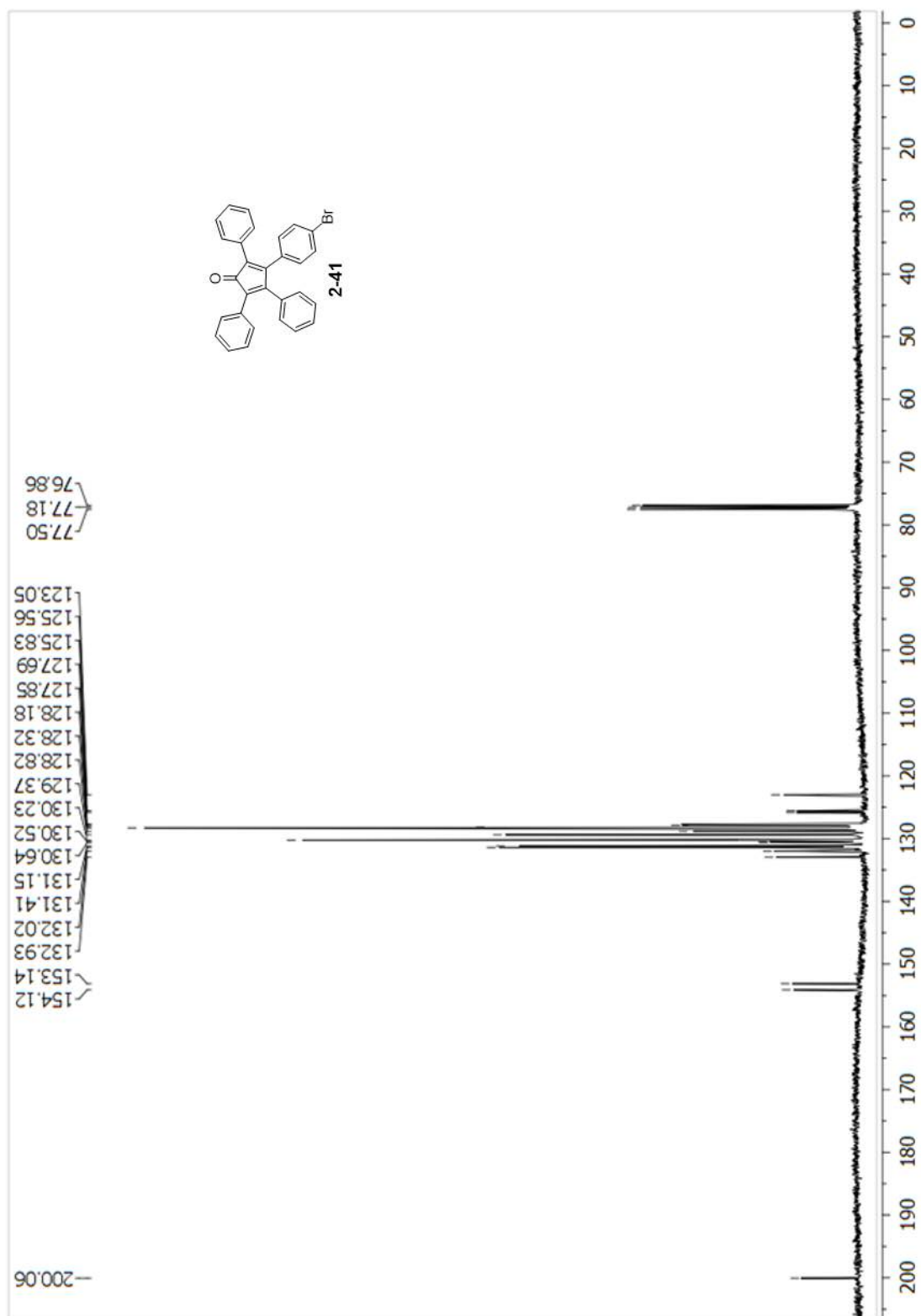
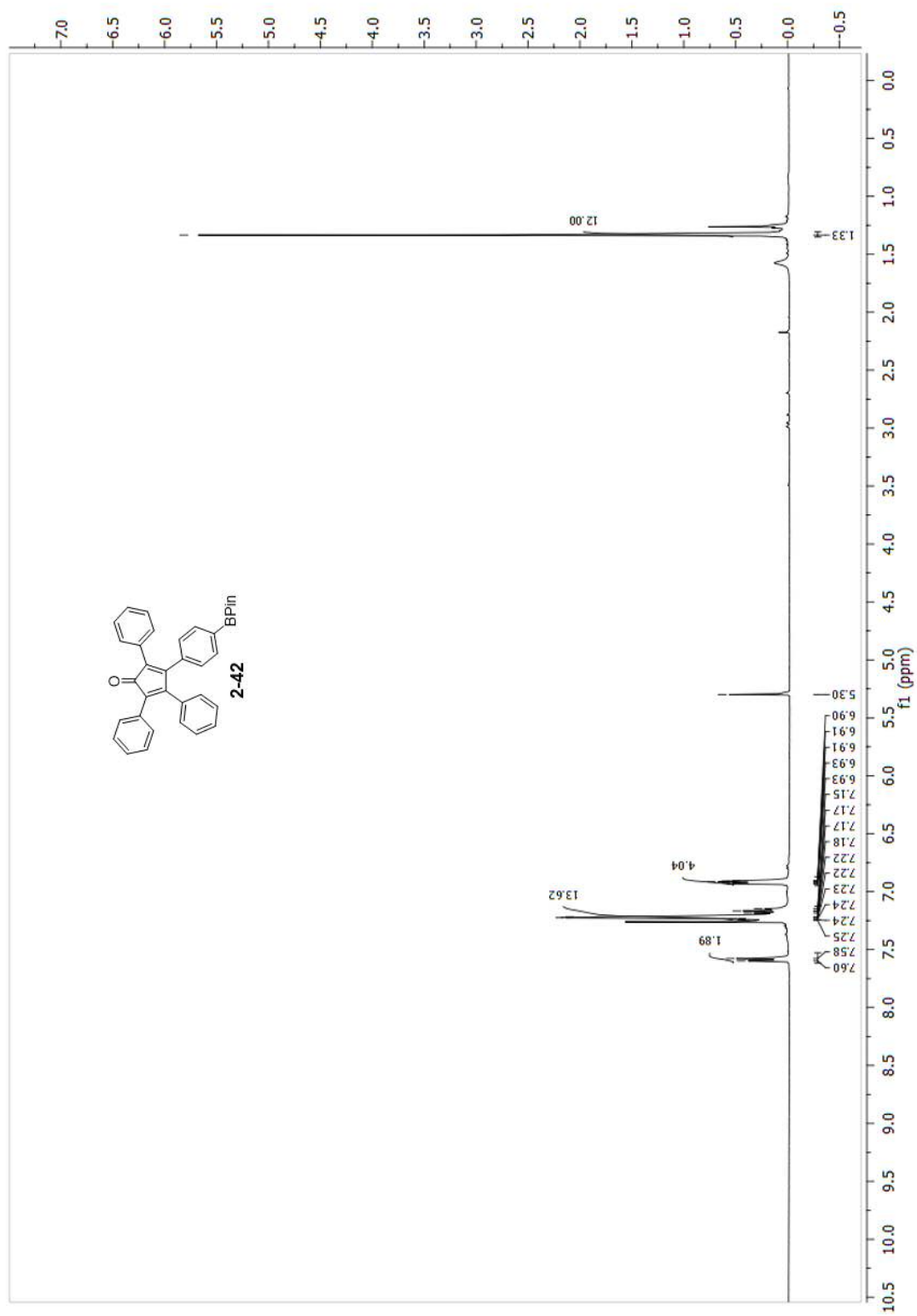


Figure A.52. $^1\text{H-NMR}$ 400 MHz, CDCl_3 .

Characterisation of 2-42

Figure A.53: $^1\text{H-NMR}$, 400 MHz, CDCl_3 .

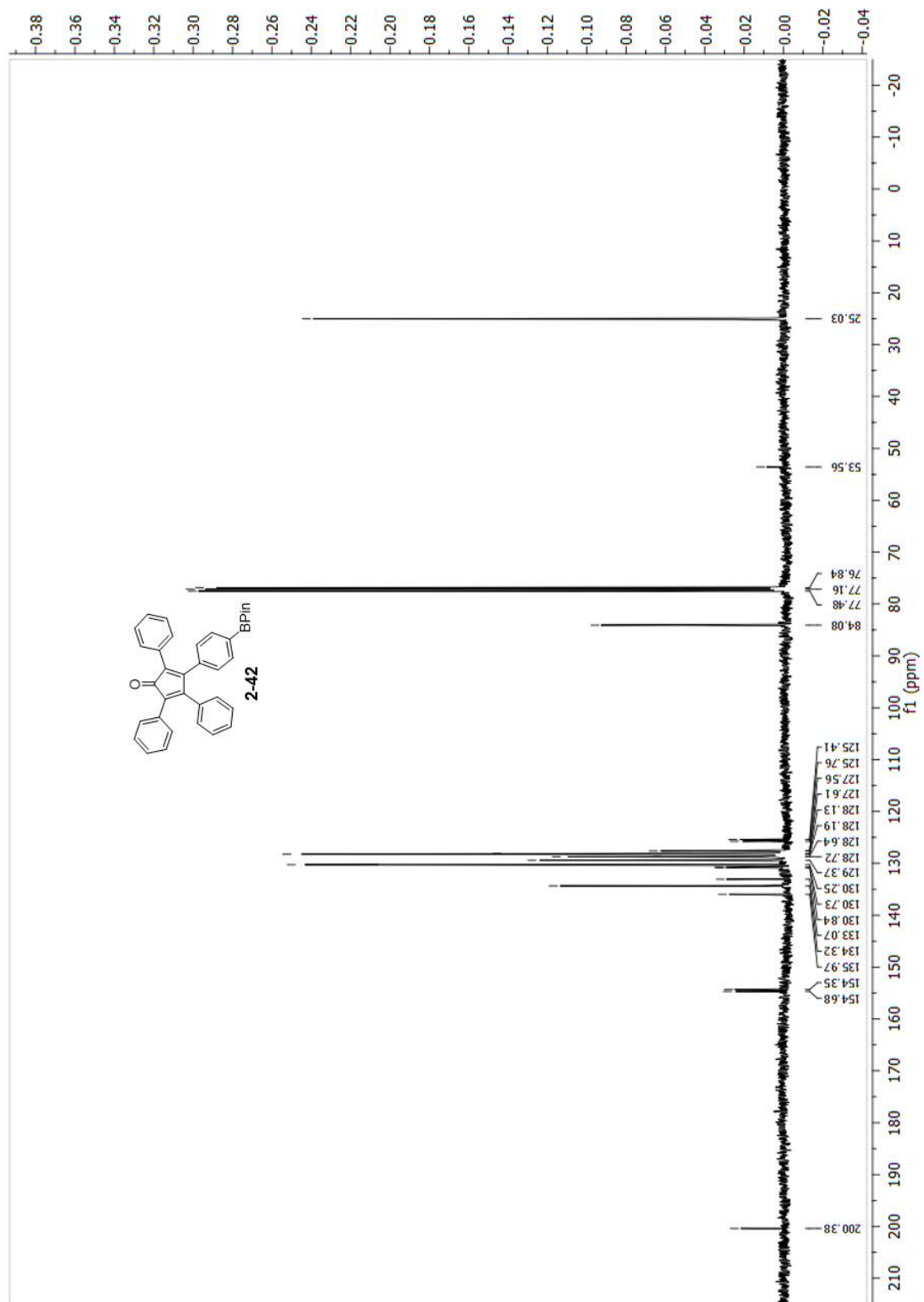
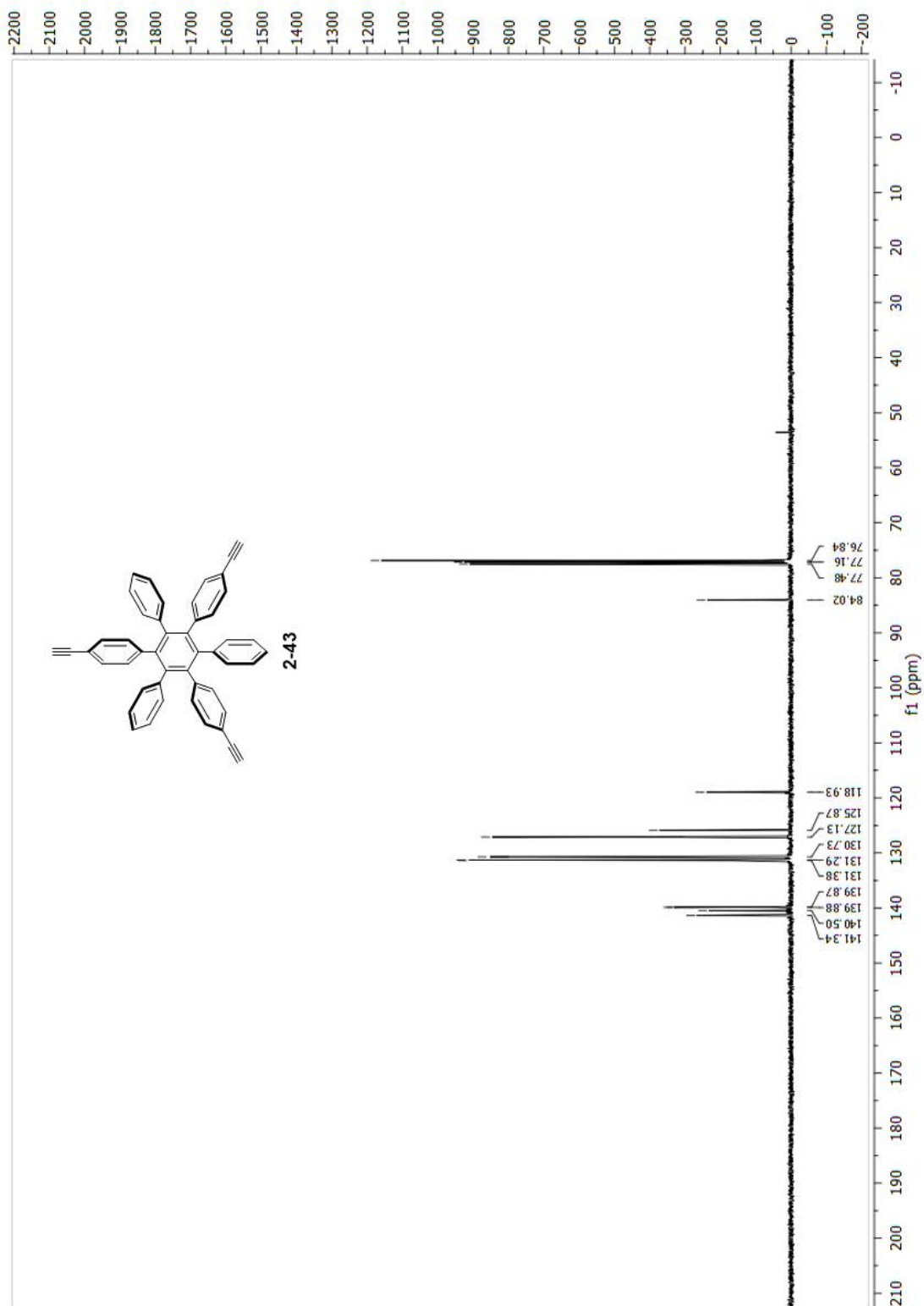
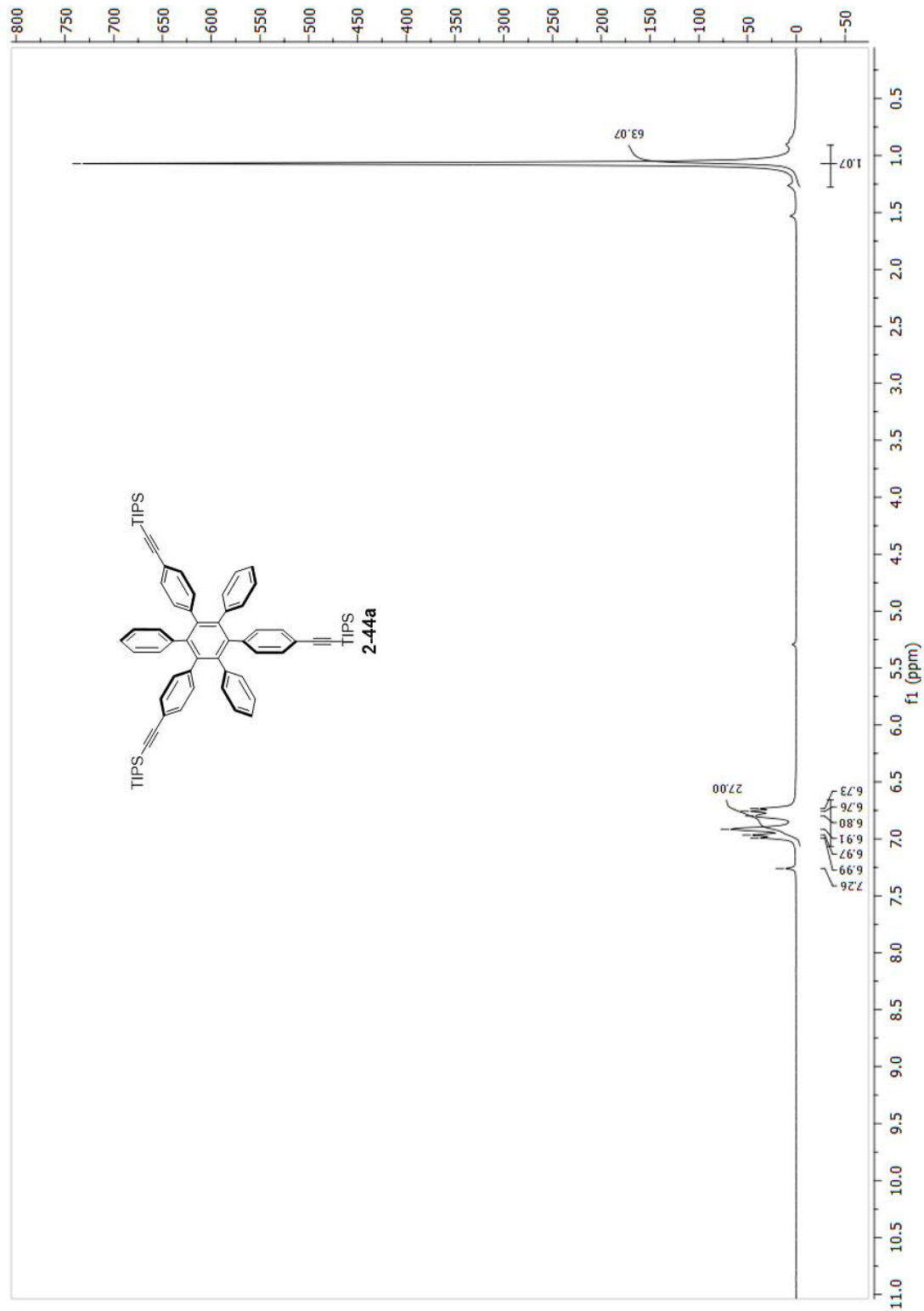


Figure A.54: ^{13}C -NMR, 100 MHz, CDCl_3 .

Characterisation of 2-43

Figure A.55: $^{13}\text{C-NMR}$, 100 MHz, CDCl_3 .

Characterisation of 2-44a

Figure A.56: $^1\text{H-NMR}$, 400 MHz, CDCl_3 .

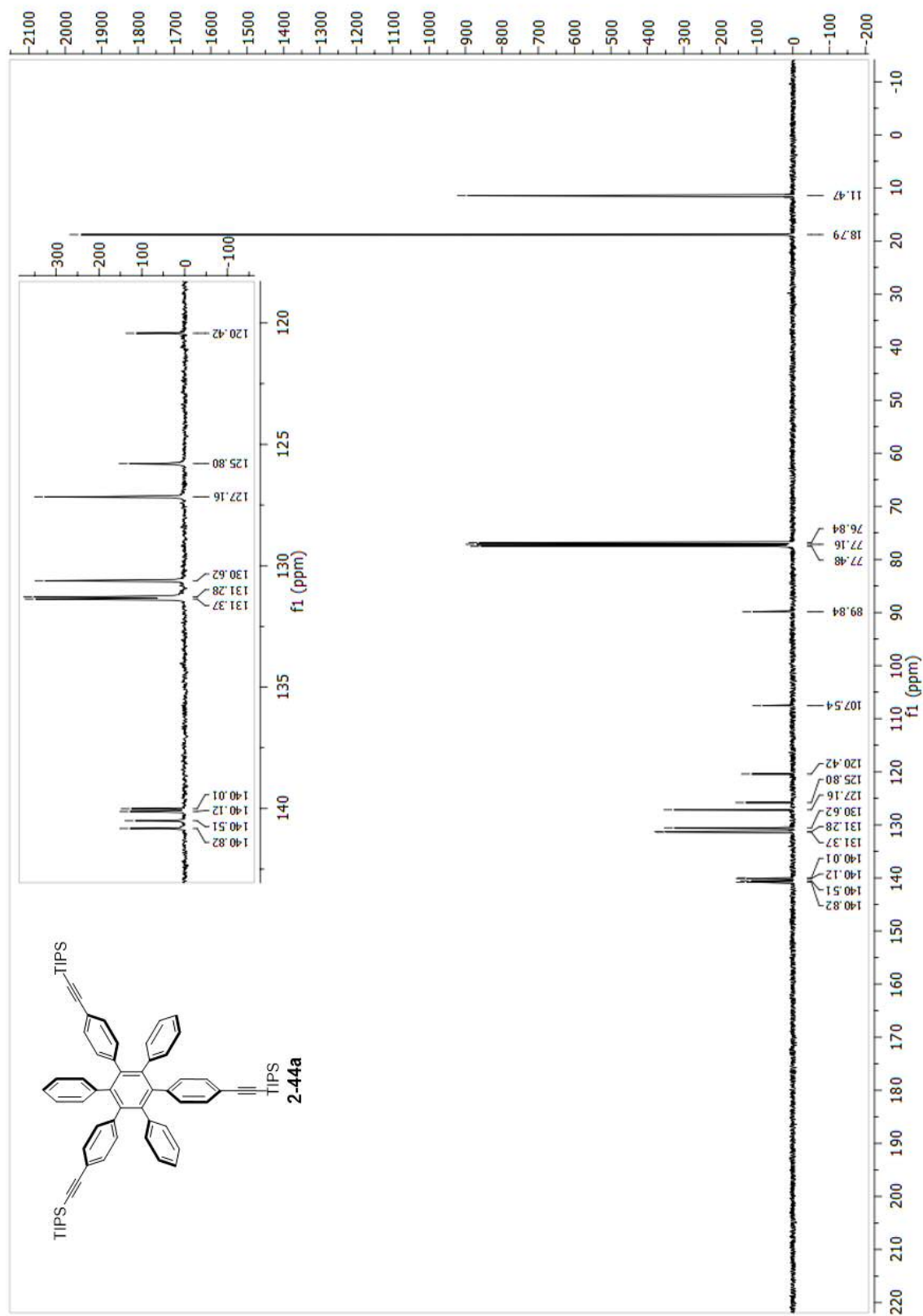
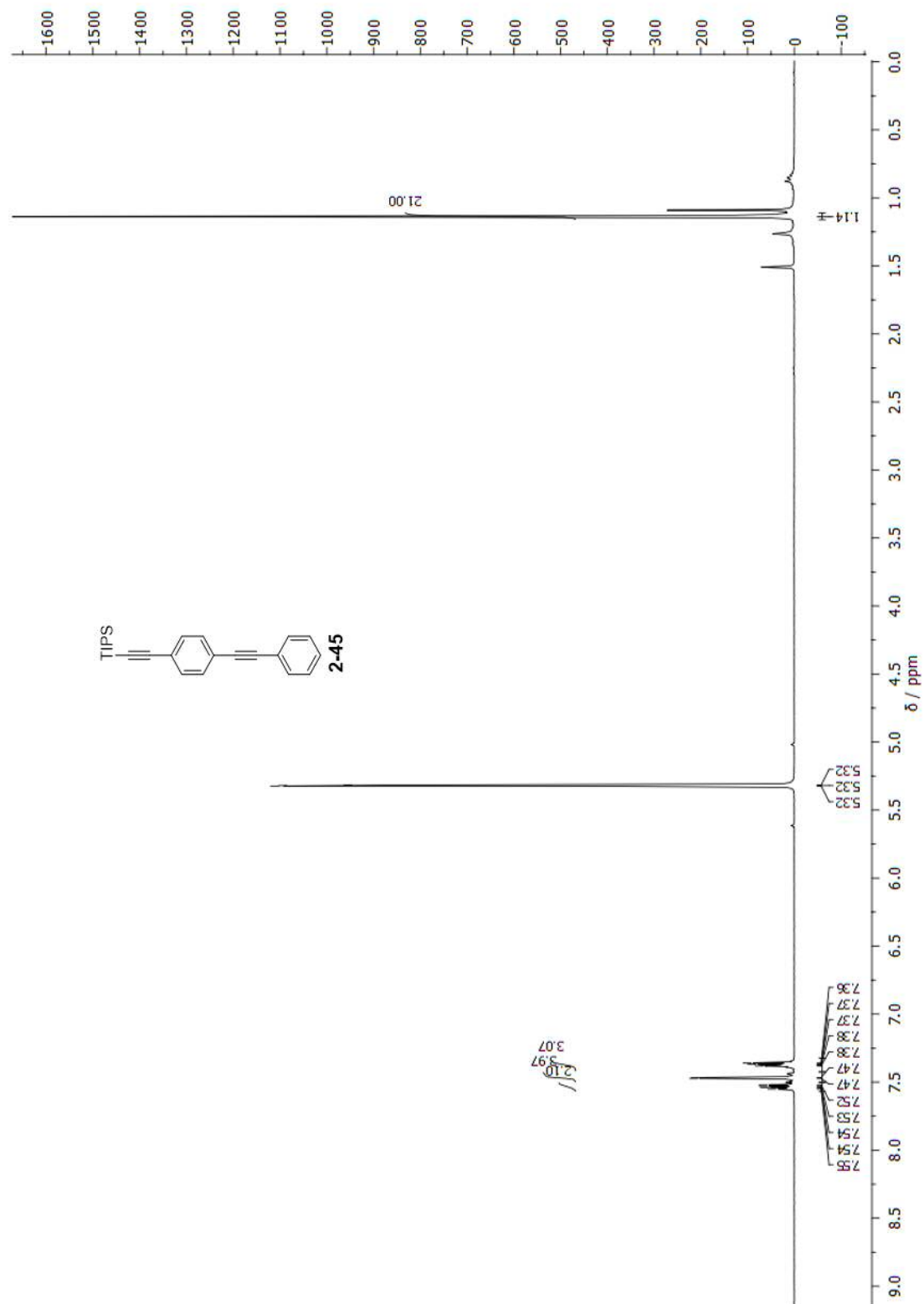


Figure A.57: ^{13}C -NMR, 100 MHz, CDCl_3 .

Characterisation of 2-45

Figure A.58: $^1\text{H-NMR}$, 400 MHz, CD_2Cl_2 .

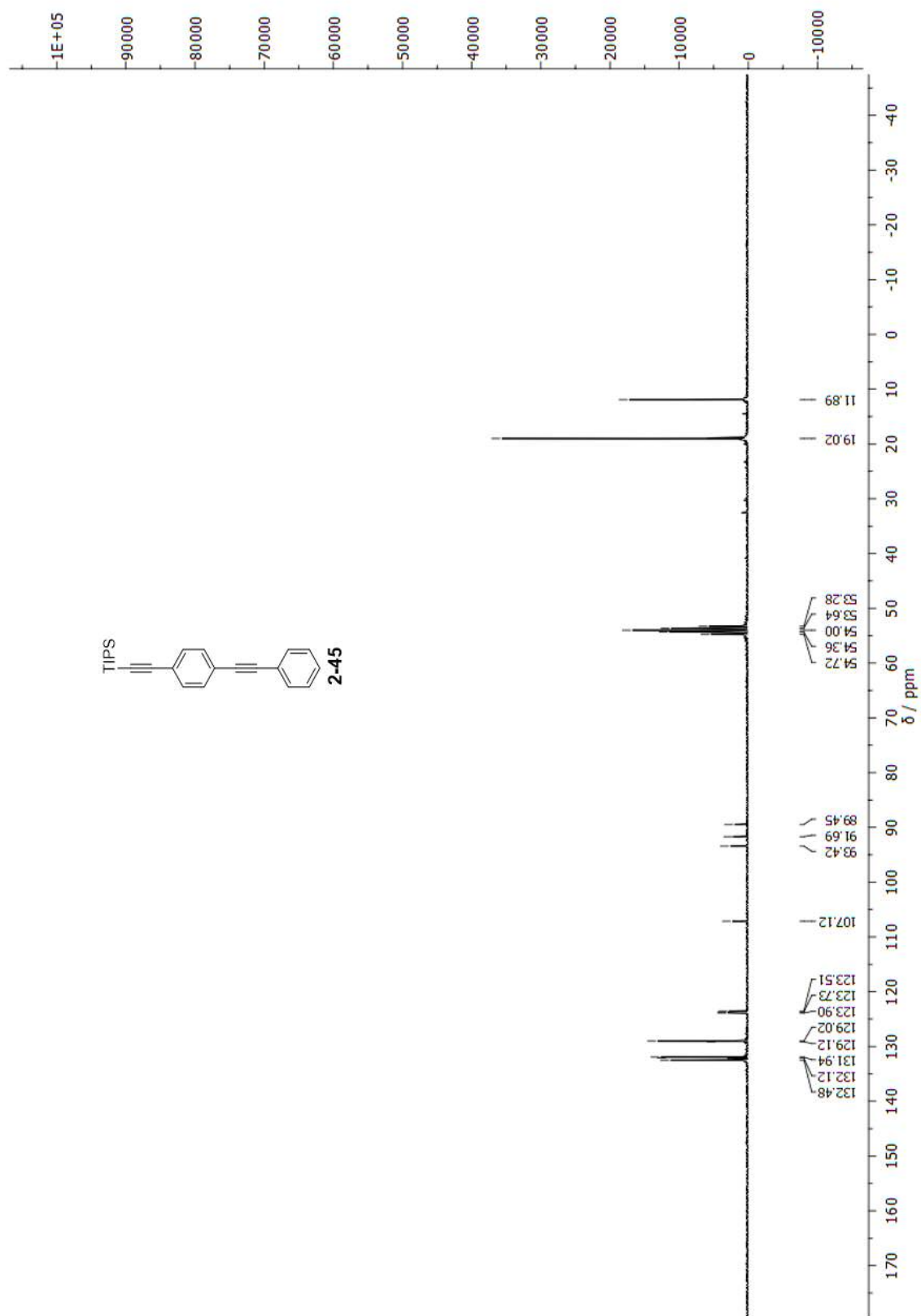
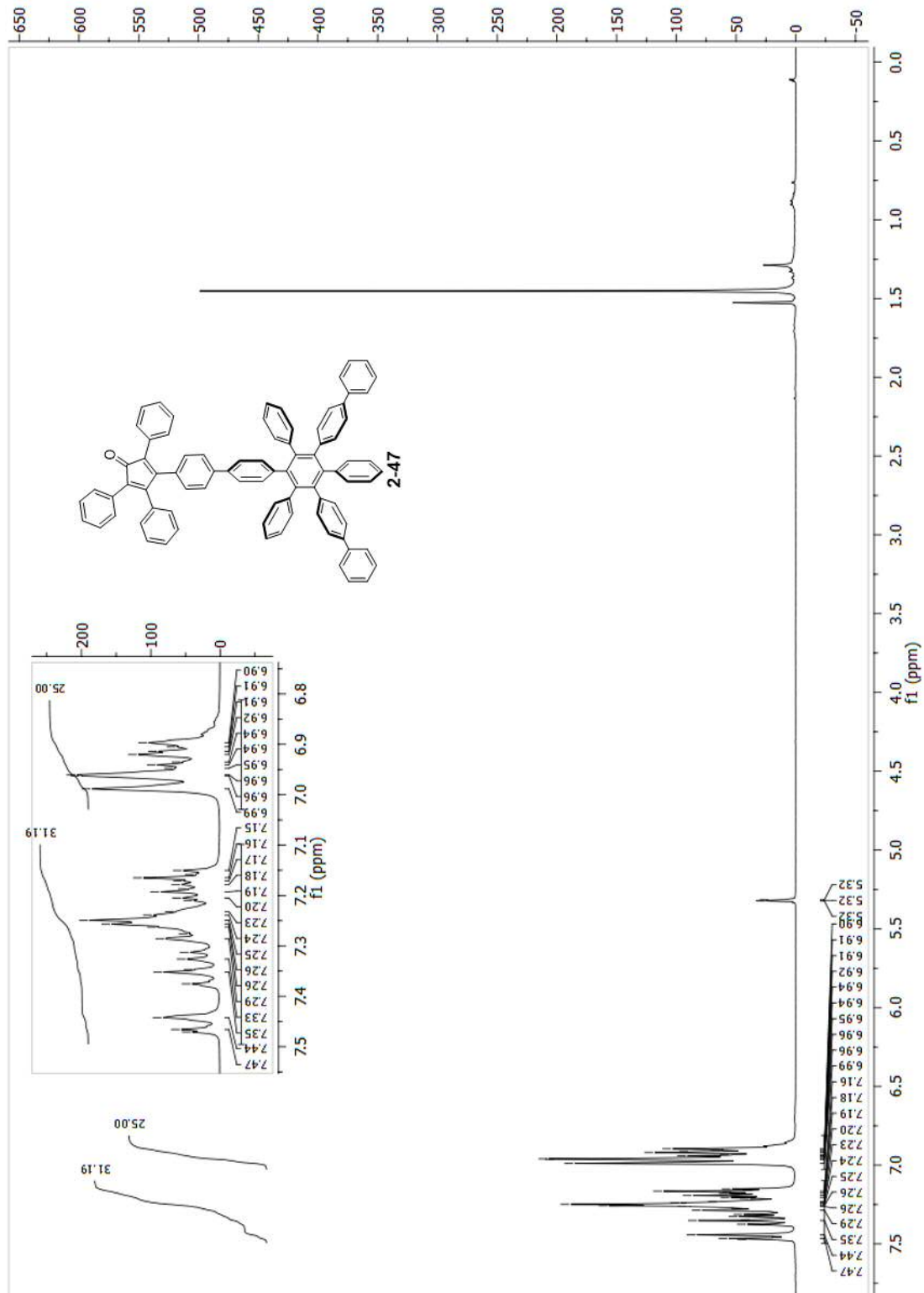


Figure A.59: $^1\text{H-NMR}$, 400 MHz, CD_2Cl_2 .

Characterisation of 2-47

Figure A.60: $^1\text{H-NMR}$, 400 MHz, CD_2Cl_2 .

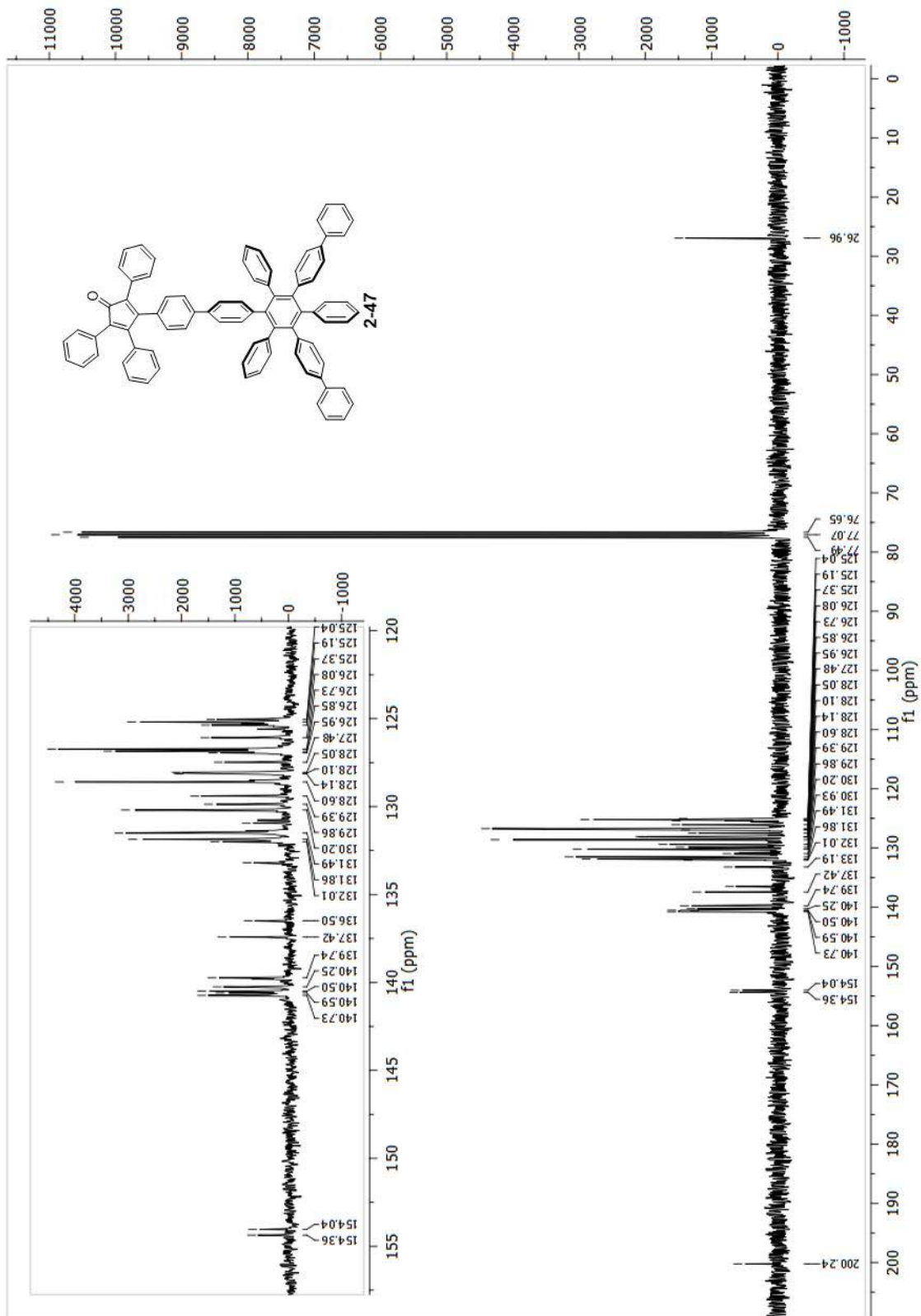
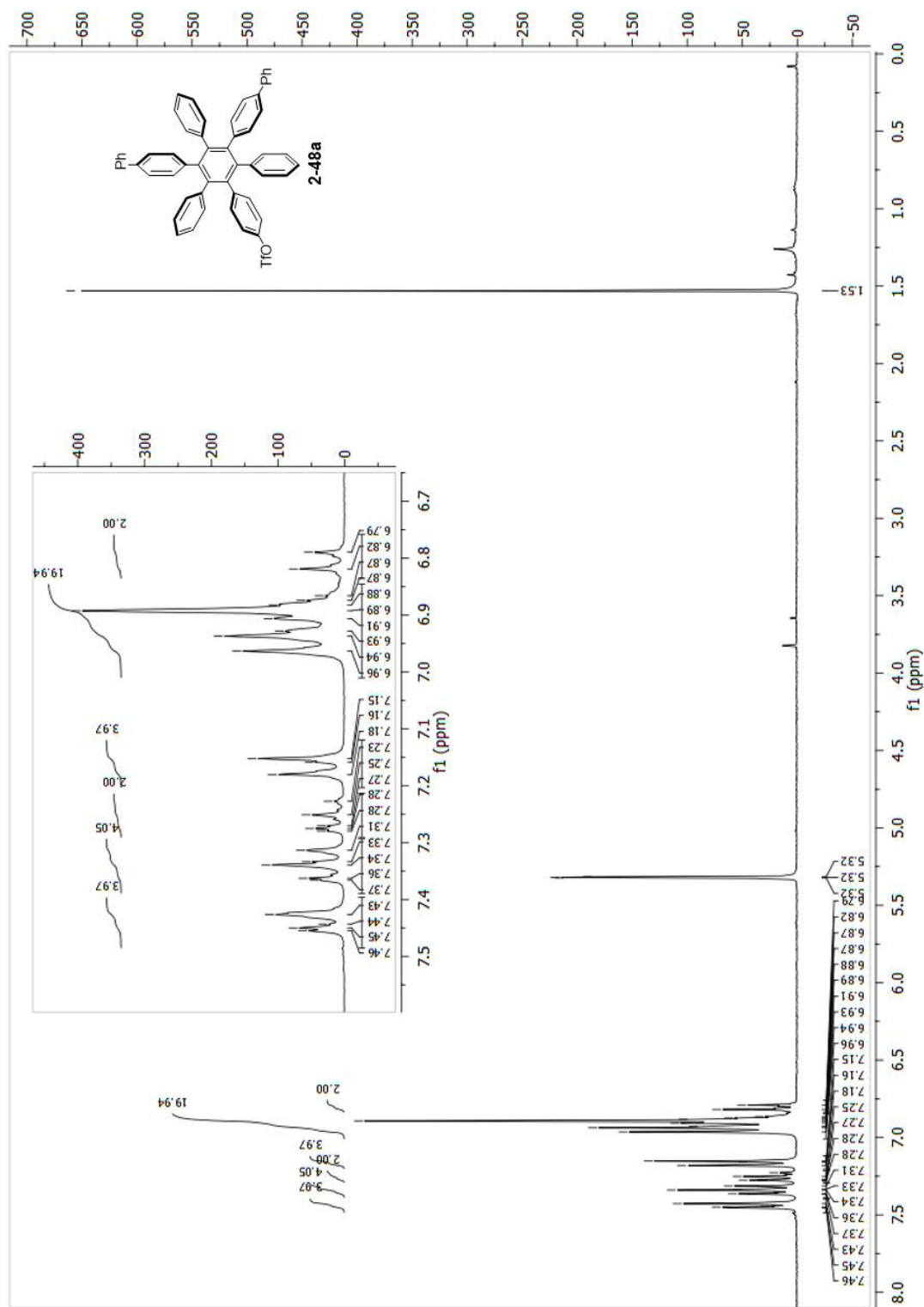


Figure A.61: ^{13}C -NMR, 100 MHz, CDCl_3 .

Characterisation of 2-48a

Figure A.62: $^1\text{H-NMR}$, 400 MHz, CD_2Cl_2 .

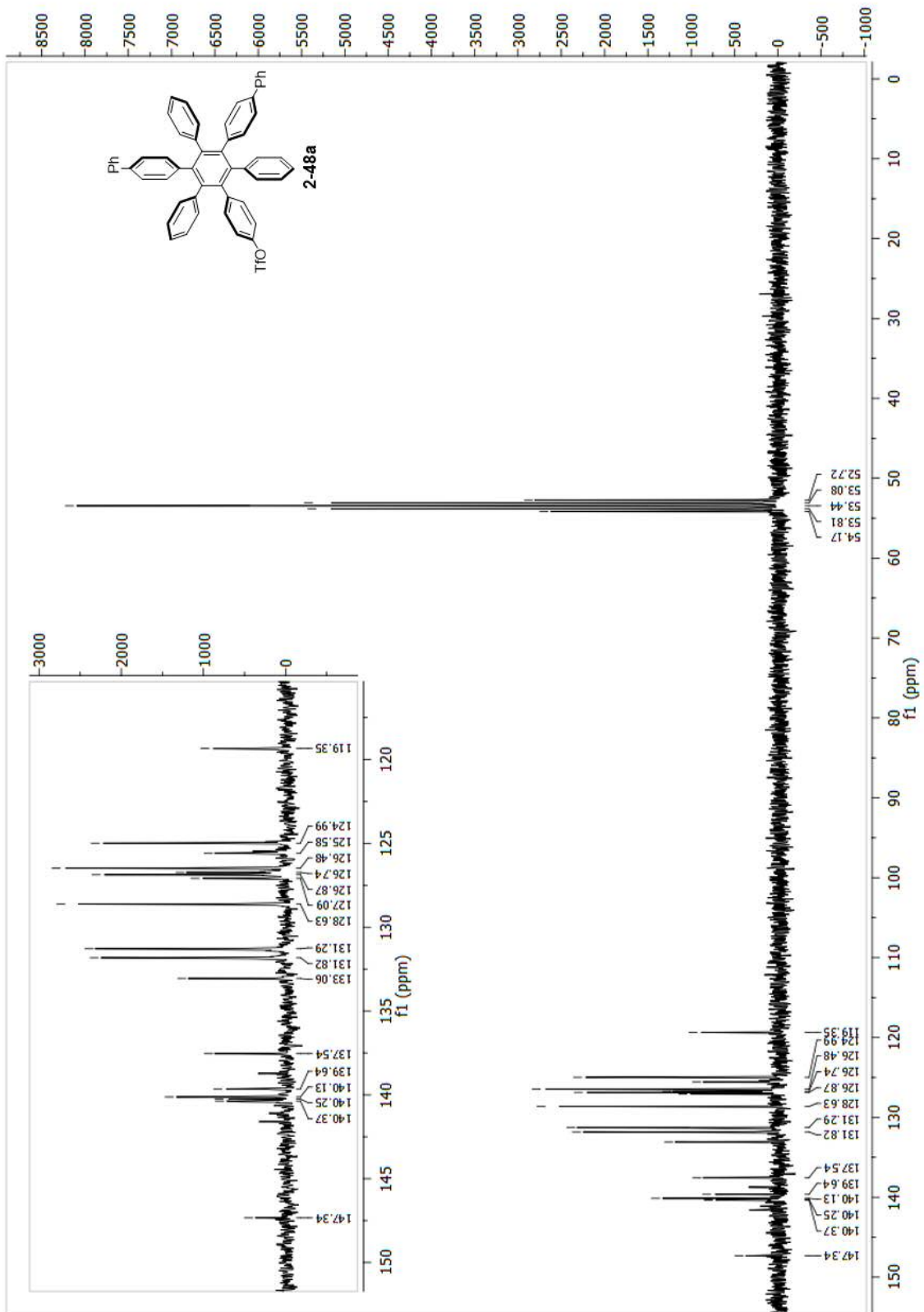
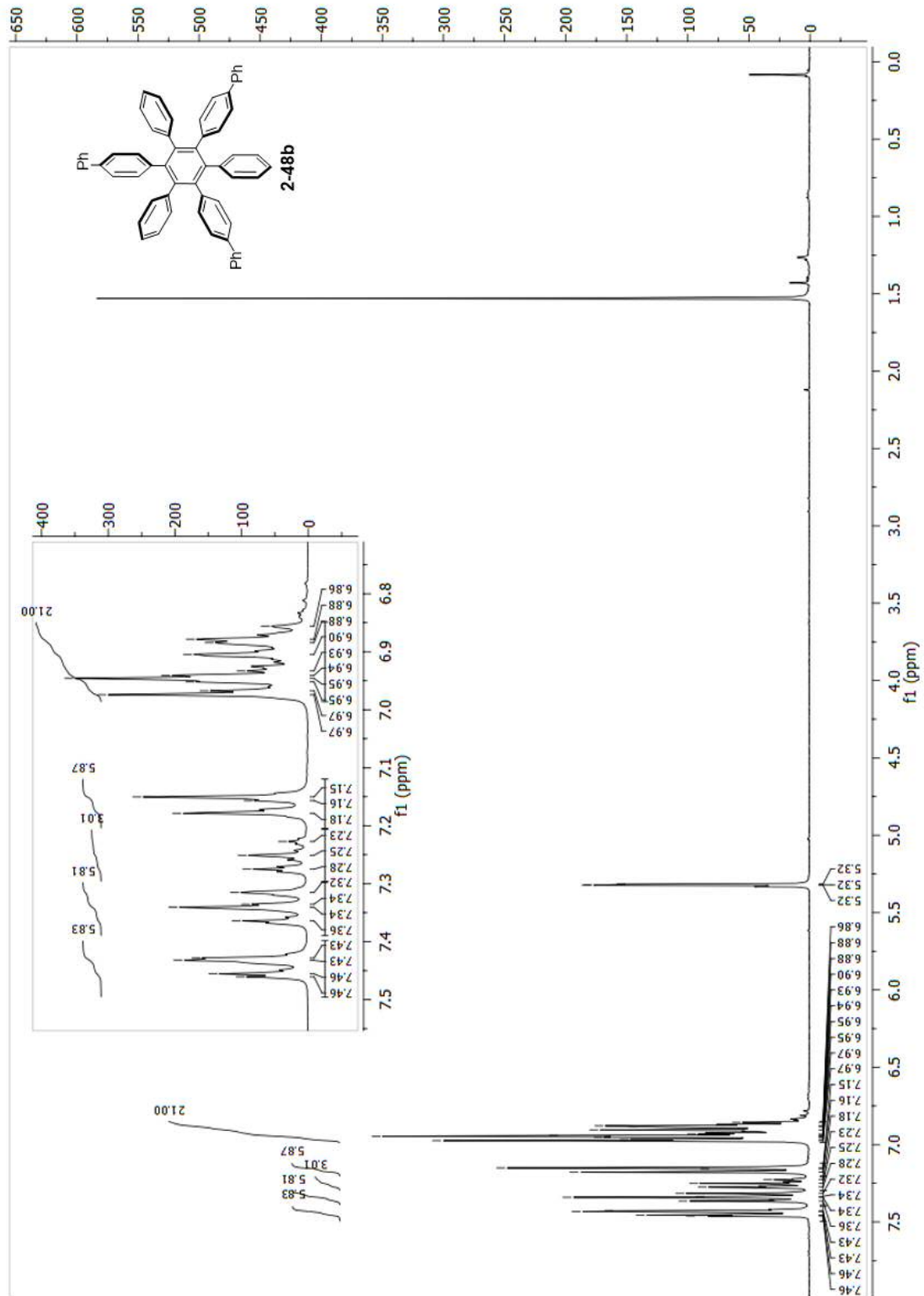


Figure A.63: ^{13}C -NMR, 100 MHz, CD_2Cl_2 .

Characterisation of 2-48b

Figure A.64: $^1\text{H-NMR}$, 400 MHz, CD_2Cl_2 .

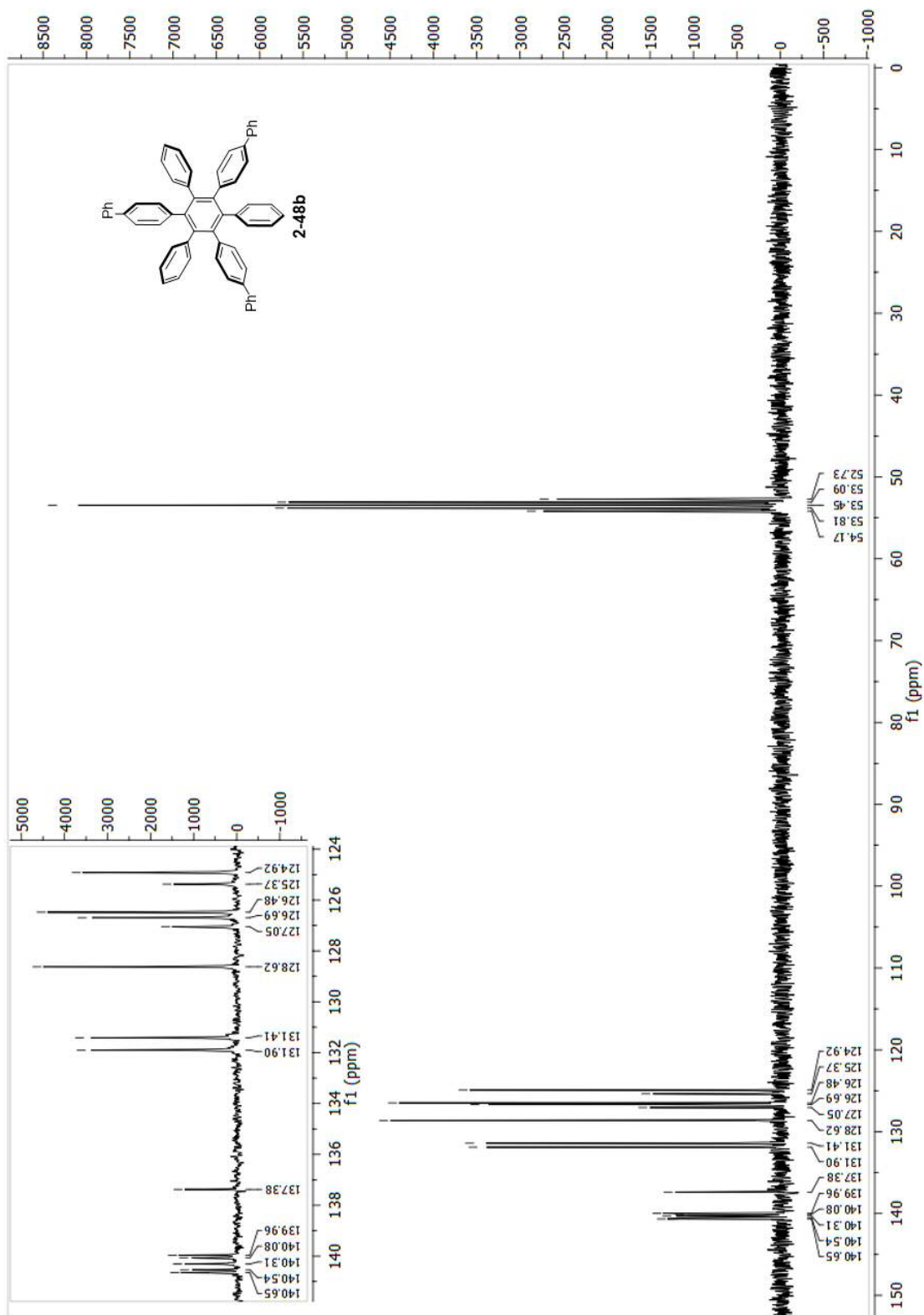
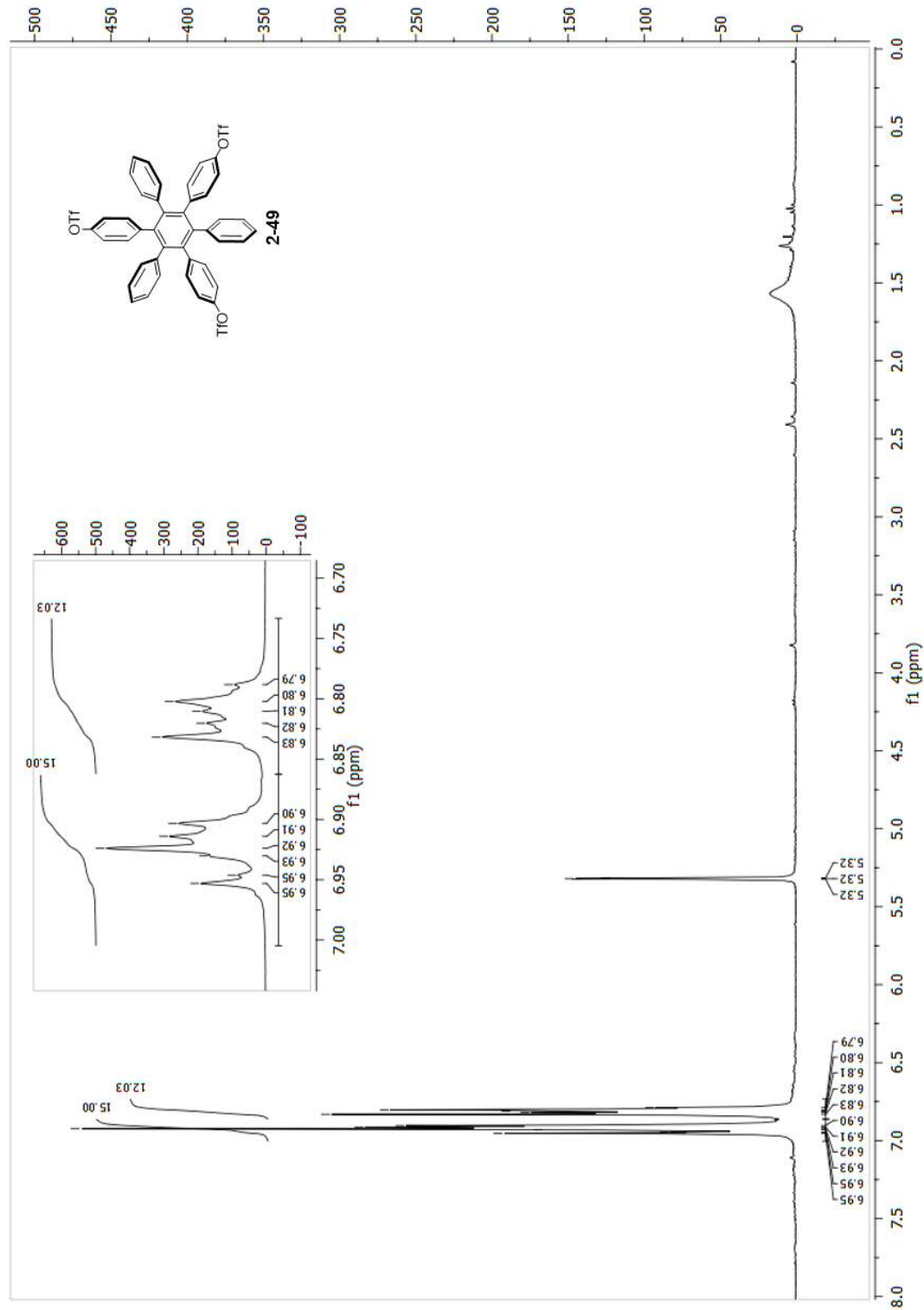


Figure A.65: ^{13}C -NMR, 100 MHz, CD_2Cl_2 .

Characterisation of 2-49

Figure A.66: $^1\text{H-NMR}$, 400 MHz, CD_2Cl_2 .

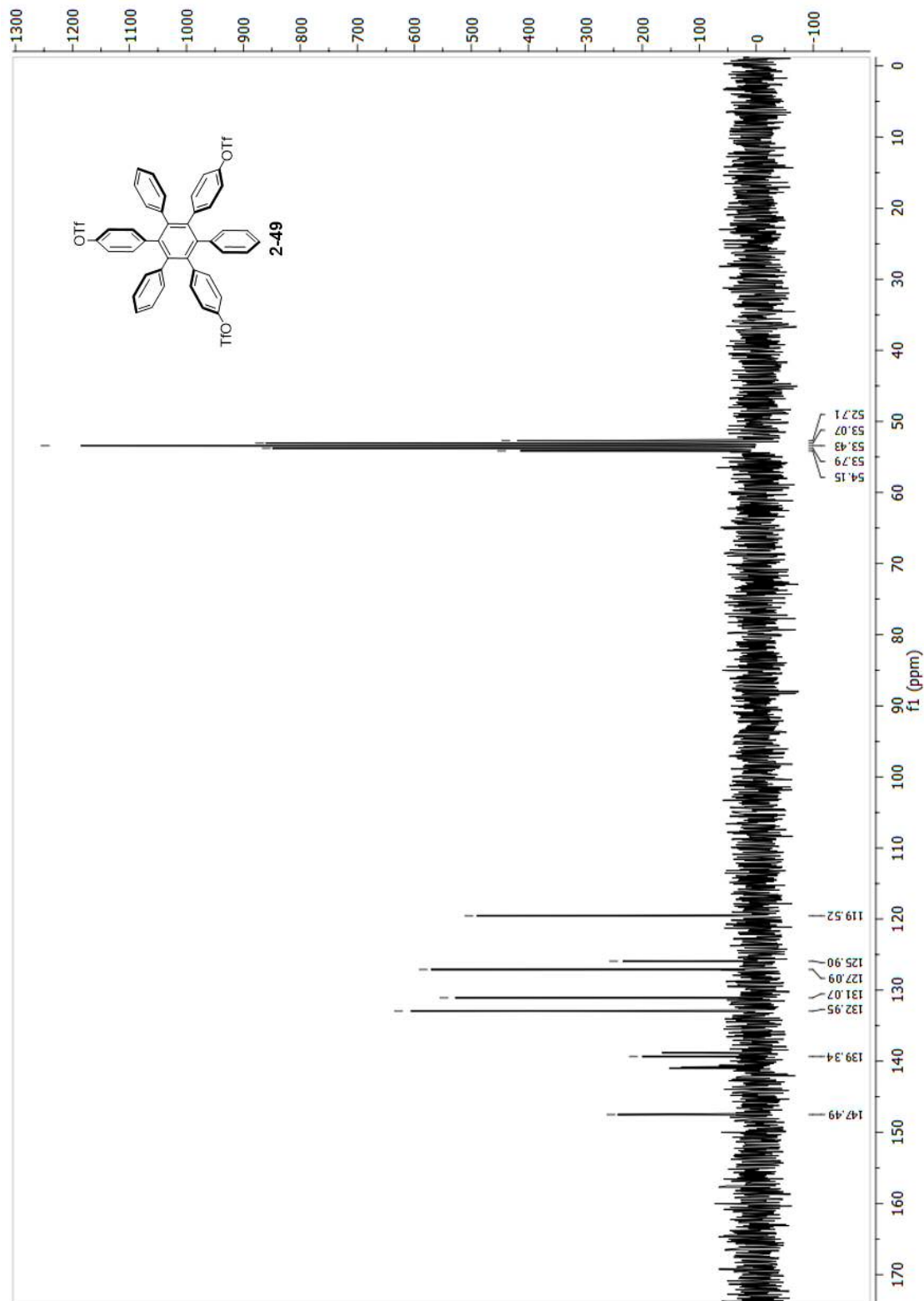
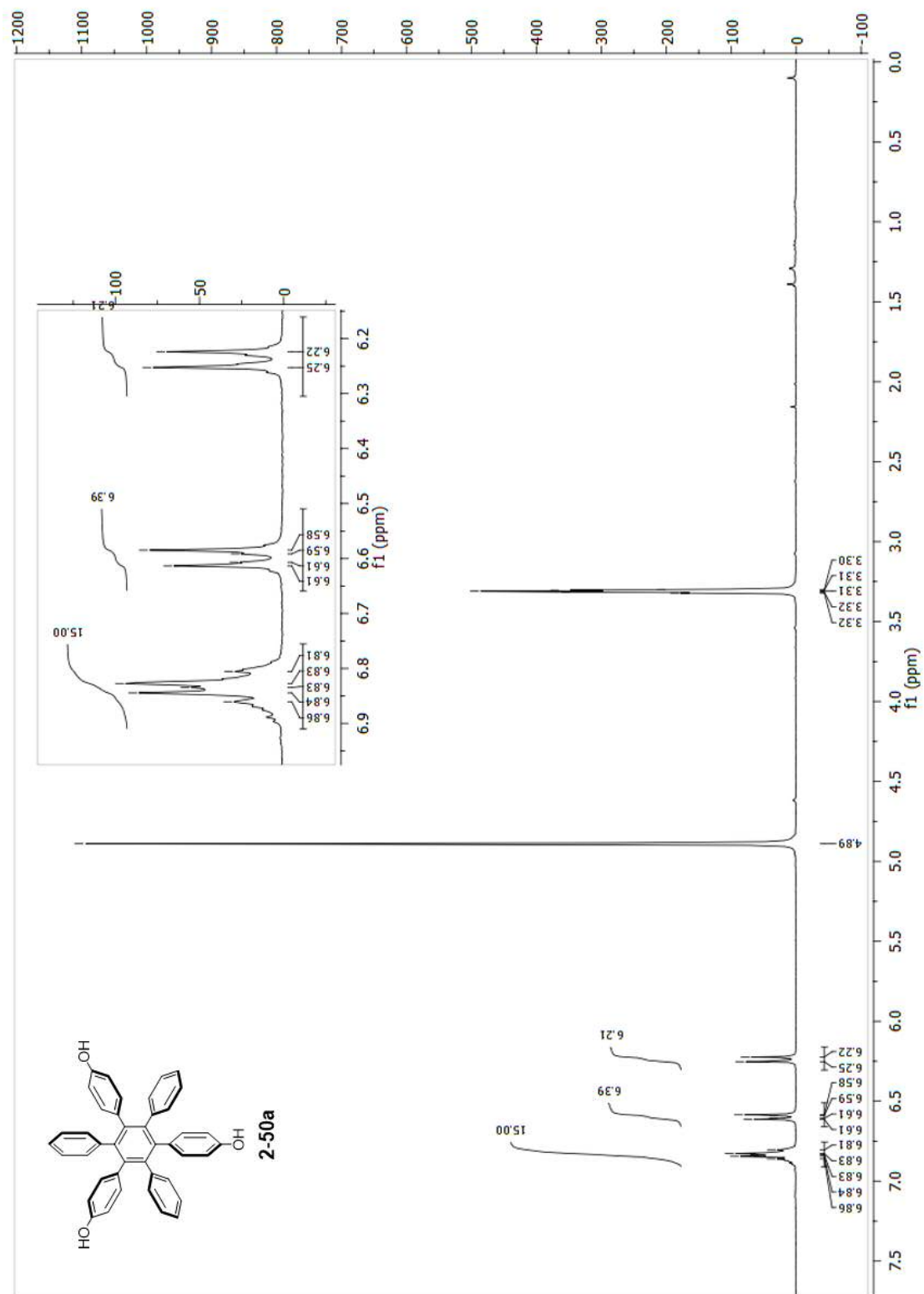


Figure A.67: ^{13}C -NMR, 100 MHz, CD_2Cl_2 .

Characterisation of 2-50a

Figure A.68: $^1\text{H-NMR}$, 400 MHz, CD_3OD .

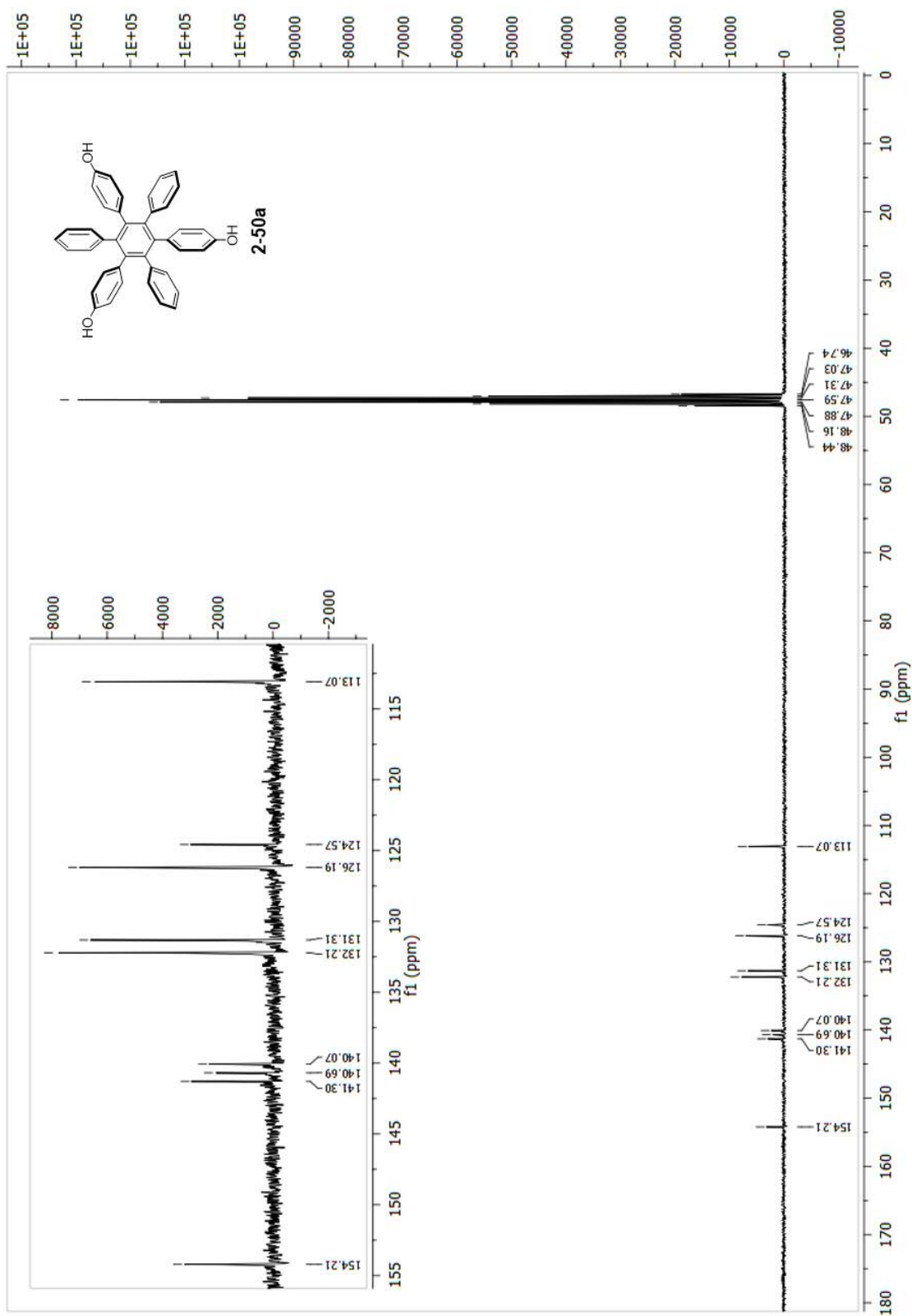
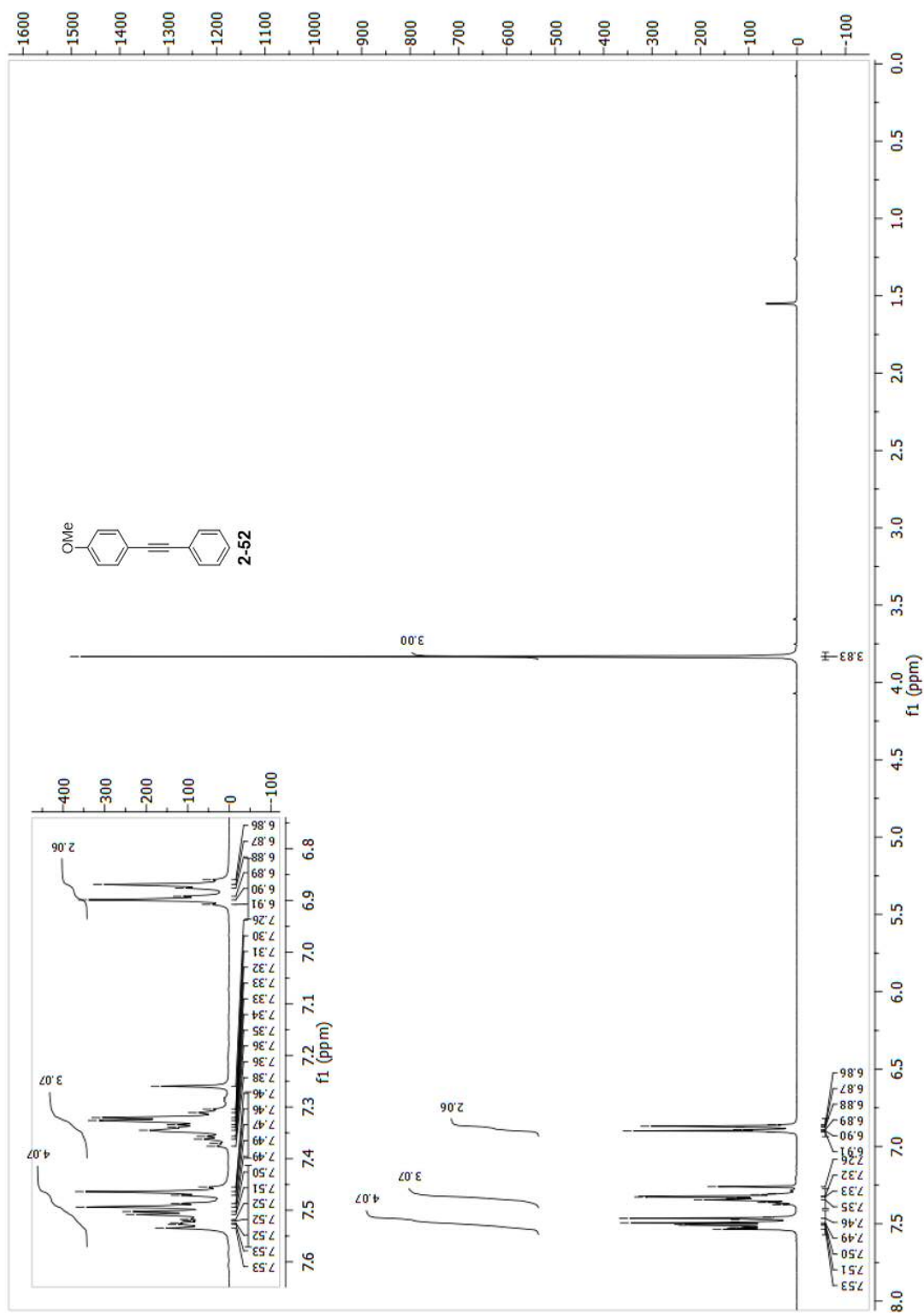


Figure A.69: ^{13}C -NMR, 100 MHz, CD_3OD .

Characterisation of 2-52

Figure A.70: ¹H-NMR, 400 MHz, CDCl₃.

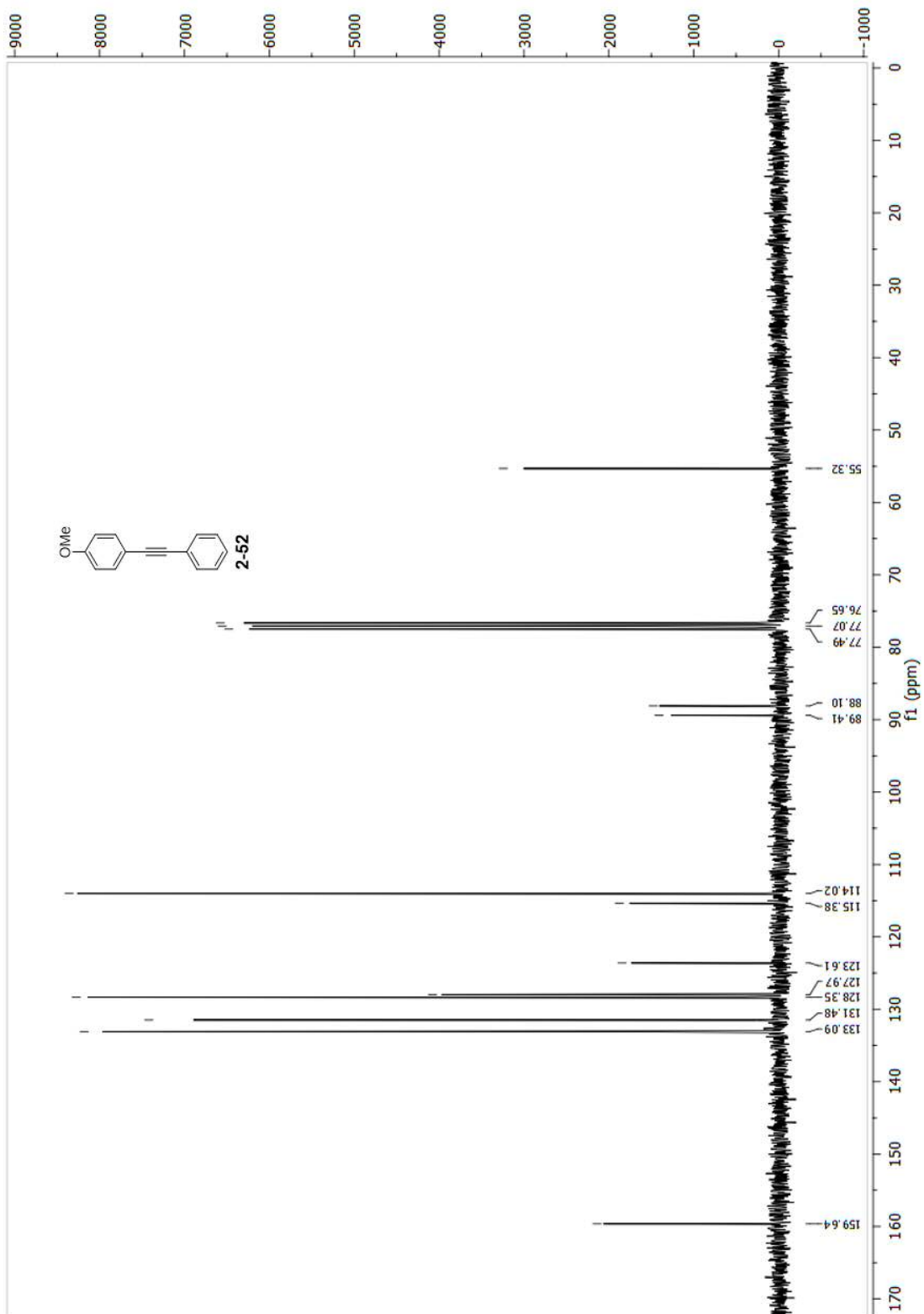
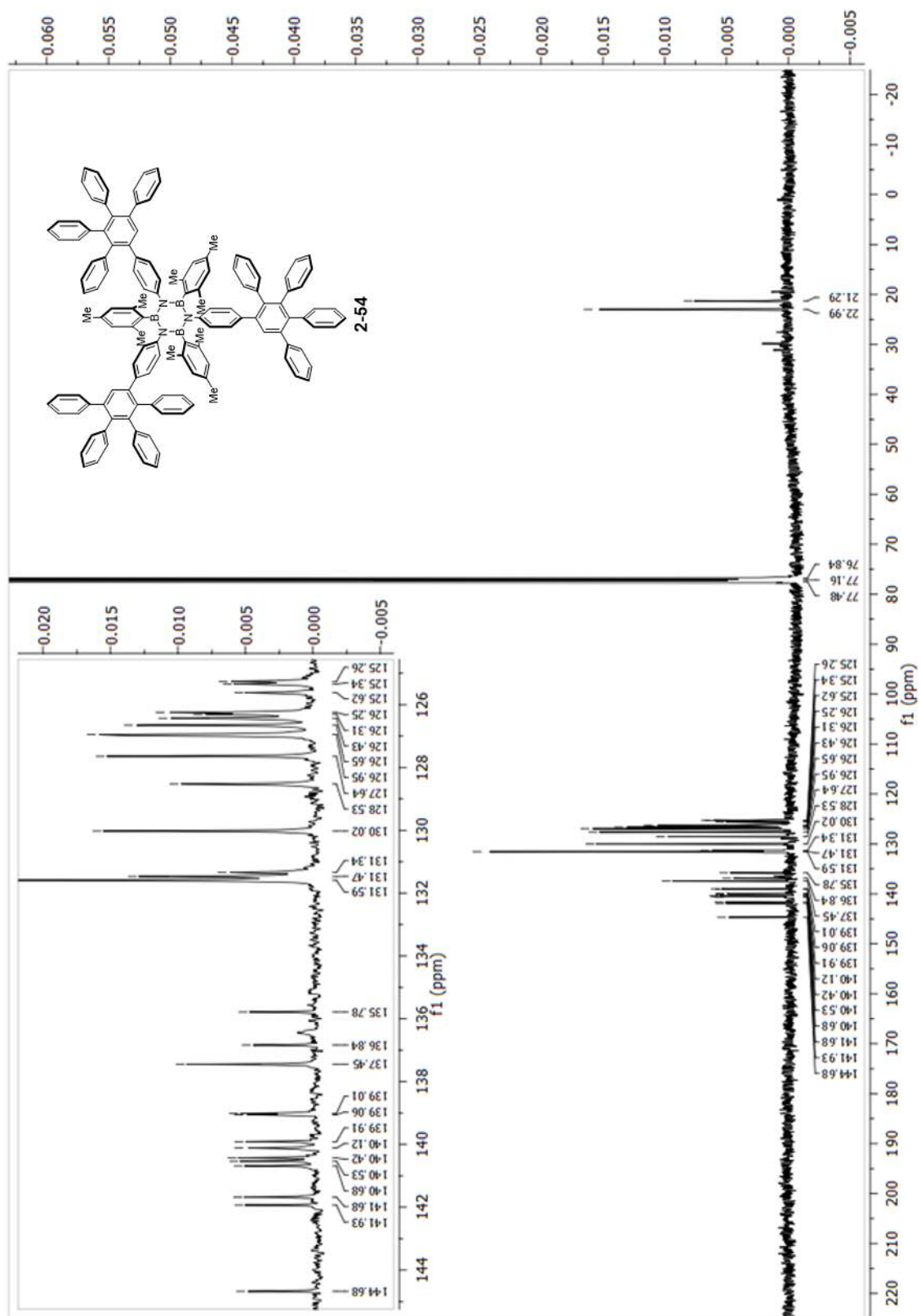


Figure A.71: ^{13}C -NMR, 100 MHz, CDCl_3 .

Characterisation of 2-54

Figure A.72: ^{13}C -NMR, 100 MHz, CDCl_3 .

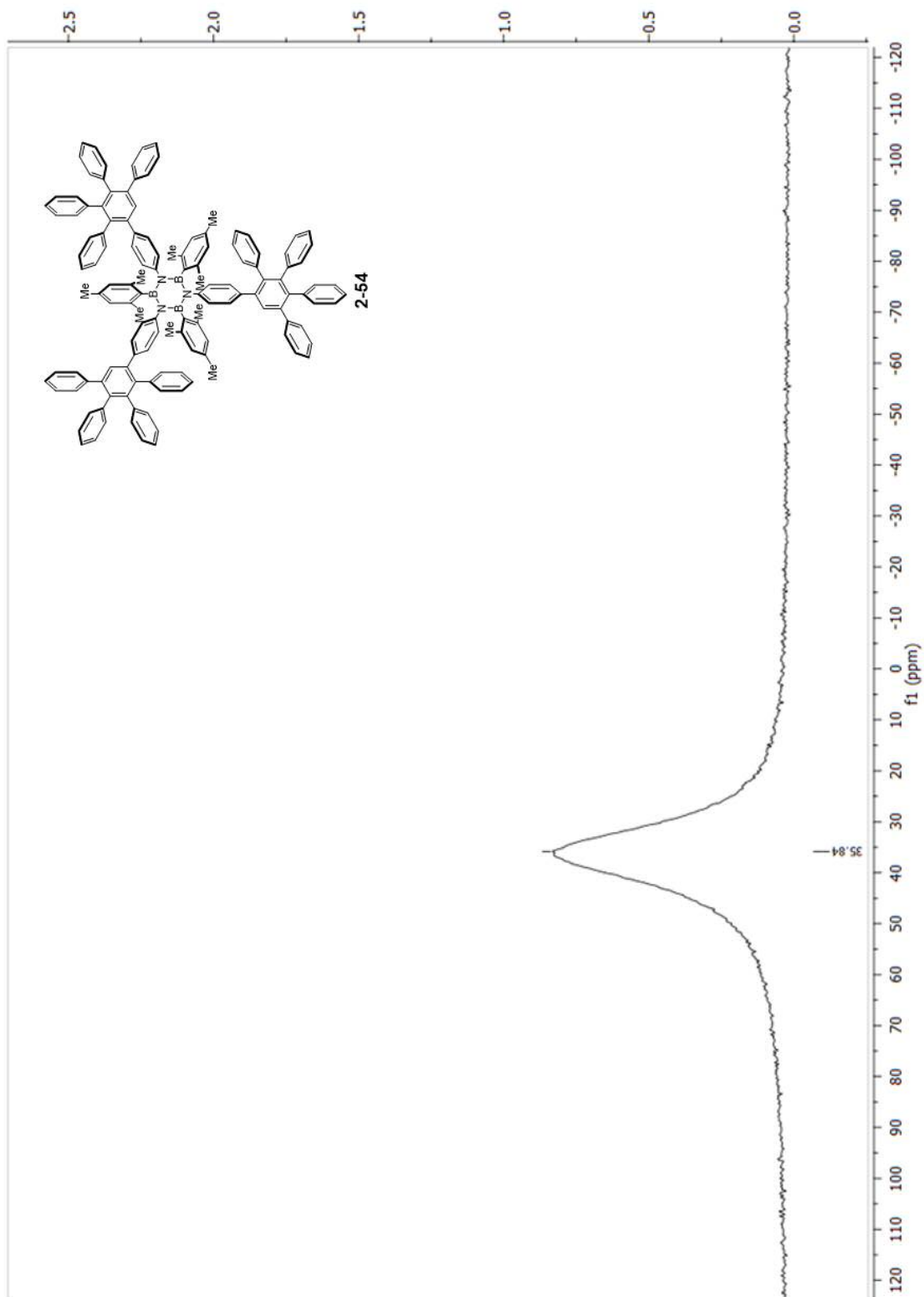


Figure A.73: ^{11}B -NMR, 128 MHz, CDCl_3 .

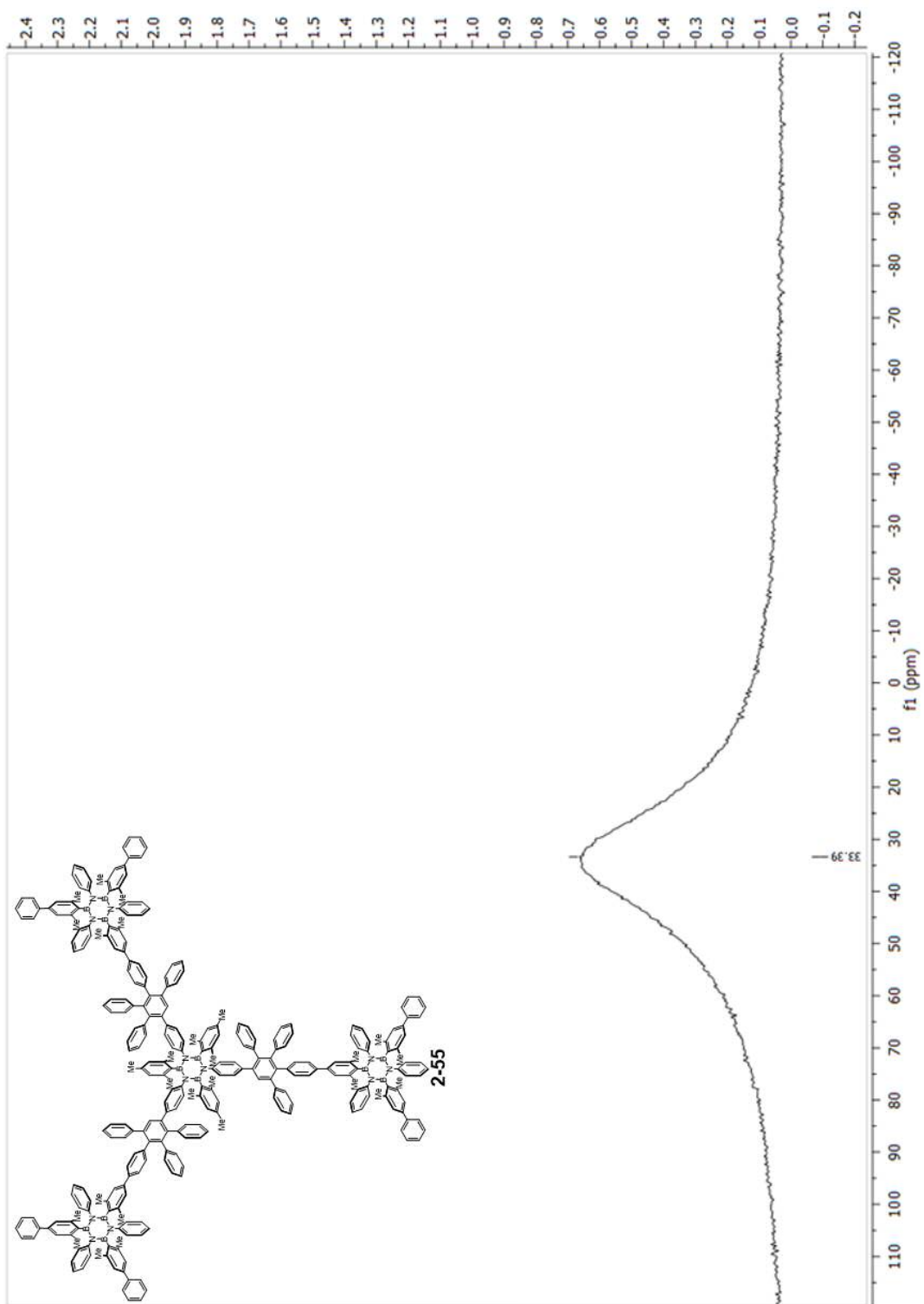


Figure A.75: ^{11}B -NMR, 128 MHz, CD_2Cl_2 .

Characterisation of 2-56

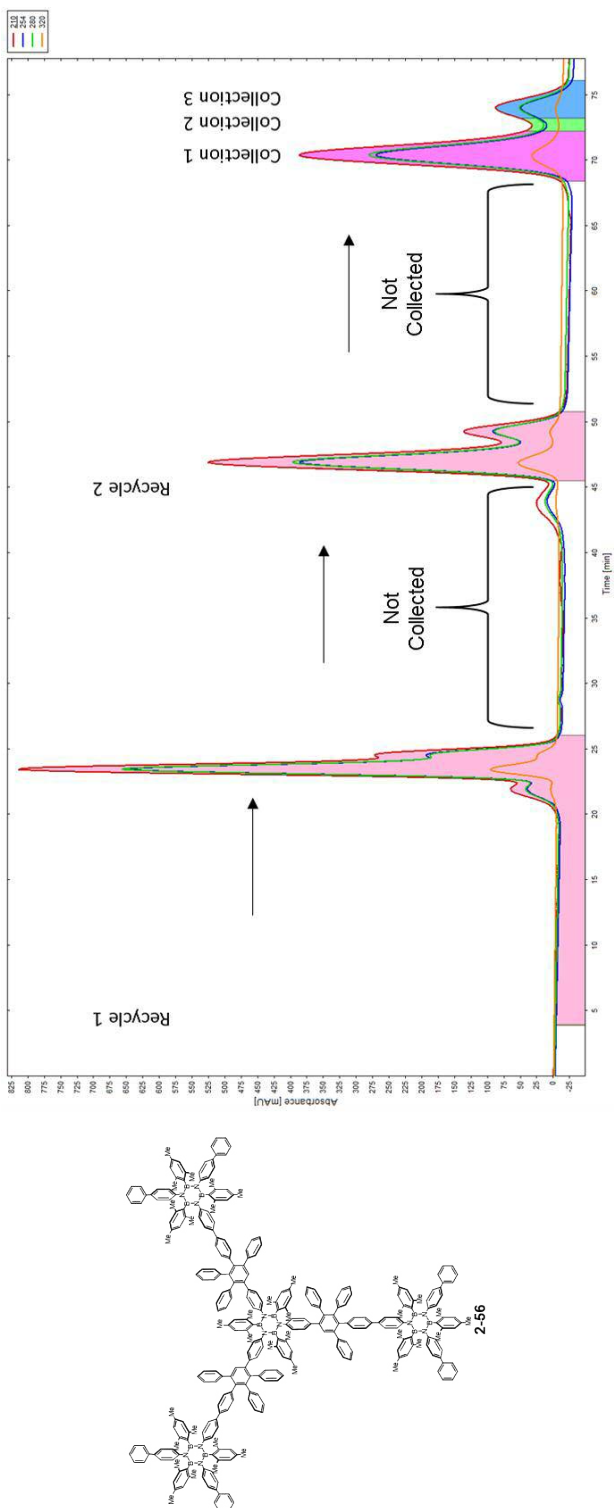


Figure A.76: Gel Permeation Chromatography (GPC), Recycling mode.

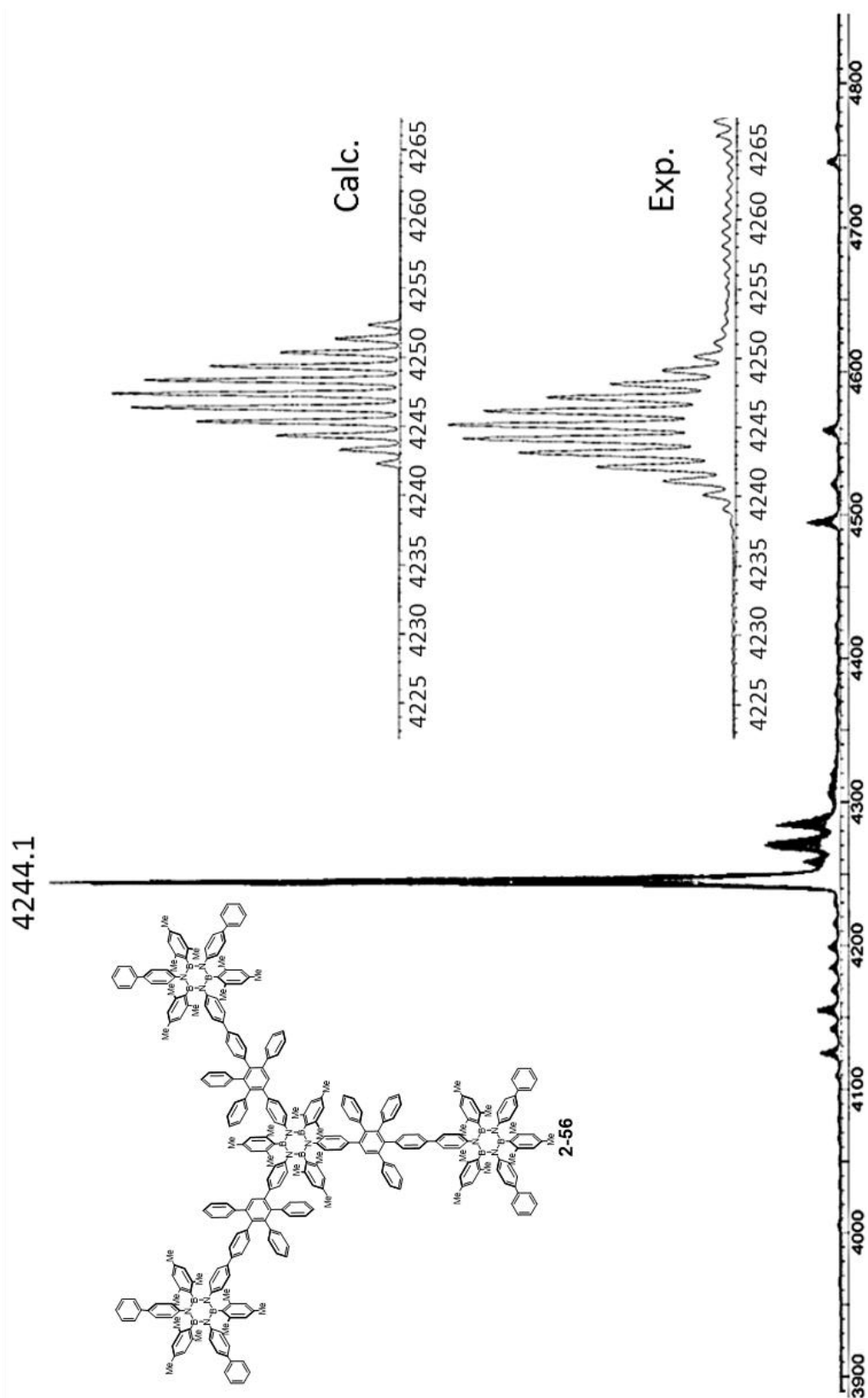


Figure A.77: MALDI-TOF Mass spectrometry of **Collection 1** (from GPC run, above), matrix: trans-2-[3-(4-tert-butyl-phenyl)-2-methyl-2-propenyldene]malonitrile (DCTB).

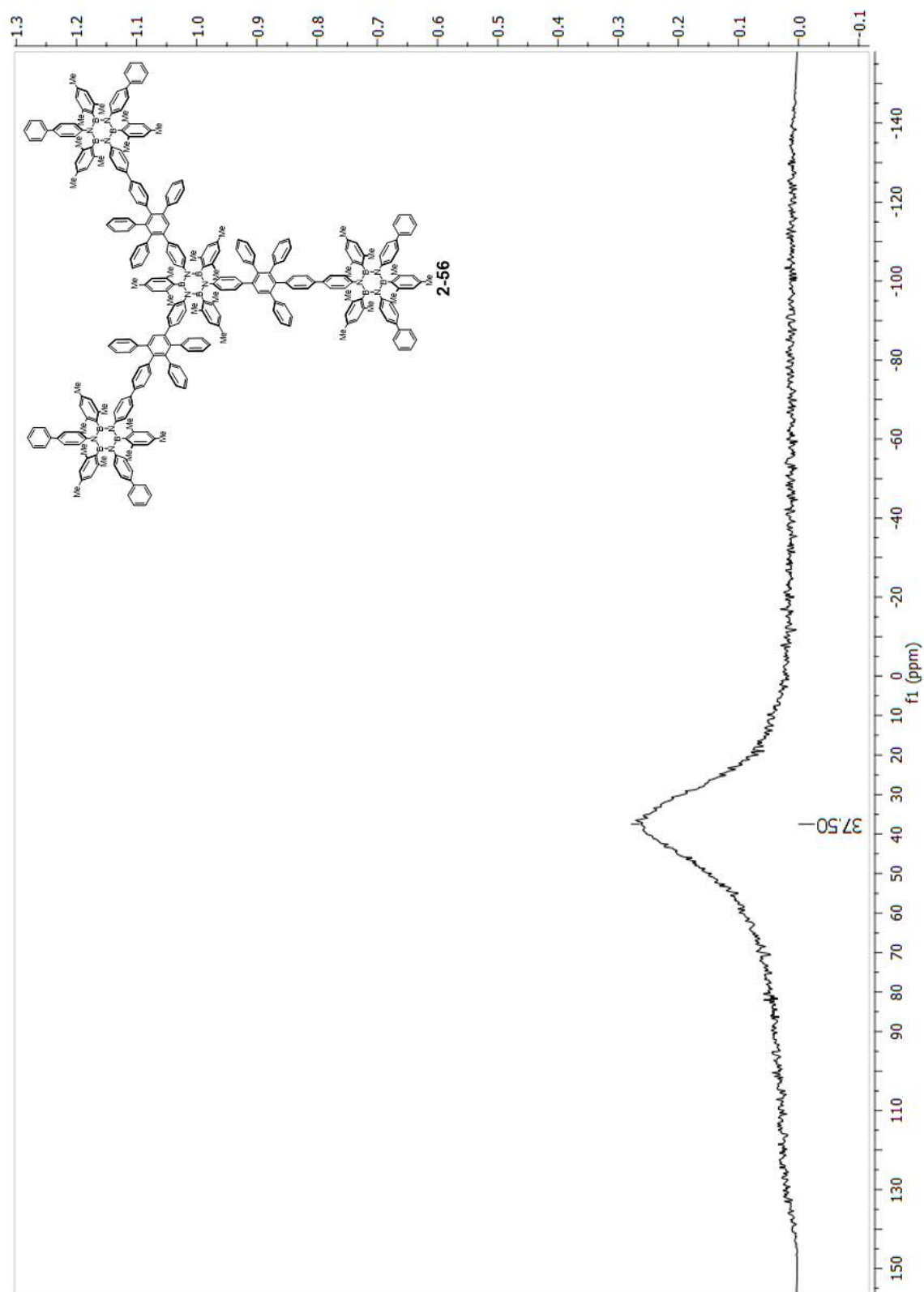


Figure A.79: ^{11}B -NMR, 128 MHz, CD_2Cl_2 .

Characterisation of 2-57

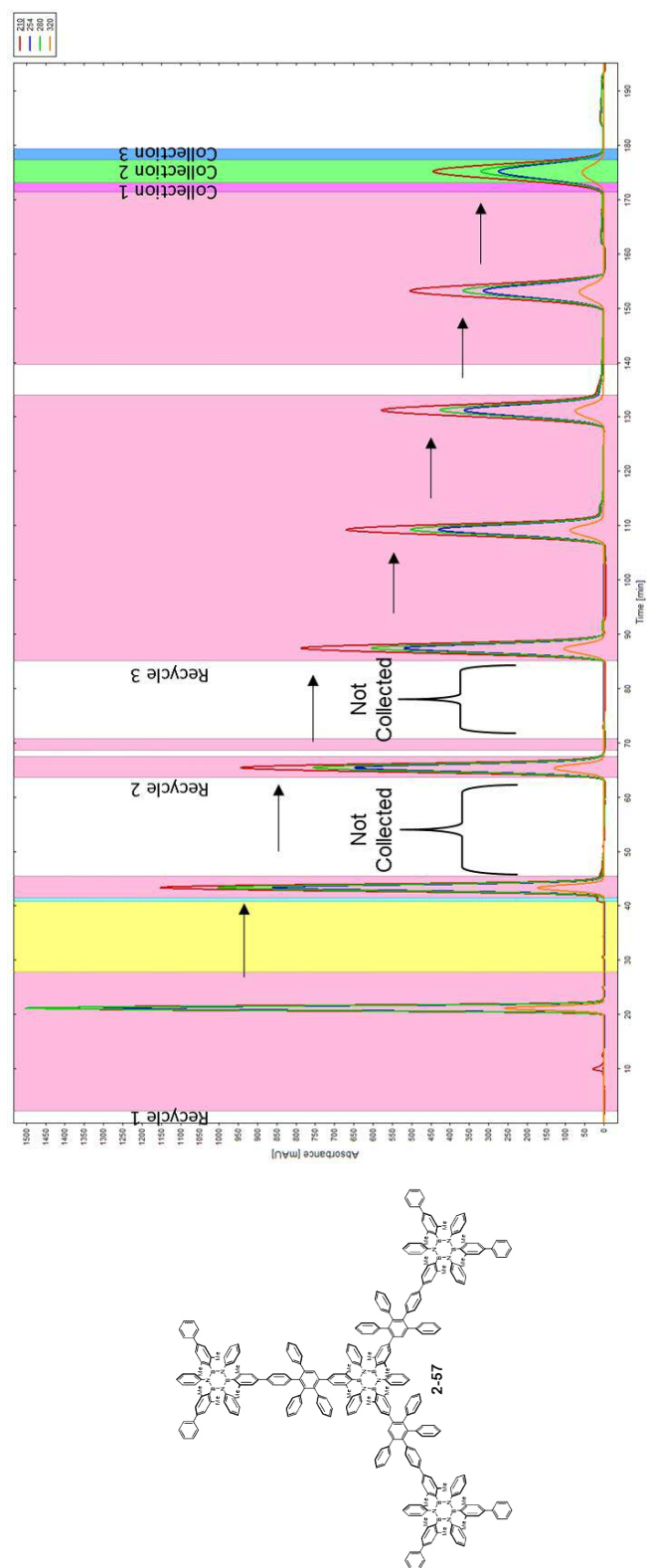


Figure A.80: Gel Permeation Chromatography (GPC), Recycling mode.

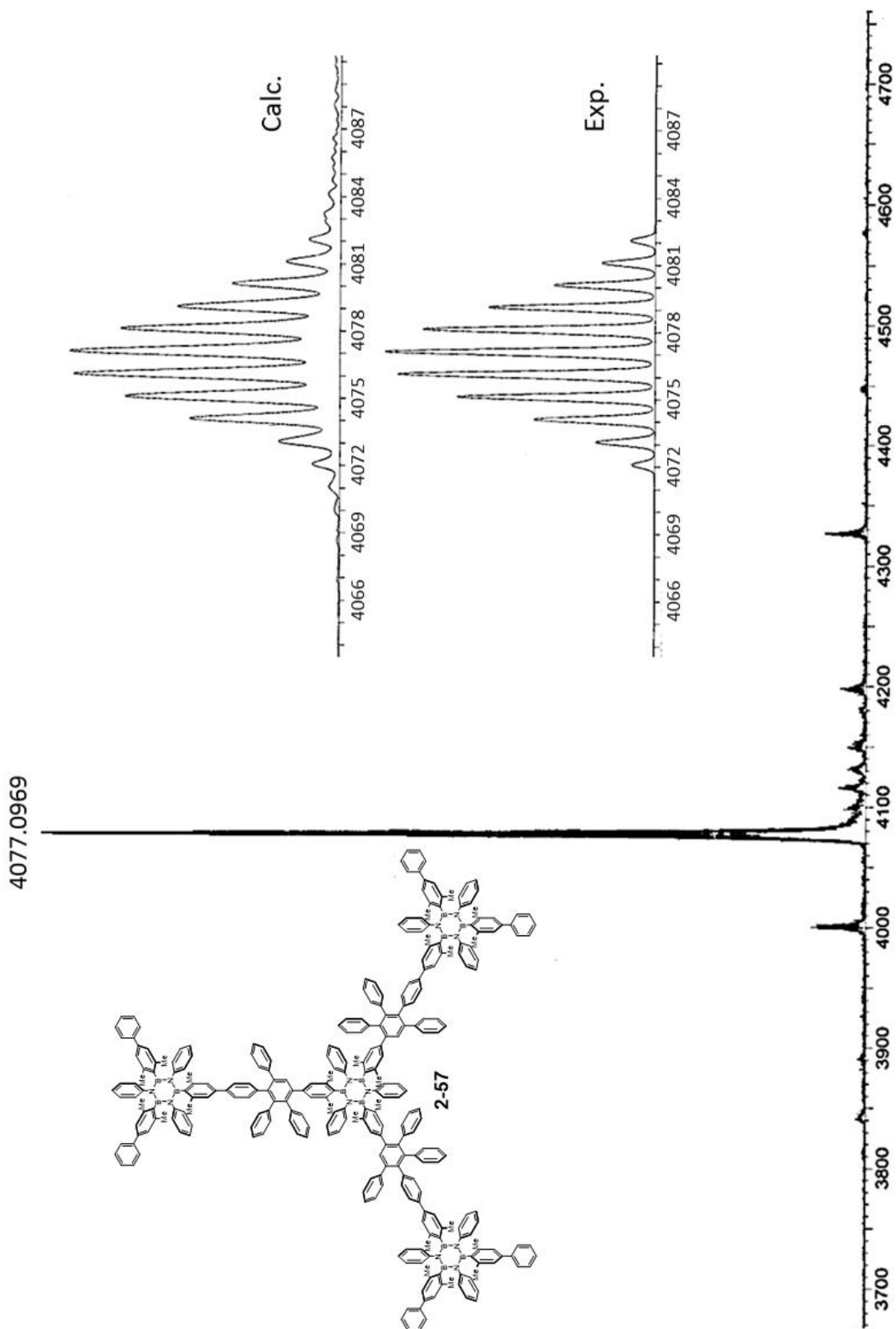


Figure A.81: MALDI-TOF Mass spectrometry of **Collection 2** (from GPC run, above), matrix: trans-2-[3-(4-tert-butyl-phenyl)-2-methyl-2-propenylidene]malonitrile (DCTB).

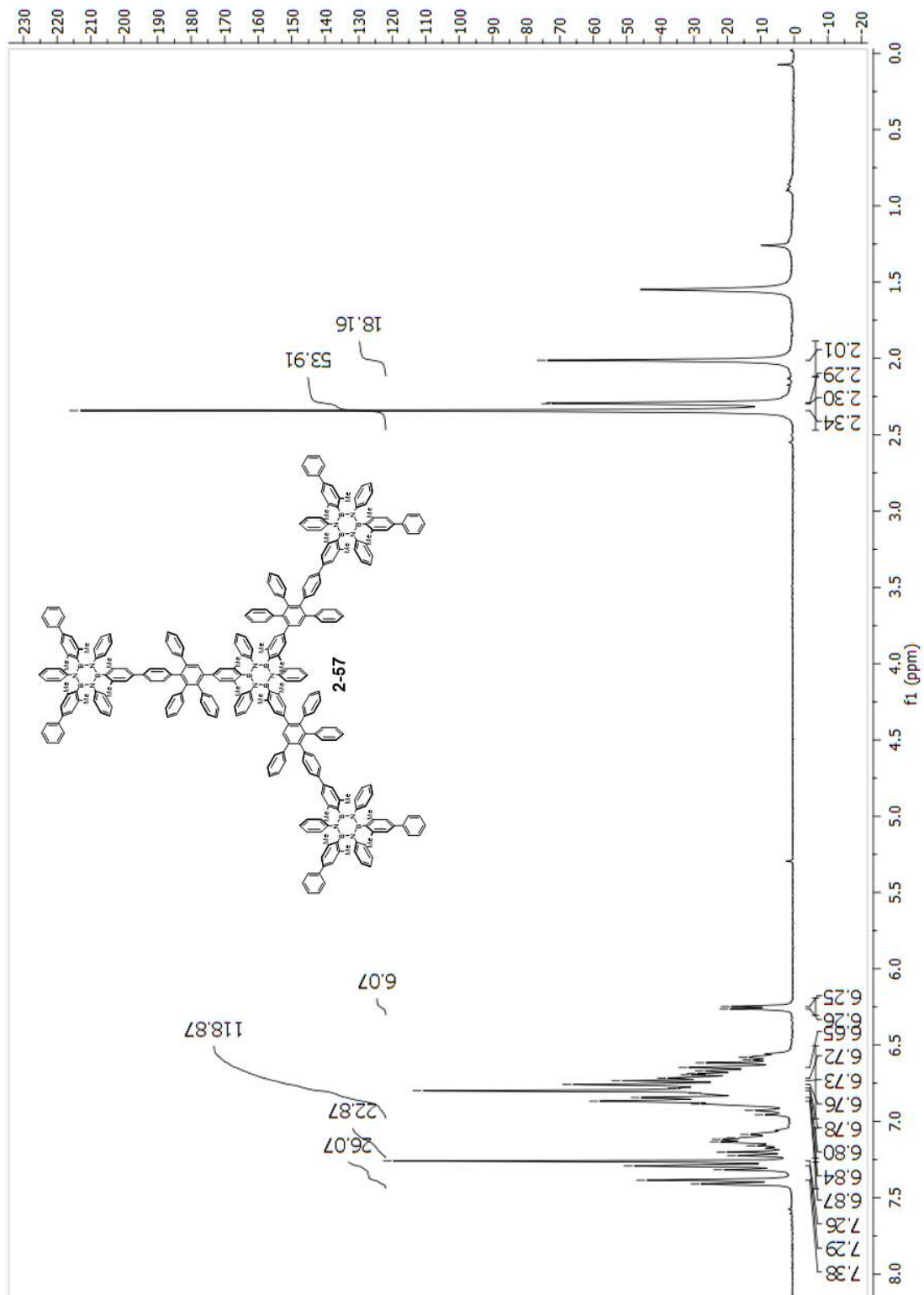


Figure A.82: $^1\text{H-NMR}$, 300 MHz, CDCl_3 .

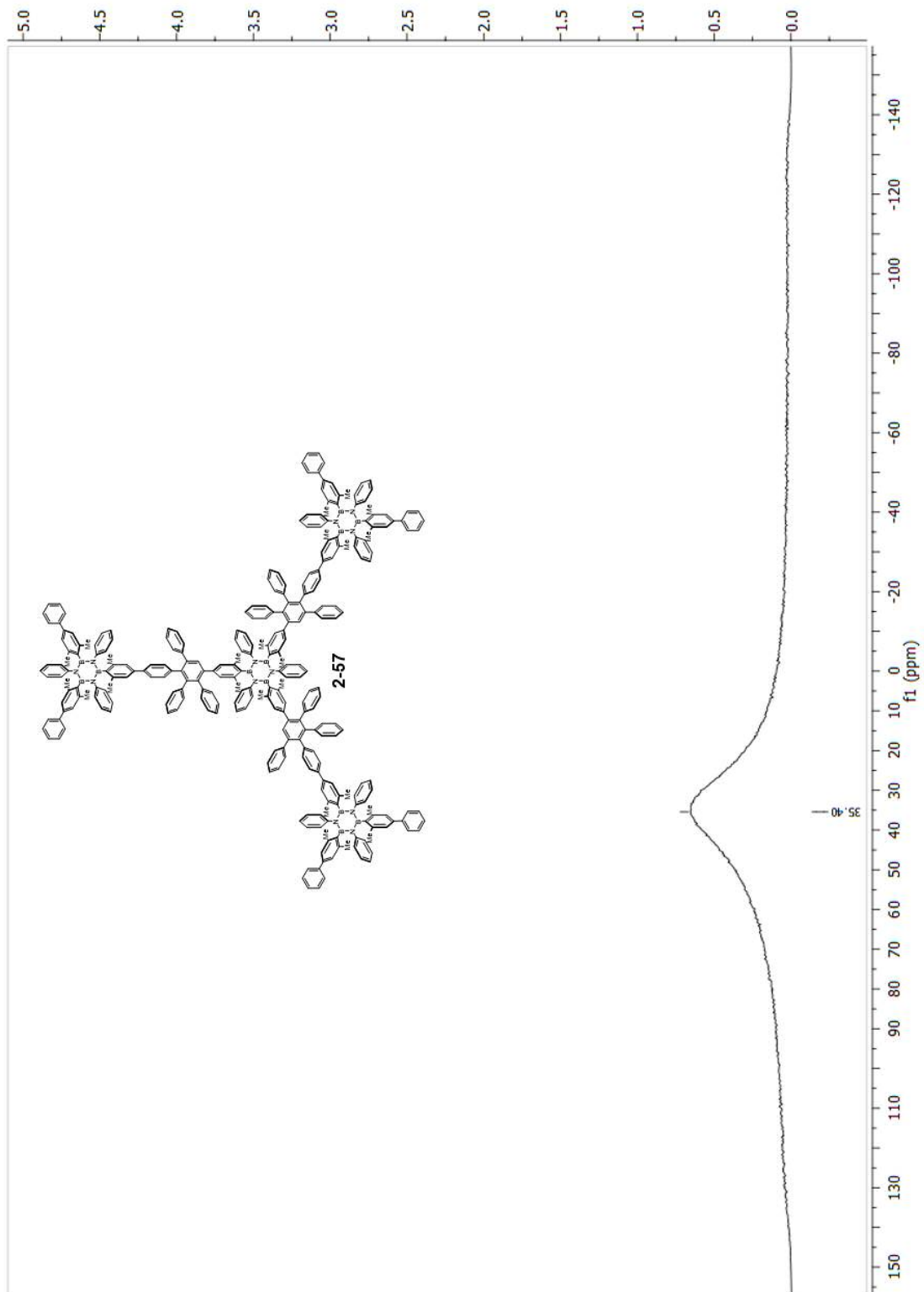
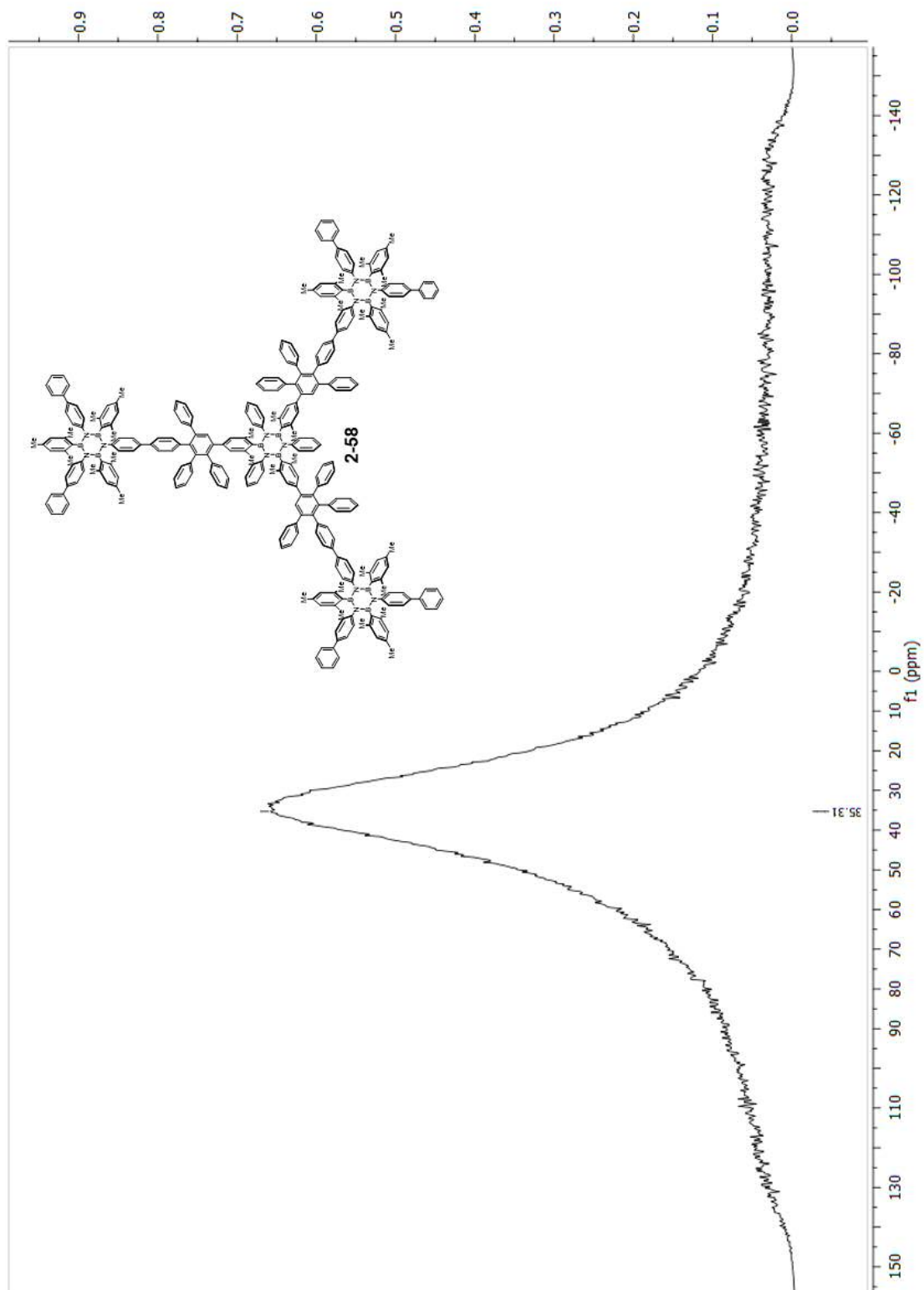


Figure A.83: ^{11}B -NMR, 128 MHz, CDCl_3 .

Characterisation of 2-58

**Figure A.84:** ^{11}B -NMR, 128 MHz, CDCl_3 .

Characterisation of 2-59

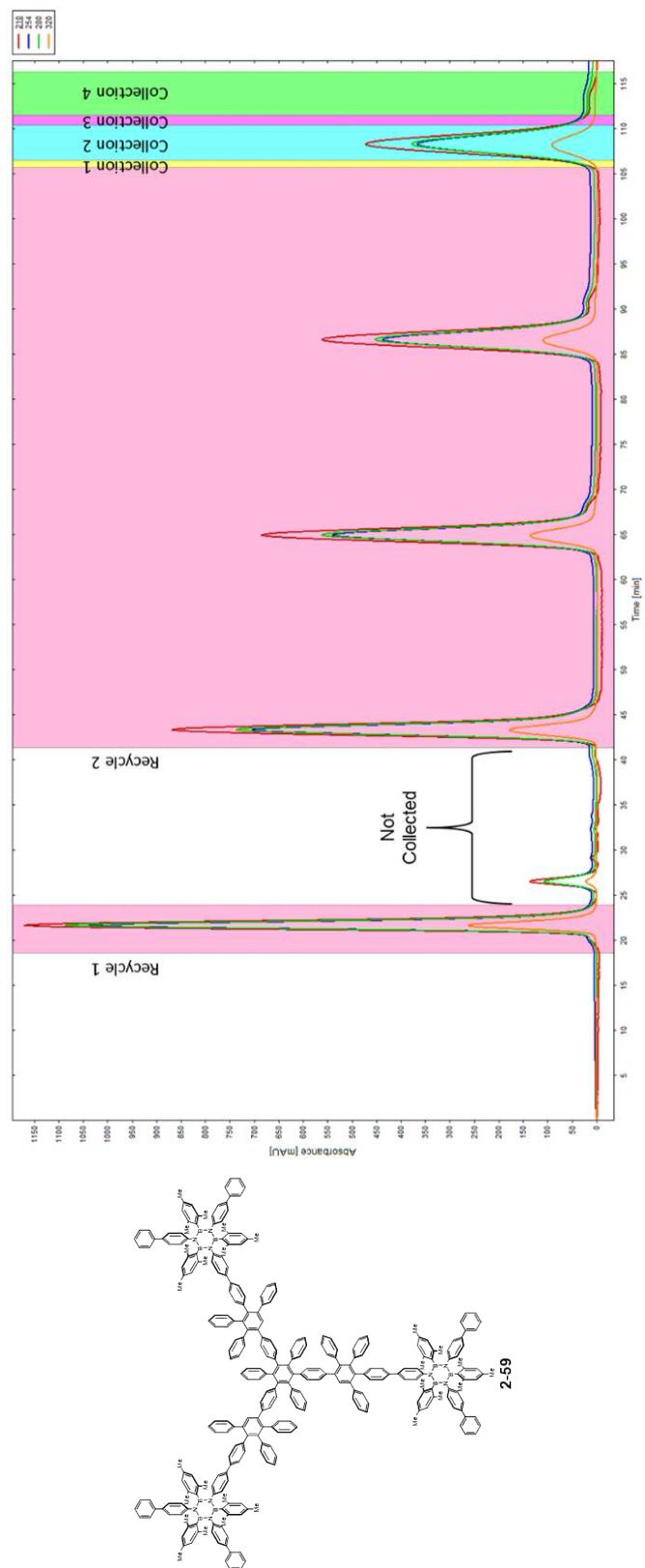


Figure A.85: Gel Permeation Chromatography (GPC), Recycling mode.

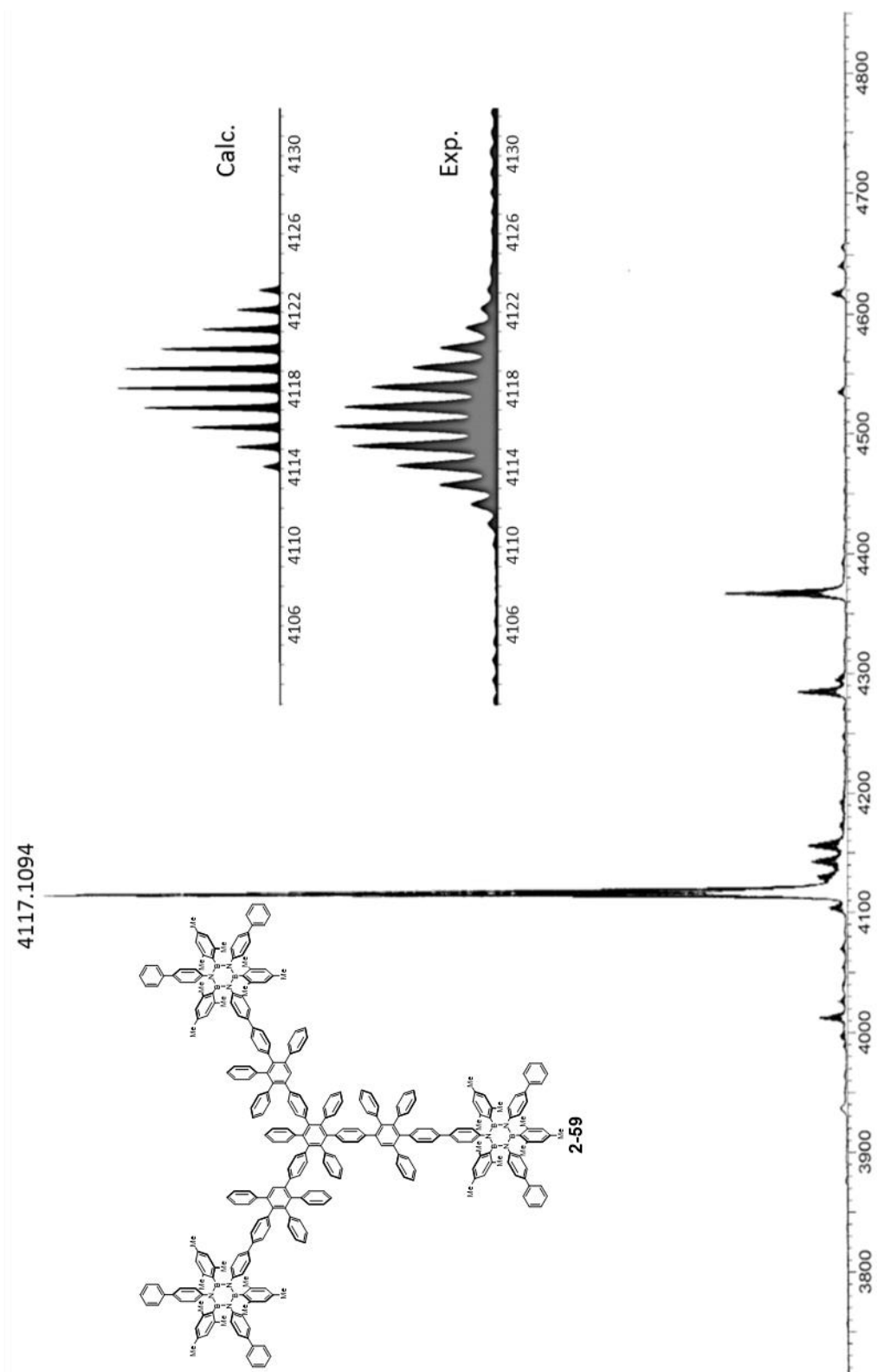


Figure A.86: MALDI-TOF Mass spectrometry of **Collection 2** (from GPC run, above), matrix: trans-2-[3-(4-tert-butyl-phenyl)-2-methyl-2-propenylidene]malonitrile (DCTB).

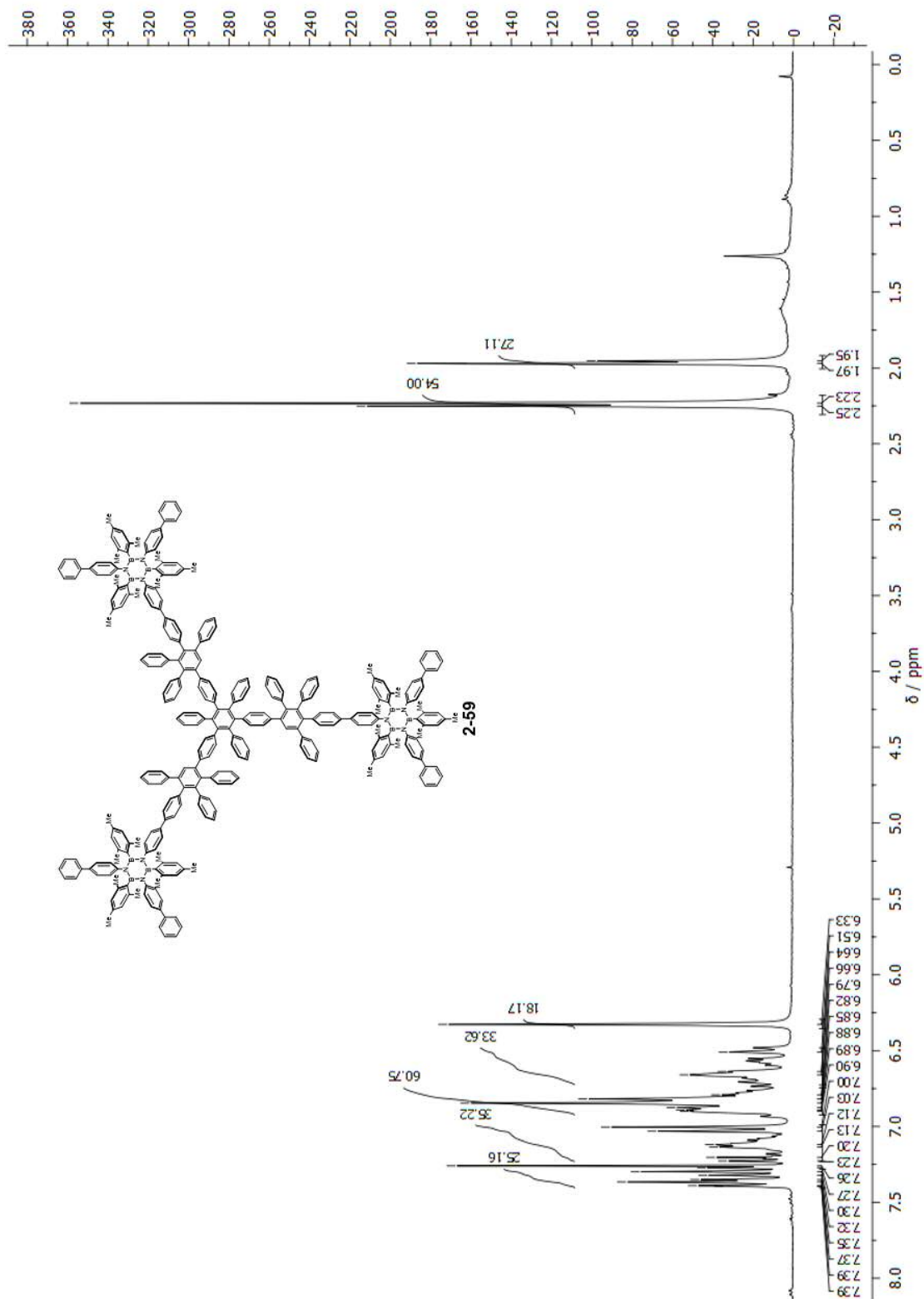
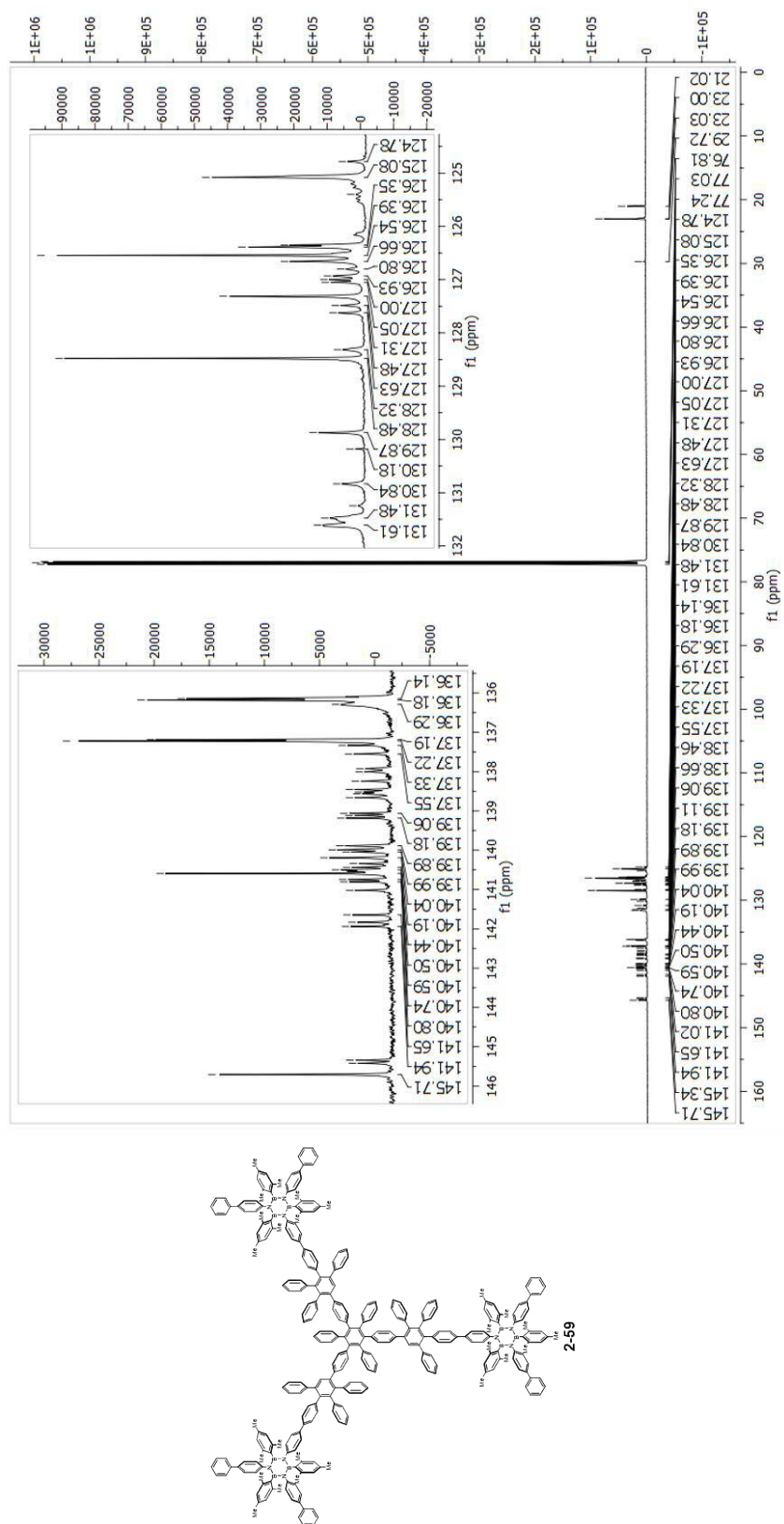


Figure A.87: $^1\text{H-NMR}$, 300 MHz, CDCl_3 .

Figure A.88: ^{13}C -NMR, 100 MHz, CDCl_3 .

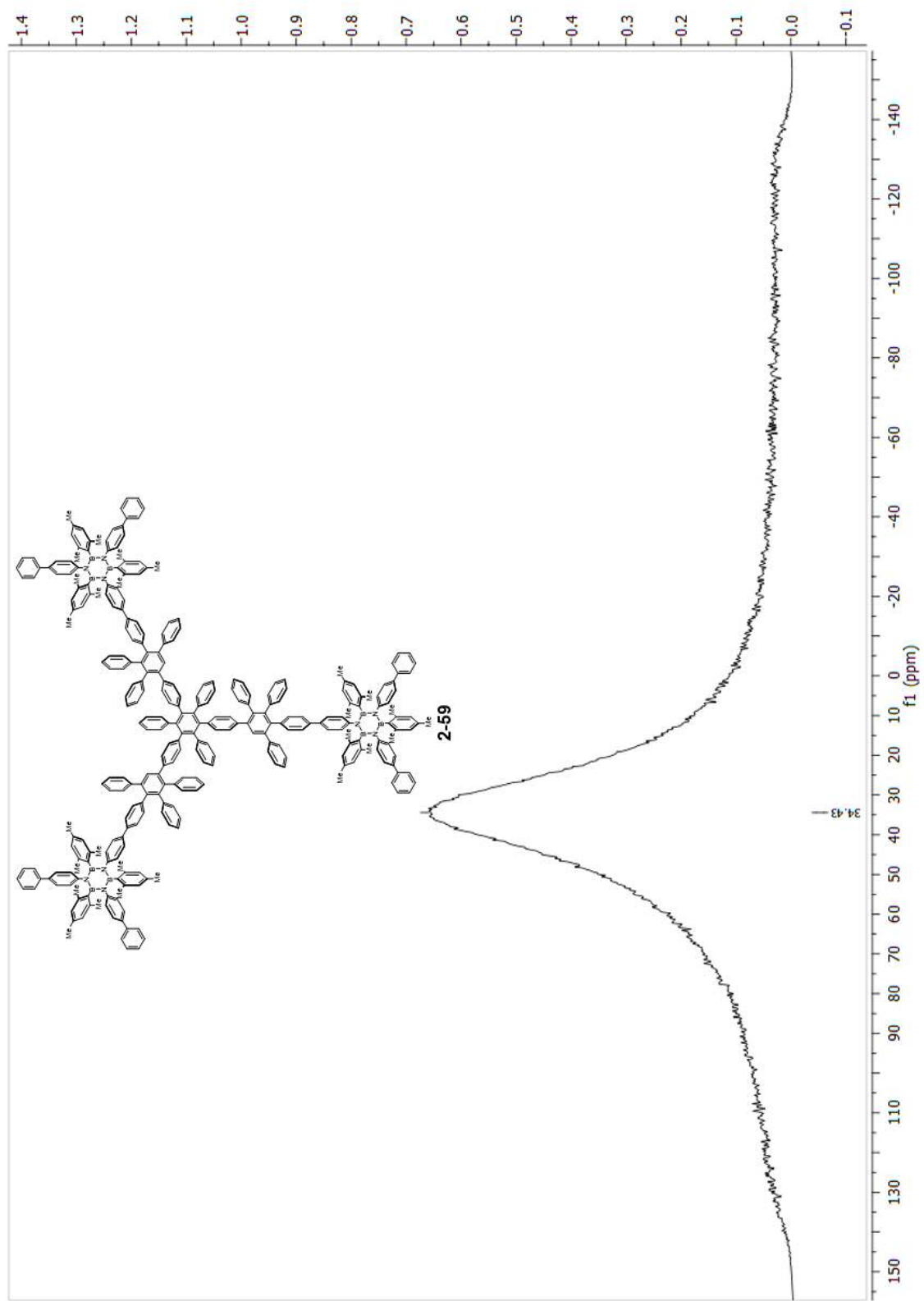


Figure A.89: ^{11}B -NMR, 128 MHz, CDCl_3 .

Characterisation of 2-60

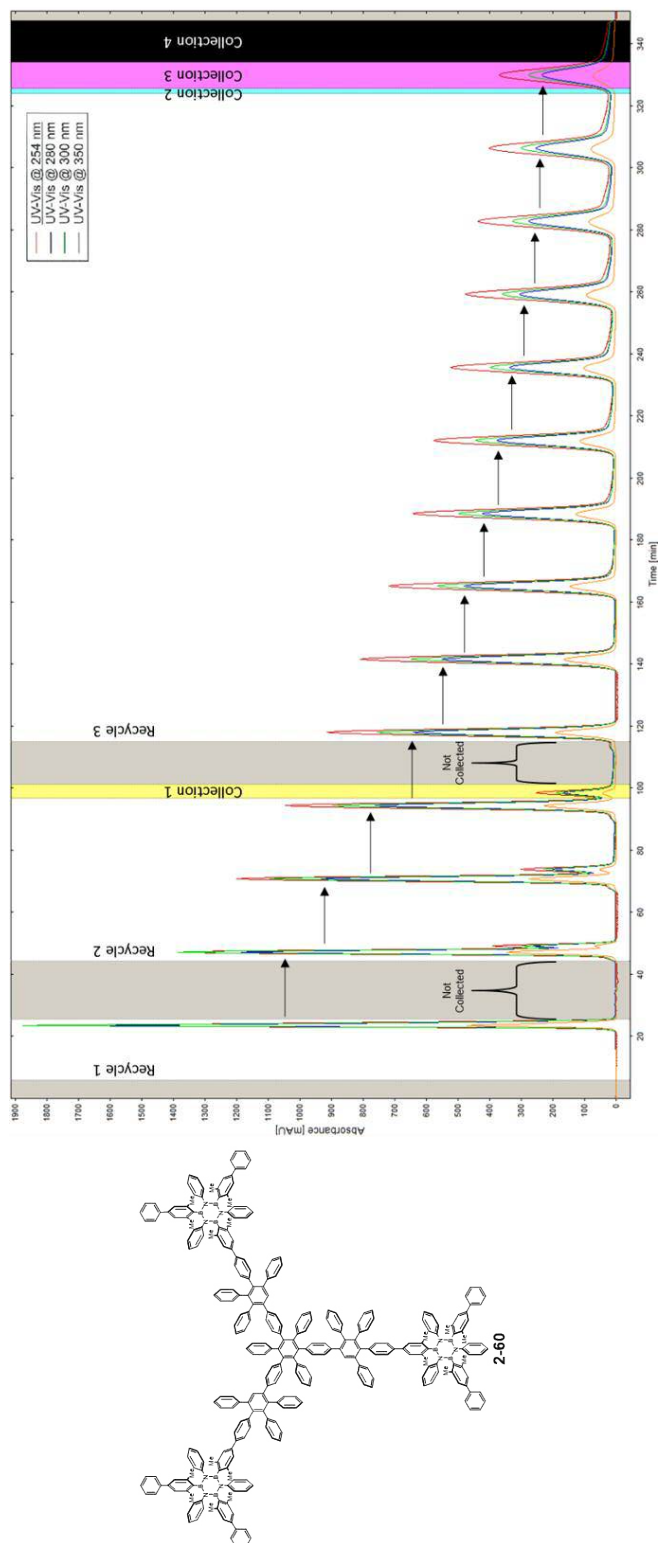


Figure A.90: Gel Permeation Chromatography (GPC), Recycling mode.

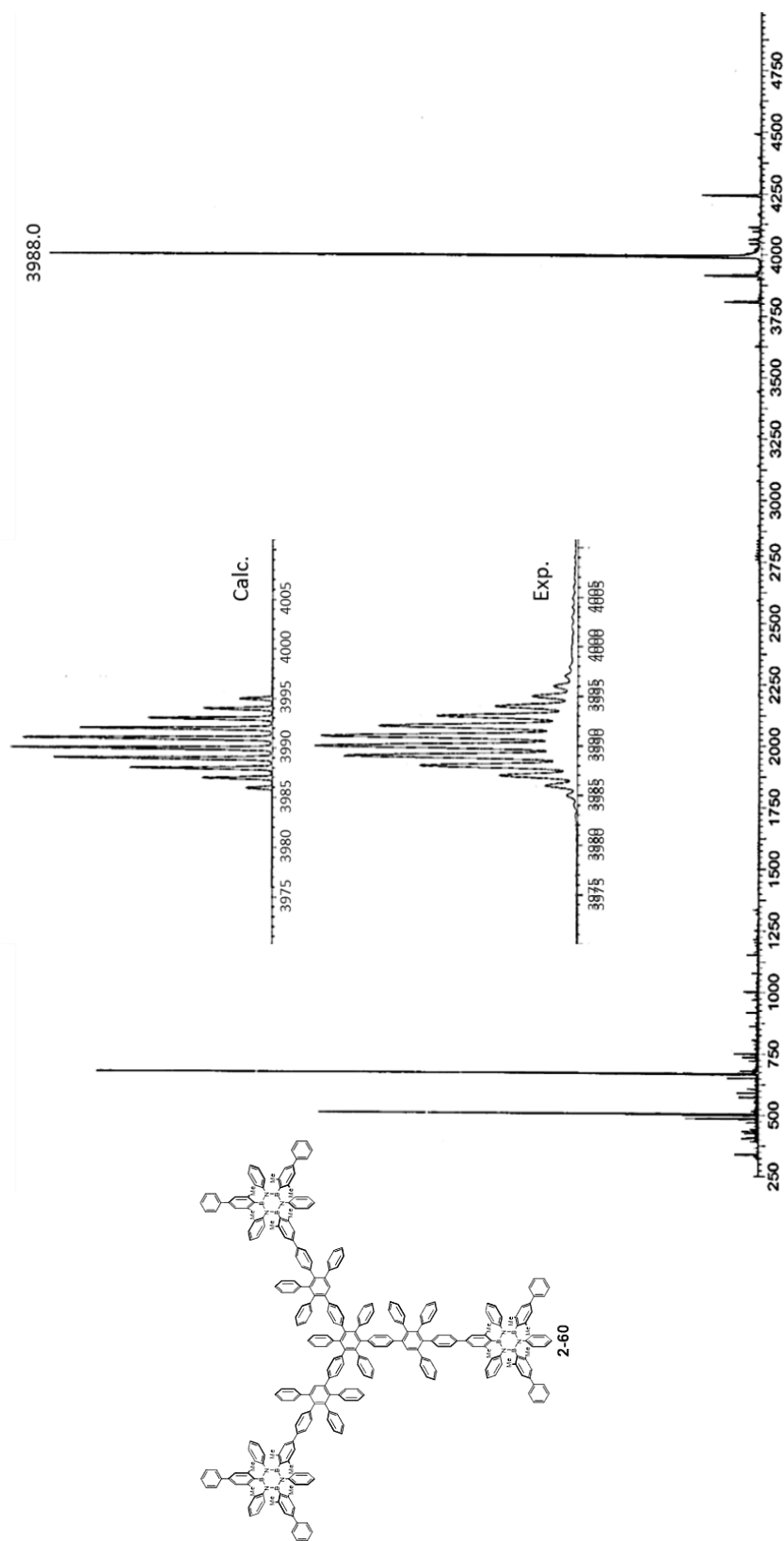


Figure A.91: MALDI-TOF Mass spectrometry of **Collection 3** (from GPC run, above), matrix: trans-2-[3-(4-tert-butyl-phenyl)-2-methyl-2-propenyldiene]malonitrile (DCTB).

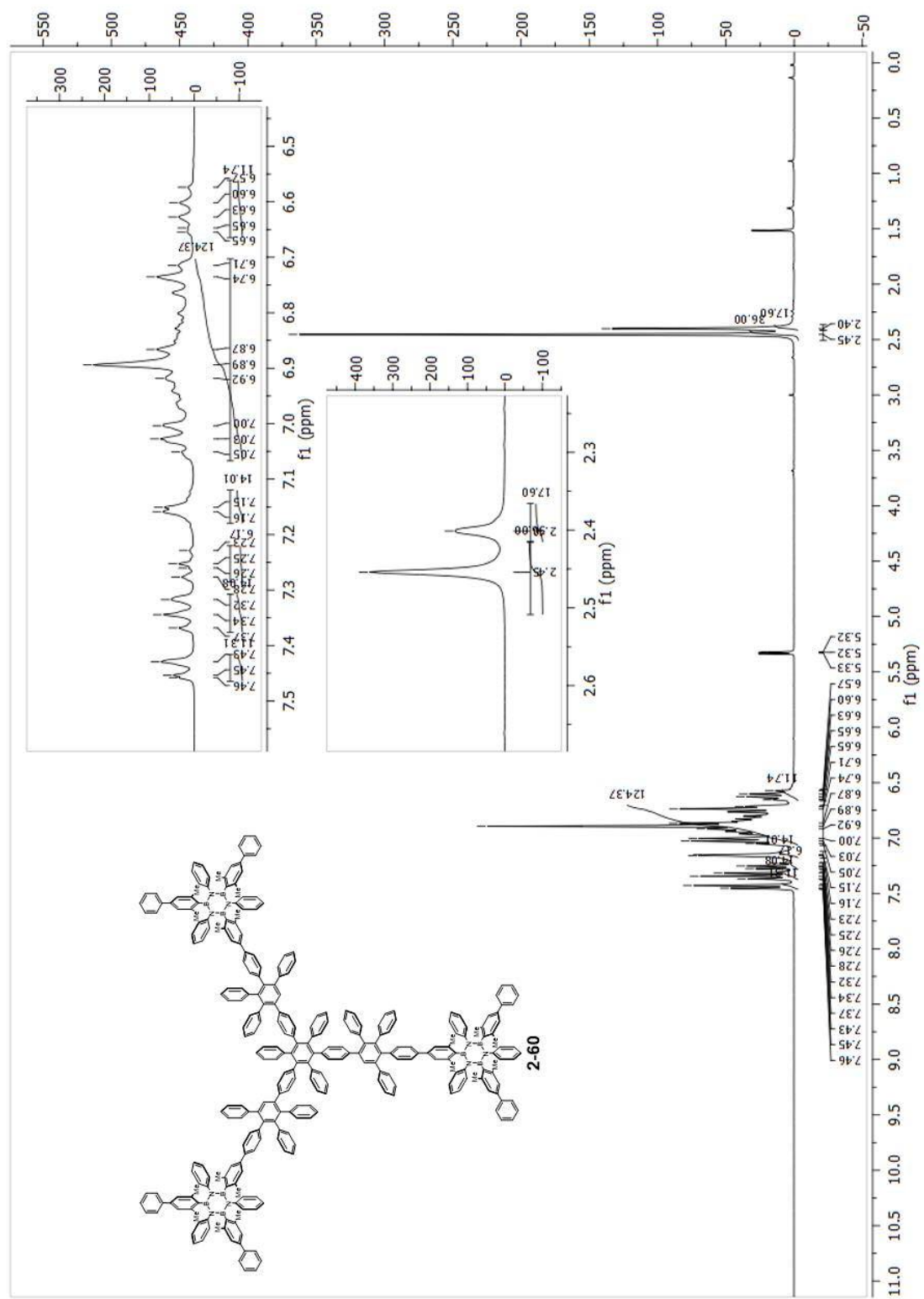


Figure A.92: $^1\text{H-NMR}$, 300 MHz, CDCl_3 .

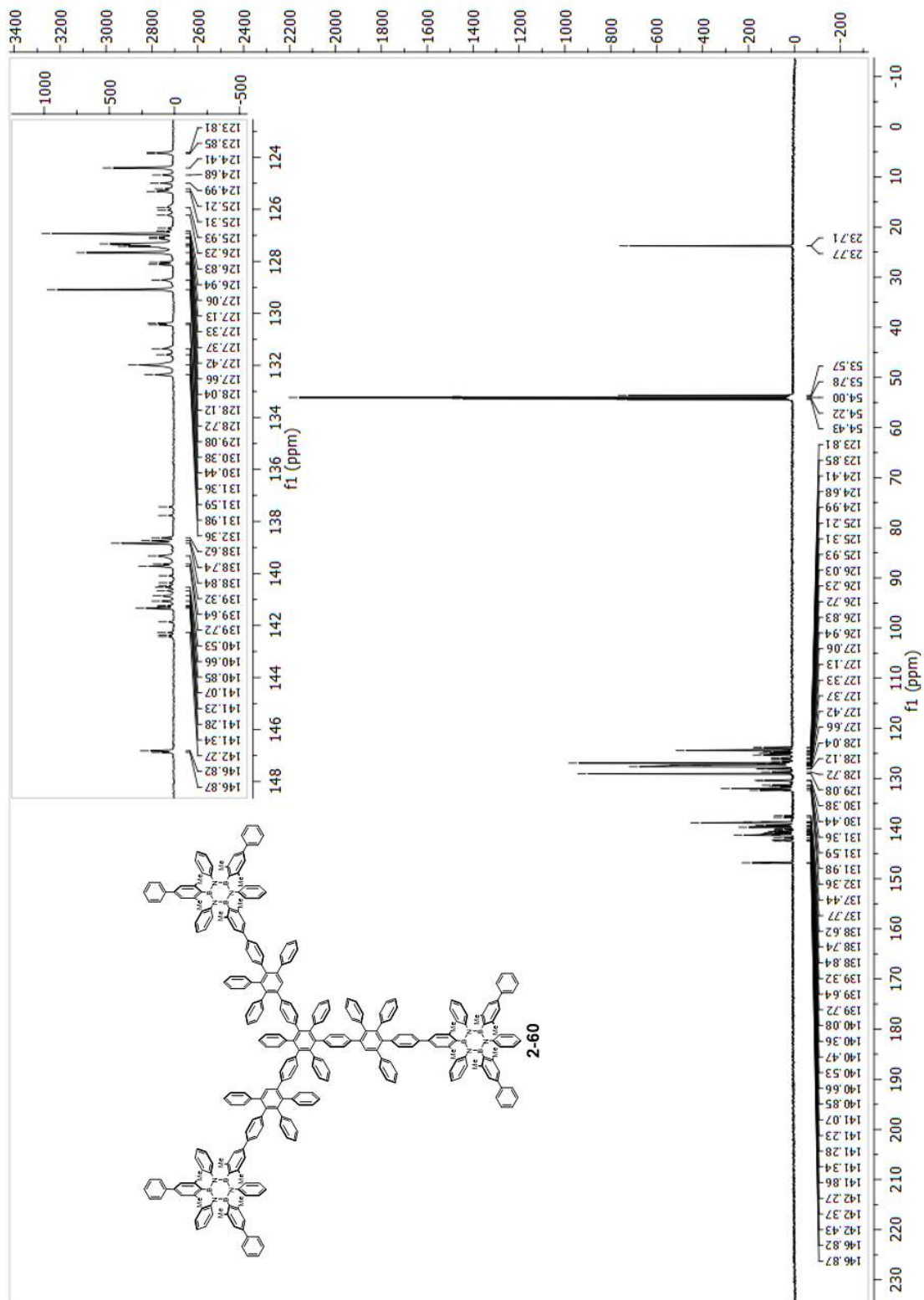


Figure A.93: ^{13}C -NMR, 100 MHz, CDCl_3 .

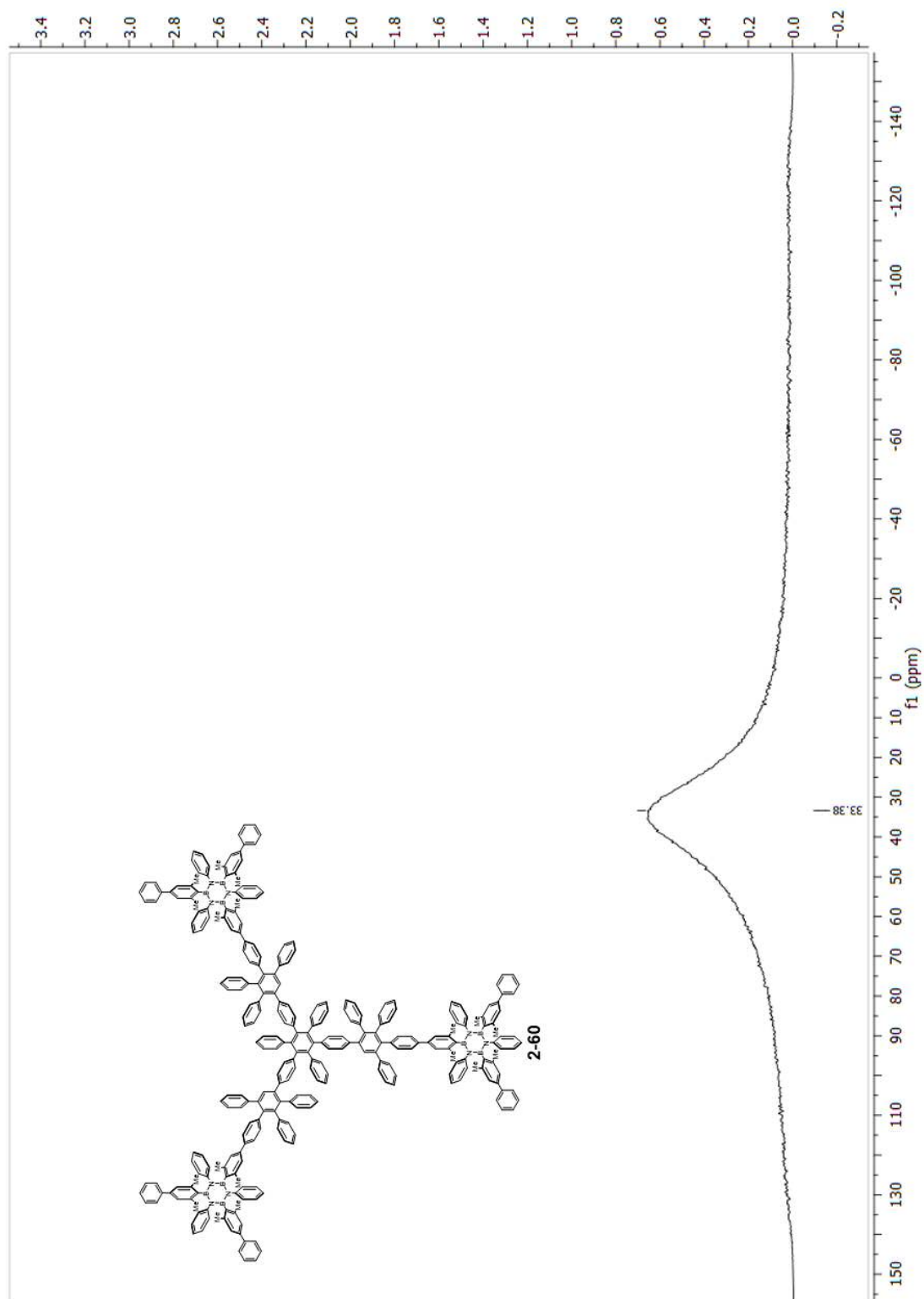


Figure A.94: ^{11}B -NMR, 128 MHz, CDCl_3 .

Characterisation of 2-61

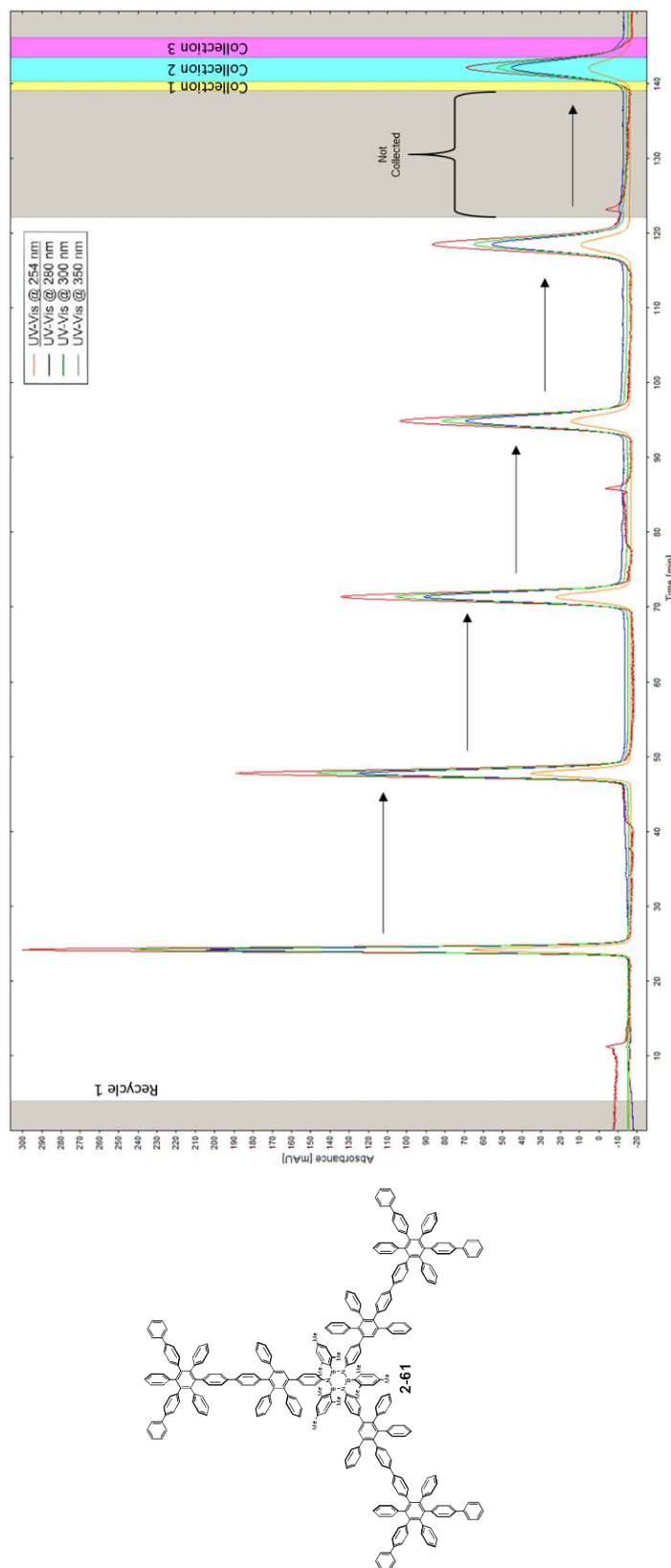


Figure A.95: Gel Permeation Chromatography (GPC), Recycling mode.

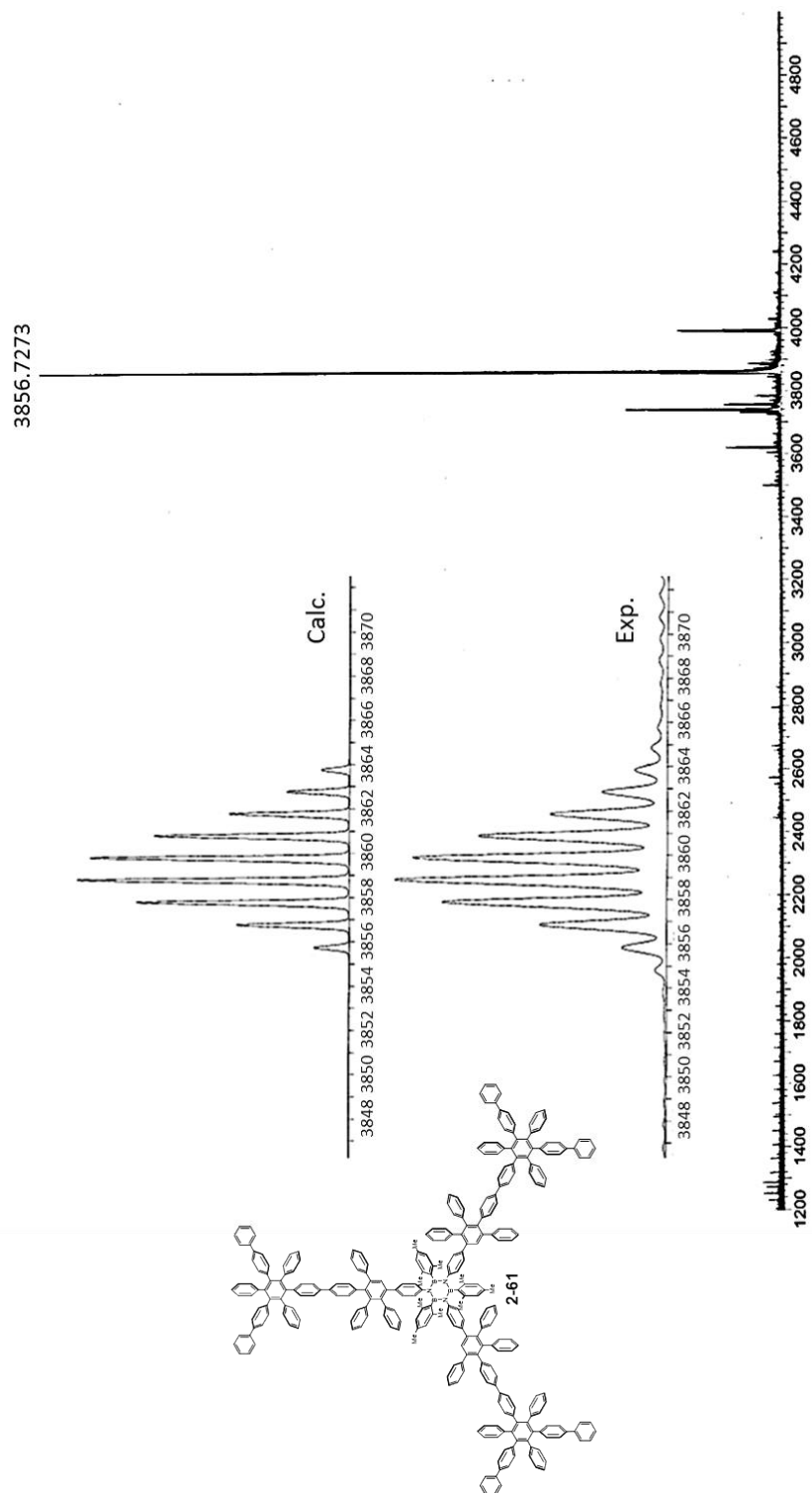


Figure A.96: MALDI-TOF Mass spectrometry of **Collection 2** (from GPC run, above), matrix: trans-2-[3-(4-tert-butyl-phenyl)-2-methyl-2-propenylidene]malonitrile (DCTB).

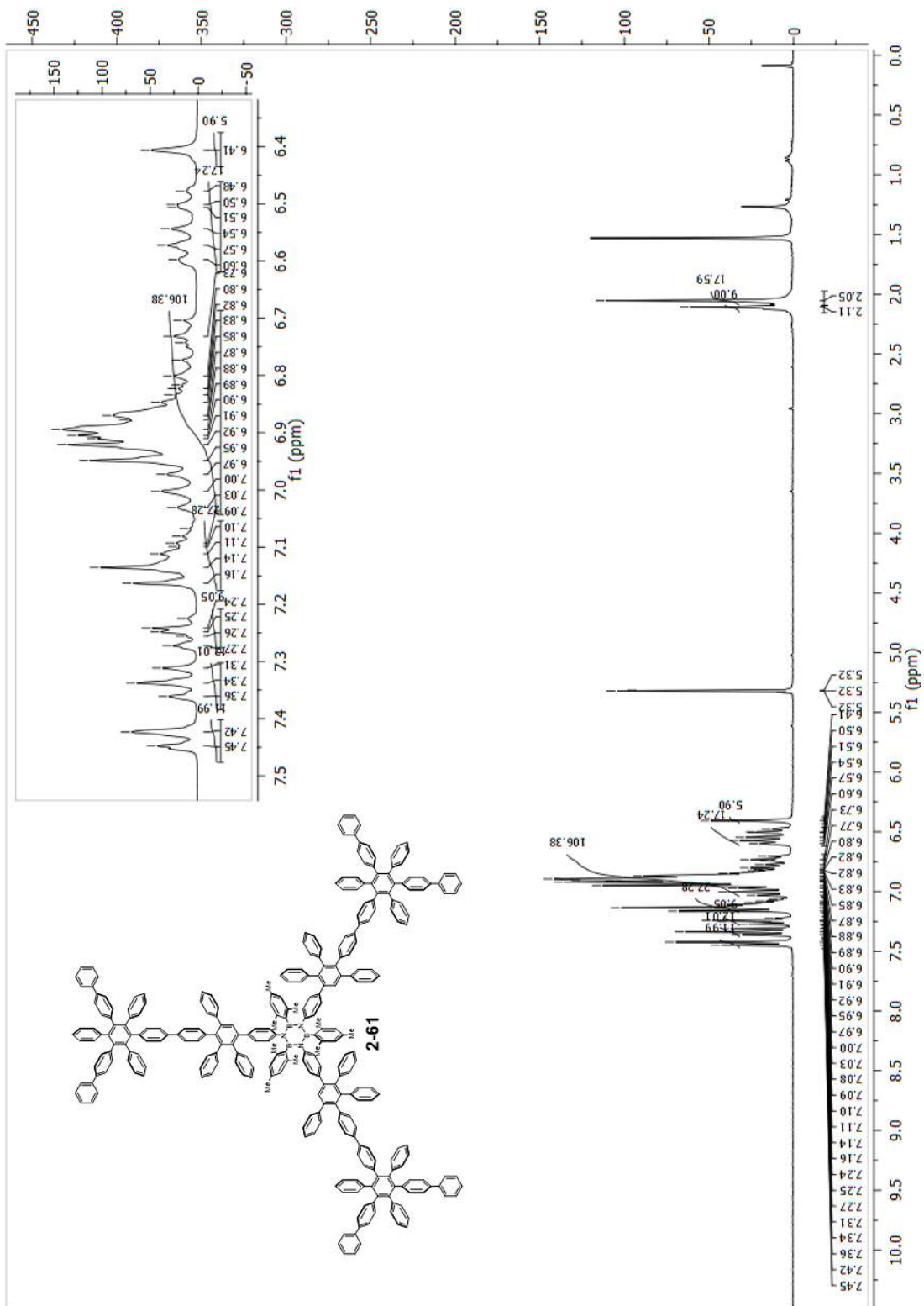


Figure A.97: $^1\text{H-NMR}$, 300 MHz, CD_2Cl_2 .

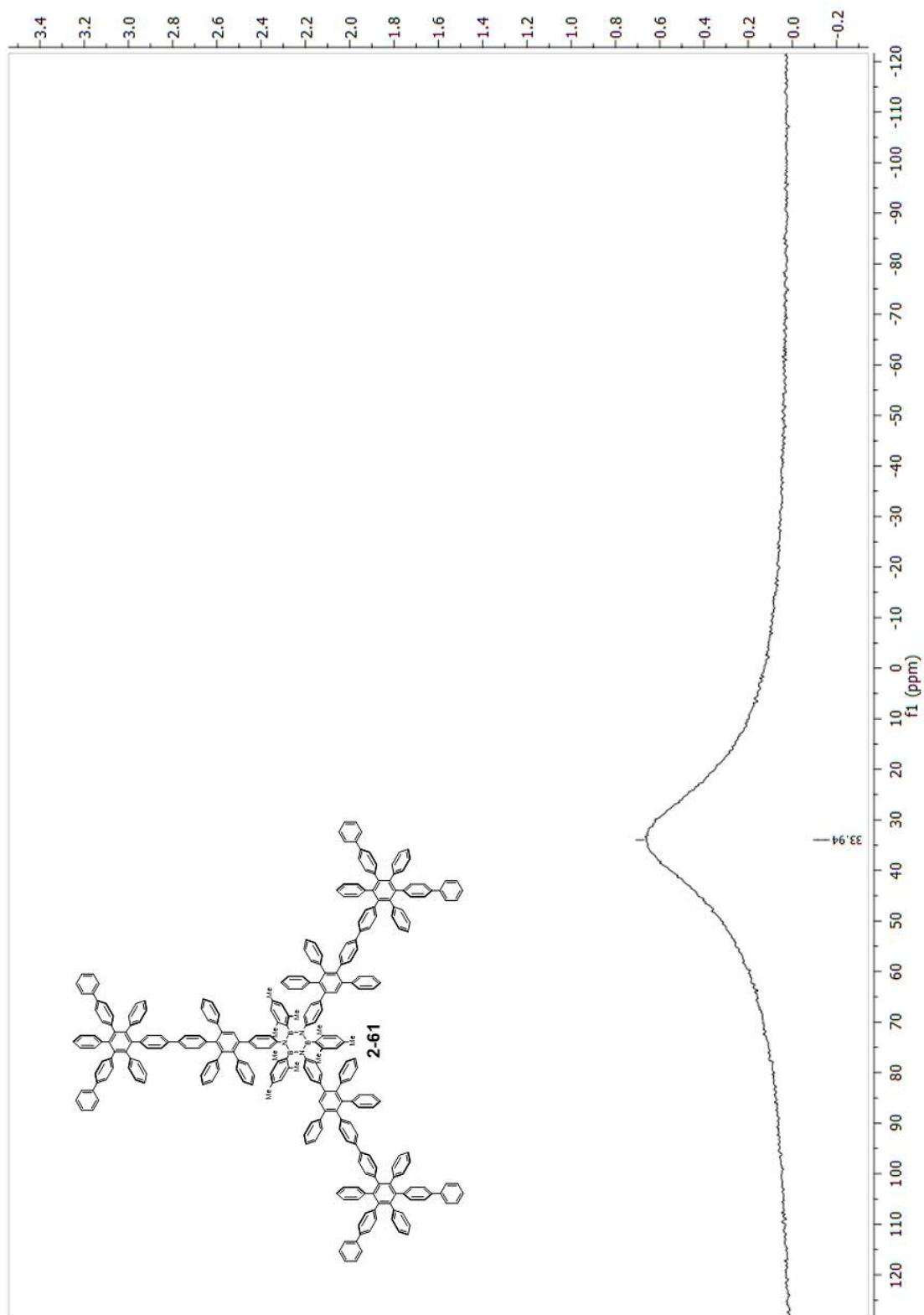


Figure A.99: ^{11}B -NMR, 128 MHz, CD_2Cl_2 .

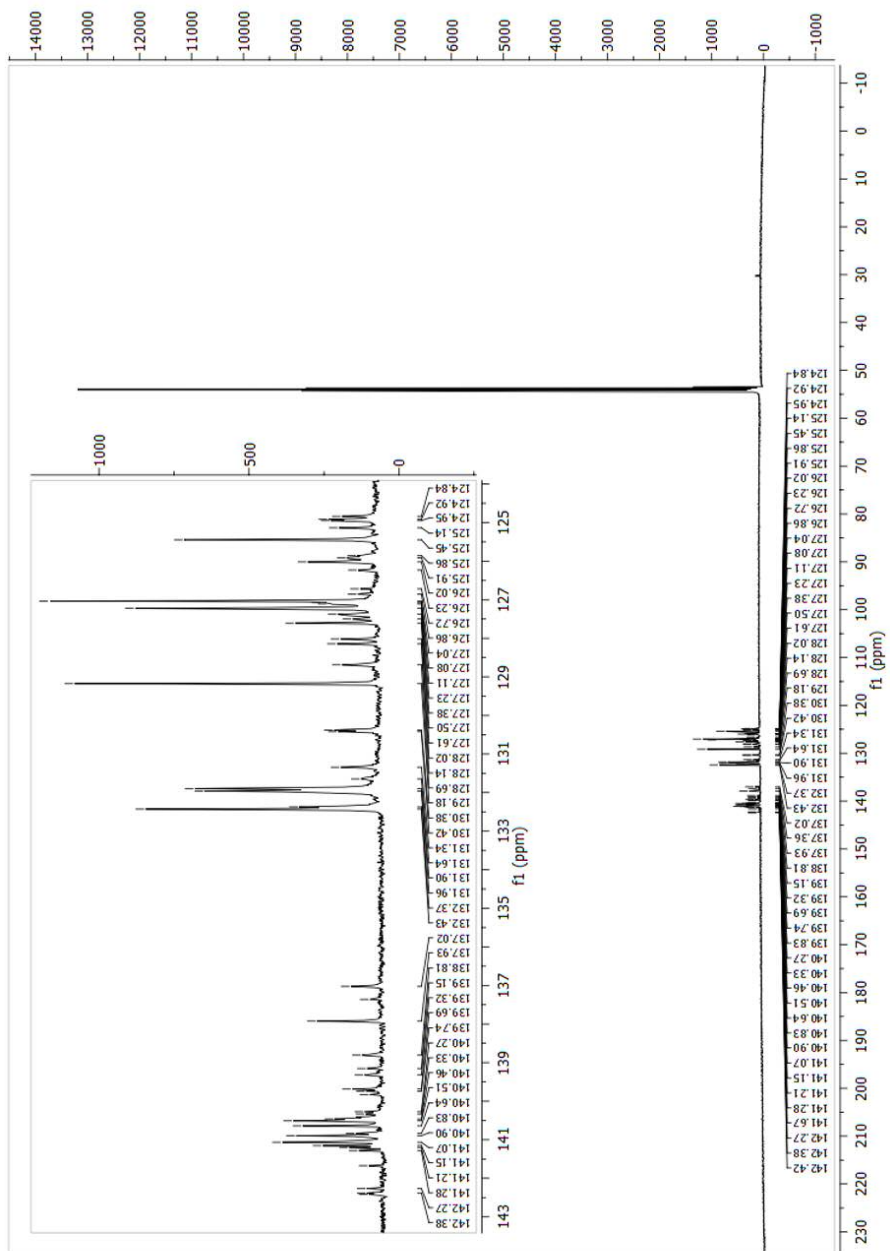
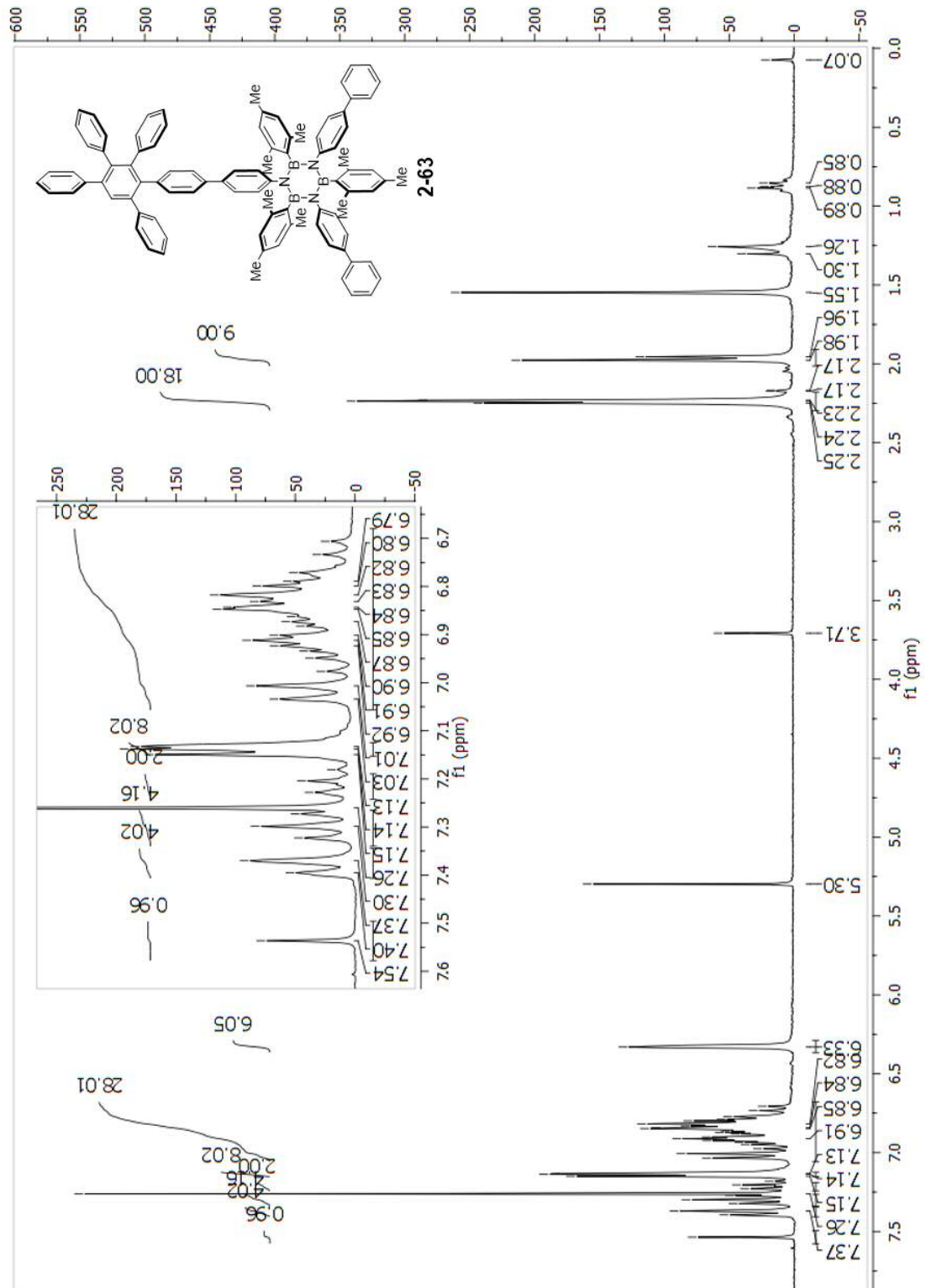


Figure A.101: ^{13}C -NMR, 100 MHz, CDCl_3 .

Characterisation of 2-63

Figure A.102: $^1\text{H-NMR}$, 400 MHz, CDCl_3 .

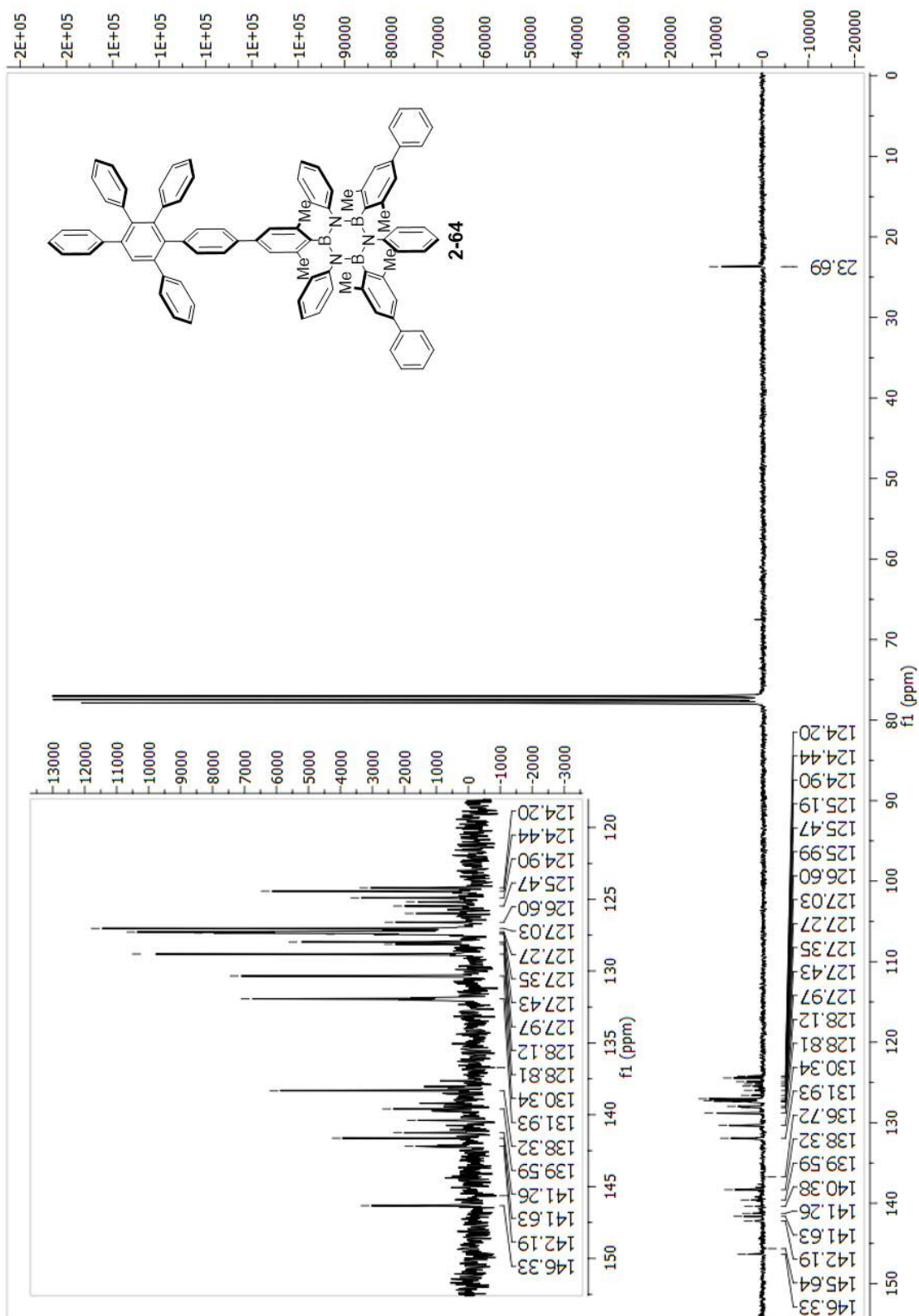
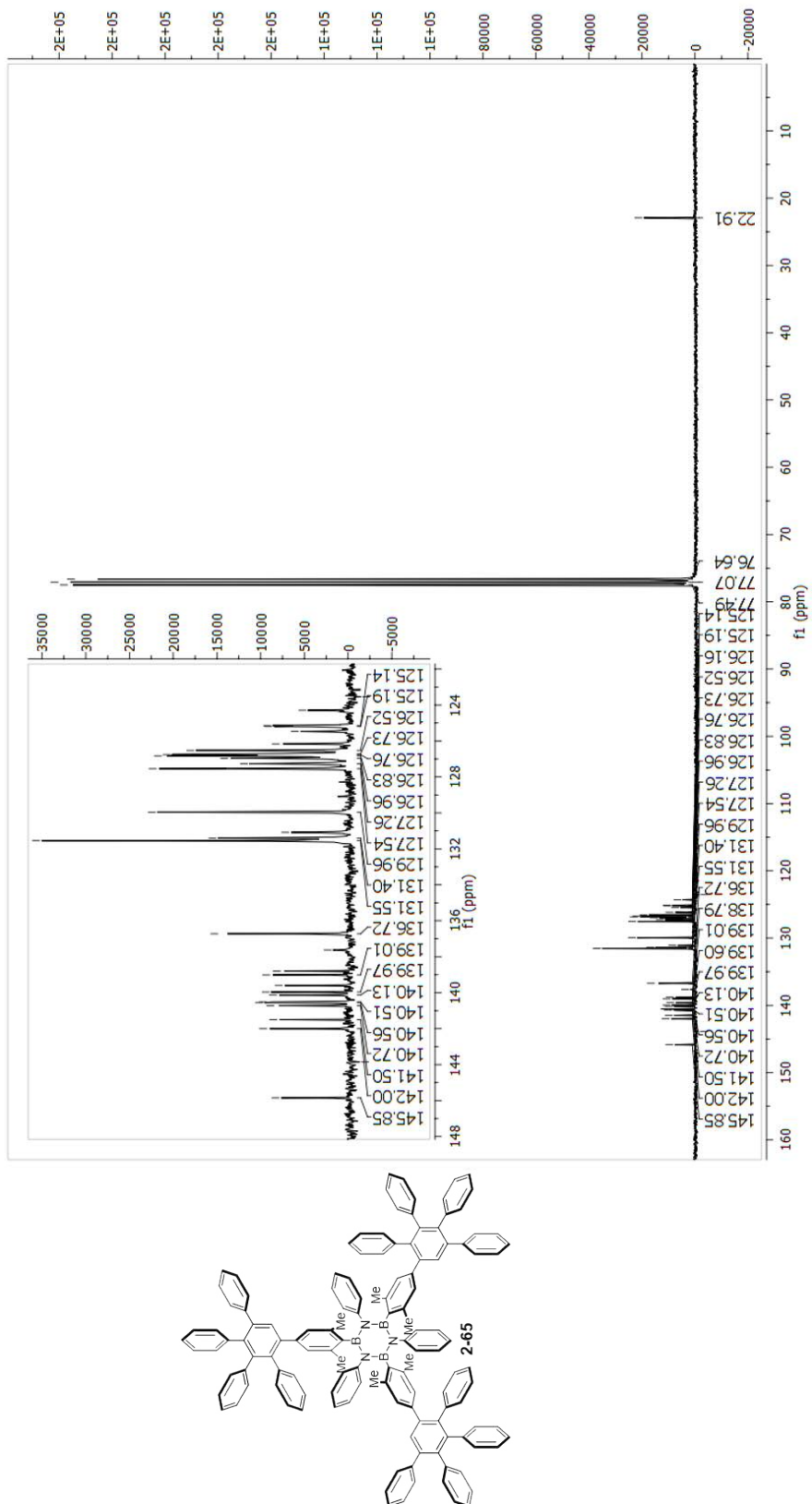
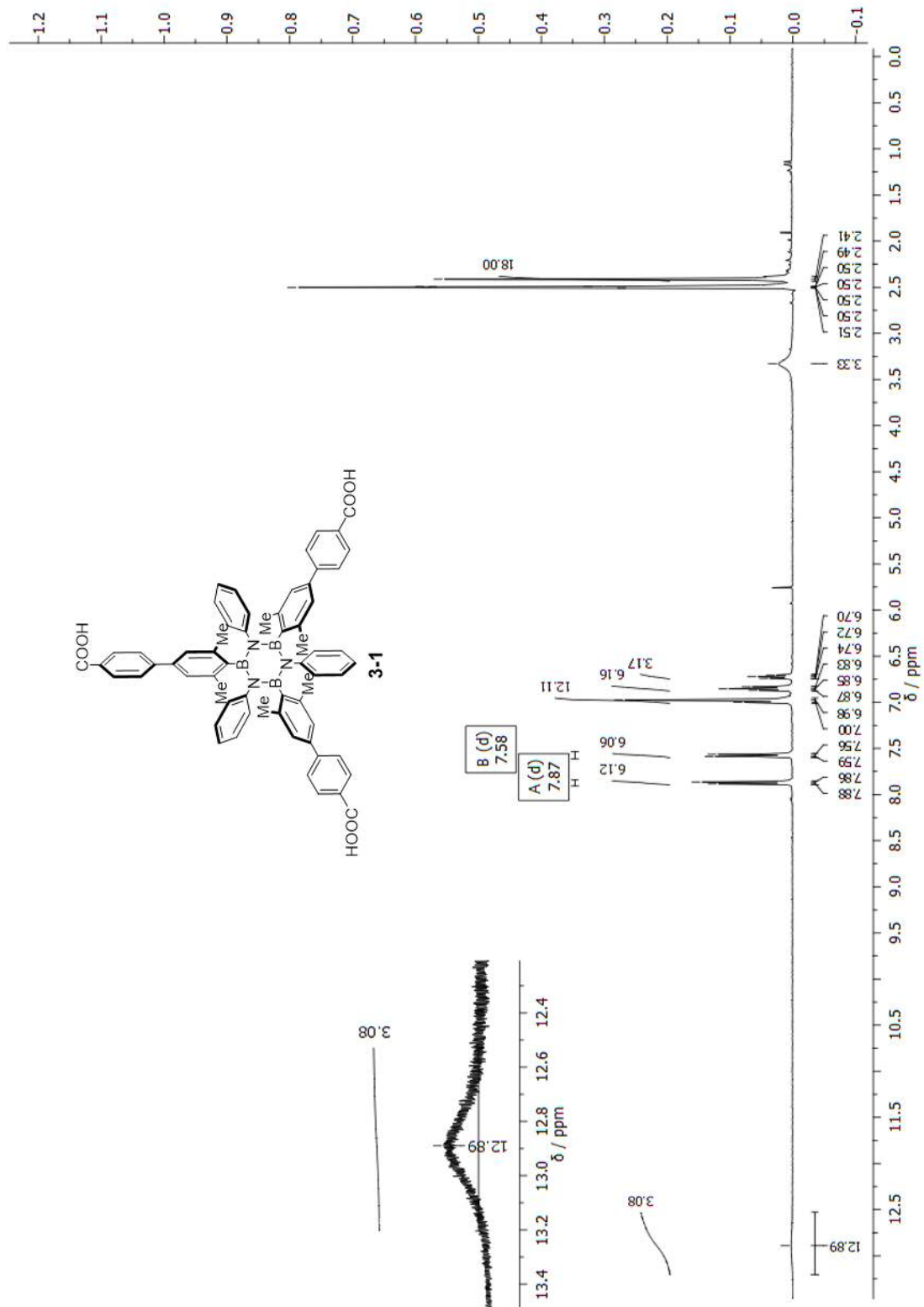


Figure A.105: ^{13}C -NMR, 100 MHz, CDCl_3 .



Characterisation of 3-1

Figure A.108: $^1\text{H-NMR}$, 400 MHz, DMSO .

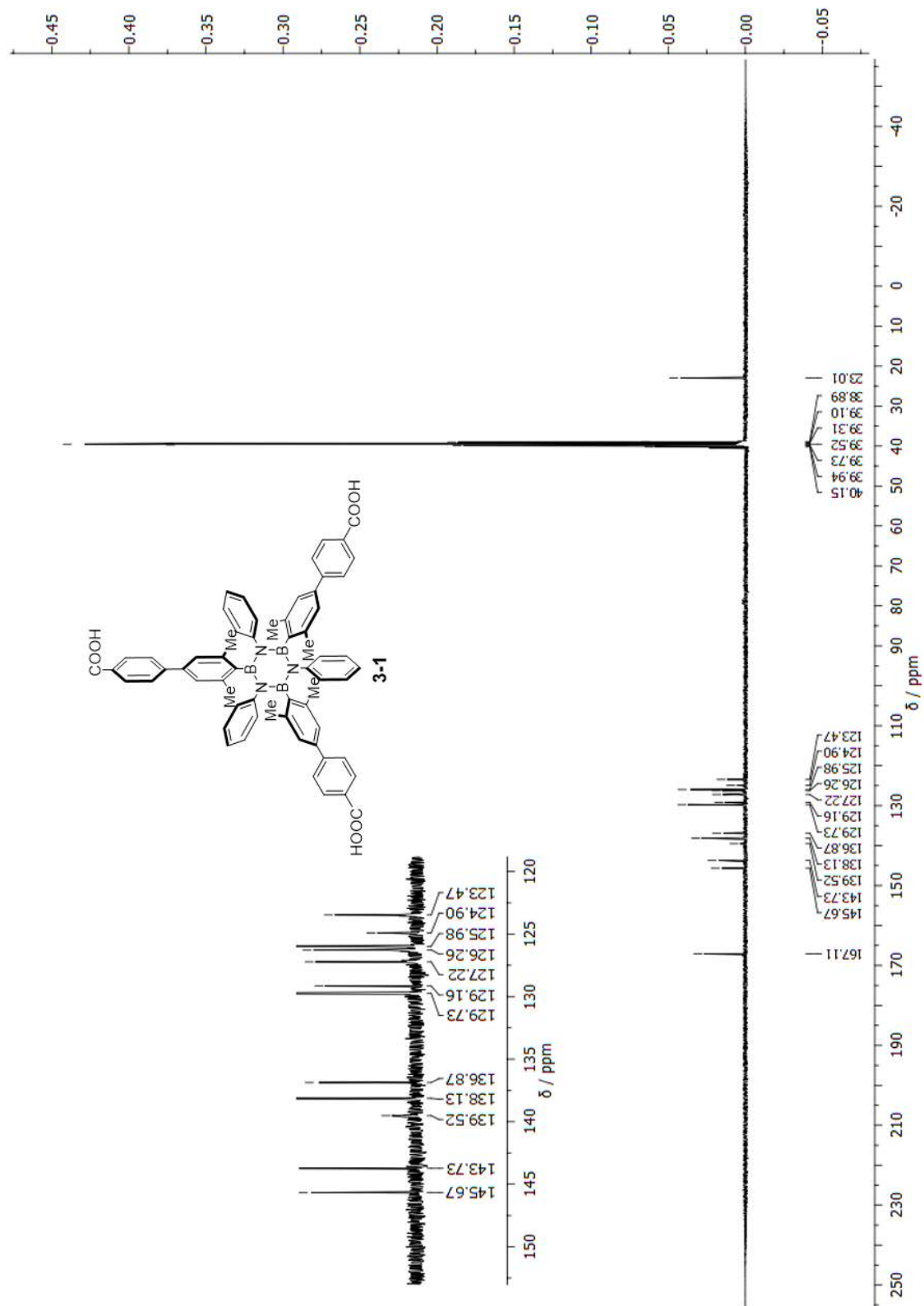


Figure A.109: ^{13}C -NMR, 400 MHz, DMSO.

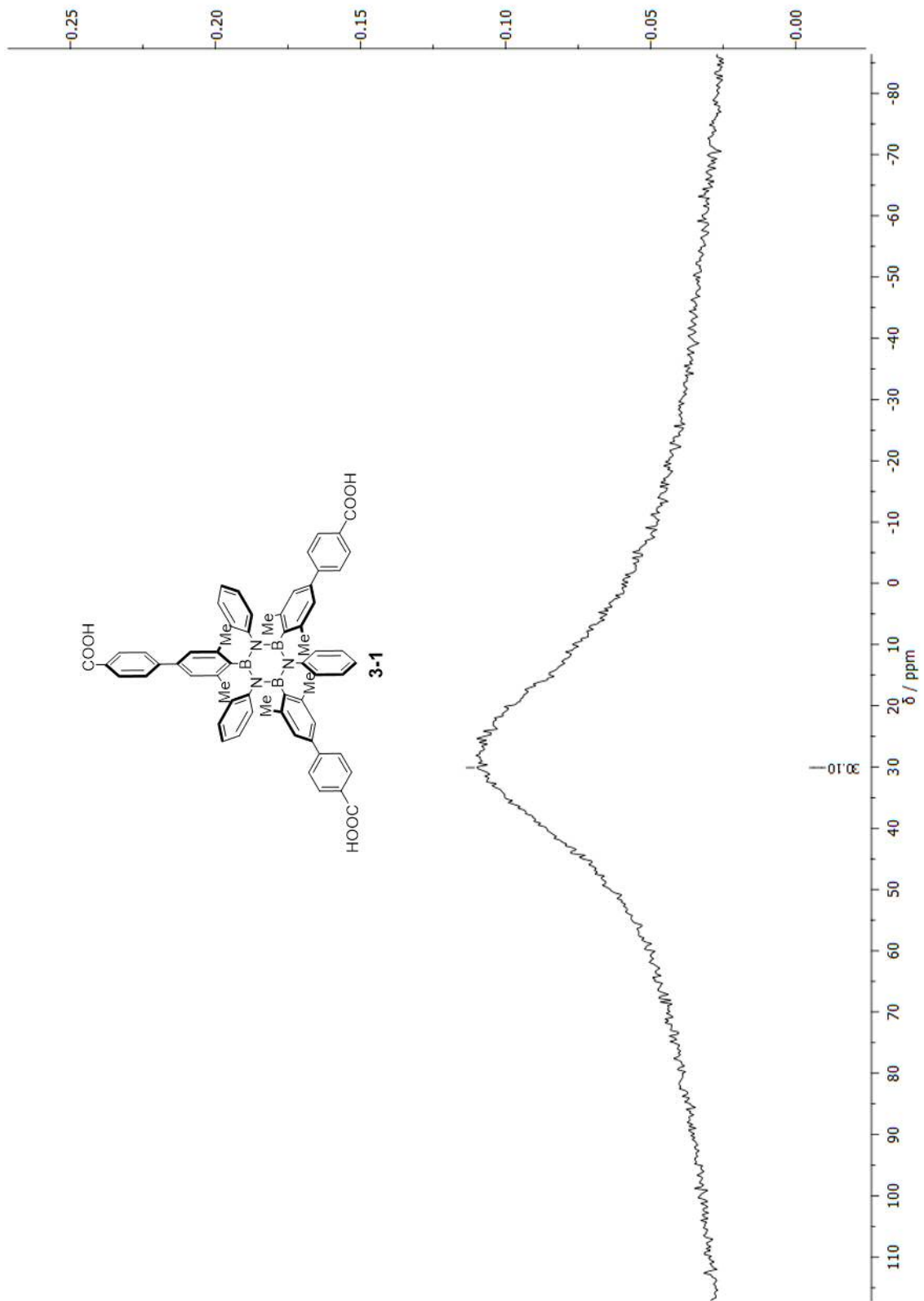
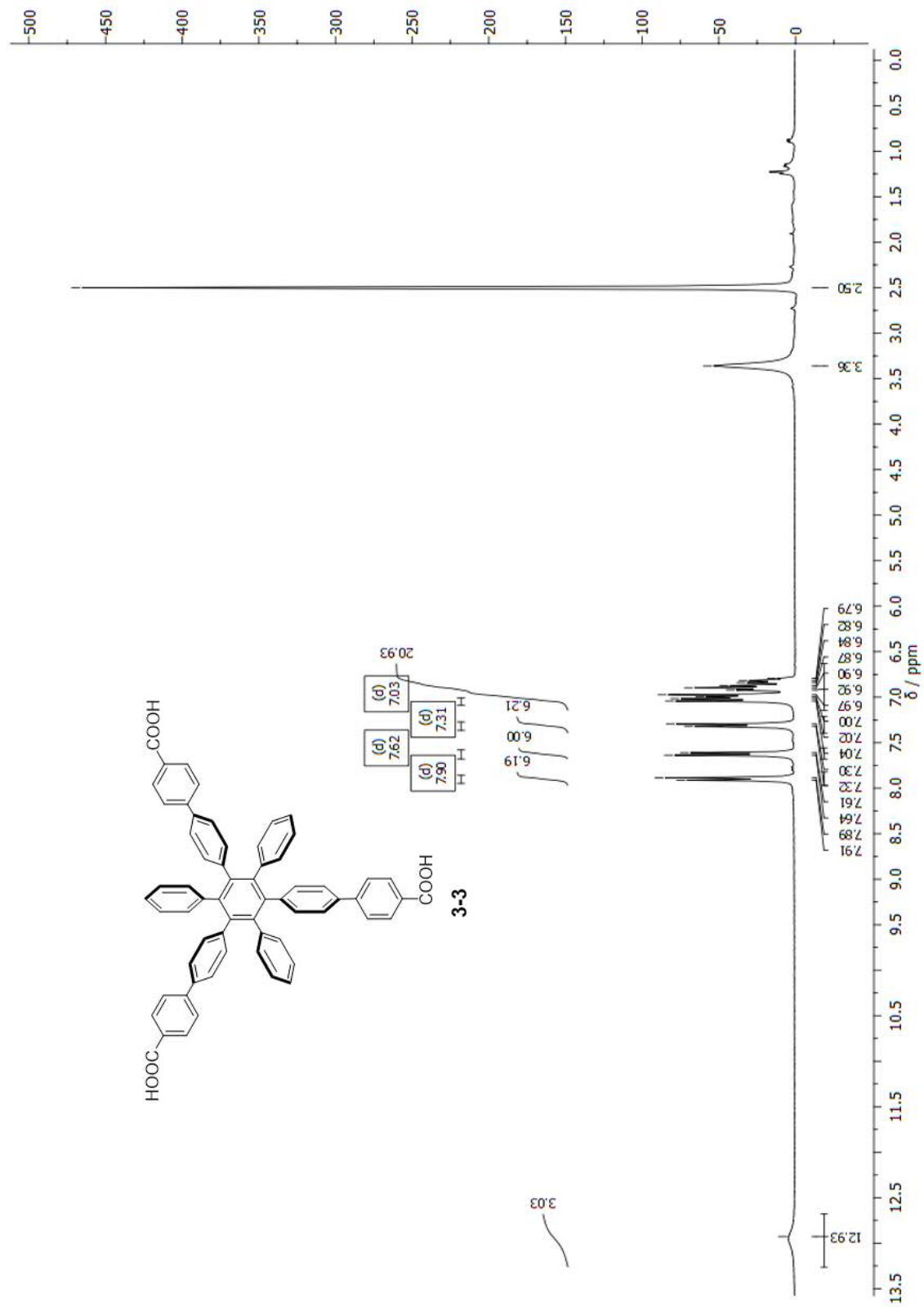


Figure A.110: ^{11}B -NMR, 128 MHz, DMSO.

Characterisation of 3-3

Figure A.111: $^1\text{H-NMR}$, 400 MHz, DMSO .

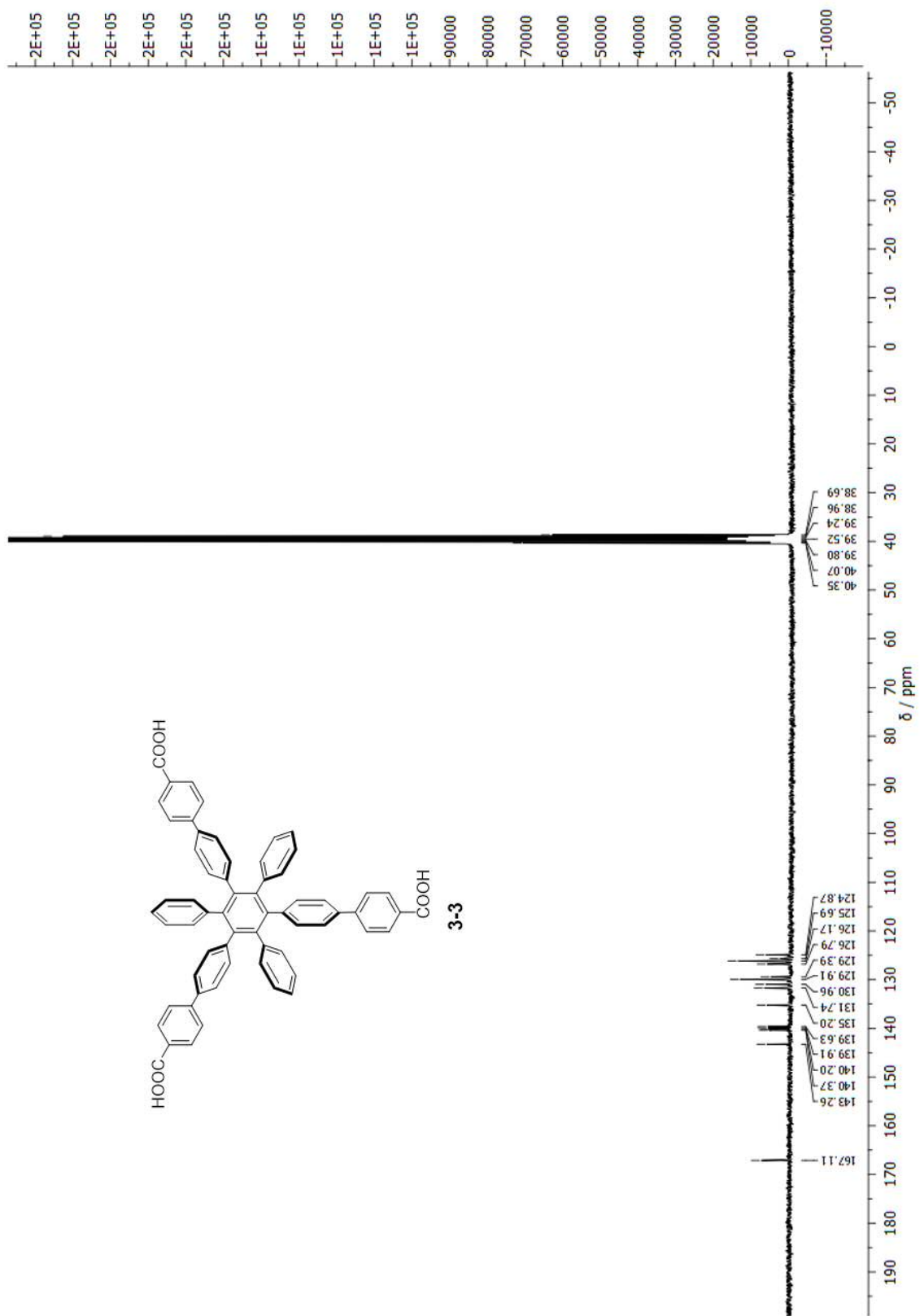
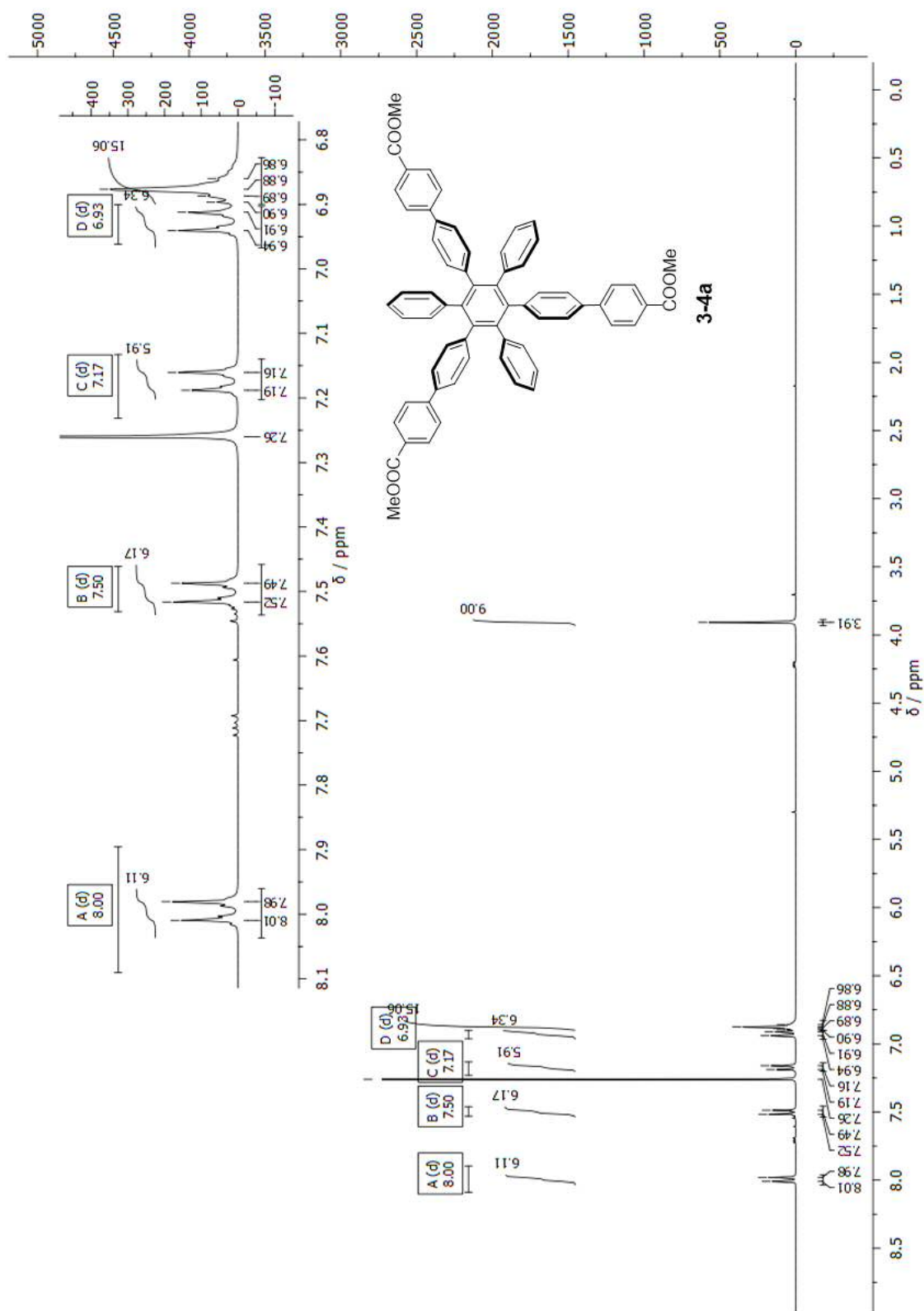


Figure A.112: ^{13}C -NMR, 400 MHz, DMSO.

Characterisation of 3-4a

Figure A.113: $^1\text{H-NMR}$, 400 MHz, CDCl_3 .

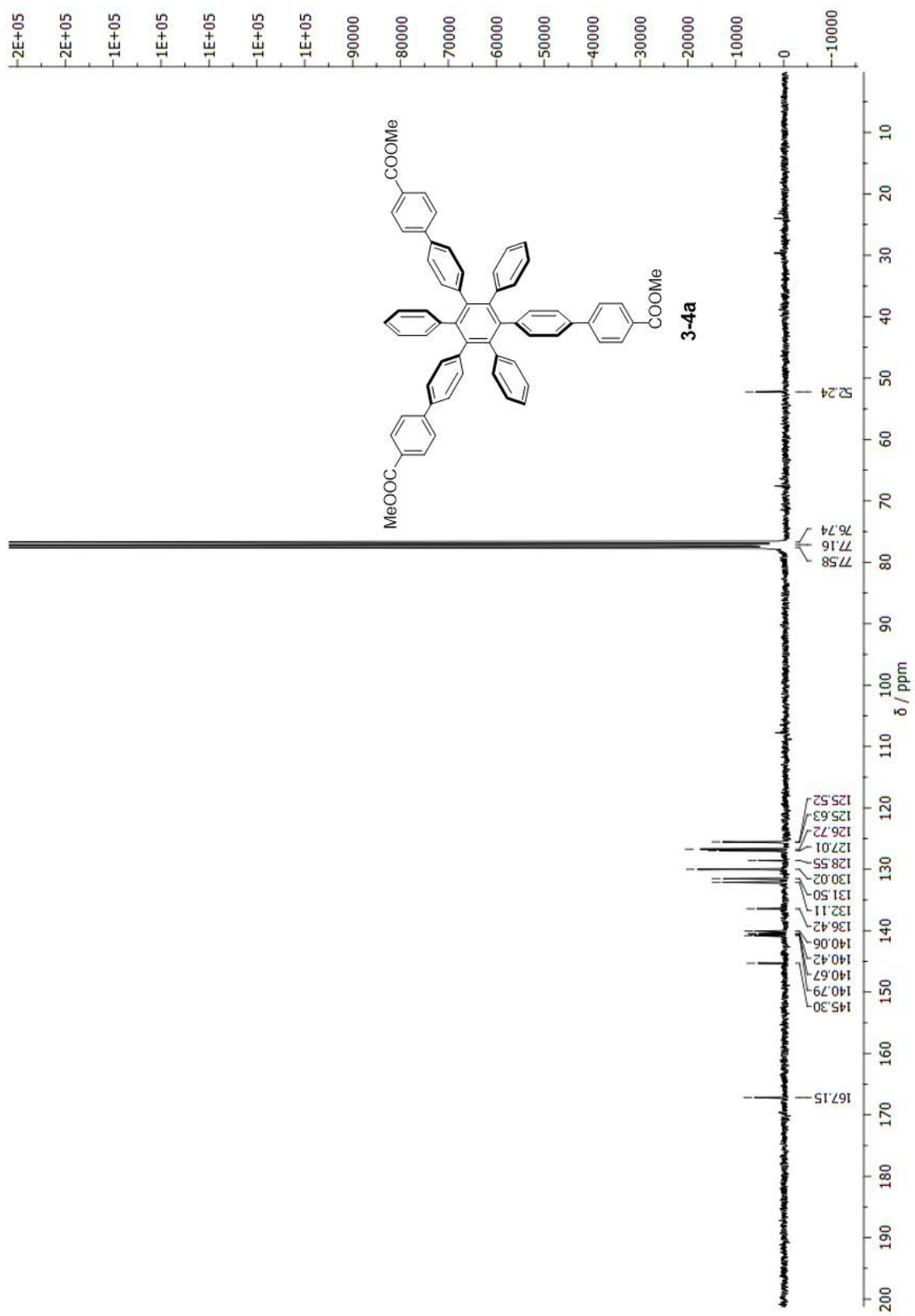
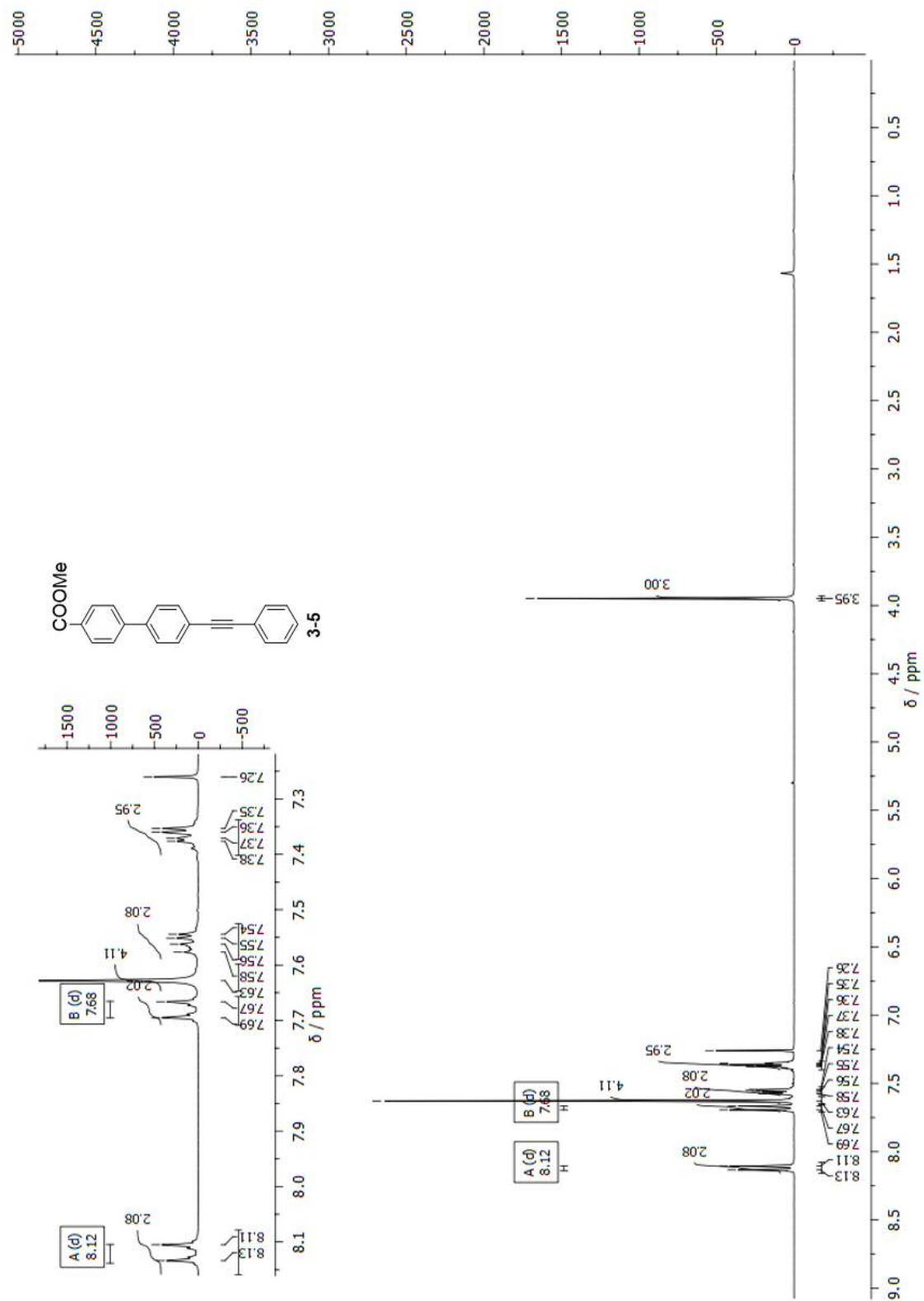
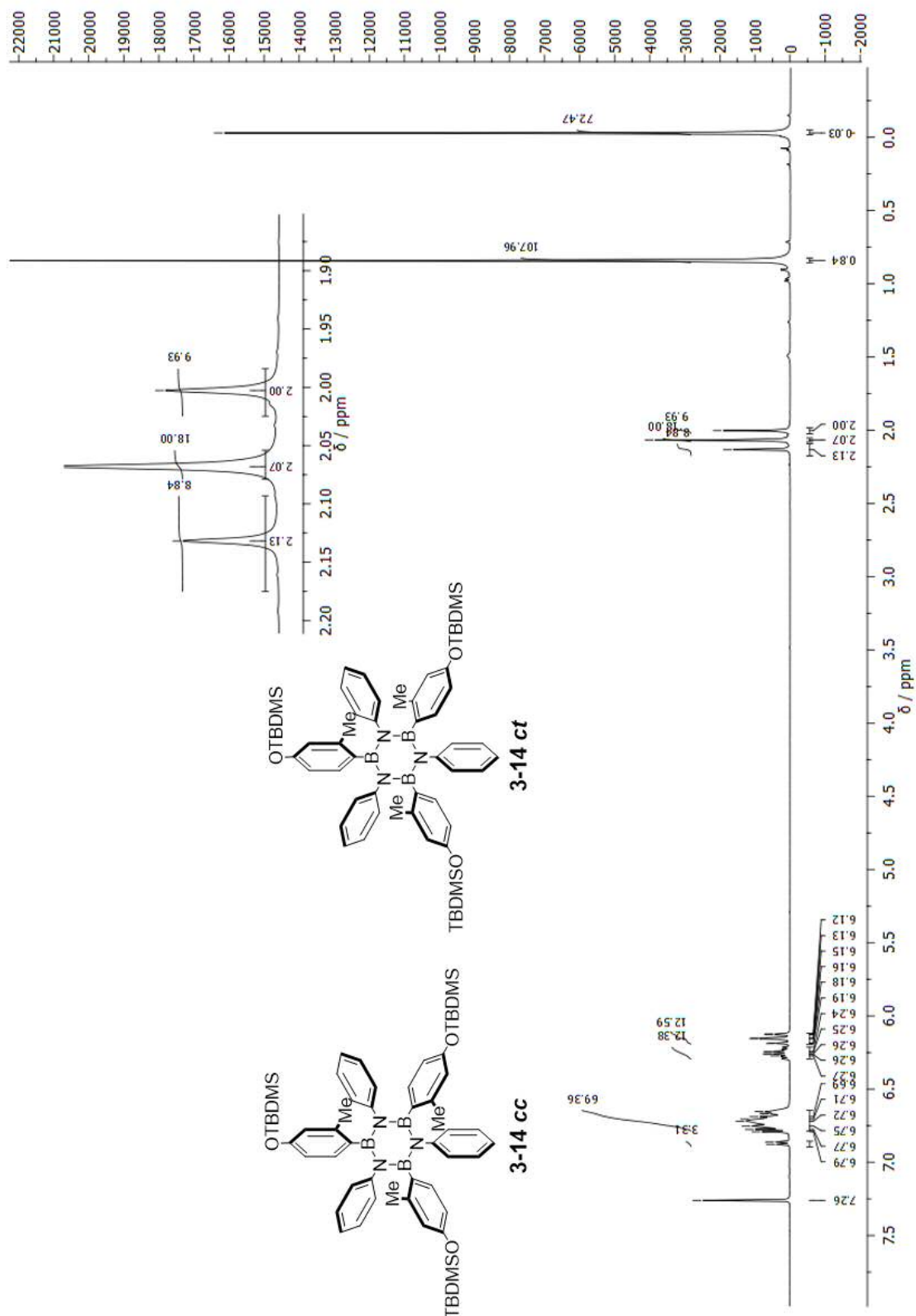


Figure A.114: ^{13}C -NMR, 400 MHz, CDCl_3 .

Characterisation of 3-5

Figure A.115: $^1\text{H-NMR}$, 400 MHz, CDCl_3 .

Characterisation of 3-14 *cc* + *ct*Figure A.116: $^1\text{H-NMR}$, 400 MHz, CDCl_3 .

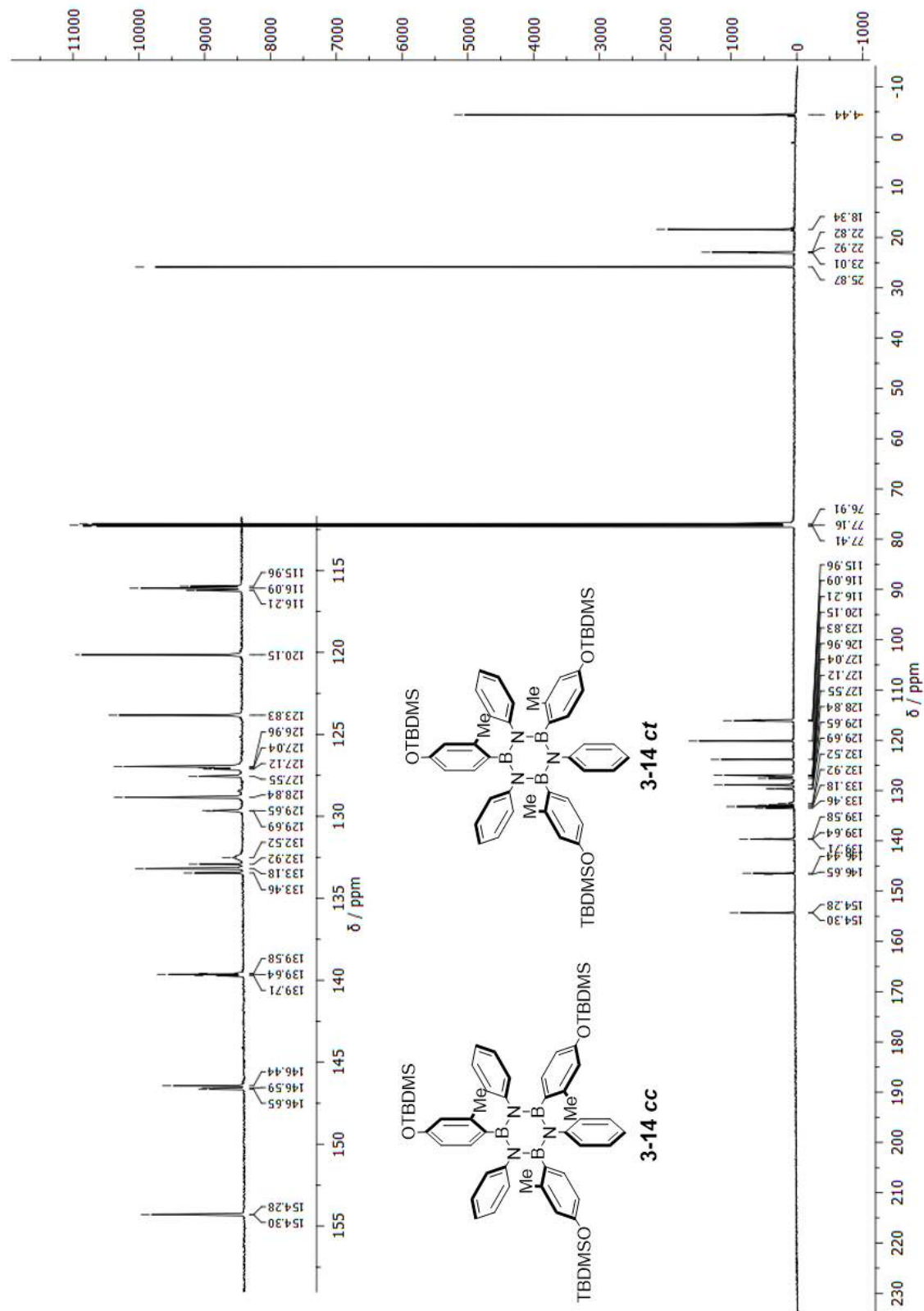
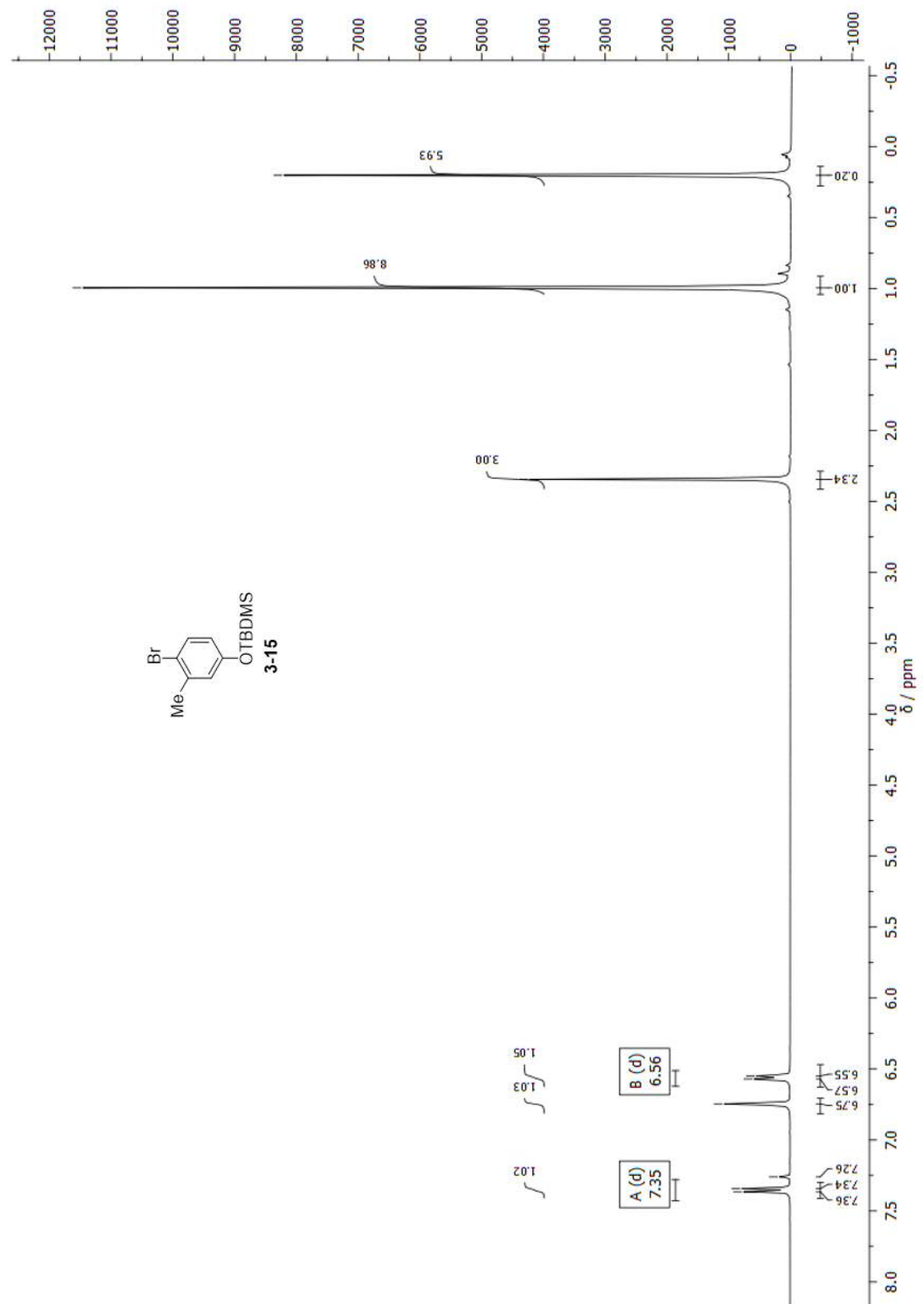


Figure A.117: ^{13}C -NMR, 400 MHz, CDCl_3 .

Characterisation of 3-15

Figure A.118: $^1\text{H-NMR}$, 400 MHz, CDCl_3 .

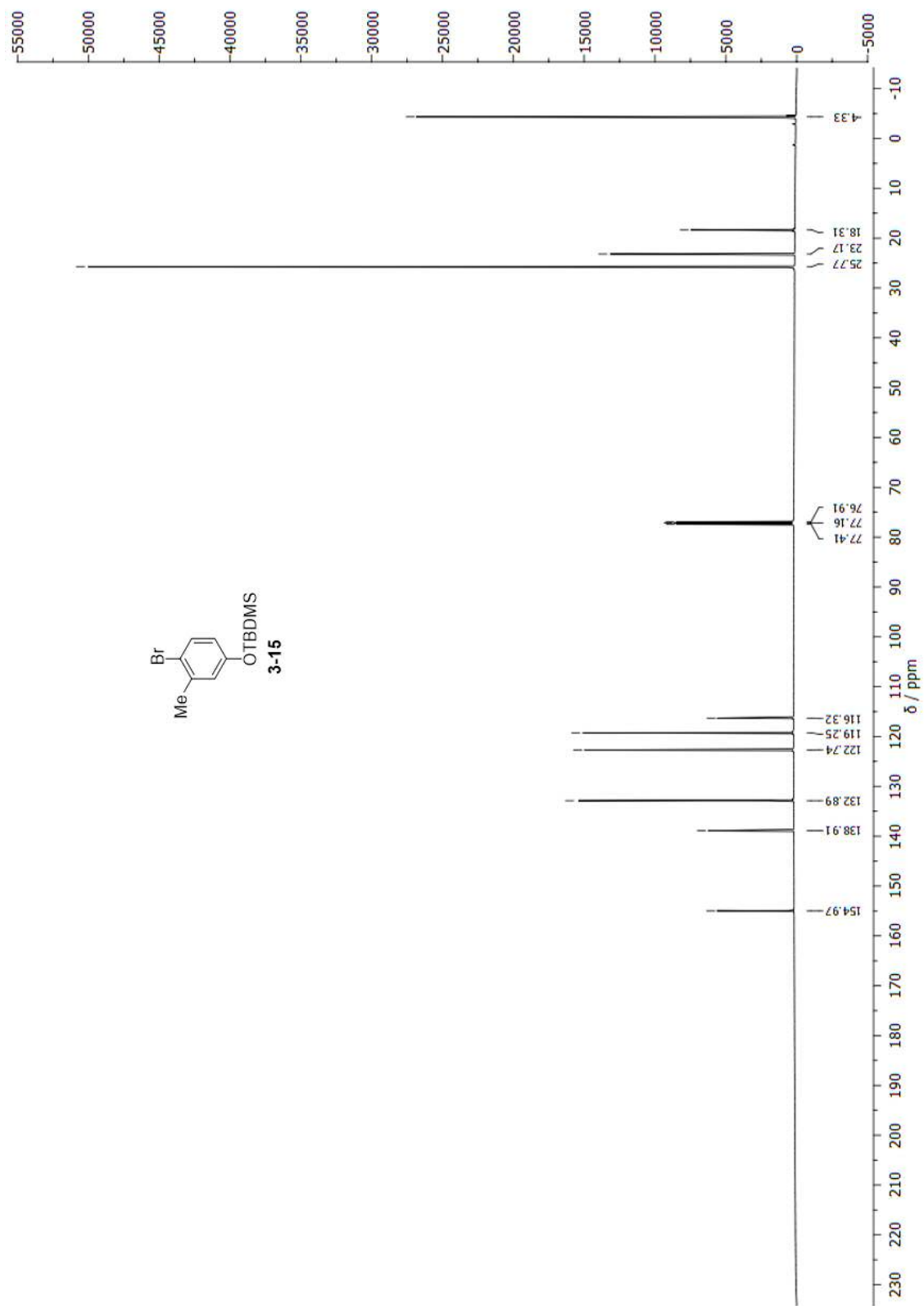
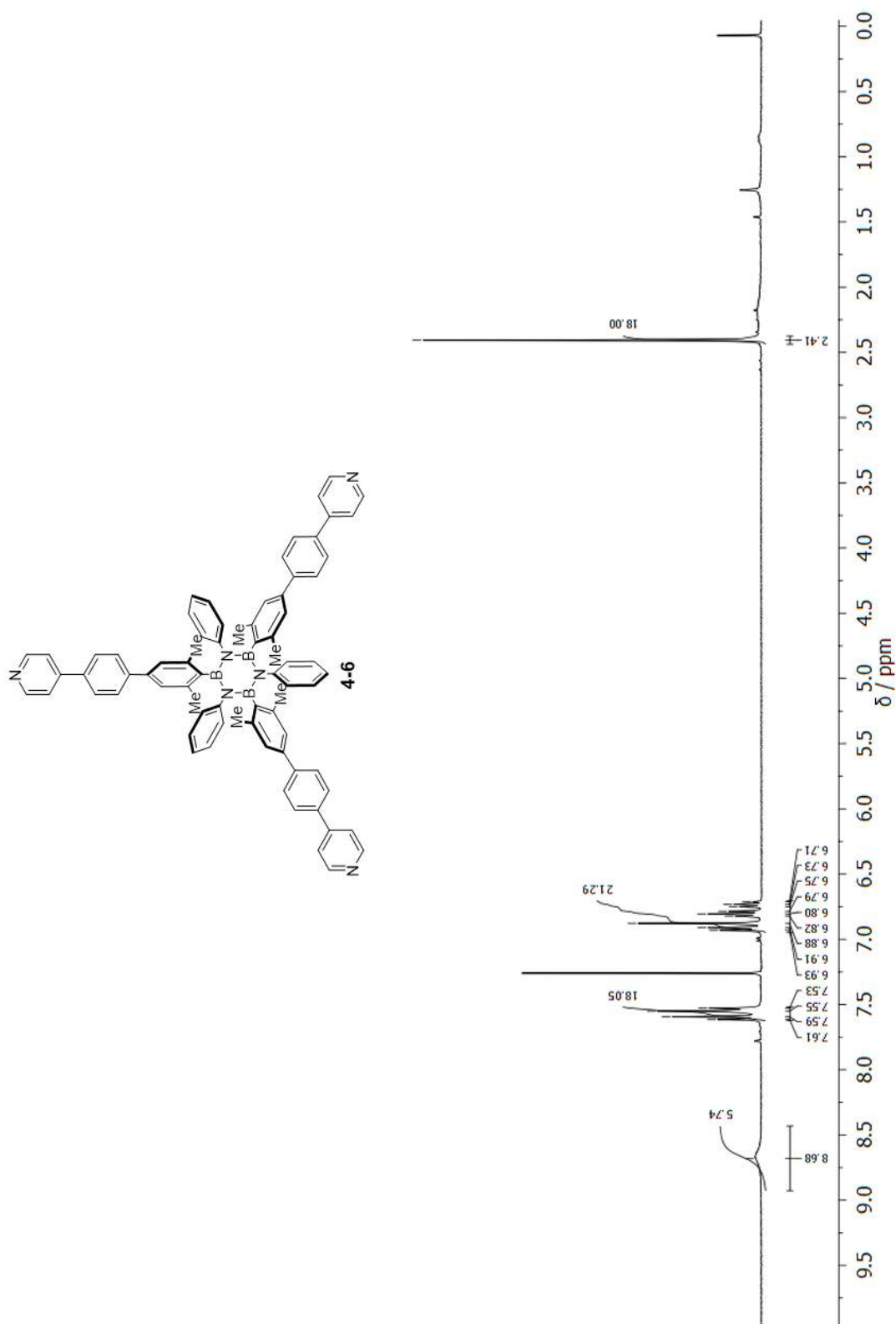


Figure A.119: ^{13}C -NMR, 400 MHz, CDCl_3 .

Characterisation of 4-6

**Figure A.120:** $^1\text{H-NMR}$, 400 MHz, CDCl_3 .

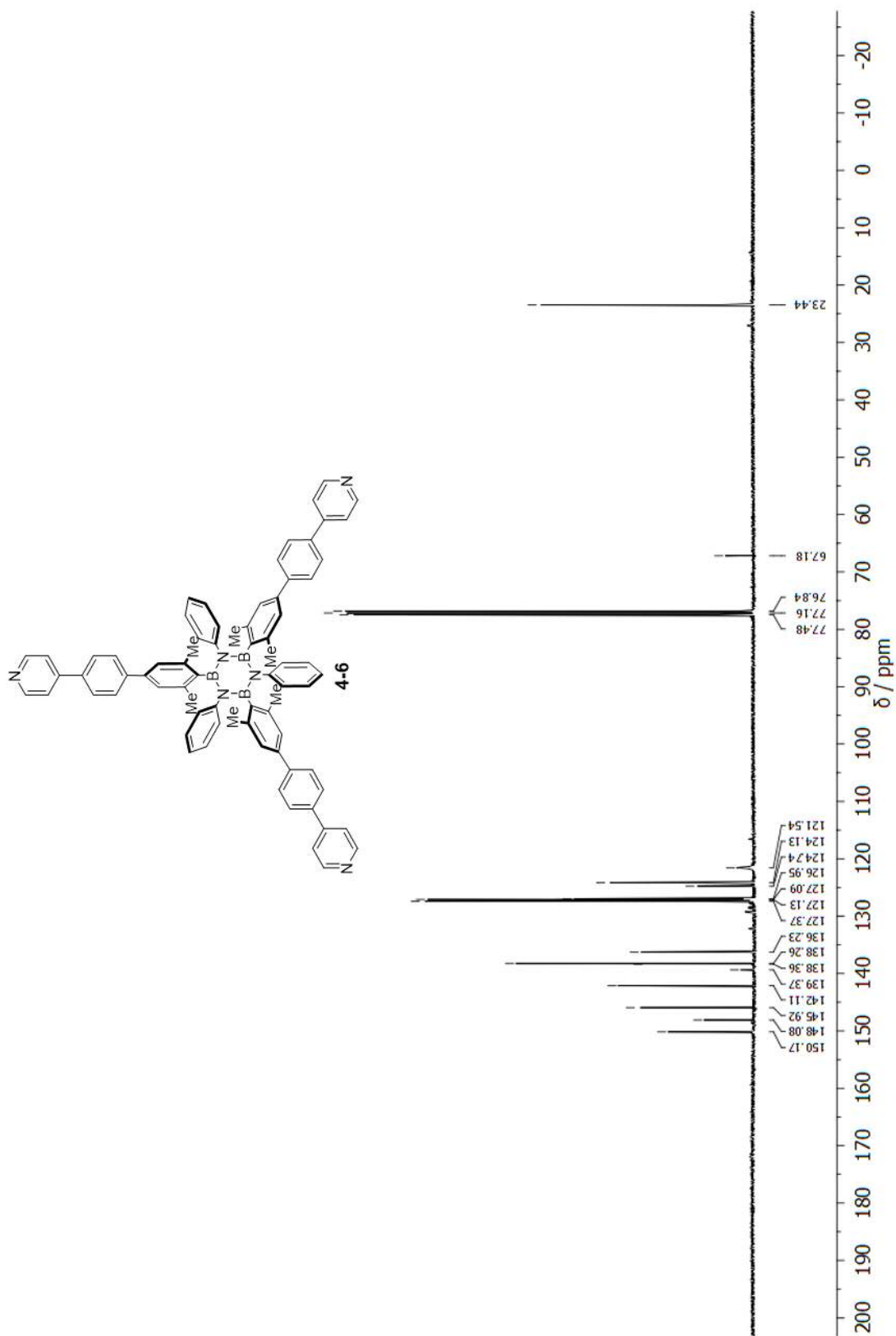


Figure A.121: ^{13}C -NMR, 100 MHz, CDCl_3 .

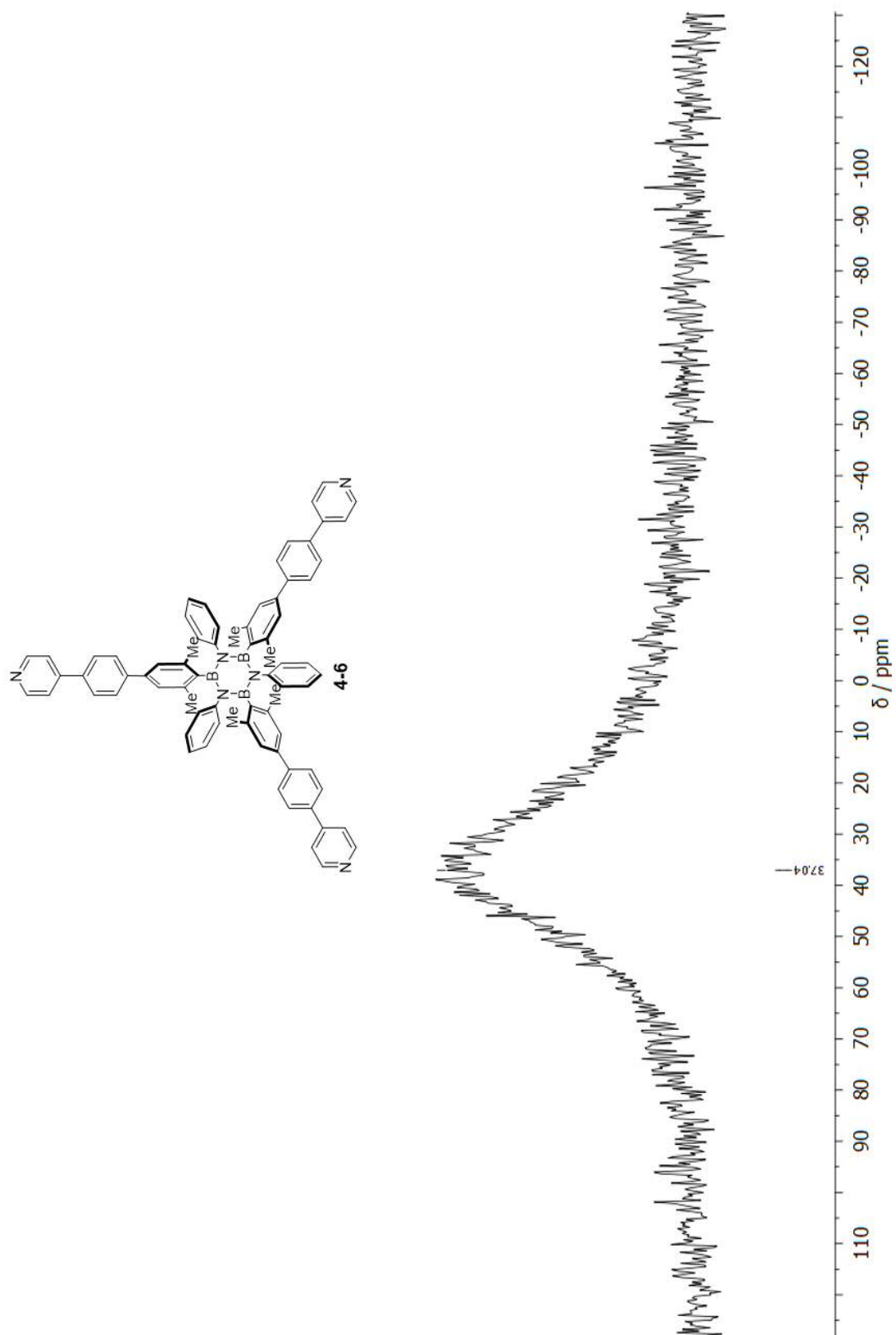
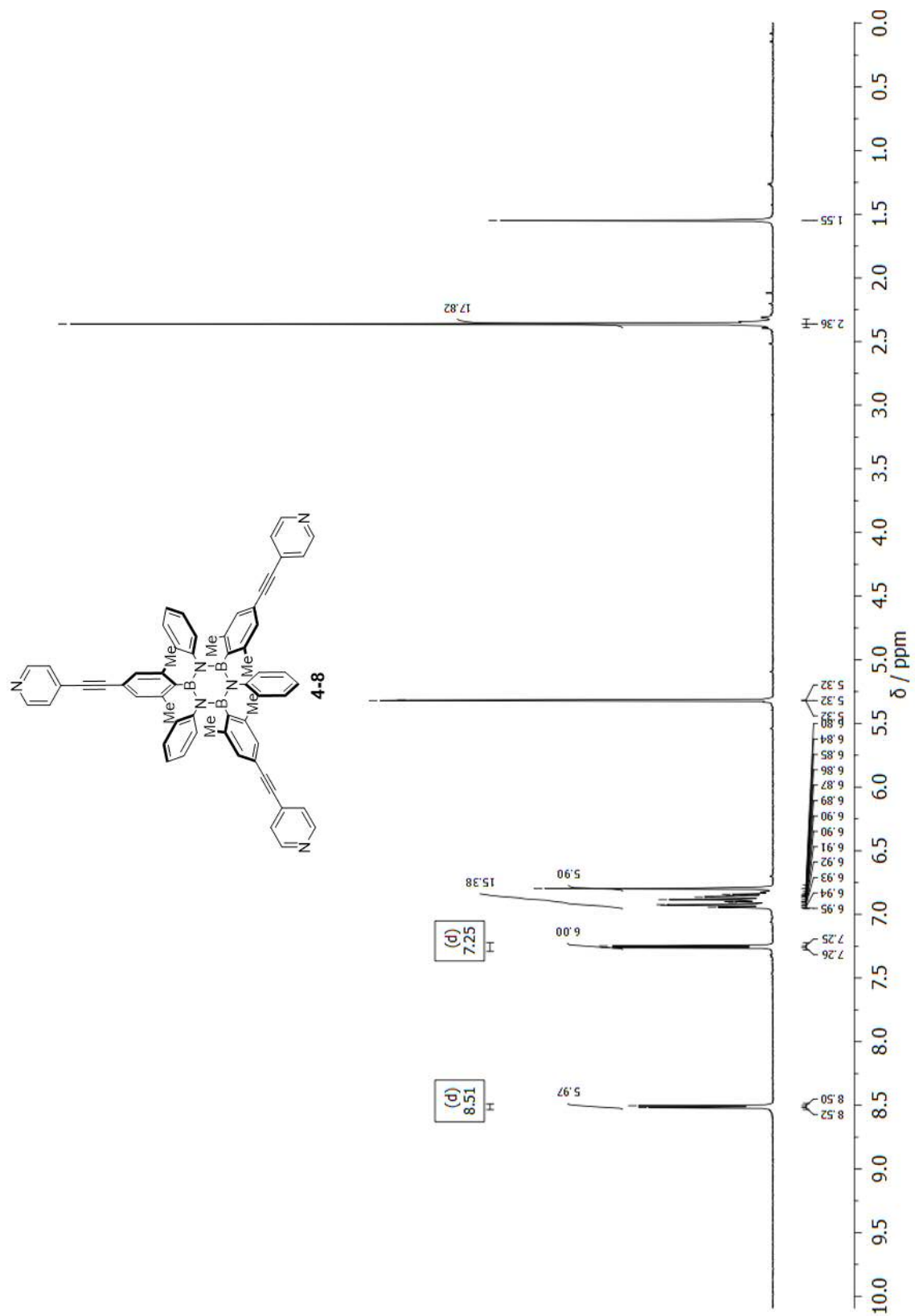


Figure A.122: ^{11}B -NMR, 128 MHz, CDCl_3 .

Characterisation of 4-8

Figure A.123: $^1\text{H-NMR}$, 400 MHz, CDCl_3 .

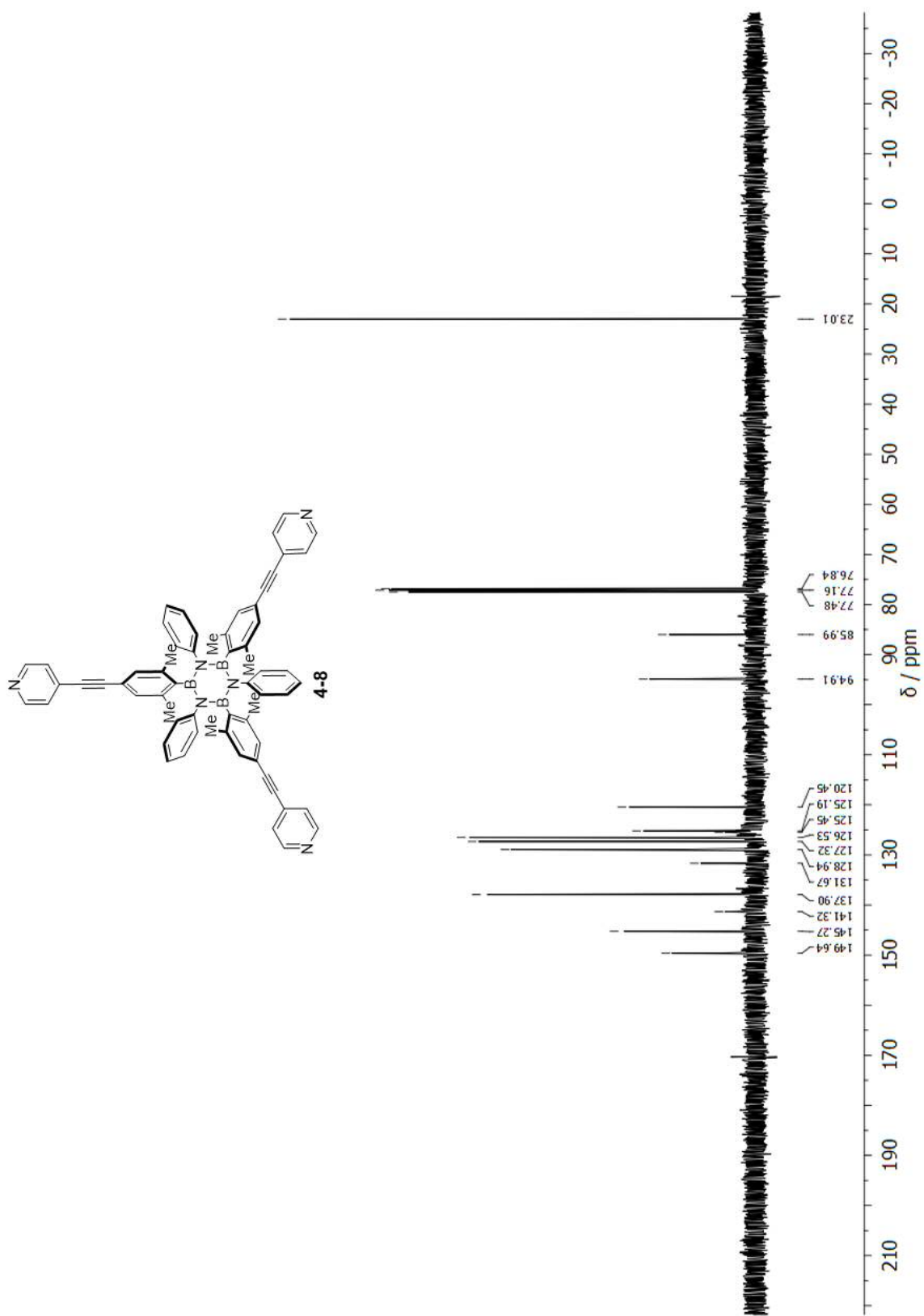


Figure A.124: ^{13}C -NMR, 100 MHz, CDCl_3 .

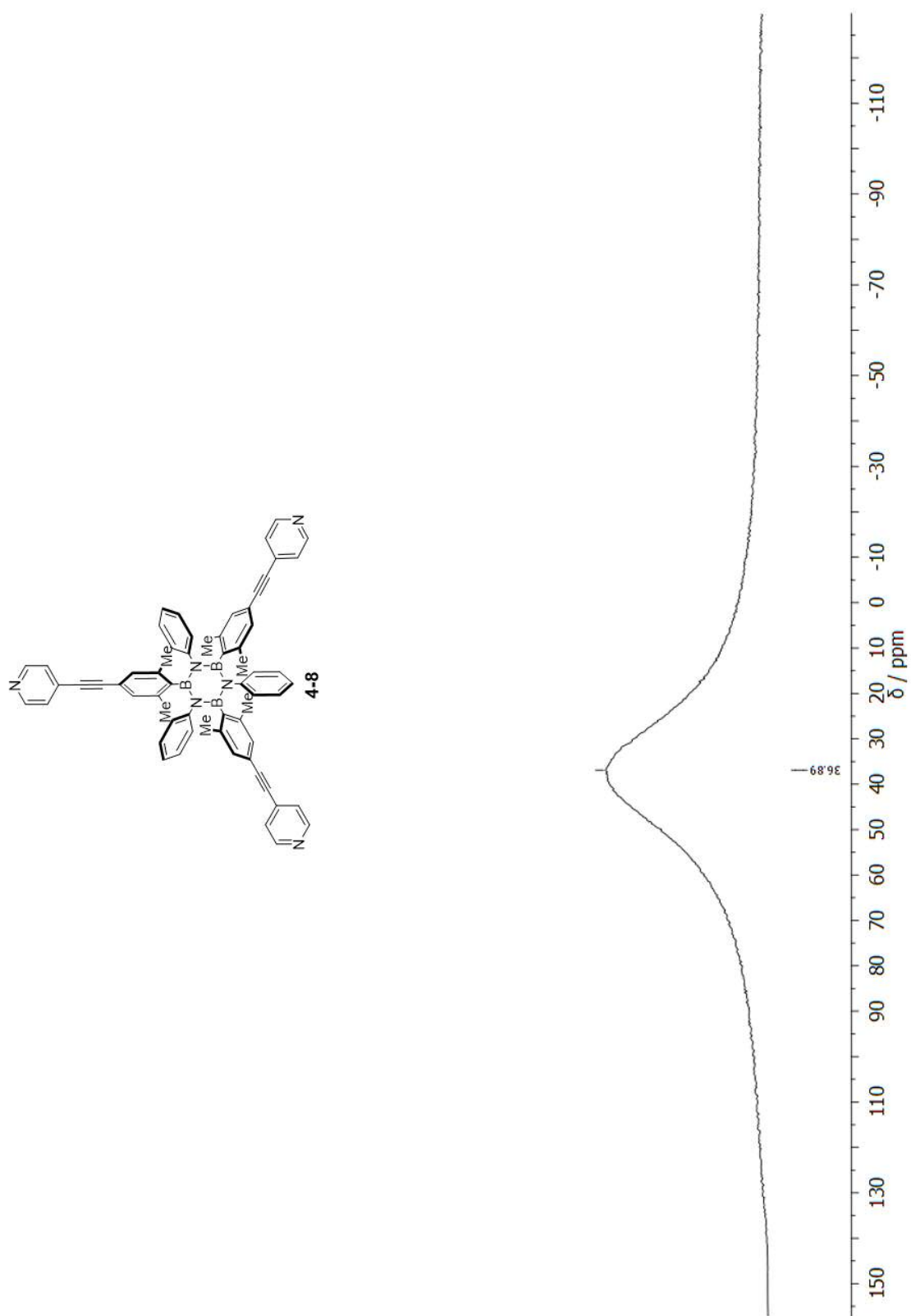


Figure A.125: ^{11}B -NMR, 128 MHz, CDCl_3 .